POLISH SOCIETY OF THEORETICAL AND APPLIED MECHANICS

JOURNAL OF THEORETICAL AND APPLIED MECHANICS

No. 3 • Vol 53

Quarterly

WARSAW, JULY 2015

JOURNAL OF THEORETICAL AND APPLIED MECHANICS
(until 1997 Mechanika Teoretyczna i Stosowana, ISSN 0079-3701)

Beginning with Vol 45, No. 1, 2007, *Journal of Theoretical and Applied Mechanics* (JTAM) has been selected for coverage in Thomson Reuters products and custom information services. Now it is indexed and abstracted in the following:

- **Science Citation Index Expanded** (also known as SciSearch®)
- **Journal Citation Reports/Science Edition**

* * * * *

Editorial Office

Building of Civil Engineering Warsaw University of Technology
Al. Armii Ludowej 16, room 650
00-637 Warszawa, Poland
phone (+48 22) 825 7180, e-mail: biuro@ptmts.org.pl

www.ptmts.org.pl/jtam.html

* * * * *

Publication supported by Ministry of Science and Higher Education of Poland

JOURNAL OF THEORETICAL AND APPLIED MECHANICS
53, 3, pp. 505-518, Warsaw 2015
DOI: 10.15632/jtam-pl.53.3.505

APPLICATION OF THE METHOD OF FUNDAMENTAL SOLUTIONS TO THE ANALYSIS OF FULLY DEVELOPED LAMINAR FLOW AND HEAT TRANSFER

Krzysztof Mrozek
Poznan University of Technology, Institute of Mechanical Technology, Poznań, Poland
e-mail: krzysztof.mrozek@put.poznan.pl

Magdalena Mierzwiczak
Poznan University of Technology, Institute of Applied Mechanics, Poznań, Poland
e-mail: magdalena.mierzwiczak@wp.pl

In this study, fully developed laminar flow and heat transfer in an internally longitudinally finned tube are investigated through application of the meshless method. The flow is assumed to be both hydrodynamically and thermally developed, with a uniform outside-the-wall temperature. The governing equations have been solved numerically by means of the method of fundamental solutions in combination with the method of particular solutions to obtain the velocity and temperature distributions. The advantage of the proposed approach is that it does not require mesh generation on the considered domain or its boundary, but uses only a cloud of arbitrarily located nodes. The results, comprising the friction factor as well as the Nusselt number, are presented for varied length values and fin numbers, as well as the thermal conductivity ratio between the tube and the flowing fluid. The results show that the heat transfer improves significantly if more fins are used.

Keywords: laminar flow, finned tube, heat transfer enhancement, method of fundamental solutions

1. Introduction

At present, many thermal engineering researchers are investigating new heat transfer enhancement methods between surfaces and the surrounding fluids. Heat transfer enhancement is of particular importance to the intensification of cooling of injection molds working in a cycle of dynamic temperature changes and equipped with cooling inserts. The aforesaid injections are the most important facet of the plastic injection molding process and affect the shape, aesthetics, technical properties and utility of compacts (Benitez-Rangel *et al.*, 2010). One of the major problems encountered during the injection process is to ensure the most efficient and uniform heat transfer from the cooled material so as to avoid generation of excessive stress causing deformation of the molds. It should be emphasized that the cooling process can make up to 70% of the time cycle, and is one of the most important stages of the injection process. So far, the most common method of heat removal through application of cooling channels relies on conventional drilling. In order to improve the cooling efficiency, we propose the use of a finned cooling channel whose main task is to increase the active surface area of the heat exchange between the injection mold and the cooling fluid.

A comprehensive report on recent advances in heat transfer enhancements was presented by Siddique *et al.* (2010), while the classification of heat transfer enhancement techniques was documented by Bergles (1998). The mechanisms of enhancing heat transfer that require external power, dubbed active methods, comprise, for example, application of stirring in the fluid vessels or surface vibration, as presented by Nesis *et al.* (1994). The passive enhancement methods are

those that do not require external power to sustain enhancement characteristics and rely on the use of: treated surfaces, rough surfaces, extended surfaces, displaced enhancement devices, swirl flow devices, coiled tubes, surface tension devices, additives for fluids and many others.

Most of the heat transfer augmentation methods presented in the literature employ fins. Laminar flow heat transfer in internally finned tubes is of particular importance in many engineering industries relying on the heating or cooling of viscous liquids or oils, and specifically including heating of the circulating fluid in solar collectors and heat transfer in heat exchangers. Internally finned tubes are commonly used in engineering applications as efficient means to improve convective heat transfer while maintaining a small size and low weight. To provide additional heat transfer surfaces, various types of internal fins are utilized. However, when an array of fins is used to enhance heat transfer, the presence of fins may increase the pressure drop in the tube and reduce the mass flow rate. For this reason, the prime engineering focus is to optimize the geometry of fins that will maximize the heat transfer rate under space and cost constraints.

Extensive work has been carried out by different researchers, e.g., Rout *et al.* (2012), to analyze a laminar heat exchanger with fins of various shapes and sizes. Experimental investigations show that the heat transfer characteristics and flow friction are greatly influenced by the fin spacing, size, and shape. Soliman and Feingold (1977) obtained an analytical solution for a fully developed laminar flow, encompassing an extensive range of fin parameters (varying height, width and number). The resulting equation of velocity distribution was rendered in the form of infinite series involving arbitrary constants evaluated by equating the velocity and its radial derivative at the boundary. In contrast, Soliman *et al.* (1980) presented numerical analysis of the momentum and energy equations using a finite difference approach. Along with dimensionless velocity, the authors determined the temperature field and defined the Nusselt number. Furthermore, the fully developed laminar flow and convective heat transfer in an internally finned tube heat exchanger were investigated numerically through application of an explicit finite-difference scheme by Tien *et al.* (2012). The authors conducted additional experiments in a closed-loop device to verify the numerical results. So far, the laminar flow heat transfer problem has mostly been resolved through utilization of the Finite Difference Method (FDM) providing the solution in a discrete form; both, the differential equation and the boundary conditions are fulfilled only in an approximate manner. The meshless Method of Fundamental Solutions (MFS) is free of the disadvantages of the above mentioned method. In MFS, the approximated solution is conveniently rendered as a continuous function with continuous derivatives. In this method, the governing equation is fulfilled exactly and the approximation lies in the fulfillment of the boundary conditions. For the homogenous differential problem of the maximum principle, the maximum error is achieved on the boundary and can be controlled by the appropriate value of the method parameters. The foundations of this dynamically developed meshless procedure were given in the 1960s by Kupradze and Aleksidze (1964). However, the modern, computerized version of the method was proposed a decade later by Mathon and Johnston (1977). The research conducted since then, and presented by Chen *et al.* (2008), allowed expanding its scope and successful application in solving the inhomogeneous differential equations, nonlinear problems, transient problems, or inverse problems. In recent years, it has become increasingly popular due to its simplicity of implementation. In such cases, the solution is approximated by linear combinations of fundamental solutions with singularities placed on a fictitious boundary lying outside the considered domain. MFS was successfully applied to resolve the potential flow problems by Johnston and Fairweather (1984), the Helmholtz problems by Tsai *et al.* (2009), the biharmonic equation by Karageorghis and Fairweather (1987), the elliptic boundary value problems by Karageorghis and Fairweather (1998), the Poisson equation by Golberg (1995), the Stokes flow problems by Alves and Silvestre (2004), and the elasticity problems by Tsai (2007). A comprehensive review of MFS was presented by Golberg and Chen (1999).

This study considers two-dimensional heat conduction through fins with a fixed volume. Both, the velocity and temperature field values are determined by means of MFS and the Method of Particular Solutions (MPS). For the velocity field, the analytical solution could be obtained with a defined and acceptable accuracy. In contrast, the temperature field problem is tackled iteratively, using the Radial Basis Function (RBF) and monomials to determine the particular solution, and MFS to work out the homogenous solutions of each iterative step. It is assumed that both, the fins and the fluid flow, are subjected to constant wall temperature conditions. The parameters of thickness, length, and number of fins as well as the thermal conductivity ratio of the fin to the working fluid are varied to obtain the friction factor as well as the Nusselt number values in the internally finned tube.

2. Analytical formulation

Figure 1 shows the cross section of the internally finned tube considered in this paper. A variable number of straight fins are evenly distributed around the circumference of the tube. Due to geometric symmetry of the flow domain, as shown in Fig. 1, the solution to the governing equations is sought only for a half of the region between the center lines of two consecutive fins Ω_f^*; i.e. between $\theta = 0$ and $\theta = \gamma$.

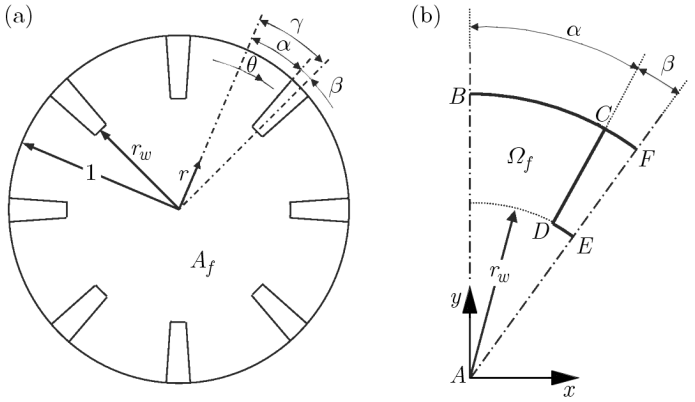

Fig. 1. Geometry of (a) the cross section of the tube and (b) a circular repeated part of the tube

2.1. Determination of velocity

This analysis is applicable to a steady, laminar, and fully developed flow with a uniform outside-the-wall temperature. Moreover, it is assumed that the fluid is Newtonian and has uniform properties, and the viscous dissipation within the fluid is neglected. On these assumptions, the momentum equation is reduced to

$$\nabla^2 w^* = \frac{1}{\mu}\frac{dp}{dz} \qquad \text{in} \quad (x^*, y^*) \in \Omega_f^* \tag{2.1}$$

where w^* is the velocity along the tube; μ – dynamic viscosity; dp/dz – gradient of pressure in the direction z. Using dimensionless variables, $r = r^*/r_0^*$, $x = x^*/r_0^*$, $y = y^*/r_0^*$, $w = w^*/[-(1/\mu)(dp/dz)r_0^*]$, where r_0^* is the inner radius of the tube, equation (2.1) can be written in a dimensionless form as

$$\nabla^2 w = -1 \qquad \text{in} \quad (x, y) \in \Omega_f \tag{2.2}$$

The boundary condition assumes the following form

$$w = 0 \qquad \text{on} \quad (x, y) \in (\overline{BC} \cup \overline{CD} \cup \overline{DE}) \tag{2.3}$$

and

$$\frac{\partial w}{\partial n} = 0 \qquad \text{on} \quad (x,y) \in (\overline{AB} \cup \overline{EA}) \tag{2.4}$$

and the dimensionless bulk velocity is obtained from the equation

$$w_b = \frac{1}{A_f} \int\limits_{A_f} w \, dA_f \tag{2.5}$$

where $A_f = A_f^*/r_0^{*2}$ is the dimensionless flow area of the tube; $A_f^* = \pi * r_0^{*2} - M\beta(r_0^{*2} - r_w^{*2})$ – the total flow area; M – number of fins in the tube; β – half of the angle subtended by one fin; $r_w = r_w^*/r_0^*$ – dimensionless radial coordinate at the tip of the fin, $L = L^*/r_0^*$ – dimensionless fin height, L^* – fin height.

The friction factor and the Reynolds number are defined as

$$f = \frac{\pi^2 \rho r_0^{*5}}{\dot{m}^2}\Big(-\frac{dp}{dz}\Big) \qquad \mathrm{Re} = \frac{2\dot{m}}{\pi r_0^* \mu} \tag{2.6}$$

where $\dot{m} = \rho A_f^* w_b^*$ is the mass flow rate of the fluid; ρ – density of the fluid.

The product $f\mathrm{Re}$ can be expressed in the dimensionless form

$$f\mathrm{Re} = \frac{\pi}{A_f}\frac{2}{w_b} \tag{2.7}$$

2.2. Determination of temperature

For a fully developed temperature profile, the dimensionless temperature $(T_w - T)/(T_w - T_b)$, where T is the fluid temperature, T_b is the bulk mean temperature, and T_w is the tube-wall temperature, does not depend on z, that is

$$\frac{\partial}{\partial z}\Big(\frac{T_w - T}{T_w - T_b}\Big) = 0 \tag{2.8}$$

After some mathematical manipulations, (2.8) gives

$$\frac{\partial T}{\partial z} = \frac{dT_w}{dz} - \frac{T_w - T}{T_w - T_b}\frac{dT_w}{dz} + \frac{T_w - T}{T_w - T_b}\frac{dT_b}{dz} \tag{2.9}$$

Considering the constant-wall-temperature boundary condition, $dT_w/dz = 0$, equation (2.9) can be reduced to

$$\frac{\partial T}{\partial z} = \frac{T_w - T}{T_w - T_b}\frac{dT_b}{dz} \tag{2.10}$$

If the flow is thermally developed and there is no axial conduction, the energy equation for the fluid flow takes the following form

$$k_f \nabla^2 T = \rho C_p w^* \frac{\partial T}{\partial z} \qquad \text{in} \quad (x^*, y^*) \in \Omega_f^* \tag{2.11}$$

where k_f is the thermal conductivity of the fluid; C_p – specific heat at constant pressure.

Introducing the dimensionless temperature of the fluid, $\Theta(x,y) = (T - T_w)/[q_w(z) r_0^*/k_f]$, where $q_w = Q/(2\pi r_0^*)$ is the average heat flux at outer tube wall; Q – total heat transfer rate at the solid-fluid interface, and employing (2.7) and (2.10) into equation (2.11), yields

$$\nabla^2 \Theta = \frac{\dot{m} C_p}{2\pi q_w r_0^*} f\mathrm{Re} w \frac{\Theta}{\Theta_b}\frac{dT_b}{dz} \tag{2.12}$$

For the energy balance of a small element Δz in the axial direction of the tube, one obtains

$$q_w(2\pi r_0^*)\Delta z = \dot{m}C_p\Big(T_b\Big|_{z+\Delta z} - T_b\Big|_z\Big) \tag{2.13}$$

As Δz approaches zero, (2.13) can be simplified to

$$\frac{dT_b}{dz} = \frac{q_w 2\pi r_0^*}{\dot{m}C_p} \tag{2.14}$$

Substituting (2.14) into (2.12) gives

$$\nabla^2\Theta = f\mathrm{Re}w\frac{\Theta}{\Theta_b} \qquad \text{in} \quad (x,y) \in \Omega_f \tag{2.15}$$

and for the solid fin, the dimensionless energy equation becomes

$$\nabla^2\Theta_s = 0 \qquad \text{in} \quad (x,y) \in \Omega_s \tag{2.16}$$

The dimensionless boundary conditions for the fluid and the fin are

$$\begin{aligned} &\frac{\partial\Theta}{\partial n} = 0 \qquad \text{in} \quad (x,y) \in (\overline{AB} \cup \overline{EA}) \\ &\frac{\partial\Theta}{\partial n} = k\frac{\partial\Theta_s}{\partial n} \quad \wedge \quad \Theta = \Theta_s \in (x,y) \in (\overline{CD} \cup \overline{DE}) \end{aligned} \tag{2.17}$$

and

$$\begin{aligned} &\frac{\partial\Theta_s}{\partial n} = 0 \qquad \text{in} \quad (x,y) \in \overline{EF} \\ &\Theta_s = 0 \qquad \text{in} \quad (x,y) \in \overline{FB} \\ &\Theta = 0 \qquad \text{in} \quad (x,y) \in \overline{BC} \end{aligned} \tag{2.18}$$

where $k = \beta k_s/k_f$ represents the ratio of thermal conductivity of the fin to the fluid, and k_s is the thermal conductivity of the fin.

The dimensionless bulk mean temperature Θ_b and the Nusselt number Nu for the flow are derived as

$$\Theta_b = \frac{\int\limits_{A_f} w(x,y)\Theta(x,y)\,dA_f}{\int\limits_{A_f} w(x,y)\,dA_f} \qquad \mathrm{Nu} = \frac{2r_0^* q_w(z)}{k_f(T_w - T_b)} = -\frac{2}{\Theta_b} \tag{2.19}$$

3. Numerical solution procedure

To solve the boundary value problem for the velocity (2.2)-(2.4) and for the temperature (2.15)-(2.18), we propose to use the MFS.

The particular solution to (2.2) has the following form

$$w^p = -\frac{1}{4}(x^2 + y^2) \tag{3.1}$$

and for the MFS, the homogenous solution can be represented as

$$w^h = \sum_{n=1}^{N} c_n \ln r_n^2 \tag{3.2}$$

where $r_n = \sqrt{(x-\widetilde{x}_n)^2 + (y-\widetilde{y}_n)^2}$ and $\{(\widetilde{x}_n, \widetilde{y}_n)\}_{n=1}^{N}$ are the coordinates of source points placed outside the considered region on a fictitious contour at a distance s from the boundary (see Fig. 2). The unknown coefficients $\{c_n\}_{n=1}^{N}$ are obtained through fulfilling boundary conditions (2.3) and (2.4) in the collocation points $\{(x_i, y_i)\}_{i=1}^{Mc}$

$$\begin{aligned} &\sum_{n=1}^{N} c_n \ln\Big((x_i-\widetilde{x}_n)^2 + (y_i-\widetilde{y}_n)^2\Big) = \frac{1}{4}(x_i^2+y_i^2) \qquad \text{on} \quad (x_i,y_i) \in (\overline{BC} \cup \overline{CD} \cup \overline{DE}) \\ &\sum_{n=1}^{N} c_n \frac{\partial}{\partial n} \ln\Big((x_i-\widetilde{x}_n)^2 + (y_i-\widetilde{y}_n)^2\Big) = \frac{1}{2}(nxx_i + nyy_i) \qquad \text{on} \quad (x_i,y_i) \in (\overline{AB} \cup \overline{EA}) \end{aligned} \tag{3.3}$$

where $n = [nx, ny]$ is the unit outward normal vector at the boundary.

If the number of collocation points Mc is equal to the number of unknown coefficients, $\{c_n\}_{n=1}^{N} Mc = N$, the system of algebraic equations (3.3) can be solved by the Gaussian elimination method. Otherwise, if $Mc > N$, system (3.3) is overdetermined and is solved through application of the least squares approach.

The dimensionless velocity profile can be expressed as

$$w = \sum_{n=1}^{N} c_n \ln r_n^2 - \frac{1}{4}(x^2+y^2) \tag{3.4}$$

Similarly, the solution to (2.16) can be written as a linear combination of fundamental solutions for the Laplace operator

$$\Theta_s(x,y) = \sum_{n=1}^{Nd} d_n \ln r_{dn} \tag{3.5}$$

where $r_{dn} = \sqrt{(x-\widetilde{x}_{dn})^2 + (y-\widetilde{y}_{dn})^2}$ and $\{(\widetilde{x}_{dn}, \widetilde{y}_{dn})\Big\}_{n=1}^{Nd}$ are source points located around the fin area.

The homogenous solution to (2.15) can be written as

$$\Theta^h(x,y) = \sum_{n=1}^{Nf} f_n \ln r_{f_n} \tag{3.6}$$

where $r_{fn} = \sqrt{(x-\widetilde{x}_{fn})^2 + (y-\widetilde{y}_{fn})^2}$ and $\{(\widetilde{x}_{fn}, \widetilde{y}_{fn})\Big\}_{n=1}^{Nf}$ are source points located around the fluid area.

To obtain the particular solution to (2.15), we propose the use of RBF and monomials. The solution can be expressed as

$$\Theta^p(x,y) = \sum_{m=1}^{Mi} a_m \psi(r_m) + \sum_{j=1}^{K} b_j q_j(x,y) \tag{3.7}$$

where $r_m = \sqrt{(x-\widehat{x}_m)^2 + (y-\widehat{y}_m)^2}$ and $\{(\widehat{x}_m, \widehat{y}_m)\}_{m=1}^{Mi}$ are interpolation points located in the fluid area, $\psi(r_m)$ is the particular solution of the RBS $\varphi(r_m)$ for the Laplace operator, and $q_j(x,y)$ is the particular solution of the monomials $p_j(x,y)$ for the Laplace operator

$$\begin{aligned} &\nabla^2 \psi(r_m) = \varphi(r_m) \qquad m = 1, \ldots, Mi \\ &\nabla^2 q_j(x,y) = p_j(x,y) \qquad j = 1, \ldots, K \end{aligned} \tag{3.8}$$

The coefficients $\{a_m\}_{m=1}^{Mi}$ and $\{b_j\}_{j=1}^{K}$ are calculated by interpolation of the right hand side of equation (2.15)

$$\begin{aligned}
&\sum_{m=1}^{Mi} a_m \varphi(r_{mi}) + \sum_{j=1}^{K} b_j p_j(\widehat{x}_i, \widehat{y}_i) = f\mathrm{Re} w(\widehat{x}_i, \widehat{y}_i)\frac{\Theta(\widehat{x}_i, \widehat{y}_i)}{\Theta_b} \qquad i = 1, \ldots, Mi \\
&\sum_{m=1}^{M} a_m p_j(\widehat{x}_m, \widehat{y}_m) = 0 \qquad j = 1, \ldots, K
\end{aligned} \tag{3.9}$$

The coefficients $\{d_n\}_{n=1}^{Nd}$ and $\{f_n\}_{n=1}^{Nf}$ are obtained through fulfilling the boundary conditions (2.17) and (2.18) in the collocation points

$$\begin{aligned}
&\sum_{n=1}^{Nf} f_n \frac{\partial \ln r_{f_{ni}}}{\partial n} = -\sum_{m=1}^{Mi} a_m \frac{\partial \psi(r_{mi})}{\partial n} - \sum_{j=1}^{K} b_j \frac{\partial q_j(x_i, y_i)}{\partial n} \\
&\quad \{(x_i, y_i)\}_{i=1}^{M1+M5} \in (\overline{AB} \cup \overline{EA}) \\
&\sum_{n=1}^{Nf} f_n \ln r_{f_{ni}} = -\sum_{m=1}^{Mi} a_m \psi(r_{mi}) - \sum_{j=1}^{K} b_j q_j(x_i, y_i) \qquad \{(x_i, y_i)\}_{i=1}^{M2} \in \overline{BC} \\
&\sum_{n=1}^{Nf} f_n \frac{\partial \ln r_{f_{ni}}}{\partial n} + \sum_{n=1}^{Nd} d_n \frac{\partial \ln r_{d_{ni}}}{\partial n} = -\sum_{m=1}^{Mi} a_m \frac{\partial \psi(r_{mi})}{\partial n} - \sum_{j=1}^{K} b_j \frac{\partial q_j(x_i, y_i)}{\partial n} \\
&\quad \{(x_i, y_i)\}_{i=1}^{M3+M4} \in (\overline{CD} \cup \overline{DE}) \\
&\sum_{n=1}^{Nf} f_n \ln r_{f_{ni}} + \sum_{n=1}^{Nd} d_n \ln r_{d_{ni}} = -\sum_{m=1}^{Mi} a_m \psi(r_{mi}) - \sum_{j=1}^{K} b_j q_j(x_i, y_i) \\
&\quad \{(x_i, y_i)\}_{i=1}^{M3+M4} \in (\overline{CD} \cup \overline{DE}) \\
&\sum_{n=1}^{Nd} d_n \frac{\partial \ln r_{d_{ni}}}{\partial n} = 0 \qquad \{(x_i, y_i)\}_{i=1}^{M3} \in \overline{EF} \\
&\sum_{n=1}^{Nd} d_n \ln r_{d_{ni}} = 0 \qquad \{(x_i, y_i)\}_{i=1}^{M4} \in \overline{CF}
\end{aligned} \tag{3.10}$$

The solution to (2.15) can be written as a sum

$$\Theta(x, y) = \sum_{n=1}^{Nf} f_n \ln r_{f_n} + \sum_{m=1}^{Mi} a_m \psi(r_m) + \sum_{j=1}^{K} b_j q_j(x, y) \tag{3.11}$$

Since the right hand side of governing equation (2.15) depends on the temperature $\Theta(x, y)$ as well as the bulk temperature value Θ_b, we developed the following iterative procedure ascertaining its successful solution. First, we assumed uniform temperature conditions throughout the area $\Theta/\Theta_b = 1$. The results are substituted into the right hand side of equation (2.15), which is then numerically solved for new values of Θ. Based on these, a new value Θ_b is calculated and all results are again substituted into the right hand side of equation (2.15). The calculations are repeated until the values of Θ converge to acceptable tolerance values and carried out in accordance with the presented algorithm.

Step 0 Input of the data M, β, k, and r_w

Step 1 Determination of the optimal parameter s characterized by the smallest error of the boundary value of temperature

Step 2 Determination of the velocity value (2.2)-(2.4) by MFS (3.1)-(3.4)

Step 3 Computation of the bulk velocity w_b, (2.5), and the product $f\mathrm{Re}$, (2.7)

Step 4 Assumption that $\Theta^0/\Theta_b^0 = 1$, $i = 1$

Step 5 Solution of interpolation problem (2.15) by RBF and monomials (3.9)

Step 6 Determination of temperature (2.15)-(2.18) by MFS (3.10) and (3.11)

Step 7 Calculation of the bulk mean temperature Θ_b^i, $(2.19)_1$, and the Nusselt number, $(2.19)_2$

Step 8 Convergence verification:

if $\delta\Theta = \|\Theta^i - \Theta^{i-1}\| \leqslant tol$ STOP,

else, take $i = i + 1$ and go to **Step 5**

4. Results and discussion

In numerical experiments, as in those employing RBF, we use the thin-plate spline function

$$\varphi(r_m) = r_m^2 \ln r_m \tag{4.1}$$

for which the particular solution for the Laplace operator has the form

$$\psi(r_m) = \frac{r_m^4 \ln r_m}{16} - \frac{r_m^4}{32} \tag{4.2}$$

and six monomials presented in Table 1.

Table 1. Monomial functions and their particular solutions

j	$p_j(x,y)$	$q_j(x,y)$
1	1	$(x^2+y^2)/4$
2	x	$x(x^2+y^2)/8$
3	y	$y(x^2+y^2)/8$
4	xy	$xy(x^2+y^2)/12$
5	x^2	$\left(x^4 + x^2y^2 - \frac{y^4}{6}\right)/14$
6	y^2	$\left(y^4 + x^2y^2 - \frac{x^4}{6}\right)/14$

An example of the distribution of collocation, the source and the interpolation points for the fluid area Ω_f and for the fin area Ω_s is shown in Fig. 2.

We calculate the number of the collocation and source points by means of the following formulas

$$\begin{aligned} M_1 &= 111 & N_1 &= M_1/3 \\ M_2 &= 4\alpha/\gamma M_1/M + 1 & N_2 &= (N_2 + N_4)/3 \\ M_3 &= M_1(1 - r_w) + 1 & N_3 &= M_3/3 \\ M_4 &= 4\beta/\gamma M_1/M + 1 & N_4 &= M_4/2 \\ M_5 &= M_1 r_w + 1 \end{aligned} \tag{4.3}$$

To interpolate the right side function in (2.15), 378 evenly located points in the considered fluid area $(\widehat{x}, \widehat{y}) \in \Omega_f$ are used. The parameter s proved to have a substantial impact on the

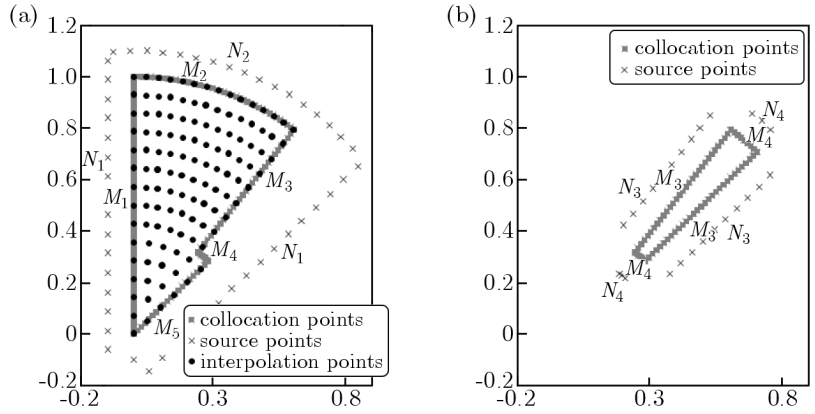

Fig. 2. Exemplary distribution of ■ Mc – collocation, × N – source, and • Mi – interpolation points (a) in the fluid area and (b) in the solid fin area

accuracy of the presented method. Therefore, at the beginning of the calculation procedure, the optimal value of s is determined, for which the maximum error of the boundary value of temperature in the control points is the lowest.

In order to verify the accuracy of the proposed algorithm, as the first test example, we have consitered a smooth tube without fins. The results of our calculations for different values of γ are presented in Table 2 and are consistent with the literature, see e.g. Soliman *et al.* (1980). This allowed us, even at this early stage, to confirm the effectiveness of the proposed algorithm.

Table 2. Numerical results of the smooth tube investigation for different γ values

M	γ [°]	s_{OPT}	fRe	Nu	$\delta\Theta$
4	45	0.2121	16	3.6787	5.35E-06
8	22.5	0.1913	16	3.6773	5.47E-06
12	15	0.1812	16	3.6735	5.44E-06
16	11.25	0.1756	16	3.6707	5.41E-06
20	9	0.1721	16	3.6688	5.42E-06
24	7.5	0.1697	16	3.6676	5.41E-06
28	6.429	0.1679	16	3.6667	5.39E-06
32	5.625	0.1666	16	3.6662	5.32E-06

Furthermore, comparison between this study and previous work of Soliman and Feingold (1977) and Soliman *et al.* (1980) has been made to validate the postulated method. Figures 3a and 3b show the comparison of Nu values obtained in this work and those of Soliman *et al.* (1980) for $k = 1, 5$, and 10 and for $M = 4$ and 8. The maximum discrepancies in Nusselt numbers proved lower than 9% for $M = 4$ and 12% for $M = 8$. This is presumably due to the hereby assumed two-dimensional heat transfer, which differs from the one-dimensional fin conductance in the tube.

Further numerical results of fRe for $\beta = 3°$, and for varying fin numbers and lengths, are presented in Fig. 4. The value of fRe increases with the increase in M for all values of L. The effect of M is much more appreciable for longer fins.

The Nusselt number, defined by $(2.19)_2$, was used as a measure of the overall performance of any heat transfer surface; in other words, Nu reflects the influence of the internal finning on the overall heat transfer performance. The calculated values of Nu corresponding to the same value of the half of the angle of one fin, $\beta = 3°$, are listed in Table 3 for $k = \{1, 5, 10, 100\}$ illustrating

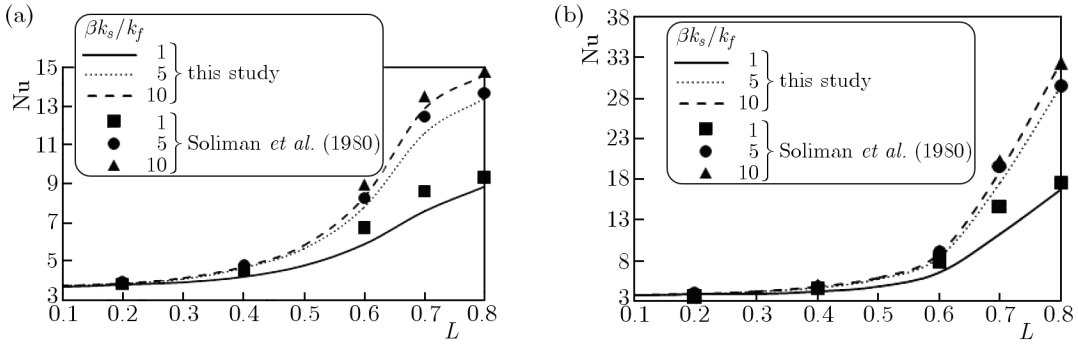

Fig. 3. Comparison of the results obtained in the present study with those presented by Soliman *et al.* (1980) for the solution of $f\mathrm{Re}$ for (a) $M = 4$ and (b) $M = 8$

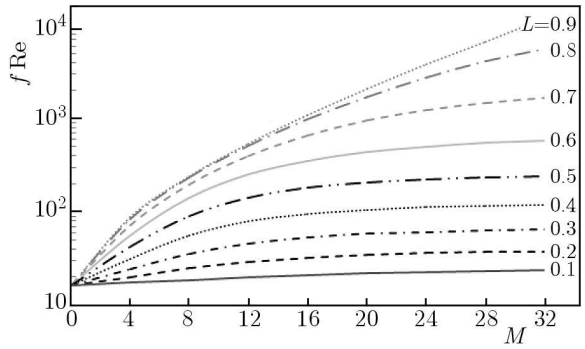

Fig. 4. The friction factor $f\mathrm{Re}$ for $\beta = 3°$

different tube geometries. Obviously, the magnitude of heat transfer enhancement depends on M, L, and k. It can be observed that for any tube geometry, the value of Nu increases as k increases. For a given value of L and k, in most cases, the maximum value of Nu is obtained for the tube with eight fins ($M = 8$). The results depicted in Table 3 also show that the effect of k is more visible for longer fins ($L \geqslant 0.7$) when there are 4, 8, or 16 of them. For the tube with eight fins and 0.8 in length, for $k = 1$ Nu $= 16.719$ and for $k = 100$ the Nusselt number was more than two times greater (Nu $= 35.254$). Comparing these results to those obtained for the smooth tube, the Nusselt number increases almost five times while, at the same time, the resistance increases more than 14 times.

A similar numerical experiment has been performed for constant values of the dimensionless flow area of the tube, $A_f = 2.7$ (Table 4). For such a geometry of the tube, which changes the angle of the fins, $\beta = (\pi - A_f)/[ML(2-L)]$, the largest value of Nu is obtained for $M = 16$ and $L = 0.8$.

However, in this case, we deal with a high resistance value, $f\mathrm{Re} = 671.92$. Considering the same example, for a fixed value of $\beta = 3°$ (Table 3),we observe that the resistance is much higher, $f\mathrm{Re} = 975.96$ (since $A_f = 2.337$ is smaller), and the value of the Nusselt number is smaller (although $\beta = 3°$ is larger). In the case of short fins ($L \leqslant 0.5$), the largest reinforcement of the heat transfer (Nu) is obtained for the tube with four fins (Table 4). This is advantageous, as in tubes with fewer fins the resistance $f\mathrm{Re}$ is lower than in their multi-finned counterparts. From the numerical experiments, it appears that in order to intensify heat transfer, it is preferable to use tubes with slim fins, since, for $M = 16$ and $L = 0.8$, better results are obtained for $\beta = 1.647$ and $A_f = 2.7$ (Table 4) than for $\beta = 3$ and $A_f = 2.337$ (Table 3).

Figures 5 and 6 illustrate the effect of the angle β of the fins of length $L = 0.8$ on the enhancement of heat conduction, Nu and resistance to flow $f\mathrm{Re}$. The results show that $f\mathrm{Re}$ and the width of the fins also play significant roles in enhancing the heat transfer.

Table 3. Overall heat transfer results for $\beta = 3^\circ$ and $A_f = \pi - M\beta L(2-L)$

		$M=4$		$M=8$		$M=16$		$M=24)$		$M=32$	
L	k	fRe	Nu	fRe	Nu	fRe	Nu	fRe	Nu	fRe	Nu
0.2	1	19.87 $A_f =$ 3.066	3.729	24.39 $A_f =$ 2.991	**3.734**	31.88 $A_f =$ 2.840	3.642	35.74 $A_f =$ 2.689	3.587	37.48 $A_f =$ 2.538	3.575
	5		3.793		**3.843**		3.739		3.662		3.662
	10		3.803		**3.852**		3.751		3.695		3.672
	100		3.812		**3.864**		3.773		3.701		3.672
0.4	1	31.47 $A_f =$ 3.008	**4.172**	55.50 $A_f =$ 2.874	4.100	93.89 $A_f =$ 2.605	3.647	110.85 $A_f =$ 2.337	3.480	117.90 $A_f =$ 2.069	3.487
	5		4.596		**4.617**		3.933		3.696		3.650
	10		**4.685**		4.681		3.981		3.737		3.684
	100		4.745		**4.758**		4.018		3.771		3.693
0.5	1	42.04 $A_f =$ 2.985	**4.737**	89.79 $A_f =$ 2.827	**4.737**	179.13 $A_f =$ 2.513	3.801	223.23 $A_f =$ 2.199	3.435	242.01 $A_f =$ 1.885	3.392
	5		5.615		**5.663**		4.255		3.748		3.637
	10		5.796		**5.809**		4.319		3.820		3.678
	100		**5.983**		5.960		4.394		3.884		3.719
0.6	1	56.12 $A_f =$ 2.966	5.816	141.01 $A_f =$ 2.790	**6.433**	354.37 $A_f =$ 2.438	4.429	503.75 $A_f =$ 2.086	3.649	575.44 $A_f =$ 1.734	3.397
	5		7.754		**8.354**		5.158		4.047		3.741
	10		8.245		**8.715**		5.281		4.121		3.784
	100		8.776		**9.088**		5.400		4.190		3.826
0.7	1	71.60 $A_f =$ 2.951	7.541	198.43 $A_f =$ 2.760	**11.219**	655.25 $A_f =$ 2.379	7.005	1228.03 $A_f =$ 1.998	4.559	1663.91 $A_f =$ 1.617	3.567
	5		11.603		**17.660**		8.654		5.352		4.025
	10		12.859		**18.983**		8.942		5.497		4.092
	100		14.363		**20.276**		9.243		5.593		4.149
0.8	1	83.13 $A_f =$ 2.941	8.845	233.49 $A_f =$ 2.739	16.719	975.96 $A_f =$ 2.337	**20.063**	2762.44 $A_f =$ 1.935	8.843	5628.56 $A_f =$ 1.533	5.000
	5		13.380		**29.398**		28.323		11.347		5.858
	10		14.614		**32.372**		29.694		11.682		5.975
	100		15.960		**35.254**		31.272		11.977		6.067

Further, it can be observed that fRe varies linearly both for $M = 4$ and $M = 8$. However, when it comes to Nu, for $M = 4$ we have found some regularity, and for $M = 8$ a significant increase in Nu has been obtained for $\beta = 1.8$ (the result comparable to that obtained for $\beta = 2.8$) and $\beta = 2.0$ (the result comparable to that obtained for $\beta = 3.0$). For both angles β we observed enhancement of heat conduction while maintaining lower resistance fRe.

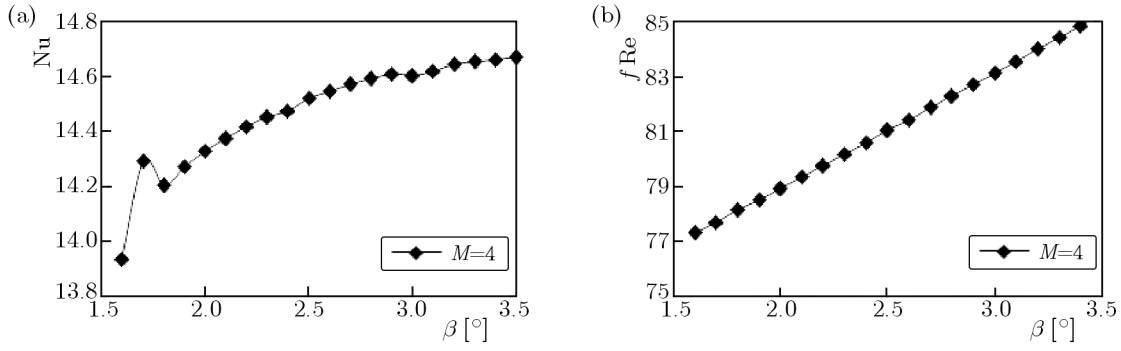

Fig. 5. The effects of the fin angle β on the Nusselt number Nu and the product of the friction factor and the Reynolds number fRe for $k = 10$, $L = 0.8$, and $M = 4$

Table 4. Overall heat transfer results for $A_f = 2.7$ and $\beta = (\pi - A_f)/[ML(2-L)]$

		$M=4$		$M=8$		$M=16$		$M=24)$		$M=32$	
L	k	fRe	Nu	fRe	Nu	fRe	Nu	fRe	Nu	fRe	Nu
0.2	1	26.33 $\beta=$ 17.57	3.526	30.11 $\beta=$ 8.785	**3.611**	34.12 $\beta=$ 4.393	3.597	35.46 $\beta=$ 2.928	3.578	36.45 $\beta=$ 2.196	3.602
	5		**3.781**		3.761		3.711		3.682		3.660
	10		**3.822**		3.800		3.717		3.690		3.675
	100		**3.860**		3.827		3.736		3.696		3.686
0.4	1	41.53 $\beta=$ 9.883	**3.992**	63.82 $\beta=$ 4.942	3.987	90.81 $\beta=$ 2.471	3.710	101.76 $\beta=$ 1.647	3.597	107.48 $\beta=$ 1.235	3.571
	5		**4.634**		4.484		4.014		3.795		3.736
	10		**4.767**		4.562		4.055		3.825		3.775
	100		**4.892**		4.634		4.098		3.876		3.791
0.5	1	54.83 $\beta=$ 8.434	**4.582**	99.61 $\beta=$ 4.217	4.539	163.91 $\beta=$ 2.108	3.940	194.40 $\beta=$ 1.406	3.683	208.19 $\beta=$ 1.054	3.604
	5		**5.758**		5.507		4.410		4.044		3.920
	10		**6.011**		5.655		4.491		4.096		3.958
	100		**6.278**		5.779		4.585		4.126		3.991
0.6	1	71.69 $\beta=$ 7.530	5.720	155.77 $\beta=$ 3.765	**6.241**	302.24 $\beta=$ 1.883	4.823	393.19 $\beta=$ 1.255	4.146	450.78 $\beta=$ 0.941	3.856
	5		8.128		**8.243**		5.664		4.712		4.260
	10		**8.742**		8.551		5.775		4.784		4.328
	100		**9.473**		8.838		5.964		4.857		4.367
0.7	1	89.15 $\beta=$ 6.951	7.505	207.91 $\beta=$ 3.475	**11.068**	505.72 $\beta=$ 1.738	8.221	782.40 $\beta=$ 1.158	6.069	1015.07 $\beta=$ 0.869	5.241
	5		12.255		**17.470**		10.333		7.254		5.992
	10		13.775		**18.660**		10.842		7.435		6.039
	100		15.625		**19.885**		11.043		7.497		6.039
0.8	1	100.42 $\beta=$ 6.589	8.730	242.48 $\beta=$ 3.294	16.685	671.92 $\beta=$ 1.647	**24.696**	1248 $\beta=$ 1.098	17.056	1821.94 $\beta=$ 0.824	12.921
	5		13.507		29.539		**36.785**		21.135		15.438
	10		14.785		32.512		**38.967**		21.879		15.737
	100		16.117		35.340		**40.993**		22.791		15.858

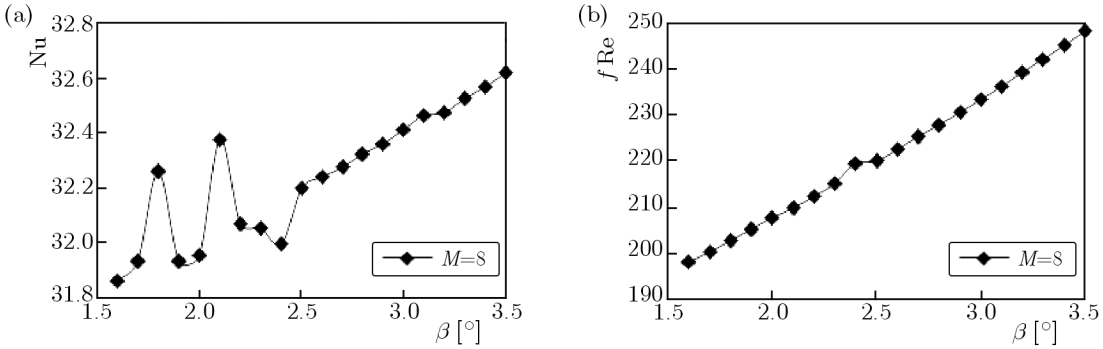

Fig. 6. The effects of the fin angle β on the Nusselt number Nu and the product of the friction factor and the Reynolds number fRe for $k = 10$, $L = 0.8$ and for $M = 8$

5. Conclusions

In this paper, we have employed MFS with RBF to investigate a fully developed laminar flow and convective heat transfer in an internally finned tube. The presented method is very easy to implement, even in the case of highly challenging domains, because requires a cloud of points only. The hereby presented numerical results, pertaining to diverse experimental data, show that MFS is an accurate and reliable numerical technique generating solutions comparable with the literature. The proposed scheme is a competitive alternative to the existing

methods of heat transfer investigation. The numerical analysis shows that the usage of finned cooling channels can not only contribute to the improvement of cooling effectiveness, but also, through proper fin placement, the enable manipulation of heat conduction in the mold. This finding is very significant from the technological point of view, as it will allow decreasing the stress strain of the mold, thereby improving its quality and mechanical properties.

Acknowledgments
The work has been supported by LIDER/006/143/L-5/13/NCBR/2014 Grant.

References

1. Alves C.J.S., Silvestre A.L., 2004, Density results using Stokeslets and a method of fundamental solutions for the Stokes equations, *Engineering Analysis with Boundary Elements*, **28**, 10, 1245-1252
2. Benitez-Rangel J.P., Trejo-Hernandez M., Morales-Hernandez L.A., Dominguez--Gonzalez A., 2010, Improvement of the injection mold process by using vibration through a mold accessory, *Materials and Manufacturing Processes*, **25**, 7, 577-580
3. Bergles E., 1998., *Handbook of Heat Transfer*, McGraw-Hill, New York, NY, USA, 3rd edition
4. Chen C.S., Karageorghis A., Smyrlis T.S. (ed.), 2008, *The Method of Fundamental Solutions – A Meshless Method. Dynamic Publishers*, Inc., Atlanta
5. Golberg M.A., 1995, The method of fundamental solutions for Poisson's equation, *Engineering Analysis with Boundary Elements*, **16**, 3, 205-213
6. Golberg M.A., Chen C.S., 1999, The method of fundamental solutions for potential, Helmholtz and diffusion problems, [In:] *Boundary integral methods: numerical and mathematical aspects. Southampton: Computational Mechanics Publications*, Golberg M.A. (Edit.), 103-176
7. Johnston R.L., Fairweather G., 1984, The method of fundamental solutions for problems in potential flow, *Applied Mathematical Modelling*, **8**, 4, 265-270
8. Karageorghis A., Fairweather G., 1987, The method of fundamental solutions for the numerical solution of the biharmonic equation, *Journal of Computational Physics*, **69**, 2, 434-59
9. Karageorghis A., Fairweather G., 1998, The method of fundamental solutions for elliptic boundary value problems, *Advances in Computational Mathematics*, **9**, 69-95
10. Kupradze V.D., Aleksidze M.A., 1964, The method of functional equations for the approximate solution of certain boundary value problems, *USSR Computational Mathematics and Mathematical Physics*, **4**, 4, 82-126
11. Mathon R., Johnston R.L., 1977, The approximate solution of elliptic boundary-value problems by fundamental solutions, *SIAM Journal on Numerical Analysis*, **14**, 4, 638-650
12. Nesis E. I., Shatalov A. F., Karmatskii N. P., 1994, Dependence of the heat transfer coefficient on the vibration amplitude and frequency of a vertical thin heater, *Journal of Engineering Physics and Thermophysics*, **67**, 1/2, 696-698
13. Rout S.K., Mishra D. P., Thatoi D. N., Acharya A. K., 2012, Numerical analysis of mixed convection through an internally finned tube, *Advances in Mechanical Engineering*, Vol.2012, Article ID 918342, p. 10
14. Siddique M., Khaled A.-R.A., Abdulhafiz N.I., Boukhary A.Y., 2010, Recent advances in heat transfer enhancements: a review report, *International Journal of Chemical Engineering*, vol. 2010, Article ID 106461, p. 28, doi:10.1155/2010/106461
15. Soliman H.M., Chau T.S., Trupp A.C., 1980, Analysis of laminar heat transfer in internally finned tubes with uniform outside wall temperature, *Journal of Heat Transfer*, **102**, 598-604
16. Soliman H.M., Feingold A., 1977, Analysis of fully developed laminar flow in longitudinal internally finned tubes, *Chemical Engineering Journal*, **14**, 119-128

17. Tien W.-K., Yeh R.-H., Hsiao, J.-C., 2012, Numerical analysis of laminar flow and heat transfer in internally finned tubes, *Heat Transfer Engineering*, **33**, 11, 957-971

18. Tsai C.C., 2007, The method of fundamental solutions for three-dimensional elasto-static problems of transversely isotropic solids, *Engineering Analysis with Boundary Elements*, **31**, 7, 586-594

19. Tsai C.C., Young D.L., Chiu C.L., Fan C.M., 2009, Numerical analysis of acoustic modes using the linear least squares method of fundamental solutions, *The Journal of Sound and Vibration*, **324**, 3/5, 1086-1100

Manuscript received January 14, 2014; accepted for print March 11, 2014

JOURNAL OF THEORETICAL AND APPLIED MECHANICS
53, 3, pp. 519-530, Warsaw 2015
DOI: 10.15632/jtam-pl.53.3.519

INCLINATION ANGLE IMPLICATIONS FOR FLUID FLOW AND MIXED CONVECTION IN COMPLEX GEOMETRY ENCLOSURE-MESHLESS NUMERICAL ANALYSES

Mohammad Najafi

Department of Mechanical and Aerospace Engineering, Science and Research Branch, Islamic Azad University, Tehran, Iran; e-mail: najafi@srbiau.ac.ir

Mehdi Nikfar

Department of Mechanical Engineering, K.N. Toosi University of Technology, Tehran, Iran

Ali Arefmanesh

Department of Mechanical Engineering, University of Kashan, Kashan, Iran

The meshless local Petrov-Galerkin (MLPG) method is extended to analyze the mixed convection and fluid flow in an inclined two-dimensional lid-driven cavity. The enclosure considered comprises two insulated vertical walls and a wavy bottom wall which is subjected to a higher constant temperature than its top counterpart, the sliding lid. For the proposed scheme, the stream function formulation with a weighting function of unity is employed. The simulation results reveal that the local Nusselt number increases with a clockwise increase in the inclination angle. Also, a decrease in the aspect ratio results in an increase in the hot wavy wall average Nusselt number.

Keywords: meshless, Petrov-Galerkin, mixed convection, rectangular cavity, wavy wall

1. Introduction

In the past two decades, a number of mesh-free numerical methods were proposed for solving partial differential equations. The principal objective of developing these methods was to get around the difficulties associated with generating a mesh in conventional numerical techniques such as the finite difference and the finite element methods. In the earlier mesh-free techniques, an auxiliary grid had been required to evaluate the integrals resulting from applying the Galerkin method to the differential equations. Hence, these methods could not be considered totally meshless. Subsequently, two truly meshless techniques, the meshless local boundary equation (MLBE) method and the meshless local Petrov-Galerkin (MLPG) method were proposed by Zhu *et al.* (2004), and Atluri and Zhu (1998), respectively. To obtain the discretized equations in the latter scheme, instead of a mesh, an arbitrary point--distribution, without any pre-specified relationship among the points, is generated in the computational domain. Subsequently, the shape functions from the moving least squares (MLS) interpolations are employed in a local weak form of the differential equations over a local subdomain. The arbitrariness of the point-distribution as well as the possibility of adding or removing points to or from pre-existing point-distributions without any considerable computational effort make the MLPG method quite appealing for domains with complex geometries such as enclosures having wavy walls.

As far as application of the MLPG method on the fluid flow and heat transfer analysis, a number of recent studies may be mentioned. Lin and Atluri (2001,2001) applied the newly--developed MLPG method to the solutions of the convection-diffusion and the Navier-Stokes (N-S) equations. They modified the local weak forms to overcome the so-called Babuska-Brezzi

conditions while solving the primitive variables form of the N-S equations. Moreover, they presented a different upwinding scheme in order to obtain stabilized solutions under high Peclet and Reynolds (Re) numbers. Arefmanesh *et al.* (2005) applied a variation of the MLPG method with unity as the test function to the convection-diffusion and the potential flow equations. Comparisons of their results with the analytical solution for the convection-diffusion equation in a square domain demonstrated high accuracy of their proposed method. More recently, Arefmanesh *et al.* (2008) used a variation of the MLPG method with the unit test function to solve a number of non-isothermal fluid flow problems. They employed the stream function-vorticity formulation to solve different test cases such as a non-isothermal lid-driven cavity flow with an inlet and an outlet. In another study, Haji Mohammadi (2008) applied the MLPG method to simulate the incompressible viscous fluid flow. He formulated his considered cases in terms of the stream function-vorticity and employed the radial basis function interpolations in his approach.

Mixed convection flow and heat transfer in an enclosure involving a moving lid has drawn extensive attention due to its broad applications in engineering, modern technology, and natural situations. Among these applications, there is cooling of electronic devices, float glass production, food processing, and fluid flow and heat transfer in solar ponds. Flow and heat transfer from irregular surfaces are often encountered in many engineering applications to enhance heat transfer such as micro-electronic devices, solar collectors, electrical machinery, etc. Moreover, roughened and wavy surfaces could be used in the cooling of electrical and nuclear components to enhance the heat transfer. On the other hand, the study of natural and mixed convection heat transfer in inclined enclosures is relevant in geophysical situations, honeycomb solar collector plates, heat exchangers and crystal growth processes from melts, etc. Determining the optimal inclination angle is of paramount importance in such cases. As far as fundamental research is concerned, tilting the enclosure allows one to study different instabilities and their corresponding interactions through making a suitable choice of the values of the external parameters. Many recent studies regarding the applications of the conventional numerical methods on mixed convection are available in the literature. Chamkha (2002) conducted a numerical simulation of unsteady and laminar mixed convection heat transfer in a square cavity in the presence of internal heat generation or absorption and a magnetic field using the finite volume method. Mixed convection heat transfer in a two-dimensional rectangular cavity consisting of isothermal side walls moving vertically and a partially-heated bottom wall was studied numerically by Guo and Sharif (2004) using the finite volume method. In another study in the same year, Oztop and Dagtekin (2004) numerically simulated a steady state two-dimensional mixed convection problem in a cavity having two differentially-heated and vertically driven side walls using the finite volume method and the SIMPLE algorithm. The study showed that both the Richardson number and the direction of the moving walls affect the fluid flow and heat transfer inside the cavity. More recently, a finite element analysis of unsteady laminar mixed convection heat transfer in a cavity with sinusoidally oscillating horizontal top-lid was carried out by Khanafer *et al.* (2007). The laminar mixed convection heat transfer in two-dimensional shallow rectangular driven cavities with an aspect ratio of 10 was studied numerically by Sharif (2007) using the FLUENT version 6 commercial code. In another study, Al-Amiri *et al.* (2007) investigated the mixed convection heat transfer and fluid flow in a lid-driven cavity being heated from a sinusoidal wavy bottom surface using the finite element method. Their results showed that the average Nusselt number increased with an increase in both the amplitude of the wavy surface and the Reynolds number. Very recently, Nasrin (2012) conducted a finite element simulation of the mixed convection in an enclosure with a wavy bottom wall maintained at a higher temperature than those of the lid and two insulated side walls. For $\mathrm{Ra} = 10^4$, $\mathrm{Re} = 100$, and $\mathrm{Pr} = 0.7$, Nasrin investigated the effects of the cavity aspect ratio, amplitude of the wavy wall and the number of undulations on the heat transfer inside the enclosure. It was concluded that increasing the wavy surface amplitude and cavity aspect ratio improved the heat transfer.

In view of the above literature survey, there is not any type of meshless numerical treatment in the literature which would be applied to the mixed convection heat transfer in an irregular geometry enclosure with a wavy bottom wall within which the flow is induced by a shear force resulting from motion of the cavity lid combined with a buoyancy force resulting from the differentially-heated cavity walls. Moreover, a comprehensive study of the mixed convection in such an enclosure for a wide range of the Grashof and Richardson numbers as well as different inclination angles remains to be carried out. In the present study, therefore, the meshless local Petrov-Galerkin method is extended to analyze the mixed convection heat transfer in a lid--driven cavity with a wavy bottom wall and the effects of the inclination angle, Grashof number, Richardson number and the aspect ratio of the cavity on the fluid flow and heat transfer are investigated.

2. Problem formulation

A mixed convection fluid flow and heat transfer within a lid-driven rectangular cavity with a wavy bottom wall is simulated numerically using the MLPG method. As depicted in Fig. 1, the height and the width of the cavity are denoted by H and L, respectively, and the aspect ratio of the cavity is defined as $A = H/L$. The left and the right walls of the cavity are insulated while the bottom wall of the enclosure, which is a wavy wall, is maintained at a constant temperature T_h, here referred to as "hot" temperature. The enclosure's top wall, which moves in its own plane from left to right with a constant speed u_l, is kept at a constant temperature T_c, here referred to as "cold" temperature, where $T_h > T_c$. The cavity is filled with a fluid with $\mathrm{Pr} = 1$. The thermo--physical properties of the fluid are considered to be constant with the exception of density in the buoyancy term which, as will be noticed, varies according to the Bousinesq approximation (Bejan, 2004).

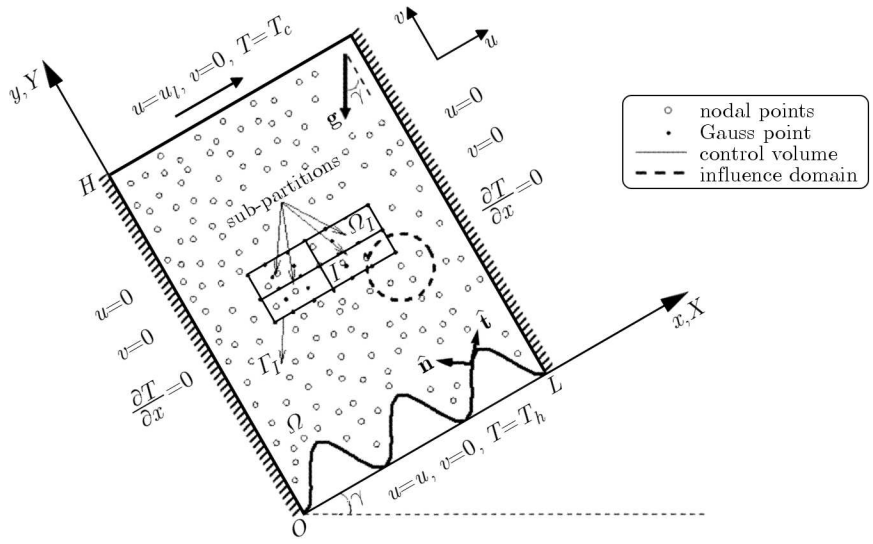

Fig. 1. Lid-driven differentially heated cavity, domain, boundary conditions and a typical control volume

The steady-state fluid flow and heat transfer in the cavity are governed by the continuity, momentum and energy equations. The natural convection term is incorporated in the momentum equation by employing the Bousinesq approximation (Bejan, 2004). In this study, the two--dimensional fluid flow problem is formulated in terms of the stream function and vorticity.

To cast the governing equations into a dimensionless form, the following dimensionless variables are introduced

$$X = \frac{x}{H} \qquad Y = \frac{y}{H}$$
$$U = \frac{u}{u_l} \qquad V = \frac{v}{u_l} \qquad \theta = \frac{T - T_c}{T_h - T_c} \tag{2.1}$$
$$\Psi = \frac{\psi}{H u_l} \qquad \Omega = \frac{\omega H}{u_l}$$

where u and v are the velocity components in the x and y-directions, respectively, ψ is the stream function and ω is the vorticity. Substituting the above dimensionless variables into the stream function, vorticity and energy equations results in the following dimensionless form of the governing equations

$$\frac{\partial^2 \Psi}{\partial X^2} + \frac{\partial^2 \Psi}{\partial Y^2} = -\Omega$$
$$U\frac{\partial \Omega}{\partial X} + V\frac{\partial \Omega}{\partial Y} = \frac{1}{\mathrm{Re}}\Big(\frac{\partial^2 \Omega}{\partial X^2} + \frac{\partial^2 \Omega}{\partial Y^2}\Big) + \mathrm{Ri}\Big(\cos\gamma\frac{\partial \theta}{\partial X} - \sin\gamma\frac{\partial \theta}{\partial Y}\Big) \tag{2.2}$$
$$U\frac{\partial \theta}{\partial X} + V\frac{\partial \theta}{\partial Y} = \frac{1}{\mathrm{RePr}}\Big(\frac{\partial^2 \theta}{\partial X^2} + \frac{\partial^2 \theta}{\partial Y^2}\Big)$$

where γ is the inclination angle of the cavity (Fig. 1). The Reynolds number Re and the Richardson number Ri are defined as

$$\mathrm{Re} = \frac{u_l H}{\nu} \qquad \mathrm{Ri} = \frac{\mathrm{Gr}}{\mathrm{Re}^2} \tag{2.3}$$

where

$$\mathrm{Gr} = \frac{g\beta(T_h - T_c)H^3}{\nu^2} \tag{2.4}$$

where ν is the kinematic viscosity of the fluid, Gr is the Grashof number, and β is the thermal expansion coefficient. The rate of heat transfer in the enclosure is obtained from the Nusselt number calculations. On the hot and the cold walls of the cavity, the local Nusselt number (Nu) is obtained from the following relation

$$\mathrm{Nu} = -\frac{\partial \theta}{\partial n} \tag{2.5}$$

The Grashof numbers used in this study are 10^4 and 10^5. Two configurations for tilting the horizontal cavity, namely, clockwise and counter-clockwise about the origin, point O (Fig. 1), are considered in this work. For each configuration, the inclination angle γ is taken as 0, 30°, 60°, and 90°. Also, for $\gamma = 0$, the simulation is carried out for three aspect ratios of $A = 0.5$, 1, and 2.

3. Numerical procedure

In the present study, the governing equations are solved numerically by the MLPG method. To implement the method, an arbitrary collection of points is selected in the computational domain (Fig. 1). Subsequently, a control volume is generated around each of the points. A typical rectangular control volume Ω_I generated around point I is shown in Fig. 1.

As the first step in developing the discretized equations for the control volume Ω_I, the weak forms of the governing equations are to be obtained. This is accomplished by multiplying the stream function, vorticity and energy equations by the test function W_I. Subsequently, the resulting equations are integrated over Ω_I. After performing the integration by parts, the weak

forms of the stream function, vorticity and energy equations for the control volume Ω_I are expressed respectively

$$
\begin{aligned}
&-\int_{\Omega_I} \nabla W_I \cdot \nabla \Psi \, d\Omega + \int_{\Gamma_I - \Gamma_I \cap \Gamma_h} W_I \frac{\partial \Psi}{\partial n} \, d\Gamma + \int_{\Gamma_I \cap \Gamma_h} W_I \frac{\partial \Psi}{\partial n} \, d\Gamma = -\int_{\Omega_I} W_I \Omega \, d\Omega \\
&\int_{\Omega_I} W_I \Big(U \frac{\partial \Omega}{\partial X} + V \frac{\partial \Omega}{\partial Y} \Big) \, d\Omega = -\frac{1}{\mathrm{Re}} \int_{\Omega_I} \nabla W_I \cdot \nabla \Omega \, d\Omega + \frac{1}{\mathrm{Re}} \int_{\Gamma_I - \Gamma_I \cap \Gamma_h} W_I \frac{\partial \Omega}{\partial n} \, d\Gamma \\
&\quad + \frac{1}{\mathrm{Re}} \int_{\Gamma_I \cap \Gamma_h} W_I \frac{\partial \Omega}{\partial n} \, d\Gamma + \mathrm{Ri} \int_{\Omega_I} W_I \Big(\frac{\partial \theta}{\partial X} \cos\gamma - \frac{\partial \theta}{\partial Y} \sin\gamma \Big) \, d\Omega \\
&\int_{\Omega_I)} W_I \Big(U \frac{\partial \theta}{\partial X} + V \frac{\partial \theta}{\partial Y} \Big) \, d\Omega = -\frac{1}{\mathrm{RePr}} \int_{\Omega_I} \nabla W_I \cdot \nabla \theta \, d\Omega + \frac{1}{\mathrm{RePr}} \int_{\Gamma_I - \Gamma_I \cap \Gamma_h} W_I \frac{\partial \theta}{\partial n} \, d\Gamma \\
&\quad + \frac{1}{\mathrm{RePr}} \int_{\Gamma_I \cap \Gamma_h} W_I \frac{\partial \theta}{\partial n} \, d\Gamma
\end{aligned}
\tag{3.1}
$$

where Γ_h is the portion of the domain boundary for which a natural boundary condition is enforced. Here, Γ_I is the boundary of the control volume Ω_I, and $\Gamma_I \cap \Gamma_h$ represents the intersection of Γ_I with Γ_h.

Next, the integrals in Eqs. (3.1) are to be evaluated. The Gaussian quadrature is employed for this purpose. To perform the numerical integrations, the control volume Ω_I is divided into a number of sub-partitions (Fig. 1). The proper number of the Gauss points for the surface and the contour integrations in each sub-domain are selected. Subsequently, the field variables are approximated at each of the Gauss points using the MLS interpolations. Considering Ω_k as the interpolation domain for a typical Gauss point k, and $S_{j,j} = 1(1)n_k$, as a collection of n_k nodal points with coordinates $x_j \in \Omega_k$ (whose influence domains cover the considered Gauss point), the unknown stream function, vorticity and temperature fields are approximated within Ω_k, respectively (Onate *et al.*, 1996),

$$
\begin{aligned}
&\overline{\Psi}^{(k)}(\mathbf{x}) = \sum_{j=1}^{n_k} N_j^{(k)}(\mathbf{x}) \widehat{\Psi}_j \qquad\qquad \overline{\Omega}^{(k)}(\mathbf{x}) = \sum_{j=1}^{n_k} N_j^{(k)}(\mathbf{x}) \widehat{\Omega}_j \\
&\overline{\theta}^{(k)}(\mathbf{x}) = \sum_{j=1}^{n_k} N_j^{(k)}(\mathbf{x}) \widehat{\theta}_j
\end{aligned}
\tag{3.2}
$$

where $\widehat{\Psi}_j$, $\widehat{\Omega}_j$, and $\widehat{\theta}_j$ are fictitious nodal values for the stream function, vorticity, and temperature, respectively. In Eqs. (3.2), $N_j^{(k)}(\mathbf{x})$, $j = 1(1)n_k$, are the MLS interpolation functions (Onate *et al.*, 1996).

Having obtained the weak formulations of the governing equations and the moving least-squares approximations of the field variables, the final step in the discretization process is to present the fully-discretized equations for a typical control volume Ω_I with the boundary Γ_I. For this purpose, the control volume Ω_I is divided into a number of sub-domains. The proper number of the Gauss points is selected in each of the sub-domains. Subsequently, the MLS interpolations for the stream function, vorticity and temperature (Eqs. (3.2)) at a typical Gauss point k are substituted into Eqs. (3.1). The resulting discretized equations are given as

$$
\begin{aligned}
&\sum_{j=1}^{n_k}\left(\int\limits_{\Gamma_I-\Gamma_I\cap\Gamma_h} W_I N_{j,n}^{(k)}(\mathbf{x})\,d\Gamma\right)\widehat{\Psi}_j = -\sum_{j=1}^{n_k}\left(\int\limits_{\Omega_I} W_I N_j^{(k)}(\mathbf{x})\,d\Omega\right)\widehat{\Omega}_j\\
&\quad -\int\limits_{\Gamma_I\cap\Gamma_h} W_I\frac{\partial\Psi}{\partial n}\,d\Gamma+\sum_{j=1}^{n_k}\left(\int\limits_{\Omega_I}\left(W_{I,X}N_{j,X}^{(k)}(\mathbf{x})+W_{I,Y}N_{j,Y}^{(k)}(\mathbf{x})\right)d\Omega\right)\widehat{\Psi}_j\\
&\sum_{j=1}^{n_k}\left(\int\limits_{\Omega_I} W_I\left(UN_{j,X}^{(k)}(\mathbf{x})+VN_{j,Y}^{(k)}(\mathbf{x})\right)d\Omega-\frac{1}{\mathrm{Re}}\int\limits_{\Gamma_I-\Gamma_I\cap\Gamma_h} W_I N_{j,n}^{(k)}(\mathbf{x})\,d\Gamma\right)\widehat{\Omega}_j\\
&\quad+\frac{1}{\mathrm{Re}}\sum_{j=1}^{n_k}\left(\int\limits_{\Omega_I}\left(W_{I,X}N_{j,X}^{(k)}(\mathbf{x})+W_{I,Y}N_{j,Y}^{(k)}(\mathbf{x})\right)d\Omega\right)\widehat{\Omega}_j=\frac{1}{\mathrm{Re}}\int\limits_{\Gamma_I\cap\Gamma_h} W_I\frac{\partial\Omega}{\partial n}\,d\Gamma\\
&\quad+\mathrm{Ri}\sum_{j=1}^{n_k}\left(\int\limits_{\Omega_I} W_I\left(N_{j,X}^{(k)}(\mathbf{x})\cos\gamma-N_{j,Y}^{(k)}(\mathbf{x})\sin\gamma\right)d\Omega\right)\widehat{\theta}_j\\
&\sum_{j=1}^{n_k}\left(\int\limits_{\Omega_I} W_I\left(UN_{j,X}^{(k)}(\mathbf{x})+VN_{j,Y}^{(k)}(\mathbf{x})\right)d\Omega-\frac{1}{\mathrm{RePr}}\int\limits_{\Gamma_I-\Gamma_I\cap\Gamma_h} W_I N_{j,n}^{(k)}(\mathbf{x})\,d\Gamma\right)\widehat{\theta}_j\\
&\quad+\frac{1}{\mathrm{RePr}}\sum_{j=1}^{n_k}\left(\int\limits_{\Omega_I}\left(W_{I,X}N_{j,X}^{(k)}(\mathbf{x})+W_{I,Y}N_{j,Y}^{(k)}(\mathbf{x})\right)d\Omega\right)\widehat{\theta}_j=\frac{1}{\mathrm{RePr}}\int\limits_{\Gamma_I\cap\Gamma_h} W_I\frac{\partial\theta}{\partial n}\,d\Gamma
\end{aligned}
\tag{3.3}
$$

The weighting function W_I is taken to be unity ($W_I = 1$) in the present study.

Similar discretized equations are obtained for all the Gauss points within the control volume Ω_I and, in turn, for all the control volumes of the domain. Assembling these equations for the control volumes and enforcing the essential boundary conditions by the direct interpolation method yield a set of algebraic equations for the stream function, vorticity and temperature. Solving this system of algebraic equations using a band solver and the Gaussian elimination process yields the unknown values of the field variables at the points.

4. Benchmarking of the code

In order to validate the numerical procedure, the fluid flow and heat transfer inside a square cavity is solved using the present method and the obtained results are compared with those of Moallemi and Jang (1992) who used the FVM. The left and the right walls of the considered cavity are insulated and the enclosure's top and bottom walls are maintained at constant temperatures T_c and T_h, respectively, with $T_h > T_c$. The top wall of the cavity moves in its own plane from the left to the right with a constant speed U_l. The simulations are performed for $\mathrm{Pr} = 1$. Figure 2 shows the streamlines and the isotherms obtained by the MLPG simulation for $\mathrm{Ri} = 1$ ($\mathrm{Gr} = 10^6$, $\mathrm{Re} = 1000$), and $\mathrm{Pr} = 1$. The results presented by Moallemi and Jang (1992) using the FVM are also shown in this figure. As it can be seen from Fig. 2, very good agreements exist between the streamlines and the isotherms obtained by the MLPG simulation and those by Moallemi and Jang (1992). Comparisons between the local Nusselt numbers for the cold and the hot walls of the cavity obtained by the proposed MLPG method for $\mathrm{Pr} = 1$, and the results of Moallemi and Jang (1992) are presented in Fig. 3. As it is observed from this figure, excellent agreements exist between the local Nusselt numbers for the two methods.

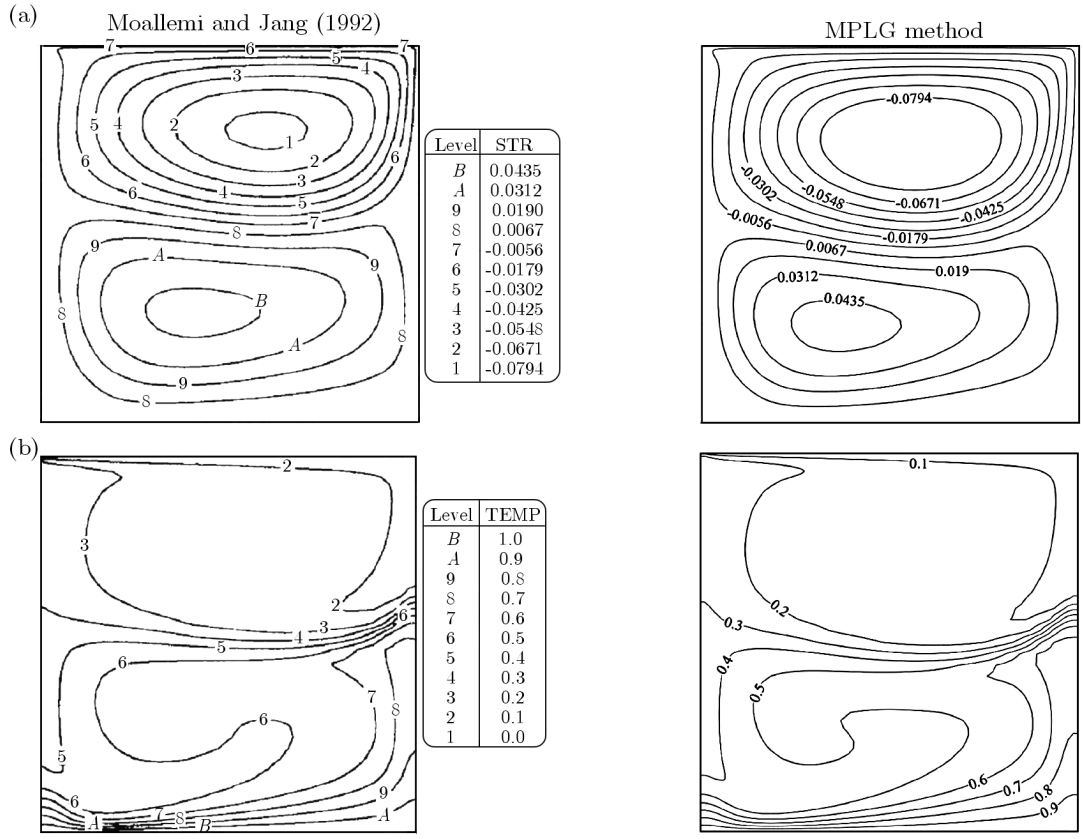

Fig. 2. Streamlines and isotherms, comparison between the MLPG method and the results of Moallemi and Jang (1992) for Ri = 1, (Gr = 10^6, Re = 1000), Pr = 1; (a) streamlines, (b) isotherms

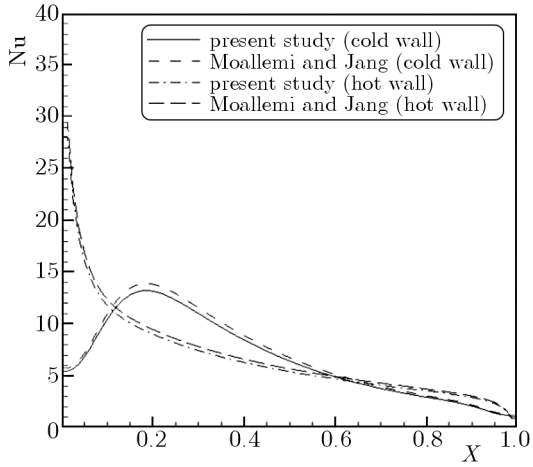

Fig. 3. Local Nusselt numbers, comparisons between the MLPG method and the results of Moallemi and Jang (1992) for Ri = 1, (Gr = 10^6, Re = 1000), and Pr = 1

5. Results and discussions

Having validated the numerical scheme, the proposed code is employed to investigate the characteristics of the mixed convection heat transfer in rectangular cavities having wavy bottom walls (Fig. 1). The geometry of the wavy surface analyzed in this study is described by $Y = 0.05(1 - \cos(6\pi X))$, where X and Y are the dimensionless Cartesian coordinates as shown in Fig. 1. The calculations are performed for a fluid with Pr = 1, for Gr = 10^4 and 10^5, and Ri = 1.

To analyze the effects of the inclination angle of the cavity γ on the fluid flow and heat transfer, the simulations are performed for two configurations of tilting the cavity clockwise and counter-clockwise directions about point O in Fig. 1. For each of the two configurations, the inclination angles of 0°, 30°, 60°, and 90° are considered. The results discussed here are for $A = 1$, Ri = 1 and 0.01, and Gr = 10^4.

Figure 4 shows the streamlines and the isotherms inside the cavity for Ri = 1 and for different inclination angles obtained by tilting the cavity counter-clockwise about point O (Fig. 1).The natural convection from the wavy hot wall intensifies with the increasing inclination angle. This, in turn, enhances the downstream eddy (DSE), and results in a relatively large counter--clockwise rotating vortex taking place in the lower portion of the cavity in the vicinity of the wavy wall with its illuminating eye coming closer to the cavity center away from the hot wavy wall. Consequently, the primary recirculation vortex weakens, and diminishes in size (Fig. 4a). The effect of the natural convection opposing the direction of the driven lid is more prominent in the vicinity of the wavy wall right edge, therefore, as it can be seen from Fig. 4b, the temperature gradients along the cold and a significant portion of the hot wall reduce substantially with the increasing inclination angle.

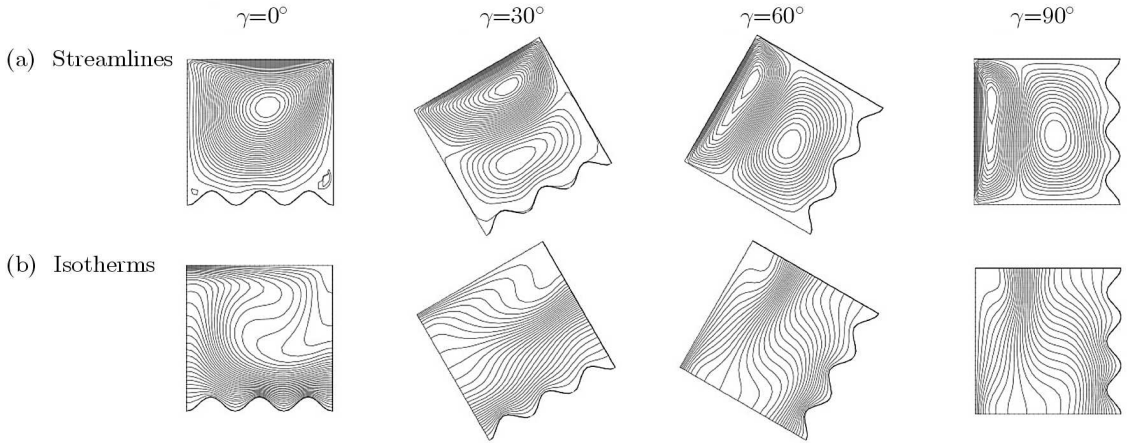

Fig. 4. Streamlines and isotherms for different counter-clockwise inclination angles, Ri = 1, Gr = 10^4, and $A = 1$; (a) streamlines, (b) isotherms

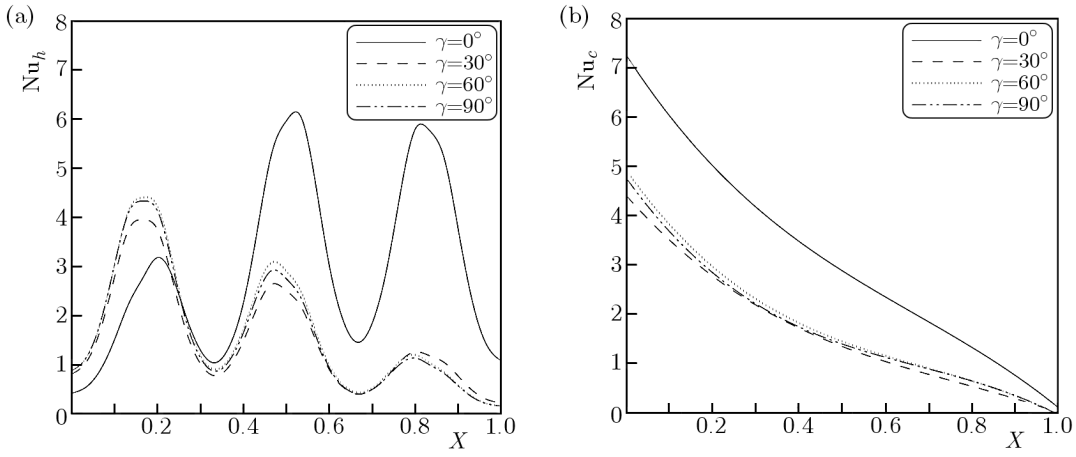

Fig. 5. Local Nusselt number distributions for different counter-clockwise inclination angles, Ri = 1, Gr = 10^4, and $A = 1$; (a) along the hot wall, (b) along the cold wall

Figures 5a and 5b show the variations of the local Nusselt number along the hot and the cold walls of the cavity for Ri = 1 and for different counter-clockwise inclination angles, respectively.

Moving from the left to the right along the hot wavy wall, it is noticed that the local Nusselt number increases in the vicinity of the first hill by increasing the inclination angle (Fig. 5a). This increase in the local Nusselt number is attributed to the enhancement of the natural convection, and the resulting boundary layer formed along the hot wavy wall. Along the remaining portions of the wavy wall, the local Nusselt number decreases substantially with an increase in the inclination angle (Fig. 5a). The reduction of the Nusselt number is due to the fact that the natural convection along the wavy wall in these regions opposes the primary recirculation vortex. Moreover, as it can be observed from Fig. 5b, the local Nusselt number along the cold wall decreases with an increase in the inclination angle which is attributed to the shrinkage of the primary vortex.

The streamlines and the isotherms inside the cavity for different inclination angles obtained by tilting the cavity clockwise are displayed in Figs. 6a and 6b, respectively. The results in these figures are obtained for Ri = 1, Gr = 10^4, and $A = 1$. By tilting the cavity clockwise about point O (Fig. 1), the natural convection along the hot wavy wall, unlike the counter--clockwise case, assists the primary recirculation vortex (Fig. 6a). This, in turn, would result in the enhancement of temperature gradients along the cold and the hot walls of the cavity (Fig. 6b). Therefore, the local Nusselt numbers along the hot and the cold cavity walls, which are depicted in Figs. 7a and 7b, respectively, increase with an increase in the inclination angle.

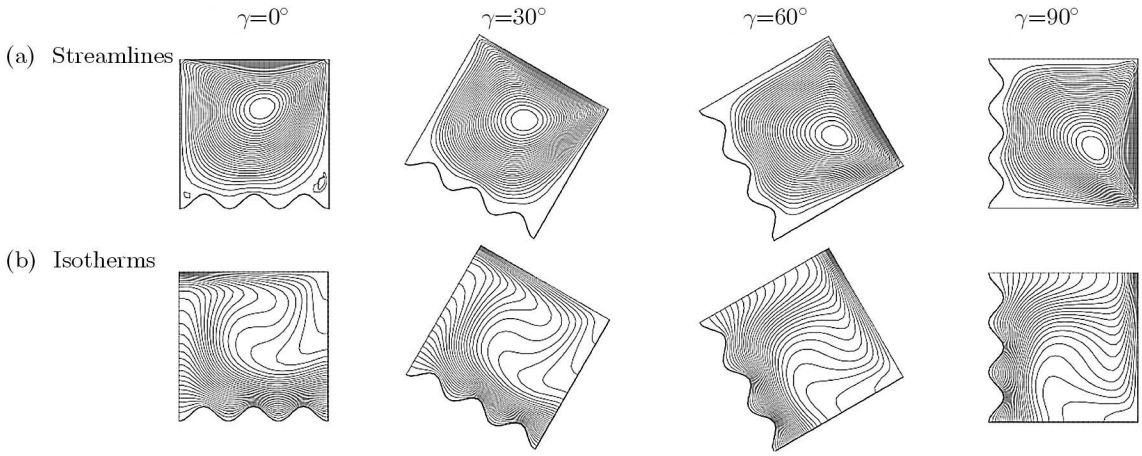

Fig. 6. Streamlines and isotherms for different clockwise inclination angles, Ri = 1, Gr = 10^4, and $A = 1$; (a) streamlines, (b) isotherms

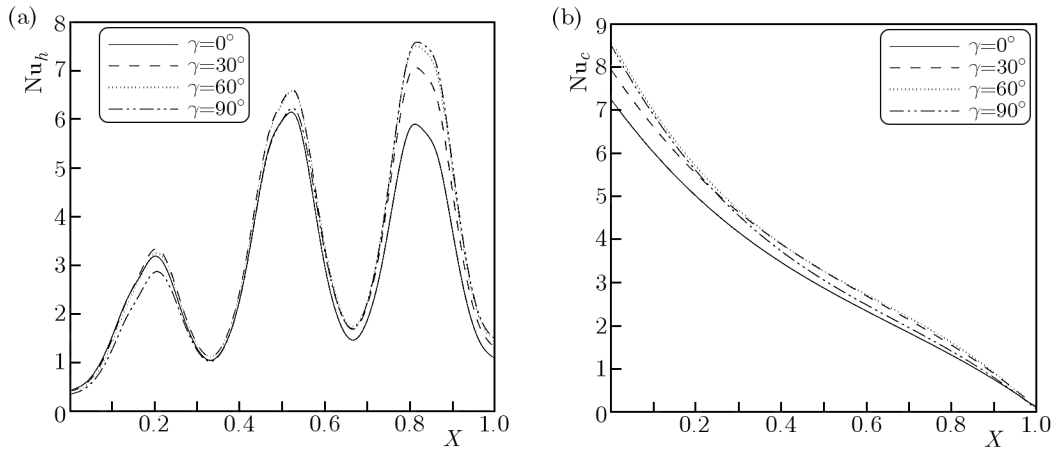

Fig. 7. Local Nusselt number distributions for different clockwise inclination angles, Ri = 1, Gr = 10^4, and $A = 1$; (a) along the hot wall, (b) along the cold wall

Figures 8a and 8b show the variations of the average Nusselt number with the inclination angle for tilting the cavity counter-clockwise and clockwise about point O (Fig. 1), respectively. The results in these figures are for Ri = 1, Gr = 10^4, and $A = 1$. It is observed in Fig. 8a that the optimal angle which provides the highest average Nusselt number while tilting the enclosure counter-clockwise is $\gamma = 0°$, i.e. the horizontal cavity. However, the optimal angle while tilting the cavity clockwise is about $\gamma = 60°$ (Fig. 8b).

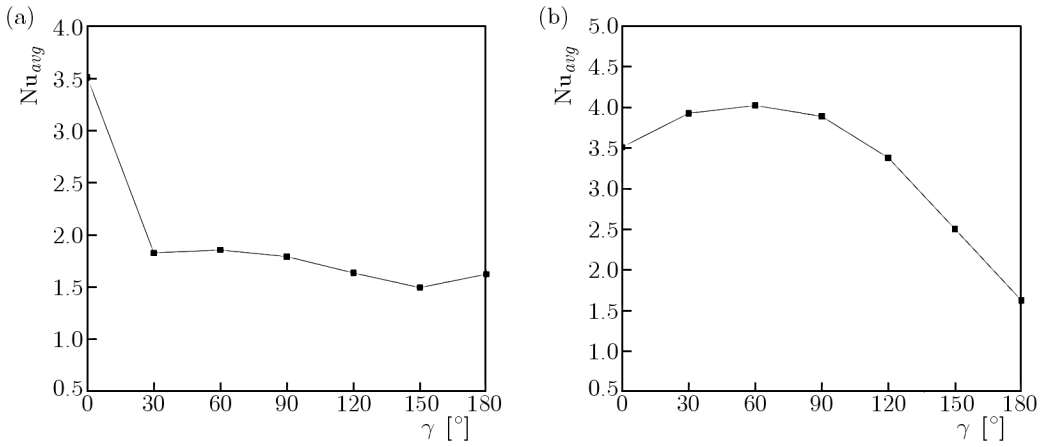

Fig. 8. Variation of the average Nusselt number with the inclination angle for Ri = 1, Gr = 10^4, and $A = 1$; (a) tilting counter-clockwise, (b) tilting clockwise

As far as the effects of the aspect ratio of the cavity on the fluid flow and heat transfer behavior are concerned, Figures 9a and 9b show the streamlines and the isotherms inside the cavity, respectively. The figures are obtained for the aspect ratios of 0.5, 1, and 2 while keeping Ri = 1 and Gr = 10^5. As it can be observed from Fig. 9a, the DSE enhances with the increasing aspect ratio of the cavity, and a relatively large counter-clockwise eddy is generated in this region (Fig. 9a). In fact, for the aspect ratio equal to two, the effect of the forced convection does not reach the bottom of the cavity. Therefore, the temperature gradient decreases in the vicinity of the hot wavy wall with increasing the aspect ratio of the cavity (Fig. 9b). As a result, the average Nusselt number of the hot wall of the cavity decreases from 6.3855 (for the aspect ratio of 0.5) to 4.5281 for the aspect ratio of 1, and to 2.6750 for the aspect ratio of 2.

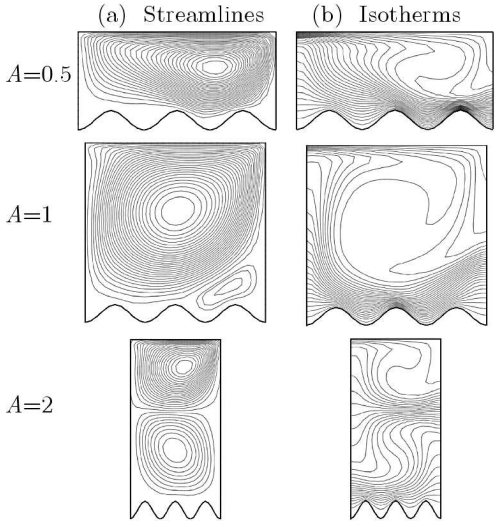

Fig. 9. Streamlines (a) and isotherms (b) inside the cavity for different aspect ratios, $\gamma = 0$, Ri = 1, and Gr = 10^5

6. Conclusions

The MLPG method is extended to numerically investigate the incompressible steady laminar flow of a fluid in an irregular geometry domain sustaining mixed convection heat transfer. The forced convective flow within the cavity is attained by a sliding top lid, while the natural convective effect is obtained by subjecting the bottom wavy wall to a higher temperature than its top sliding counterpart. The attention on this present study stems from furthering the applicability of the MLPG method by focusing on, perhaps, the most important mode of the heat transfer, the mixed convection for which the broadest spectra of engineering, technological and natural applications exist. The results show that the clockwise inclination angle tilting assists the primary recirculation vortex, causing the local Nusselt number for both the hot and cold walls to increase. The optimal inclination angle to achieve the maximum heat transfer is about 60°. Also, for zero inclination angle, the results show that a decrease in the aspect ratio enhances the hot wall average Nusselt number as the effect of the forced convection on the hot wall increases for the shorter cavity.

References

1. Al-Amiri A., Khanafer K., Bull J., Pop I., 2007, Effect of the sinusoidal wavy bottom surface on mixed convection heat transfer in a lid-driven cavity, *International Journal Heat and Mass Transfer*, **50**, 1771-1780
2. Arefmanesh A., Najafi M., Abdi H., 2005, A meshless local Petrov-Galerkin method for fluid dynamics and heat transfer applications, *Journal of Fluids Engineering*, **127**, 647-455
3. Arefmanesh A., Najafi M., Abdi H., 2008, Meshless local Petrov-Galerkin method with unity test function for non-isothermal fluid flow, *Computer Modeling in Engineering and Sciences*, **25**, 9-23
4. Atluri S.N., Zhu T., 1998, A new meshless local Petrov-Galerkin (MLPG) approach in computational mechanics, *Computational Mechanics*, **22**, 117-127
5. Atluri S.N., Zhu T., 1998, A new meshless local Petrov-Galerkin (MLPG) approach to nonlinear problems in computer modeling and simulation, *Computer Modeling in Engineering and Sciences*, **3**, 187-196
6. Bejan A., 2004, *Convection Heat Transfer*, John Wiley & Sons, New York
7. Chamkha A.J., 2002, Hydromagnetic combined convection flow in a vertical lid-driven cavity with internal heat generation or absorption, *Numerical Heat Transfer, Part A*, **41**, 529-546
8. Guo G., Sharif M.A.R., 2004, Mixed convection in rectangular cavities at various aspect ratios with moving isothermal sidewalls and constant flux heat source on the bottom wall, *International Journal of Thermal Science*, **43**, 465-475
9. Haji Mohammadi M., 2008, Stabilized meshless Petrov-Galerkin method (MLPG) for incompressible viscous fluid flows, *Computer Modeling in Engineering and Sciences*, **29**, 75-94
10. Khanafer K., Al-Amiri A.M., Pop I., 2007, Numerical simulation of unsteady mixed convection in a driven cavity using an externally excited sliding lid, *European Journal of Mechanics – B/Fluids*, **26**, 669-687
11. Lin H., Atluri S.N., 2000, Meshless local Petrov-Galerkin (MLPG) method for convection-diffusion problems, *Computer Modeling in Engineering and Sciences*, **1**, 45-60
12. Lin H., Atluri S.N., 2001, The meshless Local Petrov-Galerkin (MLPG) method for solving incompressible Navier-Stokes equations, *Computer Modeling in Engineering and Sciences*, **1**, 117-142

13. Moallemi M.K, Jang K.S., 1992, Prandtl number effects on laminar mixed convection heat transfer in a lid-driven cavity, *International Journal Heat and Mass Transfer*, **35**, 1881-1892

14. Nasrin R., 2012, Influences of physical parameters on mixed convection in a horizontal lid-driven cavity with an undulating base surface, *Numerical Heat Transfer, Part A*, **61**, 306-321

15. Onate E., Idelsohn S., Zienkiewicz O.Z., Taylor R.L., 1996, A finite point method in computational mechanics: applications to convective transport and fluid flow, *International Journal for Numerical Methods in Engineering*, **39**, 3839-3867

16. Oztop H.F., Dagtekin I., 2004, Mixed convection in two-sided lid-driven differentially heated square cavity, *International Journal Heat and Mass Transfer*, **47**, 1761-1769

17. Sharif M.A.R., 2007, Laminar mixed convection in shallow inclined driven cavities with hot moving lid on top and cooled from bottom, *Applied Thermal Engineering*, **27**, 1036-1042

18. Zhu T., Zhang J.D., Atluri S.N., 1998, Local boundary integral equation (LBIE) for solving nonlinear problems, *Computational Mechanics*, **22**, 174-186

Manuscript received June 7, 2014; accepted for print September 5, 2014

JOURNAL OF THEORETICAL
AND APPLIED MECHANICS
53, 3, pp. 531-541, Warsaw 2015
DOI: 10.15632/jtam-pl.53.3.531

MODELING OF COMBUSTION AND PROPULSION PROCESSES OF A NEW CONCEPT GUN USING A GASEOUS PROPELLANT

Ning Liu, Fei Deng, Fei Zhou, Xiangyan Zhang

School of Mechanical Engineering, Nanjing University of Science and Technology, Nanjing, China

e-mail: liunieng@gmail.com

The combustion light gas gun (CLGG) uses a low molecular weight gas as the propellant to burn, expand and propel the projectile out of the barrel with higher muzzle velocities. In order to better understand the interior ballistic process of CLGG, an multidimensional combustion and flow model for CLGG is established. It contains unsteady Reynolds-averaged Navier-Stokes (RANS) equations, the RNG k-ε two equation turbulence models, and the Eddy-Dissipation Model (EDM) of combustion. Simulation of the interior ballistic process of CLGG is carried out with a propellant of hydrogen and oxygen mixture charged at a particular initial condition. Results show that the spherical front flames spread from the ignition points which divide the flow field as burned and unburned regions in the initial period and expand to the whole flow field subsequently. The filling error of propellants in the chamber will affect the interior ballistic performance, but the impact is relatively small.

Keywords: combustion light gas gun, interior ballistics, combustion and propulsion

1. Introduction

At present, it is difficult to further improve the performance of conventional guns using the solid propellant. In order to enhance the capabilities of tube weapon, especially the muzzle velocity, many new concept guns have been studied in the world using different kinds of energy resource, such as liquid propellant gun, electrothermal gun and electromagnetic gun. We find that the combustion of solid and liquid propellants produces hot gases with similar components which limit the muzzle velocity of the projectile due to relatively high average molecular weight. Seigel pointed out that if the high muzzle velocity is desired (above 4500 m/s), the choice of the propellant is restricted to either heated hydrogen or heated helium which have low molecular weight at high temperature (Krier and Summerfield, 1979). Therefore, decreasing the molecular weight of the gas in the chamber is a significant method to achieve a higher muzzle velocity in the advanced gun technology research based on chemical energy propulsion. A new species of tube weapon called the combustion light gas gun (CLGG) meets the demand.

A combustion light gas gun uses a low molecular weight combustible gas, such as hydrogen mixed with oxygen, as the propellant. The interior ballistic process for the new concept launching principle can be simply concluded as follows: firstly, the projectile is loaded between the forward end of the gun chamber and the barrel, and then the gun chamber forms a confined space. After carrying out the projectile loading action, the cryogenic temperature fluids, i.e. hydrogen and oxygen propellants, are fed rapidly into the combustion chamber in a liquid or near liquid state using cryogenic feed system before firing. The cryogenic hydrogen and oxygen change to gaseous propellants in the chamber after flowing into the combustion chamber and form the gas mixture in the end. At firing, the gases are ignited by an electrical or laser system. When the mix approaches the ignition point, the reaction increases rapidly and the energy releases due to combustion increasing the pressure in the combustion chamber. When the pressure is

sufficiently high, the projectile is accelerated by the expansion of hot gases to the muzzle of the exit tube with higher efficiency relative to the solid propellant. The concept has been validated by laboratory experiments and a higher muzzle velocity has been achieved. The principle scheme of CLGG is shown in Fig. 1.

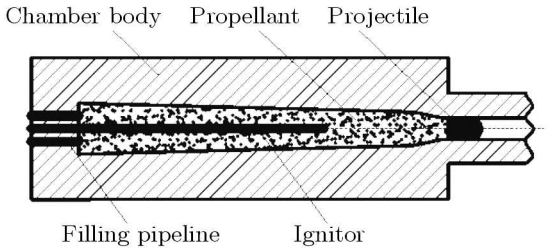

Fig. 1. Schematics of a combustion light gas gun

In fact, the concept of using a column of a low molecular gas to accelerate the projectile was applied in light gas guns (LGG) 50 years ago (Crozier and Hume, 1957). The two-stage light-gas guns are developed subsequently to accelerate projectiles up to 9-10 km/s for studies of exterior and terminal ballistics or impact experiments (Angrilli *et al.*, 2003; Munson and May, 1976). In order to further improve the muzzle velocity, the electrothermal light gas gun (ELGG) has been developed which uses electric energy to heat the hydrogen gas in the bore and achieves higher performance than the conventional LGG (Tidman and Massey, 1993). However, the hydrogen gas used in these new species of guns just plays a role of transmission of energy rather than combustion. Actually, hydrogen energy from combustion has been extensively used in many areas (Dunn, 2002), especially in the liquid rocket engines in space program since it has the best energy-to-weight ratio of any fuel (Sutton, 1992; Yeralan *et al.*, 2001). In recent years, the concern for cleaner air has aroused the interest in hydrogen as a vehicular fuel. The hydrogen-fueled internal combustion engines (HICEs) have shown the outstanding characteristics of near-zero emissions and efficiencies in excess of conventional gasoline-fueled ICEs (White *et al.*, 2006). The technology of CLGGs using hydrogen and oxygen as propellants presented here is the latest way of hydrogen application and will promote the performance of guns significantly.

The CLGG has been studied for over ten years (Kruczynski and Massey, 2007). It has been confirmed that the technology provides a minimum of 30% more muzzle energy than advanced solid propellant guns, which implies significant advantages in the firing range and projectile weight. The 16mm CLGG program was firstly conducted by GT Devices and General Dynamics Corp. Previous testing with a 16 mm CLGG achieved launching 2 gram projectile up to 4200 m/s with a hydrogen-oxygen-helium mixture, and 3800 k/s with methane-oxygen-helium mixtures. The 45mm caliber CLGG program began in 1994 and all tests firings have been conducted by Utron Inc. At present its 155mm CLGG has been set up and the firing tests have occurred. The interior ballistic study of CLGG has been carried out gradually in recent years by numerical methods. Liu and Zhang (2011) established a quasi-dimensional interior ballistic model of CLGG which assumed the space in the chamber to be composed of the burned region and the unburned region. Deng *et al.* (2013) analyzed the influence of the ignition process and the initial condition on interior ballistic characteristics of CLGG by the CFD method.

In the design and development of CLGG, an increase in the interior ballistic prediction capabilities can improve the CLGG hardware reliability and reduce the design and development costs related to experimental activities and firing tests. Both these targets require accurate modeling and numerical simulation as well as reasonable physical understanding of the complex interior ballistics launching phenomenon, which characterize the CLGG behavior and performance during the entire interior ballistic period. This paper is devoted to present the results of the interior ballistics modeling and numerical simulation of CLGG by means of unsteady

Reynolds-averaged Navier-Stokes (RANS) equations, RNG k-ε two equation turbulence models, and the Eddy-Dissipation Model (EDM) of combustion.

2. Model of interior ballistics

2.1. Basic assumptions

The CLGG is focused on providing high velocity projectile launch. It breaks with the traditional solid propellant technology. The combustion process of the premixed gases of the CLGG is complicated. In order to describe the combustion process in the chamber using a mathematical model, the following basic assumptions are proposed for the CLGG system.

(1) The combustion chamber is sealed and no mass leaks during ballistic cycle.

(2) Geometry of the combustion chamber is axisymmetric.

(3) The ignition process is ignored but some energy around the ignition points is taken into acount.

(4) The projectile moves down the barrel under the propulsion of base pressure until it reaches the starting pressure.

(5) The mixing time-scale of hydrogen and oxygen propellants is much larger than the reaction one.

2.2. Governing equations

The combustion and flow process in the chamber is a three dimensional unsteady problem. The governing equations for chemically reacting viscous flows are the compressible Navier-Stokes equations with chemical source terms for the mixture composed of gaseous propellant species, which are given as follows:

— continuity equation

$$\frac{\partial \rho}{\partial t} + \nabla \cdot (\rho \mathbf{u}) = 0 \tag{2.1}$$

— momentum equation

$$\frac{\partial \rho \mathbf{u}}{\partial t} + \nabla \cdot (\rho \mathbf{u}\mathbf{u}) = -\nabla p + \nabla \cdot [\mu(\nabla \mathbf{u} + \nabla \mathbf{u}^{\mathrm{T}})] + \rho \mathbf{g} + \mathbf{F} \tag{2.2}$$

— energy equation

$$\frac{\partial \rho e}{\partial t} + \nabla \cdot [\mathbf{u}(\rho e + p)] = \nabla \cdot (k_{eff} \nabla T) + S_h \tag{2.3}$$

— species equations

$$\frac{\partial \rho c_i}{\partial t} + \nabla \cdot (\rho \mathbf{u} c_i) = \nabla \cdot [D_i \nabla (\rho c_i)] + S_i \tag{2.4}$$

where ρ is the total density, $\mathbf{u}$ is the velocity vector, p is the pressure, T is the temperature, e is the total energy per unit mass, c_i is the volume concentration of species i, $\mathbf{F}$ is the external force source, S_h is the energy source, s_i is the mass production rate of species i due to chemical reactions, k_{eff} is the thermal conductivity which is determined by

$$k_{eff} = k_l + c_p \frac{\mu_t}{\mathrm{Pr}} \tag{2.5}$$

where k_l is the thermal conductivity of the mixture in laminar flow, Pr is the Prandtl constant with a value of 0.71-0.75.

2.3. Turbulence model

Turbulence directly affects the mixing and the combustion process in CLGG. Adequate prediction of turbulence behaviour is necessary for better understanding the CLGG performance. The RNG k-ε turbulence model derived by Yakhot and Orszag (1986) based on the Renormalization Group theory has been developed to study a number of complex flows. It yields excellent results in cases where the standard k-ε model predictions are unsatisfactory. The RNG k-ε model follows the two-equation framework of the turbulent kinetic energy equation and the turbulent energy dissipation rate equation which could be formulated as

$$\begin{aligned}
&\frac{\partial \rho k}{\partial t} + \nabla \cdot (\rho \mathbf{u} k) = \nabla \cdot \Big[\Big(\mu + \frac{\mu_t}{\sigma_k}\Big)\nabla k\Big] + P_k + P_{kb} - \rho\varepsilon \\
&\frac{\partial \rho \varepsilon}{\partial t} + \nabla \cdot (\rho \mathbf{u} \varepsilon) = \nabla \cdot \Big[\Big(\mu + \frac{\mu_t}{\sigma_\varepsilon}\Big)\nabla \varepsilon\Big] + \frac{\varepsilon}{k}[C_{\varepsilon 1}(P_k + P_{\varepsilon b} - C_{\varepsilon 2}\rho\varepsilon]
\end{aligned} \tag{2.6}$$

where the model constants are given as $C_{\varepsilon 1} = 1.42$, $C_{\varepsilon 2} = 1.68$. P_k is the turbulence production due to viscous forces, which is modeled using

$$P_k = \mu_t \nabla \mathbf{u} \cdot (\nabla \mathbf{u} + \nabla \mathbf{u}^{\mathrm{T}}) - \frac{2}{3}\nabla \cdot \mathbf{u}(3\mu_t \nabla \cdot \mathbf{u} + \rho k) \tag{2.7}$$

P_{kb} and $P_{\varepsilon b}$ represent the influence of the buoyancy forces, which are described below. The buoyancy production term P_{kb} is given as

$$P_{kb} = -\frac{\mu_t}{\rho} g \nabla \rho \qquad P_{\varepsilon b} = C_3 \max(0, P_{kb}) \tag{2.8}$$

where C_3 is the dissipation coefficient, $C_3 = 1$.

The turbulence viscosity μ_t could be expressed as follows

$$\mu_t = \rho C_\mu \frac{k^2}{\varepsilon} \tag{2.9}$$

where k is the turbulence kinetic energy, ε is the turbulence energy dissipation rate, and C_μ is the empirical coefficient with the value of 0.0845.

2.4. EDM combustion model

The eddy dissipation model (EDM) is based on the concept that the chemical reaction rate is fast relative to the transport processes, i.e. mixing rates, in the flow. When reactants mix at the molecular level, they instantaneously form products and there is no kinetic control of the reaction process. In turbulent flows, this mixing time is dominated by the eddy properties and the rate is proportional to the mixing time defined by the turbulent kinetic energy k and dissipation ε

$$\rho \overline{w}_{fu} = \alpha \overline{\rho} \frac{\varepsilon}{k} \min\Big(\overline{Y}_{fu}, \frac{\overline{Y}_{ox}}{s}, \beta \frac{\overline{Y}_{pr}}{s+1}\Big) \tag{2.10}$$

where $\overline{w}_{fu}$ is the average fuel burning rate, $\overline{Y}_{fu}$, $\overline{Y}_{ox}$ and $\overline{Y}_{pr}$ are average concentrations of the fuel, oxidizer and combustion products, respectively, α and β are adjustable parameters.

2.5. Auxiliary equations

The auxiliary equations are comprised of the equation of motion of the projectile and the equation of gas state.

The equation of projectile motion can be written as

$$\frac{dv_p}{dt} = \frac{p_d A_0}{\varphi_p m_p} \tag{2.11}$$

where m_p is the projectile mass, v_p is the projectile velocity, A_0 is the projectile base area, p_d is the projectile base pressure, φ_p is the projectile motion coefficient of second work.

The pressure in the chamber is much higher than that in normal industrial conditions. Therefore, the ideal gas equation is not suitable for the CLGG interior ballistic model. The Abel-Noble equation is applied in the paper, which is widely used in traditional solid propellant guns

$$p\Big(\frac{1}{\rho} - \alpha\Big) = RT \tag{2.12}$$

where α is the covolume.

2.6. Boundary condition and numerical method

For the transient combustion and flow problem, the appropriate initial and boundary conditions that reflect the real physical phenomenon are significant for numerical simulation. For this case, it is supposed that the gaseous propellants are well mixed before firing in the chamber with initial pressure p_0 and temperature T_0, as well as chamber volume V_0. Boundary conditions used in the simulation include no slip boundary for solid walls and moving boundary for the base face of the projectile after moving. The moving grids technique is used in the model to deal with the projectile movement. The governing equations are discretized using an element-based finite volume method. An implicit second order accurate upwind finite volume scheme is used for convection terms while the implicit second order backward Euler scheme for the transient terms. The shape functions following the standard finite element approach are applied for all the diffusion terms.

3. Results and discussions

3.1. Verification of the simulation results

The experimental data of 45mm smooth bore CLGG has been used to compare with the simulation results in order to verify the ability of the model to predict the combustion of gaseous propellants and the main performances of the interior ballistics (Kruczynski and Massey, 2007). The experimental parameters are listed in Table 1. Similar to most of the interior ballistics considerations, we supposed that the ignition occurs when the mixture temperature reaches a specified ignition value by heating the gas along the chamber axis. The simulation results of the muzzle velocity and the maximal pressure at the chamber compared with the reference results are listed in Table 2. The numerical and measured pressure history at the breech end is also shown in Fig. 2 where the experimental curve is shifted to approximately match the time of the calculated maximum pressure, i.e. about 6 ms. Overall, good agreement has been achieved between the model predictions and experimental measurements. We can observe that both the experimental and computed curves present some pressure waves which should be paid special attention to in order to avoid uncontrollable combustion in the chamber. The histories of projectile velocity and oxygen mass fraction are also shown in Figs. 3a and 3b, respectively. It can be observed in Fig. 3b that the oxygen mass fraction is about 0.045 until the projectile reaches the muzzle, i.e. 7.9% of charged oxygen is not burnt. This phenomenon will be demonstrated in the next Section.

Table 1. Initial parameters of the 45 mm CLGG (Kruczynski and Massey, 2007)

Parameter	Value
Projectile mass (m_p)	0.52 kg
Volume of power chamber (V_0)	5000 ml
Total chemical energy of the propellant (E)	3 MJ
Initial pressure (p_0)	38 MPa
Mole ratio between hydrogen and oxygen	8:1
Tube length (L)	4500 mm
Projectile starting pressure (p_s)	172.4 MPa
Number of ignition points	5

Table 2. Comparison of experimental and computed results

Parameter	Maximum pressure [MPa]	Muzzle velocity [ms^{-1}]
Experimental value	225	1700
Simulation value	229	1706

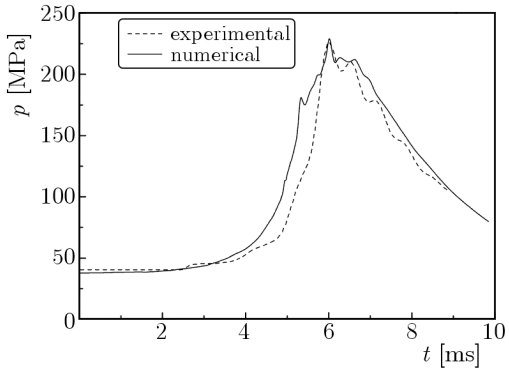

Fig. 2. Comparison between numerical and measured pressure-time traces at the breech end

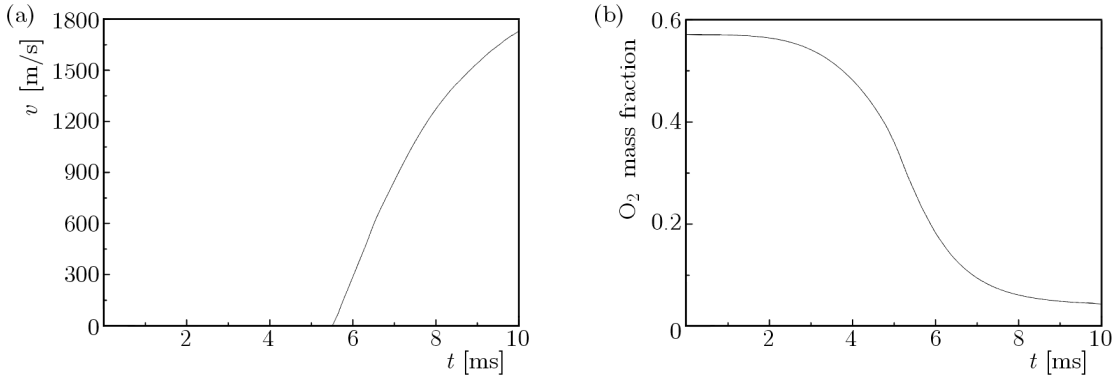

Fig. 3. (a) History of projectile velocity; (b) history of oxygen mass fraction

3.2. Interior ballistic performance of CLGG

Figure 4 shows the axial pressure distribution curves in the bore at different times where the endpoints of the curves form the base pressure as a function of the projectile displacement. The pressure difference between the breech end and the projectile base is observed in Fig. 4, and this difference becomes flat after the pressure reaches its peak value.

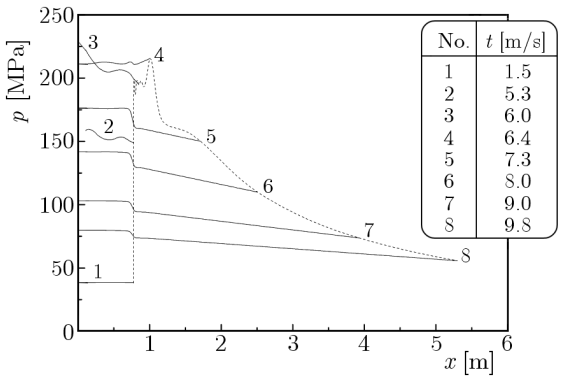

Fig. 4. Pressure distribution on the axis at different time

Figure 5 shows the temperature contours of the gun chamber. The spherical front flame spread from the five ignition points placed on the axis. Therefore, the flow field is divided into burned and unburned regions clearly by the front flame. At about 4.3 ms, the five independent burned regions begin to get in touch with each other and merge into an integral one later. It is interesting to note that the five high temperature cores in the chamber move down the tube following the gas flow after the projectile movement.

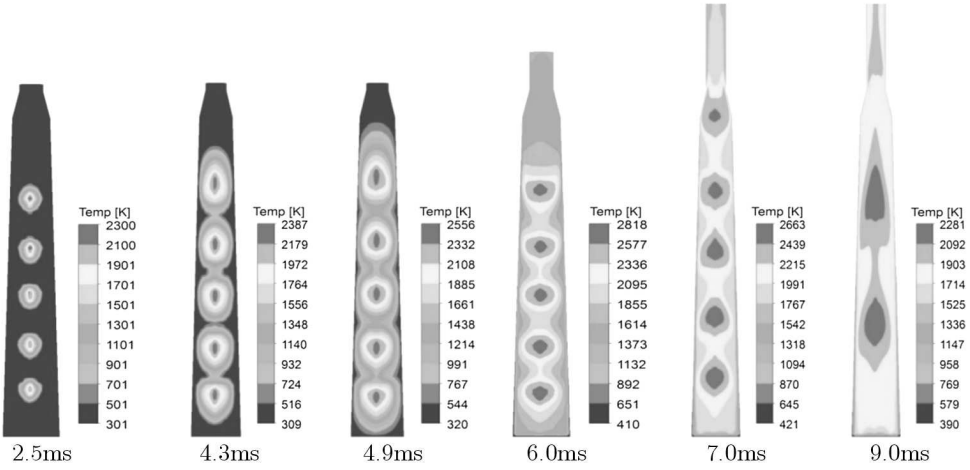

Fig. 5. Temperature contours in the gun chamber at different times

The O_2-H_2 mixture is filled in the chamber as the propellant rich with hydrogen in order to decrease the average molecular weight and to sufficiently cool the bore surface. Therefore, the oxygen quantity that participates in combustion determines the total chemical energy released during a ballistic cycle and affects the muzzle velocity of the projectile. The oxygen mass fraction distributions at different times are shown in Fig. 6. Same as that seen in Fig. 5, spherical burned regions are clearly visible around the ignition points. The oxygen quantity in the chamber decreases gradually as the burned regions expand until the oxygen burns out in most region of the field. It is important to note that there is still a certain amount of oxygen remained at the breech region until the exit of the projectile through the muzzle. This is considered to be due to weak turbulence at the breech end which leads to incomplete combustion of oxygen using the EDM model.

Figure 7 represents the pressure contours in the chamber. The pressure waves with small amplitude are observed before the pressure increasing to the peak value, whereas the pressure

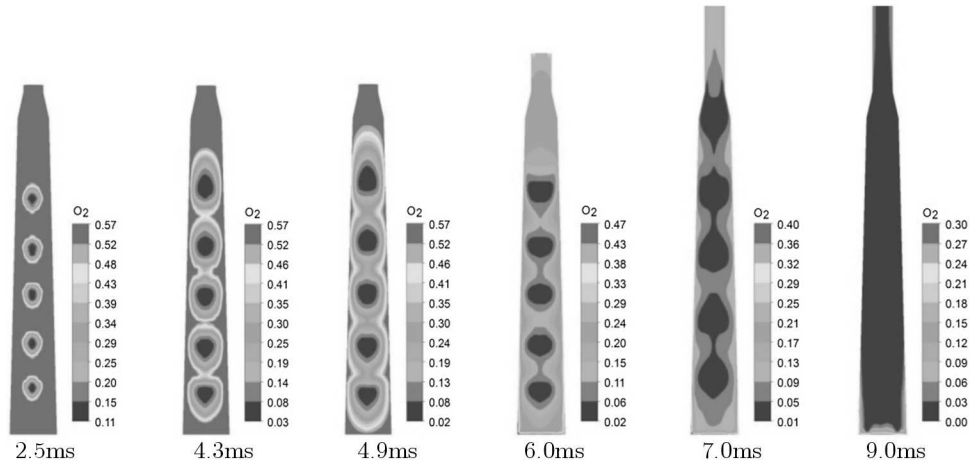

Fig. 6. Distributions of the oxygen mass fraction at different times

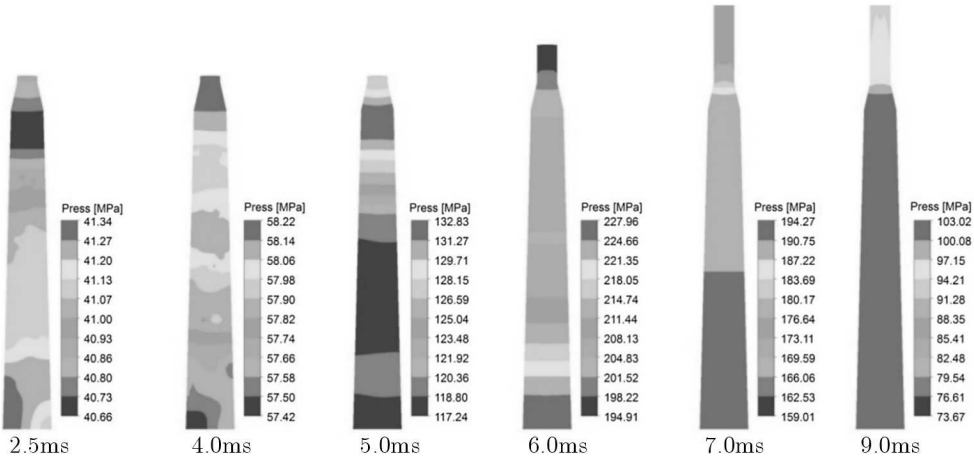

Fig. 7. Pressure distributions in the gun chamber at different times

waves disappears subsequently and the pressure decreases gradually from the breech end towards the projectile base after the maximum pressure. We can observe the distribution uniformity of pressure with time in the chamber which is also shown in Fig. 4 where the pressure distributions on the axis are plotted at different times.

4. Effects of parametric variations on the interior ballistic performance

4.1. Effect of the propellant components ratio

In order to analyze the effect of the propellant components ratio on the interior ballistic performance, we change the initial amount of hydrogen and remain the chemical energy constant. As hydrogen is rich in the chamber, it means that the amount of oxygen should remain constant. The mixture could be written as $n\mathrm{H}_2 + \mathrm{O}_2 + 2\mathrm{He}$, and we calculate three cases taking the ratio value n of 4, 8 and 12. The increasing amount of hydrogen raises the initial pressure in the chamber which enhances the maximum pressure and muzzle velocity of the projectile as presented in Figs. 8a and 8b. However, it should be noticed that the temperature significantly decreases as the amount of hydrogen increases in the chamber, as shown in Fig. 8c. It is also worthwhile to point out that for the increasing amount of hydrogen, a longer ignition time is required with the same ignition energy.

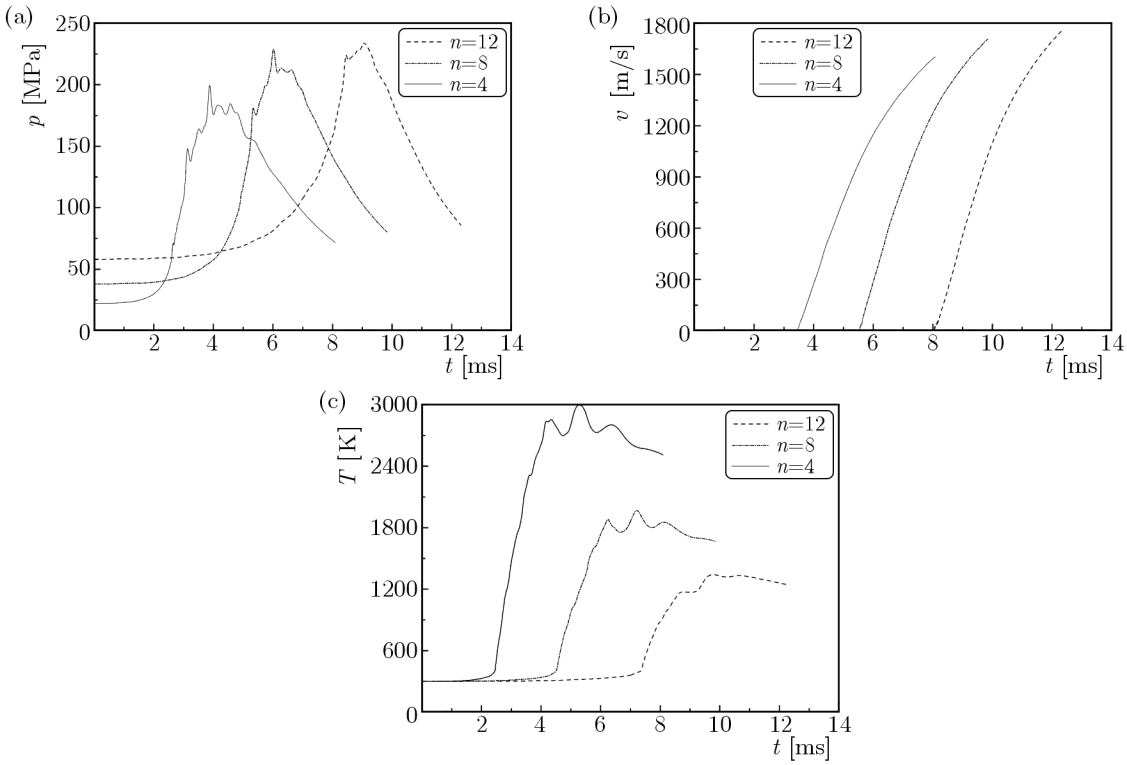

Fig. 8. Predicted pressure-time curves (a), velocity-time curves of the projectile (b) and temperature-time curves (c) for different ratios n

4.2. Effect of the filling accuracy

In the light of previous research, it has been found that one of the key technologies of CLGG is the filling accuracy control of gaseous propellants. In order to investigate the effect of filling error on the ballistic performance, we repeat the previous calculation while varying the initial amount of oxygen. We calculate the case with oxygen mass relatively increased by 10%. A comparison of pressure curves between the case with the filling error and the accurate one is shown in Fig. 9a.

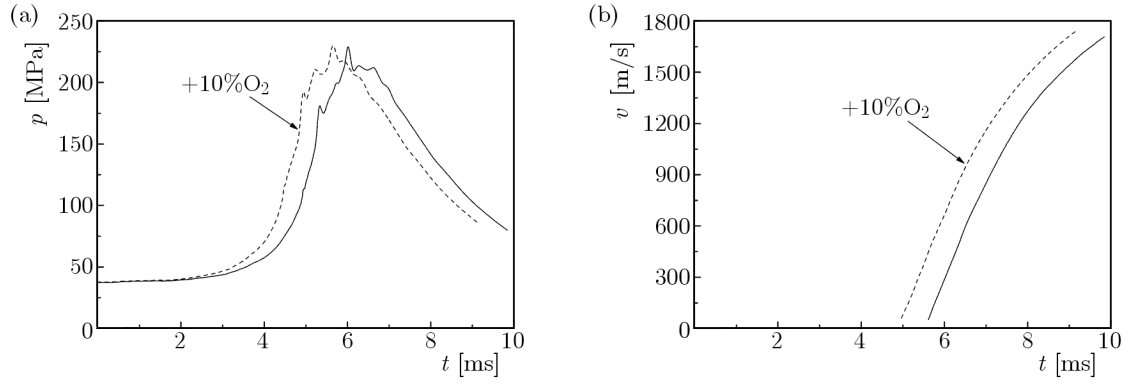

Fig. 9. Comparison of pressure curves (a) and projectile velocity curves (b) with oxygen mass relatively increased by 10%

It can be seen that the increasing of the amount of oxygen increases the pressure raising rate while the other components remain constant. The maximum pressure increases slightly from 229 MPa to 230 MPa, i.e. relatively increased by 0.4%. Meanwhile, the muzzle velocity shown in Fig. 9b varies from 1706 m/s to 1740 m/s, i.e. increased by 2% due to the additional oxygen

filled in the chamber. Thus, the filling error of propellants in the chamber affects the interior ballistic performance, but the amplitudes are relatively small.

5. Conclusions

The development of CLGG aims at providing a long range fire support such as deep strike and effective shore support, other than laboratory instruments. This paper developed a 3D combustion and flow model to study the complex interior ballistic process of CLGG. The numerical simulations based on the CFD method have shown the ability of the model to predict and analyze the main internal ballistics launching phenomenon, which provides a new approach to support and validate the experimental effort. The main conclusions are summarized as follows:

- Good agreement between the predicted and experimental results is obtained except for the ignition process which is of significant interest for future studies.
- The spherical front flames spread from the ignition points which divide the flow field into burned and unburned regions in the initial period and expand to the whole flow field subsequently. This phenomenon may help one to develop the quasi-dimensional interior ballistic model of CLGG.
- The increasing amount of hydrogen enhances the initial pressure, maximum pressure and muzzle velocity of the projectile, while the temperature significantly decreases in the process.
- The filling error of propellants in the chamber affects the interior ballistic performance, but the impact is relatively small.

References

1. Angrilli F., Pavarin D., De Cecco M., Francesconi A., 2003, Impact facility based upon high frequency two-stage light-gas gun, *Acta Astronautica*, **53**, 3, 185-189
2. Crozier W., Hume W., 1957, High-velocity, light-gas gun, *Journal of Applied Physics*, **28**, 8, 892-894
3. Deng F., Zhang X.Y., Liu N., 2013, Influences of ignition process and initial conditions on interior ballistic characteristics of combustion light gas gun (in Chinese), *Explosion and Shock Waves*, **33**, 5, 551-555
4. Dunn S., 2002, Hydrogen futures: toward a sustainable energy system, *International Journal of Hydrogen Energy*, **27**, 3, 235-264
5. Hirsch C., 2007, *Numerical Computation of Internal and External Flows (second edition): The Fundamentals of Computational Fluid Dynamics*, Butterworth-Heinemann, Oxford
6. Krier H., Summerfield M., 1979, Interior ballistics of guns, *Progress in Astronautics and Aeronautics*, **66**, AIAA, New York
7. Kruczynski D., Massey D., 2007, *Combustion Light Gas Gun Technology Demonstration*, ADA462130
8. Liu N., Zhang X.Y., 2011, Quasi-dimensional interior ballistic model and numerical simulation of combustion light gas gun, *Proceedings of the 26th International Symposium on Ballistics*, 414-419
9. Munson D., May R., 1976, Interior ballistics of a two-stage light gas gun using velocity interferometry, *AIAA Journal*, **14**, 2, 235-242
10. Sutton G.P., 1992, *Rocket Propulsion Elements – an Introduction to the Engineering of Rockets*, Wiley-Interscience, New York

11. Tidman D.A., Massey D.W., 1993, Electrothermal light gas gun, *IEEE Transactions on Magnetics*, **29**, 1, 621-624

12. White C.M., Steeper R.R., Lutz A.E., 2006, The hydrogen-fueled internal combustion engine: a technical review, *International Journal of Hydrogen Energy*, **31**, 10, 1292-1305

13. Yakhot V., Orszag S., 1986, Renormalization group analysis of turbulence. I. Basic theory, *Journal of Scientific Computing*, **1**, 3-51

14. Yeralan S., Pal S., Santoro R.J., 2001, Experimental study of major species and temperature profiles of liquid oxygen/gaseous hydrogen rocket combustion, *Journal of Propulsion And Power*, **17**, 4, 788-793

Manuscript received May 22, 2014; accepted for print October 3, 2014

JOURNAL OF THEORETICAL AND APPLIED MECHANICS
53, 3, pp. 543-555, Warsaw 2015
DOI: 10.15632/jtam-pl.53.3.543

A NUMERICAL APPROACH TO THE STANDARD MODEL OF WATER HAMMER WITH FLUID-STRUCTURE INTERACTION

Sławomir Henclik
Institute of Fluid-Flow Machinery, Polish Academy of Sciences, Gdańsk, Poland
e-mail: shen@imp.gda.pl

In the classic water hammer (WH) theory, 1D liquid flow in a quasi-rigid pipe is assumed. When the pipe is flexible or is fixed to the foundation with elastic supports, the dynamic fluid structure interaction (FSI) should be taken into account for more accurate modelling of the system behaviour. The standard model of WH-FSI for a straight pipe reach is governed by fourteen hyperbolic partial differential equations of the first order, two for 1D liquid flow and twelve for 3D motion of the pipe. This model is presented in the paper and an algorithm for its numerical solution based of the method of characteristics is proposed. Basic boundary conditions (BC) are shortly discussed. The important condition at the junction of two sub-pipes fixed to the foundation with a viscoelastic support is presented in details and a general method of its solution is proposed.

Keywords: water hammer, transient pipe flow, fluid-structure interaction, standard model, method of characteristics

1. Introduction

The water hammer (WH) phenomenon has been of scientific interest for over a century. Extensive studies on this effect can be found in the works of Wylie and Streeter (1993), Almeida and Koelle (1992), Adamkowski (2013) or Ghidaoui *et al.* (2005). WH is a result of a sudden change in pipe flow conditions due to valves operation, hydraulic machinery load variation or other reasons. During the transient the changes in liquid velocity result in pressure variations, which may travel along the pipe producing loads of the structure (pipe, supports, hydraulic devices) and perturbations to the system functioning or even its damage. WH can appear in various pipe flow systems like hydro-power installations, nuclear reactor cooling systems, engine fuel injection pipes and others. In some cases, the pipe is stiff and does not move, so the action of the liquid onto the pipe is considered as quasi-static. When the pipe is elastic or the whole piping can move on its supports, this motion forced by the unsteady flow, influences in reverse the flow variables, and the dynamic fluid-structure interaction (FSI) has to be taken into account. These effects has been examined by scientists for a few decades and the works of Wiggert *et al.* (1987), Tijsseling and Lavooij (1990), Wang and Tan (1997) or Wiggert and Tijsseling (2001) can be pointed as the reference. A specific and a complex area of potential application of WH-FSI concepts is the phenomenon of blood flow in human arteries, being an important area of research, discussed e.g. by Alastruey *et al.* (2012).

Three main factors responsible for FSI coupling are pointed in literature. The weakest is the friction between the pipe-wall and the liquid. Due to physics of WH-FSI, an unsteady friction model should be used for modelling of this effect, and one of the existed models used for classic WH, discussed e.g. by Adamkowski and Lewandowski (2006), Vitkovsky *et al.* (2006) or Urbanowicz and Zarzycki (2012) could be adopted. However, the quasi-steady model is still quite popular and often used because of its simplicity. The Poisson effect is responsible for the

second FSI coupling factor. Pressure variations induce circumferential stresses and strains in the pipe-wall which are accompanied by longitudinal ones. The latter propagates along the pipe faster than the pressure wave in the liquid and produces in the reverse action additional pressure oscillations known as the precursor (PC) wave. The third and the strongest FSI mechanism is the junction coupling (JC) effect which appears at pipe bends, knees, ends, valves, reductions, etc. In fact, this phenomenon is especially important if the pipeline is able to move as a whole structure. Due to this motion, strong interaction between the pipe and the liquid variables can occur. The motion of the junction can be also responsible for coupling between different modes of structural vibrations of neighbouring sub-pipes. As far as the friction and Poisson couplings are modelled by certain terms in the governing equations, JC is modelled by boundary conditions (BC). The JC mechanism can also be responsible for producing the WH effect by sudden motion of the structure.

In the classic water hammer theory a stiff and immovable pipe with one dimensional (1D) liquid flow is assumed. FSI is considered to be a quasi-static effect and the pipe-wall elasticity is taken into account only within the formula for the celerity of elastic waves in the liquid. Two hyperbolic partial differential equations (PDE) of the first order are used for description of the liquid flow which allows one to find the pressure p and velocity v as a function of the position x and time t. When the dynamic FSI is taken into account, two main approaches are proposed in the literature. The simpler consists of four PDEs, two for 1D liquid flow and the other two for the longitudinal motion of the straight pipe reach. These four hyperbolic equations form the four equations (4E) model of WH-FSI. In this model, the 1D approximation neglects the radial motion of the pipe and the liquid and is valid for low frequency assumption. When 3D motion of the pipe is possible, additional ten equations of lateral and torsional movement produce altogether the fourteen equations (14E) standard model of WH-FSI. For numerical modelling of the WH behaviour, the method of characteristics (MOC) is frequently used. When FSI effects are taken into account, the finite elements method (FEM) can be alternatively exploited to the structural equations, which produces the MOC-FEM technique. Pure FEM based approach are also proposed. On the other hand, the fully MOC based algorithm is proposed in the fundamental paper of Wiggert *et al.* (1987), however only general ideas of their method were presented there. A thorough presentation of the MOC approach is included in the work of Tijsseling (1993), who applied his model to a 2D pipeline system. In fact, for structural analyses, the FEM technique can be considered to be more suitable, however using a unified MOC approach to the liquid as well as to the structure is justified due to the wavy nature of the phenomenon.

In the current paper, the standard model of WH-FSI is described and a MOC based method of numerical solution for a 3D pipeline system is presented. The main steps of the algorithm are discussed and some details and novel approaches are especially explained. An important part of the method is the BC at the junction of two sub-pipes fixed to the foundation with a viscoelastic support, which is formulated as a differential equation of motion. The solution to this equation is found and presented in a compact form, convenient for numerical computations. The author does not know any other work where such a detailed 3D treatment of that problem is considered and solved.

2. Assumptions and governing equations

The coordinate system and variables used in the current approach are presented in Fig. 1.

The pipe of length L, wall thickness e, diameter D is straight, prismatic, thin-walled ($e/D \ll 1$) and slender ($D/L \ll 1$). The pipe material is linearly elastic and no buckling appears. The flow velocity v is of little relativity to the elastic waves celerity c ($v/c \ll 1$). The liquid is weakly compressible, linearly elastic and its density changes are small (pressures are low relative to the bulk modulus K, $p/K \ll 1$). The low frequency assumption applied means

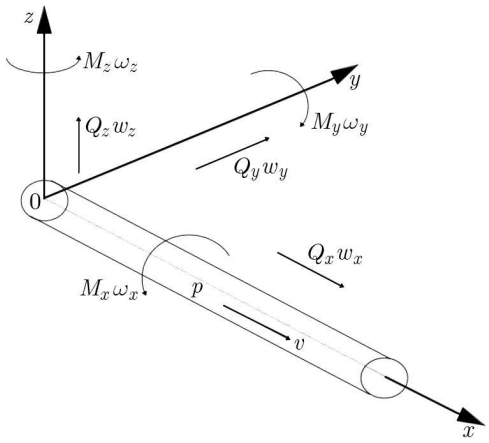

Fig. 1. Variables and coordinate system used for modelling of the WH-FSI phenomenon

neglecting of the radial inertia effects of the liquid and the pipe wall. The friction between the pipe and the liquid is taken into account and a quasi-steady model is assumed. The structural damping of the pipe material and two-phase flow are assumed not to be present. The motion of the system for a straight pipe reach is described by four uncoupled sets of PDEs. The first one consists of four equations for longitudinal motion of the system. The second set of two equations governs torsional waves in the pipe. Another two sets of four PDEs each define the lateral motion of the pipe in two perpendicular planes – vertical ($0zx$) and non-vertical ($0yx$). It is assumed that the liquid does not interact with the pipe in torsional vibrations. For the lateral movement, the Timoshenko beam model is used with the liquid being accounted as an added mass for linear motion. Liquid rotational inertia effects and the Coriolis force due to bending angular velocity are neglected.

Four equations govern the longitudinal motion of the system. Their detailed derivation can be found e.g. in Wang and Tan (1997). Two of the equations describe 1D liquid flow

$$\frac{\partial v}{\partial t}+\frac{1}{\rho}\frac{\partial p}{\partial x}=-g\sin\alpha-\frac{4\tau_s}{\rho D}\qquad\qquad \frac{\partial v}{\partial x}+\frac{1}{\rho c^2}\frac{\partial p}{\partial t}=2\nu\frac{\partial w_x}{\partial x} \tag{2.1}$$

where ν is the Poisson coefficient and ρ is liquid density. The pressure wave celerity c is given as

$$c=\sqrt{\frac{K}{\rho}}\frac{1}{\sqrt{1+\chi(1-\nu^2)}} \tag{2.2}$$

The right-side factor in the formula above expresses the influence of pipe-wall elasticity. The parameter χ used in it is defined as

$$\chi=\frac{KD}{Ee} \tag{2.3}$$

The other two equations of the 4E model govern the longitudinal pipe motion defined with velocity w_x and stresses σ_x ($\sigma_x = Q_x/A_s$, A_s is the pipe cross-section area)

$$\frac{\partial w_x}{\partial t}-\frac{1}{\rho_s}\frac{\partial \sigma_x}{\partial x}=-g\sin\alpha+\frac{\tau_s}{e\rho_s}\qquad\qquad \frac{\partial w_x}{\partial x}-\frac{1}{\rho_s c_s^2}\frac{\partial \sigma_x}{\partial t}=-\frac{\nu D}{2Ee}\frac{\partial p}{\partial t} \tag{2.4}$$

The pipe material density is ρ_s and the longitudinal elastic waves travel in it with the celerity c_s

$$c_s=\sqrt{\frac{E}{\rho_s}} \tag{2.5}$$

The gravitational term (g is acceleration of gravity) depends on the angle α between the horizon and the pipe. One can easily identify the components responsible for the Poisson and friction couplings. For the current quasi-steady liquid pipe-wall friction model, the following formula is used for determination of the shear stresses τ_s

$$\tau_s = \frac{\lambda\rho}{8}(v - w_x)|v - w_x| \tag{2.6}$$

In the equation above, λ is the Darcy-Weisbach friction factor and should be adequately determined. The pipe torsional vibrations are governed by the standard two equations (like for the rod)

$$\frac{\partial\omega_x}{\partial t} - \frac{1}{\rho_s I_0}\frac{\partial M_x}{\partial x} = 0 \qquad \frac{\partial\omega_x}{\partial x} - \frac{1}{GI_0}\frac{\partial M_x}{\partial t} = 0 \tag{2.7}$$

where M_x [Nm] is torsional moment of the force, ω_x [1/s] – angular torsional velocity, I_0 [m^4] – pipe cross-section polar moment of inertia and G [Pa] – shear modulus of the pipe material, $G = E/[2(1+\nu)]$. The shape of the above equations is the result of no-interaction assumption between the pipe and the liquid in torsional vibrations. However, if non-zero amount of accompanying water is going to be taken into account, then the factor $\rho_s I_0$ in Eq. $(2.7)_1$ should be adequately increased.

In the lateral motion at the non-vertical plane the governing equations for the Timoshenko beam model (Timoshenko and Young, 1955; Meirovitch, 1967) and the assumed coordinate system are found to be

$$\begin{aligned} &\frac{\partial w_y}{\partial t} + \frac{1}{m}\frac{\partial Q_y}{\partial x} = 0 && \frac{\partial w_y}{\partial x} + \frac{1}{T}\frac{\partial Q_y}{\partial t} = \omega_z \\ &\frac{\partial \omega_z}{\partial t} - \frac{1}{b}\frac{\partial M_z}{\partial x} = -\frac{1}{b}Q_y && \frac{\partial \omega_z}{\partial x} - \frac{1}{s}\frac{\partial M_z}{\partial t} = 0 \end{aligned} \tag{2.8}$$

The variables above are the linear velocity w_y [m/s], shear force Q_y [N], bending angular velocity ω_z [1/s] and the bending moment of force M_z [Nm]. The parameters m, b, s, T are introduced for more clear presentation of the model and the assumptions. They are defined in the following way

$$m = \rho_s A_s + \rho A_c = \rho_s A_s(1+\xi) \qquad T = \kappa G A_s \qquad b = \rho_s I \qquad s = EI \tag{2.9}$$

The form of equations $(2.9)_1$ and $(2.9)_3$ results from the water-in-pipe accounting method – the water is taken into account in the former, not in the latter. Other possibilities can be tested by proper modelling of these parameters. In Wiggert *et al.* (1987) the expression for b has included the water component as well and the current assumption was proposed by Tijsseling (1993). In fact, the influence of the weighted water component in b can be numerically tested, calibrated and concluded. The parameter ξ in $(2.9)_1$ expresses the ratio of the water-to-pipe mass and is given in

$$\xi = \frac{\rho D}{4\rho_s e} \tag{2.10}$$

In Eq. $(2.9)_3$ I [m^4] is the axial moment of inertia of the pipe cross-section, and κ in $(2.9)_2$ is the shear coefficient. A simple approach gives for a circular tube the value of $\kappa = 0.5$, but due to more detailed analyses, slightly larger values are estimated. $\kappa = 0.5+\nu/(8+6\nu)$ was proposed by Cowper (1967) and $\kappa = 0.5+\nu/(4+2\nu)$ was estimated by Hutchinson (2001). In the vertical $0xz$

plane, the equations are similar (the proper signs are the result of dextrose coordinate system) and the gravity term is also included

$$\begin{aligned} &\frac{\partial w_z}{\partial t}+\frac{1}{m}\frac{\partial Q_z}{\partial x}=-g\cos\alpha \qquad && \frac{\partial w_z}{\partial x}+\frac{1}{T}\frac{\partial Q_z}{\partial t}=-\omega_y \\ &\frac{\partial \omega_y}{\partial t}+\frac{1}{b}\frac{\partial M_y}{\partial x}=\frac{1}{b}Q_z && \frac{\partial \omega_y}{\partial x}+\frac{1}{s}\frac{\partial M_y}{\partial t}=0 \end{aligned} \tag{2.11}$$

3. Transformation of the equations

3.1. Longitudinal waves

The fundamental step of the MOC technique is linear transformation of the governing equations to get CE, which have the partial derivatives against x and t formed into absolute derivatives with time for a certain dependence $x(t)$. Such transformation applied to longitudinal equations (2.1) and (2.4) results in two sets of two equations each. They govern two coupled waves – WH and PC ones. The former propagates with the celerity c_0 (equations C0) and the equations C1 govern the PC wave which propagates with the celerity c_1. Because of the Poisson coupling, these celerities are slightly different than the original celerities c and c_s given with Eqs. (2.2) and (2.5). Moreover, these waves are not pure liquid and pure pipe waves as can be seen below. The C0 equations are

$$\frac{d}{dt}(v+Sw_1)+\varepsilon\frac{d}{dt}(r-\widetilde{S}q_1)=-(1+S)g\sin\alpha-(1-R)\frac{4\tau_s}{\rho D} \tag{3.1}$$

They are valid for the positive and negative characteristic slope ($\varepsilon=\pm1$) and the dependence $x(t)$ defined with $dx/dt=\varepsilon c_0$. The celerity of the WH wave is

$$c_0=\frac{c}{\sqrt{A}} \tag{3.2}$$

In Eq. (3.1), unified variables are used. The unified velocity w_1 is just the pipe section longitudinal velocity w_x. The unified pressure and longitudinal stresses are given by

$$r=\frac{p}{\rho c_0} \qquad q_1=\frac{\sigma_x}{\rho_s c_1} \tag{3.3}$$

The following pair of equations ($\varepsilon=\pm1$) referred to as C1 governs the PC wave

$$\frac{d}{dt}(Rv-w_1)+\varepsilon\frac{d}{dt}(\widetilde{R}r+q_1)=(1-R)g\sin\alpha-(1+S)\frac{\tau_s}{\rho_s e} \tag{3.4}$$

The characteristic slope is $dx/dt=\varepsilon c_1$ and the PC wave celerity c_1 is given as

$$c_1=c_s\sqrt{A} \tag{3.5}$$

The presented transformations are valid if the below relation holds

$$1-\gamma+\chi>0 \tag{3.6}$$

where

$$\gamma=\frac{K\rho_s}{E\rho} \tag{3.7}$$

Relation (3.6) is valid for all practical cases, and for water in metal pipe and thin-walled assumption is even stronger (> 1). It is useful to define the following parameter B

$$B = \frac{1}{2}\Big[(1-\gamma+\chi) + \sqrt{(1-\gamma+\chi)^2 + 4\gamma\chi\nu^2}\Big] \tag{3.8}$$

The correcting parameter A, which is slightly greater than 1 ($A = 1$ for $\nu = 0$) can now be presented as

$$A = 1 + \frac{\chi\nu^2}{B - \chi\nu^2} \tag{3.9}$$

The Poisson coupling parameters S, R are small ($R = S = 0$ for $\nu = 0$) and defined below

$$S = \frac{2\gamma\nu}{B} \qquad R = \xi S \tag{3.10}$$

The tilde S, R parameters are modified with the celerities ratio $\eta = c_0/c_1$ and given as

$$\widetilde{R} = R\eta \qquad \widetilde{S} = \frac{S}{\eta} \tag{3.11}$$

The developed clear form of the CE has an important advantage as it allows for preliminary analyses of physical behaviour of the system even prior to computations. If the right sides of them are assumed zero (no friction and a horizontal pipe) and the variables in the parenthesis on the left sides are considered as new "wave variables" – velocities and stresses, these equations would represent simple elastic waves. But due to the shape of the wave variables they are not pure liquid (WH) nor pure pipe (PC) waves. Thus the real physical quantities, velocities and stresses (pressures), are superpositions of the WH and PC waves. The dominant role is played by the former in liquid variables and the latter in the structure ones. These effects are possible to observe in experimental and numerical records (see Adamkowski *et al.*, 2010 or Henclik, 2010).

3.2. Torsional vibrations

Transformation of governing equations (2.7) results in compatibility equations C4

$$\frac{dw_4}{dt} - \varepsilon\frac{dq_4}{dt} = 0 \tag{3.12}$$

They are valid for the characteristic slope $dx/dt = \varepsilon c_4$, and the celerity c_4 of torsional waves is

$$c_4 = \sqrt{\frac{G}{\rho_s}} \tag{3.13}$$

The CE and unified variables, velocities w and loads q, are numbered consequently with indexes 1, 2, 3 for linear and 4, 5, 6 for angular degrees of freedom, corresponding respectively to the x, y, z axes. The variables in C4 equations are the normalized torsional angular velocity w_4 and the moment of force q_4

$$w_4 = h\omega_x \qquad q_4 = \frac{hM_x}{\rho_s I_0 c_4} \tag{3.14}$$

The parameter h [m] introduced above to get the unified variables can be in fact arbitrarily selected. But for the model homogeneity, its value is assumed to be the same as calculated further for lateral motion.

3.3. Lateral motion

Equations (2.8) of transversal movement in the non-vertical plane are transformed to CE representing shearing waves C2 coupled with bending waves C6. The equations C2 are given in

$$\frac{dw_2}{dt} + \varepsilon \frac{dq_2}{dt} = \varepsilon \Omega w_6 \tag{3.15}$$

They are valid for the dependence $x(t)$ having the slope equal to the wave celerity $dx/dt = \varepsilon c_2$

$$c_2 = \sqrt{\frac{T}{Tm}} \tag{3.16}$$

The parameter Ω on the right side of (3.15) is a result of specific normalization of the equations and is explained further in $(3.20)_2$. The C6 equations have the following form

$$\frac{dw_6}{dt} - \varepsilon \frac{dq_6}{dt} = -\Omega q_2 \tag{3.17}$$

They are valid for $dx/dt = \varepsilon c_6$, where

$$c_6 = \sqrt{\frac{s}{b}} \tag{3.18}$$

The unified variables are

$$w_2 = w_y \qquad q_2 = \frac{Q_y}{mc_2} \qquad w_6 = h\omega_z \qquad q_6 = \frac{hM_z}{bc_6} \tag{3.19}$$

The compact form of the lateral CE has been achieved by specific selection of the constant h to keep the same scaling coefficient Ω [1/s] on the right side of them. The result of this procedure is

$$h = \sqrt{\frac{b}{m}} \qquad \Omega = \sqrt{\frac{T}{b}} \tag{3.20}$$

Estimation of expression $(3.20)_1$ for the water in a metal pipe gives a value of about $D/4$ for h.

In the vertical plane, we get C3/C5 coupled CE. The shearing waves are governed by C3 equations

$$\frac{dw_3}{dt} + \varepsilon \frac{dq_3}{dt} = -g \cos \alpha - \varepsilon \Omega w_5 \tag{3.21}$$

They are valid as usual for the dependence $x(t)$ being the path of the wave that propagates with the same celerity as in the C2 case ($c_3 = c_2$). The bending waves C5 have the same celerity as in the C6 case

$$\frac{dw_5}{dt} + \varepsilon \frac{dq_5}{dt} = \Omega q_3 \tag{3.22}$$

The definition of unified variables is analogous as in the C2-C6 case.

4. Numerical method

The first step of the numerical algorithm is to integrate each CE in time within a specific time step Δt to get finite difference equations which can be solved for subsequent time moments at the x-t plane. A proper construction of the numerical scheme is required. For stability and convergence, the CFL (Courant-Fredicks-Lewy) condition (Quarteroni and Valli, 1994; Almeida and Koelle, 1992), which determines the relation between the time step Δt and space grid size Δx, is necessary

$$C_N = \frac{c\Delta t}{\Delta x} \leqslant 1 \tag{4.1}$$

It is easy to fulfill the condition for one pair of CE (one wave). Keeping C_N equal to one allows one to find the solutions without interpolation with the use of a scheme presented at the grid in Fig. 2 for the C4 torsional wave. Integrating (3.12) within the time Δt_4, we get a set of two linear equations

$$w_4 - q_4 = b_{4\mathrm{L}} \qquad w_4 + q_4 = b_{4\mathrm{R}} \tag{4.2}$$

The "history parameters" b_4 at the right side are a result of integrating the CE, and are given in

$$b_{4\mathrm{L}} = w_4^{(4\mathrm{L})} - q_4^{(4\mathrm{L})} \qquad b_{4\mathrm{R}} = w_4^{(4\mathrm{R})} + q_4^{(4\mathrm{R})} \tag{4.3}$$

The initial values of variables are taken at the beginning of C4 left (L) and right (R) characteristics as it is presented at the right part of Fig. 2. Two kinds of average parameters are defined and used consequently within the model, half of the sum and half of the difference

$$\overline{b}_4 = \frac{b_{4\mathrm{R}} + b_{4\mathrm{L}}}{2} \qquad \mathring{b}_4 = \frac{b_{4\mathrm{R}} - b_{4\mathrm{L}}}{2} \tag{4.4}$$

Now, the solutions to (4.2) at the final point F (in Fig. 2) can be presented as

$$w_4 = \overline{b}_4 \qquad q_4 = \mathring{b}_4 \tag{4.5}$$

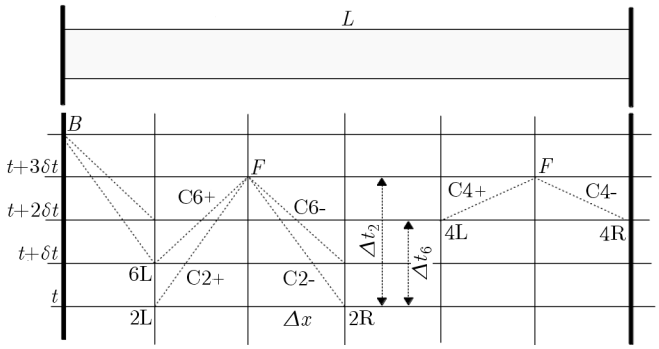

Fig. 2. A computational scheme for two coupled waves C6/C2 of the celerity ratio 3:2 (at the left) and for a single wave C4 of the time step $\Delta t_4 = \delta t$ (at the right)

A more complex case is for two coupled waves that propagate with different celerities, which is illustrated at the left part in Fig. 2 for the C2-C6 equations. If the ratio of shearing and bending waves celerities is a rational number, we can integrate each pair of CE (C2/C6) within a specific time step Δt, (Δt_2 and Δt_6 respectively), which is an integer multiplication of the elementary step δt.

In Fig. 2, the celerity ratio is 3:2 so the time step ratio is 2:3. This construction produces the same space step Δx for both waves and it is possible to move across the x-t plane and to solve the equations for the unknown variables at each node without interpolation, as we can always find the starting point in the past for any characteristics. Small modifications are required at the beginning moments, but then we can start the characteristic at any position x of the $t = 0$ line due to the known initial conditions. As an alternative, a numerical scheme with interpolation can be also considered. After integration, the following set of four linear equations for the unknown variables is found

$$\begin{aligned} w_2 + q_2 - \mu_2 w_6 &= b_{2\mathrm{L}} \qquad & w_2 - q_2 - \mu_2 w_6 &= b_{2\mathrm{R}} \\ w_6 - q_6 + \mu_6 w_2 &= b_{6\mathrm{L}} \qquad & w_6 + q_6 - \mu_6 w_2 &= b_{6\mathrm{R}} \end{aligned} \tag{4.6}$$

In the integration process, the mean values of the right-hand side variables in (3.15) and (3.17) are assumed to be the arithmetic averages of their initial and final values, which produces the following form of μ

$$\mu_i = \frac{\Omega \Delta t_i}{2} \tag{4.7}$$

The formulas for the history parameters can be easily derived and will not be presented herein. Due to the coupling between the waves, the parameters μ are assumed to be upper bounded for the stable numerical solutions, which produces an upper limit for the space size Δx of the grid mesh. An estimation made with the application of an iterative method (see Bjoerck and Dahlquist, 1974) to partially transformed equations (4.6) has given for it a value of about $D/2$. With slightly different analyses, Tijsseling (1993) suggested that the limit for an empty pipe should be $D/(2\sqrt{2})$. In fact, the real space step will be selected with numerical tests. The solutions to (4.6) are

$$w_2 = \overline{b}_2 \qquad q_2 = \frac{-\overset{\circ}{b}_2 + \mu_2 \overline{b}_6}{1 + \mu_2 \mu_6} \qquad w_6 = \frac{\overline{b}_6 + \mu_6 \overset{\circ}{b}_2}{1 + \mu_2 \mu_6} \qquad q_6 = \overset{\circ}{b}_6 \tag{4.8}$$

An analogous procedure can be applied for lateral equations C3/C5 in the vertical plane. For longitudinal motion, the results are calculated in a similar way, though a comment is necessary as the friction terms on the right-hand side of Eq. (3.1) and (3.4) are non-linear. Usually, a linearization scheme is proposed and a direct method of solution is used. However, the non-linear friction terms are small, so at the current approach they will be left within the history parameters and assumed as fixed values with the possibility of iterative improvement. One additional iteration is usually enough. Such a solution shows the advantage of using the history parameters. It is a convenient idea as the results do depend only on those parameters and they can be defined within a numerical routine in a different way for any changes in the model. Introducing material damping, changing the pipe-wall friction model or using interpolation only influences the shape of those parameters. The C0/C1 history parameters include also the gravitational term (C3/C5 ones as well). Finally, the solutions to C0/C1 are

$$v = \frac{\overline{b}_0 + S\overline{b}_1}{1 + RS} \qquad w_1 = \frac{-\overline{b}_1 + R\overline{b}_0}{1 + RS} \qquad r = -\frac{\overset{\circ}{b}_0 + \widetilde{S}\overset{\circ}{b}_1}{1 + RS} \qquad q_1 = \frac{-\overset{\circ}{b}_1 + \widetilde{R}\overset{\circ}{b}_0}{1 + RS} \tag{4.9}$$

Each group of equations is solved independently, but the same elementary time step δt is necessary for all of them to keep the effectiveness of the method. This is because the coupling between variables of different groups may occur at boundaries, thus common time nodes are required there. The common space nodes at the boundaries can be also useful. In this case, the ratios of all the wave celerities should be rational numbers. Such a condition is always true

within a certain precision, but the algorithm is effective if the integers for these ratios are not too large, so a wave-speed adjustment can be used by slightly changing the selected material or geometrical parameters of the system. This procedure is also used in other approaches, and the current author has developed and tested an algorithm allowing one to adjust all the five celerities of the elastic waves.

5. Boundary conditions

The piping is modelled as a set of straight pipes connected at junctions where certain relations are valid as the boundary conditions. In a more general case, some working elements may be also taken into account. The term non-pipe element (NPE) is used in Almeida and Koelle (1992) for them and they may be a valve, pump, turbine or other hydraulic device. NPE is assumed to be a rigid and massive element and can be fixed to the foundation with rigid or elastic supports (or staying unfixed). It is connected to individual pipes by a number of inlets-outlets for which hydraulic characteristics are determined. A simple example of NPE is a valve with its dependence between the pressure at the inlet at the left ($p_{\rm L}$) and the outlet at the right ($p_{\rm R}$) given as

$$p_{\rm L} = p_{\rm R} + \frac{1}{2}\rho(v - w_x)^2\zeta(t) \tag{5.1}$$

In the equation above, the loss factor $\zeta(t)$ is dependent on the valve opening degree, so it may change in time. For a complete valve closure, it becomes infinity what in fact changes the BC to have the form $v = w_x$. NPE will not be considered within the current model, however the junction is in fact a simple NPE of a constant and small loss factor. The mass and size of the junction can usually be neglected, but the general case can be analyzed as well. Using the current assumptions, the main dynamic liquid BC at the junction of two sub-pipes defines the pressure balance with a relation similar to (5.1). The condition is even simpler as the junction losses ζ are constant and usually small, which produces a possibility for iterative solution. A fundamental BC for the liquid is the continuity equation. For the FSI case and two sub-pipes at the junction, it has the following form

$$v^{(\rm L)} - w_x^{(\rm L)} = v^{(\rm R)} - w_x^{(\rm R)} \tag{5.2}$$

In spite of the fact that the junction is rigid, the velocities of the left and right edge of it used above are not, in general, the same as 3D motion is considered and the left and right pipe coordinate systems can be rotated (when the junction is a bend). The rigidity of the junction means it is rigid in itself and is rigidly fixed to the pipes. That is why the junction velocity $\mathbf{w}$ and pipe ends velocities $\mathbf{w}^{(\rm L)}$ and $\mathbf{w}^{(\rm R)}$ are uniquely related. In fact, they are identical for the dimensionless junction

$$\mathbf{w}^{(\rm L)} = \mathbf{w}^{(\rm R)} = \mathbf{w} \tag{5.3}$$

In this case, $\mathbf{w}$ is 6D velocity with $4, 5, 6$ components being angular velocities multiplied by h defined in $(3.20)_1$. The above is a vector equation, so when using its representation in a coordinate system, proper transform matrices of directional cosines $\mathbf{U}^{(\rm L)}$, $\mathbf{U}^{(\rm R)}$ have to be applied. If the junction size is not negligible, the above condition has to be modified because linear motion of the junction edge (the pipe end) has a component being the result of the junction rotation as a rigid body.

The motion of the junction is dependent on the way it is fixed to the foundation. For a rigid fixing, there is no motion and the BC is $\mathbf{w} = \mathbf{0}$. When the junction is unfixed or fixed with an

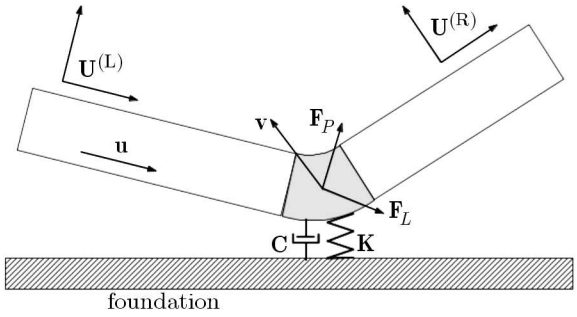

Fig. 3. Junction of two pipes fixed with a viscoelastic support

elastic support as it is presented in Fig. 3, the following junction equation of motion (EOM) should be formulated

$$\mathbf{M}\ddot{\mathbf{u}} + \mathbf{C}\dot{\mathbf{u}} + \mathbf{K}\mathbf{u} = \mathbf{F}_L + \mathbf{F}_P \tag{5.4}$$

This is 6D equation for the junction displacement $\mathbf{u}$ having three linear (1,2,3) and three angular (4,5,6) coordinates. At the right-hand side of the EOM, there are pipe and liquid forces (and moments) acting onto the junction. On the left-hand side, there is an inertia term with the matrix $\mathbf{M}$ and the forces from the elastic support with stiffness and damping matrices $\mathbf{K}$ and $\mathbf{C}$. The Kelvin-Voigt model for the support reaction is assumed. In the EOM, the convention of multiplying angular $(4, 5, 6)$ coordinates in the vector $\mathbf{u}$ by the parameter h is still valid and another one for normalization of the angular coordinates of the forces (the moments) by dividing them by h is used as well. An adequate normalization is also done to the matrices $\mathbf{M}$, $\mathbf{K}$, $\mathbf{C}$ on the left-hand side. In general, determining these matrices is a separate task, but this problem will not be discussed herein. The EOM is simplified in special cases, e.g. for massless junction $\mathbf{M} = \mathbf{0}$, for zero damping $\mathbf{C} = \mathbf{0}$ and for not supported junction $\mathbf{K} = \mathbf{0}$, $\mathbf{C} = \mathbf{0}$.

The forces on the right side of the EOM depend on the flow and pipe motion variables. The liquid forces $\mathbf{F}_L$ are mainly the result of pipe static pressures and the pipe forces $\mathbf{F}_P$ appear explicitly in the CE, though proper transformations are required. Form (5.4) of the EOM allows one to understand the junction coupling mechanism, however it is not convenient for numerical solution. The right-hand side of the EOM can be transformed using the difference form of CE discussed in Section 4 to express the liquid and pipe forces as a linear function of the junction velocity $\mathbf{w} = d\mathbf{u}/dt$ in a new time instant. Finally, the EOM can be presented in the following form

$$\widetilde{\mathbf{M}}\ddot{\mathbf{u}} + \widetilde{\mathbf{C}}\dot{\mathbf{u}} + \widetilde{\mathbf{K}}\mathbf{u} = -\mathbf{P}\mathbf{w} + \mathbf{a} \tag{5.5}$$

In the above equation, the matrices on the left-hand side (with tilde) are the original ones divided by $(\rho_s A_s c_s)$. The essence of the method is the coupling matrix $\mathbf{P}$ which is symmetric and positive definite. It depends on the pipe-junction geometry and liquid-pipe material parameters. The junction history vector $\mathbf{a}$ depends on the previous values of the system variables at the junction and its neighborhood, and changes in each time step. Both formulas for the matrix $\mathbf{P}$ and vector $\mathbf{a}$ have been determined by the author to be applied in the algorithm. To find the solution to Eq. (5.5), its left-hand side has to be transformed to a finite difference form. Applying the Newmark method to it allows one to find the junction velocity $\mathbf{w}$ in a new time instant (the variables with "0" indexes are taken at the previous time instant)

$$\mathbf{w} = \Big(\frac{2}{\Delta t}\widetilde{\mathbf{M}} + \mathbf{P} + \widetilde{\mathbf{C}} + \frac{\Delta t}{2}\widetilde{\mathbf{K}}\Big)^{-1}\Big[\mathbf{a} + \widetilde{\mathbf{M}}\Big(\frac{2}{\Delta t}\dot{\mathbf{u}}_0 + \ddot{\mathbf{u}}_0\Big) - \widetilde{\mathbf{K}}\Big(\mathbf{u}_0 + \frac{\Delta t}{2}\dot{\mathbf{u}}_0\Big)\Big] \tag{5.6}$$

The matrix in the brackets is constant for the junction and positive definite, thus the equation can be easily solved in each time step. Knowing the velocity $\mathbf{w}$, all other variables can be found.

6. Summary

The water hammer phenomenon with dynamic fluid-structure interaction is discussed in the paper. The standard mathematical model of WH-FSI and an algorithm for its numerical solution on the basis of the MOC technique is presented. The fourteen governing equations are transformed into compatibility equations developed in a convenient, compact form with the use of "unified variables" – velocities and loads. The main steps and ideas of the numerical method are discussed. The concept of using "history parameters" allows one to effectively design the algorithm. The numerical scheme uses a properly designed computational grid exploiting the technique of wave-speed adjustment but the scheme with interpolation is also possible. An important part of the algorithm is the boundary condition at the junction fixed to the foundation with a viscoelastic support. It is formulated as a differential equation of motion, transformed and effectively solved with the use of a special coupling matrix and the Newmark method. A similar approach has been applied to the 1D 4E model and it works correctly. The algorithms are now being implemented in a computer code, and the numerical results will be compared with the records from experiments which are planned for the real 3D pipeline system built in the laboratory.

Acknowledgements

The results presented in the paper have been partially developed within research project No. N N504 478839 funded by the Ministry of Science and Higher Education of Poland.

References

1. Adamkowski A., 2013, *Liquid Unsteady Flows in Closed Conduits* (in Polish), Publishing House of the Institute of Fluid-Flow Machinery, Gdansk
2. Adamkowski A., Henclik S., Lewandowski M., 2010, Experimental and numerical results of the influence of dynamic Poisson effect on transient pipe flow parameters, *25th IAHR Symposium on Hydraulic Machinery and Systems, Timisoara, Institute of Physics Conference Series: Earth and Environmental Sciencees*, DOI: 10.1088/1755-1315/12/1/012041
3. Adamkowski A., Lewandowski M., 2006, Experimental examination of unsteady friction models for transient pipe flow simulation, *ASME Journal of Fluids Engineering*, **128**, 11
4. Alastruey J., Parker K.H., Sherwin S.J., 2012, Arterial pulse wave haemodynamics, *Proceedings of the 11th International Conference on Pressure Surges*, Lisbon, 401-442
5. Almeida A.B., Koelle E., 1992, *Fluid Transients in Pipe Networks*, Computational Mechanics Publications, Boston, London
6. Bjoerck A., Dahlquist G., 1974, *Numerical Methods*, Prentice Hall, chap. 6.9.1 (Polish translation, 1987, PWN, Warsaw)
7. Cowper G.R., 1966, The shear coefficient in Timoshenko's beam theory, *Journal of Applied Mechanics*, **33**, 6, 335-340
8. Ghidaoui M., Ming Zao, Mcilnnis D., Axworthy D., 2005, A review of water hammer theory and practise, *Applied Mechanics Reviews*, **58**, 1, 49-76
9. Henclik S., 2010, Mathematical model and numerical computations of transient pipe flows with fluid-structure interaction, *Transactions of the Institute of Fluid-Flow Machinery*, **122**, 77-94
10. Hutchinson J.R., 2001, Shear coefficients for Timoshenko beam theory, *Journal of Applied Mechanics*, **68**, 1, 87-92
11. Meirovitch L., 1967, *Analytical Methods in Vibrations*, The Macmillan Company, New York

12. Quarteroni A., Valli A., 1994, *Numerical Approximation of Partial Differential Equations*, Springer-Verlag, Berlin

13. Tijsseling A.S., Lavooij C.S.W., 1990, Waterhammer with fluid-structure interaction, *Applied Scientific Research*, **47**, 273-285

14. Tijsseling A.S., 1993, Fluid – structure interaction in case of waterhammer with cavitation, PhD thesis, Delft University of Technology, Report 93-6, Faculty of Civil Engineering, http://www.win.tue.nl/∼atijssel/pdf_files/Tijsseling_1993.pdf

15. Timoshenko S., Young D.H., 1955, *Vibration Problems in Engineering*, Nostrad Co. Inc., NY

16. Urbanowicz K., Zarzycki Z., 2012, New efficient approximation of weighting function for simulations of unsteady friction losses in liquid pipe flow, *Journal of Theoretical and Applied Mechanics*, **50**, 2, 487-508

17. Vitkovsky J.P., Bergant A., Simpson A.R., Lambert M.F., 2006, Systematic evaluation of one-dimensional unsteady friction models in simple pipelines, *Journal of Hydraulic Engineering*, **132**, 7, 696-708

18. Wang Z.M., Tan S.K., 1997, Coupled analysis of fluid transient and structural dynamic responses of a pipeline system, *Journal of Hydraulic Research*, **35**, 1, 119-131

19. Wiggert D.C., Hatfield F.J., Stuckenbruck S., 1987, Analysis of liquid and structural transients in piping by the method of characteristics, *ASME Journal of Fluids Engineering*, **109**, 161-165

20. Wiggert D., Tijsseling A., 2001, Fluid transients and fluid-structure interaction in flexible liquid-filled piping, *Applied Mechanics Reviews*, **54**, 455-481

21. Wylie E.B., Streeter V.L., 1993, *Fluid Transients in Systems*, Prentice-Hall, NJ

Manuscript received August 8, 2014; accepted for print November 4, 2014

JOURNAL OF THEORETICAL AND APPLIED MECHANICS
53, 3, pp. 557-567, Warsaw 2015
DOI: 10.15632/jtam-pl.53.3.557

REFINED MODEL OF PASSIVE BRANCH DAMPER OF PRESSURE FLUCTUATIONS

Sylwester Kudźma

West Pomeranian University of Technology Szczecin, Faculty of Mechanical Engineering and Mechatronics, Szczecin, Poland; e-mail: sylwester.kudzma@zut.edu.pl

Zygmunt Kudźma

Wrocław University of Technology, Faculty of Mechanical Engineering, Wrocław, Poland
e-mail: zygmunt.kudzma@pwr.edu.pl

This paper presents an analysis of the influence of the kind of a friction model on the dimensioning of a branch pressure fluctuation damper. The mathematical model of the branch damper is defined by determining the damper input impedance and finding its minimum corresponding to the maximum effectiveness in reducing pressure fluctuations. Three kinds of friction for the oscillatory flow in the damper, i.e. a lossless line, steady friction and a nonstationary friction model, are considered. Experimental studies confirmed that the use of the nonstationary friction model in the calculation of branch damper length ensures the highest effectiveness in reducing the amplitude of pressure fluctuations characterized by a given frequency.

Keywords: pressure fluctuations, damper, noise

1. Introduction

Hydrostatic drive systems have their well-known advantages, but their main disadvantage is that they generate much noise which may disqualify such kind of drive when the increasingly more stringent noise emission standards dictated by ergonomic considerations are exceeded. For this reason, a properly designed hydrostatic drive system should not only have the expected static and dynamic properties, but also emit as little noise as possible. Directive 98/37/WE includes a general recommendation that a machine should be designed in such a way that the hazard arising from the emission of the noise generated by it is reduced (preferably at the noise generation source) to the lowest level possible owing to the technological progress and the available means of noise reduction. The directive also requires that information about the noise at the operator workstation be included in the machine documentation. The following should be specified: the equivalent sound pressure level, the instantaneous peak acoustic pressure and the acoustic power level. Noise in a hydraulic system can be generated in two ways:

- directly – the noise source (e.g. the impeller of a fan in the electric motor driving the pump) produces changes in pressure in the surrounding air,
- indirectly – time-variable forces make the components of a hydraulic system vibrate. The vibration of the surfaces of the components results in noise emission.

Indirectly generated noise is the principal noise in hydraulic systems. Changeable forces acting on the hydraulic system components arise as a result of:

- pressure fluctuations (Tijsseling, 1996),

- mechanical connection of the system components through conduits and the common mounting. A single component (e.g. a valve) may vibrate as a result of the action of the fluid, causing the vibration of the components connected with it.

One of the major noise sources in a hydraulic system is the unstable operation of the pressure relief valves due to, among other things, external excitations produced by vibration of the machine frame or the feeder cover to which the pressure relief valves are often mounted. One should note that vibrations may arise in the resonant region of the element which controls the valve. Therefore, the coincidence of the frequency range of, e.g., the foundation and that of the hydraulic valve controlling element should be avoided (Stosiak, 2012).

Experimental studies aimed at locating and identifying vibration and noise sources must be carried out in order to effectively eliminate annoying noise. Energy measuring methods are particularly suitable for locating noise sourceswhen diagnosing the acoustic condition of hydraulic machines and equipment (Kollek *et al.*, 2001). For locating noise sources, Osiński and Kollek (2013) recommend using the acoustic intensity method (AIM) with a two-microphone acoustic probe whereby a map of noise intensity around the investigated equipment can be obtained and the loudest places can be indicated.

The causes of noisiness in the hydraulic system can be divided into mechanical causes and hydraulic causes. The group of mechanical causes includes workmanship and assembly faults, excessive clearances in all moving joints, unbalanced rotating parts and so on. The main hydraulic causes are: cavitation phenomena (Kollek *et al.*, 2007), forcing pressure fluctuations and working liquid pressure surges in the pump or displacement motor chambers. In a properly designed hydraulic system, cavitation should not occur while the occurrence of working liquid pressure surges largely depends on the type of the pump. Axial multiplunger pumps are the noisiest while vane pumps and internal gear pumps are the most silent-running. The research so far has identified pressure fluctuations and the resulting vibrations as the principal causes of noise generation in hydraulic systems, see Mikota and Manhartsgruber (2003), Kudźma (2001, 2006, 2012), Wacker (1985). Thus by reducing pressure fluctuations, one can reduce the noisiness of the individual system components and thereby prolong their service life. One of the effective ways of reducing pressure fluctuations, and so the hydrostatic noise of the drive system, is the use of pressure fluctuation dampers. This paper presents a refined passive branch damper model taking into account nonstationary flow resistance.

2. The supply conduit as a long hydraulic line

Simplifying assumptions, in detail described by Kudźma (2012), are commonly made when deriving equations for the nonstationary flow of a liquid in closed conduits. On such assumptions, the (laminar and turbulent) motion of the liquid is described by the following equation, Kudźma (2012), Zarzycki (1994):
— the equation of motion towards the axis z

$$\frac{\partial v_z}{\partial t} = -\frac{1}{\rho_o}\frac{\partial p}{\partial z} + \nu\frac{1}{r}\frac{\partial}{\partial r}\Big(r\frac{\partial v_z}{\partial r}\Big) + \frac{1}{r}\frac{\partial}{\partial r}\Big(r\nu_t\frac{\partial v_z}{\partial r}\Big) \tag{2.1}$$

— the equation of continuity

$$\frac{\partial p}{\partial t} + \rho_o c_o^2\Big(\frac{\partial v_z}{\partial z} + \frac{\partial v_r}{\partial r} + \frac{v_r}{r}\Big) = 0 \tag{2.2}$$

where: v_z is the instantaneous velocity of the liquid in the conduit in the axial direction, v_r – instantaneous velocity of the liquid in the radial direction, p – instantaneous pressure of the liquid, ν – kinematic coefficient of molecular viscosity, ν_t – kinematic coefficient of turbulent

viscosity, ρ_o – steady density of the liquid, z – axial coordinate of the conduit, r – radial coordinate of the conduit, c_o – velocity of pressure wave propagation, t – time.

In the case of turbulent motion, v_z and p are quantities averaged in accordance with the Reynolds rules. By integrating equations (2.1) and (2.2) over the conduit cross section, one gets a system of equations which can be presented as follows, see Kudźma (2012), Zarzycki (1994), Zarzycki *et al.* (2007)

$$\rho_o \frac{\partial v(z,t)}{\partial t} + \frac{\partial p(z,t)}{\partial z} + \frac{2}{R}\tau_w = 0 \qquad \frac{\partial p(z,t)}{\partial t} + \rho_o c_o^2 \frac{\partial v(z,t)}{\partial z} = 0 \tag{2.3}$$

where: $v = v(z,t)$ is the average in the conduit cross section velocity of the liquid, $p = p(z,t)$ – average pressure in the conduit cross section, R – inside radius of the conduit, τ_w – shear stress on the conduit wall. The expression $(2/R)\tau_w$ in equation $(2.3)_1$ represents pressure drop due to friction, per unit length.

In the case of a laminar flow, the most accurate model of hydraulic resistance is the model with variable resistance, which takes into account pressure losses as a function of frequency. Using this model one gets the following expression for impedance Z_0 of a long hydraulic line, see Zielke (1968)

$$Z_0(s) = \frac{\dfrac{\rho_o s}{\pi R^2}}{1 - \dfrac{2J_1\left(\mathrm{j}R\sqrt{\dfrac{s}{\nu}}\right)}{\mathrm{j}R\sqrt{\dfrac{s}{\nu}}J_0\left(\mathrm{j}R\sqrt{\frac{s}{\nu}}\right)}} \tag{2.4}$$

where: s is the Laplace transformation operator, J_0, J_1 are respectively zero-order and first-order first-type Bessel functions, j – imaginary unit.

By applying the inverse Laplace transformation, Zielke (1968) obtained the following relation for the instantaneous shear stress on the conduit wall

$$\tau_w(t) = \frac{4\mu}{R}v + \frac{2\mu}{R}\int_0^t w(t-u)\frac{\partial v}{\partial t}(u)\,du \tag{2.5}$$

where: $w(t)$ is the weighting function and u is the time in the convolution integral.

The second term in equation (2.5) describes the influence of flow nonstationarity on the shear stress. It is a convolution integral of the instantaneous acceleration of the liquid and weighting function $w(t)$. The instantaneous conduit wall shear stress τ_w can be presented as the sum of quasi-steady quantity τ_{wq} and time-variable quantity τ_{wn}, see Vardy and Brown (2003)

$$\tau_w = \tau_{wq} + \tau_{wn} \tag{2.6}$$

If only the quasi-steady friction model is to be taken into account, the second term in equations (2.5) and (2.6) should be omitted, whereby only $\tau_w = \tau_{wq}$ remains. It should be noted that the quasi-steady frictional resistance models used in calculations of nonstationary states are valid only in the case of slow velocity changes, which applies to low excitation frequencies or small accelerations of the liquid.

2.1. Weighting function

The so-called weighting function, which depends on, among other things, the character of the flow, features significantly in above relation (2.5). For the laminar flow, the relation presented by Zielke (1968) is commonly used, whereas for the turbulent flow there are two main models (also

dependent on the Reynolds number) proposed by Vardy and Brown (2003, 2004) and Zarzycki (1994), Zarzycki *et al.* (2007). Since the weighting functions presented by the above authors, especially the ones for the turbulent flow, are complicated and difficult to handle in numerical computations, their approximations are used in practice. From among the weighting function approximating relations proposed in the literature, the relation presented by Urbanowicz and Zarzycki (2012), which through the appropriate scaling of the coefficients can be used for both laminar and turbulent flows, deserves special attention

$$w(\widehat{t}) = \sum_{i=1}^{26} m_i \mathrm{e}^{-n_i \widehat{t}} \tag{2.7}$$

where: $\widehat{t} = \nu t/R^2$ is dimensionless time, and the coefficients m_i, n_i assume the following values (Urbanowicz and Zarzycki, 2012):
$m_1 = 1$; $m_2 = 1$; $m_3 = 1$; $m_4 = 1$; $m_5 = 1$; $m_6 = 2.141$; $m_7 = 4.544$; $m_8 = 7.566$; $m_9 = 11.299$; $m_{10} = 16.531$; $m_{11} = 24.794$; $m_{12} = 36.229$; $m_{13} = 52.576$; $m_{14} = 78.150$; $m_{15} = 113.873$; $m_{16} = 165.353$; $m_{17} = 247.915$; $m_{18} = 369.561$; $m_{19} = 546.456$; $m_{20} = 818.871$; $m_{21} = 1209.771$; $m_{22} = 1770.756$; $m_{23} = 2651.257$; $m_{24} = 3968.686$; $m_{25} = 5789.566$; $m_{26} = 8949.468$;
$n_1 = 26.3744$; $n_2 = 70.8493$; $n_3 = 135.0198$; $n_4 = 218.9216$; $n_5 = 322.5544$; $n_6 = 499.148$; $n_7 = 1072.543$; $n_8 = 2663.013$; $n_9 = 6566.001$; $n_{10} = 15410.459$; $n_{11} = 35414.779$; $n_{12} = 80188.189$; $n_{13} = 177078.960$; $n_{14} = 388697.936$; $n_{15} = 850530.325$; $n_{16} = 1835847.582$; $n_{17} = 3977177.832$; $n_{18} = 8721494.927$; $n_{19} = 19120835.527$; $n_{20} = 42098544.558$; $n_{21} = 92940512.285$; $n_{22} = 203458923.000$; $n_{23} = 445270063.893$; $n_{24} = 985067938.878$; $n_{25} = 2166385706.058$; $n_{26} = 4766167206.672$.

The function can be easily transformed to the Laplace variable domain. Then it assumes the form

$$L[w] = \sum_{i=1}^{26} \frac{m_i}{\widehat{s} + n_i} \tag{2.8}$$

where $\widehat{s}$ is dimensionless operator of the Laplace transformation $\widehat{s} = (R^2/\nu)s$.

The values of the universal coefficients are determined in the following way, see Urbanowicz and Zarzycki (2012)

$$n_{1u} = n_1 - B^*;\ n_{2u} = n_2 - B^*;\ \ldots;\ n_{26u} = n_{26} - B^*$$
$$m_{1u} = \frac{m_1}{A^*};\ m_{2u} = \frac{m_2}{A^*};\ \ldots;\ m_{26u} = \frac{m_{26}}{A^*}$$

where

$$A^* = \sqrt{\frac{1}{4\pi}} \qquad B^* = \frac{\mathrm{Re}^{\kappa}}{12.86} = \frac{2320^{\kappa}}{12.86} \qquad \kappa = \log \frac{15.29}{\mathrm{Re}^{0.0567}} = \log \frac{15.29}{2320^{0.0567}}$$

The values of the universal coefficients of the laminar-turbulent weighting function are necessary to determine the current shape of the weighting function used in numerical computations. Thus the function defined by the universal coefficients

$$L[w] = \sum_{i=1}^{26} \frac{m_{iu}}{\widehat{s} + n_{iu}} \tag{2.9}$$

sufficiently well represents the nonstationary frictional loss model for both the laminar flow and the turbulent flow, provided that the Reynolds number is determined earlier.

Performing the Laplace transformation on equations (2.1) and (2.2) for zero initial conditions and then integrating the equations relative to the variable z with the limits of 0-L (L is the length

of the hydraulic line) one gets a matrix transition function for a long hydraulic line. Assuming a harmonic excitation, the function can be presented in the following form, see Kudźma *et al.* (2002), Zarzycki (1994), Zarzycki *et al.* (2007)

$$\begin{bmatrix} p_1 \\ q_1 \end{bmatrix} = H(\mathrm{j}\omega) \begin{bmatrix} p_2 \\ q_2 \end{bmatrix} \tag{2.10}$$

where: $H(\mathrm{j}\omega)$ is the matrix transition function, p_1, p_2, q_1, q_2 are harmonically variable deviations from the mean value of the pressure and the rate of flow respectively. When at the harmonic excitation a quasi-steady state is considered using the model with distributed parameters, the transmittance matrix assumes the following form, see Kudźma (2012) and Zarzycki (1994)

$$H(\mathrm{j}\omega) = \begin{bmatrix} h_{11} & h_{12} \\ h_{21} & h_{22} \end{bmatrix} \tag{2.11}$$

where the particular matrix terms are expressed by the relations

$$\begin{aligned} h_{11} &= \cosh(T\psi_z \mathrm{j}\omega) & h_{12} &= Z_c\psi_z \sinh(T\psi_z \mathrm{j}\omega) \\ h_{21} &= \frac{1}{Z_c\psi_z}\sinh(T\psi_z \mathrm{j}\omega) & h_{22} &= \cosh(T\psi_z \mathrm{j}\omega) \end{aligned} \tag{2.12}$$

where: $Z_c = \rho c_o/(\pi R^2)$ is the characteristic impedance of the conduit, $T = L/c_o$ – time constant. ψ_z – operator defining the influence of viscosity (a viscosity function) expressed by

$$\psi_z = \frac{\psi}{\mathrm{j}\Omega} \qquad \psi = \varepsilon + \mathrm{j}\delta \tag{2.13}$$

ε – coefficient of sinusoidal pressure wave amplitude damping, δ relates to wave phase velocity, j is the imaginary unit

$$\begin{aligned} \varepsilon &= \sqrt{\frac{-(\Omega^2 + 2b_2\Omega) + \sqrt{(\Omega^2 + 2b_2\Omega)^2 + (2b_1\Omega)^2}}{2}} \\ \delta &= \sqrt{\frac{(\Omega^2 + 2b_2\Omega) + \sqrt{(\Omega^2 + 2b_2\Omega)^2 + (2b_1\Omega)^2}}{2}} \end{aligned} \tag{2.14}$$

and

$$b_1 = \Re\Big(\frac{1}{2}R_o\frac{\pi R^4}{\mu} + 2\mathrm{j}\Omega L[w]\Big) \qquad b_2 = \Im\Big(\frac{1}{2}R_o\frac{\pi R^4}{\mu} + 2\mathrm{j}\Omega L[w]\Big) \tag{2.15}$$

where: $L[w]$ is simple Laplace transformation of the weighting function, $\Omega = \omega R^2/\nu$ – dimensionless frequency, ω – angular frequency of excitations, R_o – constant resistance calculated from the Darcy-Weisbach formula

$$R_o = \frac{\lambda \mathrm{Re}\mu}{8\pi R^4} \tag{2.16}$$

λ – dimensionless coefficient of linear frictional losses, Re – Reynolds number, μ – dynamic viscosity of the liquid. When only the quasi-steadyfrictional losses are taken into account, relations (2.14) are reduced to the form, see Zarzycki (1994)

$$\varepsilon = \sqrt{\frac{1}{2}}\Omega\sqrt{-1 + \sqrt{1 + \Big(\frac{R_o}{\Omega}\Big)^2}} \qquad \delta = \sqrt{\frac{1}{2}}\Omega\sqrt{1 + \sqrt{1 + \Big(\frac{R_o}{\Omega}\Big)^2}} \tag{2.17}$$

3. Branch damper dimensioning based on long hydraulic line equations

A branch damper is a conduit of proper length inserted at the right angle into the main conduit and stoppered at its end. The principle of operation of the branch damper is based on the interference of the pressure wave generated by an excitation with the pressure wave bounced off the damper and propagating in the opposite direction. Thus the branch damper dimensioning problem comes down to determining its length L_0 depending on the frequency of the excitations which are to be damped. There is a prevailing view that this damper is a narrow-band damper and its effectiveness in reducing pressure fluctuations is limited to one frequency – the damper resonance frequency, see Kudźma (2001, 2006), Wacker (1985), Kollek and Kudźma (1997), Mikota and Manhartsgruber (2003). It is assumed that the damping effectiveness sharply diminishes already at slight deviations from the resonance frequency. However, the above analyses were based on the ideal liquid model (not representative of the real conditions) and their conclusions have not always been corroborated in operational practice (Kudźma, 2001, 2006). A schematic of the branch damper hydraulic system is shown in Fig. 1.

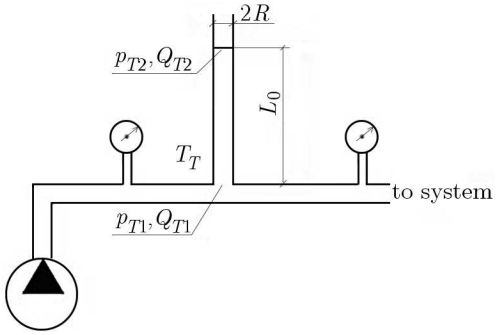

Fig. 1. Schematic of a branch damper hydraulic system

A branch damper mathematical model is defined by determining the damper input impedance and finding its minimum corresponding to the maximum pressure fluctuation reduction effectiveness. Three cases: lossless oscillatory flow, flow with quasi-steady losses and the case with the nonstationary friction model are considered. In order to carry out an analysis of the hydraulic system incorporating a branch damper one must first determine the operational impedance $Z_T(s) = p_{T1}(s)/Q_{T1}(s)$ in the supply station T_T, where $p_T(s)$ and $Q_T(s)$ are the Laplace transforms of the deviations of the pressure p_T and flow rate Q_T. Thus one should select an impedance value which ensures the minimum variation of pressure p_T. Treating the branch damper with length L_0 as a long hydraulic line, for a harmonic excitation one can write (consistently with relations (2.12) and (2.13)) the following

$$\begin{bmatrix} p_{T1} \\ Q_{T1} \end{bmatrix} = \begin{bmatrix} \cosh(T\Psi_z \mathrm{j}\omega) & Z_c\Psi_z \sinh(T\Psi_z \mathrm{j}\omega) \\ \dfrac{1}{Z_c\Psi_z}\sinh(T\Psi_z \mathrm{j}\omega) & \cosh(T\Psi_z \mathrm{j}\omega) \end{bmatrix} \begin{bmatrix} p_{T2} \\ Q_{T2} \end{bmatrix} \tag{3.1}$$

Since the flow is blocked at the damper end, $Q_{T2} = 0$, the impedance Z_d at the place where the branch is connected, according to equation (3.1), has the form

$$Z_d = \frac{\rho_o c_o \Psi_z}{\pi R^2 \tanh \frac{L_0 \Psi_z \mathrm{j}\omega}{c_o}} \tag{3.2}$$

When the lossless model is adopted, the viscosity function $\Psi_z = 1$ should be used in equation (3.2), whereas for the quasi-steady frictional losses one should use relations (2.17). The nonstationary friction model is taken into account through equations (2.13)-(2.17) and substituting $\mathrm{j}\Omega$ for $\widehat{s}$ (the dimensionless operator of the Laplace transformation) in relation (2.9).

Figure 2 shows an example of how the geometric parameters of the branch pressure fluctuation damper are determined for the basic harmonic of pump 2110 (this type of pump was used for experimental verification) manufactured by the Warsaw Waryński Construction Machinery Plant. The dominant frequency in the pump delivery fluctuation spectrum follows from the relation

$$f_i = \frac{n_p z_t K}{60} \tag{3.3}$$

where: n_p is the rotational speed of the pump shaft [rpm], z_t – number of teeth, K – next number of the harmonic component, $f_1 = 250\,\text{Hz}$, $z_t = 10$ teeth and pump shaft rotational speed $n_p = 1500\,\text{rpm}^{-1}$. From formula (3.3), after transformations, it follows that the initial damper impedance modulus $|Z_d|$ for the lossless model will be minimal when the following condition is satisfied

$$\frac{\omega_w}{c_o} L_0 = K\pi + \frac{\pi}{2} \tag{3.4}$$

where $K = 0, 1, 2, \ldots$. Using the dependence between the angular frequency ω_w and frequency f_w, and the following expression for pressure wavelength λ_f (Kudźma, 2012)

$$\lambda f = \frac{c_o}{f_w} \tag{3.5}$$

one can determine (from condition (3.5)) length L_0 of the branch damper ensuring the maximum pressure fluctuation amplitude damping for a given frequency f_w as a function of length λ_f of the pressure wave in the pipeline

$$L_0 = \frac{\lambda_f}{4} \tag{3.6}$$

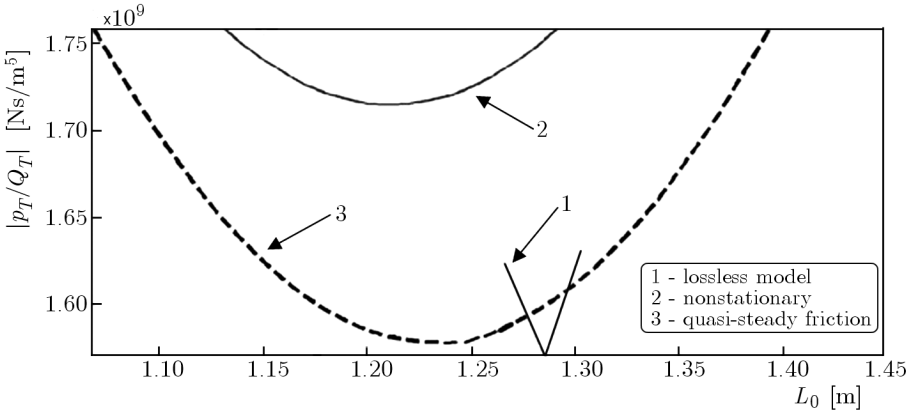

Fig. 2. Modulus of the initial impedance $|Z_d|$ of the branch damper as a function of its length L_0 for different friction models at viscosity $\mu = 30 \cdot 10^{-3}\,\text{Ns/m}^2$, pressure wave propagation velocity $c_{oszt} = 1288\,\text{m/s}$ (acc. to Kudźma (2012)) and $R = 4.5\,\text{mm}$

Numerous numerical studies, corroborated by experiments, indicate that in order to obtain the maximum pressure fluctuation damping for a given excitation frequency f_w, the damper length calculated for the ideal liquid should be shortened by the value of correction ΔL_0 determined assuming the nonstationary friction model and introducing the notion of relative change χ in damper length

$$\chi = \frac{\Delta L_0}{L_0} \tag{3.7}$$

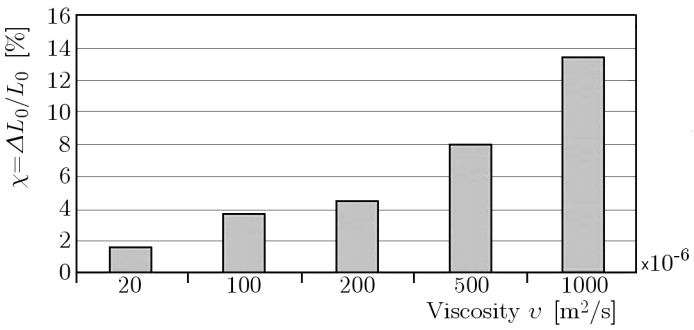

Fig. 3. Relative change χ in the branch damper length versus viscosity υ of the working medium

The numerically determined value of coefficient χ depending on the kinematic viscosity of the oil is shown in Fig. 3.

In real conditions, the optimal length of the branch damper should be calculated from relation

$$L_{0opt} = \frac{\lambda}{4}(1 - \chi) \tag{3.8}$$

4. Experimental verification

Branch damper effectiveness tests and acoustic tests were carried out in the real loader Ł-200 boom lifting gear system incorporating P2C2110C5B26A gear pump made by the Warsaw Waryński Construction Machinery Plant (the manufacturer-installed pump model). Figure 4 shows a schematic of the hydraulic system of the Ł-200 loader boom lifting gear which was placed in a sound chamber (the drive motor and the supply system were outside the chamber) with an insulating power of 50 dB.

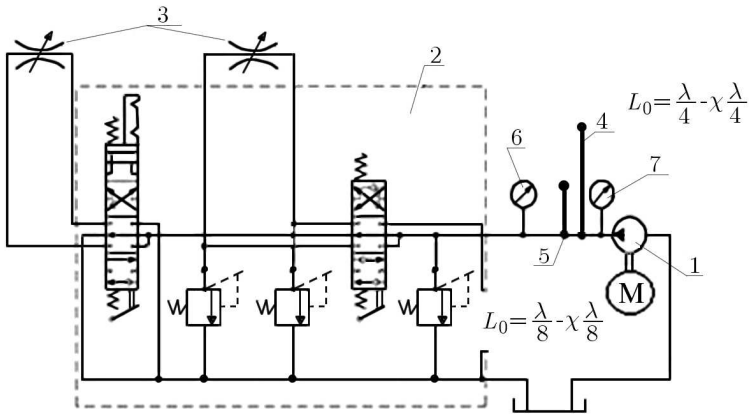

Fig. 4. Schematic of Ł-200 loader boom lifting gear hydraulic system with throttle valves and dampers: 1 – pump, 2 – distributor R1011VF1V, 3 – throttle valve, 4 – branch damper, 5 – branch damper $\lambda/8$, 6, 7 – pressure sensors

A retunable damper, with adjustable length Lo (and so with adjustable natural frequency) was designed in order to experimentally verify the method of determining (selecting a friction model) the optimal length. Figure 5 shows an axial cross section of the investigated damper. The pressure fluctuation amplitude levels p_{T1} in the hydraulic system versus branch damper length L_0 are shown in Fig. 6. The damper whose length $L_{0opt} = 1.24$ m was determined on the basis of the nonstationary friction model was found to be most effective. For the lossless model the damper length was 1.28 m, but the effectiveness of the damper was by 4 dB lower than that of the damper with the nonstationary friction model.

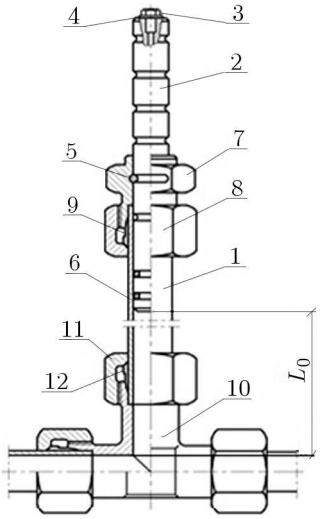

Fig. 5. Branch damper with retunable natural frequency: 1 – branch damper, 2 – piston, 3 – bleeder screw, 4 – copper washer, 5 – cotter pin, 6 – sealing ring, 7 – connector shell, 8 – connecting nut, 9 – cutting ring, 10 – coupling shell, 11 – nut, 12 – cutting ring

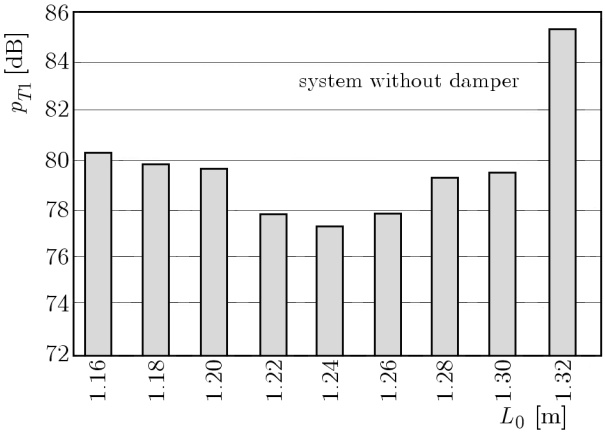

Fig. 6. Pressure fluctuation amplitude levels p_{T1} in the hydraulic system versus the branch damper length L_0 – pump delivery fluctuation first harmonic $f_1 = 250\,\text{Hz}$, average pressure $p_T = 10\,\text{MPa}$

5. Conclusion

The branch damper whose dimensioning comes down to determining its length is effective in reducing amplitudes only for specific frequencies. If in the first approximation the optimal length is assumed in accordance with $L_0 = \lambda_{f1}/4$ (leaving out oscillatory flow resistances in the damper), the pressure fluctuation amplitude damping is obtained for the basic harmonic f1and harmonic $3f_1$, i.e. generally $f_w = 2K - 1$, $K = 1, 2, 3, \ldots$. In order to suppress even harmonics, one should assume damper length $L_0 = \lambda_{f1}/8$ (λ_{f1} – the wavelength for the basic harmonic). In terms of pressure fluctuation effectiveness, the most advantageous solution is to use a double branch damper. When the flow resistances are left out and the optimum length is adopted, the particular pressure fluctuation components are suppressed completely. In real conditions, when the nonstationary friction model is assumed, the optimal length of the branch damper for a given excitation frequency is calculated from relation (3.2). One can determine the optimal branch damper length using simplified relation (3.8) and the data shown in Fig. 3. In this case, the following regularity is observed: the higher the coefficient of viscosity of the working liquid, the shorter (by 2-15%) the optimal length in comparison with the length defined by formula (3.6) for

the ideal liquid. When the double branch damper is installed in the outlet port of the pump in the Ł-200 loader boom lifting system, the pressure fluctuation amplitude is reduced several times in the whole range of the excitation frequencies, whereby the total noise (the measure of which is the sound pressure level subject to correction) is reduced by a few to about twenty $dB(A)$, depending on the system load, see Fig. 7.

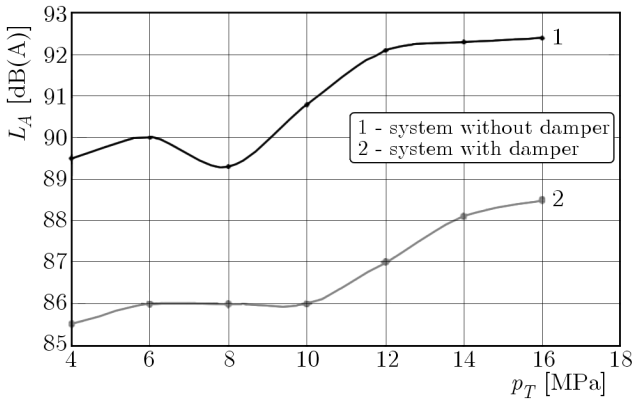

Fig. 7. Corrected sound pressure level $L_A dB(A)$ of Ł-200 loader boom lifting gear hydraulic system with the double branched damper and without damper versus the forcing pressure p_T

References

1. Directive 98/37/WE (in Polish)
2. Kollek W., Kudźma Z., 1997, Passive und active Metoden der Druckpulsation und Larminderung Hydrostatischen Systemen, *II Deutsch-Polnisches Seminar Innovation und Fortschritt in der Fluidtechnik*, Warsaw
3. Kollek W., Kudźma Z., Osiński P., 2001, The use of acoustic holography to locate noise sources in hydrostatic drive systems (in Polish), *Problemy Maszyn Roboczych*, **17**, 93-102
4. Kollek W., Kudźma Z., Stosiak M., 2008, Propagation of vibrations of the bearing elements of a heavy engineering machine (in Polish), *Transport Przemysłowy i Maszyny Robocze*, **2**, 50-53
5. Kollek W., Kudźma Z., Stosiak M., Mackiewicz J., 2007,Possibilities of diagnosing cavitation in hydraulic systems, *Archives of Civil and Mechanical Engineering*, **7**, 1, 61-73
6. Kudźma Z., 2001, Pressure fluctuation damper with retunable natural frequency (in Polish), *Czynniki stymulujące rozwój maszyn i systemów hydraulicznych, Konferencja naukowo techniczna*, Wrocław-Szklarska Poręba, 3-6.X.2001, Oficyna Wydawnicza Politechniki Wrocławskiej, Wrocław
7. Kudźma Z., 2006, Passive branch pressure fluctuation damper (in Polish), *Hydraulika i Pneumatyka*, **6**
8. Kudźma Z., 2012, *Pressure Fluctuation and Noise Damping in Hydraulic Systems in Transient and Steady States* (in Polish), Oficyna Wydawnicza Politechniki Wrocławskiej, Wrocław
9. Kudźma Z., Kudźma S., 2002, Wave phenomena in proportionally controlled hydrostatic systems (in Polish), *Hydraulika i Pneumatyka*, **6**, 15-17
10. Mikota J., Manhartsgruber B., 2003, Transientresponse dynamics of dynamic vibration absorbers for the attenuation of fluid-flow pulsations in hydraulic systems, *International Journal of Fluid Power*, **4**, 1
11. Ohmi M., Iguchi M., 1980, Flow pattern and frictional losses in pulsating pipe flow. Part 3: General representation of turbulent flow pattern, *Bulletin of JSME*, December, **23**, 186, 2029-2036

12. Ohmi M., Kyonen S., Usui T., 1985, Numerical analysis of transient turbulent flow in a liquid line, *Bulletin of JSME*, May, **28**, 239, 799-806

13. Osiński P., Kollek W., 2013, Assessment of energetistic measuring techniques and their application to diagnosis of acoustic condition of hydraulic machinery and equipment, *Archives of Civil and Mechanical Engineering*, **13**, 3

14. Stosiak M., 2012, The modelling of hydraulic distributor slide-sleeve interaction, *Archives of Civil and Mechanical Engineering*, **12**, 2, 192-197

15. Tijsseling A.S., 1996, Fluid-structure interaction in liquid-filled pipe systems: a review, *Journal of Fluids and Structures*, **10**, 109-146

16. Urbanowicz K., Zarzycki Z., 2012, New efficient approximation of weighting functions for simulations of unsteady friction losses in liquid pipe flow, *Journal of Theoretical and Applied Mechanics*, **50**, 2, 487-508

17. Vardy A.E., Brown J.M.B., 2003, Transient turbulent friction in smooth pipe flows, *Journal of Sound and Vibration*, **259**, 5, 1011-1036

18. Vardy A.E., Brown J.M.B., 2004, Transient turbulent friction in fully rough pipe flows, *Journal of Sound and Vibration*, **270**, 233-257

19. Vardy A.E., Brown J.M.B., 2007, Approximation of turbulent wall shear stress in highly transient pipe flows, *Journal of Hydraulic Engineering, ASCE*, November, 1219-1228

20. Wacker K., 1985, *Schalldampfer auslagen zum Vermindern des Larmes von Hydraulikanlagen*, Maschinenmarkt

21. Zarzycki Z., 1994,Resistances of nonstationary motion of liquid in closed conduits (in Polish), *Prace Naukowe Politechniki Szczecińskiej*, **516**

22. Zarzycki Z., Kudźma S., Kudźma Z., Stosiak M., 2007, Simulation of transient flows in hydraulic system with a long liquid line, *Journal of Theoretical and Applied Mechanics*, **45**, 4, 853-871

23. Zielke W., 1968, Frequency-dependent friction in transient pipe flow, *Transactions of the ASME, Journal of Basic Engineering*, **90**, 1, 109-115

Manuscript received June 13, 2014; accepted for print November 21, 2014

JOURNAL OF THEORETICAL AND APPLIED MECHANICS
53, 3, pp. 569-579, Warsaw 2015
DOI: 10.15632/jtam-pl.53.3.569

HEAT FLOW THROUGH A THIN COOLED PIPE FILLED WITH A MICROPOLAR FLUID

Michal Beneš
Czech Technical University, Faculty of Civil Engineering, Czech Republic
Igor Pažanin
University of Zagreb, Faculty of Science, Zagreb, Croatia; e-mail address: pazanin@math.hr
Francisco Javier Suárez-Grau
Universidad de Sevilla, Facultad de Matemáticas, Sevilla, Spain

In this paper, a non-isothermal flow of a micropolar fluid in a thin pipe with circular cross-section is considered. The fluid in the pipe is cooled by the exterior medium and the heat exchange on the lateral part of the boundary is described by Newton's cooling condition. Assuming that the hydrodynamic part of the system is provided, we seek for the micropolar effects on the heat flow using the standard perturbation technique. Different asymptotic models are deduced depending on the magnitude of the Reynolds number with respect to the pipe thickness. The critical case is identified and the explicit approximation for the fluid temperature is built improving the known result for the classical Newtonian flow as well. The obtained results are illustrated by some numerical simulations.

Keywords: pipe flow, heat conduction, micropolar fluid, asymptotic analysis

1. Introduction

The Navier-Stokes model of classical hydrodynamics is based on the assumption that the fluid particles do not posses any internal structure. However, in the case of fluids whose particles have complex shapes (e.g. polymeric suspensions, liquid crystals, muddy fluids, animal blood, even water in models with small scales), fluid particles can exhibit some microscopical effects such as rotation and shrinking. For such fluids, the local structure and micro-motions of the fluid elements cannot be ignored and one of the best-established theories covering those phenomenae is the micropolar fluid theory, introduced by Eringen (1966). Physically, micropolar fluids consist of rigid, spherical particles suspended in a viscous medium where the deformation of the particles is ignored. The individual particles may rotate (independently of the movement of the fluid) and, thus, a new vector field, the angular velocity field of rotation of particles (microrotation) is introduced to classical pressure and velocity fields. Correspondingly, one new vector equation is added expressing the conservation of the angular momentum. As a result, a non-Newtonian model is obtained representing an important generalization of the Navier-Stokes equations. As such, it describes the behavior of numerous real fluids better than the classical model, especially when the characteristic dimensions of the flow (e.g. diameter of the pipe) become very small.

Here we investigate the non-isothermal 3D flow of a micropolar fluid in a thin (or long) cylindrical pipe. The problem is described by a complex nonlinear system of PDEs in which micropolar equations are coupled with the heat conduction equation (see Lukaszewicz, 1999). The full coupled system is very difficult to be handled, especially if one wants to analytically construct an asymptotic approximation of the flow. Therefore, in this paper, we are going to consider only the heat flow in a thin pipe assuming that the velocity distribution is known. That means that the governing problem is being described by the non-stationary heat equation

with given velocity in the convection term. In view of the applications we want to model (heat exchangers, pipelines, etc.), we assume that the pipe is plunged in an ambient medium whose temperature is different from the fluid temperature. The heat exchange between the fluid and surrounding medium is being described by Robin's boundary condition resulting from Newton's cooling law. Our goal is to derive a simplified mathematical model describing the asymptotic behavior of the fluid temperature in such a situation.

Seeking primarily for the micropolar effects, one needs to focus on the convection term carrying the effects of the fluid microstructure in the velocity distribution. Following Marušić *et al.* (2008), the idea is to assume that the Reynolds number may depend on the small parameter ε (being the ratio between pipe thickness and its length) and to deduce various models depending on its magnitude with respect to ε. In the mentioned paper, classical Newtonian flow has been treated and the critical case is identified in which the effects of the convection term and the surrounding temperature are of the same order. Avoiding computation of the formal asymptotic expansion, the method employed by Marušić *et al.* (2008) is very elegant but, unfortunately, cannot be employed in the micropolar setting. The reason lies in the fact that the approximation for velocity feels the microstructure effects in its corrector (see Appendix). In view of that, we are forced to change the methodology and try to formally derive a higher-order asymptotic approximation for the fluid temperature acknowledging the effects we seek for. Starting from the non-dimensional setting and using the two-scale asymptotic technique, we manage to construct an explicit approximation in the critical case clearly showing in which way the fluid microstructure and exterior temperature affect the heat flow inside the pipe. This is especially important with regard to numerical computations.

The isothermal flow of a micropolar fluid was successfully considered both in 2D, see Dupuy *et al.* (2004, 2008) and in a more realistic 3D case, see Pažanin (2011a,b). Taking into account the thermal effects as well, non-isothermal flows have gained much attention in the recent years, see e.g. Prathap Kumar *et al.* (2010), Si *et al.* (2013), Ali and Ashraf (2014). To our knowledge, so far only simplified 2D setting (in which the microrotation is a scalar function) has been studied and the influence of the surrounding medium has been neglected in the process. For that reason, in the present paper we address the 3D problem in a cooled pipe describing a real-life situation.

2. Position of the problem

Let $B = B(0,1) \subset \mathbb{R}^2$ be a unit circle. We study the flow in a straight pipe with length L and cross-section diameter d given by $\widehat{\Omega} = \{\widehat{x} = (\widehat{x}_1, \widehat{x}_2, \widehat{x}_3) \in \mathbb{R}^3 : \ 0 < \widehat{x}_1 < L, \ (\widehat{x}_2, \widehat{x}_3) \in dB\}$. We take that the ratio $\varepsilon = d/L$ is small meaning that we consider the problem in a cylindrical pipe which is either very thin or very long. It is supposed that the pipe is filled with an incompressible micropolar fluid. Motivated by the framework of heat exchangers, we assume that the fluid inside the pipe is cooled by the exterior medium so we prescribe Newton's cooling condition on the pipe lateral boundary. As explained in Introduction, our intention is to study the thermodynamic part of the system assuming that the velocity distribution is known and given by the approximation provided in Appendix.

In such a situation, it is plausible to work with the problem written in a non-dimensional form. In view of that, we introduce the non-dimensional variable $x = (x_1, x_2, x_3) = \widehat{x}/L$ and, correspondingly, the domain $\Omega^\varepsilon = (0,1) \times \varepsilon B$. We denote by $\Gamma^\varepsilon = (0,1) \times \varepsilon \partial B$ the lateral boundary of the pipe. All physical properties of the fluid are assumed to be constant: ν – kinematic Newtonian viscosity, κ – thermal conductivity and c_p – specific heat capacity at constant pressure. We set density of the fluid to be equal to one, for the sake of notational simplicity. In the non-dimensional framework, three characteristic numbers appear: $\mathrm{Re}^\varepsilon = \nu^{-1} U_0 L$ – Reynolds number, $\mathrm{Pr} = \kappa^{-1} \nu c_p$ – Prandtl number and $\mathrm{Nu} = \beta L \kappa^{-1}$ – Nusselt number. Here U_0 denotes the

characteristic velocity of the fluid, while β stands for the heat transfer coefficient coming from Newton's cooling condition. We take the characteristic time of the process as $T_0 = L^2 c_p \kappa^{-1}$ and, correspondingly, introduce rescaled time as $t = \tau/T_0$. As a result, our problem for the unknown fluid temperature $\Phi^\varepsilon(x,t)$ can be written as follows

$$\begin{aligned} &\frac{\partial \Phi^\varepsilon}{\partial t} - \Delta \Phi^\varepsilon + \mathrm{Re}^\varepsilon \mathrm{Pr} \mathbf{v}^\varepsilon \cdot \nabla \Phi^\varepsilon = 0 \qquad \text{in} \quad \Omega^\varepsilon \times (0,T) \\ &\Phi^\varepsilon = \theta_k \qquad \text{for} \quad x_1 = k \quad (k=0,1) \end{aligned} \tag{2.1}$$

$$\frac{\partial \Phi^\varepsilon}{\partial \mathbf{n}} = \mathrm{Nu}(G - \Phi^\varepsilon) \qquad \text{on} \quad \Gamma^\varepsilon \times (0,T) \qquad\qquad \Phi^\varepsilon(x,0) = \Phi^0(x) \qquad\qquad x \in \Omega^\varepsilon \tag{2.2}$$

The fluid velocity enters the above system as the known function $\mathbf{v}^\varepsilon(x_1,x_2,x_3) = \mathbf{u}^\varepsilon(x_1,x_2/\varepsilon,x_3/\varepsilon)$ with $\mathbf{u}^\varepsilon$ being provided in Appendix. Robin's boundary condition $(2.2)_1$ models the heat exchange between the fluid inside the pipe and surrounding medium ($\mathbf{n}$ denotes exterior unit normal on Γ^ε). To simplify the calculations a little bit, exterior temperature G and boundary temperatures θ_k are assumed to be independent of cross-section variables, i.e. $G = G(x_1,t)$ and $\theta_k = \theta_k(t)$ $(k=0,1)$.

This is the formal setting of our problem. It consists of (linear) convection-diffusion equation equipped with the appropriate mixed boundary conditions for temperature. The existence and uniqueness issues for such a problem are resolved and well-known (see e.g. Ladyzhenskaya *et al.*, 1967) and, thus, are not going to be discussed here. Using asymptotic analysis with respect to ε, we want to derive a macroscopic law describing the behavior of fluid temperature clearly acknowledging the effects of the fluid microstructure and surrounding temperature.

3. Asymptotic analysis

Denoting $x' = (x_2,x_3)$, we introduce the fast variable $y' = (y_2,y_3)$ as $y' = x'/\varepsilon$. Correspondingly, we introduce the new unknown function $\varphi^\varepsilon(x_1,y',t) = \Phi^\varepsilon(x_1,\varepsilon y',t)$. Taking into account that $\mathbf{u}^\varepsilon(x_1,y') = \mathbf{u}_0(y') + \varepsilon \mathbf{u}_1(x_1,y')$ (see Appendix), φ^ε satisfies the following (rescaled) equation

$$\frac{\partial \varphi^\varepsilon}{\partial t} - \frac{1}{\varepsilon^2}\Delta_{y'}\varphi^\varepsilon - \frac{\partial^2 \varphi^\varepsilon}{\partial x_1^2} + \mathrm{PrRe}^\varepsilon\Big(u_0^1 \frac{\partial \varphi^\varepsilon}{\partial x_1} + u_1^2 \frac{\partial \varphi^\varepsilon}{\partial y_2} + u_1^3 \frac{\partial \varphi^\varepsilon}{\partial y_3} + \varepsilon u_1^1 \frac{\partial \varphi^\varepsilon}{\partial x_1}\Big) = 0 \tag{3.1}$$

The above equation is posed in $\Omega \times (0,T)$, where $\Omega = (0,1) \times B$. Here and in the sequel, we denote

$$\Delta_{y'}\phi = \frac{\partial^2 \phi}{\partial y_2^2} + \frac{\partial^2 \phi}{\partial y_3^2} \qquad\qquad \nabla_{y'}\phi = \frac{\partial \phi}{\partial y_2}\mathbf{e}_2 + \frac{\partial \phi}{\partial y_3}\mathbf{e}_3$$

for a scalar function ϕ and Cartesian basis $(\mathbf{e}_1,\mathbf{e}_2,\mathbf{e}_3)$. Newton's cooling condition $(2.2)_1$ after rescaling has the following form

$$\nabla_{y'}\varphi^\varepsilon \cdot y' = \varepsilon \mathrm{Nu}(G - \varphi^\varepsilon) \qquad \text{on} \quad \Gamma \times (0,T) \tag{3.2}$$

We express the unknown temperature φ^ε as an asymptotic expansion in powers of the small parameter ε

$$\varphi^\varepsilon(x_1,y',t) = \varphi_0(x_1,y',t) + \varepsilon\varphi_1(x_1,y',t) + \varepsilon^2\varphi_2(x_1,y',t) + \ldots \tag{3.3}$$

and substitute it in (3.1) and (3.2). It is essential to observe the following: if we kept the Reynolds number Re^ε constant (independent of ε), then we would obtain no contribution of the convection term in the macroscopic model. In fact, the exterior temperature G would completely dominate

the process and no effects of the fluid microstructure could be observed (see a) below). Thus, we adopt the idea from Marušić *et al.* (2008) and use the fact that Re^ε can be compared with the small parameter ε in a various way leading to possible different asymptotic models depending on its order of magnitude. Indeed, plugging (3.3) in (3.1) and (3.2), after collecting equal powers of ε, we detect two characteristic cases:

1. $\mathrm{Re}^\varepsilon \ll \mathcal{O}\Big(\frac{1}{\varepsilon}\Big)$

   The lowest order approximation satisfies the following problem

$$\frac{1}{\varepsilon^2}: \ \Delta_{y'}\varphi_0 = 0 \qquad \text{in} \quad B \qquad\qquad 1: \ \nabla_{y'}\varphi_0 \cdot y' = 0 \qquad \text{on} \quad \partial B, \qquad (x_1,t) \in (0,1)\times(0,T) \tag{3.4}$$

   providing $\varphi_0 = \varphi_0(x_1,t)$. The next term in the expansion is given by

$$\frac{1}{\varepsilon}: \ \Delta_{y'}\varphi_1 = 0 \qquad \text{in} \quad B \qquad\qquad 1: \ \nabla_{y'}\varphi_1 \cdot y' = \mathrm{Nu}(G-\varphi_0) \qquad \text{on} \quad \partial B$$

   For fixed $(x_1,t) \in (0,1)\times(0,T)$, this is the standard Neumann problem for the Laplace equation. Thus, it will be solvable if $\int_{\partial B} \mathrm{Nu}(G-\varphi_0)\, dy' = 0$ implying $\varphi_0 = G$. It means that, for $\mathrm{Re}^\varepsilon \ll \mathcal{O}(1/\varepsilon)$, the fluid inside the pipe assumes temperature of the surrounding medium and that the effects of the boundary temperature θ_k are negligible. Moreover, the micropolar effects do not appear even in higher-order terms.

2. $\mathrm{Re}^\varepsilon \gg \mathcal{O}\Big(\frac{1}{\varepsilon}\Big)$

   In this case, the convection term becomes dominant, but $\nabla_{y'}\varphi_0 \cdot y' = 0$ on ∂B (see (3.2)). Therefore, we conclude that the effects of the surrounding temperature G would be negligible on this assumption.

Taking into account the above discussion, we conclude that the most interesting case is when $\mathrm{Re}^\varepsilon = \mathcal{O}(1/\varepsilon)$ since it will lead to the asymptotic model in which all the effects we seek for are balanced. Thus, in the sequel, we perform careful analysis in this critical case.

3.1. Critical case $\mathrm{Re}^\varepsilon = \mathcal{O}\Big(\frac{1}{\varepsilon}\Big)$

To simplify the notation let us take $\mathrm{Re}^\varepsilon = 1/\varepsilon$. The zero order term in the asymptotic expansion is described by problem (3.4) so, as above, we conclude $\varphi_0 = \varphi_0(x_1,t)$. However, the next term is given by

$$\frac{1}{\varepsilon}: \ \Delta_{y'}\varphi_1 = \mathrm{Pr}u_0^1 \frac{\partial \varphi_0}{\partial x_1} \qquad \text{in} \quad B \qquad\qquad \varepsilon: \ \nabla_{y'}\varphi_1 \cdot y' = \mathrm{Nu}(G-\varphi_0) \qquad \text{on} \quad \partial B \tag{3.5}$$

Taking into account that $u_0^1 = 2Q(1-|y'|^2)$ (see Appendix), the compatibility condition for the existence of the solution to problem (3.5) gives

$$\mathrm{Pr}Q\frac{\partial \varphi_0}{\partial x_1} - 2\mathrm{Nu}(G-\varphi_0) = 0 \qquad \text{in} \quad (0,1)\times(0,T) \tag{3.6}$$

For fixed $t \in (0,T)$, this is in fact, a linear ODE for φ_0 (with respect to x_1) which can be easily solved. To assure uniqueness, we need one boundary condition and the natural choice is $\varphi_0(0,t) = \theta_0$. Such a choice of the boundary condition is obvious from the physical point of view (the temperature of the fluid exiting the pipe should not be prescribed in advance) and has been

rigorously justified in the case of Newtonian flow, see Marušić *et al.* (2008). Consequently, we obtain

$$\varphi_0(x_1,t)=\mathrm{e}^{-\frac{2\mathrm{Nu}}{\mathrm{Pr}Q}x_1}\left(\theta_0(t)+\frac{2\mathrm{Nu}}{\mathrm{Pr}Q}\int\limits_0^{x_1}\mathrm{e}^{\frac{2\mathrm{Nu}}{\mathrm{Pr}Q}\xi}G(\xi,t)\,d\xi\right) \tag{3.7}$$

In view of (3.6), the problem for φ_1 becomes

$$\begin{aligned}&\Delta_{y'}\varphi_1=4\mathrm{Nu}(G-\varphi_0)(1-|y'|^2) \qquad \text{in} \quad B\\ &\nabla_{y'}\varphi_1\cdot y'=\mathrm{Nu}(G-\varphi_0) \qquad \text{on} \quad \partial B\end{aligned} \tag{3.8}$$

It can be explicitly solved by passing to polar coordinates, leading to

$$\varphi_1(x_1,y',t)=\mathrm{Nu}(G-\varphi_0)\Big(|y'|^2-\frac{1}{4}|y'|^4\Big)+C(x_1,t) \tag{3.9}$$

Here $C(x_1,t)$ is a function to be determined after identifying the problem for φ_2

$$\begin{aligned}&1: \quad \frac{\partial\varphi_0}{\partial t}-\Delta_{y'}\varphi_2-\frac{\partial^2\varphi_0}{\partial x_1^2}+\mathrm{Pr}\Big(u_0^1\frac{\partial\varphi_1}{\partial x_1}+u_1^2\frac{\partial\varphi_1}{\partial y_2}+u_1^3\frac{\partial\varphi_1}{\partial y_3}+u_1^1\frac{\partial\varphi_0}{\partial x_1}\Big)=0 \qquad \text{in} \quad B\\ &\varepsilon^2: \quad \nabla_{y'}\varphi_2\cdot y'=-\mathrm{Nu}\varphi_1 \qquad \text{on} \quad \partial B, \qquad (x_1,t)\in(0,1)\times(0,T)\end{aligned} \tag{3.10}$$

The above system will be solvable if and only if

$$\begin{aligned}&\pi\frac{\partial\varphi_0}{\partial t}-\pi\frac{\partial^2\varphi_0}{\partial x_1^2}+\mathrm{Pr}\int\limits_B u_0^1\frac{\partial\varphi_1}{\partial x_1}\,dy'+\mathrm{Pr}\int\limits_B u_1^2\frac{\partial\varphi_1}{\partial y_2}\,dy'+\mathrm{Pr}\int\limits_B u_1^3\frac{\partial\varphi_1}{\partial y_3}\,dy'\\ &\quad+\mathrm{Pr}\frac{\partial\varphi_0}{\partial x_1}\int\limits_B u_1^1\,dy'=-\mathrm{Nu}\int\limits_{|y'|=1}\varphi_1\,dy'\end{aligned} \tag{3.11}$$

The components of the velocity corrector $\mathbf{u}_1$ appearing in $(3.10)_1$ have the following form (see Appendix)

$$\begin{aligned}u_1^1(x_1,y')&=\frac{1}{8}(|y'|^2-1)\Big[\Big(\frac{df_2}{dx_1}+2N^2\frac{g_3}{2R_1+R_2}\Big)y_2+\Big(\frac{df_3}{dx_1}-2N^2\frac{g_2}{2R_1+R_2}\Big)y_3\Big]\\ u_1^2(x_1,y')&=-\frac{N^2}{8R_1}g_1(x_1)(1-|y'|^2)y_3\\ u_1^3(x_1,y')&=\frac{N^2}{8R_1}g_1(x_1)(1-|y'|^2)y_2\end{aligned}$$

Taking into account expression (3.9), by direct integration we obtain that the last three integrals on the left-hand side in (3.11) are equal to zero. Thus, from (3.11) we deduce an equation for $C(x_1,t)$

$$\begin{aligned}&\mathrm{Pr}Q\frac{\partial C}{\partial x_1}+2\mathrm{Nu}C=D\\ &D(x_1,t)=\frac{\partial\varphi_0}{\partial t}-\frac{\partial^2\varphi_0}{\partial x_1^2}+\frac{7Q\mathrm{NuPr}}{24}\Big(\frac{\partial\varphi_0}{\partial x_1}-\frac{\partial G}{\partial x_1}\Big)+\frac{3}{2}\mathrm{Nu}^2(\varphi_0-G)\end{aligned}$$

Endowing it with the boundary condition $C(0,t)=0$, we get

$$C(x_1,t)=\frac{1}{\mathrm{Pr}Q}\mathrm{e}^{-\frac{2\mathrm{Nu}}{\mathrm{Pr}Q}x_1}\int\limits_0^{x_1}\mathrm{e}^{\frac{2\mathrm{Nu}}{\mathrm{Pr}Q}\xi}D(\xi,t)\,d\xi. \tag{3.12}$$

Remark 1. The corrector φ_1 is computed to satisfy equation $(3.8)_1$ and cooling condition $(3.8)_2$. Note that the boundary condition at $x_1 = 0$ could not be taken into account in the process. As a consequence, $\varphi_1(0, y', t) \neq 0$ implying $\varphi_0 + \varepsilon\varphi_1 \neq \theta_0$, i.e. the boundary temperature at the inlet is being modified by the higher-order term. We can fix that by introducing the appropriate boundary layer corrector depending on the dilated variable $(y_1, y') = (x_1/\varepsilon, x'/\varepsilon)$, see e.g. Marušić-Paloka and Pažanin (2009). However, such a corrector would have an exponential decay towards zero (as $y_1 \to +\infty$) meaning that it would not affect the approximation outside the boundary layer (it would only serve for the convergence proof which is out of the scope of the present paper). Thus, there is no reason to formally correct the approximation $\varphi_0 + \varepsilon\varphi_1$ in the vicinity of $x_1 = 0$ since the effects of such correction would not contribute to the macroscopic model except in the small boundary layer near the pipe inlet.

The corrector φ_1 is given in an explicit form by (3.9) and (3.12). We observe that there are contributions of surrounding and boundary temperature, but we find no micropolar effects at this order. Therefore, we have to continue computation and try to construct a higher-order corrector φ_2. Taking into account (3.7) and (3.9) and the expression for the velocity distribution, problem (3.10) can be written as

$$\begin{aligned}
\Delta_{y'}\varphi_2 &= \Big[-\frac{\partial\varphi_0}{\partial t} + \frac{2\mathrm{Nu}}{\mathrm{Pr}Q}\frac{\partial G}{\partial x_1} + \Big(\frac{2\mathrm{Nu}}{\mathrm{Pr}Q}\Big)^2(\varphi_0 - G)\Big](1 - 2|y'|^2) - 4\mathrm{Nu}C(1 - |y'|^2) \\
&\quad - \mathrm{Nu}^2(G - \varphi_0)(1 - |y'|^2)\Big(\frac{11}{6} + 4|y'|^2 - |y'|^4\Big) \\
&\quad + \frac{1}{2}\mathrm{PrNu}Q\frac{\partial G}{\partial x_1}(1 - |y'|^2)\Big(-\frac{7}{6} + 4|y'|^2 - |y'|^4\Big) \\
&\quad + \frac{\mathrm{Nu}}{4Q}(\varphi_0 - G)(1 - |y'|^2)H_1 y_2 + \frac{\mathrm{Nu}}{4Q}(\varphi_0 - G)(1 - |y'|^2)H_2 y_3 \qquad \text{in} \quad B \\
\nabla_{y'}\varphi_2 \cdot y' &= -\frac{3}{4}\mathrm{Nu}^2(G - \varphi_0) - \mathrm{Nu}C \qquad \text{on} \quad \partial B, \qquad (x_1, t) \in (0,1) \times (0,T)
\end{aligned} \tag{3.13}$$

Here we denote

$$H_1(x_1) = \frac{df_2}{dx_1} + 2N^2\frac{g_3}{2R_1 + R_2} \qquad H_2(x_1) = \frac{df_3}{dx_1} - 2N^2\frac{g_2}{2R_1 + R_2}$$

coming from u_1^1. Problem (3.13) can be analytically solved by introducing six auxiliary problems corresponding to each term on the right-hand side of $(3.13)_1$ and passing to polar coordinates. We leave the reader to confirm that

$$\begin{aligned}
\varphi_2(x_1, y', t) &= \Big[-\frac{\partial\varphi_0}{\partial t} + \frac{2\mathrm{Nu}}{\mathrm{Pr}Q}\frac{\partial G}{\partial x_1} + \Big(\frac{2\mathrm{Nu}}{\mathrm{Pr}Q}\Big)^2(\varphi_0 - G)\Big]\Big(\frac{1}{4}|y'|^2 - \frac{1}{8}|y'|^4\Big) \\
&\quad - \mathrm{Nu}C\Big(|y'|^2 - \frac{1}{4}|y'|^4\Big) - \mathrm{Nu}^2(G - \varphi_0)\Big(\frac{11}{24}|y'|^2 + \frac{13}{96}|y'|^4 - \frac{5}{36}|y'|^6 + \frac{1}{64}|y'|^8\Big) \\
&\quad + \frac{1}{2}\mathrm{PrNu}Q\frac{\partial G}{\partial x_1}\Big(-\frac{7}{24}|y'|^2 + \frac{31}{96}|y'|^4 - \frac{5}{36}|y'|^6 + \frac{1}{64}|y'|^8\Big) \\
&\quad + \frac{\mathrm{Nu}}{4Q}(G - \varphi_0)\Big(\frac{df_2}{dx_1} + \frac{2N^2 g_3}{2R_1 + R_2}\Big)\Big(\frac{1}{6} - \frac{1}{8}|y'|^2 + \frac{1}{24}|y'|^4\Big)y_2 \\
&\quad + \frac{\mathrm{Nu}}{4Q}(G - \varphi_0)\Big(\frac{df_3}{dx_1} - \frac{2N^2 g_2}{2R_1 + R_2}\Big)\Big(\frac{1}{6} - \frac{1}{8}|y'|^2 + \frac{1}{24}|y'|^4\Big)y_3
\end{aligned} \tag{3.14}$$

This is the end of the formal derivation. Our asymptotic solution has the following form

$$\begin{aligned}
&\varphi^{\varepsilon}_{approx}(x_1, y', t) = \varphi_0(x_1, t) + \varepsilon\varphi_1(x_1, y', t) + \varepsilon^2\varphi_2(x_1, y', t) \\
&(x_1, y') \in \Omega \qquad t \in (0, T)
\end{aligned} \tag{3.15}$$

Since the functions φ_i $(i = 0, 1, 2)$ are all given in the explicit form, see (3.7), (3.9), (3.14), we can easily detect all the effects we were originally interested for. The first part of the solution, namely $\varphi_0+\varepsilon\varphi_1$, is influenced by the effects of cooling and upstream boundary temperature, and it can be viewed as an improvement of the result by Marušić *et al.* (2008) for the classical Newtonian flow. No effects of the fluid microstructure can be seen there. However, in the second-order corrector φ_2 we can clearly observe the correction coming due to the non-Newtonian (micropolar) nature of the fluid. The correction, i.e. the difference between $\varphi_0+\varepsilon\varphi_1$ and $\varphi^{\varepsilon}_{approx}$ can be clearly observed in the numerical examples in the following Section as well.

4. Numerical examples

In this Section we aim to visually compare the function $\varphi_0+\varepsilon\varphi_1$ (representing the approximation for the Newtonian flow) with the asymptotic approximation $\varphi^{\varepsilon}_{approx}$ for the generalized micropolar flow. It must be emphasized that there is very little information in the existing literature concerning the values of micropolar parameters. We use the reference by Papautsky *et al.* (1999) where $\nu = 2.9 \cdot 10^{-3}$, $\nu_r = 2.32 \cdot 10^{-4}$, $c_a + c_d = 10^{-6}$ are reported for the micropolar viscosity constants. Furthermore, we neglect the body force $\mathbf{f}$, while $\mathbf{g}$ is taken to be a point couple, see e.g. Shu and Lee (2008) (sequence $\delta_n = n/[\pi(1 + n^2x_1^2)]$ is employed to approach the sifting property of the Dirac delta function). Exterior and boundary temperatures are assumed to be constant ($G = 10$, $\theta_0 = 35$), while for the remaining constants we take Nu = 3.66, Pr = 4.8 and $Q = 81$. Polar coordinates $(|y'|, \vartheta)$ are used to describe the domain cross-section B, and 2D comparisons for different magnitudes of the small parameter ε are presented (see Figs. 1 and 2).

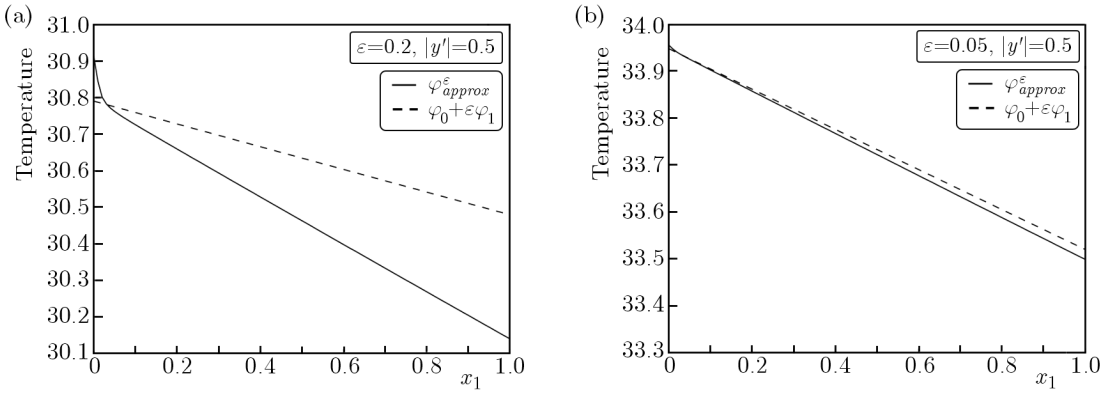

Fig. 1. Temperature distribution for the variable x_1 for a fixed $|y'|$ and polar angle $\vartheta = \pi/2$

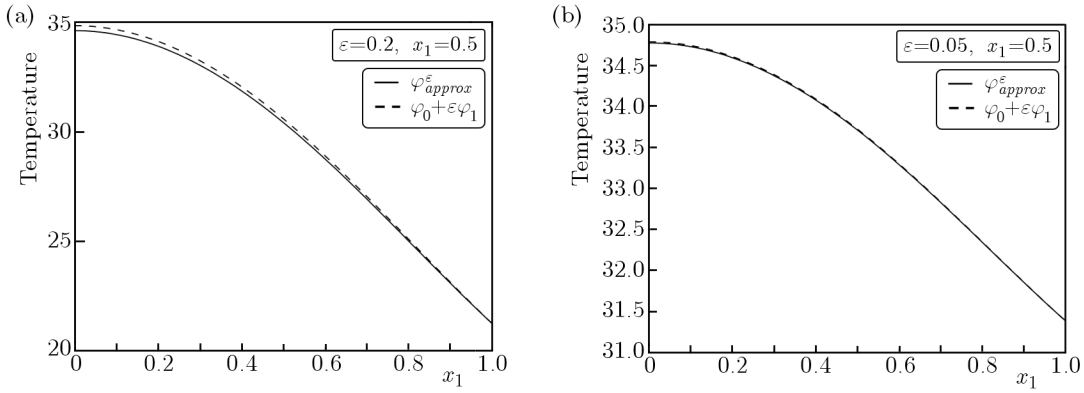

Fig. 2. Temperature distribution for the variable $|y'|$ (with $\vartheta = \pi/2$) and for a fixed x_1

5. Concluding remarks

We derived the asymptotic model describing the heat flow through a cylindrical pipe (with thickness $\mathcal{O}(\varepsilon)$) in the critical case where the effects of micropolarity, surrounding medium and entering temperature are balanced. The discussion at the beginning of Sec. 3 suggested that the critical case is reached when the Reynolds number is of order $\mathcal{O}(\varepsilon^{-1})$. As presented, the correctors in the asymptotic expansion for the fluid temperature can be explicitly computed clearly showing the difference between the classical Newtonian and micropolar flow. It is important to observe that such a more accurate approximation, is particularly interesting if ε is not too small (e.g. $\varepsilon = 0.2$ or $\varepsilon = 0.05$ as chosen in the numerical examples). Indeed, the smaller ε becomes, the difference between the Newtonian and micropolar flow becomes the less obvious (see Figs. 1 and 2). Moreover, by keeping ε in such a range, we ensure that the critical value of the Reynolds number is not exceeded, i.e. the flow stays in the laminar regime (not becoming turbulent, so we can use the laminar velocity profile from Appendix).

Let us discuss in more details the numerical results obtained in Sec. 4. First, in Fig. 1, we fix the cross-section variable and consider the temperature variations for the variable x_1. The result clearly suggests that, except in the small boundary layer near the left end of the pipe, the micropolar nature of the fluid enhances the cooling as we move along the pipe. Note that the value of the temperature at $x_1 = 0$ is a bit lower than the imposed $\theta_0 = 35$. That is essentially due to the fact that we have computed the correctors to satisfy the heat equation and the cooling condition, while the boundary condition at the pipe inlet has been neglected. Consequently, a boundary layer appear (in the vicinity of $x_1 = 0$) having no influence on the effective flow far from the pipe inlet, as explained in Remark 1. On the other hand, by fixing x_1, from Fig. 2 we deduce that the micropolar effects enhances the cooling far from the pipe lateral boundary. Indeed, as we approach the boundary, those effects become negligible due to the influence of the surrounding temperature.

To conclude, we believe that the above observations could improve the known engineering practice by acknowledging the obtained micropolar effects on the cooling process.

Appendix A. Approximation for the velocity

For reader's convenience, here we provide an asymptotic approximation for the fluid velocity used in the main part of the paper. For detailed (formal) derivation, we refer the reader to Pažanin (2013). Rigorous justification can be recovered from Pažanin (2011).

We start from the linearized micropolar equations (see Lukaszewicz, 1999)

$$\begin{aligned} &-(\nu+\nu_r)\Delta\widehat{\mathbf{u}}^\varepsilon + \nabla\widehat{p}^\varepsilon = 2\nu_r \operatorname{rot}\widehat{\mathbf{w}}^\varepsilon + \widehat{\mathbf{f}} \\ &\operatorname{div}\widehat{\mathbf{u}}^\varepsilon = 0 \qquad \text{in} \quad \widehat{\Omega}^\varepsilon \\ &-(c_a+c_d)\Delta\widehat{\mathbf{w}}^\varepsilon - (c_0+c_d-c_a)\nabla\operatorname{div}\widehat{\mathbf{w}}^\varepsilon + 4\nu_r\widehat{\mathbf{w}}^\varepsilon = 2\nu_r\operatorname{rot}\widehat{\mathbf{u}}^\varepsilon + \widehat{\mathbf{g}} \end{aligned} \tag{A.1}$$

The unknowns are: velocity $\widehat{\mathbf{u}}^\varepsilon$, pressure $\widehat{p}^\varepsilon$ and microrotation $\widehat{\mathbf{w}}^\varepsilon$. Positive constants ν_r, c_0, c_a, c_d represent new viscosity coefficients coming from the asymmetry of the stress tensor. Due to the pipe thickness, the body force $\widehat{\mathbf{f}} = \widehat{\mathbf{f}}(\widehat{x_1})$ and body couple $\widehat{\mathbf{g}} = \widehat{\mathbf{g}}(\widehat{x_1})$ are assumed to depend only on the variable going along the pipe. We use standard Dirichlet boundary conditions for the velocity and microrotation and prescribe the pressure drop $\widehat{q}_0 - \widehat{q}_L$ between the pipe ends

$$\begin{aligned} &\widehat{\mathbf{u}}^\varepsilon = 0 \qquad \text{on} \quad \widehat{\Gamma}^\varepsilon \qquad\qquad \mathbf{e}_1\times\widehat{\mathbf{u}}^\varepsilon = 0 \\ &\widehat{p}^\varepsilon = \widehat{q}_i \qquad \text{for} \quad \widehat{x}_1 = i \quad (i=0,L) \qquad\qquad \widehat{\mathbf{w}}^\varepsilon = 0 \qquad \text{on} \quad \partial\widehat{\Omega}^\varepsilon \end{aligned} \tag{A.2}$$

Since we need to work in non-dimensional framework, we introduce

$$x_1 = \frac{\widehat{x}_1}{L} \qquad y_2 = \frac{\widehat{x}_2}{\varepsilon L} \qquad y_3 = \frac{\widehat{x}_3}{\varepsilon L} \qquad \mathbf{u}^\varepsilon = \frac{\widehat{\mathbf{u}}^\varepsilon}{U_0} \qquad \mathbf{w}^\varepsilon = \frac{L}{U_0}\widehat{\mathbf{w}}^\varepsilon$$
$$p^\varepsilon = \frac{\varepsilon^2 L}{U_0(\nu+\nu_r)}\widehat{p}^\varepsilon \qquad \mathbf{f} = \frac{\varepsilon^2 L^2}{U_0(\nu+\nu_r)}\widehat{\mathbf{f}} \qquad \mathbf{g} = \frac{\varepsilon^2 L}{U_0(\nu+\nu_r)}\widehat{\mathbf{g}}$$

When considering micropolar flows, three non-Newtonian characteristic numbers appear

$$R_1 = \frac{c_a + c_d}{(\nu+\nu_r)L^2} \qquad R_2 = \frac{c_0 + c_d - c_a}{(\nu+\nu_r)L^2} \qquad N^2 = \frac{\nu_r}{\nu+\nu_r} \tag{A.3}$$

The parameters R_i are related to characteristic length of the microrotation effects, while N characterizes the coupling between the equations for velocity and microrotation. Note that for $N = 0$, the above system becomes decoupled and $(A.1)_1$ and $(A.1)_2$ reduce to classical Navier-Stokes equations. In view of that, equations (A.1) in the dimensionless form read

$$\begin{aligned}
&-\Delta_{y'}\mathbf{u}^\varepsilon - \varepsilon^2\frac{\partial^2\mathbf{u}^\varepsilon}{\partial x_1^2} + \frac{1}{\varepsilon}\nabla_{y'}p^\varepsilon + \frac{\partial p^\varepsilon}{\partial x_1}\mathbf{e}_1 \\
&\quad = 2N^2\Big[\varepsilon\Big(\frac{\partial w_3^\varepsilon}{\partial y_2} - \frac{\partial w_2^\varepsilon}{\partial y_3}\Big)\mathbf{e}_1 + \varepsilon\,\mathrm{rot}_{y'}w_1^\varepsilon - \varepsilon^2\frac{\partial w_3^\varepsilon}{\partial x_1}\mathbf{e}_2 + \varepsilon^2\frac{\partial w_2^\varepsilon}{\partial x_1}\mathbf{e}_3\Big] + \mathbf{f} \\
&\mathrm{div}_{y'}\mathbf{u}^\varepsilon + \varepsilon\frac{\partial u_1^\varepsilon}{\partial x_1} = 0 \\
&-R_1\Big(\Delta_{y'}\mathbf{w}^\varepsilon + \varepsilon^2\frac{\partial^2\mathbf{w}^\varepsilon}{\partial x_1^2}\Big) - R_2\Big[\nabla_{y'}(\,\mathrm{div}_{y'}\mathbf{w}^\varepsilon) + \varepsilon\frac{\partial}{\partial x_1}(\,\mathrm{div}_{y'}\mathbf{w}^\varepsilon)\mathbf{e}_1 \\
&\quad + \varepsilon\nabla_{y'}\Big(\frac{\partial w_1^\varepsilon}{\partial x_1}\Big) + \varepsilon^2\frac{\partial^2 w_1^\varepsilon}{\partial x_1^2}\mathbf{e}_1\Big] + 4N^2\varepsilon^2\mathbf{w}^\varepsilon \\
&\quad = 2N^2\Big[\varepsilon\Big(\frac{\partial u_3^\varepsilon}{\partial y_2} - \frac{\partial u_2^\varepsilon}{\partial y_3}\Big)\mathbf{e}_1 + \varepsilon\,\mathrm{rot}_{y'}u_1^\varepsilon - \varepsilon^2\frac{\partial u_3^\varepsilon}{\partial x_1}\mathbf{e}_2 + \varepsilon^2\frac{\partial u_2^\varepsilon}{\partial x_1}\mathbf{e}_3\Big] + \mathbf{g}
\end{aligned} \tag{A.4}$$

where

$$\mathrm{div}_{y'}\mathbf{v} = \frac{\partial v_2}{\partial y_2} + \frac{\partial v_3}{\partial y_3} \qquad \mathrm{rot}_{y'}v_i = \frac{\partial v_i}{\partial y_3}\mathbf{e}_2 - \frac{\partial v_i}{\partial y_2}\mathbf{e}_3 \qquad v_i = \mathbf{v}\cdot\mathbf{e}_i$$

Now we construct the approximation for the fluid velocity $\mathbf{u}^\varepsilon$ by plugging the asymptotic expansions

$$\begin{aligned}
&\mathbf{u}^\varepsilon(x_1, y') = \mathbf{u}_0(x_1, y') + \varepsilon\mathbf{u}_1(x_1, y') + \dots \\
&\mathbf{w}^\varepsilon(x_1, y') = \mathbf{w}_0(x_1, y') + \varepsilon\mathbf{w}_1(x_1, y') + \dots \\
&p^\varepsilon(x_1, y') = p_0(x_1) + \varepsilon p_1(x_1, y') + \dots
\end{aligned} \tag{A.5}$$

into system (A.4) and collecting the terms with equal powers of ε. The zero-order approximation turns out to be the standard Poiseuille solution given by

$$\begin{aligned}
&\mathbf{u}_0(y') = 2Q(1 - |y'|^2)\mathbf{e}_1 \\
&Q = \frac{1}{\pi}\int\limits_B u_0^1\,dy' = \frac{1}{8}\Big(q_0 - q_1 + \int\limits_0^1 f_1(\xi)\,d\xi\Big)
\end{aligned} \tag{A.6}$$

Since we observe no effects of the microstructure here, we have to derive a lower-order term $\mathbf{u}_1$ from the velocity expansion. Continuing computation, we arrive at

$$u_1^1(x_1,y') = \frac{1}{8}(|y'|^2-1)\Big[\Big(\frac{df_2}{dx_1}+2N^2\frac{g_3}{2R_1+R_2}\Big)y_2+\Big(\frac{df_3}{dx_1}-2N^2\frac{g_2}{2R_1+R_2}\Big)y_3\Big]$$
$$u_1^2(x_1,y') = -\frac{N^2}{8R_1}g_1(x_1)(1-|y'|^2)y_3 \tag{A.7}$$
$$u_1^3(x_1,y') = \frac{N^2}{8R_1}g_1(x_1)(1-|y'|^2)y_2$$

Finally, our asymptotic approximation for the fluid velocity reads

$$\mathbf{u}^\varepsilon(x_1,y') = \mathbf{u}_0(y') + \varepsilon\mathbf{u}_1(x_1,y') \qquad (x_1,y')\in\Omega \tag{A.8}$$

Acknowledgements

The first author of this work has been supported by the project GAČR 13-18652S. The second author has been supported by the Croatian Science Foundation (project 3955: *Mathematical modeling and numerical simulations of processes in thin or porous domains*). The third author has been supported by the projects MTM2011-24457 of the Ministerio de Economía y Competitividad and FQM309 of the Junta de Andalucía. The authors would like to thank the referee for his/her helpful comments and suggestions.

References

1. Ali K., Ashraf M., 2014, Numerical simulation of the micropolar fluid flow and heat transfer in a channel with a shrinking and a stationary wall, *Journal of Theoretical and Applied Mechanics*, **52**, 557-569
2. Dupuy D., Panasenko G., Stavre R., 2004, Asymptotic methods for micropolar fluids in a tube structure, *Mathematical Models and Methods in Applied Sciences*, **14**, 735-758
3. Dupuy D., Panasenko G., Stavre R., 2008, Asymptotic solution for a micropolar flow in a curvilinear channel, *Zeitschrift für Angewandte Mathematik und Mechanik*, **88**, 793-807
4. Eringen A.C., 1966, Theory of micropolar fluids, *Journal of Mathematics and Mechanics*, **16**, 1, 1-18
5. Ladyzhenskaya O.A., Solonnikov V.A., Uraltseva N.N., 1967, Linear and quasilinear equations of parabolic type, *Translations of Mathematical Monographs*, **23**, American Mathematical Society, Providence, R.I.
6. Lukaszewicz G., 1999, *Micropolar Fluids: Theory and Applications*, Birkhäuser, Boston
7. Marušić S., Marušić-Paloka E., Pažanin I., 2008, Effects of strong convection on the cooling process for a long or thin pipe, *C.R. Mécanique*, **336**, 493-499
8. Marušić-Paloka E., Pažanin I., 2009, Non-isothermal fluid flow through a thin pipe with cooling, *Journal of Applied Analysis*, **88**, 495-515
9. Papautsky I., Brazzle J., Ameel T., Frazier A.B., 1999, Laminar fluid behaviour in microchannels using micropolar fluid theory, *Sensors and Actuators A: Physical*, **73**, 101-108
10. Pažanin I., 2011a, Asymptotic behavior of micropolar fluid flow through a curved pipe, *Acta Applicandae Mathematicae*, **116**, 1-25
11. Pažanin I., 2011b, Effective flow of micropolar fluid through a thin or long pipe, *Mathematical Problems in Engineering*, **2011**, Article ID 127070, 18 pages
12. Pažanin I., 2013, Modeling of solute dispersion in a circular pipe filled with micropolar fluid, *Mathematical and Computer Modelling*, **57**, 2366-2373

13. Prathap Kumar J., Umavathi J.C., Chamkha A.J., Pop I., 2010, Fully-developed free-convective flow of micropolar and viscous fluids in a vertical channel, *Applied Mathematical Modelling*, **34**, 1175-1186

14. Si X., Zheng L., Lin P., Zhang X., Zhang Y., 2013, Flow and heat transfer of a micropolar fluid in a porous channel with expanding or contracting walls, *International Journal of Heat and Mass Transfer*, **67**, 885-895

15. Shu J.-J., Lee J.S., 2008, Fundamental solutions for micropolar fluids, *Journal of Engineering Mathematics*, **61**, 69-78

Manuscript received October 16, 2014; accepted for print December 9, 2014

JOURNAL OF THEORETICAL AND APPLIED MECHANICS
53, 3, pp. 581-591, Warsaw 2015
DOI: 10.15632/jtam-pl.53.3.581

ELASTIC BUCKLING OF A TRIANGULAR FRAME SUBJECT TO IN-PLANE TENSION

Krzysztof Magnucki

Poznan University of Technology, Institute of Applied Mechanics, Poznań, Poland
e-mail: krzysztof.magnucki@put.poznan.pl

Szymon Milecki

Institute of Rail Vehicles, TABOR, Poznań, Poland

The paper is devoted to elastic buckling of a symmetrical triangular frame under tensile in-plane load. Three mathematical models of the triangular frame are formulated. The first model deals with the pre-buckling state, the second one with the in-plane buckling state, and the third one with the lateral buckling state of the frame. The FEM-numerical model of the frame is formulated and the critical loads are calculated. The comparison of the results obtained in the analytical and numerical-FEM analysis is presented in tables and graphs in figures.

Keywords: triangular frame, elastic buckling, critical load, mathematical model

1. Introduction

The theoretical basis of buckling problems of structures is elaborated in many papers and monographs. Horne and Merchant (1965) described the problem of stability of frames. Thompson and Hunt (1973) presented a general theory of elastic stability of structures. Budiansky (1974) presented the theory of buckling and post-buckling behaviour of elastic structures. Chen and Liu (1987) described the theory of stability and implementation for structures. Bažant and Cedolin (1991) presented an extensive review of stability problems of structures: columns, frames, thin-walled beams, plates and shells. Simitses and Hodges (2006) presented the fundamentals of structural stability for columns, beams, rings and arches. Van der Heijden (2008) described the elastic stability of solids and structures formulated and studied by professor W.T. Koiter. Kaveh and Salimbahram (2007) presented a methodology for efficient calculation of buckling loads for symmetric rectangular frame structures. Şakar *et al.* (2012) presented FEM study of dynamic stability of a multi-span rectangular frame subjected to periodic loading.

The problem of triangular frame stability has been presented in literature only in several publications. For example, Magnucki and Milecki (2012) presented flat elastic buckling of the brake triangle in freight wagons, while Sobaś (2010) described the strength problems, especially the fatigue strength of the brake triangles.

The subject of theoretical study presented in this paper is a symmetrical triangular frame under tensile in-plane load (Fig. 1). The vertex C of the frame is fixed, whereas the vertexes A and B are simply supported in the plane of the triangular frame.

The arms of length L_1 are connected with a cross-beam of length L_2. The cross-section of the arms is rectangular, while the cross-section of the cross-beam is a circular ring (Fig. 2).

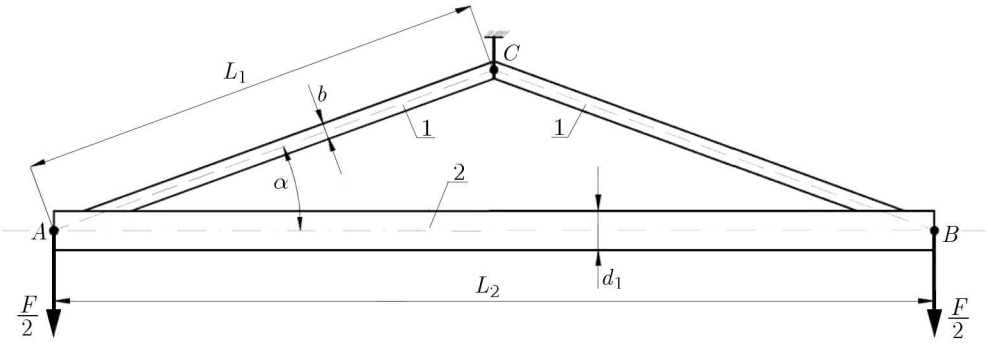

Fig. 1. Scheme of the symmetrical triangular frame with the load

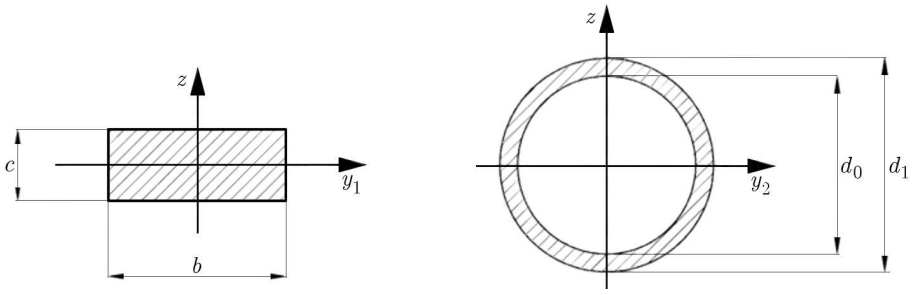

Fig. 2. Cross-section of the arms – 1 and cross-beam – 2

2. Mathematical models

2.1. Pre-buckling state

A half of the symmetrical triangular frame with the load F, internal normal force N_2 and bending moment M_2 for the pre-buckling state is shown in Fig. 3.

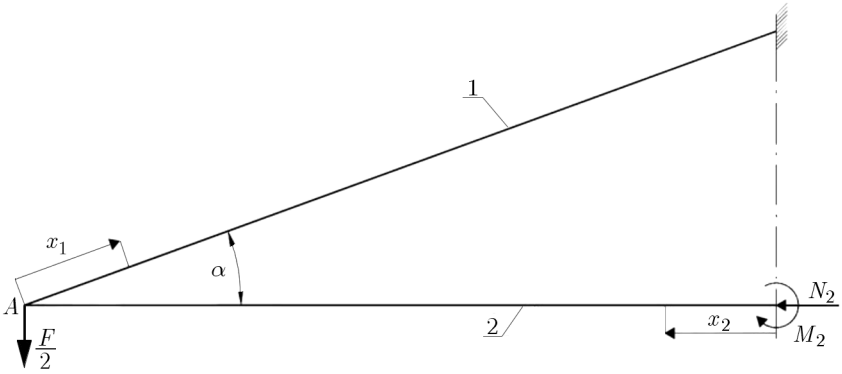

Fig. 3. Scheme of a half of the frame for the pre-buckling state

The normal forces $N(x_i)$ and bending moments $M_b(x_i)$ in the elements of the frame:

- arm – 1

$$N(x_1) = N_1 = N_2 \cos\alpha + \frac{1}{2}F\sin\alpha \qquad M_b(x_1) = \Big(N_2 \sin\alpha - \frac{1}{2}F\cos\alpha\Big)x_1 + M_2 \tag{2.1}$$

- cross-beam – 2

$$N(x_2) = N_2 \qquad M_b(x_2) = M_2 \tag{2.2}$$

The elastic strain energy of the frame is

$$U_\varepsilon = \frac{1}{2EA_1}\int_0^{L_1}[N(x_1)]^2\,dx_1 + \frac{1}{2EJ_z^{(1)}}\int_0^{L_1}[M_b(x_1)]^2\,dx_1 + \frac{1}{2EA_2}\int_0^{L_2/2}[N(x_2)]^2\,dx_2 + \frac{1}{2EJ_z^{(2)}}\int_0^{L_2/2}[M_b(x_2)]^2\,dx_2 \tag{2.3}$$

where $A_1 = bc$, $A_2 = \pi(d_1^2 - d_0^2)/4$ are the areas of the cross-sections of the arm and the cross-beam, $J_z^{(1)} = bc^3/12$, $J_z^{(2)} = \pi(d_1^4 - d_0^4)/64$ – inertia moments of the cross-sections of the arm and the cross-beam, E – Young's modulus.

Taking into account the theorem of Menabrea, two conditions are formulated

$$\frac{\partial U_\varepsilon}{\partial N_2} = \frac{1}{A_1}\int_0^{L_1}N(x_1)\cos\alpha\,dx_1 + \frac{1}{J_z^{(1)}}\int_0^{L_1}M_b(x_1)x_1\sin\alpha\,dx_1 + \frac{1}{A_2}\int_0^{L_2/2}N_2\,dx_2 = 0$$
$$\frac{\partial U_\varepsilon}{\partial M_2} = \frac{1}{J_z^{(1)}}\int_0^{L_1}M_b(x_1)\,dx_1 + \frac{1}{J_z^{(2)}}\int_0^{L_2/2}M_2\,dx_2 = 0 \tag{2.4}$$

Thus, after integration, two equations are obtained

$$\alpha_{11}\frac{M_2}{L_2} + \alpha_{12}N_2 = \frac{1}{2}\beta_1 F \qquad \alpha_{21}\frac{M_2}{L_2} + \alpha_{22}N_2 = \frac{1}{8}F \tag{2.5}$$

from which

$$N_2 = \frac{1}{2}\frac{\alpha_{11} - 4\beta_1\alpha_{21}\alpha_{11}}{\alpha_{22} - \alpha_{12}\alpha_{21}}F \qquad M_2 = \frac{1}{8}\frac{4\beta_1\alpha_{22} - \alpha_{12}}{\alpha_{11}\alpha_{22} - \alpha_{12}\alpha_{21}}FL_2 \tag{2.6}$$

where

$$\alpha_{11} = \frac{A_2L_2^2}{4J_z^{(1)}}\frac{\sin\alpha}{\cos^2\alpha} \qquad \alpha_{12} = 1 + \frac{A_2}{A_1}\cos\alpha + \frac{A_2L_2^2}{12J_z^{(1)}}\frac{\sin^2\alpha}{\cos^3\alpha}$$
$$\beta_1 = \Big(\frac{A_1L_2^2}{12J_z^{(1)}\cos^2\alpha} - 1\Big)\frac{A_2}{A_1}\sin\alpha \qquad \alpha_{21} = 1 + \frac{J_z^{(1)}}{J_z^{(2)}}\cos\alpha \qquad \alpha_{22} = \frac{1}{4}\tan\alpha$$

Thus, the normal tension force of arm (2.1) is as follows

$$N_1 = \frac{1}{2}\Big(\frac{\alpha_{11} - 4\beta_1\alpha_{21}}{\alpha_{11}\alpha_{22} - \alpha_{12}\alpha_{21}}\cos\alpha + \sin\alpha\Big)F \tag{2.7}$$

The normal force N_2 $(2.6)_1$ is a compressive force acting on the cross-beam which causes buckling of the frame.

2.2. Flat buckling state – critical load

The critical state for the flat buckling of the symmetrical triangular frame is demonstrated by symmetrical flexure of the cross-beam and the angles of rotation of the vertexes A and B in the xy plane. A scheme of the flat buckling mode for one half of the frame is shown in Fig. 4. Short discussion of this buckling problem was presented by Bažant and Cedolin (1991).

The detailed scheme of the load and displacements for the arm and the cross-beam of the frame is presented in Fig. 5.

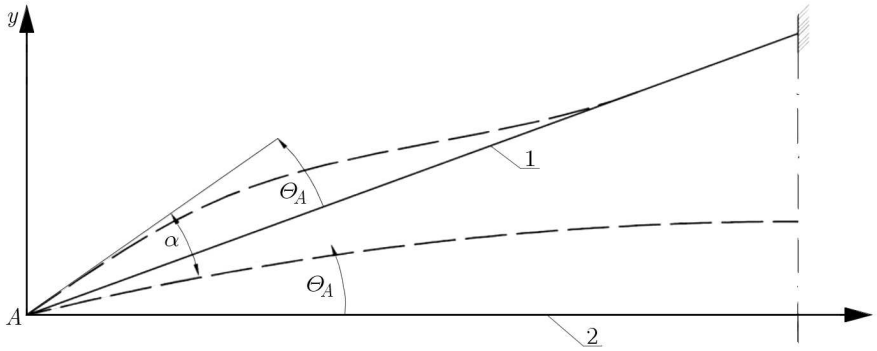

Fig. 4. Scheme of the flat buckling mode

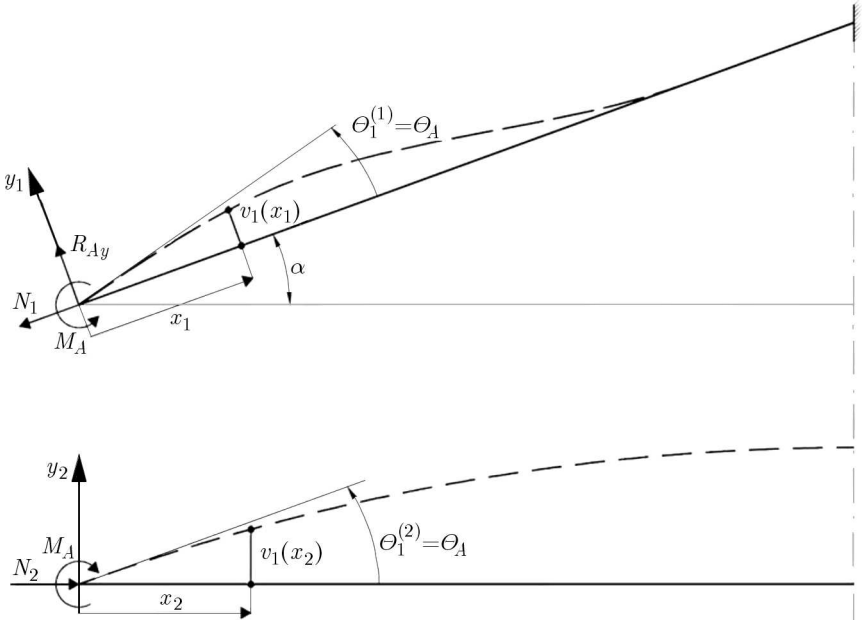

Fig. 5. Scheme of the load and displacements for the flat buckling state

The bending moment in the arm

$$M_b(x_1) = M_A - N_1 v_1(x_1) - R_{Ay} x_1 \tag{2.8}$$

The differential equation of the bending line of the arm

$$EJ_z^{(1)} \frac{d^2 v_1}{dx_1^2} - N_1 v_1(x_1) = -M_A + R_{Ay} x_1 \tag{2.9}$$

or

$$\frac{d^2 v_1}{dx_1^2} - k_{1y}^2 v_1(x_1) = -\frac{M_A}{EJ_z^{(1)}} + \frac{R_{Ay} x_1}{EJ_z^{(1)}} \tag{2.10}$$

where $k_{1y} = \sqrt{N_1/(EJ_z^{(1)})}$ is a coefficient.

The solution of this equation is in the form

$$v_1(x_1) = C_1^{(1)} \sinh(k_{1y} x_1) + C_2^{(1)} \cosh(k_{1y} x_1) + \frac{M_A}{N_1} - \frac{R_{Ay}}{N_1} x_1 \tag{2.11}$$

where $C_1^{(1)}$, $C_2^{(1)}$ are the integration constants.

The boundary conditions are as follows

$$v_1(0) = 0 \qquad v_1(L_1) = 0 \qquad \left.\frac{dv_1}{dx_1}\right|_{L_1} = 0 \tag{2.12}$$

from which

$$C_1^{(1)} = \frac{M_A}{N_1}\frac{1 + k_{1y}L_1\sinh(k_{1y}L_1) - \cosh(k_{1y}L_1)}{k_{1y}L_1\cosh(k_{1y}L_1) - \sinh(k_{1y}L_1)} \qquad C_2^{(1)} = -\frac{M_A}{N_1} \tag{2.13}$$

and the reaction

$$R_{Ay} = k_{1y}M_A\Big[\frac{1 + k_{1y}L_1\sinh(k_{1y}L_1) - \cosh(k_{1y}L_1)}{k_{1y}L_1\cosh(k_{1y}L_1) - \sinh(k_{1y}L_1)}\cosh(k_{1y}L_1) - \sinh(k_{1y}L_1)\Big] \tag{2.14}$$

Thus, the angle of the A vertex rotation in the xy plane is

$$\theta_A^{(1)} = \left.\frac{dv_1}{dx_1}\right|_0 = \frac{M_A L_1}{EJ_z^{(1)}} f_{1y}(k_{1y}L_1) \tag{2.15}$$

where

$$f_{1y}(k_{1y}L_1) = \frac{1}{k_{1y}L_1}\Big\{\sinh(k_{1y}L_1) - \frac{1 + k_{1y}L_1\sinh(k_{1y}L_1) - \cosh(k_{1y}L_1)}{k_{1y}L_1\cosh(k_{1y}L_1) - \sinh(k_{1y}L_1)}[\cosh(k_{1y}L_1) - 1]\Big\} \tag{2.16}$$

Similarly, the bending moment in the cross-beam is

$$M_b(x_2) = -M_A + N_2 v_2(x_2) \tag{2.17}$$

The differential equation of the bending line

$$\frac{d^2v_2}{dx_2^2} + k_2^2 v_2(x_2) = \frac{M_A}{EJ_z^{(2)}} \tag{2.18}$$

where $k_2 = \sqrt{N_2/(EJ_z^{(2)})}$ is a coefficient.

The solution of this equation is

$$v_2(x_2) = C_1^{(2)}\sinh(k_2x_2) + C_2^{(2)}\cosh(k_2x_2) + \frac{M_A}{N_2} \tag{2.19}$$

The boundary conditions

$$v_2(0) = 0 \qquad v_2(L_2) = 0 \tag{2.20}$$

from which the integration constants are

$$C_1^{(2)} = -\frac{M_A}{N_2}\frac{1 - \cos(k_2L_2)}{\sin(k_2L_2)} \qquad C_2^{(2)} = -\frac{M_A}{N_2} \tag{2.21}$$

Thus, the angle of the A vertex rotation in the xy plane is

$$\theta_A^{(2)} = \left.\frac{dv_2}{dx_2}\right|_0 = -\frac{M_A L_2}{EJ_z^{(2)}}\frac{1 - \cos(k_2L_2)}{k_2L_2\sin(k_2L_2)} \tag{2.22}$$

The consistency condition for the angles of in-plane rotation of the vertex A for the arm and cross-beam

$$\theta_A^{(1)} = \theta_A^{(2)} \tag{2.23}$$

from which the nonlinear algebraic equation is in the following form

$$k_{Jzz} f_{1y}(k_{1y} L_1) + 2\frac{1-\cos(k_2 L_2)}{k_2 L_2 \sin(k_2 L_2)} = 0 \tag{2.24}$$

where $k_{Jzz} = J_z^{(2)}/(J_z^{(1)} \cos\alpha)$ is a dimensionless parameter.

Taking into account the normal forces N_2 $(2.6)_1$ and N_1 (2.7), the critical load from this equation is determined.

2.3. Lateral buckling state – critical load

The critical state for the lateral buckling of the triangular frame is demonstrated by symmetrical flexure of the cross-beam in the xz plane and the corresponding angles of rotation of the vertexes A and B. A scheme of the lateral buckling mode for the half of the frame is shown in (Fig. 6).

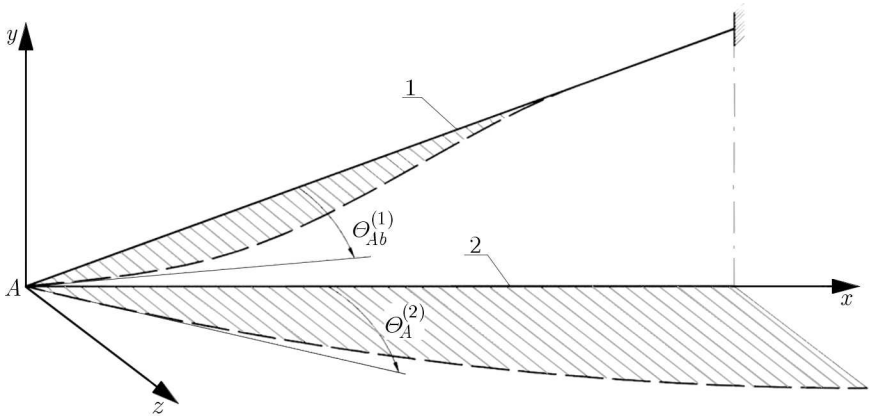

Fig. 6. Scheme of the lateral buckling mode

The flexure of the cross-beam in the xz plane causes bending and torsion of the arms. A scheme of the moments in the vertex A is shown in Fig. 7.

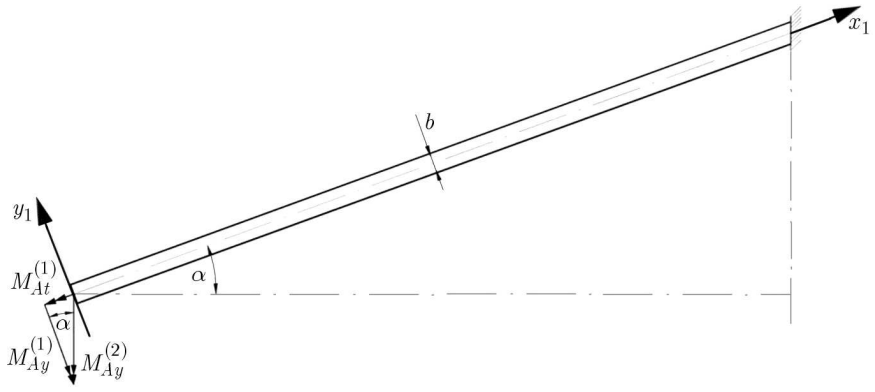

Fig. 7. Scheme of the moments in the vertex A

The bending moment $M_{Ay}^{(1)}$ and torsional moment $M_{At}^{(1)}$ in the vertex A for the arm are

$$M_{Ay}^{(1)} = M_{Ay}^{(2)} \cos\alpha \qquad M_{At}^{(1)} = M_{Ay}^{(2)} \sin\alpha \tag{2.25}$$

where $M_{Ay}^{(2)}$ is the bending moment in the vertex A for the cross-beam.

Analogically, the bending angle $\theta_{Ab}^{(1)}$ and torsion angle $\theta_{At}^{(1)}$ in the vertex A for the arm are

$$\theta_{Ab}^{(1)} = \theta_{A}^{(2)} \cos\alpha \qquad \theta_{At}^{(1)} = \theta_{A}^{(2)} \sin\alpha \tag{2.26}$$

where $\theta_{A}^{(2)}$ is the bending angle in the vertex A for the cross-beam.

The detailed scheme of the load and displacements for the arm and the cross-beam of the frame is presented in Fig. 8.

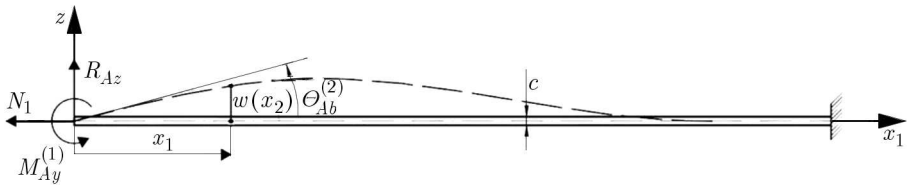

Fig. 8. Scheme of the load and displacements for lateral buckling state

The bending moment in the arm is

$$M_b(x_1) = M_{Ay}^{(1)} - N_1 w_1(x_1) - R_{Az} x_1 \tag{2.27}$$

This bending problem is analogous to the bending of the arm for flat buckling state (10), thus the bending angle of the vertex A is

$$\theta_{Ab}^{(1)} = \left.\frac{dw_1}{dx_1}\right|_0 = \frac{M_{Ay}^{(1)} L_1}{E J_y^{(1)}} f_{1z}(k_{1z} L_1) \tag{2.28}$$

where

$$f_{1z}(k_{1z}L_1) = \frac{1}{k_{1z}L_1}\Big\{\sinh(k_{1z}L_1) - \frac{1 + k_{1z}L_1\sinh(k_{1z}L_1) - \cosh(k_{1z}L_1)}{k_{1z}L_1\cosh(k_{1z}L_1) - \sinh(k_{1z}L_1)}[\cosh(k_{1z}L_1) - 1]\Big\} \tag{2.29}$$

and $k_{1z} = \sqrt{N_1/(EJ_y^{(1)})}$ is a coefficient, $J_y^{(1)} = b^3 c/12$ – inertia moment of the cross-sections of the arm.

The torsion angle $\theta_{At}^{(1)}$ in the vertex A

$$\theta_{At}^{(1)} = \frac{M_{At}^{(1)} L_1}{G J_t^{(1)}} = 2(1+\nu)\frac{M_{At}^{(1)} L_1}{E J_t^{(1)}} \tag{2.30}$$

where: $G = E/[2(1+\nu)]$ is the shear modulus of elasticity, ν – Poisson's ratio, and the torsional constant $J_t^{(1)}$ of the rectangular cross-section

• for $b \leqslant c$

$$J_t^{(1)} = \mu b^3 c \qquad \mu = \frac{1}{3} - \Big[0.178 + 0.153\frac{b}{c} - 0.138\Big(\frac{b}{c}\Big)^2\Big] \tag{2.31}$$

• for $c \leqslant b$

$$J_t^{(1)} = \mu b c^3 \qquad \mu = \frac{1}{3} - \Big[0.178 + 0.153\frac{c}{b} - 0.138\Big(\frac{c}{b}\Big)^2\Big] \tag{2.32}$$

The bending moment in the cross-beam is

$$M_b(x_2) = -M_{Ay}^2 + N_2 w_2(x_2) \tag{2.33}$$

This bending problem is analogous to the bending of the cross-beam for flat buckling state (2.17), thus the bending angle of the vertex A is

$$\theta_A^{(2)} = \left.\frac{dw_2}{dx_2}\right|_0 = -\frac{M_{Ay}^{(2)} L_2}{E J_z^{(2)}} \frac{1-\cos(k_2 L_2)}{k_2 L_2 \sin(k_2 L_2)} \tag{2.34}$$

Taking into account expressions (2.26) for the bending angle $\theta_{Ab}^{(1)}$ and torsion angle $\theta_{At}^{(1)}$, the consistency condition for the angles of the vertex A is as follows

$$\theta_{Ab}^{(1)} \cos\alpha + \theta_{At}^{(1)} \sin\alpha = \theta_A^{(2)} \tag{2.35}$$

Substituting expressions (2.28) and (2.30) into equation (2.35) and making simple transformation, the nonlinear algebraic equation is obtained in the following form

$$k_{Jzy} f_{1z}(k_{1z} L_1) \cos^2\alpha + 2(1+\nu) k_{Jzt} \sin^2\alpha + 2\frac{1-\cos(k_2 L_2)}{k_2 L_2 \sin(k_2 L_2)} = 0 \tag{2.36}$$

where: $k_{Jzy} = J_z^{(2)}/(J_y^{(1)} \cos\alpha)$, $k_{Jzt} = J_z^{(2)}/(J_t^{(1)} \cos\alpha)$ are dimensionless parameters.

Taking into account the normal forces N_2 $(2.6)_1$ and N_1 (2.7), the critical load from this equation is determined.

2.4. Example of the triangular frame – values of the critical load

An examplary calculation of the critical load is carried out for a symmetrical triangular frame: length of the cross-beam $L_2 = 1352\,\text{mm}$, angle between the arms and the cross-beam $\alpha = \pi/9$, diameters of the cross-section of the cross-beam $d_0 = 50\,\text{mm}$, $d_1 = 60\,\text{mm}$, area of the cross section of the arms $A_1 = 1000\,\text{mm}^2$ and material constants $E = 2 \cdot 10^5\,\text{MPa}$, $\nu = 0.3$. Models with different b parameter have been investigated. Values of other parameters are the same as the parameters of the construction which is used in railway industry. The values of critical loads $F_{CR,\,Flat}^{(Anal)}$ and $F_{CR,\,Lat}^{(Anal)}$ have been calculated on the basis of non-linear algebraic equations (2.24) and (2.36), respectively. The results of calculations are specified in Table 1.

Table 1. Values of critical loads – analytical solution

b [mm]	15	20	25	31.623	35	40	50	60
$F_{CR,\,Flat}^{(Anal)}$ [kN]	360.6	403.0	448.2	510.0	541.5	587.1	672.5	747.8
$F_{CR,\,Lat}^{(Anal)}$ [kN]	363.9	394.6	403.4	399.2	388.7	377.1	357.1	342.8

Flat buckling occurs when the width b of the arm is small ($b \leqslant 18\,\text{mm}$), and the lateral buckling occurs for greater width ($18\,\text{mm} \leqslant b$).

3. Numerical FEM model

3.1. FEM model of the triangular frame

The symmetrical triangular frame is a beam structure (Fig. 9), hence it is modeled with beam elements – system SolidWorks Simulation 2013 (Fig. 10). The model of the frame is defined in the rectangular coordinate system. The loading force is applied to the vertexes of the frame (Fig. 11).

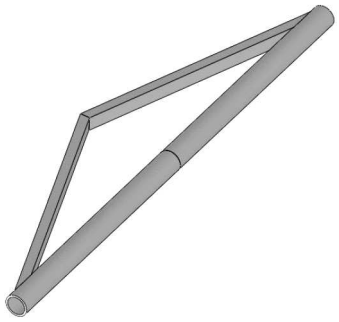

Fig. 9. Numerical model of triangular frame

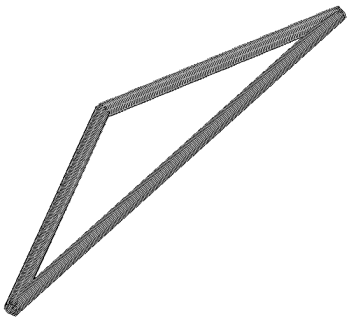

Fig. 10. Discretization of numerical model with the beam elements

Fig. 11. Boundary conditions and loads of the numerical model

3.2. Example of the triangular frame – values of the critical load

An examplary calculation of the critical load is carried out for the symmetrical triangular frame: length of the cross-beam $L_2 = 1352\,\text{mm}$, angle between arms and the cross-beam $\alpha = \pi/9$, diameters of the cross-section of the cross-beam $d_0 = 50\,\text{mm}$, $d_1 = 60\,\text{mm}$, the area of the cross section of the arms $A_1 = 1000\,\text{mm}^2$ and material constants $E = 2 \cdot 10^5\,\text{MPa}$, $\nu = 0.3$. The values of critical loads $F^{(FEM)}_{CR,\,Flat}$ and $F^{(FEM)}_{CR,\,Lat}$ are calculated on the basis of the finite element method. The results of calculations are specified in Table 2. An examplary FEM calculation of the triangular frame with dimension $b = 25\,\text{mm}$ is shown in Fig. 12.

Flat buckling, similarly to the analytical model, occurs when the width b of the arm is small ($b \leqslant 18\,\text{mm}$), and the lateral buckling occurs for greater width ($18\,\text{mm} \leqslant b$).

Table 2. The values of critical loads – FEM solution

b [mm]	15	20	25	31.623	35	40	50	60
$F_{CR,\,Flat}^{(FEM)}$ [kN]	353.7	390.7	435.6	492.4	520.9	562.1	638.2	704.7
$F_{CR,\,Lat}^{(FEM)}$ [kN]	361.6	393.5	400.5	393.2	385.5	373.4	352.7	338.6

Fig. 12. Scheme of the FEM model of the triangular frame

4. Comparison analysis

The values of critical loads calculated analytically and numerically (FEM) are similar. The difference between them is less than 3%. Comparison of these values is graphically shown for flat buckling (Fig. 13) and for lateral buckling (Fig. 14).

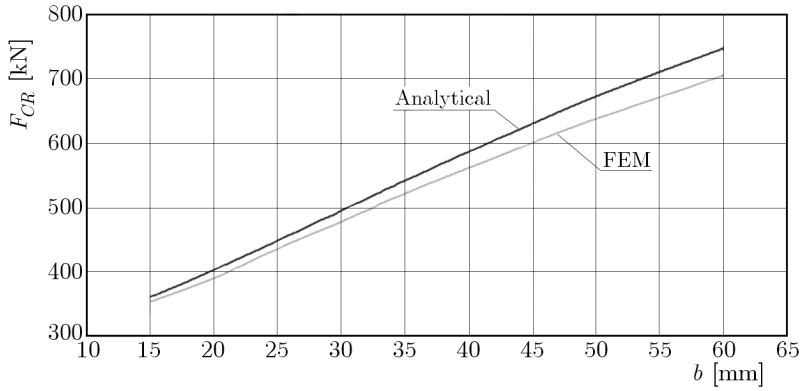

Fig. 13. Comparison of the critical values obtained from the analytical and numerical (FEM) methods for flat buckling

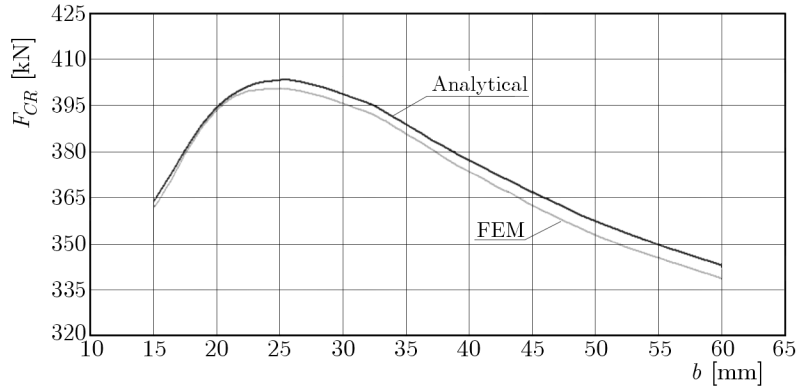

Fig. 14. Comparison of the critical values obtained from the analytical and numerical (FEM) methods for lateral buckling

5. Conclusions

Theoretical studies of the buckling problem of the symmetrical triangular frame carried out on the basis of the analytical and numerical FEM models allow one to conclude that:

- flat buckling of the frame occurs when the width b of the arm is small ($b \leqslant 18\,\mathrm{mm}$),
- lateral buckling of the frame occurs when the width b of the arm is greater ($18\,\mathrm{mm} \leqslant b$),
- maximum of the critical load exists for the width $b = 25\,\mathrm{mm}$,
- the analytical model of the frame accurately describes the flat and lateral buckling phenomena. The analytical and FEM results comply with each other.

The presented study, considering the lateral buckling, has not been undertaken before.

References

1. Budiansky B., 1974, Theory of buckling and post-buckling behaviour of elastic structures, *Advances in Applied Mechanics*, **14**, 1-65
2. Bažant Z.P., Cedolin L., 1991, *Stability of Structures. Elastic, Inelastic, Fracture, and Damage Theories*, Oxford University Press, New York, Oxford
3. Chen W.F., Liu E.M., 1987, *Structural Stability: Theory and Implementation*, Elsevier, New York
4. Horne M.Z., Merchant W., 1965, *The Stability of Frames*, Pergamon Press, New York
5. Kaveh A., Salimbahrami B., 2007, Buckling load of symmetric plane frames using canonical forms, *Computers and Structures*, **85**, 1420-1430
6. Magnucki K., Milecki S., 2012, Elastic stability of a brake triangle (in Polish), *Modelowanie Inżynierskie*, **44**, 199-208
7. Simitses G.J., Hodges D.H., 2006, *Fundamentals Structural Stability*, Butterworth-Heinemann, an imprint of Elsevier
8. Şakar G., Öztürk, Sabuncu M., 2012, Dynamic stability of multi-span frames subjected to periodic loading, *Journal of Constructional Steel Research*, **70**, 65-70
9. Sobaś M., 2010, New generation of brake triangles for freight care (in Polish), *Pojazdy Szynowe*, **3**, 21-30
10. Thompson J.M.T., Hunt G.W., 1973, *A General Theory of Elastic Stability*, John Wiley & Sons, London, New York, Sydney, Toronto
11. Van der Heijden A.M.A. (Editor), 2008, *W.T. Koiter's Elastic Stability of Solids and Structures*, Cambridge University Press, Cambridge, New York, Melbourne, Madrid, Cape Town, Singapore, São Paulo

Manuscript received August 26, 2014; accepted for print December 19, 2014

JOURNAL OF THEORETICAL AND APPLIED MECHANICS
53, 3, pp. 593-604, Warsaw 2015
DOI: 10.15632/jtam-pl.53.3.593

AN INTERNAL-STATE-VARIABLE BASED VISCOELASTIC-PLASTIC MODEL FOR POLYMERS

Cyprian Suchocki

Warsaw University of Technology, Department of Mechanics and Armament Technology, Warsaw, Poland
e-mail: c.suchocki@imik.wip.pw.edu.pl

In this study, a new viscoelastic-plastic constitutive model which has been formulated by utilizing the formalism of stress-like internal state variables is introduced. The developed constitutive equation allows for a good description of the inelastic material response of polymeric materials over a wide range of strain rates. An algorithm for numerical integration of the model equations has been derived. The FE implementation of the constitutive equation is widely discussed and the results of solving several exemplary problems are presented.

Keywords: polymers, rheology, constitutive equation, finite element method

Nomenclature

b	–	Knowles material parameter
$\mathbf{B}, \overline{\mathbf{B}}$	–	left Cauchy-Green (C-G) and isochoric left C-G deformation tensor
$\mathbf{C}, \overline{\mathbf{C}}$	–	right and isochoric right C-G deformation tensor
$\boldsymbol{\mathcal{C}}, \boldsymbol{\mathcal{C}}^{ve-p}$	–	elasticity tensor and viscoelastic-plastic material tensor
$\boldsymbol{\mathcal{C}}^{\tau c}$	–	material tensor related to convected stress rate
$\boldsymbol{\mathcal{C}}^{MJ}$	–	material Jacobian tensor used by Abaqus
$\mathbf{D}$	–	strain rate tensor
D_1	–	inverse of bulk modulus
$\mathbf{e}_k$	–	unit vector of Cartesian base, $k = 1, 2, 3$,
$\mathbf{F}, \overline{\mathbf{F}}$	–	deformation gradient and isochoric deformation gradient tensor
$\mathbf{H}_k$	–	viscoelastic overstress tensor $k = 1, 2, \ldots, N$
$\widetilde{\mathbf{H}}_k$	–	endochronic overstress tensor $k = 1, 2, \ldots, P$
$\mathbf{I}$	–	fourth order identity tensor
$\mathbf{I}_{\mathbf{C}^{-1}}$	–	fourth order identity tensor in reference configuration
$\boldsymbol{\mathcal{I}}$	–	auxiliary fourth order tensor
$I_k, \overline{I}_k$	–	algebraic invariants of right and of isochoric right C-G deformation tensor, $k = 1, 2, 3$
$\overline{J}_k$	–	algebraic invariants of material time derivative of isochoric right C-G deformation tensor, $k = 1, 2, 3$
J	–	Jacobian determinant
$\mathbf{L}$	–	velocity gradient tensor
$\mathbf{Q}$	–	orthogonal tensor
$\mathbf{S}, \overline{\mathbf{S}}$	–	second Piola-Kirchhoff (P-K) and auxiliary second P-K total stress tensor
$\mathbf{S}_0$	–	second P-K elastic stress tensor
$\mathbf{T}$	–	Lagrange total stress tensor
t	–	time since loading
U	–	volumetric stored elastic energy potential

$\mathbf{W}$	–	spin tensor
$W, \overline{W}$	–	stored and isochoric stored elastic energy potential
z, ζ	–	fictitious time variable at time t and at time τ
τ, τ'	–	time and auxiliary time variable
λ_k	–	stretch ratio in k-th direction, $k = 1, 2, 3$
$\boldsymbol{\tau}, \boldsymbol{\sigma}$	–	Kirchhoff and Cauchy stress tensors
μ, κ	–	Knowles material shear modulus and Knowles material hardening parameter
Γ_k	–	k-th relaxation coefficient, $k = 1, 2, \ldots, N$
γ_k	–	k-th endochronic coefficient, $k = 1, 2, \ldots, P$
τ_k	–	k-th relaxation time, $k = 1, 2, \ldots, N$
$\widetilde{D}_k$	–	k-th endochronic parameter, $k = 1, 2, \ldots, N$
$\mathbf{1}$	–	second order identity tensor
$\mathrm{DEV}\,[\bullet]$	–	operator extracting deviatoric part of a tensor in reference configuration
$\otimes$	–	dyadic product operator
$(\bullet)^{\nabla}$	–	Zaremba-Jaumann (Z-J) objective rate operator

1. Introduction

In recent years, various constitutive equations of viscoelasticity and viscoplasticity have been developed in order to describe the mechanical properties of thermoplastic polymers and resins. Ayoub *et al.* (2011) presented a viscoplastic model aimed at capturing the large strain response of polyethylene over a wide range of strain rates. A better approximation of the stress-strain relation of polyethylene, however for a narrower range of the strain rates, was achieved by Bergström and Bischoff (2010) who developed the so-called three network viscoplastic model. Abdul Hameed *et al.* (2014) formulated a constitutive model based on the multiplicative split of the deformation gradient. It was further used to simulate the monotonic stress-strain curves of polyethylene. Bardella (2001) developed a nonlinear viscoelastic constitutive model oriented for the description of the epoxy resin behavior during cyclic loadings and creep.

Instead of modeling the mechanical behavior of a polymer over the entire range of physically possible strains, some researchers focus on improving the constitutive equations for the spectrum of small and moderate deformations which are usually experienced by the structural elements. Drozdov and Christiansen (2007) developed a viscoplastic constitutive model aimed at predicting the stresses in high density polyethylene (HDPE) subjected to the cyclic loadings in tension. Hassan *et al.* (2011) utilized an overstress-based viscoplasticity theory to model the hysteresis loops of ultra high molecular weigth polyethylene (UHMWPE) for the maximum strains equal to 10%. Ben Hadj Hamouda *et al.* (2007) developed a viscoplastic model to capture the nonlinear stress-strain relation, creep and relaxation of the medium density polyethylene (MDPE). Monotonic stress-strain curves with the maximum strain of 12% were analyzed. Krairi and Doghri (2014) proposed a model utilizing the additive split of the strain tensor into viscoelastic and viscoplastic components. Monotonic and cyclic stress-strain curves were approximated for both polyamide (PA) and HDPE with the maximum axial strain of 14%.

Constitutive theories based on the endochronic plasticity theory enjoy recently an increasingly high interest. This theory was originally developed by Pipkin and Rivlin (1965). Kästner *et al.* (2012) proposed a viscoplastic constitutive equation for polyprophylene (PP) based on the generalized Maxwell mechanistic model. The polymer viscosity was assumed to depend on the non-equilibrium overstress while endochronic plasticity was used to help modeling the hysteresis loop. Strains up to 5% in tension were analyzed and infinitesimal strain tensor was used. This approach was later generalized to large displacements and large rotations by Alkas Yonan *et al.* (2013) for the purpose of modeling the inelastic response of polyvinylchloride (PVC).

All the mentioned above constitutive theories require determination of about twenty material parameters. The numerical algorithms used for integrating the models are usually complicated.

In the current study, a new viscoelastic-plastic constitutive model for thermoplastics and resins is presented. The model is an extension of the popular nonlinear viscoelasticity theory proposed by Holzapfel (2010) and widely used in FE codes. The formalism of internal stress-like state variables previously used by Suchocki (2013) to develop a nonlinear viscoelastic model for polymers is extended by taking advantage of the endochronic plasticity framework (Pipkin and Rivlin, 1965). The common assumptions of isothermal deformations and treating the effects of volumetric viscoelasticity as negligible have been applied. It was experimentally observed that irreversible volume changes are usually small (e.g. Wu, 2005). Thus, the postulate of plastic incompressibility is well established and utilized by the classical theory of plasticity. This assumption is adopted in the constitutive model formulated in the present study for sake of simplicity. The constitutive equation has a modular structure which enables adjusting it for a specific polymeric material. It is applied to capture the inelastic behavior of polyethylene. For that purpose the specific values of the material parameters have been determined. It is found that the proposed constitutive model accurately reproduces the stress relaxation curve and the hysteresis loop for the deformation rate magnitude from the interval 0.0005-0.05 s^{-1}. The constitutive equation is discretized and an algorithm for efficient numerical computations is presented. The implementation of the model into the FE software Abaqus is discussed.

2. Decoupled finite elasticity

In this section, the basic notions of hyperelasticity are presented. A material is called hyperelastic if it posseses a stored-energy function $W = W(\mathbf{C})$ (Holzapfel, 2010). In the case of material isotropy, this function must be invariant with respect to a rotation $\mathbf{Q}$, i.e.

$$W(\mathbf{C}) = W(\mathbf{Q}\mathbf{C}\mathbf{Q}^{\mathrm{T}}) \tag{2.1}$$

This requirement is fulfilled if W is a function of algebraic invariants of $\mathbf{C}$.

In terms of FEM, it is profitable to decouple the volumetric and isochoric responses within the constitutive model. This is facilitated by utilizing proper multiplicative decomposition of the deformation gradient tensor $\mathbf{F}$

$$\mathbf{F} = \mathbf{F}_{vol}\overline{\mathbf{F}} \qquad \mathbf{F}_{vol} = J^{\frac{1}{3}}\mathbf{1} \qquad \overline{\mathbf{F}} = J^{-\frac{1}{3}}\mathbf{F} \qquad \overline{\mathbf{C}} = \overline{\mathbf{F}}^{\mathrm{T}}\overline{\mathbf{F}} = J^{-\frac{2}{3}}\mathbf{C} \tag{2.2}$$

where $\mathbf{F}_{vol}$ and $\overline{\mathbf{F}}$ represent purely volumetric and isochoric deformations, respectively. Consequently, the algebraic invariants of $\overline{\mathbf{C}}$

$$\overline{I}_1 = \operatorname{tr}\overline{\mathbf{C}} \qquad \overline{I}_2 = \frac{1}{2}[(\operatorname{tr}\overline{\mathbf{C}})^2 - \operatorname{tr}\overline{\mathbf{C}}^2] \qquad \overline{I}_3 = \det\overline{\mathbf{C}} = 1 \tag{2.3}$$

The stored-energy function is formulated in a decoupled form

$$W(\mathbf{C}) = U(J) + \overline{W}(\overline{\mathbf{C}}) \tag{2.4}$$

where U and $\overline{W}$ are the stored-energy components associated with the volumetric and isochoric deformations, respectively. The stored-energy function as given by (2.4) results in

$$\mathbf{S} = Jp\mathbf{C}^{-1} + J^{-\frac{2}{3}}\operatorname{DEV}[\overline{\mathbf{S}}] \tag{2.5}$$

where

$$p = \frac{\partial U}{\partial J} \qquad \operatorname{DEV}[\overline{\mathbf{S}}] = \overline{\mathbf{S}} - \frac{1}{3}(\overline{\mathbf{S}}\cdot\overline{\mathbf{C}})\overline{\mathbf{C}}^{-1} \qquad \overline{\mathbf{S}} = 2\frac{\partial\overline{W}}{\partial\overline{\mathbf{C}}} \tag{2.6}$$

and $\operatorname{DEV}[\bullet] = [\bullet] - \frac{1}{3}([\bullet]\cdot\overline{\mathbf{C}})\overline{\mathbf{C}}^{-1}$ is an operator extracting a deviator of a tensor in the reference configuration, whereas $\overline{\mathbf{S}}$ is an auxiliary stress tensor.

3. Internal-state-variable based viscoelastic-plastic model

The total stress is assumed in the form of a sum

$$\mathbf{S} = \mathbf{S}_0 + \sum_{k=1}^{P} \widetilde{\mathbf{H}}_k + \sum_{j=1}^{N} \mathbf{H}_j \tag{3.1}$$

where the components $\mathbf{S}_0$ and $\widetilde{\mathbf{H}}_k$ $(k = 1, 2, \ldots, P)$ describe the equilibrium material response, whereas $\mathbf{H}_j$ $(j = 1, 2, \ldots, N)$ account for the viscoelastic effects. $\mathbf{S}_0$ is taken in the decoupled form, i.e.

$$\mathbf{S}_0 = \mathbf{S}_0^{vol} + \mathbf{S}_0^{iso} \qquad \mathbf{S}_0^{vol} = J\frac{\partial U}{\partial J}\mathbf{C}^{-1} \qquad \mathbf{S}_0^{iso} = 2J^{-\frac{2}{3}}\,\mathrm{DEV}\Big[\frac{\partial \overline{W}}{\partial \overline{\mathbf{C}}}\Big] \tag{3.2}$$

The evolution of overstresses $\widetilde{\mathbf{H}}_k$ is governed by the equations of the form

$$\dot{\widetilde{\mathbf{H}}}_k + \frac{1}{\widetilde{D}_k M(|\dot{\overline{\mathbf{C}}}|)}\widetilde{\mathbf{H}}_k = \gamma_k \dot{\mathbf{S}}_0^{iso} \qquad k = 1, 2, \ldots, P \tag{3.3}$$

where

$$M(|\dot{\overline{\mathbf{C}}}|) = \overline{J}_2^{-\frac{1}{2}} \qquad \overline{J}_2 = \mathrm{tr}\,\dot{\overline{\mathbf{C}}}^2 \tag{3.4}$$

This specific choice of M enables one to eliminate the time from Eq. (3.3), thus making the evolution of $\widetilde{\mathbf{H}}_k$ rate-independent. By integrating Eq. (3.3), it is found that

$$\widetilde{\mathbf{H}}_k(t) = \int_0^{z(t)} \gamma_k \mathrm{e}^{-\frac{z-\zeta}{\widetilde{D}_k}} \frac{\partial \mathbf{S}_0^{iso}(\zeta)}{\partial \zeta}\, d\zeta \tag{3.5}$$

where the following equalities are used

$$\dot{\zeta} = \frac{1}{M(|\dot{\overline{\mathbf{C}}}|)} \qquad \zeta(\tau) = \int_{-\infty}^{\tau} \frac{d\tau'}{M(\tau')} \qquad \zeta(t) = z \tag{3.6}$$

Substituting Eqs (3.4) into Eq. $(3.6)_2$ leads to the result

$$\zeta(\tau) = \int_{-\infty}^{\tau} \big[\dot{\overline{\mathbf{C}}}(\tau') \cdot \dot{\overline{\mathbf{C}}}(\tau')\big]^{\frac{1}{2}}\, d\tau' \qquad (\dot{\bullet}) = \frac{d}{d\tau'}(\bullet) \tag{3.7}$$

which in turn gives

$$\zeta(\tau) = \int_{-\infty}^{\tau} \big[d\overline{\mathbf{C}}(\tau') \cdot d\overline{\mathbf{C}}(\tau')\big]^{\frac{1}{2}} \tag{3.8}$$

The variable ζ is a fictious internal time associated with the material. For this reason the overstresses defined by Eq. (3.5) are called endochronic. Equation (3.5) is a special case of the stress-strain relation proposed by Pipkin and Rivlin (1965). The stress tensor $\mathbf{S}_0$ together with the endochronic overstresses $\widetilde{\mathbf{H}}_k$ $(k = 1, 2, \ldots, P)$ form up the elasto-plastic part of the constitutive equation which is responsible for reproducing the hysteresis loop of the modeled

polymeric material. The strain rate effects are captured by the viscoelastic overstresses $\mathbf{H}_j$ $(j = 1, 2, \ldots, N)$ which evolve in time according to the following differential equation

$$\dot{\mathbf{H}}_j + \frac{1}{\tau_j}\mathbf{H}_j = \Gamma_j \dot{\mathbf{S}}_0^{iso} \qquad j = 1, 2, \ldots, N \tag{3.9}$$

After time integrating Eq. (3.9), one obtains

$$\mathbf{H}_j(t) = \int_{-\infty}^{t} \Gamma_j \mathrm{e}^{-\frac{t-\tau}{\tau_j}} \frac{\partial \mathbf{S}_0^{iso}(\tau)}{\partial \tau}\, d\tau \tag{3.10}$$

For the purpose of modeling the mechanical properties of thermoplastics and resins, the stored-energy function $\overline{W}$ is adopted in the form proposed by Knowles (1977). The advantages of using the isochoric Knowles function were discussed by Suchocki (2011). The volumetric strain energy is assumed in the standard form, thus

$$\overline{W} = \frac{\mu}{2b}\Big\{\Big[1 + \frac{b}{\kappa}(\overline{I}_1 - 3)\Big]^{\kappa} - 1\Big\} \qquad U = \frac{1}{D_1}(J-1)^2 \tag{3.11}$$

Summing up, the developed constitutive equation utilizes four elasticity constants, $2P$ endochronic plasticity constants and $2N$ constants of viscoelasticity all of which are independent.

4. Discretization of constitutive equation

Below a numerical algorithm for the incremental integration of the developed model is introduced. For the time increment $n+1$, the total stress is, according to Eq. (3.1), given by the equation

$$\mathbf{S}_{n+1} = \mathbf{S}_{0\,n+1} + \sum_{k=1}^{P} \widetilde{\mathbf{H}}_{k\,n+1} + \sum_{j=1}^{N} \mathbf{H}_{j\,n+1} \tag{4.1}$$

The reccurence-update formula for the integration of Eq. (3.3) is obtained using the central difference method, thus the following approximations are utilized

$$\dot{y}\Big|_{n+\frac{1}{2}} \approx \frac{y_{n+1} - y_n}{\Delta t} = \frac{\Delta y_{n+1}}{\Delta t} \qquad y\Big|_{n+\frac{1}{2}} \approx y_n + \frac{1}{2}\Delta y_{n+1} \tag{4.2}$$

Applying the rules given by Eqs (4.2) to Eq. (3.3) one obtains the following formula

$$\widetilde{\mathbf{H}}_{k\,n+1} = \frac{\Big(1 - \frac{1}{\widetilde{D}_k}\frac{\Delta z_{n+1}}{2}\Big)\widetilde{\mathbf{H}}_{k\,n} + \gamma_k(\mathbf{S}_{0\,n+1}^{iso} - \mathbf{S}_{0\,n}^{iso})}{1 + \frac{1}{\widetilde{D}_k}\frac{\Delta z_{n+1}}{2}} \tag{4.3}$$

where

$$\Delta z_{n+1} = (\Delta \overline{\mathbf{C}}_{n+1} \cdot \Delta \overline{\mathbf{C}}_{n+1})^{\frac{1}{2}} \tag{4.4}$$

The integration of Eq. (3.9) is performed by means of the reccurence-update formula developed by Taylor *et al.* (1970), i.e.

$$\mathbf{H}_{j\,n+1} = \mathrm{e}^{-\frac{\Delta t}{\tau_j}}\mathbf{H}_{j\,n} + \Gamma_j \frac{1 - \mathrm{e}^{-\frac{\Delta t}{\tau_j}}}{\frac{\Delta t}{\tau_j}}(\mathbf{S}_{0\,n+1}^{iso} - \mathbf{S}_{0\,n}^{iso}) \tag{4.5}$$

Equations (4.1), (4.3) and (4.5) form up a discretized set of equations which can be utilized for numerical simulations. For the use of FEM, a material tangent stiffness tensor has to be defined in addition. The derivation of a tangent stiffness is discussed further in the text.

5. Exemplary application

In order to check the ability of the developed viscoelastic-plastic constitutive equation to fit the experimental data, it has been employed to capture the mechanical properties of UHMWPE which is a popular biomaterial with numerous applications in orthopaedics, such as hip joint implants, elbow implants or artificial intervertebral discs for instance.

For the purpose of modeling the inelastic behavior of UHMWPE, a version of the developed constitutive equation has been adopted with $N = 3$ viscoelastic overstresses and $P = 1$ endochronic overstress. The graphic interpretation of the model can be seen in Fig. 1.

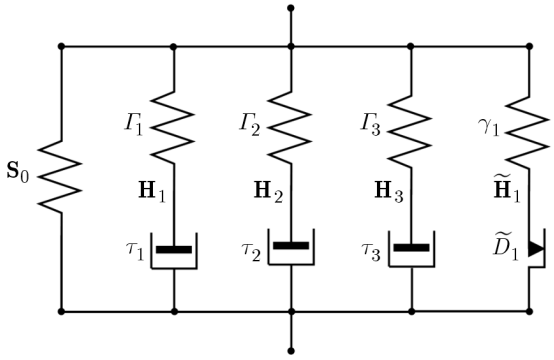

Fig. 1. Mechanical scheme of the rheological model assumed for UHMWPE

A number of mechanical tests have been performed on cylindrical specimens machined from a UHMWPE rod. The dimensions of the specimens are $\emptyset 17$ and $l_0 = 21\,\mathrm{mm}$. A medical grade polyethylene CHIRULEN 1050 has been used. All the experiments have been conducted on MTS Bionix 2500 testing machine at a constant room temperature of 20°C.

A number of loading-unloading compression tests at a constant deformation rate $\dot{\lambda}$ has been performed. The used values of the deformation rate are 0.0005, 0.005 and $0.05\,\mathrm{s}^{-1}$ with λ equal to 0.93 as the minimum stretch ratio. Furthermore, a relaxation test in compression has been carried out. The specimen has been loaded with a constant deformation rate of $0.003\,\mathrm{s}^{-1}$ and subsequently allowed to relax for 30 minutes.

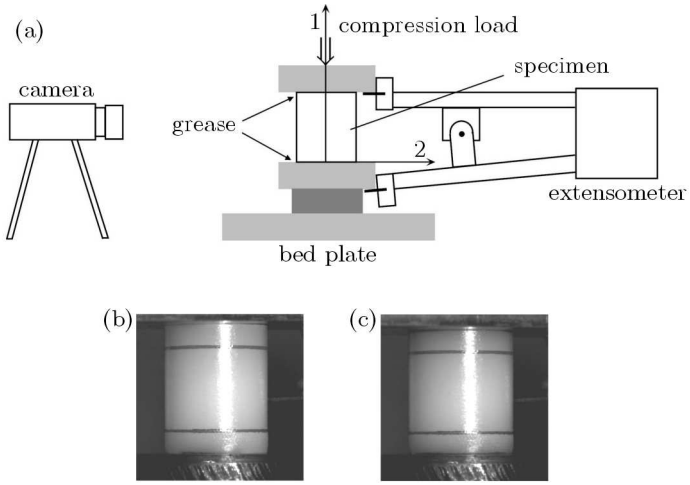

Fig. 2. (a) Experimental set-up. (b) View of undeformed specimen. (c) View of deformed specimen

The specimen stretch ratios in both axial an perpendicular directions have been measured using a video extensometer. The axial deformation has been at the same time measured with a strain gauge extensometer in order to verify the measured values. A sketch of the experimental setup can be seen in Fig. 2. A Poisson ratio of 0.46 has been determined, which justifies adopting an assumption of material incompressibility.

The material parameters of the constitutive equation have been evaluated using the least squares method. Thus, the following error function has been minimized

$$\mathcal{F}(\mathbf{p}) = \sum_{k=1}^{P} [(T_{11}(\mathbf{p}))_k - (\widetilde{T}_{11})_k]^2 \tag{5.1}$$

where $T_{11}(\mathbf{p})$ is the theoretical and $\widetilde{T}_{11}$ is the experimental Lagrange stress in the axial direction of the specimen at the time instant t_k ($k = 1, 2, \ldots, P$). The column matrix $\mathbf{p} = [\mu, b, \kappa, \gamma_1, \widetilde{D}_1, \Gamma_1, \Gamma_2, \Gamma_3, \tau_1, \tau_2, \tau_3]^{\mathrm{T}}$ contains the material parameters being optimized. The experimental data from three loading-unloading tests at various deformation rates together with the data from the relaxation test have been utilized to form up the minimized objective function given by Eq. (5.1). The results of the curve fitting are shown in Fig. 3, whereas the determined values of the material constants of elasticity, viscoelasticity and plasticity have been collected in Table 1. The inverese of the bulk modulus D_1 does not participate in the optimization. In FE implementation, D_1 is set to a value corresponding to the bulk modulus high enough to account for the material near incompressibility.

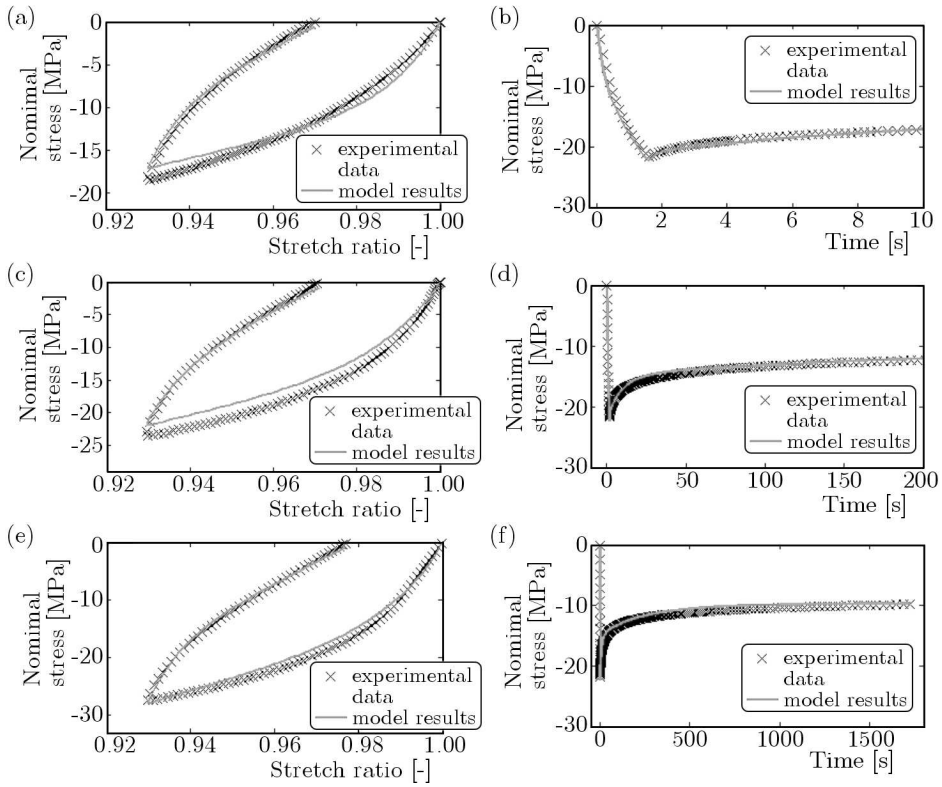

Fig. 3. Fitting of the viscoelastic-plastic constitutive model to the experimental data. Loading-unloading compression tests with the deformation rate of: (a) $0.0005\,\mathrm{s}^{-1}$, (b) $0.005\,\mathrm{s}^{-1}$, (c) $0.05\,\mathrm{s}^{-1}$ and stress relaxation tests with the relaxation time of: (d) 10 s, (e) 200 s, (f) 1700 s

Table 1. Model parameters for UHMWPE

Elastic constants		Viscoelastic constants				Plastic constants			
μ	52.56 MPa	Γ_1	2.89	τ_1	0.16 s	γ_1	3.25	$\widetilde{D}_1$	0.029
b	209.28	Γ_2	0.93	τ_2	8.803 s				
κ	0.81	Γ_3	0.62	τ_3	279.16 s				
D_1	0.00033 MPa^{-1}								

6. Finite element implementation

The linearized constitutive equation used for the FE implementation is obtained by taking a directional derivative of Eq. (4.1) with respect to $\mathbf{C}_{n+1}$. Thus, for the $n+1$ increment

$$\Delta\mathbf{S}_{n+1} = \boldsymbol{\mathcal{C}}^{ve-p}_{n+1} \cdot \frac{1}{2}\Delta\mathbf{C}_{n+1} \qquad \boldsymbol{\mathcal{C}}^{ve-p}_{n+1} = 2\frac{\partial\mathbf{S}_{n+1}}{\partial\mathbf{C}_{n+1}} \tag{6.1}$$

where the approximate material tangent tensor takes the form

$$\boldsymbol{\mathcal{C}}^{ve-p}_{n+1} = \boldsymbol{\mathcal{C}}^{vol}_{0\,n+1} + \left[1 + \sum_{k=1}^{P}\gamma_k\Big(1 + \frac{\Delta z_{n+1}}{2\widetilde{D}_k}\Big)^{-1} + \sum_{j=1}^{N}\Gamma_j\frac{1-\mathrm{e}^{-\frac{\Delta t}{\tau_j}}}{\frac{\Delta t}{\tau_j}}\right]\boldsymbol{\mathcal{C}}^{iso}_{0\,n+1} \tag{6.2}$$

The incremental constitutive rate equation given by Eq. (6.1) can be expressed using the Zaremba-Jaumann (Z-J) objective rate of the Kirchhoff stress $\boldsymbol{\tau}$, thus

$$\boldsymbol{\tau}^{\nabla}_{n+1} = J_{n+1}\boldsymbol{\mathcal{C}}^{MJ}_{n+1} \cdot \Delta\mathbf{D}_{n+1} \tag{6.3}$$

where the incremental Z-J objective rate of the Kirchhoff stress

$$\boldsymbol{\tau}^{\nabla}_{n+1} = \Delta\boldsymbol{\tau}_{n+1} - \Delta\mathbf{W}_{n+1}\boldsymbol{\tau}_{n+1} - \boldsymbol{\tau}_{n+1}\Delta\mathbf{W}^{\mathrm{T}}_{n+1} \tag{6.4}$$

and

$$\begin{aligned}
\Delta\mathbf{W}_{n+1} &= \frac{1}{2}\Big[\Delta\mathbf{F}_{n+1}\mathbf{F}^{-1}_{n+1} - (\Delta\mathbf{F}_{n+1}\mathbf{F}^{-1}_{n+1})^{\mathrm{T}}\Big]\\
\Delta\mathbf{D}_{n+1} &= \frac{1}{2}\Big[\Delta\mathbf{F}_{n+1}\mathbf{F}^{-1}_{n+1} + (\Delta\mathbf{F}_{n+1}\mathbf{F}^{-1}_{n+1})^{\mathrm{T}}\Big]\\
\Delta\mathbf{F}_{n+1} &= \mathbf{F}_{n+1}\mathbf{F}^{-1}_{n}
\end{aligned} \tag{6.5}$$

The material stiffness tensor takes the corresponding form

$$\boldsymbol{\mathcal{C}}^{MJ}_{n+1} = \frac{1}{J_{n+1}}(\boldsymbol{\mathcal{C}}^{\tau c}_{n+1} + \boldsymbol{\mathcal{I}}_{n+1}) \tag{6.6}$$

where

$$\begin{aligned}
\boldsymbol{\mathcal{C}}^{\tau c}_{n+1} &= (F_{iP}F_{jQ}F_{kR}F_{lS}\mathcal{C}^{ve-p}_{PQRS})_{n+1}\mathbf{e}_i\otimes\mathbf{e}_j\otimes\mathbf{e}_k\otimes\mathbf{e}_l\\
\boldsymbol{\mathcal{I}}_{n+1} &= \frac{1}{2}(\delta_{ik}\tau_{jl} + \tau_{ik}\delta_{jl} + \delta_{il}\tau_{jk} + \tau_{il}\delta_{jk})_{n+1}\mathbf{e}_i\otimes\mathbf{e}_j\otimes\mathbf{e}_k\otimes\mathbf{e}_l
\end{aligned} \tag{6.7}$$

and $\mathbf{e}_k$ $(k=1,2,3)$ are the unit vectors of the Cartesian basis. The Kirchhoff stress in Eq. (6.4) is determined from the stress transformation law, i.e.

$$\boldsymbol{\tau}_{n+1} = \mathbf{F}_{n+1}\mathbf{S}_{n+1}\mathbf{F}^{\mathrm{T}}_{n+1} \tag{6.8}$$

where the second Piola-Kirchhoff stress, $\mathbf{S}_{n+1}$ is calculated utilizing Eq. (4.1).

Substitution of Eq. (6.2) into Eq. $(6.7)_1$ results in the following form of the material stiffness in the current configuration

$$\boldsymbol{\mathcal{C}}^{\tau c}_{n+1} = \boldsymbol{\mathcal{C}}^{vol}_{n+1} + \left[1 + \sum_{k=1}^{P}\gamma_k\Big(1 + \frac{\Delta z_{n+1}}{2\widetilde{D}_k}\Big)^{-1} + \sum_{j=1}^{N}\Gamma_j\frac{1-\mathrm{e}^{-\frac{\Delta t}{\tau_j}}}{\frac{\Delta t}{\tau_j}}\right]\boldsymbol{\mathcal{C}}^{iso}_{n+1} \tag{6.9}$$

where

$$\boldsymbol{\mathcal{C}}^{vol} = \frac{2}{D_1}J(J-1)(\mathbf{1}\otimes\mathbf{1} - 2\mathbf{I}) + J^2\frac{2}{D_1}\mathbf{1}\otimes\mathbf{1} \tag{6.10}$$

and

$$\begin{aligned}\boldsymbol{\mathcal{C}}^{iso} &= \frac{2}{3}\mu\Big[1+\frac{b}{\kappa}(\overline{I}_1-3)\Big]^{\kappa-1}\overline{I}_1\Big(\mathbf{I}+\frac{1}{3}\mathbf{1}\otimes\mathbf{1}\Big)-\frac{2}{3}J^{-\frac{2}{3}}\mu\Big[1+\frac{b}{\kappa}(\overline{I}_1-3)\Big]^{\kappa-1}(\mathbf{B}\otimes\mathbf{1}+\mathbf{1}\otimes\mathbf{B})\\ &+2J^{-\frac{4}{3}}\mu\frac{b(\kappa-1)}{\kappa}\Big[1+\frac{b}{\kappa}(\overline{I}_1-3)\Big]^{\kappa-2}\mathbf{B}\otimes\mathbf{B}\\ &-\frac{2}{3}J^{-\frac{2}{3}}\mu\frac{b(\kappa-1)}{\kappa}\Big[1+\frac{b}{\kappa}(\overline{I}_1-3)\Big]^{\kappa-2}\overline{I}_1(\mathbf{B}\otimes\mathbf{1}+\mathbf{1}\otimes\mathbf{B})\\ &+\frac{2}{9}\mu\frac{b(\kappa-1)}{\kappa}\Big[1+\frac{b}{\kappa}(\overline{I}_1-3)\Big]^{\kappa-2}\overline{I}_1^2\mathbf{1}\otimes\mathbf{1}\end{aligned} \tag{6.11}$$

are, respectively, the volumetric and isochoric components of the elasticity tensor corresponding to the stored-energy functions as given in Eqs (3.11), cf Suchocki (2011).

The viscoelastic-plastic model has been implemented into FE software Abaqus by taking advantage of the user subroutine UMAT (UserMATerial), which is called by the FE solver during every iteration of the Newton-Raphson numerical procedure (Hibbit *et al.* 2008). The written subroutine calculates Cauchy stress tensor and material Jacobian defined in Eq. (6.6) for each finite element. These quantities are subsequently used by Abaqus to form up the element stiffness matrix. Finally, the global stiffness matrix is assembled by Abaqus using the element stiffness matrices. The calculations done by the written subroutine UMAT are listed further in the text. The user subroutines used in other FE programs to define custom constitutive equations have a similar structure.

In order to verify the performance of the developed UMAT code, several exemplary simulations have been performed using the Abaqus FEM program. The simulations involved a 15 mm×15 mm×15 mm UHMWPE block undergoing ramp tension test, ramp compression test and sinusoidal deformation with variable amplitude. In the first approach, the polymeric block is meshed using a single finite element C3D8H[1]. Subsequently, all the simulations are conducted using the polyethylene block meshed with 125 elements. In each of the simulated processes the excitation was kinematic, i.e. the frontal face of the block performs a designated displacement program. The displacement distribution and the used boundary conditions are depicted in Fig. 4. Due to the assumed incompressibility, the deformation gradient tensor has the following components

$$\mathbf{F}_{3\times3}=\begin{bmatrix}\lambda_1 & 0 & 0\\ 0 & \frac{1}{\sqrt{\lambda_1}} & 0\\ 0 & 0 & \frac{1}{\sqrt{\lambda_1}}\end{bmatrix} \tag{6.12}$$

where λ_1 denotes the stretch ratio in the direction x (Fig. 4).

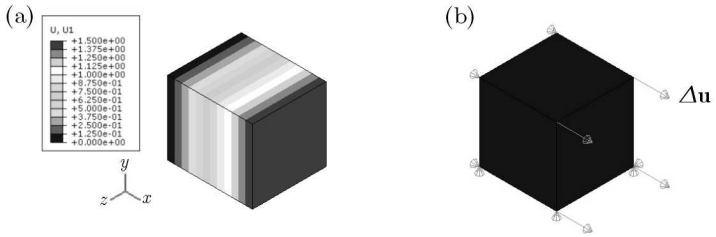

Fig. 4. Homogeneous deformation of a single finite element. (a) Distribution of the displacement component in the tension/compression direction. (b) Applied boundary conditions

All the simulations have been repeated utilizing programs written in MATLAB in which the discretized equations presented in Section 4 are used to calculate the stresses for the given deformation histories.

[1]Cubic, three-dimensional, 8 nodes, hybrid.

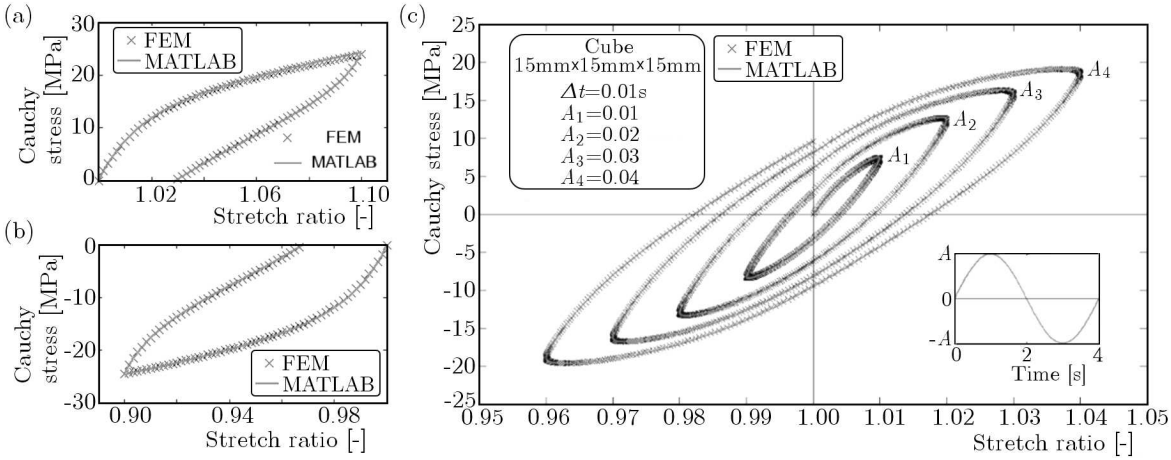

Fig. 5. Polyethylene block undergoing (a) ramp tension and (b) ramp compression tests with the deformation rate of $0.003\,\mathrm{s}^{-1}$ and (c) cyclic deformation history – a sinusoidal function with the increasing amplitude A

Algorithm for the implementation in Abaqus

Input: $\mathbf{F}_{n+1}$, no. of direct and shear stress components

1. Calculate strain measures from the current increment

$$\mathbf{C}_{n+1} = \mathbf{F}^{\mathrm{T}}_{n+1}\mathbf{F}_{n+1} \qquad \overline{\mathbf{F}}_{n+1} = J^{-\frac{1}{3}}_{n+1}\mathbf{F}_{n+1} \qquad \overline{\mathbf{B}}_{n+1} = \overline{\mathbf{F}}_{n+1}\overline{\mathbf{F}}^{\mathrm{T}}_{n+1}$$

2. Extract variables from the previous increment
3. Calculate elastic stresses from the current increment

$$\mathbf{S}^{vol}_{0\,n+1} = J_{n+1}p_{n+1}\mathbf{C}^{-1}_{n+1} \qquad p_{n+1} = \partial_{J_{n+1}}U(J_{n+1})$$
$$\mathbf{S}^{iso}_{0\,n+1} = J^{-\frac{2}{3}}_{n+1}\,\mathrm{DEV}\,[\overline{\mathbf{S}}_{n+1}] \qquad \overline{\mathbf{S}}_{n+1} = 2\partial_{\overline{\mathbf{C}}_{n+1}}\overline{W}(\overline{\mathbf{C}}_{n+1})$$
$$\mathbf{S}_{0\,n+1} = \mathbf{S}^{vol}_{0\,n+1} + \mathbf{S}^{iso}_{0\,n+1}$$

4. Update endochronic and viscoelastic overstresses ($k = 1, 2, \ldots, P$), ($j = 1, 2, \ldots, N$)

$$\Delta z_{n+1} = (\Delta\overline{\mathbf{C}}_{n+1} \cdot \Delta\overline{\mathbf{C}}_{n+1})^{\frac{1}{2}} \qquad \Delta\overline{\mathbf{C}}_{n+1} = \overline{\mathbf{C}}_{n+1} - \overline{\mathbf{C}}_{n}$$
$$\widetilde{\mathbf{H}}_{k\,n+1} = \frac{\left(1 - \frac{1}{\widetilde{D}_k}\frac{\Delta z_{n+1}}{2}\right)\widetilde{\mathbf{H}}_{k\,n} + \gamma_k(\mathbf{S}^{iso}_{0\,n+1} - \mathbf{S}^{iso}_{0\,n})}{1 + \frac{1}{\widetilde{D}_k}\frac{\Delta z_{n+1}}{2}}$$
$$\mathbf{H}_{j\,n+1} = \mathrm{e}^{-\frac{\Delta t}{\tau_j}}\mathbf{H}_{j\,n} + \Gamma_j\frac{1 - \mathrm{e}^{-\frac{\Delta t}{\tau_j}}}{\frac{\Delta t}{\tau_j}}(\mathbf{S}^{iso}_{0\,n+1} - \mathbf{S}^{iso}_{0\,n})$$

5. Calculate total stress from the current increment

$$\mathbf{S}_{n+1} = \mathbf{S}_{0\,n+1} + \sum_{k=1}^{P}\widetilde{\mathbf{H}}_{k\,n+1} + \sum_{j=1}^{N}\mathbf{H}_{j\,n+1} \qquad \boldsymbol{\sigma}_{n+1} = \frac{1}{J_{n+1}}\mathbf{F}_{n+1}\mathbf{S}_{n+1}\mathbf{F}^{\mathrm{T}}_{n+1}$$

6. Calculate viscoelastic-plastic stiffness from the current increment
7. Store stresses and isochoric C-G tensor from the current increment

In Fig. 5, the results of ramp tension (Fig. 5a) and compression (Fig. 5b) are shown. In the case of ramp tension simulation, the material is deformed at a constant rate $\dot{\lambda}_1 = -0.003\,\mathrm{s}^{-1}$ until the stretch ratio $\lambda_1 = 1.1$ is reached. Subsequently, unloading is performed at the deformation rate of $\dot{\lambda}_1 = 0.003\,\mathrm{s}^{-1}$. The compression process was simulated analogously.

In Fig. 5c, the results of sinusoidal loading simulation are presented. The simulated process comprises of four periods, each performed at different amplitude.

The predictions of the FEM simulations utilizing UMAT are in a good agreement with the results produced by MATLAB programs (see Fig. 5). All the simulations have been performed utilizing the material parameter values collected in Table 1.

7. Conclusions

In this study, a new viscoelastic-plastic model for thermoplastic polymers and resins is presented. The model is formulated by utilizing the formalism of stress-like internal state variables. It has been implemented into the FE software Abaqus and applied to model the inelastic behavior of polyethylene with very good results.

References

1. Abdul-Hameed H., Messager T., Zaïri F., Naït-Abdelaziz M., 2014, Large-strain viscoelastic-viscoplastic constitutive modeling of semi-crystalline polymers and model identification by deterministic/evolutionary approach, *Computational Materials Science*, **90**, 241-252
2. Alkas Yonan S., Soyarslan C., Haupt P., Kwiatkowski L., Tekkaya A.E., 2013, A simple finite strain non-linear visco-plastic model for thermoplastics and its application to the simulation of incremental cold forming of polyvinylchloride (PVC), *International Journal of Mechanical Sciences*, **66**, 192-201
3. Ayoub G., Zaïri F., Fréderix C., Gloaguen J.M., Naït-Abdelaziz M., Seguela R., Lefebvre J.M., 2011, Effects of crystal content on the mechanical behaviour of polyethylene under finite strains: experiments and constitutive modelling, *International Journal of Plasticity*, **27**, 492-511
4. Bardella L., 2001, A phenomenological constitutive law for the nonlinear viscoelastic behaviour of epoxy resins in the glassy state, *European Journal of Mechanics – A/Solids*, **20**, 907-924
5. Ben Hadj Hamouda H., Laiarinandrasana L., Piques R., 2007, Viscoplastic behaviour of a medium density polyethylene (MDPE): constitutive equations based on double nonlinear deformation model, *International Journal of Plasticity*, **23**, 1307-1327
6. Bergström J.S., Bischoff J.E., 2010, An advanced thermomechanical constitutive model for UHMWPE, *International Journal of Structural Changes in Solids*, **2**, 1, 31-39
7. Drozdov A.D., Christiansen J. de C., 2007, Cyclic viscoplasticity of high-density polyethylene/montmorillonite clay nanocomposite, *European Polymer Journal*, **43**, 1, 10-25
8. Hassan T., Colak O.U., Clayton P.M., 2011, Uniaxial strain and stress-controlled cyclic responses of ultrahigh molecular weigth polyethylene: experiments and model simulations, *Journal of Engineering Materials and Technology*, **133**, 021010-1–021010-9
9. Hibbit B., Karlsson B., Sorensen P., 2008, *ABAQUS Theory Manual*, Hibbit, Karlsson & Sorensen Inc.
10. Holzapfel G.A., 2010, *Nonlinear Solid Mechanics*, John Wiley & Sons Ltd., New York
11. Knowles J.K., 1977, The finite anti-plane shear field near the tip of a crack for a class of incompressible elastic solids, *International Journal of Fracture*, **13**, 5, 611-639

12. Krairi A., Doghri I., 2014, A thermodynamically-based constitutive model for thermoplastic polymers coupling viscoelasticity, viscoplasticity and ductile damage, *International Journal of Plasticity*, **60**, 163-181

13. Kästner M., Obst M., Brummund J., Thielsch K., Ulbricht V., 2012, Inelastic behavior of polymers – experimental characterization, formulation and implementation of a material model, *Mechanics of Materials*, **52**, 40-57

14. Pipkin A.C., Rivlin R.S., 1965, Mechanics of rate-independent materials, *ZAMP*, **16**, 3, 313-327

15. Suchocki C., 2011, A finite element implementation of Knowles stored-energy function: theory, coding and applications, *The Archive of Mechanical Engineering*, **58**, 319-346

16. Suchocki C., 2013, A quasi-linear viscoelastic rheological model for thermoplastics and resins, *Journal of Theoretical and Applied Mechanics*, **51**, 1, 117-129

17. Taylor R.L., Pister K.S., Goudreau G.L., 1970, Thermomechanical analysis of viscoelastic solids, *International Journal for Numerical Methods in Engineering*, **2**, 45-59

18. Wu H.C., 2005, *Continuum Mechanics and Plasticity*, CRC Press, New York

Manuscript received October 26, 2014; accepted for print January 7, 2015

JOURNAL OF THEORETICAL AND APPLIED MECHANICS
53, 3, pp. 605-616, Warsaw 2015
DOI: 10.15632/jtam-pl.53.3.605

LINEAR MATRIX INEQUALITIES CONTROL DRIVEN FOR NON-IDEAL POWER SOURCE ENERGY HARVESTING

Douglas C. Ferreira
UFMT – Federal University of Mato Grosso, Mechanical Engineering Department, Rondonópolis, MT, Brazil
e-mail: dcferreira@ufmt.br

Fábio R. Chavarette
UNESP – Universidade Estadual Paulista, Mathematical Sciences Department, Ilha Solteira, SP, Brazil
e-mail: fabioch@mat.feis.unesp.br

Nelson J. Peruzzi
UNESP – Universidade Estadual Paulista, Mathematical Sciences Department, Jaboticabal, SP, Brazil
e-mail: peruzzi@fcav.unesp.br

The dynamic model of a linear energy harvester excited by a non-ideal power source is coupled to a controller to maximum vibration adjustment. Numerical analysis is taken to evaluate the energy harvested keeping the vibration optimized for the maximum interaction to the energy source using linear matrix inequalities for control driven. The dimensionless power output, actuation power and net output power is determined. As a result, it is possible to verify that the total energy harvested via exogenous vibration using the proposed controller is increased up to 65 times when in comparison to the open loop system.

Keywords: energy harvesting, efficiency, control, non-ideal excitation

1. Introduction

Harnessing energy from environment to supply low power devices can be accomplished from sources as thermal gradients, solar radiation and vibration (Huesgen *et al.*, 2008; Cepnik *et al.*, 2011; Miller *et al.*, 2011). Concerning the vibration there are three main groups of harvesters: electrostatic, electromagnetic and piezoelectric (Roundy *et al.*, 2003).

Although harvesting to be a sustainable source of energy, it is still not efficient enough and its use is limited to very little power devices, and enhancing its capacity represents a science frontier. The energy harvesting system main application in the present is for remote sensor nodes, wireless systems and smart structures actuators (Miller *et al.*, 2011; Roundy *et al.*, 2003). To enhance energy harnessed, there are several project solutions focusing in matching the natural frequency according to the vibration source, nevertheless the resonance solution has restrictions for power source and scale.

Regarding the power source, an important consideration is that the environmental vibration has low power and wide range, and normally is random resulting in difficulties for a design to be coincident with the resonance. Considering the scale, it is notable that recent studies concerning the enhancement of energy harvesting efficiency produced better piezoelectric materials (Yeager and Trolier-Mckinstry, 2012; Baek *et al.*, 2011; Kim *et al.*, 2012) and now the designed harvesters are facing new barrier applications of micro sizing. As most power sources from ambient vibration have low frequency, it is difficult to design a small harvester resulting in his natural frequency to be coincident with the resonance.

Some project solutions regard to tuning a device to the resonance (Challa *et al.*, 2008; Eichhorn *et al.*, 2009) that can be accomplished by mechanical, magnetic and piezoelectric adjustments (Peters *et al.*, 2009; Tang *et al.*, 2013). The mechanical adjustment requires known excitation frequency and high cost energy to tuning, magnetic adjustment has limited tuning result and faces a limited micro sizing requirements, and the piezoelectric adjustment is a promising frontier to enhance energy harvesting capability (Zhu *et al.*, 2010). First studies using piezoelectric adjustment results in negative net output power (Roundy and Zhang, 2005) but latter studies from Zhu *et al.* (2010) found a mistake in Roundy and Zhang (2005) formulation that not considered mean voltage to active power determination. A piezoelectric tuning solution with positive net output power was numerically and experimentally proven by Lallart and Inman (2010) and Lallart and Guyomar (2010). According to Wang and Inman (2012), the state of the art of enhancement of energy harvesting capability relies in control projects formulation which characterizes the mean objective of this study.

The proposed solution considers that vibration excitation has low energy and the vibration generated by the harvester can influence the source which characterizes a non-ideal power source (Balthazar *et al.*, 2003; Balthazar and Dantas, 2004; Chavarette, 2012). For a limited power in controller systems, the input vibration control influences the own controller which characterizes a non-ideal system (Souza *et al.*, 2008). Thus the model of movement sums the feedback term increasing the number of degrees of freedom (Piccirillo *et al.*, 2008). According to Balthazar *et al.* (2003), when the vibration source is near natural frequency there appears a jump phenomenon which it is not possible while arriving the resonance as the maximum vibration response.

In this study, the proposed controller is based on Linear Matrix Inequalities (LMI) theory. The dynamic systems control for vibration maximization is performed by optimum control $H\infty$ as a convex optimization problem involving Linear Matrix Inequalities – LMI (Chilali and Gahinet, 1996). The LMI can be in form of linear inequalities, linear convex inequalities or matrix inequalities. Several restriction formats of control theory as Lyapunov and Riccati inequalities can be described via LMI (Antwerp and Braatz, 2000). The LMI has large use in control, mainly because sustains the stability of a system based in restrictions and can incorporated in dynamical systems with not singular parameters that vary within a known range (Wan and Kothare, 2003; Andrea *et al.*, 2008).

To explore controller efficiency, this study is conducted according to a bimorph energy harvester (Erturk and Inman, 2011) and the use of non-ideal power source (Balthazar *et al.*, 2003; Balthazar and Dantas, 2004; Chavarette, 2012). The definition of a Linear Matrix Inequalities controller (LMI) to set up a harvester to optimize interaction to the power source to take advantage of full range of vibration is the main propose of this study.

Considering the paper organization: Section 2 presents the harvester model, Section 3 presents the controller definition, Section 4 presents the efficiency analysis and Section 5 presents the final remarks from this investigation and acknowledgements.

2. Harvester model

A non-ideal excitation can be modeled for an unbalanced mass receiving torque by a DC motor as shown in Fig. 1 (Balthazar *et al.*, 2003; Balthazar and Dantas, 2004; Chavarette, 2012).

This arrangement is based in Kononenko model and can be mathematically modeled according to equations (2.1) where m_1 is DC motor mass, m_0 is unbalanced mass, l is dumping, k is rigidity, r is the eccentricity distance from the unbalanced mass to the torque source, $(I + m_0 r^2)$ is moment of inertia of the unbalanced mass, and the state variables are X for the beam tip position and φ for the unbalanced mass angular position. The net torque is a function of angular

velocity $\dot{\varphi}$ and described for $S(\dot{\varphi}) = a - b\dot{\varphi}$ (Palácios *et al.*, 2003; Tusset *et al.*, 2013), where a is the net torque applied by the DC motor and b is the resistive net torque constant

$$\begin{aligned}(m_1 + m_0)\ddot{X} + l\dot{X} + kX &= m_0 r(\dot{\varphi}^2 \cos\varphi + \ddot{\varphi}\sin\varphi)\\ (I + m_0 r^2)\ddot{\varphi} - m_0 r\ddot{X}\sin\varphi &= S(\dot{\varphi})\end{aligned} \tag{2.1}$$

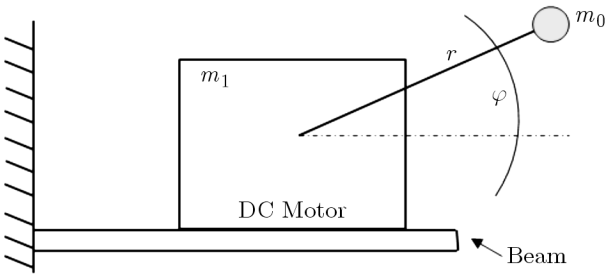

Fig. 1. Non-ideal power source (Chavarette, 2012)

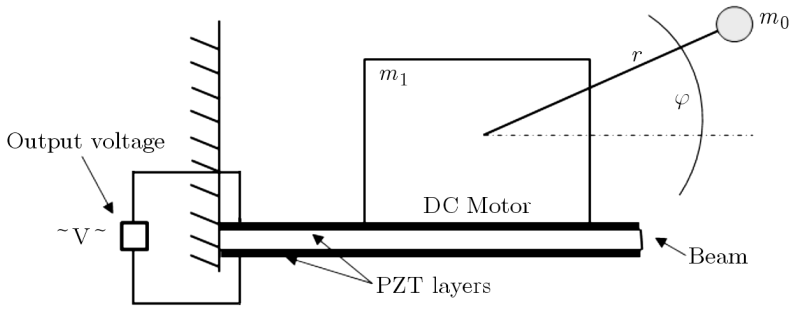

Fig. 2. Energy harvester system (Erturk and Inman, 2011) coupled to non-ideal power source (Chavarette, 2012)

An energy harvester defined by Erturk and Inman (2011) with two layers of a piezoelectric material and an output voltage was coupled to the non-ideal power source as shown in Fig. 2. It is dimensionlessly modeled according to the resonance as given by equations (2.2), where ζ is damping factor, χ is piezoelectric mechanical coupling coefficient, Λ is reciprocal of time constant, κ is piezoelectric electric coupling coefficient, μ is unbalanced mass eccentricity, ξ is unbalanced mass eccentricity for moment of inertia, α is the net torque applied by the DC motor and β is the resistive net torque constant. The dimensionless state variables are x for tip beam position, z for the angular position of the unbalanced mass and ν for the output voltage

$$\begin{aligned}&\ddot{x} + 2\zeta\dot{x} + \frac{1}{2}x - \chi\nu = \mu(\dot{z}^2\cos z + \ddot{z}\sin z)\\ &\ddot{z} = \xi\ddot{x}\sin z + \alpha - \beta\dot{z}\\ &\dot{\nu} + \Lambda\nu + \kappa\dot{x} = 0\end{aligned} \tag{2.2}$$

Isolating $\ddot{x}$, $\dot{\nu}$ and $\ddot{z}$, equation (2.2) can be presented by

$$\begin{aligned}\ddot{x} &= \frac{-\frac{1}{2}x - 2\zeta\dot{x} + \chi\nu + \mu\dot{z}^2\cos z + (\alpha - \beta\dot{z})\mu\sin z}{1 - \mu\xi(\sin z)^2}\\ \ddot{z} &= \frac{\left(-\frac{1}{2}x - 2\zeta\dot{x} + \chi\nu\right)\xi\sin z + \mu\xi\dot{z}^2\cos z\sin z + \alpha - \beta\dot{z}}{1 - \mu\xi(\sin z)^2}\\ \dot{\nu} &= -\kappa\dot{x} - \Lambda\nu\end{aligned} \tag{2.3}$$

Adopting $x = x_1$, $z = x_3$ and $\nu = x_5$ and rearranging the terms, the space-state form of equations (2.3) is given by

$$\begin{aligned}
\dot{x}_1 &= x_2 \\
\dot{x}_2 &= \frac{-\frac{1}{2}x_1 - 2\zeta x_2 + \chi x_5 + \mu x_4^2 \cos x_3 + (\alpha - \beta x_4)\mu \sin x_3}{1 - \mu\xi(\sin x_3)^2} \\
\dot{x}_3 &= x_4 \\
\dot{x}_4 &= \frac{\left(-\frac{1}{2}x_1 - 2\zeta x_2 + \chi x_5\right)\xi \sin x_3 + \mu\xi x_4^2 \cos x_3 \sin x_3 + \alpha - \beta x_4}{1 - \mu\xi(\sin x_3)^2} \\
\dot{x}_5 &= -\kappa x_2 - \Lambda x_5
\end{aligned} \tag{2.4}$$

Applying Jacobian, the matrix form of equations (2.4) is given as

$$\begin{Bmatrix} \dot{x}_1 \\ \dot{x}_2 \\ \dot{x}_3 \\ \dot{x}_4 \\ \dot{x}_5 \end{Bmatrix} = \begin{bmatrix} 0 & 1 & 0 & 0 & 0 \\ -\frac{1}{2} & -2\zeta & \mu\alpha & 0 & \chi \\ 0 & 0 & 0 & 1 & 0 \\ 0 & 0 & -\frac{1}{2}\xi & -\beta & 0 \\ 0 & -\kappa & 0 & 0 & -\Lambda \end{bmatrix} \begin{Bmatrix} x_1 \\ x_2 \\ x_3 \\ x_4 \\ x_5 \end{Bmatrix} \tag{2.5}$$

The main propose of this study is to design a controller to optimize vibration response and, consequently, energy the harvesting performance. In this case, a Linear Matrix Inequalities controller is arranged to maximize the displacement and velocity. As the output voltage has directly influenced by velocity and displacement, it is expected to increase the output voltage and, then, the efficiency.

3. Controller definition

To ensure the maximum energy harvested, the controller it is coupled using Linear Matrix Inequalities (LMI) according to Optimum Control $H\infty$. An LMI Control Driven utilizes feedback state to optimize the interaction between exogenous the excitation $w(t)$ and the resulting signal $y(t)$ (Andrea *et al.*, 2008). A sufficient condition for LMI control is the existence of a matrix $\mathbf{X} = \mathbf{X}' \in \mathcal{R}^{n\times n}$ and $\mathbf{Y} \in \mathcal{R}^{m\times n}$ satisfying equations

$$\begin{aligned}
&\min \mu \\
&\begin{vmatrix} \mathbf{AX} + \mathbf{XA}' - \mathbf{B}_2\mathbf{Y} - \mathbf{Y}'\mathbf{B}_2' & \mathbf{XC}' + \mathbf{Y}'\mathbf{D}' & \mathbf{B}_1 \\ \mathbf{CX} + \mathbf{DY} & -\mathbf{I} & \mathbf{0} \\ \mathbf{B}_1' & \mathbf{0} & -\mu\mathbf{I} \end{vmatrix} < \mathbf{0} \\
&|\mathbf{X}| > 0
\end{aligned} \tag{3.1}$$

The space-state model for the proposed controlled system is given by equations (3.2), and explained in a schematic flow chart in Fig. 3

$$\dot{\mathbf{x}} = \mathbf{Ax} + \mathbf{B}_1\mathbf{w} + \mathbf{B}_2\mathbf{u} \qquad \mathbf{y} = \mathbf{Cx} \tag{3.2}$$

where $\mathbf{A}$ is the state matrix, $\mathbf{B}_1$ is the excitation vector, $\mathbf{B}_2$ is the feedback state vector and $\mathbf{C}$ is the actuation vector and control signal, in this case, a singular control signal.

The previous study conducted by Erturk and Inman (2011) defined parameters for a bimorph cantilever according to the resonance $\zeta = 0.01$, $\chi = 0.05$, $\kappa = 0.5$, $\Lambda = 0.05$, and the studies conducted by Balthazar *et al.* (2003), Balthazar and Dantas (2004) and Chavarette (2012)

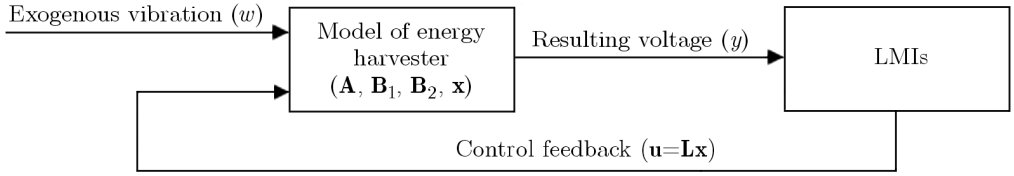

Fig. 3. Dynamic control scheme

defined the parameters for non-ideal excitation $\mu = 0.2$, $\xi = 0.3$ and $\beta = 1.5$. Replacing the parameters in the state matrix according to equation (2.5) the matrices for equation (3.2) are shown as in the following

$$\mathbf{A} = \begin{bmatrix} 0 & 1 & 0 & 0 & 0 \\ -0.5 & -0.02 & 0.2\alpha & 0 & 0.05 \\ 0 & 0 & 0 & 1 & 0 \\ 0 & 0 & -0.15 & -1.5 & 0 \\ 0 & -0.5 & 0 & 0 & -0.05 \end{bmatrix}$$

$$\mathbf{B}_1 = \begin{bmatrix} 1 \\ 1 \\ 1 \\ 1 \\ 1 \end{bmatrix} \qquad \mathbf{B})_2 = \begin{bmatrix} 1 \\ 1 \\ 1 \\ 1 \\ 1 \end{bmatrix} \qquad \mathbf{C} = \begin{bmatrix} 1 & 0 & 0 & 0 & 0 \end{bmatrix} \tag{3.3}$$

4. Efficiency analysis

For the designed controller the initial parameters are used to excite the beam, and then a LMI controller is set up to the maximum interaction between the excited beam and the external exogenous excitation, in this case, a non-ideal power source. When LMIs are feasible, there is a matrix $\mathbf{X}$ and a feedback matrix $\mathbf{L}$ for the space-state that optimizes the system behavior, given by equation (3.4)

$$\mathbf{L} = \mathbf{Y}\mathbf{X}^{-1} \tag{4.1}$$

Once $\mathbf{L}$ is determined, it is possible to determine a feedback space-state matrix for the system ($\mathbf{A}_f$), given by equation (3.5)

$$\mathbf{A}_f = \mathbf{A} - \mathbf{B}_2\mathbf{L} \tag{4.2}$$

The variable parameter is the dimensionless net torque applied by the DC motor α that will assume values ranging from 0.4 to 5.0.

4.1. System response for $\alpha = 0.4$

Considering $\alpha = 0.4$ and substituting matrices $\mathbf{A}$, $\mathbf{B}_1$, $\mathbf{B}_2$ and $\mathbf{C}$ given in equations (3.3) in LMIs given in equations (3.1) and solving the inequalities, the resulting feedback matrix $\mathbf{L}$ for a feasible system is

$$\mathbf{L} = 10^3 \begin{bmatrix} 6.1648 & 0.0004 & -0.0000 & -0.0007 & -0.0000 \end{bmatrix}$$

Taking into consideration the feedback state matrix $\mathbf{A}_f$, it is possible to calculate the feedback parameters, comparing to the original matrix $\mathbf{A}$ in (3.3) as shown in Table 3.

Table 3. Feedback parameters for $\alpha = 0.4$

Feedback parameters	ζ	χ	κ	Λ	μ	ξ	β
Value	0.2308	0.0749	0.9416	0.0251	0.2988	0.2210	0.8244

Table 4. System eigenvalues (10^3) for $\alpha = 0.4$

λ_1	$-6.1635 + 0.0000\mathrm{i}$
λ_2	$-0.0015 + 0.0000\mathrm{i}$
λ_3	$-0.0005 + 0.0002\mathrm{i}$
λ_4	$-0.0005 - 0.0002\mathrm{i}$
λ_5	$-0.0001 + 0.0000\mathrm{i}$

The controlled system exhibits stable behavior since all the eigenvalues have the real part negative as shown in Table 4.

Performing Runge-Kutta fourth order algorithm for solving the ordinary differential equations in equation (2.4) for open loop (without control) parameters given in Section 3 and for controlled system parameters given in Table 3, it is possible to visualize the total energy from the system to compare the efficiency from the open loop to the controlled system as shown in Fig. 4. Th following initial conditions are considered $x(0) = 1$, $\dot{x}(0) = 0$, $\nu(0) = 0$, $z(0) = 0$ and $\dot{z}(0) = 0$ and time samples from 0 to 2500 in the interval of 0.1 totalizing 25 000 samples in Figs. 4a-4d and samples from 2000 to 2500 in the interval of 0.1 totalizing 5000 samples in Fig. 4d to exclude transient behavior.

The controlled system presents greater displacements, velocity and output voltage in comparison to the open loop system. To explore control performance, the dimensionless net torque applied by the DC motor assumes the values $\alpha = 0.5$, $\alpha = 1.3$ and $\alpha = 5.0$, considering parameters below the resonance, at the resonance and beyond it, the feedback vector $\mathbf{L}$ and feedback parameters are given in Table 5.

Table 5. Feedback parameters $\alpha = 0.5$, $\alpha = 1.3$ and $\alpha = 4.0$

α	$\mathbf{L}$ (10^3)	Feedback parameters
0.5	$[4.7795, 0.0004, -0.0000, -0.0007, -0.0000]$	$\zeta = 0.2304$, $\chi = 0.0742$, $\kappa = 0.9408$ $\Lambda = 0.0258$, $\mu = 0.2689$, $\xi = 0.2311$ $\beta = 0.8449$
1.3	$[2.2552, 0.0005, -0.0000, -0.0007, -0.0000]$	$\zeta = 0.2537$, $\chi = 0.0691$, $\kappa = 0.9873$ $\Lambda = 0.0309$, $\mu = 0.2173$, $\xi = 0.2551$ $\beta = 0.8212$
5.0	$[2.4482, 0.0006, 0.0000, -0.0007, -0.0000]$	$\zeta = 0.3096$, $\chi = 0.0639$, $\kappa = 1.0991$ $\Lambda = 0.0361$, $\mu = 0.1957$, $\xi = 0.3425$ $\beta = 0.8231$

Making use of the Runge-Kutta fourth order method for solving ordinary differential equations in (2.4) for open loop (without control) parameters given in Section 3 and for the controlled system parameters given in Table 5 we find analogous results for the initial conditions $x(0) = 1$, $\dot{x}(0) = 0$, $\nu(0) = 0$, $z(0) = 0$ and $\dot{z}(0) = 0$ and time samples from 0 to 2500 in the interval of 0.1 totalizing 25 000 samples in Figs. 5a, 5c, 5e and samples from 2000 to 2500 in the interval of 0.1 totalizing 5000 samples to exclude transient behavior in Figs. 5b, 5d, 5f.

It is possible to verify that the system energy is greater for the control system when out of the resonance for $\alpha = 0.5$ and $\alpha = 5.0$. When the system is at the resonant behavior at $\alpha = 1.3$,

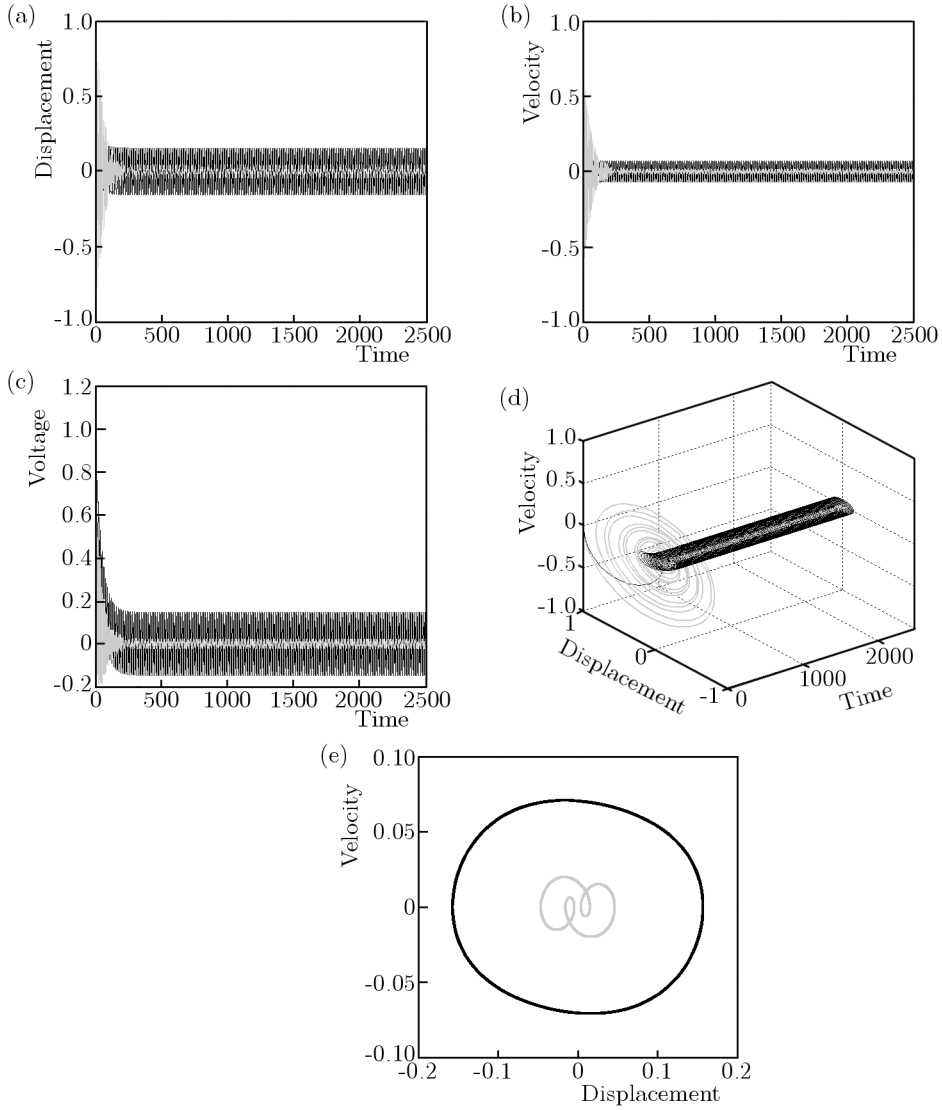

Fig. 4. System behavior for $\alpha = 0.4$ (open loop system – grey line, controlled system – black line); (a) displacement, (b) velocity, (c) output voltage, (d) phase portrait time sample and (e) phase portrait without transient

it is not possible for the controller to get more energy than the resonance, and the controlled system gives less energy than the open loop system.

According Tang and Zuo (2011), the system output power (P) is given by equation (4.3) related to the output voltage root mean square (V_{rms}) squared, divided by the load resistance (R)

$$P = \frac{V_{rms}^2}{R} \tag{4.3}$$

As the model is dimensionless, a dimensionless output power (Φ) given for the root mean square of the dimensionless output voltage (ν_{rms}) squared, divided by the dimensionless load resistance (Ψ), as shown in (4.4), is considered

$$\Phi = \frac{\nu_{rms}^2}{\Psi} \tag{4.4}$$

For the propose of numerical simulation, a value of the load resistance $\Psi = 0.1$ and for α ranging from 0.5 to 5.0 the dimensionless output power Φ values given in Table 6 are assumed.

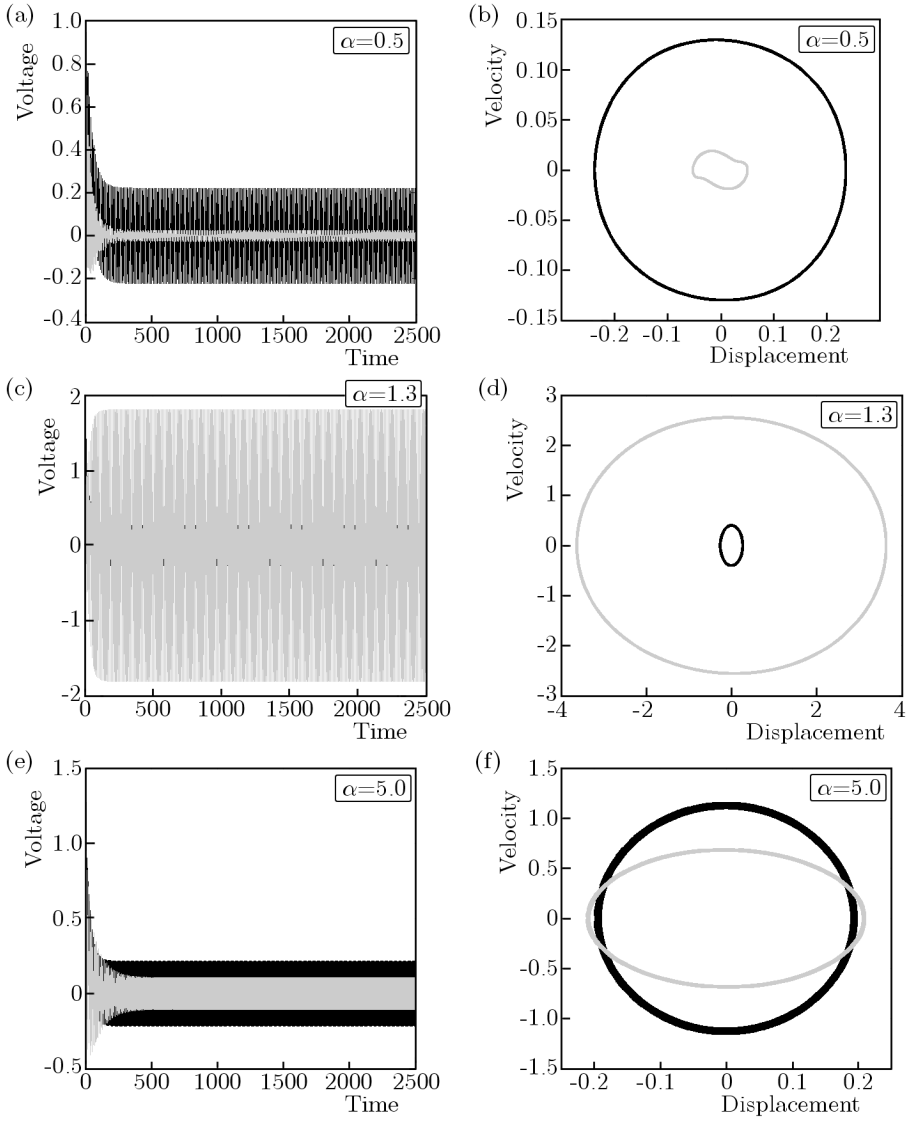

Fig. 5. System behavior (open loop system – grey line, controlled system – black line); (a), (c), (e) output voltage, (b), (d), (f) phase portrait without transient

Table 6. Dimensionless power Φ for α ranging from 0.4 to 5.0

Net torque (α)	Φ – Open loop	Φ – Controlled
0.4	0.0247	0.1695
0.5	0.0250	0.3040
1.3	16.0565	0.4015
5.0	0.0953	0.2995

Expanding the investigation for other values of the net torque (α), the resulting dimensionless power (Φ) is given in Fig. 6.

The LMI control show the efficiency of enhancing the system dimensionless output power as shown in Fig. 6 and not considering the resonance effect where the dimensionless output power is greater in the open loop system. This fact is explained because the higher energy orbit available in the system is the resonance behavior. To better visualize the control efficiency, the resonance net torque is shown in Fig. 7.

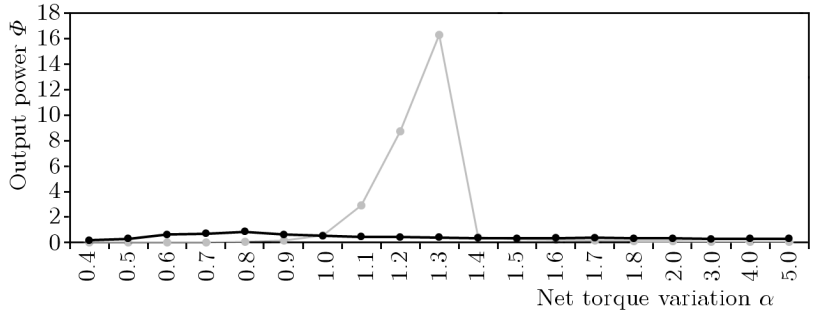

Fig. 6. Dimensionless output power (Φ) of the open loop compared to the controlled system; open loop system – grey line, controlled system – black line

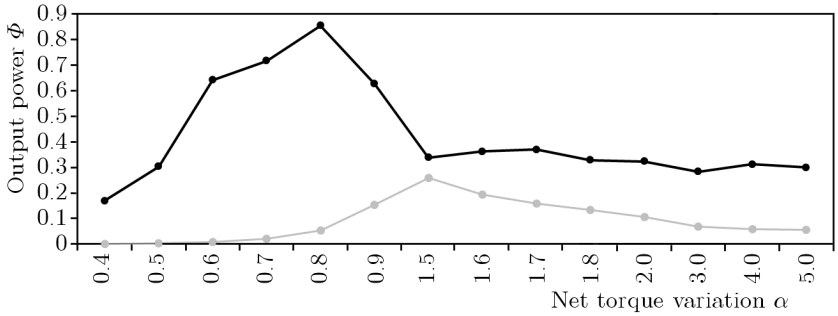

Fig. 7. Dimensionless output power (Φ) of the open loop compared to the controlled system; open loop system – grey line, controlled system – black line. Suppressing the resonance behavior

To evaluate the dimensionless net output power (Φ_{net}), Roundy and Zang (2005) compared the frequency of the open loop system to the controlled system, and later Lallart and Inman (2010) used the same evaluation to compare the output power from the open loop and controlled systems. In both cases, the power used for control (action power) is referred to the amount of change of the system parameters, in other words, it is the energetic cost to change the system behavior. Based on experimentally proven evaluations, the action power (Φ_{act}) is determined by applying the Runge-Kutta fourth order method to solve the ordinary differential equations in (2.4) for the absolute difference of the open loop and controlled parameters of each net torque (α). The results are shown in Fig. 8.

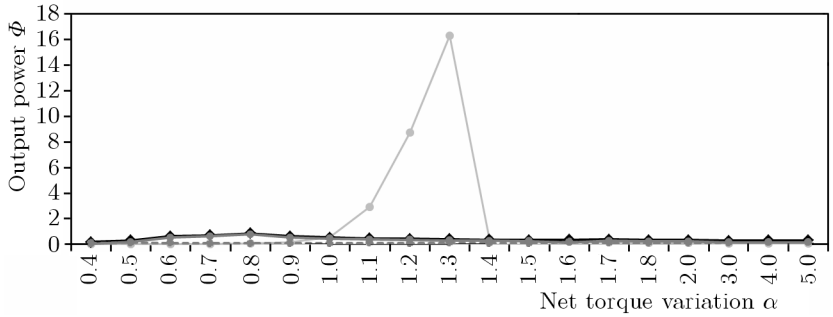

Fig. 8. Output power for the open loop system (grey line); output power for the controlled system (black line); actuation power (dotted line); net output power (solid dark grey line)

To better visualize the control efficiency, the resonance net torque is depicted in Fig. 9. The summary of power gains resulting from the control is shown in Table 7.

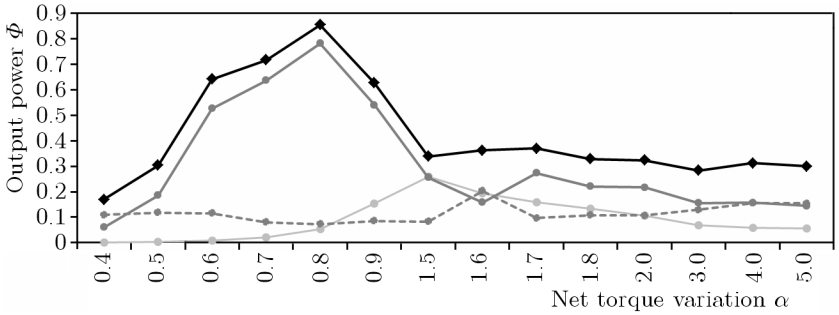

Fig. 9. Output power for the open loop system (grey line); output power for the controlled system (black line); actuation power (dotted line); net output power (solid dark grey line). Suppressing the resonance behavior

Table 7. Summary of dimensionless net power gains for the controlled system

α	0.4	0.5	0.6	0.7	0.8	0.9	1.0	1.1	1.2	1.3
Net power gain	40.69	59.67	65.85	31.70	14.99	3.54	0.77	0.13	0.04	0.02
α	1.4	1.5	1.6	1.7	1.8	2.0	3.0	4.0	5.0	
Net power gain	0.68	0.99	0.82	1.74	1.64	2.03	2.28	2.65	2.59	

5. Final remarks

Various studies regarding the energy harvesting have been carried out for the last few years to enhance the capability of the energy harvesters. In the same direction, this investigation presents a study of control of the dynamic behavior based on Linear Matrix Inequalities Optimum $H\infty$ method and a non-ideal excitation as the power source. As the main result, it has been possible to verify a significant increase in the system energy available for harvesting when applying a controller to the system. Velocity and displacement have direct effect on the output voltage and, consequently, on the output power for energy harvesting. The proposed controller is able to increase the net output power up to 65 times. Table 8 shows the comparison of other studies with the present research.

Table 8. Comparison of the obtained results with other works

Author	Resulting frequency band [Hz]
Roundy and Zhang (2005)	61.8-67.0
Wu *et al.* (2006)	91.0-94.5
Peters *et al.* (2009)	66.0-89.0
Lallart and Inman (2010)	8.1-112.0
This work	all the band

Whereas other energy harvesting methods, such as piezoelectric tuning, increase the resonant band, this control approach enhances energy not regarding the band but focusing on the output power optimization with considerable efficiency for small power excitations.

In this study, the parameters are considered constant, however in a real situation, damping and electrical coupling parameters depend on environmental conditions, for example humidity and temperature. Such variation in the parameters results in polytopic uncertainties. Thus, instead of an optimum method, a robust LMI method is required (Andrea *et al.*, 2008) which characterizes possible research continuation. The energy sink due to controller circuit is result

of the electronic architecture and is not explored in this study as another possible research exploration area.

Acknowledgments

The authors would like to thank CNPq (Proc. No. 301769/2012-5) and Federal University of Mato Grosso (UFMT) for funding this research.

References

1. Andrea C.Q., Pinto J.O.P., Assunção E., Teixeira M.C.M., Galotto L.J., 2008, Optimum control $H\infty$ of non-linear systems with fuzzy Takagi-Sugeno models (in Portuguese), *Controle and Automação*, **19**, 3
2. Antwerp J.G., Braatz R.D., 2000, A tutorial on linear and bilinear matrix inequalities, *Journal of Process Control*, **10**, 363-385
3. Baek S.H., Park J., Kim D.M., Aksyuk V.A., Das R.R., Bu S.D., Felker D.A., et al., 2011, Giant piezoelectricity on Si for hyperactive MEMS, *Science*, **334**
4. Balthazar J.M., Dantas M.J.H., 2004, On local analysis of oscillations of a non-ideal and non-linear mechanical model, *Meccanica*, **39**, 4, 313-330
5. Balthazar J.M., Mook D.T., Weber H.I., Brasil R.M.L.R.F., Fenili A., Belato D., Felix P.J.L., 2003, An overview on non-ideal vibrations, *Meccanica*, **38**, 613-621
6. Cepnik C., Radler O., Rosenbaum S., Ströhla T., Wallrabe U., 2011, Effective optimization of electromagnetic energy harvesters through direct computation of the electromagnetic coupling, *Sensors and Actuators*, **167**, 416-421
7. Challa V.R., Prasad M.G., Shi Y., Fisher F.T., 2008, A vibration energy harvesting device with bidirectional resonance frequency tenability, *Smart Materials and Structures*, **17**
8. Chavarette F.R., 2012, On an optimal linear control of a chaotic non-ideal Duffing system, *Advances in Mechanical Engineering*, **2**, 3
9. Chilali M., Gahinet P., 1996, $H\infty$ design with pole placement constrains: an LMI approach, *IEEE Transactions on Automatic Control*, **41**, 3
10. Eichhorn C., Goldschmidtboeing F., Porro Y., Woias P., 2009, A piezoelectric harvester with an integrated frequency tuning mechanism, *PowerMEMS*, Washington DC, USA, December 1-4
11. Erturk A., Inman D., 2011, Broadband piezoelectric power generation on high-energy orbits of the bistable Duffing oscillator with electromechanical coupling, *Journal of Sound and Vibration*, **330**, 2339-2353
12. Huesgen T., Woias P., Kockmann N., 2008, Design and fabrication of MEMS thermoelectric generators with high temperature efficiency, *Sensors and Actuators A*, 423-429
13. Kim S., Leung A., Koo C.Y., Kuhn L., Jiang W., Kim D., Kingon A.I., 2012, Lead-free (Na0.5K0.5)(Nb0.95Ta0.05)O3-BiFeO3 thin films for MEMS piezoelectric vibration energy harvesting devices, *Materials Letters*, **69**, 24-26
14. Lallart M., Guyomar D., 2010, Piezoelectric conversion and energy harvesting enhancement by initial energy injection, *Applied Physics Letters*, **97**
15. Lallart M., Inman D.J., 2010, Frequency self-tuning scheme for broadband vibration energy harvesting, *Journal of Intelligent Material Systems and Structures*, **21**, 897-906
16. Miller L.M., Halvorsen E., Dong T., Wright P.K., 2011, Modeling and experimental verification of low-frequency MEMS energy harvesting from ambient vibrations, *Journal of Micromechanics and Microengineering*, **21**, 045029, pp. 13

17. Palácios J.L., Balthazar J.M., Brasil R.M.L.F.R., 2003, A short note on a nonlinear system vibrations under two non-ideal excitations, *Journal of the Brazilian Society of Mechanical Sciences and Engineering*, **XXV**, 391-395

18. Peters C., Maurath D., Schock W., Mezger F., Manoli Y., 2009, A closed-loop wide-range tunable mechanical resonator for energy harvesting systems, *Journal of Micromechanics and Microengineering*, **19**, pp. 9

19. Piccirillo V., Balthazar J.M., Pontes Jr. B.R., Felix J.L.P., 2008, On a nonlinear and chaotic non-ideal vibrating system with shape memory alloy (SMA), *Journal Of Theoretical and Applied Mechanics*, **46**, 597-620

20. Roundy S., Wright P.K., Rabaey J., 2003, A study of low level vibrations as a power source for wireless sensor nodes, *Computer Communications*, **26**, 1131-1144

21. Roundy S., Zhang Y., 2005, Toward self-tuning adaptive vibration-based microgenerators, *Proceedings of Smart Structures, Devices and Systems*, **5649**, 373-384

22. Souza S.L.T., Caldas I.L., Viana R.L., Balthazar J.M., 2008, control and chaos for vibro-impact and non-ideal oscillators, *Journal of Theoretical and Applied Mechanics*, **46**, 641-664

23. Tang L., Yaowen Y., Soh C.K., 2013, Broadband vibration energy harvesting techniques, [In:] *Advances in Energy Harvesting Methods* (Chapter Two), N. Elvin and A. Erturk (Eds.), Springer Science & Business Media, New York

24. Tang X., Zuo L., 2011, Enhanced vibration energy harvesting using dual-mass systems, *Journal of Sound and Vibration*, **330**, 5199-5209

25. Tusset A.M., Balthazar J.M., Felix J.L.P., 2013, On elimination of chaotic behavior in a non-ideal portal frame structural system, using both passive and active controls, *Journal of Vibration and Control*, **19**, 6, 803-813

26. Wan Z., Kothare M.V., 2003, An efficient off-line formulation of robust model predictive control using linear matrix inequalities, *Automatica*, **39**, 837-846

27. Wang Y., Inman J.D., 2012, A survey of control strategies for simultaneous vibration suppression and energy harvesting via piezoceramics, *Journal of Intelligent Material Systems and Structures*, **23**, 18, 2021-2037

28. Wu W.-J., Chen Y.-Y., Lee B.-S., He J.-J., Peng Y.-T., 2006, Tunable resonant frequency power harvesting devices, *Proceedings of Smart Structures and Materials*, **6169**, 55-62

29. Yeager C.B., Trolier-Mckinstry S., 2012, Epitaxial Pb(Zrx,Ti1-x)O3 (0.30?x?0.63) films on (100)MgO substrates for energy harvesting applications, *Journal of Applied Physics*, **112**

30. Zhu, D., Tudor, M. J., Beeby, S. P., 2010, Strategies for increasing the operating frequency range of vibration energy harvesters: a review, *Measurement Science and Technology*, **21**, pp. 29

Manuscript received February 5, 2014; accepted for print January 9, 2015

JOURNAL OF THEORETICAL AND APPLIED MECHANICS
53, 3, pp. 617-628, Warsaw 2015
DOI: 10.15632/jtam-pl.53.3.617

INVERSE METHOD FOR A ONE-STAGE SPUR GEAR DIAGNOSIS

Ali Akrout, Dhouha Tounsi, Mohamed Taktak, Mohamed Slim Abbes, Mohamed Haddar

Mechanics, Modelling and Production Research Laboratory (LA2MP), National School of Engineers of Sfax, University of Sfax, Sfax, Tunisia; e-mail: mohamed.taktak@fss.rnu.tn; mohamed.taktak.tn@gmail.com

In this paper, a source separation approach based on the Blind Source Separation (BSS) is presented. In fact, the Independent Component Analysis (ICA), which is the main technique of BSS, consists in extracting different source signals from several observed mixtures. This inverse method is very useful in many fields such as telecommunication, signal processing and biomedicine. It is also very attractive for diagnosis of mechanical systems such as rotating machines. Generally, dynamic responses of a given mechanical system (displacements, accelerations and speeds) measured through sensors are used as inputs for the identification of internal defaults. In this study, the ICA concept is applied to the diagnosis of a one-stage gear mechanism in which two types of defects (the eccentricity error and the localized tooth defect)are introduced. The finite element method allows determination of the signals corresponding to the acceleration in some locations of the system, and those signals may be used also in the ICA algorithm. Hence, the vibratory signatures of each defect can be identified by the ICA concept. Thus, a good agreement is obtained by comparing the expected default signatures to those achieved by the developed inverse method.

Keywords: Independent Component Analysis (ICA), source identification, gear mechanism, geometrical defects

1. Introduction

Diagnosis, without disassembling different parts of a given machine, represents the main purpose to be achieved in the defect detection practice. This procedure allows the industry to save time and money. That is why many approaches found in the literature can be considered as tools to realize non destructive diagnosis of machines. Usually, any internal default or external force which excites mechanical systems can be identified by frequency analysis. That allows the determination of the internal default excitation frequencies or the external excitation forces. However, the knowledge of the different excitation frequencies existing in the spectrum of the system vibratory signal is insufficient to determine the type of defaults, its amplitude and its position in the system. To surpass these limitations, various methods have been developed in order to solve the source separation problem leading to different algorithms which can be used for modal analysis of structures and dynamic systems (Antoni *et al.*, 2004; Poncelet *et al.*, 2007; Kerschen *et al.*, 2007; Abbès *et al.*, 2011; Akrout *et al.*, 2012a,b). One of these techniques is the Blind Source Separation (BSS) which was presented by many researchers (Antoni and Braum, 2005) and (Antoni, 2005). It consists in separating an independent linear mixture source signal without any information about the sources by using only the measured vibratory response of the system. The separation procedure is based on the statistical independency of sources.

In the last few years, an increasing number of works using the ICA concept for detecting defects in mechanical systems have been found. Many researchers have developed different algorithms based on the ICA technique for the diagnosis of rotating machines (Servière and Fabry,

2004) and (Taktak *et al.*, 2012), bearings (Shalvi and Weinstein, 1990) and structures (Zang and Friswel, 2004), (Akrout *et al.*, 2012a,b).

In this paper, the ICA method is applied to diagnosis a one-stage spur gear system. The spur gear represents a device that ensures transmission of movement in various mechanical systems. In a gear mechanism, there appear frequently many internal defaults which generate disturbances in the dynamic responses. By using the ICA concept, both the amplitude and the frequency are used to localize the defaults.

After presentation of the separation method including the definition of the ICA in Section 2, Section 3 presents the separation hypothesis of the ICA concept and the associated different steps. Section 4 presents the results and the discussion of the application of this technique to a one-stage spur gear to identify its internal defaults.

It is also worth mentioning that in our previous work (Taktak *et al.*, 2012), the observed signals (accelerations) are determined on two nodes of a discretized crankcase flexible plate. However, in this article, the vibratory responses are calculated in the pinion and the gear centre, respectively.

2. Inverse method for dynamic problem: the Independent Component Analysis (ICA)

2.1. ICA definition

The ICA method was defined by Comon (1990) as a statistical technique that aims at decomposing a random signal $\mathbf{X}$ (measured signal) into a linear combination of independent signals (source signals). Then, the ICA problem is formulated as follows

$$\mathbf{X} = \mathbf{AS} \tag{2.1}$$

where $\mathbf{X}$ is a column vector of M output observations, which represents an instantaneous linear mixture of source signals $\mathbf{S}$ defined by a column vector of N sources. $\mathbf{A}$ is a $M \times N$ mixing matrix. The equation of the ICA concept is described as follows (Zang *et al.*, 2004; Abbès *et al.*, 2011; Akrout *et al.*, 2012)

$$X_j(t) = \sum_{i=1}^{N} a_{ji} S_i(t) \qquad j = 1, \ldots, M \tag{2.2}$$

2.2. ICA indeterminacies

In spite of its advantages in separating source signals, two ambiguities are inherent to the ICA method: it aims at identification of both source signals and the mixing matrix with certain indeterminacies that include arbitrary scaling and permutation. The mixture model can be expressed as follows (Antoni, 2005; Tong *et al.*, 1991)

$$\mathbf{X} = \mathbf{AP}^{-1}\mathbf{PS} \tag{2.3}$$

where $\mathbf{P}$ is the permutation matrix.

In the same way, the observations can be rewritten as follows

$$\mathbf{X} = \mathbf{AD}^{-1}\mathbf{DS} \tag{2.4}$$

$\mathbf{D}$ is a diagonal matrix. So any scalar multiplier to one of the source S_i could be avoided by dividing the corresponding column of the matrix $\mathbf{A}$.

These two indeterminacies imply that it is impossible to obtain a unique determination of the original sources. So the separating matrix **B** is estimated by the product **BA** which is equal to the diagonal matrix **D** up to the permutation matrix **P**

$$\mathbf{BA} = \mathbf{DP} \tag{2.5}$$

In order to reduce the shape indeterminacy in the model and save the waveform of the original signals, a constraint of unit variance is imposed on the sources **S** to eliminate the scale factor (Antoni, 2005; Tong *et al.*, 1991)

$$E[\mathbf{SS}^{+}] = \mathbf{I} \tag{2.6}$$

where (+) denotes the conjugate, and **I** is the $N \times N$ identity matrix.

The ICA concept assumes that the sources Si must be statically independent uncorrelated and have a non-Gaussian distribution. Then, to perform the estimated source signals task and the mixing matrix **A**, the ICA requires some separation assumptions which are presented in the following section.

2.3. Separation assumptions

2.3.1. Statistical independency of the sources

The separation can be achieved only when all the components of the separating system are mutually and statically independent. The components of a random vector **X** are mutually independent if and only if the probability density of the vector **X** is equal to the marginal probability density (Akrout *et al.*, 2012a,b; Hyvärinen and Oja, 2000)

$$P_x(x) = \prod_{i=1}^{N} P_{x_i}(x_i) \tag{2.7}$$

Many formulations are used to assure the statistical independence of the sources such as the mutual information which is based on the Kulback divergence (Comon, 1990)and the likelihood estimation (Geata and Lacoume, 1990).

2.3.2. Uncorrelated sources

The statistical independence of the sources imposes that the sources must be uncorrelated. So, two variables Y_1 and Y_2 are uncorrelated if and only if their covariance is equal to zero (Akrout *et al.*, 2012a,b; Comon, 1990)

$$E\{Y_1Y_2\} - E\{Y_1\}E\{Y_2\} = 0 \tag{2.8}$$

2.4. Non-Gaussianity distribution of the sources

Another very useful hypothesis in the source separation is the non-Gaussianity of the sources (Akrout *et al.*, 2012a,b; Comon, 1990). This criterion is especially essential in the case of stationary white sources since the non-Gaussianity of the sources is needed to achieve the separation.

The Gaussianity of a signal is defined as the difference between the distributions of the signal and the Gaussian signal with the same power. Instantaneous linear mixture sources can be separated by maximizing the non-Gaussianity of the output signal, which is obtained by a linear combination of the observations.

The non-Gaussianity can be evaluated by the kurtosis or the fourth order cumulate. The Kurtosis of a variable y is expressed as follows (Comon, 1990)

$$Kurt(y) = E\{y^4\} - 3(E\{y^2\})^2 \tag{2.9}$$

Another measure of non-Gaussianity which can be used is the negentropy theory which is based on the theoretical quantity of the differential entropy (Wiggins, 1978).The differential entropy of a variable y with a density $f(y)$ can be defined as follows (Hyvärinen and Oja, 2000)

$$H(y) = -\int f(y)\log(f(y))\,dy \tag{2.10}$$

So, the negentropy which is equal to zero for the Gaussian variable can be written as follows (Hyvärinen and Oja, 2000)

$$J(y) = H(y_{gauss}) - H(y) \tag{2.11}$$

where y_{gauss} is a random variable which has the same covariance matrix as y. So, the negentropy is always non negative and it is equal to zero in the case of Gaussian variable.

3. ICA steps

3.1. Pre-processing for ICA

Before applying the ICA algorithm and to guarantee the uncorrolatedness of the sources, it is useful to do some pre-processing. These pre-processings make the ICA estimation easy. These pre-processings are presented in the following sections.

3.1.1. Centring

The first pre-treatment is the centring. Each observed vector $\mathbf{X}$ must be centred, i.e., subtracts its mean vector $m = E\{\mathbf{X}\}$; so, $\mathbf{X}$ will be the zero mean variable which implies that $\{S\}$ is the zero mean as well (Hyvärinen and Oja, 2000).

3.1.2. Whitening

The second pre-treatment used in ICA is whitening of the observations $\mathbf{X}$. This means that before applying the ICA algorithm, we transform the vector $\mathbf{X}$ to a white vector $\widetilde{\mathbf{X}}$ which has uncorrelated components, and the variance of its components is equal to unity and (Thirion--Moreau, Moreau, 2000)

$$\widetilde{\mathbf{X}} = \mathbf{WX} \tag{3.1}$$

$\mathbf{W}$ is the whitening matrix, it is determined by the eigenvalues decomposition of the covariance matrix which is defined by

$$R_x(0) = E\{\mathbf{XX}^+\} = \mathbf{AA}^+ = \mathbf{UDU}^{\mathrm{T}} \tag{3.2}$$

where $\mathbf{U}$ is the eigenvector orthogonal matrix of $E\{\mathbf{XX}^{\mathrm{T}}\}$ and $\mathbf{D}$ is the diagonal matrix of its eigenvalues.

So,we can write

$$E\{(\mathbf{WX})(\mathbf{WX})^+\} = \mathbf{WW}^+E\{\mathbf{XX}^+\} = \mathbf{I} \tag{3.3}$$

Then, the whitening matrix can be defined as follows

$$\mathbf{W} = \mathbf{D}^{-1/2}\mathbf{U}^{\mathrm{T}} \tag{3.4}$$

This transformation allows definition of a new matrix $\widetilde{\mathbf{A}}$

$$\widetilde{\mathbf{X}} = \mathbf{D}^{-1/2}\mathbf{U}^{\mathrm{T}}\mathbf{A}\mathbf{S} = \widetilde{\mathbf{A}}\mathbf{S} \tag{3.5}$$

$\widetilde{\mathbf{A}}$ is an orthogonal mixing matrix, then we can write

$$E\{\widetilde{\mathbf{X}}\widetilde{\mathbf{X}}^{\mathrm{T}}\} = \widetilde{\mathbf{A}}E\{\mathbf{S}\mathbf{S}^{\mathrm{T}}\}\widetilde{\mathbf{A}}^{\mathrm{T}} = \widetilde{\mathbf{A}}\widetilde{\mathbf{A}}^{\mathrm{T}} = \mathbf{I} \tag{3.6}$$

So, the whitening of the observations contributes to reduction of the number of parameters to be estimated. Instead of estimating n^2 parameters, only the elements of the new orthogonal matrix $\widetilde{\mathbf{A}}$ are considered. We noticed that an orthogonal matrix has $n(n-1)/2$ degrees of freedom (Hyvärinen and Oja, 2000).

3.2. ICA algorithm

3.2.1. Kurtosis maximization

In the literature, many contrast functions have been proposed. Among them the Kurtosis defined by the normalized fourth order marginal cumulate is the commonly used statistical quantity in the ICA concept (Comon, 1994). The kurtosis was firstly used in blind separation of seismic signals and digital communication (Shalvi and Weinstein, 1990; Wiggins, 1978).

The separation of sources using ICA is based on the determination of each column of the separating matrix $\mathbf{W}$. Then it determines the source related to this column. The extracting vector of the mixing matrix can be defined as follows (Akrout *et al.*, 2012a,b; Zarzoso and Comon, 2010)

$$\mathbf{Y} = \mathbf{W}^{\mathrm{H}}\mathbf{X} \tag{3.7}$$

where $\mathbf{Y}$ is the estimated source and $\mathbf{W}$ is the separating matrix, $(\cdot)^{\mathrm{H}}$ denotes the conjugate transpose operator. $\mathbf{W}$ must maximize the Kurtosis in order to guarantee the non-Gaussianity distribution. This Kurtosis is defined as follows (Akrout *et al.*, 2012a,b; Zarzoso and Comon, 2010)

$$K(\omega) = \frac{E\{|y|^4\} - 2E^2\{|y|^2\} - |E\{y^2\}|^2}{E^2\{|y|^2\}} \tag{3.8}$$

In order to maximize this function, an exact line search of the absolute Kurtosis contrast is performed, which is defined as (Zarzoso and Comon, 2010)

$$\mu_{opt} = \arg\left(K(w + \mu g)\right) \tag{3.9}$$

where g is the search direction defined as the gradient $g = \nabla_w(K(\omega))$. The exact line search is determined after determination of roots of a fourth degrees polynomial, so the roots leading to the absolute maximum of the contrast along the search direction are chosen.

After the determination of the column of the separating matrix, a deflation approach is considered in order to extract the source corresponding to the determined column.

3.2.2. Deflation approach

The deflation approach allows escaping from a multiple inputs/multiple outputs system into a system with a single input/multiple outputs. The deflation approach is used to extract successively the sources. This ensures that each source is chosen once with multiplying the exact factor. After the determination of the column vector of the separation matrix $\mathbf{W}$ by maximizing the kurtosis contrast, the deflation approach is used in order to determine the estimated source.

4. Diagnosis of a one-stage gear mechanism

The purpose of this part is to provide an illustration of the capability of the ICA algorithm to separate and extract signals from a given mechanical system which is a one-stage spur gear mechanism. The ICA concept is applied to this system and the source identification results are presented and discussed.

4.1. System presentation

The studied system is a one-stage spur gear mechanism. It can be divided into two blocks as presented in Fig. 1a. The first block is composed by the input shaft (1) and a pinion. The second block is constituted by the gear and the output shaft (2). Both the pinion and the gear are supposed to be rigid. The shafts, which are assumed to be flexible, are discretized by two node beam finite elements (Fig. 1b) with 6 degrees of freedom per node.

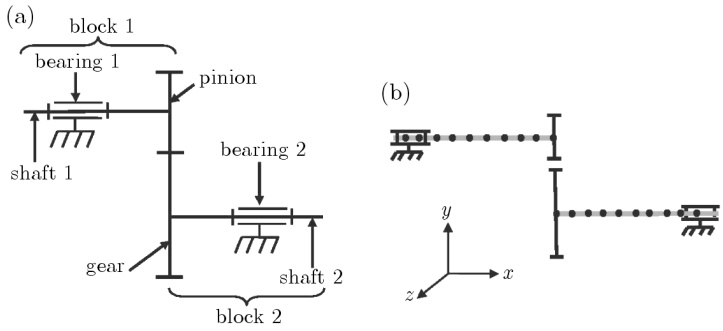

Fig. 1. Studied case: (a) model of a one-stage spur gear, (b) discretized single spur gear

The shafts are supported by bearings each modelled by two linear springs. The gear mesh stiffness is modelled by a linear spring acting on the line of action of the meshing teeth.

The expression of the displacement on the line of action is expressed as (Chaari *et al.*, 2008)

$$\delta(t) = (z_1 - z_2)\sin\gamma + (y_1 - y_2)\cos\gamma + \theta_{xp} r_{bp} + \theta_{xg} r_{bg} \tag{4.1}$$

where z_i and y_i $(i = 1, 2)$ are respectively the centre displacements of the pinion and gear. θ_{xp} and θ_{xg} are angular rotations of the pinion and the gear centre, respectively. r_{bp} and r_{bg} are the basis radius of the pinion and the gear, respectively. γ is the pressure angle.

The equation of motion of the system is defined as (Chaari *et al.*, 2008)

$$\mathbf{M}\ddot{\mathbf{q}} + \mathbf{C}\dot{\mathbf{q}} + \mathbf{K}(t)\mathbf{q} = \mathbf{F}_{ext} \tag{4.2}$$

where $\mathbf{M}$, $\mathbf{C}$ and $\mathbf{K}(t)$ are respectively the global mass, damping and stiffness matrices of the whole system. $\mathbf{q}$ is the vector of degrees of freedom, $\mathbf{F}_{ext}$ is the external applied forces vector.

The mass matrix $\mathbf{M}$ is a diagonal matrix which can be written as follows (Chaari *et al.*, 2008)

$$\mathbf{M} = \begin{bmatrix} \mathbf{M}_1 & \mathbf{0} & \mathbf{0} & \mathbf{0} \\ \mathbf{0} & \mathbf{M}_p & \mathbf{0} & \mathbf{0} \\ \mathbf{0} & \mathbf{0} & \mathbf{M}_g & \mathbf{0} \\ \mathbf{0} & \mathbf{0} & \mathbf{0} & \mathbf{M}_2 \end{bmatrix} \tag{4.3}$$

$\mathbf{M}_i$ $(i = 1, 2)$ is the mass matrix of the ith shaft; $\mathbf{M}_p$ and $\mathbf{M}_g$ are respectively the mass matrices of the pinion and the gear (Chaari *et al.*, 2008).

$\mathbf{K}(t)$ includes the shafts stiffness, bearing stiffness and the time varying gear mesh stiffness matrix.The stiffness matrix of the shafts is determined by the FE model presented in Fig. 1b.

Then, the matrix $\mathbf{K}(t)$ can be divided into a mean stiffness matrix $\overline{\mathbf{K}}$ and a fluctuating one $\mathbf{K}_{GS}(t)$ (Chaari *et al.*, 2008)

$$\mathbf{K}(t) = \overline{\mathbf{K}} + \mathbf{K}_{GS}(t)$$
$$\overline{\mathbf{K}} = \begin{bmatrix} \mathbf{K}_{shaft'1'} & \mathbf{K}_{C1} & \mathbf{0} & \mathbf{0} \\ \mathbf{K}_{C1}^{\mathrm{T}} & \mathbf{K}_{bearing'1'} & \mathbf{0} & \mathbf{0} \\ \mathbf{0} & \mathbf{0} & \mathbf{K}_{bearing'2'} & \mathbf{K}_{C2} \\ \mathbf{0} & \mathbf{0} & \mathbf{K}_{C2}^{\mathrm{T}} & \mathbf{K}_{shaft'2'} \end{bmatrix} \tag{4.4}$$

$\mathbf{K}_{shaft'i'}$ and $\mathbf{K}_{bearing'i'}$ $(i = 1, 2)$ are the stiffness matrices of the ith shaft. $\mathbf{K}_{C1}$ and $\mathbf{K}_{C2}$ are the coupling matrices between the bearings and shafts. The bearing stiffness matrices contain the translation stiffness along with the z and y directions (Chaari *et al.*, 2008) ($K_{y1} = K_{z1} = K_{y2} = K_{z2} = 10^8$ N/m).

$\mathbf{K}_{GS}(t)$ is the fluctuation stiffness matrix defined as follows (Chaari *et al.*, 2008)

$$\mathbf{K}_{GS}(t) = \begin{bmatrix} 0 & 0 & 0 & 0 & 0 & 0 & 0 & 0 & 0 & 0 & 0 & 0 \\ 0 & s_4 & s_5 & s_6 & 0 & 0 & 0 & -s_4 & -s_5 & s_8 & 0 & 0 \\ 0 & s_5 & s_3 & s_7 & 0 & 0 & 0 & -s_5 & s_3 & s_9 & 0 & 0 \\ 0 & s_6 & s_7 & s_{10} & 0 & 0 & 0 & -s_6 & s_7 & s_{12} & 0 & 0 \\ 0 & 0 & 0 & 0 & 0 & 0 & 0 & 0 & 0 & 0 & 0 & 0 \\ 0 & 0 & 0 & 0 & 0 & 0 & 0 & 0 & 0 & 0 & 0 & 0 \\ 0 & 0 & 0 & 0 & 0 & 0 & 0 & 0 & 0 & 0 & 0 & 0 \\ 0 & -s_4 & -s_5 & -s_6 & 0 & 0 & 0 & s_4 & s_5 & -s_8 & 0 & 0 \\ 0 & -s_5 & -s_3 & -s_7 & 0 & 0 & 0 & s_5 & s_3 & -s_9 & 0 & 0 \\ 0 & s_8 & s_9 & s_{12} & 0 & 0 & 0 & -s_8 & -s_9 & s_{11} & 0 & 0 \\ 0 & 0 & 0 & 0 & 0 & 0 & 0 & 0 & 0 & 0 & 0 & 0 \\ 0 & 0 & 0 & 0 & 0 & 0 & 0 & 0 & 0 & 0 & 0 & 0 \end{bmatrix} K_e(t) \tag{4.5}$$

where $K_e(t)$ is the time varying gear mesh stiffness.

The terms s_i $(i = 1, \ldots, 12)$ are given in Table 1.

Table 1. Coefficients s_i

s_1	$\sin\gamma$	s_7	$r_{bp}\sin\gamma$
s_2	$\cos\gamma$	s_8	$r_{bg}\cos\gamma$
s_3	$\sin^2\gamma$	s_9	$r_{bg}\sin\gamma$
s_4	$\cos^2\gamma$	s_{10}	r_{bp}^2
s_5	$\sin\gamma\cos\gamma$	s_{11}	r_{bg}^2
s_6	$r_{bp}\cos\gamma$	s_{12}	$r_{bg}r_{bp}$

The damping matrix of the system is determined from a combination between the mass matrix of the system and the mean stiffness matrix

$$\mathbf{C} = \alpha\mathbf{M} + \beta\overline{\mathbf{K}} \tag{4.6}$$

where α and β are two constants which influence the stability of the system. The properties of the studied system are presented in Tables 2 and 3.

4.2. Geometrical and teeth defect models

In order to disturb the dynamic response of the studied system, some defects have been introduced into the spur gear. The vibration sources (internal and external excitations) of the dynamic transmission are multiple. However, the internal sources have considerable effects on

Table 2. Parameters of the spur gear (Hidaka *et al.*, 1979)

	Pinion	Gear
Teeth numbers	20	40
Mass [kg]	0.6659	2.663
Inertia Moment [kg m^2]	$2.996 \cdot 10^{-4}$	0.0048
Base diameter circle [m]	0.0564	0.1128
Rotation speed [rpm]	1500	750
Torque [Nm]	10	-20
Module [mm]	3	
Pressure angle [deg]	20	
Gear mesh frequency [Hz]	500	

Table 3. Parameters of the input and output shafts (Hidaka *et al.*, 1979)

Shaft characteristics	value
Material	steel
Young's modulus [MPa]	$2 \cdot 10^5$
Length [m]	0.45
Section [m^2]	$3.84 \cdot 10^{-3}$
Poisson's coefficient	0.29
Density [kg/m^3]	7858

the dynamic response of the system. As examples, of internal excitation sources, we can mention assembly defects which are characterized by an excitation frequency which corresponds to the rotation frequency of the shafts as well as geometric deviation which is characterized by an excitation frequency corresponding to the gear mesh rotation frequency.

The geometric deviation comes mainly from manufacturing defects; they are duplicated typically at the gear mesh frequency. We can distinguish the profile error which presents the difference between the actual profile and the theoretical profile of the teeth. According to Munro (1967), the profile error which is duplicated on each tooth, induces a transmission error marked at the gear mesh frequency and its harmonics.

The eccentricity error represents the difference between the real and theoretical location of the axes of the gear polar moment of inertia. Munro (1967) shows that the eccentricity of the wheel is characterized by the presence of a main peak at the rotation frequency in the spectrum of the static transmission.

Furthermore, teeth defects, such as spalling, breakage and crack, can affect considerably the dynamic behaviour of the gear transmission. In that case, several dynamic models have been developed in order to achieve some diagnosis solutions (Munro, 1967; Chaari *et al.*, 2009).

The eccentricity error and the localized tooth defect have the following expressions (Hidaka *et al.*, 1979; Wajag and Kahraman, 2002)

$$F_{def_1} = K_e(t)e_c \sin(2\pi f_r t) \qquad F_{def_2} = K_e(t)e_c \sin(2\pi f_{en} t) \tag{4.7}$$

where f_r is the rotation frequency of the shaft, e_c is the excitation amplitude, f_{en} is the gear mesh frequency. Therefore, the equation of motion of the spur gear transmission can be expressed as follows

$$\mathbf{M}, \ddot{\mathbf{q}} + \mathbf{C}\dot{\mathbf{q}} + \mathbf{K}(t)\mathbf{q} = \mathbf{F} - \mathbf{F}_{def1} - \mathbf{F}_{def2} \tag{4.8}$$

Equation (4.10) is solved using the New mark method. Then, vibratory responses of the system are determined and used to reconstruct the forces related to different system failures.

4.3. Numerical simulation

As mentioned above, the first step in the simulation process is the introduction of both eccentricity and tooth defaults. The waveforms of the two internal defects introduced in the gear transmission are presented in Figs. 2 and 3. The first one (Fig. 2) corresponds to the temporary evolution of the eccentricity error. The second one (Fig. 3) corresponds to the time evolution of the tooth defect.

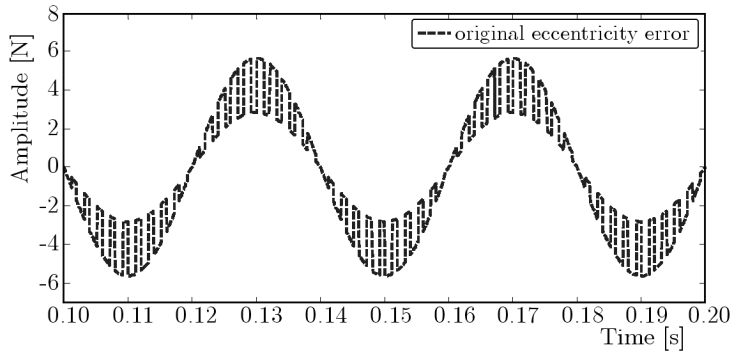

Fig. 2. Time-evolution of the eccentricity error

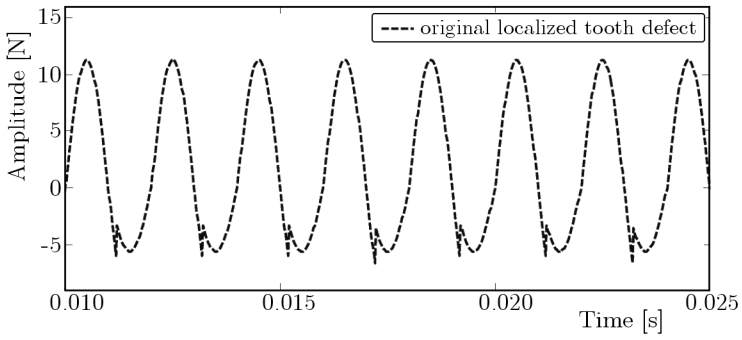

Fig. 3. Time-evolution of the localized tooth defect

In order to extract the original sources, the observed signals (accelerations) are determined at both the centre of the pinion and the centre of the gear and by taking into account the presence of the tooth failure and the eccentricity error. The rotational speed of the pinion is equal to $N = 1500\,\mathrm{tr/min}$. The period is $T_e = 0.002\,\mathrm{s}$ which corresponds to the gear mesh frequency $f_e = 500\,\mathrm{Hz}$.

Then, these calculated dynamic reponses are used as inputs in the ICA separation algorithm to estimate the waveforms of the real internal defects in the spur gear as well as the excitation frequency and, finally, to identify the type of defect.

After determination of the observed signals, the ICA algorithm is applied to determine the estimated sources which correspond to the internal defects of the spur gear. The presence of the rotation frequency of the shaft in the spectrum of the estimated sources indicates clearly the position defect with the corresponding waveform. So, the eccentricity error can be identified. If only the gear mesh frequency and its harmonics are observed, we can stipulate that there is a tooth failure with the waveform and we can distinguish between the different tooth failures which may exist.

Figure 4 presents the evolution of the estimated source extracted by the ICA method from the observed signals versus time superimposed with the original source, which presents the eccentricity error. The estimated source has almost the same waveform and amplitude as the original source. The two sources have the same excitation frequency.

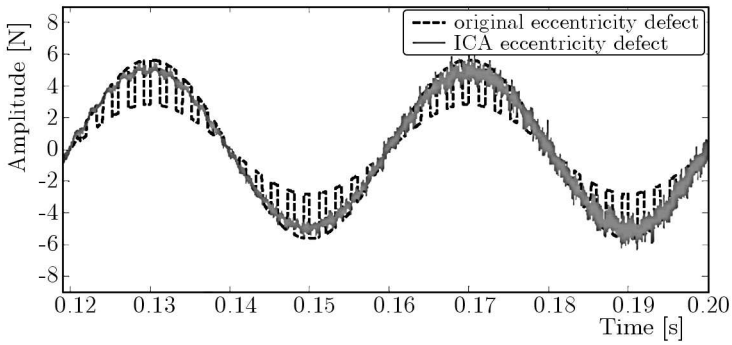

Fig. 4. Original and estimated time-evolution of the eccentricity defect

In Fig. 5, the spectrum of the estimated source corresponding to the eccentricity error is presented. We notice the presence of a peak at the rotation frequency of the shaft which is equal to 25 Hz and other peaks at the gear mesh frequency and its harmonics that correspond to the excitation frequency of the eccentricity error.

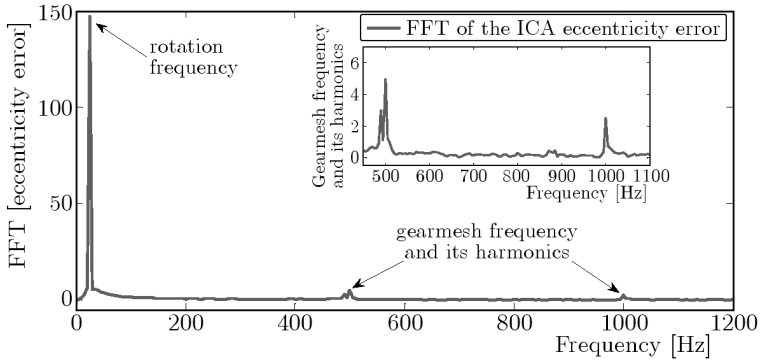

Fig. 5. Spectrum of the estimated signal of the eccentricity defect

Figure 6 shows the time-evolution of both original and estimated source corresponding to the tooth defect. So, one can clearly see the efficiency of the developed inverse method for reconstruction of the introduced internal defects. The amplitudes and the waveforms of the original and the estimated excitation source are almost identical.

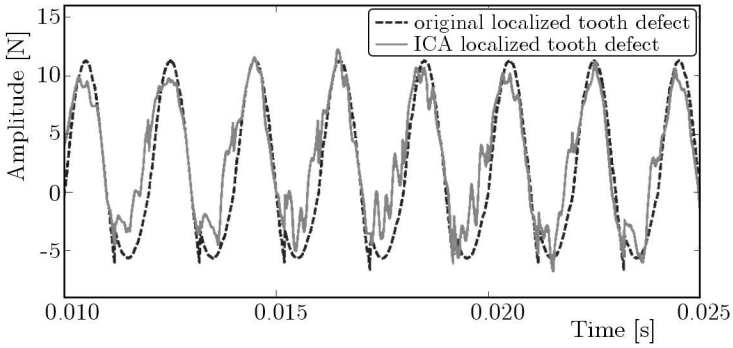

Fig. 6. Original and estimated time-evolution of the localized tooth defect

In Fig. 7, the spectrum of the second estimated source is presented. Here, we noticed the presence of three peaks corresponding to the gear mesh frequency and its harmonics. Hence, the excitation frequency of the tooth defect can be identified ($f_e = 500$ Hz).

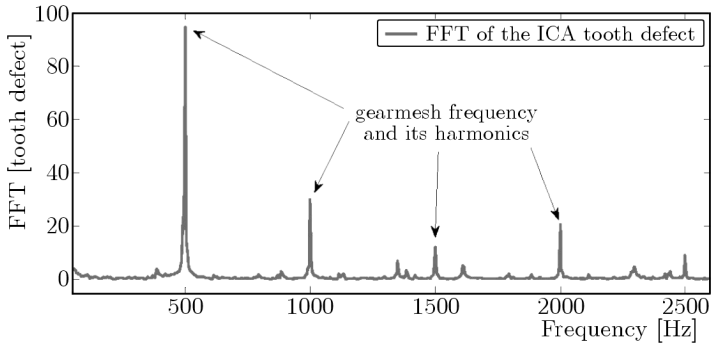

Fig. 7. Spectrum of the estimated signal of the second defect

From all the results presented above, we conclude that the estimated sources reconstructed by the developed inverse method(ICA algorithm) have the same waveforms and excitation frequencies as the internal defects considered present in the system. So, the ICA method gives good results for dynamic diagnosis of a one-stage spur gear and can be employed for other complicated mechanical systems.

5. Conclusion

In this paper, the ICA method has been presented and applied to a mechanical system defined bya one-stage spur gear in order to identify the eventual internal defects. Two different types of internal defects have been introduced in the equation of motion: the eccentricity error and tooth defect. Then, by using the dynamic response signals as inputs in the ICA algorithm, we have succeeded to recover the estimated sources which correspond to real internal sources introduced in the gear system. So, the usefulness of the proposed method is demonstrated.

References

1. Abbès M.S., Miladi Chaabane M., Akrout A., Fakhfakh T., Haddar M., 2011, Vibratory behavior of a double panel system by the operational modal analysis, *International Journal of Modeling, Simulation and Scientific Computing*, **2**, 4, 459-479

2. Akrout A., Miladi Chaabane M., Hammami L., Haddar M., 2012, Edge stiffness effects on laminated double glazing system dynamical behaviour by the operational modal analysis, *Journal of Mechanics of Materials and Structures*, **7**, 8/9, 837-859

3. Akrout A., Tounsi D., Taktak M., Abbes M.S., Haddar M., 2012, Estimation of dynamic system's excitation forces by the independent components analysis, *International Journal of Applied Mechanics*, **4**, 3

4. Antoni J., Garibaldi L.,Marchesiello S., Sidahmed M., 2004, New separation techniques for output-only modal analysis, *Shock and Vibration*, **11**, 227-242

5. Antoni J., 2005, Blind separation of vibration components: principles and demonstration, *Mechanical Systems and Signal Processing*, **19**, 1166-1180

6. Antoni J., Braun S., 2005, Special issue on blind source separation: editorial, *Mechanical Systems and Signal Processing*, **19**, 1163-1165

7. Chaari F., Baccar W., Abbès M.S., Haddar M., 2008,Effect of spelling or tooth breakage on gearmesh stiffness and dynamic response of a one-stage spur gear transmission, *European Journal of Mechanics A/Solids*, **27**, 691-705

8. Chaari F., Fakhfakh T., Haddar M., 2009, Analytical modelling of spur gear tooth crack and influence on gearmesh stiffness, *European Journal of Mechanics A/Solids*, **28**, 461-468

9. Comon P., 1990, Separation of sources using higher-order cumulants, *Actes Advanced Algorithms and Architectures for Signal Processing IV*, San Diego, Californie, 1152, 170-181

10. Comon P., 1994, Independent component analysis: a new concept? *Signal Processing*, **36**, 287-314

11. Gaeta M., Lacoume J.L., 1990, *Maximum Likelihood Estimators Applied to the Non Gaussian Source Separation*, Saint-Martin-d'Heres, France

12. Hidaka T., Terauchi Y., Dohi K., 1979, On the relation between the run out errors and the motion of the center of sun gear in a Stoeckicht planetary gear, *Bulletin of JSME*, **22**, 167, 748-754

13. Hyvärinen A., Oja E., 2000, Independent component analysis: algorithms and applications, *Neural Networks*, **13**, 3/5, 411-430

14. Kerschen G., Poncelet F., Golinval J.C., 2007, Physical interpretation of independent component analysis in structural dynamics, *Mechanical Systems and Signal Processing*, **21**, 1561-1575

15. Munro R., 1967, Gear transmission error, *AGMA Paper*, **239**, 10

16. Poncelet F., Kerschen G., Golinval J.C., Verhelst D., 2007, Output-only modal analysis using blind source separation techniques, *Mechanical Systems and Signal Processing*, **21**, 2335-2358

17. Servière C., Fabry P., 2004, Blind source separation of noisy harmonic signals for rotating machine diagnosis, *Journal of Sound and Vibration*, **272**, 317-339

18. Shalvi O., Weinstein E., 1990, New criteria for blind deconvolution of non-minimum phase systems (channels), *IEEE Transactions Information Theory*, **36**, 2, 312-321

19. Taktak M., Tounsi D., Akrout A., Abbès M.S., Haddar M., 2012, One stage spur gear transmission crankcase diagnosis using the independent components method, *International Journal of Vehicle Noise and Vibration*, **8**, 4, 387-400

20. Thi H.L.N., Jutten C., 1995, Blind source separation for convolutive mixtures, *Signal Processing*, **45**, 209-229

21. Thirion-Moreau N., Moreau E., 2000, New criteria for blind signal separation, *IEEE Workshop on Statistical Signal and Array Processing*, 344-348

22. Tong L., Liu R.W., Soon V.C., Huang Y.F., 1991, Indeterminacy and identifiability of blind identification, *IEEE Transactions on Circuits and Systems*, **38**, 499-509

23. Wajag P., Kahraman A., 2002, Influence of tooth profile modification on helical gear durability, *ASME Transactions, Journal of Mechanical Design*, **124**, 501-510

24. Wiggins R.A., 1978, Minimum entropy deconvolution, *Geoexploration*, **16**, 21-35

25. Zang C., Friswel M.I., Imregun M., 2004, Structural damage detection using independent component analysis, *Structural Health Monitoring*, **3**, 1, 69-83

26. Zarzoso V., Comon P., 2010, Robust independent component analysis by iterative maximization of the Kurtosis contrast with algebraic optimal step size, *IEEE Transactions on Neural Networks*, **21**, 2

Manuscript received April 8, 2014; accepted for print January 30, 2015

JOURNAL OF THEORETICAL AND APPLIED MECHANICS
53, 3, pp. 629-642, Warsaw 2015
DOI: 10.15632/jtam-pl.53.3.629

ON FREE VIBRATIONS OF THIN FUNCTIONALLY GRADED PLATE BANDS RESTING ON AN ELASTIC FOUNDATION

Jarosław Jędrysiak, Magda Kaźmierczak-Sobińska
Lodz University of Technology, Department of Structural Mechanics, Łódź, Poland
e-mail: jarek@p.lodz.pl; magda.kazmierczak@p.lodz.pl

In this note free vibrations of plate bands with functionally graded properties, resting on an elastic foundation, are investigated. On the micro-level, these plate bands have a tolerance--periodic structure. It can be shown that in dynamic problems of those objects, the effect of the microstructure size plays a role. This effect can be described in the framework of the tolerance model, which is presented here for these bands. Obtained results are evaluated introducing the asymptotic model. Both fundamental and higher free vibration frequencies of these plate bands are calculated using the Ritz method. The effects of differences of material plate properties in the cell on the microlevel and of the foundation are shown.

Keywords: thin functionally graded plate band, microstructure size, free vibrations, material properties, elasic foundation

1. Introduction

In the civil engineering, plates interacting with the subsoil are often used as elements of building foundations or reinforcements of roads foundations. In many cases, the first approximation of the subsoil can be a model of Winkler's foundation.

In this paper, free vibrations of thin functionally graded plate bands with span L (along the x_1-axis) interacting with elastic Winkler's foundation are considered. It is assumed that these plate bands have the functionally graded structure along their span on the macrolevel, but on the microlevel their structure is, so called, tolerance-periodic in x_1, i.e. nearly periodic, cf. Jędrysiak (2010), Jędrysiak and Michalak (2011), Kaźmierczak and Jędrysiak (2010, 2011, 2013). Hence, the plate bands are called thin functionally graded plate bands, cf. Jędrysiak (2010). The plate material properties are assumed to be independent of the x_2-coordinate. The size of microstructure is determined by length l of "the cell", being very small compared to the plate span L. A fragment of the plate band is shown in Fig. 1.

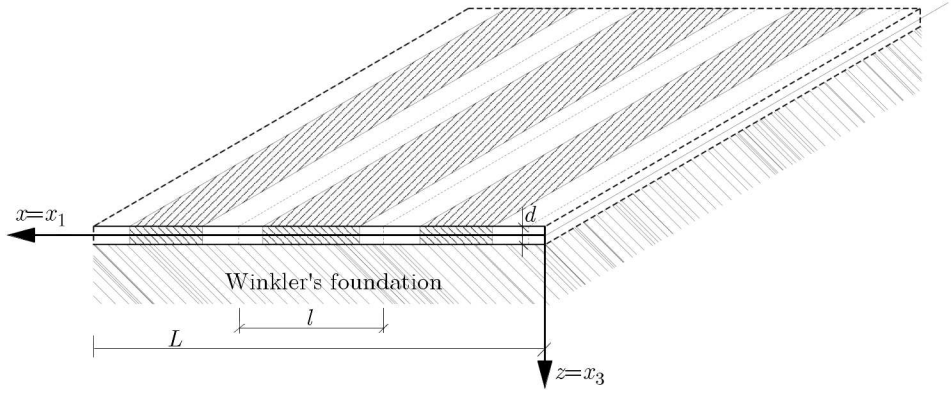

Fig. 1. A fragment of a thin functionally graded plate band interacting with Winkler's foundation

Vibrations of such plates are described by a partial differential equation with highly oscillating, tolerance-periodic, non-continuous coefficients. Because analysis of these plates is too complicated using the equation of the plate theory, different averaged models have been proposed. These models are usually described by partial differential equations with smooth, slowly-varying coefficients.

Functionally graded structures can be described by approaches applied to analyse macroscopically homogeneous media, e.g. periodic, cf. Suresh and Mortensen (1998). Between these models it can be mentioned those based on the asymptotic homogenization method for periodic solids, cf. Bensoussan *et al.* (1978). Models of such kind for periodic plates can be found in a series of papers, e.g. Kohn and Vogelius (1984). Other models are based on the microlocal parameters approach, cf. Matysiak and Nagórko (1989), or the nonstandard homogenization, cf. Nagórko (1998). However, the effect of the microstructure size on the dynamic plate behaviour is neglected in the governing equations of those models. Composite plates can be also parts of more complicated structures such as thin-walled composite columns or beams, cf. Kołakowski (2009, 2012), Królak *et al.* (2009), Kubiak (2006). Moreover, nonhomogeneous Winkler's type solids can be approximations of foam cores in three layered composite plates, cf. Magnucka-Blandzi (2011). Theoretical and numerical results of different problems of functionally graded structures are presented in many papers. Jha *et al.* (2013) analysed free vibrations of functionally graded thick plates with shear and normal deformations effects. The static response of functionally graded plates and shells was investigated using higher order deformation theories by Oktem *et al.* (2012). Vibrations of FG-type plates were analysed using a collocation method with higher-order plate theories by Roque *et al.* (2007). Free vibrations of shells were presented by Tornabene *et al.* (2011). Problems of functionally graded plates resting on a foundation were also considered, e.g. by Tahouneh and Naei (2014) with using the three-dimensional elasticity theory by Yajuvindra Kumar and Lal (2012), where vibrations of nonhomogeneous plates with varying thickness interacting with a foundation were analysed. A list of papers of various theoretical and numerical results of thermomechanical problems of functionally graded structures can be found in Jędrysiak (2010), Woźniak *et al.* (2008, 2010). Unfotunately, the effect of the microstructure size is usually neglected in the governing equations of those models.

This effect can be taken into account in the governing equations in the framework of the tolerance modelling, cf. Woźniak and Wierzbicki (2000), Woźniak *et al.* (2008, 2010). Various thermomechanical problems of periodic structures were investigated in a series of papers applying this method, e.g. dynamics of periodic plane structures by Wierzbicki and Woźniak (2000), vibrations of medium-thickness plates by Baron (2006), static problems of thin plates with moderately large deflections by Domagalski and Jędrysiak (2012), nonlinear vibrations of beams by Domagalski and Jędrysiak (2014), vibrations of thin plates resting on an elastic nonhomogeneous foundation by Jędrysiak (1999, 2003), vibrations of medium-thickness plates resting on an elastic foundation by Jędrysiak and Paś (2005, 2014), vibrations with damping of plate strips with a periodic system of concentrated masses by Marczak and Jędrysiak (2014), vibrations of wavy-type plates by Michalak (2002), vibrations of thin plates with stiffeners by Nagórko and Woźniak (2002), vibrations of thin cylindrical shells by Tomczyk (2007, 2013). These papers show that the effect of the microstructure size plays a crucial role in nonstationary (and some stationary) problems of periodic structures.

The tolerance modelling method is also applied to similar thermomechanical problems of functionally graded structures, e.g. Jędrysiak (2010), Woźniak *et al.* (2010). Some applications to dynamic and stability problems for thin transversally graded plates with the microstructure size bigger than the plate thickness were shown by Jędrysiak and Michalak (2011), Kaźmierczak and Jędrysiak (2010, 2011, 2013, 2014); for thin functionally graded plates with the microstructure size of an order of the plate thickness by Jędrysiak (2013, 2014), Jędrysiak and Pazera (2014); for functionally graded skeletonal shells by Michalak (2012); for heat conduction in functionally

graded hollow cylinders by Ostrowski and Michalak (2011); for thin longitudinally graded plates by Michalak and Wirowski (2012), Wirowski (2012). An extended list of papers can be found in the books by Woźniak *et al.* (2008, 2010).

The main aims of this paper are four. The first of them is to formulate the tolerance and the asymptotic models of vibrations for thin transversally graded plate bands. The second aim is to apply these models to calculate free vibration frequencies of a simply supported plate band interacting with Winkler's foundation using the Ritz method. The third is to analyse the effect of various distribution functions of material properties and the effect of the foundation on the frequencies. The fourth aim is to show the effect of differences in the cell between material properties (Young's modulus and mass densities) on the frequencies.

2. Formulation of the problem

Considerations are assumed to be independent of the x_2-coordinate. Let us denote $x = x_1$, $z = x_3$, $x \in [0, L]$, $z \in [-d/2, d/2]$, with d as a constant plate thickness. The plate band is described in the interval $\Lambda = (0, L)$, with "the basic cell" $\Delta \equiv [-l/2, l/2]$ in the interval $\overline{\Lambda}$, where l is the length of the basic cell, satisfying conditions: $d \ll l \ll L$. By $\Delta(x) \equiv (x - l/2, x + l/2)$ a cell with the centre at $x \in \Lambda$ is denoted. It is assumed that the plate band is made of two elastic isotropic materials, perfectly bonded across interfaces. The materials are characterised by Young's moduli E', E'', Poisson's ratios ν', ν'' and mass densities ρ', ρ''. Similarly, the elastic foundation is made of two various materials characterised by Winkler's coefficients k', k''. Let $E(x)$, $\Delta(x)$, $k(x)$, $x \in \Lambda$, be tolerance-periodic, highly-oscillating functions in x, but Poisson's ratio $\nu \equiv \nu' = \nu''$ constant. Assuming $E' \neq E''$ and/or $\rho' \neq \rho''$, the plate material structure can be treated as functionally graded in the x-axis direction. Similarly, for $k' \neq k''$, the foundation structure is functionally graded. Let ∂ denote the derivative with respect to x, and $w(x, t)$ ($x \in \overline{\Lambda}$, $t \in (t_0, t_1)$) be deflection of the plate band.

Tolerance-periodic functions in x describe the plate band properties – the mass density per unit area of the midplane μ, the rotational inertia ϑ and the bending stiffness B

$$\mu(x) \equiv d\rho(x) \qquad \vartheta(x) \equiv \frac{d^3}{12}\rho(x) \qquad B(x) \equiv \frac{d^3}{12(1-\nu^2)}E(x) \tag{2.1}$$

respectively. Free vibrations of thin functionally graded plate bands, on the well known Kirchhoff plate theory assumptions, can be described by the partial differential equation of the fourth order with respect to the deflection w

$$\partial\partial[B\partial\partial w] + \mu\ddot{w} - \partial(\vartheta\partial\ddot{w}) + kw = 0 \tag{2.2}$$

with highly-oscillating, non-continuous, tolerance-periodic coefficients.

3. Foundations of the modelling

3.1. Introductory concepts

Following the book edited by Woźniak *et al.* (2010) and the book by Jędrysiak (2010), some introductory concepts of the tolerance modelling are used, i.e. the averaging operator, tolerance system, slowly-varying function $SV^{\alpha}_{\xi}(\Lambda, \Delta)$, tolerance-periodic function $TP^{\alpha}_{\xi}(\Lambda, \Delta)$, highly oscillating function $HO^{\alpha}_{\xi}(\Lambda, \Delta)$, fluctuation shape function $FS^{2}_{\xi}(\Lambda, \Delta)$, where ξ is the tolerance parameter and α is a positive constant determining kind of the function. Some of these concepts are reminded below.

A cell at $x \in \Lambda_\Delta$ is denoted by $\Delta(x) = x + \Delta$, $\Lambda_\Delta = \{x \in \Delta : \Delta(x) \subset \Lambda\}$. The basic concept of the modelling technique is the averaging operator, for an integrable function f defined by

$$\langle f\rangle(x) = \frac{1}{l}\int\limits_{\Delta(x)} f(y)\,dy \qquad x \in \Lambda_\Delta \qquad y \in \Delta(x) \tag{3.1}$$

If f is a function tolerance-periodic in x, its averaged value by (3.1) is slowly-varying in x.

Let $h(\cdot)$ be a highly oscillating function defined on $\overline{\Lambda}$, $h \in HO^2_\xi(\Lambda, \Delta)$, continuous together with the gradient $\partial^1 h$ and with a piecewise continuous and bounded gradient $\partial^2 h$. The function $h(\cdot)$ is the fluctuation shape function of the 2-nd kind, $FS^2_\xi(\Lambda, \Delta)$, if it depends on l as a parameter and the condition $\langle \mu h\rangle(x) \approx 0$ holds for every $x \in \Lambda_\Delta$, where $\mu > 0$ is a certain tolerance-periodic function, l is the microstructure parameter.

3.2. Fundamental assumptions

Following the books by Woźniak *et al.* (2010), Jędrysiak (2010) and applying the introductory concepts, the following fundamental modelling assumptions can be formulated.

The micro-macro decomposition is the first assumption, in which the deflection w appears in the form

$$w(x,t) = W(x,t) + h^A(x)V^A(x,t) \qquad A = 1,\dots,N \qquad x \in \Lambda \tag{3.2}$$

with $W(\cdot,t)$, $V^A(\cdot,t) \in SV^2_\xi(\Lambda, \Delta)$ (for every t) as basic kinematic unknowns (W is called the macrodeflection; V^A are called the fluctuation amplitudes) and $h^A(\cdot) \in FS^2_\xi(\Lambda, \Delta)$ as the known fluctuation shape functions.

In the tolerance averaging approximation, being the second modelling assumption, the terms of an order of $O(\xi)$ are treated as negligibly small in the course of modelling.

4. The tolerance modelling procedure

The modelling procedure of the tolerance averaging technique was shown by Woźniak *et al.* (2010) and for thin functionally graded plates by Jędrysiak (2010). Below, it is outlined.

The formulation of the action functional is the first step

$$\mathcal{A}(w(\cdot)) = \int\limits_\Lambda \int\limits_{t_0}^{t_1} \mathcal{L}(y, \partial\partial w(y,t), \partial\dot{w}(y,t), \dot{w}(y,t), w(y,t))\,dt\,dy \tag{4.1}$$

where the lagrangean $\mathcal{L}$ is given by

$$\mathcal{L} = \frac{1}{2}(\mu\dot{w}\dot{w} + \vartheta\partial\dot{w}\partial\dot{w} - B\partial\partial w\partial\partial w - kww) \tag{4.2}$$

From the principle of stationary action to functional (4.1) combined with (4.2), after some manipulations, known equation (2.2) of free vibrations for thin functionally graded plate bands interacting with Winkler's foundation is derived.

The next step of the tolerance modelling is substituting micro-macro decomposition (3.2) into lagrangean (4.2). Applying averaging operator (3.1) and the tolerance averaging approximation, the tolerance averaged form $\langle\mathcal{L}_h\rangle$ of lagrangean (4.2) is obtained in the third step

$$\begin{aligned}\langle\mathcal{L}_h\rangle = -\frac{1}{2}\{&(\langle B\rangle\partial\partial W + 2\langle B\partial\partial h^B\rangle V^B)\partial\partial W + \langle k\rangle WW + 2W\langle kh^B\rangle V^B + \langle\vartheta\rangle\partial\dot{W}\partial\dot{W}\\ &+ (\langle kh^Ah^B\rangle + \langle B\partial\partial h^A\partial\partial h^B\rangle)V^AV^B - \langle\mu\rangle\dot{W}\dot{W} + (\langle\vartheta\partial h^A\partial h^B\rangle - \langle\mu h^Ah^B\rangle)\dot{V}^A\dot{V}^B\}\end{aligned} \tag{4.3}$$

where the macrodeflection W and the fluctuation amplitudes V^A, $A = 1, \ldots, N$, are new basic kinematic unknowns. The known fluctuation shape functions V^A are introduced in micro-macro decomposition (3.2).

Using the principle of stationary action to the averaged functional $\mathcal{A}_h$ combined together with lagrangean (4.3), the system of governing equations is derived.

5. Model equations

From the principle of stationary action applied to the averaged functional $\mathcal{A}_h$ with lagrangean (4.3), after some manipulations, the following system of equations for W and V^A is obtained

$$\begin{aligned} &\partial\partial(\langle B\rangle\partial\partial W + \langle B\partial\partial h^B\rangle V^B) + \langle k\rangle W + \underline{\langle kh^A\rangle} V^A + \langle\mu\rangle\ddot{W} - \langle\vartheta\rangle\partial\partial\ddot{W} = 0 \\ &\langle B\partial\partial h^A\rangle\partial\partial W + \underline{\langle kh^A\rangle} W = -(\langle B\partial\partial h^A\partial\partial h^B\rangle + \underline{\langle kh^A h^B\rangle})V^B \\ &\quad - (\underline{\langle\mu h^A h^B\rangle} + \underline{\langle\vartheta\partial h^A\partial h^B\rangle})\ddot{V}^B \end{aligned} \tag{5.1}$$

The above equations are a system of $N+1$ differential equations constituting the tolerance model of thin functionally graded plate bands. The underlined terms in these equations depend on the microstructure parameter l. Hence, this model allows one to take into account the effect of the microstructure size on free vibrations of these plates. The coefficients of equations (5.1) are slowly-varying functions in x. It can be observed that boundary conditions for these plate bands (in $\Lambda = (0, L)$) are formulated only for the macrodeflection W (on edges $x = 0, L$) but not for the fluctuation amplitudes V^A, $A = 1, \ldots, N$.

It can be observed that after neglecting terms with the parameter l in equations $(5.1)_2$, the algebraic equations for fluctuation amplitudes V^A are obtained

$$V^A = -(\langle B\partial\partial h^A\partial\partial h^B\rangle)^{-1}\langle B\partial\partial h^B\rangle\partial\partial W \tag{5.2}$$

Substituting formula (5.2) into $(5.1)_1$, the following equation for W is derived

$$\partial\partial\Big((\langle B\rangle - \langle B\partial\partial h^A\rangle(\langle B\partial\partial h^A\partial\partial h^B\rangle)^{-1}\langle B\partial\partial h^B\rangle)\partial\partial W\Big) + \langle k\rangle W + \langle\mu\rangle\ddot{W} = 0 \tag{5.3}$$

The above equation together with micro-macro decomposition (3.2) represents the asymptotic model of thin functionally graded plate bands. Governing equation (15) with equations (5.2) of this model can be obtained using also the formal asymptotic modelling procedure, cf. Woźniak *et al.* (2010), Kaźmierczak and Jędrysiak (2011, 2013). It can be observed that this procedure leads to model equations without terms describing the effect of the microstructure size on free vibrations of these plates. Hence, in the framework of the asymptotic model, the macrobehaviour of these plate bands can be only investigated.

6. Example: free vibrations of plate bands

6.1. Introduction

Free vibrations of a simply supported thin plate band with span L along the x-axis interacting with Winkler's foundation are considered. The properties of the plate band are

$$\rho(\cdot, z), E(\cdot, z) = \begin{cases} \rho', E' & \text{for} \quad z \in \big((1-\gamma(x))l/2, (1+\gamma(x))l/2\big) \\ \rho'', E'' & \text{for} \quad z \in [0, (1-\gamma(x))l/2] \cup [(1+\gamma(x))l/2, l] \end{cases} \tag{6.1}$$

with a distribution function of material properties $\gamma(x)$, see Fig. 2. Moreover, it is assumed that the foundation is homogeneous with the Winkler's coefficient $k = \text{const}$.

Our considerations are restricted only to one fluctuation shape function, i.e. $A = N = 1$. Denote $h \equiv h^1$, $V \equiv V^1$. Hence, micro-macro decomposition (3.2) of the deflection $w(x,t)$ has the form

$$w(x,t) = W(x,t) + h(x)V(x,t)$$

where $W(\cdot,t), V(\cdot,t) \in SV_\xi^2(\Lambda,\Delta)$ for every $t \in (t_0,t_1)$, $h(\cdot) \in FS_\xi^2(\Lambda,\Delta)$.

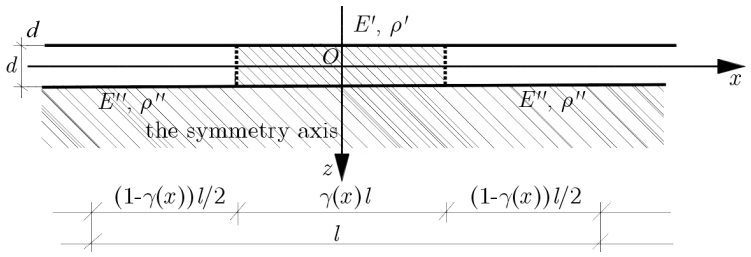

Fig. 2. "Basic cell" of the functionally graded plate band interacting with Winkler's foundation

The cell structure is shown in Fig. 2. Thus, the periodic approximation of the fluctuation shape function $h(x)$ has the form

$$\widetilde{h}(x,z) = \Lambda^2[\cos(2\pi z/l) + c(x)] \qquad z \in \Delta(x) \qquad x \in \Lambda$$

where the parameter $c(x)$ is a slowly-varying function in x and is determined by $\langle \widetilde{\mu}\widetilde{h} \rangle = 0$

$$c = c(x) = \{\sin[\pi\widetilde{\gamma}(x)](\rho' - \rho'')\}\Big\{\pi\{\rho'\widetilde{\gamma}(x) + \rho''[1 - \widetilde{\gamma}(x)]\}\Big\}^{-1}$$

where $\widetilde{\gamma}(x)$ is the periodic approximation of the distribution function of the material properties $\gamma(x)$. The parameter $c(x)$ is treated as constant in the calculations of derivatives $\partial\widetilde{h}$, $\partial\partial\widetilde{h}$.

Under denotations:

$$\begin{aligned}
&\breve{B} = \langle B \rangle && \widehat{B} = \langle B\partial\partial h \rangle && \overline{B} = \langle B\partial\partial h\partial\partial h \rangle && \breve{K} = \langle k \rangle \\
&\widetilde{K} = l^{-2}\langle kh \rangle && \overline{K} = l^{-4}\langle khh \rangle && \breve{\mu} = \langle \mu \rangle && \overline{\mu} = l^{-4}\langle \mu hh \rangle \\
&\breve{\vartheta} = \langle \vartheta \rangle && \overline{\vartheta} = l^{-2}\langle \vartheta\partial h\partial h \rangle
\end{aligned} \tag{6.2}$$

tolerance model equations (5.1) can be written as

$$\begin{aligned}
&\partial\partial(\breve{B}\partial\partial W + \widehat{B}V) + \breve{K}W + l^2\widetilde{K}V + \breve{\mu}\ddot{W} - \breve{\vartheta}\partial\partial\ddot{W} = 0 \\
&\widehat{B}\partial\partial W + l^2\widetilde{K}W + (\overline{B} + l^4\overline{K})V + l^2(l^2\overline{\mu} + \overline{\vartheta})\ddot{V} = 0
\end{aligned} \tag{6.3}$$

however, plate band equation (5.3) has the form

$$\partial\partial[(\breve{B} - \widehat{B}^2/\overline{B})\partial\partial W] + \breve{K}W + \breve{\mu}\ddot{W} - \breve{\vartheta}\partial\partial\ddot{W} = 0 \tag{6.4}$$

Equation (6.4) describes free vibrations of this plate band within the asymptotic model. All coefficients of model equations (6.3) and (6.4) are slowly-varying functions in x.

6.2. The Ritz method applied to the model equations

Equations (6.3) or (6.4) have slowly-varying functional coefficients. Analytical solutions to them are too difficult to find. Hence, approximate formulas fo free vibrations frequencies can be derived using the known Ritz method, cf. Kaźmierczak and Jędrysiak (2010). In order to obtain these formulas, relations of the maximum strain energy $\mathcal{A}_{max}$ and the maximal kinetic energy $\mathcal{V}_{max}$ have to be determined.

Solutions to equation (6.4) and equations (6.3) are assumed in form satisfying the boundary conditions for the simply supported plate band

$$W(x,t) = A_W \sin(\alpha x)\cos(\omega t) \qquad V(x,t) = A_V \sin(\alpha x)\cos(\omega t) \tag{6.5}$$

where α is the wave number, ω is the free vibrations frequency. Introducing denotations

$$\begin{aligned}
\breve{B} &= \frac{d^3}{12(1-\nu^2)} \int_0^L \{E''[1-\widetilde{\gamma}(x)] + \widetilde{\gamma}(x)E'\}[\sin(\alpha x)]^2\, dx \\
\widehat{B} &= \frac{\pi d^3}{3(1-\nu^2)}(E'-E'') \int_0^L \sin(\pi\widetilde{\gamma}(x))[\sin(\alpha x)]^2\, dx \\
\overline{B} &= \frac{(\pi d)^3}{3(1-\nu^2)} \int_0^L \{(E'-E'')[2\pi\widetilde{\gamma}(x) + \sin(2\pi\widetilde{\gamma}(x))] + 2\pi E''\}[\sin(\alpha x)]^2\, dx \\
\breve{\mu} &= d\int_0^L \{[1-\widetilde{\gamma}(x)]\rho'' + \widetilde{\gamma}(x)\rho'\}[\sin(\alpha x)]^2\, dx \\
\breve{\vartheta} &= \frac{d^3}{12}\int_0^L \{[1-\widetilde{\gamma}(x)]\rho'' + \widetilde{\gamma}(x)\rho'\}[\cos(\alpha x)]^2\, dx \\
\overline{\mu} &= \frac{d}{4\pi}\int_0^L \{(\rho'-\rho'')[2\pi\widetilde{\gamma}(x) + \sin(2\pi\widetilde{\gamma}(x))] + 2\pi\rho''\}[\sin(\alpha x)]^2\, dx \\
&\quad + \frac{d}{\pi}(\rho'-\rho'')\int_0^L c(x)[\pi c(x)\widetilde{\gamma}(x) - 2\sin(\pi\widetilde{\gamma}(x))][\sin(\alpha x)]^2\, dx \\
&\quad + d\rho''\int_0^L [c(x)]^2[\sin(\alpha x)]^2\, dx \\
\overline{\vartheta} &= \frac{\pi d^3}{12}\int_0^L \{(\rho'-\rho'')[2\pi\widetilde{\gamma}(x) - \sin(2\pi\widetilde{\gamma}(x))] + 2\pi\rho''\}[\sin(\alpha x)]^2\, dx \\
\breve{K} &= k\int_0^L [\sin(\alpha x)]^2\, dx \\
\widetilde{K} &= k\int_0^L c(x)[\sin(\alpha x)]^2\, dx = \frac{k(\rho'-\rho'')}{\pi}\int_0^L \frac{\sin(\pi\widetilde{\gamma}(x))}{\rho'\widetilde{\gamma}(x) + \rho''[1-\widetilde{\gamma}(x)]}[\sin(\alpha x)]^2\, dx \\
\overline{K} &= \frac{1}{2}k\int_0^L c(x)[\sin(\alpha x)]^2\, dx = \frac{k(\rho'-\rho'')}{2\pi}\int_0^L \frac{\sin[\pi\widetilde{\gamma}(x)]}{\rho'\widetilde{\gamma}(x) + \rho''[1-\widetilde{\gamma}(x)]}[\sin(\alpha x)]^2\, dx
\end{aligned} \tag{6.6}$$

and using (6.5), the formulas of the maximum energies – strain $\mathcal{E}_{max}$ and kinetic $\mathcal{V}_{max}$ – in the framework of the tolerance model, take the form

$$\begin{aligned}
\mathcal{E}_{max}^{TM} &= \frac{1}{2}[(\breve{B}A_W^2\alpha^2 - 2\widehat{B}A_W A_V)\alpha^2 + \breve{K}A_W^2 + 2l^2\widetilde{K}A_W A_V + (\overline{B} + l^4\overline{K})A_V^2] \\
\mathcal{V}_{max}^{TM} &= \frac{1}{2}[A_W^2(\breve{\mu} + \breve{\vartheta}\alpha^2) + A_V^2 l^2(l^2\overline{\mu} + \overline{\vartheta})]\omega^2
\end{aligned} \tag{6.7}$$

For the asymptotic model, they can be written as

$$\mathcal{E}^{AM}_{max} = \frac{1}{2}[(\breve{B}A_W^2\alpha^2 - 2\widehat{B}A_W A_V)\alpha^2 + \breve{K}A_W^2 + \overline{B}A_V^2] \qquad \mathcal{V}^{AM}_{max} = \frac{1}{2}A_W^2(\breve{\mu} + \breve{\vartheta}\alpha^2)\omega^2 \tag{6.8}$$

The conditions of the Ritz method take the form

$$\frac{\partial(\mathcal{E}_{max} - \mathcal{V}_{max})}{\partial A_W} = 0 \qquad \frac{\partial(\mathcal{E}_{max} - \mathcal{V}_{max})}{\partial A_V} = 0 \tag{6.9}$$

Using (6.9) to relations (6.7), after some manipulations, the following formulas are obtained

$$(\omega_{-,+})^2 \equiv \frac{l^2(l^2\overline{\mu} + \overline{\vartheta})(\alpha^4\breve{B} + \breve{K}) + (\breve{\mu} + \alpha^2\breve{\vartheta})(\overline{B} + l^4\overline{K})}{2(\breve{\mu} + \alpha^2\breve{\vartheta})l^2(l^2\overline{\mu} + \overline{\vartheta})} \tag{6.10}$$

$$\mp\frac{\sqrt{[l^2(l^2\overline{\mu} + \overline{\vartheta})(\alpha^4\breve{B} + \breve{K}) - (\breve{\mu} + \alpha^2\breve{\vartheta})(\overline{B} + l^4\overline{K})]^2 + 4(l^2\widetilde{K} - \alpha^2\widehat{B})^2 l^2(\breve{\mu} + \alpha^2\breve{\vartheta})(l^2\overline{\mu} + \overline{\vartheta})}}{2(\breve{\mu} + \alpha^2\breve{\vartheta})l^2(l^2\overline{\mu} + \overline{\vartheta})}$$

for the lower ω_- and the higher ω_+ free vibrations frequencies, respectively, in the framework of the tolerance model.

For asymptotic model conditions (6.9) applied to equations (6.8) lead, after some manipulations, to the following formula

$$\omega^2 \equiv [(\alpha^4\breve{B} + \breve{K})\overline{B} - \alpha^4\widehat{B}^2][(\breve{\mu} + \breve{\vartheta}\alpha^2)\overline{B}]^{-1} \tag{6.11}$$

of the lower free vibration frequency ω.

6.3. Results

Calculations are made for the following distribution functions of the material properties $\gamma(x)$

$$\begin{aligned} &\widetilde{\gamma}(x) = \sin^2\frac{\pi x}{L} \qquad \widetilde{\gamma}(x) = \cos^2\frac{\pi x}{L} \qquad \widetilde{\gamma}(x) = \Big(\frac{x}{L}\Big)^2 \\ &\widetilde{\gamma}(x) = \sin\frac{\pi x}{L} \qquad \widetilde{\gamma}(x) = \frac{1}{2} \end{aligned} \tag{6.12}$$

where formula $(6.12)_5$ determines an example of a periodic plate band.

Let us also introduce dimensionless frequency parameters for the free vibration frequencies ω and ω_-, ω_+ determined by equations (6.11) and (6.10), respectively

$$\begin{aligned} &\Omega^2 \equiv 12(1-\nu^2)(E')^{-1}l^2\omega^2 \qquad (\Omega_-)^2 \equiv 12(1-\nu^2)(E')^{-1}l^2(\omega_-)^2 \\ &(\Omega_+)^2 \equiv 12(1-\nu^2)(E')^{-1}l^2(\omega_+)^2 \end{aligned} \tag{6.13}$$

Moreover, a dimensionless parameter of the foundation is introduced

$$\kappa \equiv 12(1-\nu^2)(E')^{-1}kd$$

Results of calculations are shown in Figs. 3-6, where the results obtained by the tolerance or asymptotic models for plate bands with the simply supported edges are presented. Calculations are made for Poisson's ratio $\nu = 0.3$, wave number $\alpha = \pi/L$, ratio $l/L = 0.1$, ratios of plate thickness $d/l = 0.1$, 0.01 and ratios of the foundation $\kappa = 5 \cdot 10^{-5}$, 0.05. Figures 3 and 4 show plots of the lower frequency parameters versus both ratios $E''/E' - \rho''/\rho'$, but Figs. 5 and 6 present diagrams of the higher frequency parameters versus these both ratios. Plots in Figs. 3a, 4a, 5a, 6a are made for $\kappa = 5 \cdot 10^{-5}$, but in Figs. 3b, 4b, 5b, 6b for $\kappa = 0.05$. Moreover, in Figs. 3 and 4, a comparison of the lower frequency parameters versus both ratios $E''/E' - \rho''/\rho'$ calculated in the framework of the tolerance model (formulas $(6.13)_2$ and $(6.10)_1$) and of the asymptotic model (formulas $(6.13)_1$ and (6.11)) is presented. Plots shown in Figs. 3 and 5 are made for $d/l = 0.1$, but in Figs. 4 and 6 they are for $d/l = 0.01$.

From the results shown in Figs. 3-6 some remarks and comments are formulated.

1° The lower frequency parameters calculated by the asymptotic model, (6.11), and the tolerance model, $(6.10)_1$, depend on the plate thickness ratio d/l and the parameter of foundation κ, see Figs. 3 and 4:

- The lower frequency parameters calculated by the asymptotic model, (6.11), and the tolerance model, $(6.10)_1$, are nearly identical for thicker plates, e.g. $d/l = 0.1$, and weaker foundations, e.g. $\kappa = 5 \cdot 10^{-5}$, see Fig. 3a.
- However, higher values of these parameters are found from the tolerance model for smaller thickness of plates, $d/l < 0.1$, and for stronger foundations, $\kappa > 5 \cdot 10^{-5}$, see Figs. 3b and 4.
- Differences between these frequency parameters depend on the plate thickness ratio d/l and the parameter of foundation κ. They increase with a decrease in the plate thickness, $d/l > 0$, and an increase in the stiffness of foundation, $\kappa > 5 \cdot 10^{-5}$, e.g. $d/l = 0.01$, $\kappa = 0.05$, see Fig. 3b.

2° The effect of distribution functions of the material properties $\gamma(x)$ on the lower frequency parameters for various ratios $E''/E' \in [0,1]$, $\rho''/\rho' \in [0,1]$ for the simply supported plate band can be observed in Figs. 3 and 4:

- The highest values of these frequency parameters are obtained for all pairs of ratios $(E''/E', \rho''/\rho')$ from the above intervals of the function $\gamma(x)$ by $(6.12)_2$ and for smaller thickness of the plates, $d/l < 0.1$, or for stronger foundations, cf. $\kappa > 5 \cdot 10^{-5}$, see Figs. 3b and 4.
- The highest values of these frequency parameters for thicker plates, e.g. $d/l = 0.1$, or for weaker foundations, e.g. $\kappa = 5 \cdot 10^{-5}$, see Fig. 3a, are obtained:
  - for $\gamma(x)$ by $(6.12)_2$ and for pairs of ratios $(E''/E', \rho''/\rho')$ such that $E''/E' > (E''/E')_0 > 0$, $\rho''/\rho' < (\rho''/\rho')_0((E''/E')_0) > 0$, where $(\rho''/\rho')_0$ depends on $(E''/E')_0$,
  - for $\gamma(x)$ by $(6.12)_4$ and for pairs of ratios $(E''/E', \rho''/\rho')$ such that $E''/E' < (E''/E')_0 > 0$, $\rho''/\rho' > (\rho''/\rho')_0((E''/E')_0) > 0$, where $(\rho''/\rho')_0$ depends on $(E''/E')_0$ (unfortunately, it is not visible in this form of these diagrams)

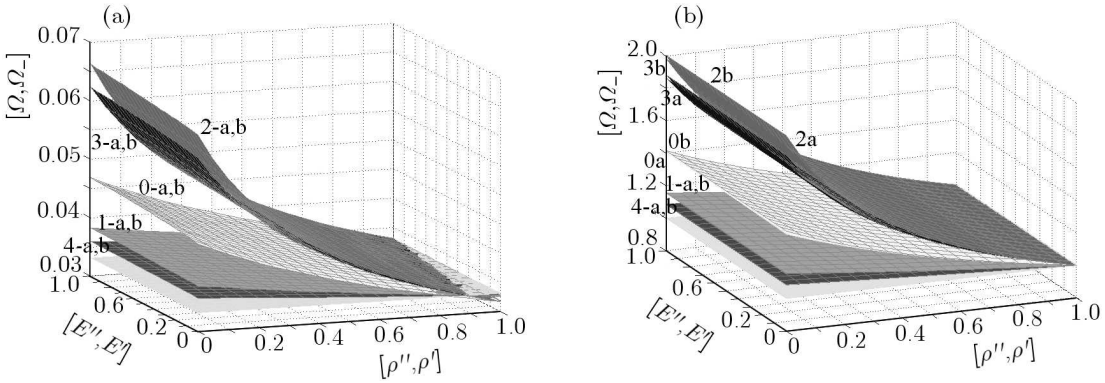

Fig. 3. Plots of the dimensionless frequency parameters Ω and Ω_- of lower free vibration frequencies versus ratios $E''/E' - \rho''/\rho'$ by the asymptotic model (surfaces a), the tolerance model (surfaces b), made for: (a) $d/l = 0.1$, $\kappa = 5 \cdot 10^{-5}$; (b) $d/l = 0.1$, $\kappa = 0.05$ ($1 - \gamma$ by $(6.12)_1$; $2 - \gamma$ by $(6.12)_2$; $3 - \gamma$ by $(6.12)_3$; $4 - \gamma$ by $(6.12)_4$; $0 - \gamma$ by $(6.12)_5$; the grey plane is related to the frequency parameter for the homogeneous plate band, i.e. $E''/E' = \rho''/\rho' = 1$)

- The smallest values of these frequency parameters are obtained for all pairs of ratios $(E''/E', \rho''/\rho')$ from the above intervals of the function $\gamma(x)$ by $(6.12)_4$ and for smaller thickness of the plates, $d/l < 0.1$, or for stronger foundations, cf. $\kappa > 5 \cdot 10^{-5}$, see Figs. 3b and 4.

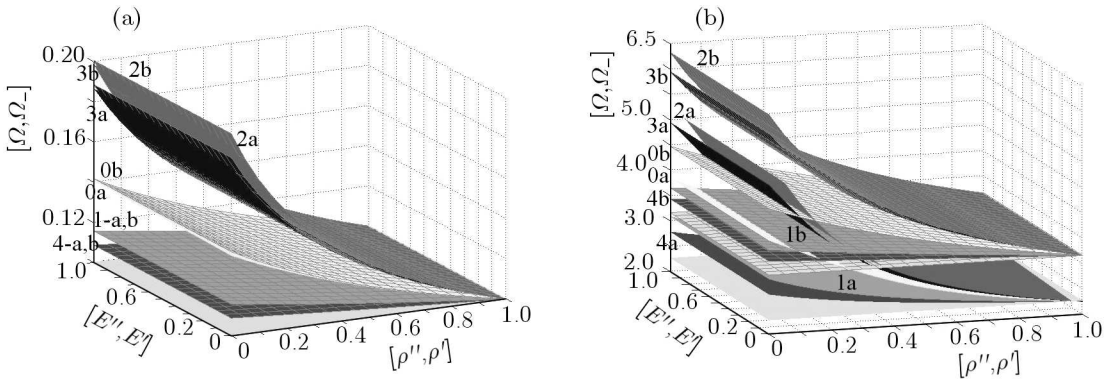

Fig. 4. Plots of the dimensionless frequency parameters Ω and Ω_- of lower free vibration frequencies versus ratios $E''/E' - \rho''/\rho'$ by the asymptotic model (surfaces a), the tolerance model (surfaces b), made for: (a) $d/l = 0.01$, $\kappa = 5 \cdot 10^{-5}$; (b) $d/l = 0.01$, $\kappa = 0.05$ ($1 - \gamma$ by $(6.12)_1$; $2 - \gamma$ by $(6.12)_2$; $3 - \gamma$ by $(6.12)_3$; $4 - \gamma$ by $(6.12)_4$; $0 - \gamma$ by $(6.12)_5$; the grey plane is related to the frequency parameter for the homogeneous plate band, i.e. $E''/E' = \rho''/\rho' = 1$)

- The smallest values of these frequency parameters for thicker plates, e.g. $d/l = 0.1$, or for weaker foundations, e.g. $\kappa = 5 \cdot 10^{-5}$, see Fig. 3a, are obtained:
  - for $\gamma(x)$ by $(6.12)_4$ and for pairs of ratios $(E''/E', \rho''/\rho')$ such that $E''/E' > (E''/E')_1 > 0$, $\rho''/\rho' < (\rho''/\rho')_1((E''/E')_1) > 0$, where $(\rho''/\rho')_1$ depends on $(E''/E')_1$,
  - for $\gamma(x)$ by $(6.12)_2$ and for pairs of ratios $(E''/E', \rho''/\rho')$, such that $E''/E' > (E''/E')_2 > 0$, $\rho''/\rho' > (\rho''/\rho')_2((E''/E')_2) > 0$, where $(\rho''/\rho')_2$ depends on $(E''/E')_2$ (unfortunately, it is not visible in this form of diagrams),
  - for $\gamma(x)$ by $(6.12)_3$ and for pairs of ratios $(E''/E', \rho''/\rho')$, such that $(E''/E')_2 > E''/E' < (E''/E')_3 > 0$, $(\rho''/\rho')_2((E''/E')_2) > \rho''/\rho' > (\rho''/\rho')_3((E''/E')_3) > 0$, where $(\rho''/\rho')_2$, $(\rho''/\rho')_3$ depend on $(E''/E')_2$, $(E''/E')_3$, respectively (not visible in this form of diagrams),
  - for $\gamma(x)$ by $(6.12)_5$ (periodic plate band) and for pairs of ratios $(E''/E', \rho''/\rho')$, such that $(E''/E')_1 > E''/E' > (E''/E')_3 > 0$, $(\rho''/\rho')_1((E''/E')_1) < \rho''/\rho' < (\rho''/\rho')_3((E''/E')_3) > 0$, where $(\rho''/\rho')_1$, $(\rho''/\rho')_3$ depend on $(E''/E')_1$, $(E''/E')_3$, respectively (not visible in this form of diagrams).

3° Figure 3 shows also an interesting feature that for the distribution functions of the material properties $\gamma(x)$ used and for rather thicker plates, e.g. $d/l = 0.1$, and weaker foundations, e.g. $\kappa = 5 \cdot 10^{-5}$, the lower frequency parameters are higher or smaller than this parameter for the homogeneous plate band made of a stronger material, i.e. $\rho''/\rho' = E''/E' = 1$ (the grey plane in Fig. 3a).

4° The effect of distribution functions of the material properties $\gamma(x)$ on higher frequency parameters for various ratios $E''/E' \in [0, 1]$, $\rho''/\rho' \in [0, 1]$ for the simply supported plate band can be observed in Figs. 5 and 6:

- The highest values of these frequency parameters for rather very thin plates, e.g. d/l=0.01, and for stronger foundations, e.g. $\kappa = 0.05$, see Fig. 6a, are obtained:
  - for $\gamma(x)$ by $(6.12)_3$ and for pairs of ratios $(E''/E', \rho''/\rho')$ such that $E''/E' > (E''/E')_0 > 0$, $\rho''/\rho' < (\rho''/\rho')_0((E''/E')_0) > 0$, where $(\rho''/\rho')_0$ depends on $(E''/E')_0$,
  - for $\gamma(x)$ by $(6.12)_2$ and for pairs of ratios $(E''/E', \rho''/\rho')$ such that $E''/E' < (E''/E')_0 > 0$, $\rho''/\rho' > (\rho''/\rho')_0((E''/E')_0) > 0$, where $(\rho''/\rho')_0$ depends on $(E''/E')_0$.

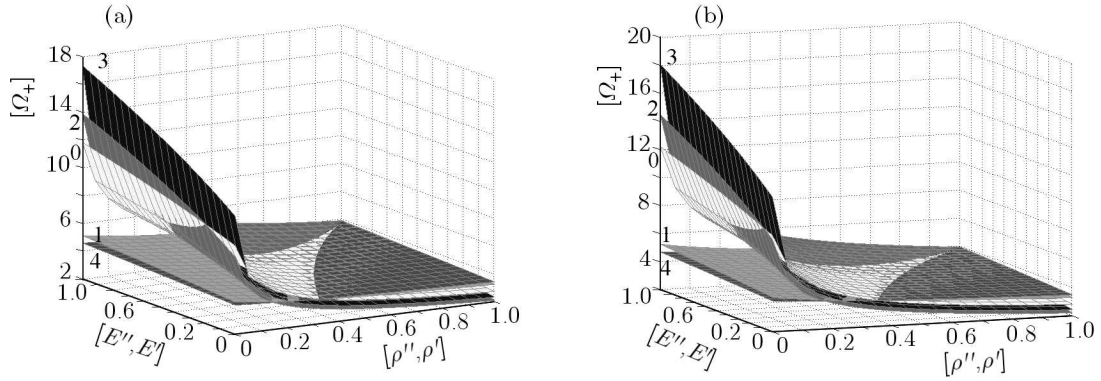

Fig. 5. Plots of the dimensionless frequency parameters Ω_+ of higher free vibration frequencies versus ratios $E''/E' - \rho''/\rho'$, made for: (a) $d/l = 0.1$, $\kappa = 5 \cdot 10^{-5}$; (b) $d/l = 0.1$, $\kappa = 0.05$ ($1-\gamma$ by $(6.12)_1$; $2-\gamma$ by $(6.12)_2$; $3-\gamma$ by $(6.12)_3$; $4-\gamma$ by $(6.12)_4$; $0-\gamma$ by $(6.12)_5$)

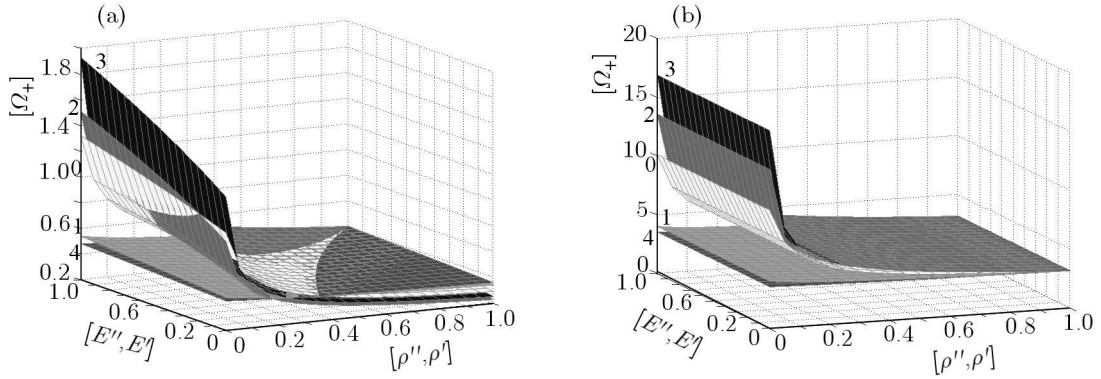

Fig. 6. Plots of the dimensionless frequency parameters Ω_+ of higher free vibration frequencies versus ratios $E''/E' - \rho''/\rho'$, made for: (a) $d/l = 0.01$, $\kappa = 5 \cdot 10^{-5}$; (b) $d/l = 0.01$, $\kappa = 0.05$ ($1-\gamma$ by $(6.12)_1$; $2-\gamma$ by $(6.12)_2$; $3-\gamma$ by $(6.12)_3$; $4-\gamma$ by $(6.12)_4$; $0-\gamma$ by $(6.12)_5$)

- The highest values of these frequency parameters for thicker plates, e.g. $d/l > 0.01$, and for weaker foundations, e.g. $\kappa \leqslant 0.05$, see Figs. 5 and 6a, are obtained:
  - for $\gamma(x)$ by $(6.12)_4$ and for pairs of ratios $(E''/E', \rho''/\rho')$ such that $E''/E' < (E''/E')_0 > 0$, $\rho''/\rho' > (\rho''/\rho')_0((E''/E')_0) > 0$, where $(\rho''/\rho')_0$ depends on $(E''/E')_0$,
  - for $\gamma(x)$ by $(6.12)_5$ (periodic plate band) and for pairs of ratios $(E''/E', \rho''/\rho')$ such that $(E''/E')_1 > E''/E' > (E''/E')_0 > 0$, $(\rho''/\rho')_1((E''/E')_1) < \rho''/\rho' < (\rho''/\rho')_0((E''/E')_0) > 0$, where $(\rho''/\rho')_0$, $(\rho''/\rho')_1$ depend on $(E''/E')_0$, $(E''/E')_1$, respectively,
  - for $\gamma(x)$ by $(6.12)_2$ and for pairs of ratios $(E''/E', \rho''/\rho')$ such that $E''/E' > (E''/E')_1 > 0$, $(\rho''/\rho')_2((E''/E')_2) < \rho''/\rho' < (\rho''/\rho')_1((E''/E')_1) > 0$, where $(\rho''/\rho')_1$, $(\rho''/\rho')_2$ depend on $(E''/E')_1$, $(E''/E')_2$, respectively,
  - for $\gamma(x)$ by $(6.12)_3$ and for pairs of ratios $(E''/E', \rho''/\rho')$ such that $(E''/E')_2 > E''/E' > (E''/E')_1 > 0$, $(\rho''/\rho')_2((E''/E')_2) > \rho''/\rho' < (\rho''/\rho')_1((E''/E')_1) > 0$, where $(\rho''/\rho')_1$, $(\rho''/\rho')_2$ depend on $(E''/E')_1$, $(E''/E')_2$, respectively.
- The smallest values of the higher frequency parameters for rather very thin plates, e.g. $d/l = 0.01$, and for stronger foundations, e.g. $\kappa = 0.05$, see Fig. 6b, are obtained for $\gamma(x)$ by $(6.12)_4$ and for all pairs of ratios $(E''/E', \rho''/\rho')$.
- The smallest values of these frequency parameters for thicker plates, e.g. $d/l > 0.01$, and for weaker foundations, e.g. $\kappa \leqslant 0.05$, see Figs. 5 and 6a, are obtained:

– for $\gamma(x)$ by $(6.12)_3$ and for all pairs of ratios $(E''/E', \rho''/\rho')$ such that $E''/E' > (E''/E')_3 > 0$, $\rho''/\rho' < (\rho''/\rho')_3((E''/E')_3) > 0$, where $(\rho''/\rho')_3$ depends on $(E''/E')_3$,
– for $\gamma(x)$ by $(6.12)_2$ and for pairs of ratios $(E''/E', \rho''/\rho')$ such that $E''/E' < (E''/E')_3 > 0$, $\rho''/\rho' > (\rho''/\rho')_3((E''/E')_3) > 0$, where $(\rho''/\rho')_3$ depends on $(E''/E')_3$.

7. Remarks

Using the tolerance modelling to the known differential equation of thin plates resting on Winkler's foundation, the averaged tolerance model equations of functionally graded plate bands are obtained. From the differential equation with non-continuous, tolerance-periodic coefficients, a system of differential equations with slowly-varying coefficients is derived. It should be noted that the tolerance model equations have terms dependent on the microstructure parameter l, and describe the effect of the microstructure size on the behaviour of these plates. However, the asymptotic model equation neglects this effect.

Free vibration frequencies of the simply supported plate band have been analysed in the example for various distribution functions of the material properties $\gamma(x)$, different ratios of material properties E''/E', ρ''/ρ' and of the plate thickness d/l as well as various parameters of foundation κ.

Analysing results of this example, it can be observed that:

1° Using both the presented models – the tolerance and the asymptotic one, lower free vibrations frequencies can be analysed.

2° Lower and higher free vibrations frequencies decrease with an increase in the ratio ρ''/ρ', but they increase with the increasing ratio E''/E'.

3° The asymptotic model cannot be applied to analyse lower free vibrations frequencies of rather very thin plates (with the ratio $d/l = 0.01$) and rather strong foundations (with the foundation parameter $\kappa = 0.05$), see Fig. 4b.

4° For thicker plates (e.g. $d/l = 0.1$) and weaker foundations ($\kappa = 5 \cdot 10^{-5}$), microstructured plates can be made applying different distribution functions of the material properties $\gamma(x)$ such that their lower fundamental free vibrations frequencies are smaller or higher than these frequencies for the homogeneous plate made of a stronger material (plates with the ratios $E''/E' = \rho''/\rho' = 1$) for different pairs of the ratios $(E''/E', \rho''/\rho')$.

Hence, the tolerance model can be used as a certain tool to analyse various vibration problems of thin functionally graded plates under consideration, for instance – higher order vibrations related to the microstructure of the plates. Other dynamic problems of such plates will be shown in forthcoming papers.

Acknowledgements

This contribution has been supported by the National Science Centre of Poland under grant No. 2011/01/N/ST8/07758.

References

1. Baron E., 2006, On modelling of periodic plates having the inhomogeneity period of an order of the plate thickness, *Journal of Theoretical and Applied Mechanics*, **44**, 3-18
2. Bensoussan A., Lions J.-L., Papanicolaou G., 1978, *Asymptotic Analysis for Periodic Structures*, North-Holland, Amsterdam

3. Domagalski Ł., Jędrysiak J., 2012, On the elastostatics of thin periodic plates with large deflections, *Meccanica*, **47**, 1659-1671

4. Domagalski Ł., Jędrysiak J., 2014, Nonlinear vibrations of periodic beams, *Journal of Vibrations in Physical Systems*, **26**, 73-78

5. Jędrysiak J., 1999, Dynamics of thin periodic plates resting on a periodically inhomogeneous Winkler foundation, *Archive of Applied Mechanics*, **69**, 345-356.

6. Jędrysiak J., 2003, Free vibrations of thin periodic plates interacting with an elastic periodic foundation, *International Journal of Mechanical Sciences*, **45**, 1411-1428

7. Jędrysiak J., 2010, *Thermomechanics of Laminates, Plates and Shells with Functionally Graded Structure* (in Polish), Wyd. PŁ Łódź

8. Jędrysiak J., 2013, Modelling of dynamic behaviour of microstructured thin functionally graded plates, *Thin-Walled Structures*, **71**, 102-107

9. Jędrysiak J., 2014, Free vibrations of thin functionally graded plates with microstructure, *Engineering Structures*, **75**, 99-112

10. Jędrysiak J., Michalak B., 2011, On the modelling of stability problems for thin plates with functionally graded structure, *Thin-Walled Structures*, **49**, 627-635

11. Jędrysiak J., Paś A., 2005, On the modelling of medium thickness plates interacting with a periodic Winkler's subsoil, *Electronic Journal of Polish Agricultural Universities*, **8**, www.ejpau.media.pl

12. Jędrysiak J., Paś A., 2014, Dynamics of medium thickness plates interacting with a periodic Winkler's foundation: non-asymptotic tolerance modelling, *Meccanica*, **49**, 1577-1585

13. Jędrysiak J., Pazera E., 2014, Free vibrations of thin microstructured plates, *Journal of Vibrations in Physical Systems*, **26**, 93-98

14. Jha D.K., Kant Tarun, Singh R.K., 2013, Free vibration response of functionally graded thick plates with shear and normal deformations effects, *Composite Structures*, **96**, 799-823

15. Kaźmierczak M., Jędrysiak J., 2010, Free vibrations of transversally graded plate bands, *Electronic Journal of Polish Agricultural Universities*, **13**, 4, www.ejpau.media.pl

16. Kaźmierczak M., Jędrysiak J., 2011, Tolerance modelling of vibrations of thin functionally graded plates, *Thin-Walled Structures*, **49**, 1295-1303

17. Kaźmierczak M., Jędrysiak J., 2013, A new combined asymptotic-tolerance model of vibrations of thin transversally graded plates, *Engineering Structures*, **46**, 322-331

18. Kaźmierczak-Sobińska M., Jędrysiak J., 2014, Vibrations of thin functionally graded plates with tolerance-periodic microstructure, *Journal of Vibrations in Physical Systems*, **26**, 99-104

19. Kohn R.V., Vogelius M., 1984, A new model for thin plates with rapidly varying thickness, *International Journal of Solids and Structures*, **20**, 333-350

20. Kołakowski Z., 2009, Some aspects of the axial extension mode in an elastic thin-walled beam-column, *Journal of Theoretical and Applied Mechanics*, **50**, 147-168

21. Kołakowski Z., 2012, Static and dynamic interactive buckling of composite columns, *Journal of Theoretical and Applied Mechanics*, **47**, 177-192

22. Królak M., Kowal-Michalska K., Mania R.J., Świniarski J., 2009, Stability and load carrying capacity of multi-cell thin-walled columns of rectangular cross-sections, *Journal of Theoretical and Applied Mechanics*, **47**, 435-456

23. Kubiak T., 2006, Interactive buckling in thin-walled beam-columns with widthwise varying orthotropy, *Journal of Theoretical and Applied Mechanics*, **44**, 75-90

24. Magnucka-Blandzi E., 2011, Mathematical modelling of a rectangular sandwich plate with a metal foam core, *Journal of Theoretical and Applied Mechanics*, **49**, 439-455

25. Matysiak S.J., Nagórko W., 1989, Microlocal parameters in the modelling of microperiodic plates, *Ingenieur-Archiv*, **59**, 434-444

26. Marczak J., Jędrysiak J., 2014, Analysis of vibrations of plate strip with concentrated masses using tolerance averaging technique, *Journal of Vibrations in Physical Systems*, **26**, 161-168

27. Michalak B., 2002, On the dynamic behaviour of a uniperiodic folded plates, *Journal of Theoretical and Applied Mechanics*, **40**, 113-128

28. Michalak B., 2012, Dynamic modeling of thin skeletonal shallow shells as 2D structures with nonuniform microstructures, *Archive of Applied Mechanics*, **82**, 949-961

29. Michalak B., Wirowski A., 2012, Dynamic modelling of thin plate made of certain functionally graded materials, *Meccanica*, **47**, 1487-1498

30. Nagórko W., 1998, Two methods of modelling of periodic nonhomogeneous elastic plates, *Journal of Theoretical and Applied Mechanics*, **36**, 291-303

31. Nagórko W., Woźniak C., 2002, Nonasymptotic modelling of thin plates reinforced by a system of stiffeners, *Electronic Journal of Polish Agricultural Universities*, **5**, 2, www.ejpau.media.pl

32. Oktem A.S., Mantari J.L., Guedes Soares C., 2012, Static response of functionally graded plates and doubly-curved shells based on a higher order shear deformation theory, *European Journal of Mechanics – A/Solids*, **36**, 163172

33. Ostrowski P., Michalak B., 2011, Non-stationary heat transfer in a hollow cylinder with functionally graded material properties, *Journal of Theoretical and Applied Mechanics*, **49**, 385-397

34. Roque C.M.C., Ferreira A.J.M., Jorge R.M.N., 2007, A radial basis function approach for the free vibration analysis of functionally graded plates using a refined theory, *Journal of Sound and Vibration*, **300**, 1048-1070

35. Suresh S., Mortensen A., 1998, *Fundamentals of Functionally Graded Materials*, The University Press Cambridge

36. Tahouneh V., Naei M.H., 2014, A novel 2-D six-parameter power-law distribution for three-dimensional dynamic analysis of thick multi-directional functionally graded rectangular plates resting on a two-parameter elastic foundation, *Meccanica*, **49**, 91-109

37. Tomczyk B., 2007, A non-asymptotic model for the stability analysis of thin biperiodic cylindrical shells, *Thin-Walled Structures*, **45**, 941-944

38. Tomczyk B., 2013, Length-scale effect in dynamics and stability of thin periodic cylindrical shells, *Scientific Bulletin of the Lodz University of Technology*, **1166**, series: Scientific Transactions, **466**, Wyd. PŁ, Łódź

39. Tornabene F., Liverani A., Caligiana G., 2011, FGM and laminated doubly curved shells and panels of revolution with a free-form meridian: A 2-D GDQ solution for free vibrations, *International Journal of Mechanical Sciences*, **53**, 443-470

40. Wierzbicki E., Woźniak C., 2000, On the dynamics of combined plane periodic structures, *Archive of Applied Mechanics*, **70**, 387-398

41. Wirowski A., 2012, Self-vibration of thin plate band with non-linear functionally graded material, *Archives of Mechanics*, **64**, 603-615

42. Woźniak C., et al. (Eds.), 2010, *Mathematical Modeling and Analysis in Continuum Mechanics of Microstructured Media*, Wyd. PŚl, Gliwice

43. Woźniak C., Michalak B., Jędrysiak J. (Eds.), 2008, *Thermomechanics of Heterogeneous Solids and Structures*, Wyd. PŁ, Łódź

44. Woźniak C., Wierzbicki E., 2000, *Averaging Techniques in Thermomechanics of Composite Solids*, Wyd. PCz, Częstochowa

45. Yajuvindra Kumar, Lal R., 2012, Vibrations of nonhomogeneous orthotropic rectangular plates with bilinear thickness variation resting on Winkler foundation, *Meccanica*, **47**, 893-915

Manuscript received August 28, 2014; accepted for print February 10, 2015

JOURNAL OF THEORETICAL AND APPLIED MECHANICS
53, 3, pp. 643-652, Warsaw 2015
DOI: 10.15632/jtam-pl.53.3.643

THE COMBINED HEAT TRANSFER OF RADIATION AND MIXED CONVECTION ANALYSIS IN A LID-DRIVEN TRAPEZOIDAL CAVITY

Malihe Mohammadi, Seyyed Abdolreza Gandjalikhan Nassab
Department of Mechanical Engineering, School of Engineering, Shahid Bahonar University, Kerman, Iran
e-mail: mohammadi2345@yahoo.com

In this paper, the effect of radiation heat transfer on mixed convection in a lid-driven trapezoidal cavity is studied numerically. The governing equations of mixed convection are solved based on the SIMPLE algorithm and the solution of the radiative transfer equation inside the participating medium is carried out using the discrete ordinates method, simultaneously. To study the heat transfer and flow characteristics, sensitivity analysis is carried out based on the two parameters including the optical thickness and radiation-conduction parameter. Several interesting results are obtained such as sweep behavior on the isotherms, streamlines and convective Nusselt number with optical thicknesses.

Keywords: mixed convection, radiation, lid-driven trapezoidal cavity

1. Introduction

The mixed convection process inside a lid-driven cavity is found in many engineering applications such as solar collectors, cooling of electronic devices, heat exchangers (Cheng and Liu, 2010). Study of the literature shows that the problem is considered along two different parts, those are square or rectangular geometry and irregular geometries. The majority of previous works investigated the effect of several boundary conditions on flow and temperature characteristics inside a lid-driven square or rectangular cavity (Moallemi and Jang, 1992; Prasad and Koseff, 1996; Shankar *et al.*, 2002; Oztop, 2006). Chen and Cheng (2004, 2005) studied the flow and temperature characteristics for mixed convective inside an arc-shaped lid-driven cavity by considering variable inclination angle. Recently, few literatures items have been reported on topic of mixed convective flow inside a lid-driven trapezoidal cavity. The analysis of flow and temperature characteristics inside irregular geometries is very important for advance of heating and cooling arrangements or material processing systems (Bhattacharya *et al.*, 2013). In most of the studies on the mixed convection in lid-driven cavities, the role of the radiative heat transfer is neglected. Therefore, the objective of this work is to study the effect of radiative heat transfer on mixed convection in a lid-driven trapezoidal cavity numerically. To achieve this purpose, the flow and heat transfer characteristics is investigated for a broad range of optical thickness ($0 < \tau < 100$) and radiation-conduction parameters ($0.5 < RC < 10$) at the Richardson number equal to 10. The lid-driven trapezoidal cavity is considered as emitting, absorbing and isotropically scattering participating with gray gasses. The governing equations are solved by using the finite volume method and the radiative transfer equation by the discrete ordinates method (DOM). Also, the SIMPLE algorithm of Patankar and Spalding (1972) has been employed to couple the velocity and pressure fields. It should be mentioned that analysis of combined radiative heat transfer and mixed convection in a lid-driven trapezoidal cavity is carried out for the first time in the present work.

Nomenclature

C_p – specific heat [J/(kg·K)]
g – gravitational acceleration [m/s^2]
I – radiation intensity [W/m^2]
I^* – dimensionless radiation intensity
k – thermal conductivity [W/(m·K)]
L – the enclosure height [m]
p – fluid dynamic pressure [Pa]
P – dimensionless pressure
q_c, q_r – convective and radiative heat flux [W/m^2]
RC – radiation-conduction parameter
S – radiation source term
S^* – dimensionless radiation source term
T – temperature [K]
T_c, T_h – top wall cold and hot temperature [K]
U_0 – moving lid velocity [m/s]
(u, v) – the x- and y-velocity components [m/s]
(U, V) – dimensionless the x- and y-velocity components
(x, y) – dimensional Cartesian coordinate [m]
(X, Y) – dimensionless Cartesian coordinate
α – thermal diffusivity [m^2/s]
β – extinction coefficient [m^{-1}], or thermal coefficient expansion [k^{-1}]
ε – emissivity of wall
$\theta, \theta_1, \theta_2$ – dimensionless temperature and dimensionless temperature parameters
μ – dynamic viscosity [N·s/m^2]
ν – kinematic viscosity [m^2/s]
ρ – density [kg/m^3]
σ_a, σ_s – absorbing and scattering coefficient [m^{-1}]
τ – optical thickness
Φ – scattering phase function
ω – scattering albedo
Ω – solid angle

and

$\mathrm{Gr} = g\beta(T_h - T_c)L^3)/\nu^2$, $\mathrm{Pr} = \nu/\alpha$, $\mathrm{Re} = LU_0/\nu$, $\mathrm{Ri} = \mathrm{Gr}/\mathrm{Re}^2$, Pe – Grashof, Prandtl, Reynolds, Richardson and Peclet number, respectively
Nu, Nu_t – Nusselt and total Nusselt number at bottom wall, respectively
$\mathrm{Nu}_c, \mathrm{Nu}_r$ – convective and radiative Nusselt number, respectively

2. Mathematical model

The schematic diagram of a lid-driven trapezoidal cavity is shown in Fig. 1. The top lid of the cavity moves in the x-direction with constant velocity U_0. The horizontal walls are isothermal and the temperature of bottom wall T_h is higher than that of the moving wall T_c. Also, the side walls are assumed with linear temperature distribution in the range of $T_c < T < T_h$, and their inclination angle is equal to 45°. All thermo-physical properties of the fluid except the density are assumed to be constant. The fluid into the enclosure is considered as a gray participating medium and all walls are considered to be black.

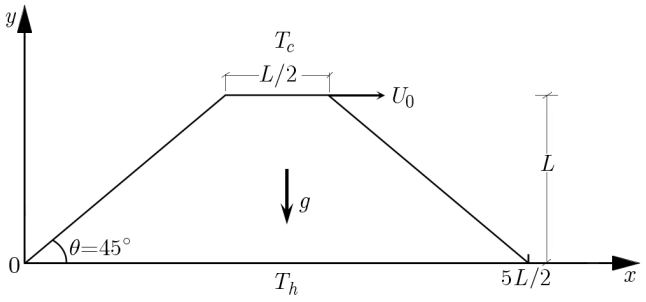

Fig. 1. Schematic model of the trapezoidal cavity

The governing equations containing continuity, momentum and energy for a two-dimensional, steady, laminar and constant property flow assuming the Boussinesq approximation in a dimensional form can be written as

$$\begin{aligned}
&\frac{\partial u}{\partial x}+\frac{\partial v}{\partial y}=0\\
&u\frac{\partial u}{\partial x}+v\frac{\partial u}{\partial y}=-\frac{1}{\rho}\frac{\partial p}{\partial x}+\vartheta\Big(\frac{\partial^2 u}{\partial x^2}+\frac{\partial^2 u}{\partial y^2}\Big)\\
&u\frac{\partial v}{\partial x}+v\frac{\partial v}{\partial y}=-\frac{1}{\rho}\frac{\partial p}{\partial y}+\vartheta\Big(\frac{\partial^2 v}{\partial x^2}+\frac{\partial^2 v}{\partial y^2}\Big)+g\beta(T-T_c)\\
&u\frac{\partial T}{\partial x}+v\frac{\partial T}{\partial y}=\frac{k}{\rho C_p}\Big(\frac{\partial^2 T}{\partial x^2}+\frac{\partial^2 T}{\partial y^2}\Big)-\frac{1}{\rho C_p}\nabla\cdot\mathbf{q}_r
\end{aligned}\tag{2.1}$$

The radiative source term in the energy equation which appears as divergence of radiative flux $\nabla\cdot\mathbf{q}_r$ is dependent on the local radiation intensities (Modest, 2003)

$$\nabla\cdot\mathbf{q}_r=\sigma_a\left(4\pi I_b(\mathbf{r})-\int\limits_{4\pi} I(\mathbf{r},\mathbf{s})\,d\Omega\right)\tag{2.2}$$

The local radiation intensity is calculated by solving the radiative transfer equation. This equation for the participating medium in the direction vector $\mathbf{s}$ can be expressed as (Modest, 2003)

$$(\mathbf{s}\cdot\nabla)I(\mathbf{r},\mathbf{s})=-\beta I(\mathbf{r},\mathbf{s})+\sigma_a I_b(\mathbf{r})+\frac{\sigma_s}{4\pi}\int\limits_{4\pi} I(\mathbf{r},\mathbf{s})\Phi(\mathbf{s},\mathbf{s}')\,d\Omega'\tag{2.3}$$

In this study, the phase function $\Phi(\Omega,\Omega')$ is equal to unity because of the assumption of isotropic scattering.

For diffusely reflecting walls in Eq. (2.3), the radiative boundary condition is

$$I(\mathbf{r}_w,\mathbf{s})=\varepsilon_w I_b(\mathbf{r}_w)+\frac{1-\varepsilon_w}{\pi}\int\limits_{\mathbf{n}_w\cdot\mathbf{s}<0} I(\mathbf{r}_w,\mathbf{s})|\mathbf{n}_w\cdot\mathbf{s}'|\,ds'\qquad\mathbf{n}_w\cdot\mathbf{s}>0\tag{2.4}$$

The discrete ordinates method is used to solve the equation of radiative transfer equation (Eq. (2.3)). In this method, Eq. (2.3) is replaced by a set of n equations for a finite number of n different directions $\mathbf{s}_i$, and each integral is replaced by a quadrature series of the following form

$$(\mathbf{s}_i\cdot\nabla)I(\mathbf{r},\mathbf{s}_i)=-\beta I(\mathbf{r},\mathbf{s}_i)+\sigma_a I_b(\mathbf{r})+\frac{\sigma_s}{4\pi}\sum_{j=1}^{n} w_j I(\mathbf{r},\mathbf{s}_j)\Phi(\mathbf{s}_j,\mathbf{s}_i)\qquad i=1,2,3,\ldots,n\tag{2.5}$$

with the boundary conditions

$$I(\mathbf{r}_w,\mathbf{s}_i)=\varepsilon_w I_b(\mathbf{r}_w)+\frac{1-\varepsilon_w}{\pi}\sum_{|\mathbf{n}_w|,|\mathbf{s}_j|<0})w_j I(\mathbf{r}_w,\mathbf{s}_j)|\mathbf{n}_w,\mathbf{s}_j|\tag{2.6}$$

In the above equations, w_k is the weighting factor for each discrete ordinate. The original equation by this angular approximation is transformed to a set of coupled differential equations. Equation (2.5) in Cartesian coordinates becomes

$$\begin{aligned} &\xi_i\frac{\partial I_i}{\partial x}+\nu_i\frac{\partial I_i}{\partial y}+\mu_i\frac{\partial I_i}{\partial z}+\beta I_i=\beta S_i \\ &S_i=(1-\omega)I_b+\frac{\omega}{4\pi}\sum_{j=1}^{n}w_j I(\mathbf{r},\mathbf{s}_j)\Phi(\mathbf{s}_j,\mathbf{s}_i) \qquad i=1,2,3,\ldots,n \end{aligned} \tag{2.7}$$

in which ξ_m, ν_m, μ_m are the directional cosines of $\mathbf{s}_i$.

Non-dimensional Eqs. (2.1)-(2.3) are obtained using the following dimensionless variables

$$\begin{aligned} &X=\frac{x}{L} && Y=\frac{y}{L} && U=\frac{u}{U_0} && V=\frac{v}{U_0} \\ &\theta=\frac{T-T_c}{T_h-T_c} && P=\frac{p}{\rho U_0^2} && \mathrm{Re}=\frac{\rho U_0 L}{\mu} && \theta_1=\frac{T_c}{T_h-T_c} \\ &\theta_2=\frac{T_h}{T_c} && I^*=\frac{I}{\sigma T_h^4} && S^*=\frac{S}{\sigma T_h^4} && \tau=\beta L \\ &1-\omega=\frac{\sigma_a}{\beta} && \mathrm{Pr}=\frac{\vartheta}{\alpha} && \mathrm{Pe}=\mathrm{Re}\,\mathrm{Pr} && \mathrm{Gr}=\frac{g\beta(T_h-T_c)L^3}{\vartheta^2} \\ &RC=\frac{\sigma T_h^3 L}{k} && q_r^*=\frac{q_r}{\sigma T_h^4} \end{aligned} \tag{2.8}$$

The non-dimensional form of Eqs. (2.1)-(2.3) can be written as

$$\begin{aligned} &\frac{\partial U}{\partial X}+\frac{\partial V}{\partial Y}=0 \\ &U\frac{\partial U}{\partial X}+V\frac{\partial U}{\partial Y}=-\frac{\partial P}{\partial X}+\frac{1}{\mathrm{Re}}\Big(\frac{\partial^2 U}{\partial X^2}+\frac{\partial^2 U}{\partial Y^2}\Big) \\ &U\frac{\partial V}{\partial X}+V\frac{\partial V}{\partial Y}=-\frac{\partial P}{\partial Y}+\frac{1}{\mathrm{Re}}\Big(\frac{\partial^2 V}{\partial X^2}+\frac{\partial^2 V}{\partial Y^2}\Big)+\frac{\mathrm{Gr}}{\mathrm{Re}^2}\theta \\ &\frac{\partial}{\partial X}\Big(U\theta-\frac{1}{\mathrm{Pe}}\frac{\partial\theta}{\partial X}\Big)+\frac{\partial}{\partial Y}\Big(V\theta-\frac{1}{\mathrm{Pe}}\frac{\partial\theta}{\partial Y}\Big)+\frac{\tau(1-\omega)RC\theta_1\theta_2}{\mathrm{Pe}}\left[\frac{4}{\theta_2^4}\Big(\frac{\theta}{\theta_1}+1\Big)^4-\sum_{i=1}^{n}I_i^* w_i\right]=0 \end{aligned} \tag{2.9}$$

The modified boundary conditions are:
— on the upper wall

$$U=1 \qquad V=0 \qquad \theta=0 \tag{2.10}$$

— on the lower wall

$$U=0 \qquad V=0 \qquad \theta=1 \tag{2.11}$$

— on the inclined walls

$$U=0 \qquad V=0 \qquad \theta=1-Y \tag{2.12}$$

The convective, radiative and total Nusselt number at the walls are determined using the heat fluxes as

$$\mathrm{Nu}_c=\frac{q_c L}{k\Delta T} \qquad \mathrm{Nu}_r=\frac{q_r L}{k\Delta T} \qquad \mathrm{Nu}_t=\mathrm{Nu}_c+\mathrm{Nu}_r \tag{2.13}$$

3. Numerical solution procedure

The applied numerical method to solve the governing equations (Eqs. (2.9)) is a line-by-line iteratively method based on the SIMPLE algorithm. The equations are discretized using the finite control volume technique on staggered control volumes for the x and y velocity components. The RTE is solved using the DOM method to calculate the radiation source term in the energy equation (Modest, 2003). This calculations are written in a FORTRAN program. The convergence criterion for solving the governing equations is assumed that the amount of residual terms between two consecutive iteration is less than 10^{-6}, and the convergence criterion for the RTE is

$$\max\left|\frac{I_p^{*n} - I_p^{*n-1}}{I_p^{*n}}\right| \leqslant 10^{-5} \tag{3.1}$$

4. Validation of the code

To validate the pure mixed convection case, comparison is performed with the studied problem by Bhattacharya *et al.* (2013). The schematic of this problem is a two-dimensional trapezoidal enclosure with cold top wall (lid), hot bottom wall and adiabatic inclined walls. The distribution of the Nusselt number at the bottom wall for Re = 100, Gr = 10^5 and Pr = 0.7 is shown in Fig. 2. We can conclude that there is a good consistency between the present numerical results and those reported by Bhattacharya *et al.* (2013).

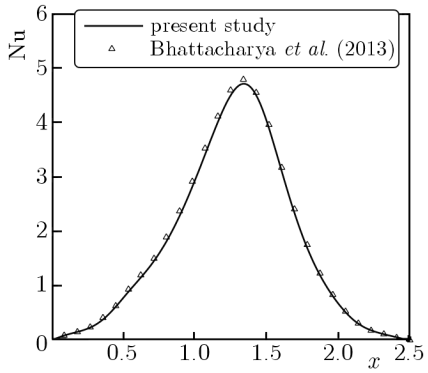

Fig. 2. Nusselt number profile at the bottom wall, $RC = 10$, Re = 100, Gr = 10^5 and Pr = 0.7

To investigate validity of the discrete ordinates method, since no study exists on the combined heat transfer of mixed convection and radiation in a lid-driven cavity, a combined conductive-radiative heat transfer problem is considered. This problem was studied by Mahapatra *et al.* (2006). The schematic is a square enclosure of length L, containing an absorbing, emitting, and scattering medium. A plot of the mid-plane temperature inside the medium for $RC = 10$, $\varepsilon = 1.0$, $\tau = 1.0$ and $\omega = 0.5$ is shown in Fig. 3. It is shown that the present numerical results are in accordance with the theoretical ones reported by Mahapatra *et al.* (2006).

Also, to get grid-independent solutions, the maximum total Nusselt number at the bottom wall for three different radiation-conduction parameters and optical thicknesses for three cases are shown in Table 1. As it is seen, the amount of the total Nusselt number is different only in the second or third decimal places. Therefore, we used a uniform mesh with 90×80 grid numbers for all cases.

Also, the maximum total Nusselt number at the bottom wall with $S4$ and $S6$ approximations at Re = 100, Gr = 10^5, Pr = 0.7 is shown in Table 2. These results demonstrate that there is very little difference between $S4$ and $S6$ approximations. Thus, to reduce computational effort, $S4$ approximation is used for all cases.

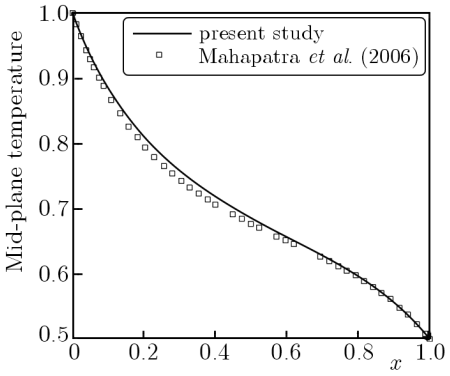

Fig. 3. Variation of mid-plane temperature, $\varepsilon = 1.0$ and $\tau = 1.0$

Table 1. Grid independence study in terms of the total Nusselt number at Re = 100, Gr = 10^5 and Pr = 0.7

Grid Size	$\tau = 0$	$\tau = 0.5$	$\tau = 1$	$RC = 0.5$	$RC = 2$	$RC = 5$
80×70	13.325	11.799	10.927	7.169	2.432	13.916
90×80	13.310	11.781	10.916	7.157	9.418	13.903
100×90	13.313	11.781	10.907	7.148	9.408	13.895

Table 2. Angular quadrature study in terms of the total Nusselt number at Re = 100, Gr = 10^5 and Pr = 0.7

	$\tau = 0$	$\tau = 0.5$	$\tau = 1$	$RC = 0.5$	$RC = 2$	$RC = 5$
$S4$	13.310	11.781	10.916	7.157	9.418	13.903
$S6$	13.380	11.836	10.944	7.160	9.436	13.951

5. Results and discussion

In this study, the effect of radiative heat transfer on the heat transfer and flow characteristics of the mixed convection in a lid-driven trapezoidal cavity is investigated numerically. Figures 4 and 5 indicate the isotherms and streamlines at Ri = 10 for different optical thicknesses and also for the pure mixed convection case. Optical thickness $\tau = 0$ shows the results for a radiatively transparent medium. These figures demonstrate the sweep behavior on the isotherms and streamlines. An increase in the optical thickness from $\tau = 0$ to $\tau = 2$ makes the difference between isotherms for the pure mixed convection and the radiative case increases as well. But when the optical thickness increases from $\tau = 2$ to $\tau = 100$, the isotherms of pure mixed convection case will be obtained. In fact, for high values of optical thickness, the radiation intensity cannot permeate the cavity, and it is absorbed near the walls.

This phenomenon is also seen for the streamlines along the optical thickness, such that by increasing the optical thickness from $\tau = 0$ to $\tau = 10$ the difference between streamlines for the pure mixed convection and the radiative case increases. But by further increasing of the optical thickness the reverse behavior is observed.

In Fig. 6, the effect of radiation-conduction parameter (RC) on the thermal behavior of the system at Ri = 10 is shown. This parameter shows the relative importance of the radiative heat transfer mechanism compared with its conduction counterpart. As can be seen in Fig. 6, as the RC parameter increases due to changing the dominant heat transfer mechanism from conduction to radiation, the difference between the isotherms for the radiative and pure mixed convection case increases.

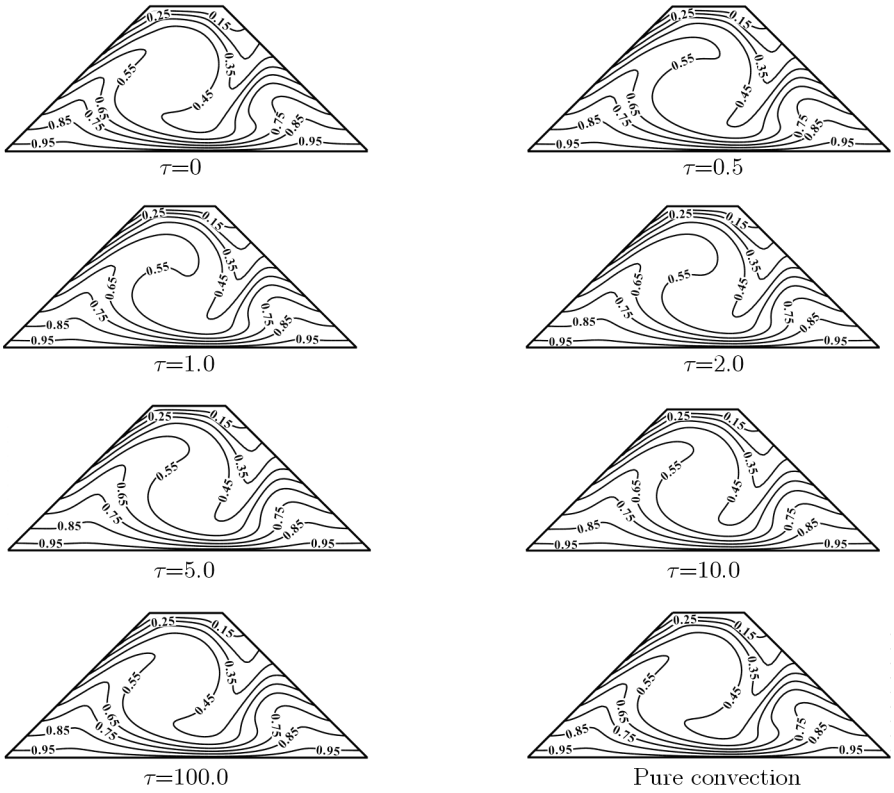

Fig. 4. Isotherms for different optical thicknesses and the pure mixed convection case at Ri = 10

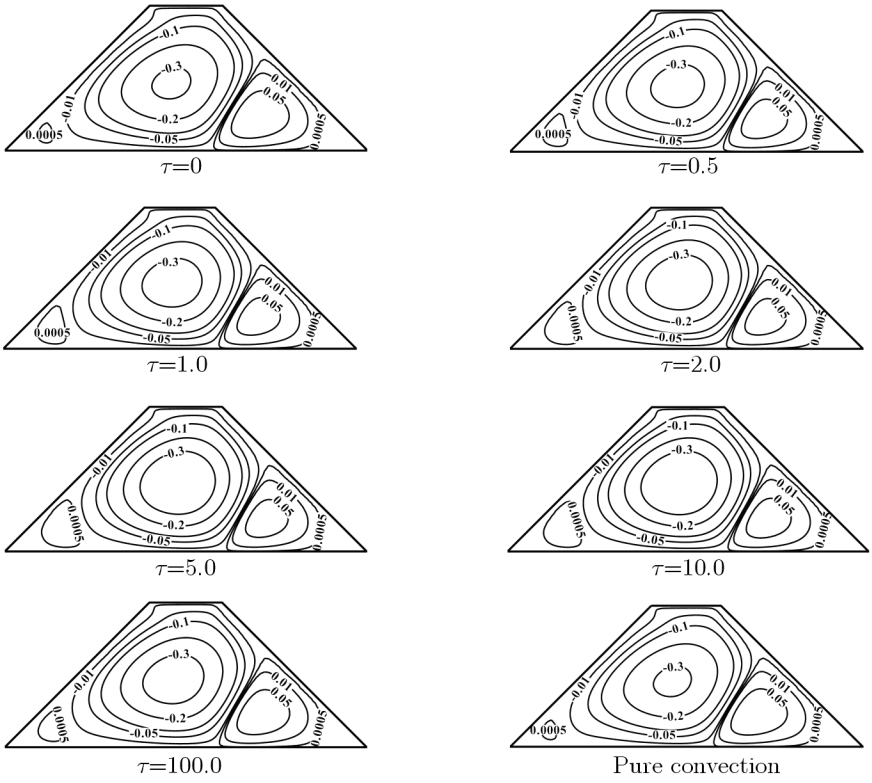

Fig. 5. Streamlines for different optical thicknesses and pure mixed convection at Ri = 10

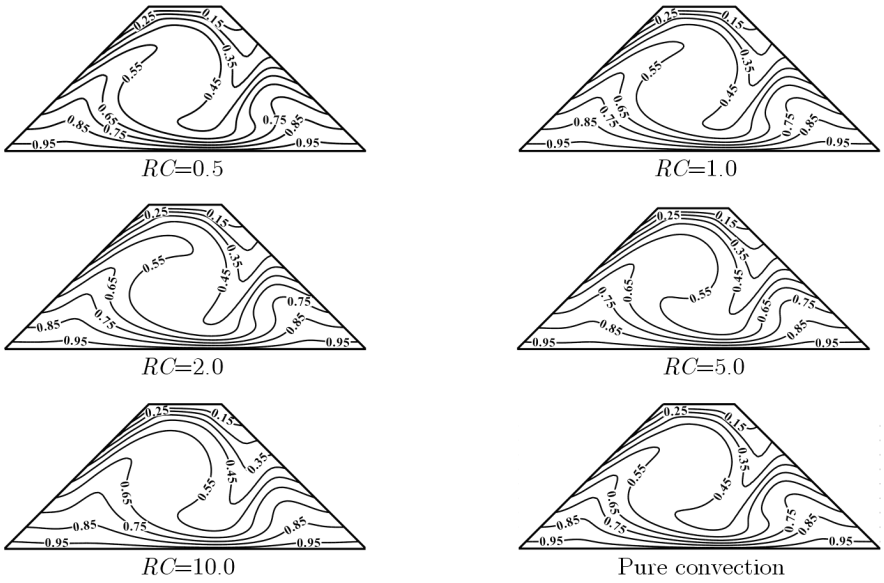

Fig. 6. Isotherms for different radiation-conduction parameters and pure mixed convection at Ri = 10

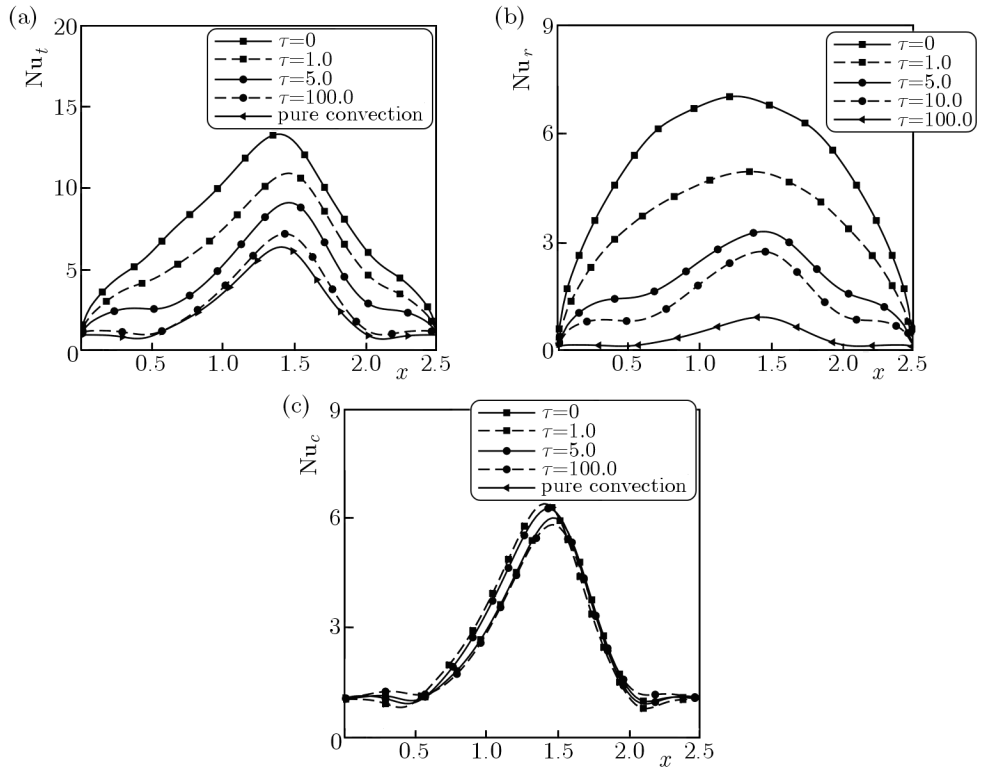

Fig. 7. The effect of optical thicknesses on the Nusselt number distribution along the bottom wall; (a) total Nusselt number, (b) radiative Nusselt number, (c) convective Nusselt number

The radiative, convective and total Nusselt numbers along the bottom wall for different optical thicknesses at Ri = 10 are shown in Figs. 7a-7c. As it is seen in Fig. 7a, as optical thickness increases, the total Nusselt number decreases. This figure shows that the radiatively transparent medium ($\tau = 0$) has the maximum amount of the total Nusselt number and the pure mixed convection case has the smallest total Nusselt number. Therefore, it can be deducted that the radiatively transparent medium has the maximum amount of thermal exchange with the environment. Figure 7b shows that as the optical thickness increases, the radiative Nusselt

number decreases. This is because of the increasing gas absorption, hence the radiative heat flux at the bottom wall decreases. Figure 7c indicates that there is sweep behavior in the convective Nusselt number. By increasing the optical thickness from $\tau = 0$ to $\tau = 5$, the convective Nusselt number decreases at the core of the cavity ($0.5 < X < 1.5$) and after that, with an increase in the optical thicknesses, the convective Nusselt number increases until it reaches the pure mixed convection, while near the inclined walls reverse behavior is observed on the convective Nusselt number with optical thickness.

Figures 8a-8c show the effect of the radiation-conduction parameter on the radiative, convective and total Nusselt numbers along the bottom wall at Ri = 10. Figures 8a and 8b display that the total and radiative Nusselt numbers increase with an increase in the RC parameter. But the convective Nusselt number decreases at the core of cavity ($0.5 < X < 1.5$) with this parameter. This is because in high values of the RC parameter, the radiative heat transfer is the dominant mechanism.

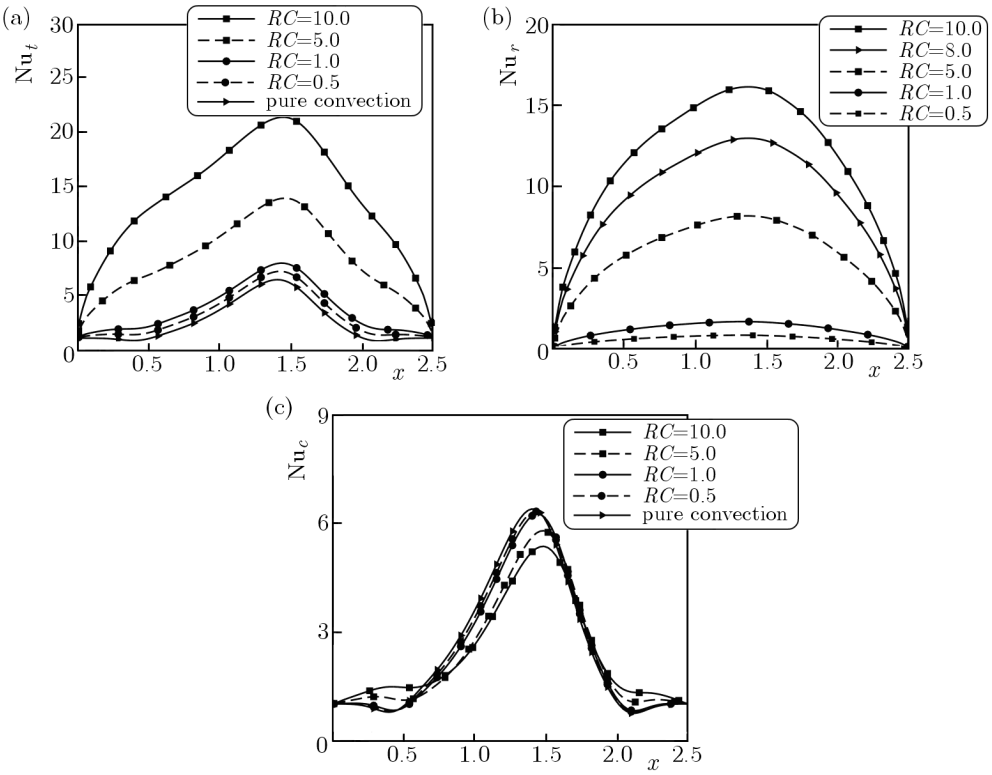

Fig. 8. The effect of radiation-conduction parameter on the Nusselt number distribution along the bottom wall; (a) total Nusselt number, (b) radiative Nusselt number, (c) convective Nusselt number

6. Conclusions

Mixed convection combined with radiation heat transfer in a lid-driven trapezoidal cavity has been analyzed numerically in the present study. The finite volume method has been chosen to solve the continuity, momentum and energy equations and the discrete ordinates method for the radiative transfer equation. The medium has been considered as emitting, absorbing and isotropically scattering with gray gases. The heat transfer and flow characteristics have been studied in the range of radiation-conduction parameter ($0.5 \leqslant RC \leqslant 10$) and optical thickness ($0 \leqslant \tau \leqslant 100$). The obtained results have shown that in a radiatively transparent medium, the radiative heat transfer is the dominant mechanism. It has the maximum heat transfer, whereas the pure convection case has the minimum heat transfer with the environment. Also,

as the optical thickness increases, the contribution of radiation in comparison with convection decreases until pure mixed convection is obtained. But, by increasing the radiation-conduction parameter, the contribution of radiative heat transfer increases.

References

1. Bhattacharya M., Basak T., Oztop H.F., Varol Y., 2013, Mixed convection and role of multiple solutions in lid-driven trapezoidal enclosures, *International Journal of Heat and Mass Transfer*, **63**, 366-388
2. Chen C.L., Cheng C.H., 2004, Experimental and numerical study of mixed convection and flow pattern in a lid-driven arc-shape cavity, *Heat and Mass Transfer*, **41**, 58-66
3. Cheng C.H., Chen C.L., 2005, Numerical study of effects of inclination on buoyancy-induced flow oscillation in a lid-driven arc-shaped cavity, *Numerical Heat Transfer Applications*, **48**, 77-97
4. Cheng T.S., Liu W.H., 2010, Effect of temperature gradient orientation on the characteristics of mixed convection flow in a lid-driven square cavity, *Computers and Fluids*, **39**, 965-978
5. Mahapatra S.K., Dandapat B.K., Sarkar A., 2006, Analysis of combined conduction and radiation heat transfer in presence of participating medium by the development of hybrid method, *Journal of Quantitative Spectroscopy and Radiative Transfer*, **102**, 277-292
6. Moallemi M.K., Jang K.S., 1992, Prandtl number effects on laminar mixed convection heat-transfer in a lid-driven cavity, *International Journal of Heat and Mass Transfer*, **35**, 1881-1892
7. Modest M.F., 2003, *Radiative Heat Transfer*, McGraw-Hill, New York
8. Oztop H.F., 2006, Combined convection heat transfer in a porous lid-driven enclosure due to heater with finite length, *International Communications in Heat and Mass Transfer*, **33**, 772-779
9. Patankar S.V., Spalding D.B., 1972, A calculation procedure for heat, mass and momentum transfer in three-dimensional parabolic flows, *International Journal of Heat and Mass Transfer*, **15**, 1787-1806
10. Prasad A.K., Koseff J.R., 1996, Combined forced and natural convection heat transfer in a deep lid driven cavity flow, *International Journal of Heat and Fluid*, **17**, 460-467
11. Shankar P.N., Meleshko V.V., Nikiforovich E.I., 2002, Slow mixed convection in rectangular containers, *Journal of Fluid Mechanics*, **471**, 203-217

Manuscript received November 8, 2014; accepted for print February 10, 2015

JOURNAL OF THEORETICAL AND APPLIED MECHANICS
53, 3, pp. 653-664, Warsaw 2015
DOI: 10.15632/jtam-pl.53.3.653

ON SUPPRESSION OF CHAOTIC MOTIONS OF A PORTAL FRAME STRUCTURE UNDER NON-IDEAL LOADING USING A MAGNETO-RHEOLOGICAL DAMPER

Angelo Marcelo Tusset, Vinicius Piccirillo
Federal University of Technology-Paraná – UTFPR, Ponta Grossa, PR, Brazil
e-mail: tusset@utfpr.edu.br; piccirillo@utfpr.edu.br

José Manoel Balthazar
University Paulista State – UNESP, Rio Claro, SP, Brazil; e-mail: jmbaltha@rc.unesp.br

Reyolando Manoel Lopes Rebello da Fonseca Brasil
Federal University of ABC – UFABC, Santo Andre, SP, Brasil; e-mail: reyolando.brasil@ufabc.edu.br

We consider chaotic motions of a portal frame structure under non-ideal loading. To suppress this chaotic behavior, a controlling scheme is implemented. The control strategy involves application of two control signals and nonlinear feedforward control to maintain a desired periodic orbit, and state feedback control to bring the system trajectory into the desired periodic orbit. Additionally, the control strategy includes an active magneto-rheological damper to actuate the system. The control force of the damper is a function of the voltage applied in the coil of the damper that is based on the force given by the controller.

Keywords: feedback control, feedforward control, MR damper

1. Introduction

The study of non-ideal vibrating systems, that is, when the excitation is influenced by the response of the system, has been considered a major challenge in theoretical and practical engineering research (as examples, among others, see Bolla *et al.* (2007), Castão *et al.* (2010), Samantaray *et al.* (2010), Djanan *et al.* (2013). In this work, we observed chaotic vibrations of a portal frame structural system mathematical model under non-ideal loading. We intend not only to suppress large amplitude oscillations but also to reduce them to a periodic orbit. The suppression of chaos and keeping the oscillations into a desired periodic orbit was obtained using active control considering the Optimal Linear Feedback (OLFC) proposed by Rafikov and Balthazar (2004) and the use of a magnetorheological (MR) damper modeled considering the hysteresis phenomenon.

The MR damper uses an MR fluid which is basically composed of micrometer-sized particles of iron suspended in an oil base. The MR response of MR fluids is a result of polarization induced in the suspended particles by application of an external field. The interaction between the resulting induced dipoles makes the particles form columnar structures parallel to the applied field, increasing the viscous characteristics of the device (Kasemi *et al.*, 2012; Dutta and Chakraborty, 2014). These magnetic properties permit its use as a damper controlled by an electrical current (Tusset and Balthazar, 2013; Tusset *et al.*, 2012, 2013). When using MR damper control for suppression of unwanted oscillations, the viscosity of the internal fluid varies according to a variable electrical current or voltage (Tusset *et al.*, 2009; Piccirillo *et al.*, 2014). According to Cetin *et al.* (2011), there are two main approaches in the literature to describe the hysteresis dynamic behavior of MR dampers. One of them is the Bouc-Wen hysteresis model proposed

by Spencer *et al.* (1997), and other one is the LuGre hysteresis model that has been obtained from the nonlinear friction model proposed in (Jimenez and Alvarez, 2002, 2005; Terasawa *et al.*, 2004; Sakai *et al.*, 2003). In Dyke *et al.* (1996), the Bouc-Wen model of an MR damper was implemented with successful results to a three-story frame model. Cetin *et al.* (2011) used the LuGre friction model of an MR damper to a six-story frame model. Although Bouc-Wen model can accurately predict MR damper dynamics for active or semi-active control, it is too complex and difficult to implement (Cetin *et al.*, 2011). On the other hand, Cetin *et al.* (2011) observed that the LuGre Model is more versatile than the Bouc-Wen model in semi-active control systems, therefore, in this work, the LuGre friction model is preferred over the Bouc-Wen model.

The organization of this paper is as follows: in Section 2, the mathematical model of the portal frame under a non-ideal excitation is described and numerical simulations necessary to analyze the dynamics of the system are performed. In Section 3, the control of chaotic motion by the application of the OLFC method is presented. Section 4 presents the mathematical model of the MR damper as a function of the applied voltage in its coil and numerical simulations necessary to analyze the dynamics of the controlled system. In Section 5, the robustness of the control techniques is tested by including parameters uncertainties on the control signals. The final remarks and the acknowledgments are in Sections 6.

2. Formulation of the engineering problem

Here, we will consider the horizontal motion of a portal frame under a non-ideal excitation (see Fig. 1a) and the approximated schematic model of the system, represented by coupled oscillators (see Fig. 1b).

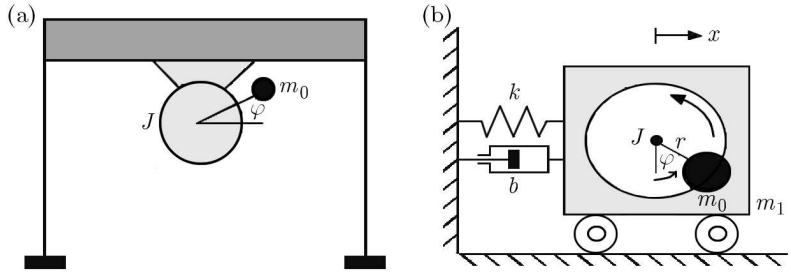

Fig. 1. (a) Non-ideal portal frame; (b) schematic of a non-ideal oscillator

The parameters of this coupled dynamical system consist of $m_0, m_1, k_1, k_{nl}, c_1, x_1, \varphi, J, r, d, s$, the mass, unbalanced mass, linear stiffness, non-linear stiffness, linear damping, displacement, angular displacement, inertia moment, eccentricity of the unbalanced mass. d is related to the voltage applied across the armature of the DC motor and s is a constant for each model of the DC motor considered. The resulting mathematical model of the structure is a Duffing-like equation

$$\begin{aligned}&(m_1+m_0)\ddot{x}+b\dot{x}-k_l x+k_{nl}x^3=m_0 r(\ddot{\varphi}\sin\varphi+\dot{\varphi}^2\cos\varphi)\\&(J+r^2m_0)\ddot{\varphi}-rm_0\ddot{x}\sin\varphi=L(\dot{\varphi})=d-s\dot{\varphi}\end{aligned}\tag{2.1}$$

Next, we render Eqs. (2.1) dimensionless in terms of new variables defined by: $\tau=\omega t$, $x_1=x/x^*$, and $x_3=\varphi/\varphi^*$, where x^* and φ^* are constant characteristics. Equations (2.1) can be represented in a state space, in dimensionless form, as

$$\begin{aligned}&x_1'=x_2 \qquad && x_2'=-\alpha x_2+\beta_1 x_1-\beta_3 x_1^3+\delta_1\sin(\varphi^* x_3)x_4'+\delta_1\cos(\varphi^* x_3)x_4^2\\&x_3'=x_4 \qquad && x_4'=\rho_1\sin(x_3)x_2'-\rho_3 x_4+\rho_2\end{aligned}\tag{2.2}$$

where

$$\alpha = \frac{b}{(m_1+m_0)\omega} \qquad \omega = \sqrt{\frac{k_1}{m_1+m_0}} \qquad \beta_1 = \frac{k_l}{(m_1+m_0)\omega^2}$$
$$\beta_3 = \frac{k_{nl}x^{*2}}{(m_1+m_0)\omega^2} \qquad \delta_1 = \frac{m_0 r\varphi^*}{(m_1+m_0)x^*} \qquad \rho_2 = \frac{d}{(J+r^2m_0)\omega^2\varphi^*}$$
$$\delta_2 = \frac{m_0 r\varphi^{*2}}{(m_1+m_0)x^*} \qquad \rho_1 = \frac{rm_0x^*}{(J+r^2m_0)\varphi^*} \qquad \rho_3 = \frac{s\omega\varphi^*}{(J+r^2m_0)\omega^2\varphi^*}$$

2.1. Numerical simulations

Numerical simulations are performed using Matlab® ode45 integrator with $h = 0.01$ and considering parameters:$\alpha = 0.1$, $\beta_1 = 1$, $\beta_3 = 2$, $\delta_1 = 8.373$, $\rho_1 = 0.05$, $\rho_2 = 100$ and $\rho_3 = 200$ (Tusset *et al.*, 2013). System (2.2) displays chaotic motions, as shown in Fig. 2.

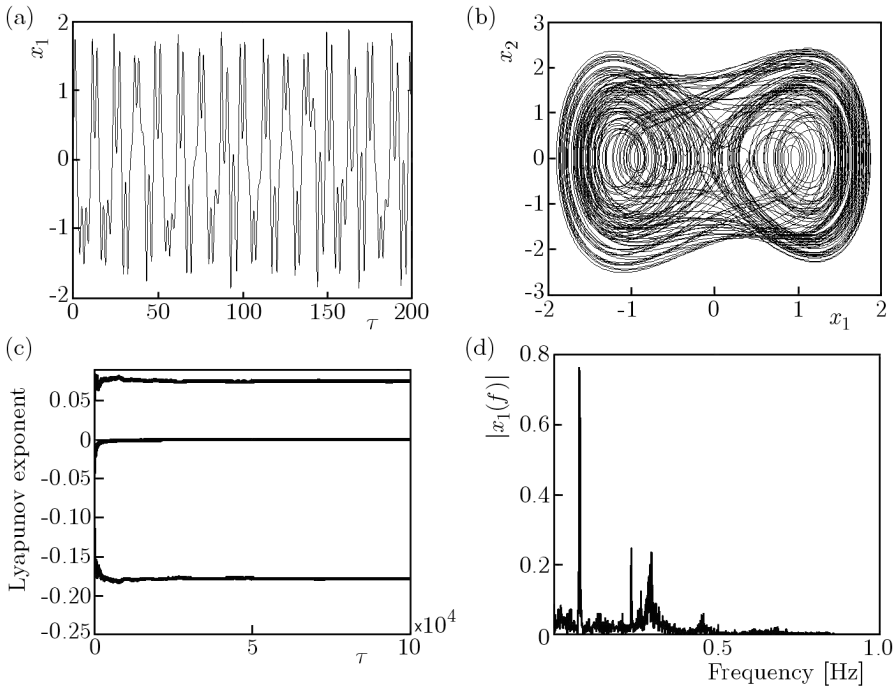

Fig. 2. (a) Displacement; (b) phase diagram; (c) Lyapunov exponent; (d) frequency spectrum

Computation of the first Lyapunov exponent $\lambda_1 = 0.075$ confirms chaotic behavior for the parameters used.

3. Proposed active control

Consider now the introduction of a controllable damper in the system, as shown in Fig. 3.

Introduction of the control U leads system (2.2) to

$$\begin{aligned} x_1' &= x_2 & x_2' &= -\alpha x_2 + \beta_1 x_1 - \beta_3 x_1^3 + \delta_1 \sin(x_3) x_4' + \delta_1 \cos(x_3) x_4^2 + U \\ x_3' &= x_4 & x_4' &= \rho_1 \sin(x_3) x_2' - \rho_3 x_4 + \rho_2 \end{aligned} \tag{3.1}$$

where

$$U = u^* + u \tag{3.2}$$

u^* will be the feedforward control and u the feedback control.

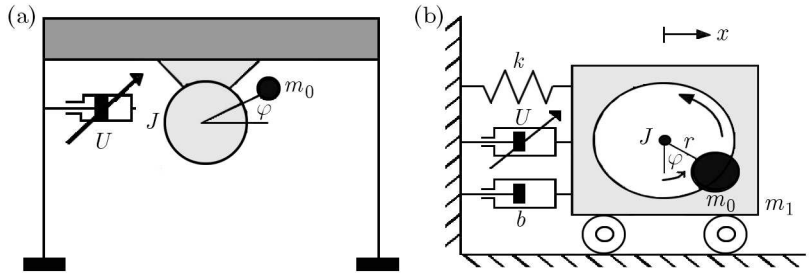

Fig. 3. (a) Portal frame with active control; (b) schematic oscillator with active control

Since the objective of this work is to control x_1 and x_2, the variables x_3 and x_4 will be considered only as disturbances of the system. Thus

$$u^* = x_2^{*\prime} + \alpha x_2^* - \beta_1 x_1^* + \beta_3 x_1^{*3} - \delta_1 \sin(x_3) x_4' - \delta_1 \cos(x_3) x_4^2 \tag{3.3}$$

Substituting (3.3) into (3.1) and defining the deviation of the desired trajectory as

$$\mathbf{y} = \begin{bmatrix} x_1 - x_1^* & x_2 - x_2^* \end{bmatrix}^{\mathrm{T}} \tag{3.4}$$

we rewrite system (3.1) in matrix form

$$\dot{\mathbf{y}} = \mathbf{A}\mathbf{y} + \mathbf{G}(\mathbf{y}, \mathbf{x}^*) + \mathbf{B}\mathbf{u} \tag{3.5}$$

where

$$\mathbf{A} = \begin{bmatrix} 0 & 1 \\ \beta_1 & -\alpha \end{bmatrix} \qquad \mathbf{B} = \begin{bmatrix} 0 \\ 1 \end{bmatrix} \qquad \mathbf{G}(y, x^*) = \begin{bmatrix} 0 \\ -\beta_3 (y_1 + x_1^*)^3 + \beta_3 x_1^{*3} \end{bmatrix}$$

The feedback control $\mathbf{u}$ can be found solving Eq. (3.6)

$$\mathbf{u} = -\mathbf{R}^{-1}\mathbf{B}^{\mathrm{T}}\mathbf{P}\mathbf{y} \tag{3.6}$$

According to Rafikov *et al.* (2008), if there are matrices $\mathbf{Q}$ and $\mathbf{R}$ ($\mathbf{Q}$ symmetric positive definite) such that

$$\mathbf{Q}^* = \mathbf{Q} - \mathbf{G}^{\mathrm{T}}(\mathbf{y}, \mathbf{x}^*)\mathbf{P} - \mathbf{P}\mathbf{G}(\mathbf{y}, \mathbf{x}^*) \tag{3.7}$$

is positive definite, the matrix $\mathbf{G}$ restricted, then the control $\mathbf{u}$ is optimal and transfers the non-linear systems from any initial state to the final state $\mathbf{y}(\infty) = \mathbf{0}$

$$J = \int_0^\infty (\mathbf{y}^{\mathrm{T}}\mathbf{Q}^*\mathbf{y} + \mathbf{u}^{\mathrm{T}}\mathbf{R}\mathbf{u})\, dt \tag{3.8}$$

The symmetric matrix $\mathbf{P}$ can be found from the Riccati algebraic equation

$$\mathbf{P}\mathbf{A} + \mathbf{A}^{\mathrm{T}}\mathbf{P} - \mathbf{P}\mathbf{B}\mathbf{R}^{-1}\mathbf{B}^{\mathrm{T}}\mathbf{P} + \mathbf{Q} = \mathbf{0} \tag{3.9}$$

For the optimal control verification (3.6), function (3.7) is numerically calculated using

$$L(t) = \mathbf{y}^{\mathrm{T}}\widetilde{\mathbf{Q}}\mathbf{y} \tag{3.10}$$

The sufficient criterion to guarantee that control (3.8) is optimal is that $L(t)$ is positive definite (Rafikov *et al.*, 2008).

3.1. Numerical simulations

Let us define the desired trajectory as being a periodic orbit $x_1^* = 0.01\cos(\pi\tau)$. As can be seen, in Fig. 2d, the choice of this orbit allows the system to keep out of the resonance region and with a low amplitude value of the displacement. Defining matrices

$$\mathbf{Q} = \begin{bmatrix} 1000 & 0 \\ 0 & 1000 \end{bmatrix} \qquad \mathbf{R} = [0.001]$$

and solving the Riccati algebraic equation (3.9), we obtain the optimal feedback control (3.6)

$$u = -1001(x_1 - x_1^*) - 1001.9(x_2 - x_2^*) \tag{3.11}$$

Substituting feedforward control (3.3) and the optimal feedback control (3.11) into (3.1), we will obtain trajectories shown in Fig. 4.

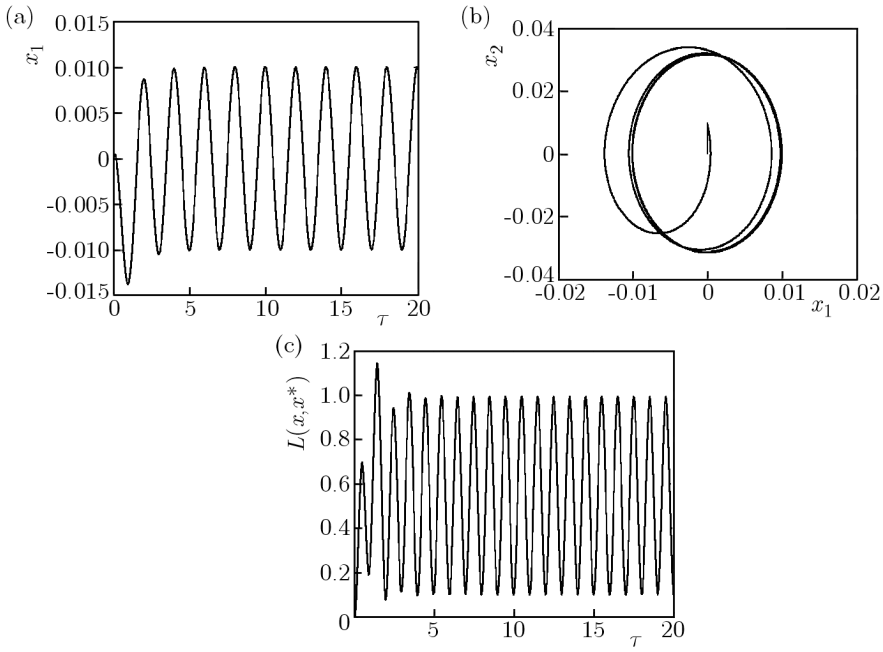

Fig. 4. (a) Displacement with active control; (b) phase portrait with active control; (c) $L(t)$ calculated in the optimal trajectory

As can be observed in Figs. 4a and 4b, the control is effective in reducing the displacement amplitude and frequency desired, and is optimal as shown in Fig. 4c.

4. Proposed control by MR damper with hysteresis

The MR damper has hysteresis effects due to a nonlinear friction mechanism. Many research efforts have been devoted to the modeling of this nonlinear behavior. An alternative is the LuGre friction model (Sakai *et al.*, 2003) which was originally developed to describe nonlinear friction phenomena (Jimenez and Alvarez, 2002).

The friction mechanism is a phenomenon in which two surfaces make contact at a number of asperities at the microscopic level. In the modified LuGre friction model (Jimenez and Alvarez, 2002), this mechanism is expressed by the average behavior of the bristles. In (Sakai *et al.*, 2003; Cetin *et al.*, 2011), another MR damper model based on the LuGre model is described as

$$\begin{aligned} F &= \sigma_a z + \sigma_0 z v + \sigma_1 \dot{z} + \sigma_2 \dot{x} + \sigma_b \dot{x} v \\ \dot{z} &= \dot{x} - \sigma_0 a_0 |\dot{x}| z \end{aligned} \tag{4.1}$$

where F is the damping force, v is the input voltage, $z(t)$ is the internal state variable [m], $\dot{x}$ is the velocity of the damper piston [m/s], σ_0 is the stiffness of $z(t)$ influenced by v [N/(mV)], σ_1 is the damping coefficient of $z(t)$ [Ns/m], σ_2 is the viscous damping coefficient [Ns/m], σ_a is the stiffness of $z(t)$ [N/m], σ_b is the viscous damping coefficient influenced by v [Ns/(mV)], a_0 is the constant value [V/N].

As can be seen in equation $(4.1)_1$, the LuGre model has a parameter that represents the voltage applied to the coil of the damper v. This parameter allows one to control the force of the MR damper through the control of the voltage v making the LuGre model the most suitable for the active control system.

4.1. Control of oscillations using an active MR damper

For numerical simulations we will consider $\dot{x}$ in equations (4.1) as $\dot{x} = -0.01\pi \sin(\pi\tau)$, and the parameters: $\sigma_0 = 8{\cdot}10^5$, $\sigma_1 = 1.6{\cdot}10^3$, $\sigma_2 = 1.5{\cdot}10^2$, $\sigma_a = 4{\cdot}10^5$, $\sigma_b = 8{\cdot}10^2$ and $a_0 = 3{\cdot}10^{-3}$ (Sakai *et al.*, 2003). In Fig. 5, one can observe the force the damper MR $(4.1)_1$.

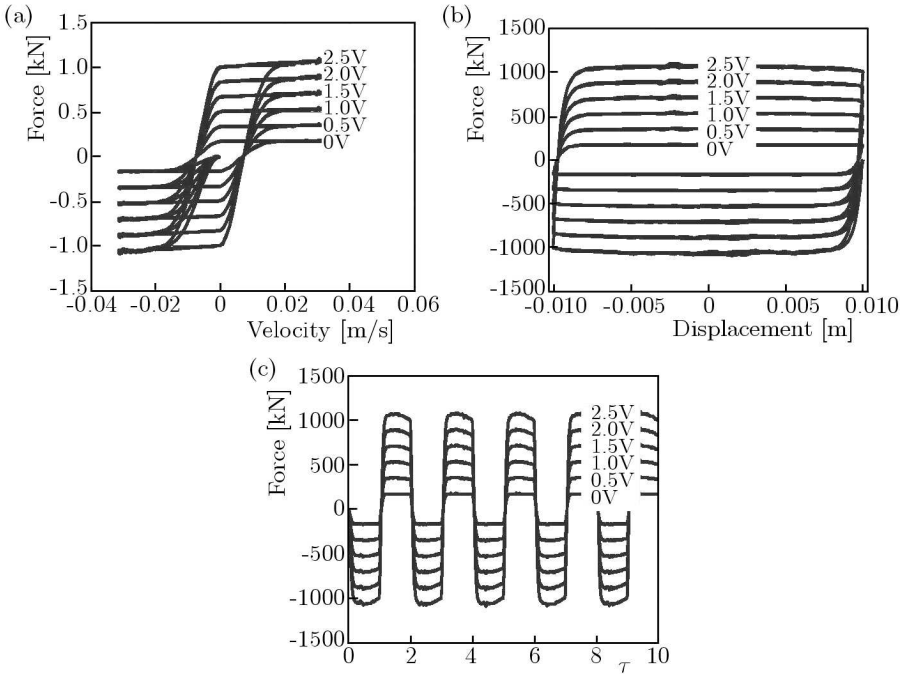

Fig. 5. Characteristics of the MR damper as a function of voltage: (a) force vs. velocity, (b) force vs. displacement, (c) force vs. time

The MR damper semi-active system and the damping force can be controlled by controlling the applied voltage in the damper coil. According to Tusset *et al.* (2013), one can numerically determine the voltage v required for the force of the MR damper F $(4.1)_1$ to coincide with the desired control force U, (3.2), obtained from the control strategy.

Considering $F = U$, the voltage to be applied can be determined by solving the following function

$$\Gamma(v) = \sigma_a z + \sigma_0 z v + \sigma_1 \dot{z} + \sigma_2 \dot{x} + \sigma_b \dot{x} v - U \tag{4.2}$$

Through Eq. (4.2), we can determine the voltage being applied to the control system considering the force estimated by the control method, such as control proposed in this paper. In Fig. 6, we can see the force applied to control the oscillations.

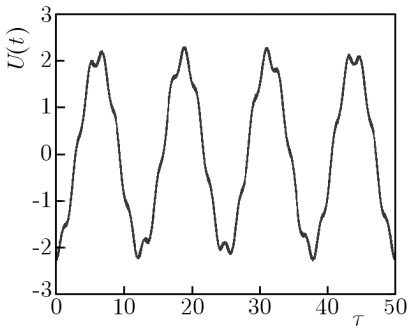

Fig. 6. Force used to control the non-ideal system

Considering forces U (Fig. 6) and F (Fig. 5) normalized, the voltage to be applied is determined by solving numerically function (4.2). In Fig. 7, we see the values of z, $\dot{z}$ and $\dot{x}$ used in equation (4.2).

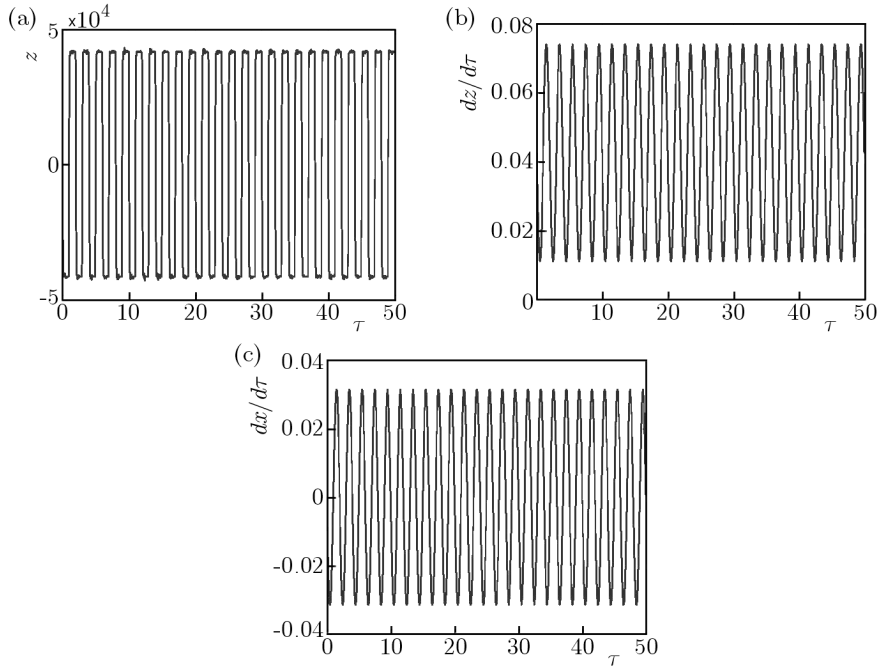

Fig. 7. (a) Internal state variable $z(\tau)$; (b) derivative of internal state variable $\dot{z}(\tau)$; (c) velocity of the piston of the damper $\dot{x}(\tau)$

In Fig. 8, we can see the voltage control estimated considering Eq. (4.2) and values from Fig. 7.

Considering these results, we can observe that the proposed methodology allowed the control of the voltage (Fig. 8) considering the force U in Fig. 6 and Eq. (4.2).

4.2. Control of oscillations using a passive MR damper

The objective of introducing a passive MR damper to the portal frame structure shown in Fig. 9 is to control the displacement of the portal frame in the same scale considered in the proposed active control.

Next, we will consider the introduction of a passive MR damper U_p into system (2.2)

$$\begin{aligned} x_1' &= x_2 & x_2' &= -\alpha x_2 + \beta_1 x_1 - \beta_3 x_1^3 + \delta_1 \sin(x_3) x_4' + \delta_1 \cos(x_3) x_4^2 - U_p \\ x_3' &= x_4 & x_4' &= \rho_1 \sin(x_3) x_2' - \rho_3 x_4 + \rho_2 \end{aligned} \tag{4.3}$$

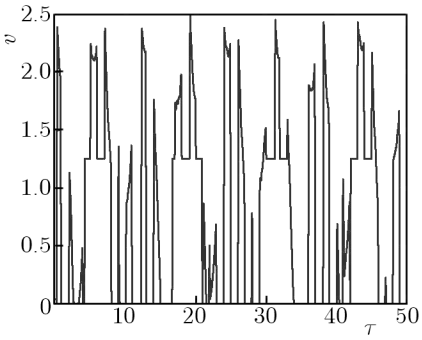

Fig. 8. Voltage used to control the non-ideal system

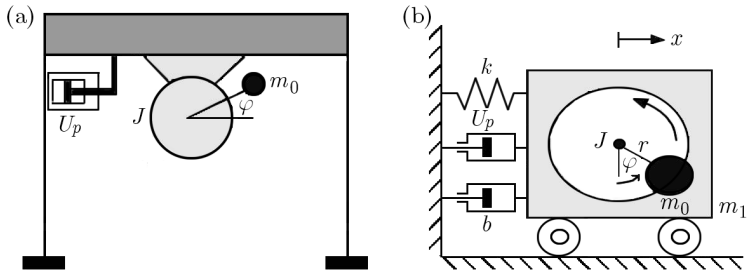

Fig. 9. (a) Portal frame with passive control; (b) schematic oscillator with passive control

where

$$U_p = \sigma_a z + \sigma_0 z v + \sigma_1 \dot{z} + \sigma_2 \dot{x} + \sigma_b \dot{x} v \tag{4.4}$$

and z is obtained by solving Eq. $(4.1)_2$.

In Figs. 10-13, we can observe motions of the portal frame for different constant voltages v applied to the MR damper, (4.4).

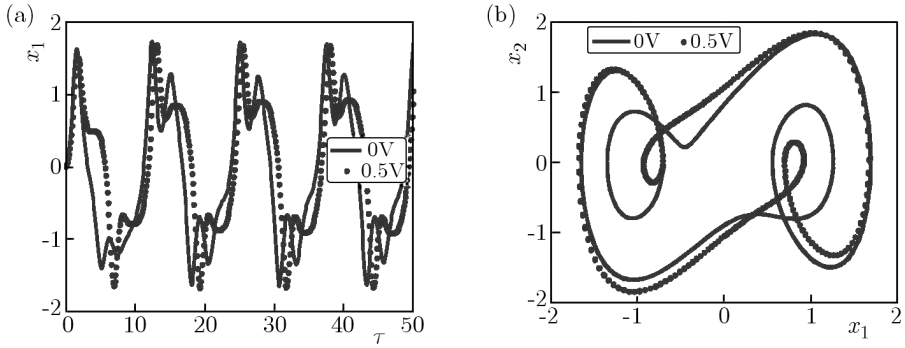

Fig. 10. Voltage $\nu = 0\,\mathrm{V}$ and $\nu = 0.5\,\mathrm{V}$: (a) displacement, (b) phase portrait

We can observe that as we increase the value of voltage, the amplitude of the displacement reduces and shifts the equilibrium point of origin. We also observe that for $\nu = 2.5\,\mathrm{V}$ the amplitudes are smaller than those obtained with the active damper. For $\nu = 2.3808\,\mathrm{V}$ we have the same displacement amplitude for the active damper and passive damping, as can be seen in Fig. 14.

As it can be seen in Fig. 14, it is possible to maintain the system on periodic orbits using the MR damper energized with $\nu = 2.3808\,\mathrm{V}$. One factor which compromises this control strategy is that the system stabilizes after a long time $\tau > 113.5$, and it is not recommended to keep the coil of the MR damper energized continuously for long periods, as required by the proposed active control (Fig. 8).

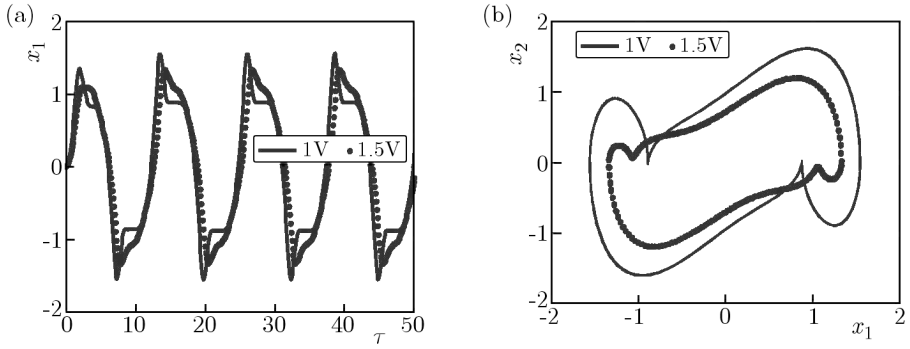

Fig. 11. Voltage $\nu = 1\,\mathrm{V}$ and $\nu = 1.5\,\mathrm{V}$: (a) displacement, (b) hase portrait

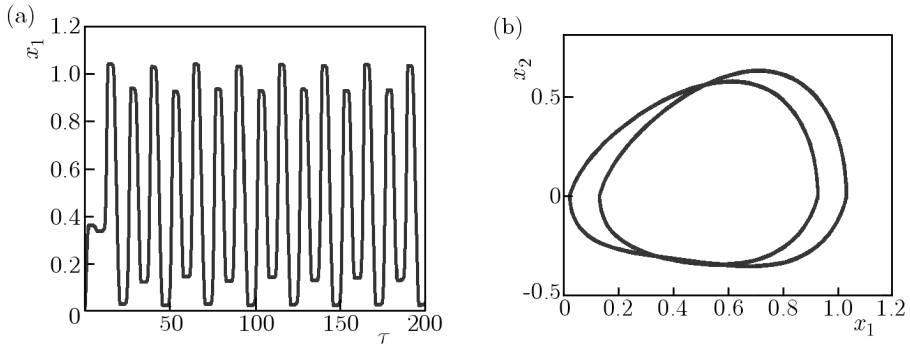

Fig. 12. Voltage $\nu = 2\,\mathrm{V}$: (a) displacement, (b) phase portrait

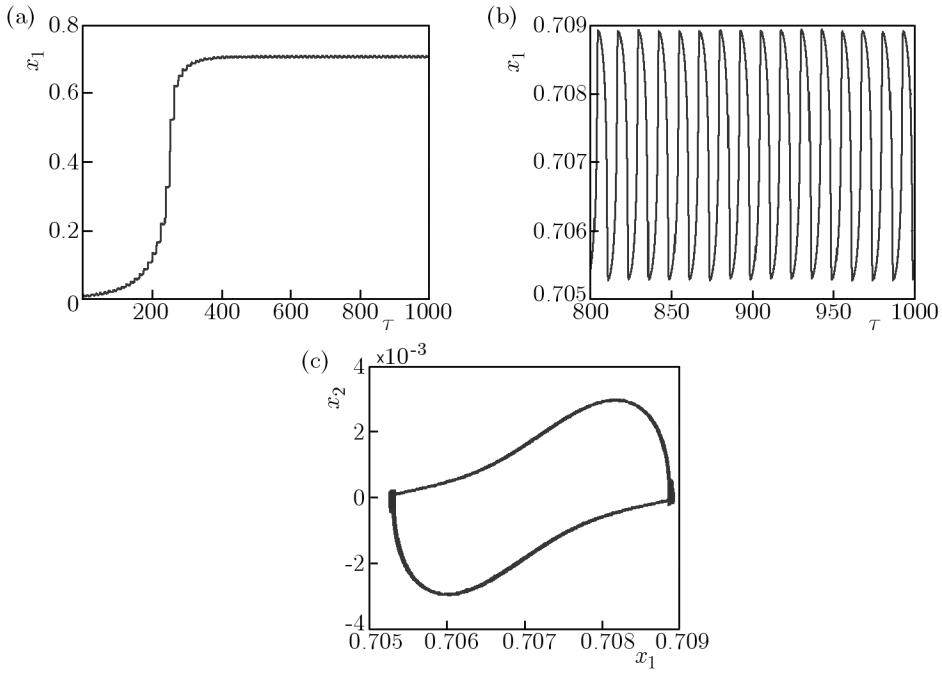

Fig. 13. Voltage $\nu = 2.5\,\mathrm{V}$: (a) displacement for $0 \leqslant \tau \leqslant 1000$, (b) displacement for $800 \leqslant \tau \leqslant 1000$, (c) phase portrait

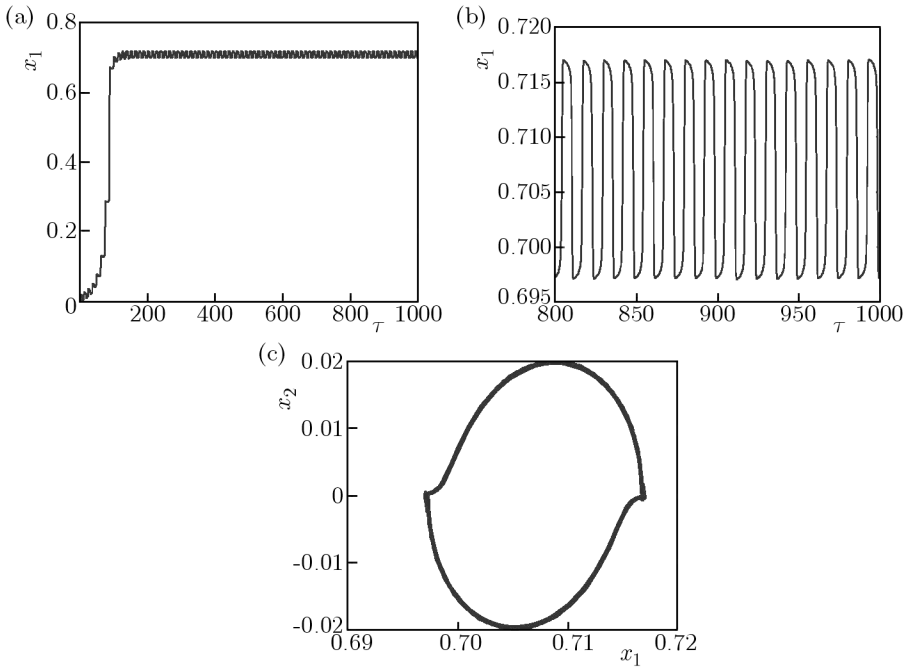

Fig. 14. Voltage $\nu = 2.3808\,\mathrm{V}$: (a) displacement for $0 \leqslant \tau \leqslant 1000$, (b) displacement for $800 \leqslant \tau \leqslant 1000$, (c) phase portrait

5. Active control with uncertainties

The parameters used in the control strategy are obtained from a certain data set. The data set provides parametric errors due to measurement errors or model uncertainties. To consider the effect of parameter uncertainties on the performance of the controller, the parameters used in the proposed control will be considered having a random error of ±20% (Balthazar *et al.*, 2014).

In order to consider the effect of parameter uncertainties on the performance of the controller, the real unknown parameters of the system are supposed to be as follows: $\widehat{\alpha} = 0.08 + 0.04r(t)$, $\widehat{\beta}_1 = 0.8 + 0.4r(t)$, $\widehat{\beta}_3 = 1.6 + 0.8r(t)$, $\widehat{\delta}_1 = 6.6984 + 3.3492r(t)$, $\widehat{\rho}_1 = 0.04 + 0.02r(t)$, $\widehat{\rho}_2 = 80 + 40r(t)$ and $\widehat{\rho}_3 = 160 + 80r(t)$, where $r(t)$ are normally distributed random functions. To analyze the sensitivity of the error, we consider

$$\begin{bmatrix} e_1 \\ e_2 \end{bmatrix} = \begin{bmatrix} x_1 - \widehat{x}_1 \\ x_2 - \widehat{x}_2 \end{bmatrix} \tag{5.1}$$

where x_i is obtained for the control without parametric errors and $\widehat{x}_i$ is obtained for the control with the parametric error $(i = 1, 2)$.

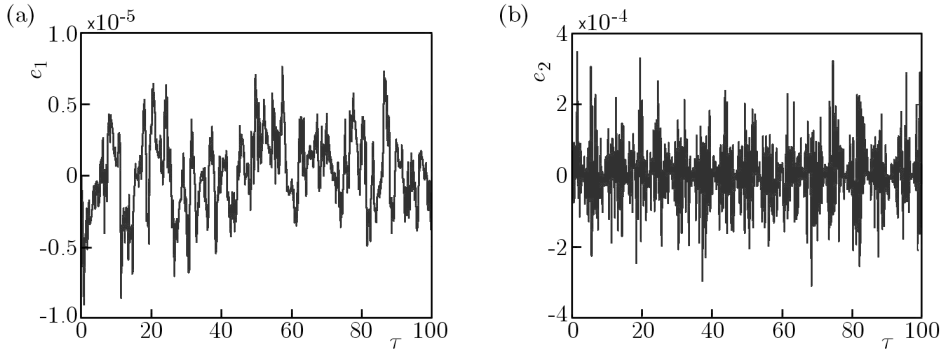

Fig. 15. Error of uncertainty in parameters: (a) $x_1 - \widehat{x}_1$, (b) $x_2 - \widehat{x}_2$

In Fig. 15, we can observe the sensitivity of the proposed active control with parametric errors.

As can be observe in Fig. 15, the proposed active control is somewhat sensitive to parametric errors being under 10^{-4}.

6. Conclusions

As can be seen in Figs. 4a and 4b, with the proposed association of feedforward control u^* (3.3) and feedback u (3.11), it is possible to control the oscillations of the studied portal frame structure under non-ideal loading into periodic orbits, and the control is optimal (Fig. 4c). Our model of the MR damper force (4.2) allows us to determine the electrical current to be applied to the dampers, as shown in Fig. 8. Regarding the use of the passive control, it is possible to observe that to keep the system in a periodic displaced orbit, the origin must be changed. Thus, the active control is more indicated, as it keeps the oscillations around the origin. With respect to the parametric sensitivity, the active control proved to be less sensitive than the passive control.

With the results obtained, we can conclude that the proposed active control using a MR damper is more appropriate than the use of a passive MR damper.

Acknowledgments

The authors acknowledge the financial support by FAPESP and CNPq (grant: 420026/2013-4 and grant: 484729/2013-6), both Brazilian research funding agencies.

References

1. Balthazar J.M., Tusset A.M., Bueno A.M., 2014, TM-AFM nonlinear motion control with robustness analysis to parametric errors in the control signal determination, *Journal of Theoretical and Applied Mechanics*, **52**, 1, 93-106
2. Bolla M., Balthazar J.M., Felix J.L.P., Mook D.T., 2007, On an approximate analytical solution to a nonlinear vibrating problem, excited by a non-ideal motor, *Nonlinear Dynamics*, **50**, 841-847
3. Castão K.A.L., Goes L.C.S., Balthazar J.M., 2010, A note on the attenuation of the sommerfeld effect of a non-ideal system taking into account a MR damper and the complete model of a DC motor, *Journal of Vibration and Control*, **17**, 7, 1112-1118
4. Cetin S., Zergeroglu E., Sivrioglu S., Yuksek I., 2011, A new semiactive nonlinear adaptive controller for structures using MR damper: Design and experimental validation, *Nonlinear Dynamics*, **66**, 4, 731-743
5. Djanan A.A.N., Nbendjo B.R.N., Woafo P., 2013, Electromechanical control of vibration on a plate submitted to a non-ideal excitation, *Mechanics Research Communications*, **54**, 72-82
6. Dutta S., Chakraborty G., 2014, Performance analysis of nonlinear vibration isolator with magneto-rheological damper, *Journal of Sound and Vibration*, **333**, 5097-5114
7. Dyke S.J., Spencer B.F. Jr., Sain M.K., Carlson J.D., 1996, Modeling and control of magnetorheological dampers for seismic response reduction, *Smart Materials and Structures*, **5**, 565-575
8. Jimenez R., Alvarez L., 2002, Real time identification of structures with magnetorheological dampers, *Proceedings of the 41st IEEE Conference on Decision and Control*, 1017-1022
9. Jimenez R., Alvarez L., 2005, LuGre friction model for a magnetorheological damper, *Structural Control and Health Monitoring*, **12**, 91-116

10. Kasemi B., Muthalif A.G.A., Rashid M.M., Fathima S., 2012, Fuzzy-PID Controller for semi-active vibration control using magnetorheological fluid damper, *Procedia Engineering*, **41**, 1221-1227

11. Piccirillo V., Tusset A.M., Balthazar J.M., 2014, Dynamical jump attenuation in a non-ideal system through magneto rheological damper, *Journal of Theoretical and Applied Mechanics*, **52**, 2, 595-604

12. Rafikov M., Balthazar J.M., Tusset A.M., 2008, An optimal linear control design for nonlinear systems, *Journal of the Brazilian Society of Mechanical Sciences and Engineering*, **30**, 279-284

13. Rafikov M., Balthazar J.M., 2004, On an optimal control design for Rössler system, *Physics Letters A*, **333**, 241-245

14. Sakai C., Ohmori H., Sano A., 2003, Modeling of MR damper with hysteresis for adaptive vibration control, *Proceedings of the 42nd IEEE Conference on Decision and Control*, 3840-3845

15. Samantaray A.K., Dasgupta S.S., Bhattacharyya R., 2010, Sommerfeld effect in rotationally symmetric planar dynamical systems, *International Journal of Engineering Science*, **48**, 21-36

16. Spencer Jr. B.F., Dyke S.J., Sain M.K., Carlson J.D., 1997, Phenomenological model of a magnetorheological damper, *ASCE Journal of Engineering Mechanics*, **3**, 230-238

17. Terasawa T., Sakai C., Ohmori H., Sano A., 2004, Adaptive identification of MR damper for vibration control, *Proceedings of the 43rd IEEE Conference on Decision and Control*, 14-17

18. Tusset A.M., Balthazar J.M., 2013, On the chaotic suppression of both ideal and non-ideal Duffing based vibrating systems, using a magnetorheological damper, *Differential Equations and Dynamical Systems*, **21**, 105-121

19. Tusset A.M., Balthazar J.M., Felix J.L.P., 2013, On elimination of chaotic behavior in a non-ideal portal frame structural system, using both passive and active controls, *Journal of Vibration and Control*, **19**, 803-813

20. Tusset A.M., Balthazar J.M., Chavarette F.R., Felix J.L.P., 2012, On energy transfer phenomena, in a nonlinear ideal and nonideal essential vibrating systems, coupled to a (MR) magneto-rheological damper, *Nonlinear Dynamics*, **69**, 1859-1880

21. Tusset A.M., Rafikov M., Balthazar J.M., 2009, Intelligent controller design for magneto-rheological damper based on quarter-car model, *Journal of Vibration and Control*, **15**, 1907-1920

Manuscript received May 9, 2014; accepted for print February 10, 2015

JOURNAL OF THEORETICAL AND APPLIED MECHANICS
53, 3, pp. 665-672, Warsaw 2015
DOI: 10.15632/jtam-pl.53.3.665

NUMERICAL ANALYSIS OF STRESS INTENSITY FACTOR AND T-STRESS IN PIPELINE OF STEEL P264GH SUBMITTED TO LOADING CONDITIONS

Hassane Moustabchir

Équipe Science et Ingénierie des Matériaux (ESIM), Département de Physique, Université My Ismaïl, Errachidia, Morocco; e-mail: hmoustabchir74@gmail.com

Jamal Arbaoui

ENSTA Bretagne, LBMS/DFMS, Brest Cedex, France; e-mail: jamal.arbaoui@ensta-bretagne.fr

Azari Zitouni

LaBPS, Université Paul Verlaine Metz,Ecole Nationale d'Ingénieurs de Metz, Metz, France

Said Hariri

TPCIM, Ecole des Mines de Douai, Douai Cedex, France

Ihor Dmytrakh

Karpenko Physico-Mechanical Institute of National Academy of Sciences of Ukraine, Lviv, Ukraine

Stress singularities occur at crack tips, corners and material interfaces. The stress intensity factors and T-stresses are coefficients of structural components where the active stress singular and first regular stress terms, respectively, are denoted by William's eigen function expansion series. A finite element analysis by CASTEM 2000 have been undertaken in order to determine the evolution of the T-stress and stress intensity factor terms in mode I for an arc of pipeline specimens with an external surface crack. A stress difference method described by Moustabchir *et al.* (2012) are adapted and, in the following step, the volumetric method is then embedded to compute the SIFs and T-stress near the crack tip. Different crack geometries combined with different length-to-thickness ratios are examined for the T-stress and stress-intensity factor. The revisited stress difference method employed here shows to be an accurate and robust scheme for evaluating the T-stress/SIFs in an arc of the pipeline.

Keywords: T-stress, Stress Intensity Factor (SIF), Finite Element Method (FEM), Stress Difference Method (SDM), volumetric method

1. Introduction

Fracture behavior of materials is generally characterized by a single parameter such as the SIF. Traditionally, the SIF has been used in the determination of initiation and propagation of cracks in brittle materials. However, the introduction of a second fracture parameter, as well as the T-stress, allows better understanding of the effect of structural and loading configuration at the crack tip, even that the physical significance of this parameter inserted is limited. To correlate the higher term effects with an appropriate physical parameter, a difficult task to simplify the higher terms to define the T-stress term was conducted (Nakamura and Parks, 1991; Du and Hancock, 1991). The T-stress is defined as constant stress acting parallel to the crack and its magnitude is proportional to the nominal stress in the vicinity of the crack. A positive T-stress strengthens the level of crack tip stress triaxiality and leads to high crack tip constraint; while a negative T-stress reduces the level of crack tip stress triaxiality and leads to the loss of the crack tip constraint. It was noted (Nakamura and Parks, 1991; Smith *et al.*, 2001) that T-stress, which is the non-singular linear elastic stress component parallel to the crack, characterizes the

local crack tip stress field for an elastic linear material, and the elastic plastic material with the restriction of small-scale yielding conditions.

In this paper, we revise the method described by Moustabchir *et al.* (2012) using directly single Finite Element (FE) analysis by CASTEM 2000 program. The Stress Difference Method (SDM) adapted here is developed to compute the elastic T-stress efficiently and accurately by evaluating $(\sigma_{xx} - \sigma_{yy})$ at a point ahead of the crack tip. The powerful idea shows that the errors acquired in the numerical values of σ_{xx} and σ_{yy} near the of crack tip evolve with x, i.e. the distance from the crack tip, and their difference eliminates the errors effectively. For a homogeneous material, we calculate the T-stress using the difference of the normal stresses along $\theta = 0$, i.e. $(\sigma_{xx} - \sigma_{yy})$, which is a method that can lead to significant numerical errors due to the recovery of stresses very close to the crack tip. We then present a volumetric method for computing T-stress and stress intensity factor K_I in mode I by modifying the stress difference method, the so-called Modified Stress Difference Method (MSDM). Details of the volumetric method were well explained by Pluvinage (2003). Condequently, in Section 4, we pay attention to it presenting a clear evidence that it agrees with our case studied. The physical meaning of the results is discussed, giving a better solution to the detection of the pipelines integrity.

2. Finite element analysis

In an isotropic linear elastic body containing a three-dimensional crack subject to a symmetric loading, the stresses developed in front of the crack for each dimension can be written as a series expansion (2012). Near the crack tip (see details of the crack tip in Fig. 1), the higher order terms of the series expansion are negligible, thus the stresses for mode I fracture can be written

$$\begin{aligned}
\sigma_{xx} &= \frac{K_I}{\sqrt{\pi r}} \cos\frac{\theta}{2}\Big(1 - \sin\frac{\theta}{2}\sin\frac{3\theta}{2}\Big) + T & \sigma_{yy} &= \frac{K_I}{\sqrt{\pi r}} \cos\frac{\theta}{2}\Big(1 + \sin\frac{\theta}{2}\sin\frac{3\theta}{2}\Big) \\
\sigma_{zz} &= \frac{K_I}{\sqrt{\pi r}} 2\nu \cos\frac{\theta}{2} + E\varepsilon_{zz} + \nu T & \sigma_{xy} &= \frac{K_I}{\sqrt{\pi r}} \sin\frac{\theta}{2}\cos\frac{\theta}{2}\cos\frac{3\theta}{2} \\
\sigma_{xz} &= \sigma_{yz} = 0
\end{aligned} \tag{2.1}$$

where K_I is mode I local stress intensity factor, E is Young's modulus and ν is Poisson's ratio. Here, T is the elastic T-stress representing tension/compression acting parallel to the cracked plane.

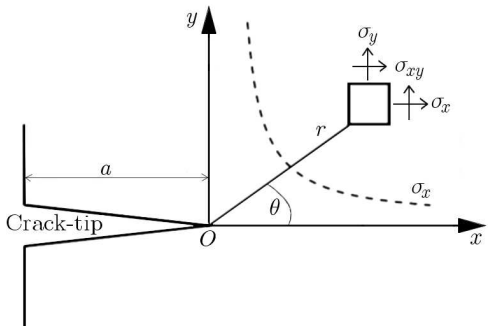

Fig. 1. Crack-tip cartesian coordinates (x, y) and polar coordinates (r, θ)

The subscripts x, y and z in Fig. 1 describe the local Cartesian co-ordinate system formed by the plane normal to the crack front and the plane tangential to the crack front point; r and θ are the local polar co-ordinates.

In mode I loading, equation (2.1) (state of σ_{xx}) shows that the stress comprises a singular term and the T part

$$T = (\sigma_{xx} - \sigma_{yy})_{r=0,\,\theta=0} \tag{2.2}$$

The T-stress developed varies with different crack geometries and loading. It plays the dominant role on shape and size of the plastic zone, while estimating the degree of local crack tip yielding, and also in quantifying the fracture toughness. In a particular case of $K_{II} = 0$, Mostafavi *et al.* (2010) stated that T must be proportional to the reference stress σ_{xx} and, therefore, it can be normalized to obtain biaxial stress ratios

$$\beta = \frac{T\sqrt{\pi r}}{K_I} \tag{2.3}$$

The finite element method has been used to determine the crack-tip parameters T and K for the an arc of pipe specimens. The structures are modeled by CASTEM 2000 code in two dimensions under plane strain conditions using free-meshed isoparametric quadrilateral elements, with quarter-point singularity elements at the crack-tip. Only one half of the test apparatus has been modelled due to symmetry in the geometry and loading conditions. The mesh generated for the elastic analyses comprises 31485 elements and 63526 nodes. The arc of pipeline fracture specimen geometry is illustrated in Fig. 2a. A fan-like mesh focused at the crack tip (on the plane perpendicular to the crack front, see Fig. 2b) is employed because this yields more accurate T-stress values. Furthermore, a detailed mesh sensitivity study has shown that further refinement

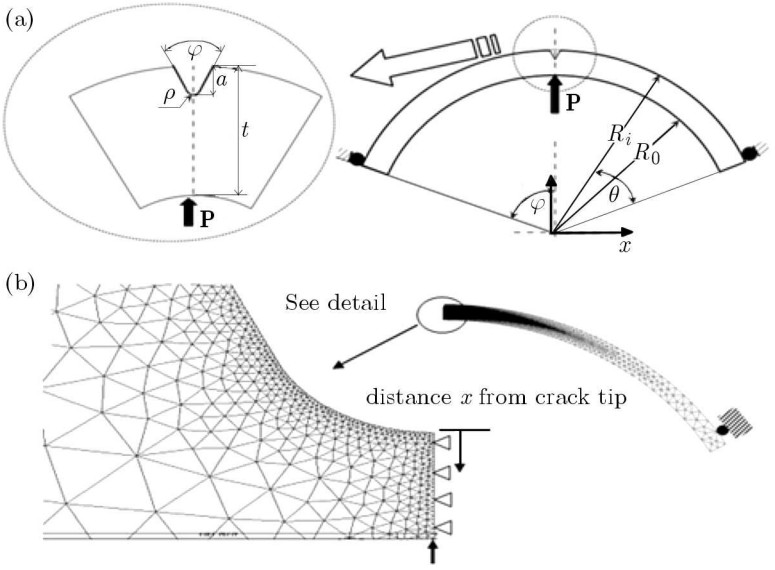

R_i [mm]	P [N]	Φ [°]	θ [°]	φ [°]	ρ [mm]	a [mm]	t [mm]
219.55	150	60	60	45	0.15	1.22-4.88	6.1

Fig. 2. (a) Geometry of sample with boundary conditions and loading configuration using an arc of the pipe. (b) Typical 2D finite-element mesh used to model the cracked arc of the pipe for elastic analysis

of the mesh leads to small changes only ($< 1\%$). The wall thickness of the pipeline is 6.1 mm and length 40 mm. The specimen is loaded by a concentrate force ($P = 150$ N) on the top of the TPB specimen in the symmetric plane. The support and the symmetric boundary conditions are also used in this model. The material used in this survey is steel P264GH. The stress/strain curve of the material is represented by the Ramberg-Osgood curve generated during the hardening processes and expressed as

$$\frac{\varepsilon}{\varepsilon_0} = \frac{\sigma}{\sigma_y} + \alpha\Big(\frac{\sigma}{\sigma_y}\Big)^n \tag{2.4}$$

In Eq. (2.4), ε_0, σ_y, α and n are constants, and $E\varepsilon_0 = \sigma_y$. A model that encloses deformation plasticity processes with only a small geometry change as well as continuum model is invoked. We take $\alpha = 1$ and $\sigma_y = 410\,\text{MPa}$. Two values of the strain hardening exponent n are embedded, with the values of $n = 1$ and $n = 0.0446$. The case of $n = 1$ corresponds to the elastic path. A series of finite element analyses are performed for different crack length ratios a/t. The chemical compositions of the material samples are included in Table 1, and the true stress versus strain curve that shows the behavior for this material are plotted in Fig. 3.

Table 1. Chemical composition of material specimens (weight %)

Material	C	Mn	S	Si	P	Al	Fe
Tested steel	0.135	0.665	0.002	0.195	0.013	0.027	Bal.
Steel P264GH according to Standard EN10028.2-92	0.18	1	0.015	0.4	0.025	0.02	Bal.

Table 2. Mechanical properties of steel P264GH

Young's modulus	$E = 207000\,\text{MPa}$
Poisson's ratio	$\nu = 0.3$
Yield stress	$\sigma_y = R_e = 410\,\text{MPa}$
Ultimate tensile strength	$R_m = 440\,\text{MPa}$
Elongation to fracture	$A = 35\%$

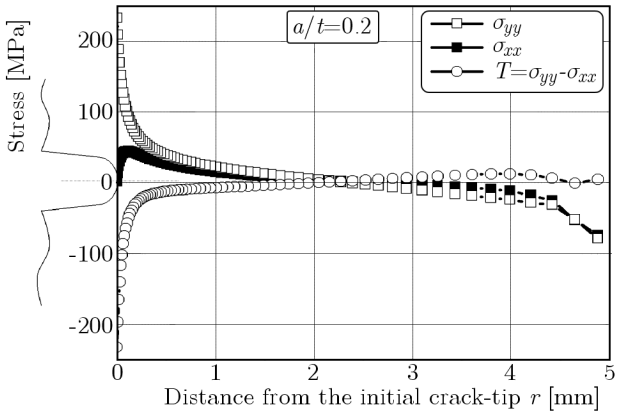

Fig. 3. T-stress definition by the stress difference method ($a/t = 0.2$)

3. Mode I stress intensity factors and T-stresses results

The calculated mode I stress intensity factor K_I and the T-stress are plotted in Fig. 4. T-stress variations presented in Fig. 3 (at the near crack tip $x < 1\,\text{mm}$) denote that T is more sensitive for all cases and the results from the arc of pipe specimens show that the SDM does not provide a constant value of T. It first increases with the crack length and then decreases rapidly. Later, it decreases slowly along the distance x for any ratio of a/t. When the ratio $a/t < 0.4$ is reached and the distance from crack tip $x > 0.23\,\text{mm}$, the T-stress seems to remain constant at $0 \sim -25\,\text{MPa}$, while T decreases strongly with the increase of the crack length when $a/t \geqslant 0.4$. The change of sign of the T-stress from positive to negative may be due to the fact that the magnitude of the local moment closing the crack increases with an increase in the crack depth. The negative values for the arc of pipe specimens indicate a low crack front constraint and an extended plastic

deformation around the crack front. This conforms to the solutions of the T-stress for a 2D single edge crack under tension (Smith *et al.*, 2001; Mostafavi *et al.*, 2010; Moustabchir, 2012; Lu and Meshii, 2014). The T-stress becomes more negative when the free surface is closed due to the loss of crack-front constraint.

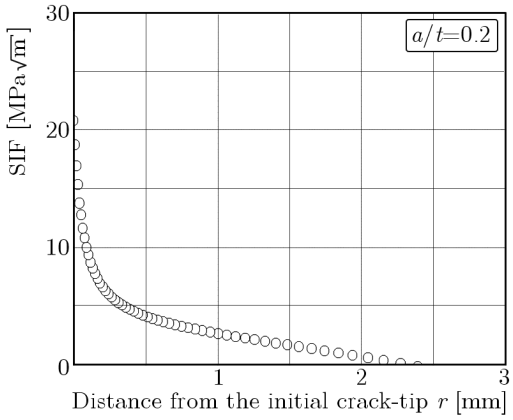

Fig. 4. An example of evaluation of different stresses for $a/t = 0.2$

Notably, the T-stress has always the same value ($T = 23.3\,\mathrm{MPa}$) at a distance $x = 0.24\,\mathrm{mm}$ for any given crack length. It is worth noting that the T-stress variations with the crack depth and the crack length for the bending loading case are in agreement with the results reported by Wang and Bell (2004) for plates and Jayadevan *et al.* (2005) (work devoted to studies on the pipes behavior). However, the variation of T-stress with crack depth in plates is just the reverse of that observed in pipes under bending (Wang, 2003). This is evidenced when the crack depthincrease, while the T-stress in pipes under bending decreases slowly and remains negative (see Fig. 3). It strongly increases for the plate from a negative to a high positive value (Wang, 2003). In Fig. 4, we show the results obtained from the bending loading. Variations of the SIF presented as the ratio of $d/t = 36$ show that the decrease in the SIF with crack length is not monotonic as verified by 2D analyses. With an increasing of the ratio a/t, the SIF increases strongly at the crack tip (Fig. 4). The effect of crack length is more pronounced for short cracks compared to long cracks. Furthermore, for the shortest crack, an increase in the SIF with crack depth becomes marginal for the ratio $a/t = 0.2$. The results were confirmed by the powerful research developed in works by Jayadevan *et al.* (2005).

Note that the stress intensity factors always increases for a distance of $x < 0.115\,\mathrm{mm}$ for any ratios a/t and then decreases along the crack length. K always has a maximum at $x \approx 0.11$ for any given cracklength. In Fig. 4, we present the results obtained from variations of the SIF for deep cracks ($a/t = 0.2$-0.8). The SIF increases strongly with an increase in the crack length and becomes positive until reaching the maximum value for $a/t = 0.6$, then decreases for negative values. Note that for $a/t = 0.7$, the SIF vanishes.

In order to normalize the effect of the T-stress relatively to the stress intensity factor in mode I, Mostafavi *et al.* (2010) proposed in Eq. (2.3) a dimensionless parameter called the biaxiality ratio β. Figure 5 shows the variation of the biaxiality ratio versus the ratio of crack length-to-width a/t for various distances near the tip-crack. The sign of the biaxiality ratio changes from positive to negative values as the distance from the crack tip increases. Near the crack tip and for the shortest crack, $a/t < 0.4$, the ratio $T\sqrt{\pi a}/K_I$ decreases strongly along a certain distance and then reaches a positive value. On the other hand, for $a/t \geqslant 0.4$, T-stresses change from positive to negative values when $x < 0.3\,\mathrm{mm}$. Considering a slight imperfection under mode I loading, Hadj Meliani *et al.* (2010) found that the crack path is stable for negative T-stresses and unstable for positive T-stresses.

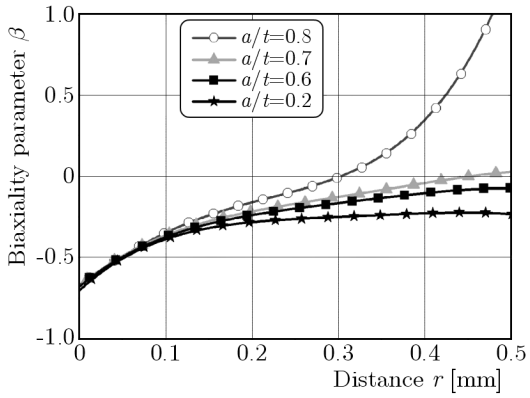

Fig. 5. Biaxiality ratio for an arc of the pipe specimen; (a) distribution of $T\sqrt{\pi a}/K_I$ along the crack length, (b) biaxiality ratio versus the crack length-to-width ratio a/t for mode I near the tip crack

A distance from the crack tip greater than 0.3 mm is sufficient for most problems, except when a/t is large, see Fig. 6. Fracture criteria that include the SIFs and T-stress can be implemented in the present code and used to predict the crack initiation angle. These remarks are in agreement with the results from well-known authors, see e.g. Ayatollah *et al.* (1998). The variations of the biaxiality ratio versus the crack length-to-width ratio a/t for two specimens (SENB and SENT) published by Fett (1997) using the boundary collocation method, also the method proposed by Kim and Paulino (2003) using the FEM and by Sutradhar and Paulino (2004) employing the interaction integral method, are compared to the present results using an arc of a pipe subject to bending loading (Fig. 3). At the notch of the crack, Fig. 5 shows that the stress difference method (SDM) provides a constant value for $T\sqrt{\pi a}/K_I$ and the sign remains the same between 2.6 and 2.8 for any ratio a/t.

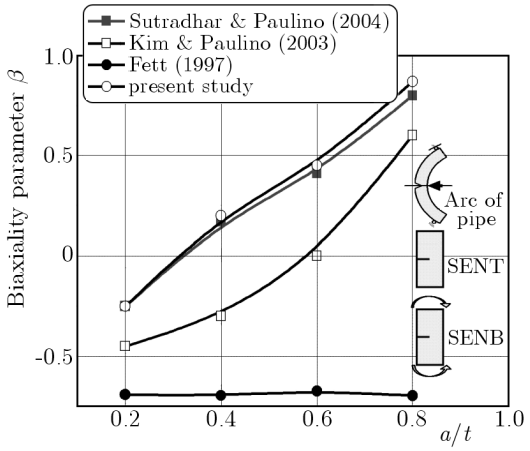

Fig. 6. Biaxiality ratio versus a/t for various specimens at the notch of the crack

4. Evaluation of the SIF and T-stress by the volumetric method

The elastic and elastic-plastic normal stress intensity factor distribution at the notch tip exhibits a decreasing trend with distance from the notch tip. A careful analysis demonstrated for this configuration was initiated by Pluvinage (2003). It characterized three zones, as shown in Fig. 7: the first one is very near the notch tip where the normal SIF is practically constant and/or increasing to its maximum value K_I^{max}, the intermediate zone and the third one are considered as the location where the pseudo stress intensity factor singularity can be simulated.

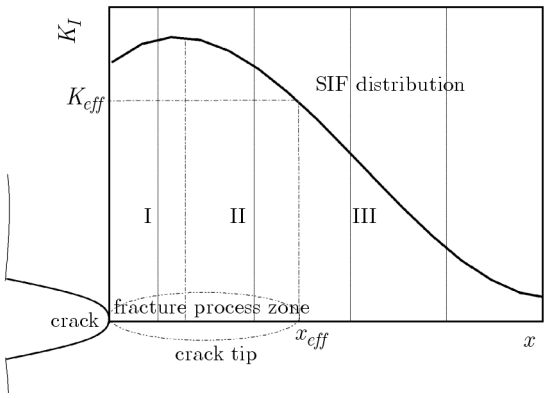

Fig. 7. Schematic SIF distribution at the notch tip for definition of fracture parameters – the effective SIF and effective distance

It is assumed that the fracture process needs a physical volume. This assumption is supported by the fact that fracture resistance is affected by the loading mode, structure geometry and scale effect. The values of the hot spot in the neighborhood of any point in the fracture process volume are taken into account. This volume is assumed to be quasi-cylindrical by analogy to the notch plastic zone, which has a similar shape. The diameter of this cylinder is called the effective distance x_{eff}. The effective stress intensity factor and the effective T-stress can be estimated by averaging the value of SIF distribution along this effective distance (Pluvinage, 2003).

Although many works have estimated the stress intensity factors with the presence of T-stress of an arc of a pipe, they have exclusively used the fracture mechanics to estimate the toughness. According to recent investigations, other methods are applied to predict the T-stress and stress intensity factors. One of these methods, named the volumetric approach, is concerned with the modification of the Stress Difference Method (SDM). The volumetric approach is a macro-mechanical method and it uses an elastic-plastic distribution and the stress intensity factor gradient evolution to predict the stress intensity factor. The main idea of this method is the application of the effective stress intensity factor to the region near notch roots and examination of intrinsic characteristics of this small size as well as the essential zone by consideration of numerical SIF results including non-linear behavior of materials.

5. Concluding remarks and extensions

- In mode I, the T-stress can be obtained by direct use of the stress difference method (SDM) along the crack. The SDM, applied to evaluate the T-stress and SIFs, provides an accurate and robust scheme for calculating the fracture parameters.
- The numerical results obtained by CASTEM 2000 are in good agreement with known results for single cracks. In general, the T-stress computations are more time-consuming than those for SIFs. This observation is in agreement with analogous studies in the FEM fields.
- The results for T are strongly highlighted near the crack tip and far away from the crack tip, and depend on the geometrical parameters.
- In general, the T-stress has larger domain dependence or contour dependence than the stress intensity factors or the J-integral. The data for T-stresses as well as mode I stress intensity factor K_I are represented by simple fit relations.
- The ratio obtained from the numerical results by several researchers showed some difference from the predicted stress intensity factor in mode I with and without presence of the T-stress. It can be reasonably predicted from the regression result and using the relation-

ship $(K_I/K_{IC})^2 + \alpha(T/T_{crit})^2$ where α is an empirical constant and T_{crit} is the critical T-stress.

- The data for T-stresses as well as for mode I stress intensity factor are represented by simple fit relations.

References

1. Ayatollah M.R., Pavier M.J., Smith D.J., 1998, Determination of T-stress from finite element analysis for mode I and mixed mode I/II loading, *International Journal of Fracture*, **91**, 283-298
2. CASTEM 2000.http://www-cast3m.cea.fr/cast3m/index.jsp
3. Du Z.-Z., Hancock J.W., 1991, The effect of non-singular stresses on crack-tip constraint, *Journal of the Mechanics and Physics of Solids*, **39**, 555-567
4. Fett T., 1997, A Green's function for T-stresses in an edge cracked rectangular plate, *Engineering Fracture Mechanics*, **57**, 365-373
5. Hadj Meliani M., Azari Z., Pluvinage G., Matvienko Yu.G., 2010, The effective T-stress estimation and crack paths emanating from U-notches, *Engineering Fracture Mechanics*, **77**, 1682-1692
6. Jayadevan K.R., Thaulow C., Østby E., Berg B., Skallerud B., Holthe K., Nyhus B., 2005, Structural integrity of pipelines: T-stress by line-spring, *Fatigue and Fracture of Engineering Materials and Structures*, **28**, 467-488
7. Kim J.-H., Paulino G.H., 2003, T-stress, mixed-mode stress intensity factors, and crack initiation angles in functionally graded materials: a unified approach using the interaction integral method, *Computer Methods in Applied Mechanics and Engineering*, **192**, 1463-1494
8. Lu K., Meshii T., 2014, Three-dimensional T-stresses for three-point-bend specimens with large thickness variation, *Engineering Fracture Mechanics*, **116**, 197-203
9. Mostafavi M., Smith D.J., Pavier M.J., 2010, Reduction of measured toughness due to out-of-plane constraint in ductile fracture of aluminium alloy specimens, *Fatigue and Fracture of Engineering Materials and Structures*, **33**, 724-739
10. Moustabchir H., Azari Z., Hariri S., Dmytrakh I., 2012, Three-dimensional t-stress to predict the directional stability of crack propagation in a pipeline with external surface crack, *Key Engineering Materials*, **498**, 31- 41
11. Nakamura T., Parks D.M., 1991, Determination of elastic T -stress along three-dimensional crack fronts using an interaction integral, *International Journal of Solids and Structures*, **29**, 1597-1611
12. Pluvinage G., 2003, *Fracture and Fatigue Emanating from Stress Concentrators*, Kluwer Publisher, Springer link. 978, 1-4020
13. Smith D.J., Ayatollahi M.R., Pavier M.J., 2001, The role of T-stress in brittle fracture for linear elastic materials under mixed-mode loading, *Fatigue and Fracture of Engineering Materials and Structures*, **24**, 137-150
14. Sutradhar A., Paulino G.H., 2004, The simple boundary element method for transient heat conduction in functionally graded materials, *Computer Methods in Applied Mechanics and Engineering*, **193**, 4511-4539
15. Wang X., 2003, Elastic T-stress solutions for semi-elliptical surface cracks in infinite thickness plates, *Engineering Fracture Mechanics*, **70**, 731-756
16. Wang X., Bell R., 2004, Elastic T-stress solutions for semi-elliptical surface cracks infinite thickness plates subject to non-uniform stress distributions, *Engineering Fracture Mechanics*, **71**, 1477-1496

Manuscript received October 13, 2014; accepted for print February 11, 2014

JOURNAL OF THEORETICAL AND APPLIED MECHANICS
53, 3, pp. 673-682, Warsaw 2015
DOI: 10.15632/jtam-pl.53.3.673

WAVE PROPAGATION IN PIEZOELECTRIC RINGS WITH RECTANGULAR CROSS-SECTIONS

Xiaoming Zhang
School of Mechanical and Power Engineering, Henan Polytechnic University, Jiaozuo, P.R. China
e-mail: zxmworld11@163.com

Youchao Wang
School of Materials Science and Engineering, Henan Polytechnic University, Jiaozuo, P.R. China
e-mail: wangyc@hpu.edu.cn

Huitao Chen
School of Mechanical and Power Engineering, Henan Polytechnic University, Jiaozuo, P.R. China
e-mail: huitaochen@hpu.edu.cn

The ring ultrasonic transducers are widely used in the ocean engineering and medical fields. This paper employs an extended orthogonal polynomial approach to solve the guided wave propagation in two-dimensional structures, i.e. piezoelectric rings with rectangular cross--sections. The extended polynomial approach can overcome the drawbacks of the conventional orthogonal polynomial approach which can be used to solve wave propagation in one-dimensional structures. Through numerical comparison with the available results for a rectangular aluminum bar, the validity of the present approach is illustrated. The dispersion curves and displacement and electric potential distributions of various rectangular piezoelectric rings are calculated, and the effects of different radius to thickness ratios, width to height ratios and polarizing directions on the dispersion curves are illustrated.

Keywords: piezoelectric rings, orthogonal polynomial, guided wave, dispersion curves

1. Introduction

With the development of materials and advances in manufacturing technology, piezoelectric materials having electromechanical coupling effects have found extensive applications in many smart devices, and the behavior of the selected wave mode can directly affect the performance of the devices. Thus, it is very important to study the wave characteristics in piezoelectric structures. Much effort has been made both theoretically and experimentally to study wave propagation in piezoelectric structures by scientists and engineers, which is essential for the application of piezoelectric materials. Wave propagation along piezoelectric cylindrical rods of hexagonal 6, 622, and 6 mm crystal symmetry was discussed by Wilson and Morrison (1977). The propagating nature of the elastic and electric wave in bone and porous PZT was investigated by Chakraborty (2009). Using the extended Durbin method, Ing *et al.* (2013) investigated the transient elastic waves propagating in a two-layered piezoelectric medium The wave propagation behavior in layered piezoelectric structures and functionally graded piezoelectric material structures has also been studied by many researches with different methods, such as the transfer matrix method (Cai *et al.*, 2001), the layer element method (Han *et al.*, 2004), the orthogonal polynomial series method (Yu and Ma, 2008; Yu *et al.*, 2013; Singh and Rokne, 2013), and so on.

As a common structure, hollow cylinder has been paid considerable attention on the wave propagation. For piezoelectric media, Paul and Venkatesan (1987) and Shul'ga (2002) studied three dimensional electroelastic waves and the axisymmetric waves in a hollow piezoelectric

ceramic cylinder. Puzyrev and Storozhev (2011) studied the problem of electroelastic waves propagating in piezoelectric hollow cylinders of sector cross section and analyzed mode asymptotic behavior and amplitude distributions of wave characteristics. Zenkour (2012) developed an analytical solution to the axisymmetric problem of a radially polarized piezoelectric hollow cylinders subjected to electric, thermal and mechanical load. Using the Legendre orthogonal polynomial approach developed by Lefebvre *et al.* (1999) to solve the waves in multilayered plates, Yu *et al.* (2009) investigated the wave characteristics in functionally graded piezoelectric hollow cylinders. These investigations focused on one-dimensional structures, i.e. the hollow cylinders are infinite in axial direction and have a finite dimension in only one direction. But in practical applications, many piezoelectric elements have very finite dimensions in two directions. One-dimensional models are not suitable for these structures. Thus, it is significant to study the wave characteristics in 2-D piezoelectric structures, such as a piezoelectric ring with rectangular cross-section. The ring ultrasonic transducer has been widely used in ocean engineering and medical fields. But few investigations on the wave propagation in ring transducers have been reported.

In this paper, we present an extended orthogonal polynomial series approach to solve the wave propagation in a 2-D structure, i.e. a piezoelectric ring with rectangular cross-section. The present approach can overcome the drawbacks of the conventional orthogonal polynomial approach which can only deal with the one-dimensional structures that have a finite dimension in only one direction, such as the axially infinite hollow cylinder, horizontally infinite flat plate. The dispersion curves and displacement and electric potential distributions of various piezoelectric rings with rectangular cross sections are shown. The effects of different width to height ratios, radius to thickness ratios and polarizing directions on the wave characteristics are also illustrated. The investigating results can be used to direct the design and optimization of the piezoelectric ring transducers.

2. Mathematics and formulation of the problem

In this seciton, we derive the analytical formulation of the problem in cylindrical coordinate (r, θ, z) with the z-axis coinciding with the axis of the ring. Considering an orthotropic ring with rectangular cross-section, h is height in z direction and a, b denote the inner and outer radius respectively, as shown in Fig. 1. The radius to thickness ratio is defined as $\eta = b/(b-a)$ and the width to height ratio is d/h. The polarizing direction is in r or z direction. In this paper, traction free and open circuit boundary conditions are assumed.

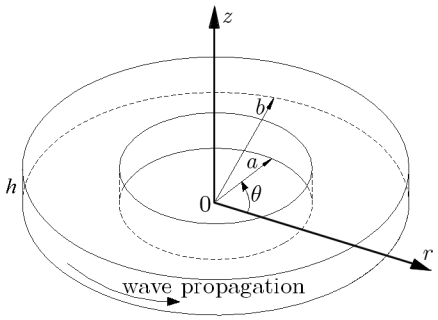

Fig. 1. Schematic of a piezoelectric ring with rectangular cross-section

In cylindrical coordinate, the dynamic equation for the piezoelectric ring is governed by

$$\begin{aligned}
&\frac{\partial T_{rr}}{\partial r} + \frac{1}{r}\frac{\partial T_{r\theta}}{\partial \theta} + \frac{\partial T_{rz}}{\partial z} + \frac{T_{rr} - T_{\theta\theta}}{r} = \rho \frac{\partial^2 u_r}{\partial t^2} \\
&\frac{\partial T_{r\theta}}{\partial r} + \frac{1}{r}\frac{\partial T_{\theta\theta}}{\partial \theta} + \frac{\partial T_{\theta z}}{\partial z} + \frac{2T_{r\theta}}{r} = \rho \frac{\partial^2 u_\theta}{\partial t^2}
\end{aligned} \tag{2.1}$$

$$\frac{\partial T_{rz}}{\partial r}+\frac{1}{r}\frac{\partial T_{\theta z}}{\partial \theta}+\frac{\partial T_{zz}}{\partial z}+\frac{T_{rz}}{r}=\rho\frac{\partial^2 u_z}{\partial t^2}$$
$$\frac{\partial D_r}{\partial r}+\frac{1}{r}\frac{\partial D_\theta}{\partial \theta}+\frac{\partial D_z}{\partial z}+\frac{D_r}{r}=0$$

where u_i, T_{ij} and D_i denote mechanical displacement, the stress and electric displacement components respectively; ρ is the density of the material.

The strain-displacement relations are

$$\begin{aligned}
&\varepsilon_{rr}=\frac{\partial u_r}{\partial r} && \varepsilon_{\theta\theta}=\frac{1}{r}\frac{\partial u_\theta}{\partial \theta}+\frac{u_r}{r} && \varepsilon_{zz}=\frac{\partial u_z}{\partial z}\\
&\varepsilon_{\theta z}=\frac{1}{2}\Big(\frac{\partial u_\theta}{\partial z}+\frac{\partial u_z}{r\partial \theta}\Big) && \varepsilon_{rz}=\frac{1}{2}\Big(\frac{\partial u_r}{\partial z}+\frac{\partial u_z}{\partial r}\Big) && \varepsilon_{r\theta}=\frac{1}{2}\Big(\frac{1}{r}\frac{\partial u_r}{\partial \theta}+\frac{\partial u_\theta}{\partial r}-\frac{u_\theta}{r}\Big)
\end{aligned} \tag{2.2}$$

where ε_{ij} denotes the strain.

The constitutive equations for the piezoelectric ring with radial polarizing direction can be written in the following form

$$\begin{aligned}
T_{\theta\theta}&=C_{11}\varepsilon_{\theta\theta}+C_{12}\varepsilon_{zz}+C_{13}\varepsilon_{rr}+e_{31}\frac{\partial \Phi}{\partial r}\\
T_{zz}&=\Big(C_{12}\varepsilon_{\theta\theta}+C_{22}\varepsilon_{zz}+C_{23}\varepsilon_{rr}+e_{32}\frac{\partial \Phi}{\partial r}\Big)\mathrm{I}(r,z)\\
T_{rr}&=\Big(C_{13}\varepsilon_{\theta\theta}+C_{23}\varepsilon_{zz}+C_{33}\varepsilon_{rr}+e_{33}\frac{\partial \Phi}{\partial r}\Big)\mathrm{I}(r,z)\\
T_{rz}&=\Big(2C_{44}\varepsilon_{rz}+e_{24}\frac{\partial \Phi}{\partial z}\Big)\mathrm{I}(r,z)\\
T_{r\theta}&=\Big(2C_{55}\varepsilon_{r\theta}+e_{15}\frac{1}{r}\frac{\partial \Phi}{\partial \theta}\Big)\mathrm{I}(r,z)\\
T_{\theta z}&=2C_{66}\varepsilon_{\theta z}\mathrm{I}(r,z)
\end{aligned} \tag{2.3}$$

and

$$\begin{aligned}
D_\theta&=2e_{15}\varepsilon_{r\theta}-\epsilon_{11}\frac{1}{r}\frac{\partial \Phi}{\partial \theta}\\
D_z&=\Big(2e_{24}\varepsilon_{rz}-\epsilon_{22}\frac{\partial \Phi}{\partial z}\Big)\mathrm{I}(r,z)\\
D_r&=\Big(e_{31}\varepsilon_{\theta\theta}+e_{32}\varepsilon_{zz}+e_{33}\varepsilon_{rr}-\epsilon_{33}\frac{\partial \Phi}{\partial r}\Big)\mathrm{I}(r,z)
\end{aligned} \tag{2.4}$$

where Φ denotes the electric potential. C_{ij}, e_{ij} and ϵ_{ij} are the elastic, piezoelectric and dielectric coefficients given in the crystallographic axes, respectively. $\mathrm{I}(r,z)$ is the rectangular window function, introduced so as to meet the stress-free boundary conditions ($T_{rr}=T_{r\theta}=T_{rz}=T_{\theta z}=T_{zz}=D_r=D_z=0$ at the four boundaries), defined as

$$\mathrm{I}(y,z)=\begin{cases}1 & 0\leqslant y\leqslant d \quad \text{and} \quad 0\leqslant z\leqslant h\\ 0 & \text{elsewhere}\end{cases} \tag{2.5}$$

For a free harmonic plane wave propagating in the circumferential direction in a ring, we assume the displacement components, to be of the form

$$\begin{aligned}
&u_r(r,\theta,z,t)=\exp(\mathrm{i}kb\theta-\mathrm{i}\omega t)U(r,z) && u_\theta(r,\theta,z,t)=\exp(\mathrm{i}kb\theta-\mathrm{i}\omega t)V(r,z)\\
&u_z(r,\theta,z,t)=\exp(\mathrm{i}kb\theta-\mathrm{i}\omega t)W(r,z) && \varphi(r,\theta,z,t)=\exp(\mathrm{i}kb\theta-\mathrm{i}\omega t)X(r,z)
\end{aligned} \tag{2.6}$$

where $U(r,z)$, $V(r,z)$ and $W(r,z)$ denote the mechanical displacement amplitudes in the radial, circumferential and axial directions respectively, and $X(r,z)$ represents the amplitude of electric potential. ω is the angular frequency, and k is the magnitude of the wave vector.

Substituting Eqs. (2.2)-(2.6) into Eq. (2.1), the governing differential equations in terms of mechanical displacement and electric potential components, gives

$$
\begin{aligned}
&[C_{33}(r^2U_{,rr}+rU_{,r})-C_{11}U-k^2b^2C_{55}U+C_{44}r^2U_{,zz}-\mathrm{i}kb(C_{11}+C_{55})V+(C_{23}-C_{12})rW_{,z}\\
&\quad+\mathrm{i}kb(C_{13}+C_{55})rV_{,r}+(C_{23}+C_{44})r^2W_{,rz}+e_{33}(r^2X_{,rr}+rX_{,r})-e_{31}rX_{,r}-k^2b^2e_{15}X\\
&\quad+e_{24}r^2X_{,zz}]I(r,z)+[C_{33}r^2U_{,r}+C_{13}r(\mathrm{i}kbV+U)+C_{23}r^2W_{,z}+e_{33}r^2X_{,r}]I(r,z)_{,r}\\
&\quad+[C_{44}r^2(U_{,z}+W_{,r})+e_{24}r^2X_{,z}]I(r,z)_{,z}=-\rho r^2\omega^2U\\
&[C_{55}(r^2V_{,rr}+rV_{,r})-(C_{55}+(kb)^2C_{11})V+\mathrm{i}kb(C_{13}+C_{55})rU_{,r}+C_{66}r^2V_{,zz}\\
&\quad+\mathrm{i}kb(C_{11}+C_{66})U+\mathrm{i}kb(C_{12}+C_{66})rW_{,z}+(e_{31}+e_{15})rX_{,r}+2e_{15}X]I(r,z)\\
&\quad+C_{66}(r^2V_{,z}+\mathrm{i}kbrW)I(r,z)_{,z}+[C_{55}(r^2V_{,r}+rV+\mathrm{i}kbrU)+e_{15}rX]I(r,z)_{,r}=-\rho r^2\omega^2V\\
&[C_{44}(r^2W_{,rr}+rW_{,r})+C_{22}r^2W_{,zz}-(kb)^2C_{66}W+(C_{12}+C_{44})rU_{,z}+(C_{23}+C_{44})r^2U_{,rz}\\
&\quad+\mathrm{i}kb(C_{12}+C_{66})rV_{,z}+e_{24}rX_{,z}+(e_{24}+e_{32})r^2X_{,rz}]I(r,z)+[C_{12}r(\mathrm{i}kbV+U)\\
&\quad+C_{23}r^2U_{,r}+C_{22}r^2W_{,z}+e_{32}r^2X_{,r}]I(r,z)_{,z}+[C_{44}r^2(W_{,r}+U_{,z})+e_{24}r^2X_{,z}]I(r,z)_{,r}\\
&\quad=-\rho r^2\omega^2V\\
&[e_{33}(r^2U_{,rr}+rU_{,r})-k^2b^2e_{15}U+e_{31}rU_{,r}+e_{24}r^2U_{,zz}+(e_{31}+e_{15})rV_{,r}-e_{15}V\\
&\quad+(e_{24}+e_{32})r^2W_{,rz}+e_{24}rW_{,z}-\epsilon_{33}(r^2X_{,rr}+rX_{,r})-\epsilon_{22}r^2X_{,zz}+(kb)^2\epsilon_{11}X]I(r,z)\\
&\quad+[e_{24}r^2U_{,z}+e_{24}r^2W_{,r}-\epsilon_{22}r^2X_{,z}]I(r,z)_{,z}\\
&\quad+[e_{31}rU+e_{33}r^2U_{,r}+e_{31}rV+e_{32}r^2W_{,z}-\epsilon_{33}r^2X_{,r}]I(r,z)_{,r}=0
\end{aligned}
\tag{2.7}
$$

where subscript comma indicates partial derivative.

To solve the coupled wave equation, we expand $U(r,z)$, $V(r,z)$, $W(r,z)$ and $X(r,z)$ into products of two Legendre orthogonal polynomial series

$$
\begin{aligned}
U(r,z)&=\sum_{m,j=0}^{\infty}p^1_{m,j}Q_m(r)Q_j(z) \qquad & V(r,z)&=\sum_{m,j=0}^{\infty}p^2_{m,j}Q_m(r)Q_j(z)\\
W(r,z)&=\sum_{m,j=0}^{\infty}p^3_{m,j}Q_m(r)Q_j(z) \qquad & X(r,z)&=\sum_{m,j=0}^{\infty}p^4_{m,j}Q_m(r)Q_j(z)
\end{aligned}
\tag{2.8}
$$

where $p^i_{m,j}$ $(i=1,2,3,4)$ is the expansion coefficients and

$$
Q_m(r)=\sqrt{\frac{2m+1}{b-a}}P_m\Big(\frac{2r-b-a}{b-a}\Big) \qquad Q_n(z)=\sqrt{\frac{2n+1}{h}}P_n\Big(\frac{2z-h}{h}\Big) \tag{2.9}
$$

with P_m and P_n representing the mth and the nth Legendre polynomial. The summation over the polynomials can be halted at some finite value $m=M$ and $n=N$, when higher order terms become essentially negligible.

Multiplying each equation by $Q_j(r)Q_l(z)\mathrm{e}^{-j\omega t}$ with j and l running respectively from zero to M and zero to N, and integrating over z from zero to h and r from a to b and taking advantage of the orthonormality of the polynomials $Q_m(r)$ and $Q_n(z)$, Eqs. (2.7) can be reorganized into a form of the system problem

$$
\begin{aligned}
A^{jlmn}_{11}p^1_{m,n}+A^{jlmn}_{12}p^2_{m,n}+A^{jlmn}_{13}p^3_{m,n}+A^{jlmn}_{14}p^4_{m,n}&=-\omega^2M_{jlmn}p^1_{m,n}\\
A^{jlmn}_{21}p^1_{m,n}+A^{jlmn}_{22}p^2_{m,n}+A^{jlmn}_{23}p^3_{m,n}+A^{jlmn}_{24}p^4_{m,n}&=-\omega^2M_{jlmn}p^2_{m,n}\\
A^{jlmn}_{31}p^1_{m,n}+A^{jlmn}_{32}p^2_{m,n}+A^{jlmn}_{33}p^3_{m,n}+A^{jlmn}_{34}p^4_{m,n}&=-\omega^2M_{jlmn}p^3_{m,n}\\
A^{jlmn}_{41}p^1_{m,n}+A^{jlmn}_{42}p^2_{m,n}+A^{jlmn}_{43}p^3_{m,n}+A^{jlmn}_{44}p^4_{m,n}&=0
\end{aligned}
\tag{2.10}
$$

where $A_{\alpha\beta}^{jlmn}$ $(\alpha,\beta=1,2,3,4)$ and M_{jlmn} are the elements of a non-symmetric matrix.

Equations $(2.10)_4$ can be written as

$$p_{m,n}^4=-\left(A_{44}^{jlmn}\right)^{-1}\left(A_{41}^{jlmn}p_{m,n}^1+A_{42}^{jlmn}p_{m,n}^2+A_{43}^{jlmn}p_{m,n}^3\right) \tag{2.11}$$

Substituting Equation (2.11) into equations $(2.10)_1$, $(2.10)_2$ and $(2.10)_3$, gives

$$\begin{aligned}
&\left[A_{11}^{jlmn}-A_{14}^{jlmn}\left(A_{44}^{jlmn}\right)^{-1}A_{41}^{jlmn}\right]p_{m,n}^1+\left[A_{12}^{jlmn}-A_{14}^{jlmn}\left(A_{44}^{jlmn}\right)^{-1}A_{42}^{jlmn}\right]p_{m,n}^2\\
&\quad+\left[A_{13}^{jlmn}-A_{14}^{jlmn}\left(A_{44}^{jlmn}\right)^{-1}A_{43}^{jlmn}\right]p_{m,n}^3=-\omega^2M_{jlmn}p_{m,n}^1\\
&\left[A_{21}^{jlmn}-A_{24}^{jlmn}\left(A_{44}^{n,m}\right)^{-1}A_{41}^{jlmn}\right]p_{m,n}^1+\left[A_{22}^{jlmn}-A_{24}^{jlmn}\left(A_{44}^{jlmn}\right)^{-1}A_{42}^{jlmn}\right]p_{m,n}^2\\
&\quad+\left[A_{23}^{jlmn}-A_{24}^{jlmn}\left(A_{44}^{jlmn}\right)^{-1}A_{43}^{jlmn}\right]p_{m,n}^3=-\omega^2M_{jlmn}p_{m,n}^1\\
&\left[A_{31}^{jlmn}-A_{34}^{jlmn}\left(A_{44}^{jlmn}\right)^{-1}A_{41}^{jlmn}\right]p_{m,n}^1+\left[A_{32}^{jlmn}-A_{34}^{jlmn}\left(A_{44}^{jlmn}\right)^{-1}A_{42}^{jlmn}\right]p_{m,n}^2\\
&\quad+\left[A_{33}^{jlmn}-A_{34}^{jlmn}\left(A_{44}^{jlmn}\right)^{-1}A_{43}^{jlmn}\right]p_{m,n}^3=-\omega^2M_{jlmn}p_{m,n}^1
\end{aligned} \tag{2.12}$$

Then, Eqs. (2.12) can be recognized into

$$\begin{bmatrix}\overline{A}_{11}^{jlmn} & \overline{A}_{12}^{jlmn} & \overline{A}_{13}^{jlmn}\\ \overline{A}_{21}^{jlmn} & \overline{A}_{22}^{jlmn} & \overline{A}_{23}^{jlmn}\\ \overline{A}_{31}^{jlmn} & \overline{A}_{32}^{jlmn} & \overline{A}_{33}^{jlmn}\end{bmatrix}\begin{Bmatrix}p_{m,n}^1\\ p_{m,n}^2\\ p_{m,n}^3\end{Bmatrix}=-\omega^2\begin{bmatrix}M_{jlmn} & 0 & 0\\ 0 & M_{jlmn} & 0\\ 0 & 0 & M_{jlmn}\end{bmatrix}\begin{Bmatrix}p_{m,n}^1\\ p_{m,n}^2\\ p_{m,n}^3\end{Bmatrix} \tag{2.13}$$

So, Eq. (2.13) forms the eigenvalue problem to be solved. The eigenvectors $p_{m,n}^i$ $(i=1,2,3)$ allow the components of the displacement and $p_{m,n}^4$ determines the electric potential distribution. The eigenvalue ω^2 gives angular frequency.

3. Numerical results

The computer programs in terms of the extended orthogonal polynomial approach have been written using Mathematica to calculate the dispersion curves and displacement and electric potential distributions for the piezoelectric rings. The physical properties of the piezoelectric material, PZT-4, are listed in Table 1. Here, the elastic constants of the radial polarizing ring and axial polarizing rings are the same to have a clear comparison.

Table 1. Material parameters of the piezoelectric materials

Property	C_{11}	C_{12}	C_{13}	C_{22}	C_{23}	C_{33}	C_{44}	C_{55}	C_{66}
r-polarization	13.9	7.8	7.4	13.9	7.4	11.5	2.56	2.56	3.05
	e_{15}	e_{24}	e_{31}	e_{32}	e_{33}	ϵ_{11}	ϵ_{22}	ϵ_{33}	ρ
	12.7	12.7	−5.2	−5.2	15.1	650	650	560	7.5
a-polarization	e_{34}	e_{16}	e_{23}	e_{21}	e_{22}	ϵ_{11}	ϵ_{22}	ϵ_{33}	ρ
	12.7	12.7	−5.2	−5.2	15.1	650	560	650	7.5

Units: C_{ij} $[10^{10}\mathrm{N/m^2}]$, ϵ_{ij} $[10^{-11}\mathrm{F/m}]$, e_{ij} $[\mathrm{C/m^2}]$, ρ $[10^3\mathrm{kg/m^3}]$

3.1. Approach validation

To the authors' knowledge, there are not published results on the wave propagation for a piezoelectric ring with rectangular cross-section so far. In order to check the effectiveness of the present approach and validate the computer program, we calculate a 16 mm by 5 mm rectangular aluminum bar and make a comparison with previous results. The material parameters are $\rho = 2.7 \cdot 10^3\,\mathrm{kg/m^3}$, $C_{11} = C_{22} = C_{33} = 10.78 \cdot 10^{10}\,\mathrm{Pa}$, $C_{12} = C_{13} = C_{23} = 5.494 \cdot 10^{10}\,\mathrm{Pa}$, $C_{44} = C_{55} = C_{66} = 2.645 \cdot 10^{10}\,\mathrm{Pa}$. Figure 2 is the corresponding dispersion curves, of which lines are from Loveday (2006), and dotted lines are obtained from the present approach. As can be seen, the agreement between the present approach and the previous results is quite good.

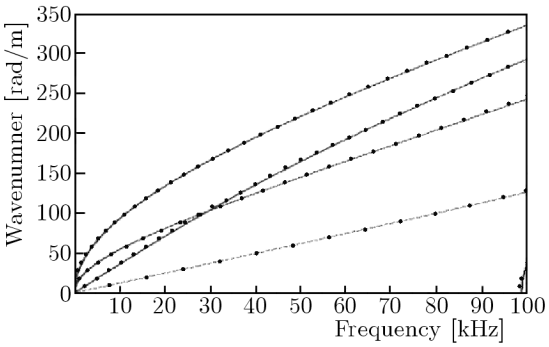

Fig. 2. Dispersion of propagating waves in a rectangular waveguide; lines: Philip W. Loveday's results, dotted lines: the authors' results

3.2. Guided waves in piezoelectric rings with rectangular cross-sections

Figure 3 shows the dispersion curves of the first four order modes for the PZT-4 ring with a square cross section and for the corresponding non-piezoelectric one with $h = 1\,\mathrm{mm}$, $a = 9\,\mathrm{mm}$, $b = 10\,\mathrm{mm}$ and $\eta = 10$. It can be seen that piezoelectricity has a significant effect on the dispersion curves. For any one specific mode, the phase velocities of non-piezoelectric ring are smaller than those of the corresponding piezoelectric one, and the piezoelectric effect is very little on the low order modes at low frequency and becomes stronger as the wave number and mode order increase. The wave number is usually very big and the operating frequency is very high in micro-scale SAW devices. So, the piezoelectric effects will be prominent.

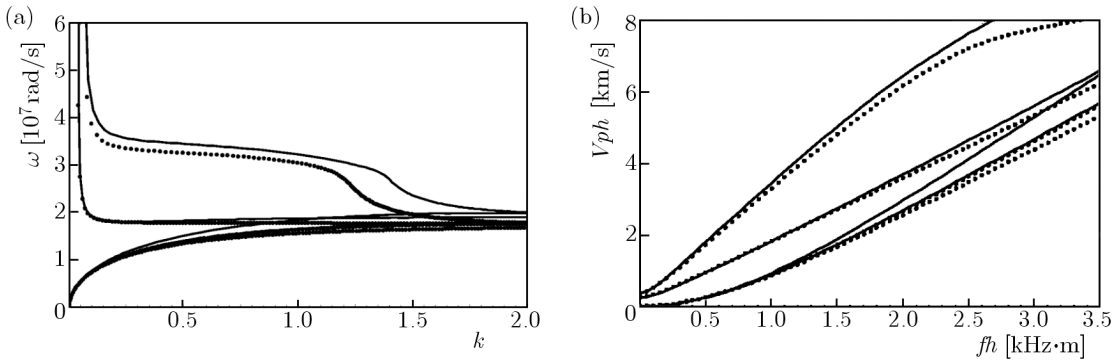

Fig. 3. Dispersion curves of the first four order modes for a square ring with $\eta = 10$: (a) phase velocity spectra, (b) frequency spectra, solid line, piezoelectric; dotted line, non-piezoelectric

Figures 4 and 5 show the dispersion curves of the PZT-4 rings with different radius to thickness ratios ($\eta = 10$, $\eta = 2$) and different width to height ratios ($d/h = 1/2$, $d/h = 1/4$, $d/h = 1/10$), respectively. Figure 6 illustrates the dispersion curves of the PZT-4 ring with

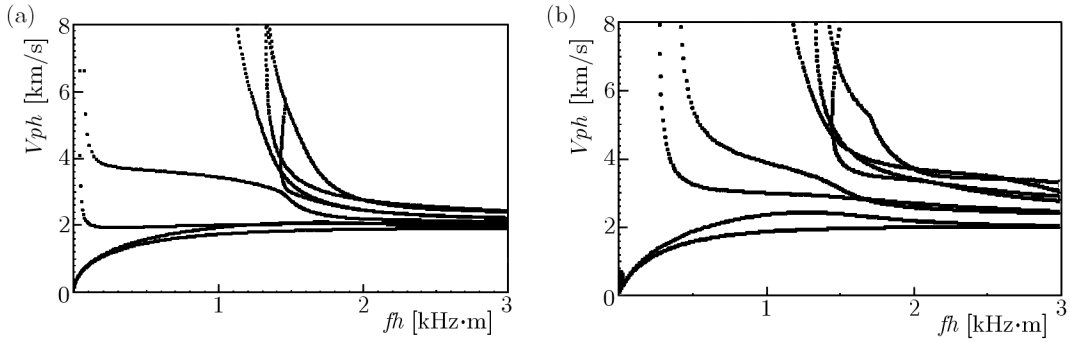

Fig. 4. Phase velocity dispersion curves for piezoelectric square rings: (a) $\eta = 10$, (b) $\eta = 2$

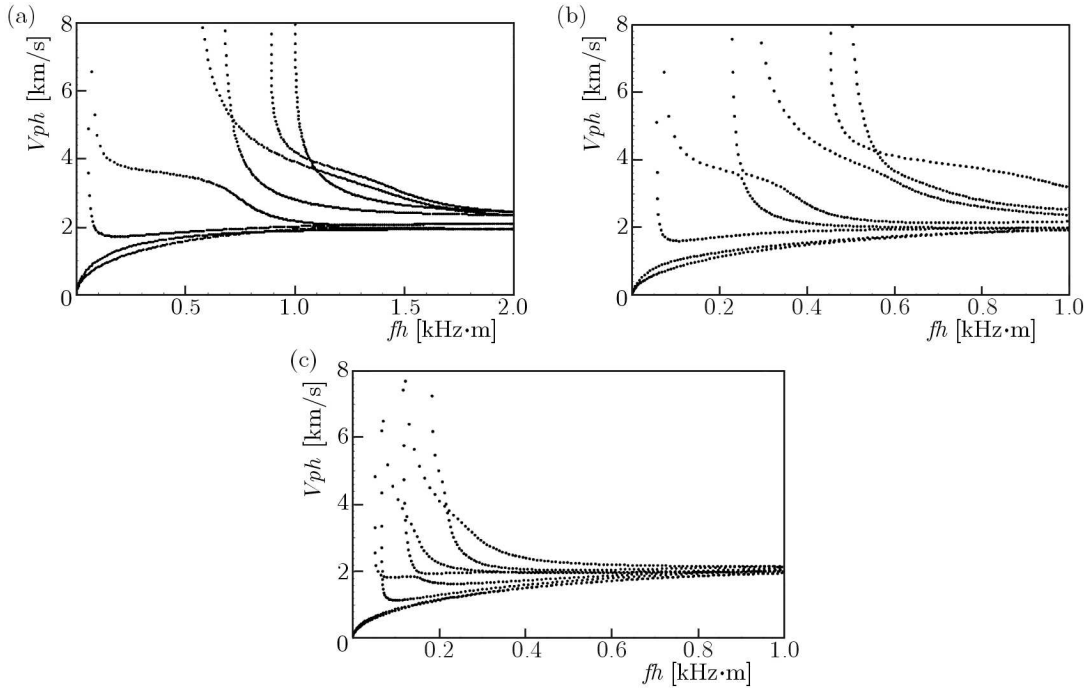

Fig. 5. Phase velocity dispersion curves for piezoelectric rectangular rings with different width to thickness ratios: (a) $d/h = 1/2$, (b) $d/h = 1/4$, (c) $d/h = 1/10$

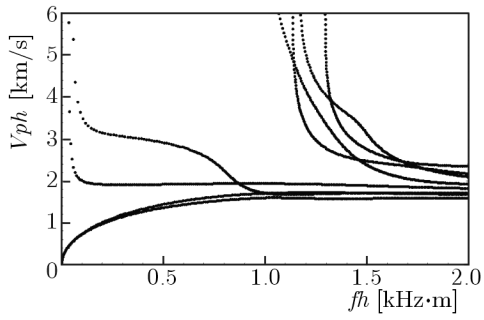

Fig. 6. Phase velocity dispersion curves for a piezoelectric rectangular ring with axial polarization

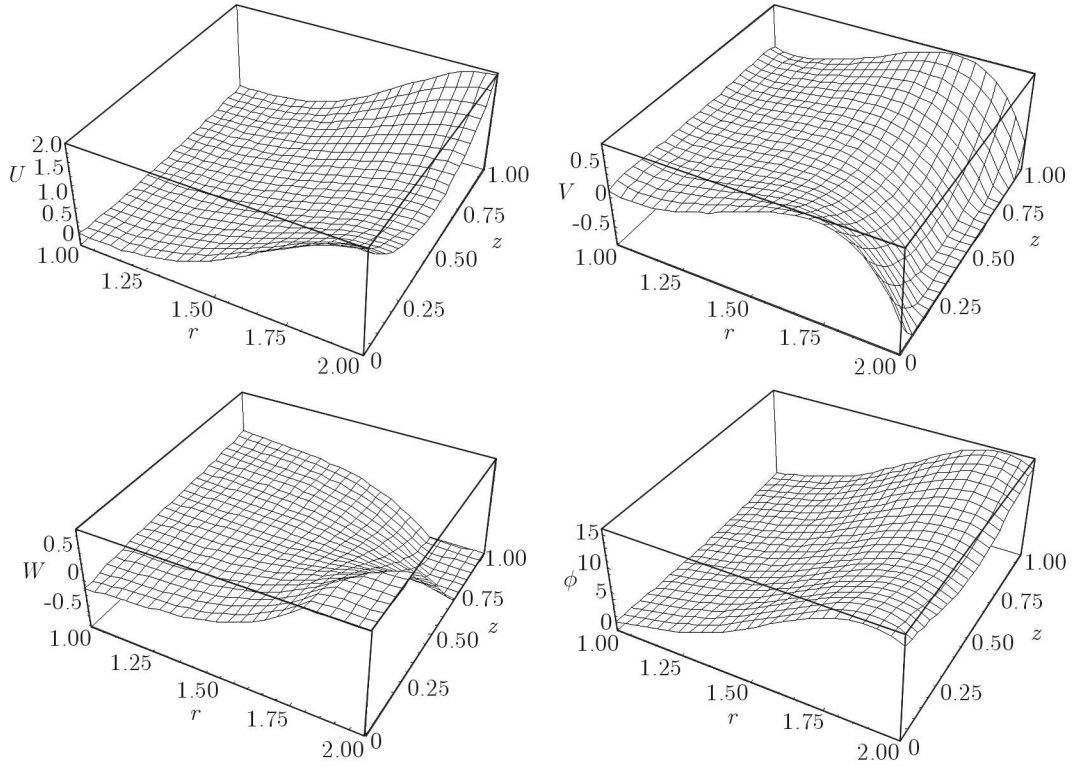

Fig. 7. Mechanical displacement and electric potential profiles of the first mode for a piezoelectric square ring with $\eta = 2$ at $kd = 4.1$

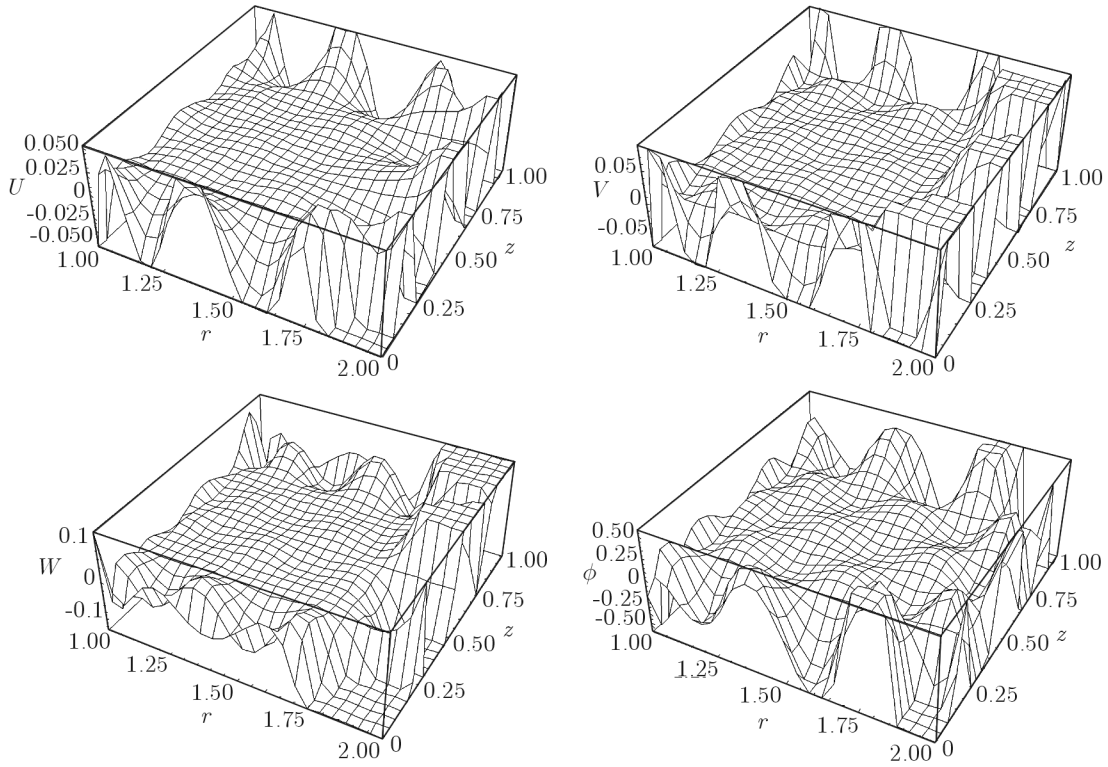

Fig. 8. Mechanical displacement and electric potential profiles of the first mode for a piezoelectric square ring with $\eta = 2$ at $kd = 4.1$

axial polarization. From the curves, we find that different radius to thickness ratios and width to height ratios and polarizing direction all have significant influence on the dispersion curves. The first two modes have no cut-off frequencies, which is different from that for an infinite hollow cylinder in which only the first mode has no cut-off frequencies. In an infinite hollow cylinder, only the thickness direction is a finite dimension, but there are two finite dimensions in a rectangular ring. With the width to height ratio increasing, the difference between the first mode dispersion curve and the second one becomes small, and the cut-off frequencies become small.

The displacement and electric potential profiles of the first mode for a square ring with$\eta = 10$ at $kd = 4.1$ and $kd = 40.1$ are respectively shown in Figs. 7 and 8. We notice that displacement u and v and electric potential distributions are symmetry and displacement w is antisymmetry in axial direction, This is because the geometry and material propreties are symmetric in axial direction. The displacement and electric potential profiles distribute mainly near the outside edge at small wavenumber case and distribute around the four boundaries at big wavenumber case.

4. Conclusions and prospects

The formulation to analyze the guided wave in piezoelectric rings with rectangular cross-sections using the extended orthogonal polynomial approach has been presented in this paper. According to the numerical results, we can draw the following conclusions:

(a) The effects of the piezoelectricity on dispersion curves become stronger with the wave number and mode order increasing.

(b) The width to height ratio, radius to thickness ratio and polarization all can significantly influence the guided wave characteristics in piezoelectric rings.

(c) The displacement and electric potential distributions are symmetry in axial direction and distribute mainly near the outside edge.

So, through changing the width to height ratio and the radius to thickness ratio of the piezoelectric ring, we can obtain the ring transducers with the dispersion features and field distributions that we want.

We consider that the present approach could be of interest in non-destructive testing evaluation, and can deal with 2D structures with more complex cross sections and multi-field coupled 2D structures.

Acknowledgments

The work is supported by the National Natural Science Foundation of China (No. 11272115) and Doctoral Fund of Henan Polytechnic University (No. B2009-81) and Foundation for Distinguished Young Scholars of Henan Polytechnic University (No. J2013-08) and by the high-performance grid computing platform of Henan Polytechnic University.

References

1. Cai C., Liu G.R., Lam K.Y., 2001, A technique for modelling multiple piezoelectric layers, *Smart Materials And Structures*, **10**, 689

2. Chakraborty A., 2009, Wave Propagation in Porous Piezoelectric Media, *Computer Modeling in Engineering and Sciences*, **40**, 105

3. Han X., Liu G.R., Ohyoshi T., 2004, Dispersion and characteristic surfaces of waves in hybrid multilayered piezoelectric circular cylinders, *Computational Mechanics*, **33**, 334-344

4. Ing Y.S., Liao H.F., Huang K.S., 2013, The extended Durbin method and its application for piezoelectric wave propagation problems, *International Journal of Solids and Structures*, **50**, 4000-4009

5. Lefebvre J.E., Zhang V., Gazalet J., Gryba T., 1999, Legendre polynomial approach for modeling free-ultrasonic waves in multilayered plates, *Journal of Applied Physics*, **85**, 3419-3427

6. Loveday P.W., 2006, Numerical comparison of patch and sandwich piezoelectric transducers for transmitting ultrasonic waves, *Smart Structures and Materials. International Society for Optics and Photonics*, **6166**, 1-8

7. Paul H.S., Venkatesan M., 1987, Vibrations of a hollow circular cylinder of piezoelectric ceramics, *The Journal of the Acoustical Society of America*, **82**, 952-956

8. Puzyrev V., Storozhev V., 2011, Wave propagation in axially polarized piezoelectric hollow cylinders of sector cross section, *Journal of Sound and Vibration*, **330**, 4508-4518

9. Shul'ga H.A., 2002, Propagation of harmonic waves in anisotropic piezoelectric cylinders. Homogeneous piezoceramic waveguides, *International Applied Mechanics*, **38**, 933-953

10. Singh B.M., Rokne J., 2013, Propagation of SH waves in layered functionally gradient piezoelectric-piezomagnetic structures, *Philosophical Magazine*, **93**, 1690-1700

11. Wilson L.O., Morrison J.A., 1977, Wave propagation in piezoelectric rods of hexagonal crystal symmetry, *Journal of Mechanics and Applied Mathematics*, **30**, 387-395

12. Yu J.G., Lefebvre J.E., Guo Y.Q., 2013, Wave propagation in multilayered piezoelectric spherical plates, *Acta Mechanica*, **224**, 1335-1349

13. Yu J.G., Ma Q.J., 2008, Circumferential wave in functionally graded piezoelectric cylindrical curved plates, *Acta Mechanica*, **198**, 171-190

14. Yu J.G., Wu B., Chen G.Q., 2009, Wave characteristics in functionally graded piezoelectric hollow cylinders, *Archive of Applied Mechanics*, **79**, 807-824

15. Zenkour A.M., 2012, Piezoelectric behavior of an inhomogeneous hollow cylinder with thermal gradient, *International Journal of Thermophysics*, **33**, 1288-1301

Manuscript received May 6, 2014; accepted for print February 17, 2015

JOURNAL OF THEORETICAL AND APPLIED MECHANICS
53, 3, pp. 683-695, Warsaw 2015
DOI: 10.15632/jtam-pl.53.3.683

NANO-PARTICLES TRANSPORT IN A CONCENTRIC ANNULUS: A LATTICE BOLTZMANN APPROACH

Hamoon Pourmirzaagha
Department of Mechanical and Aerospace Engineering, Ramsar Branch, Islamic Azad University, Ramsar, Iran; e-mail: h.poormirzaagha@sina.kntu.ac.ir

Hamid Hassanzadeh Afrouzi
Young Researchers Club, Babol Branch, Islamic Azad University, Babol, Iran; e-mail: hamidhasanzade@yahoo.com

Abbasali Abouei Mehrizi
Young Researchers and Elite Club, Karaj Branch, Islamic Azad University, Karaj, Iran; e-mail: abbasabouei@gmail.com

A combination of the lattice Boltzmann method and lagrangian Runge-Kutta procedure is used to study dispersion and removal of nano-particles in a concentric annulus. The effect of aspect ratio, Rayleigh number and particles diameter are examined on particles removal and their dispersion characteristics. Simulations are performed for the Rayleigh number ranges from 10^3 to 10^5 and aspect ratio of 2, 3 and 4. Higher aspect ratios have led to weaker recirculation strength. The finest particles move on stochastic path due to the effect of Brownian motion. The Brownian motion has a greater effect on the removal of nano--particles with respect to thermophoresis.

Keywords: LBM, nano-particles, dispersion, removal, Brownian motion, thermophoresis

1. Introduction

Natural convection heat transfer in an enclosure occurs in various industrial and engineering applications. Many investigations have been done to study these phenomena in different situations. Heat exchangers as cooling systems in reactors and electrical components of heating and cooling system are some of these examples (Abouei Mehrizi *et al.*, 2013; Jourabian *et al.*, 2013). Dispersion, deposition and removal of solid particles are considered as important cases in numerous industrial, environmental and biological applications. Heat transfer enhancement (Hassanzadeh and Farhadi, 2013; Abouei Mehrizi *et al.*, 2013), air quality (Chen *et al.*, 2006) are some others challages in environmental and biological systems. Studies show that deposition micro-particles and nano-particles on cooling or heating surfaces can improve the systems and significantly increases energy consumption (Rahman *et al.*, 2006; Vessakosol and Charoensuk, 2010). Golovin and Putnam (1962) studied the deposition efficiency of ribbon particles in potential flows. Vasak *et al.* (1992) investigated solid particles deposition on channel walls in various ranges of flow conditions. One of the major issues in a severe accident scenario is accurate prediction of the deposition rate in adition of understanding and quantifying the removal mechanisms of micro size aerosol particles in buoyancy driven flows inside containments. Puragliesi *et al.* (2011) investigated micro-particle deposition in the turbulent buoyancy driven flow in a DHC (differentially heated cavity). They employed DNS (Direct Numerical Simulation) for flow field simulation. Their results showed that the largest influence on micro-particles deposition is caused by the gravity effect in such a situation. They discussed the contribution of different forces on the removal of micro-particles in details. Akbar *et al.* (2009) focused on the behavior of micro-particles in a laminar free convection in a square enclosure. A numerical analysis was performed by Golkarfard *et al.* (2012) to investigate the transport and deposition

of aerosols in convection flow in a cavity in the presence of built-in heated obstacles and a driven lid. They analyzed the effect of thermophoresis on deposition of particles, and their result showed that thermophoresis decreases the deposition. The authors performed some researches on the transport of micro-particles in a forced convection flow (Hassanzadeh Afrouzi *et al.*, 2012b) and buoyancy driven flow (Hassanzadeh Afrouzi *et al.*, 2012) employing the lattice Boltzmann method. Annular shapes are applicable geometry in engineering and industry. The geometry of the circular annulus is found in transmission cables, solar collectors-receivers, vapor condenser, heat exchangers. Kuehn and Goldstein (1976, 1978) reviewed studies on the free convection in an annulus. It is very important to reach accurate characteristics of the flow field at particle position to calculate the lagrangian particle tracking procedure. The lattice Boltzmann method (LBM) is a suitable numerical technique based on kinetic theory for modeling the physics of fluids systems (Abouei Mehrizi *et al.*, 2012, 2013). In the most recently published papers, the analyzes were done on micro-particles, in which the effects such as the Brownian motion and thermophoresis are not substantial contributors to the particle diffusion mechanism. There is also a lack of understanding of the contribution of specific forces.

In the present study, the contribution of Brownian motion and thermophoresis on the transport of nano-particles is discussed by analysing some case without considering the Brownian motion force and some cases without considering both the Brownian motion and thermophoresis. The lattice Boltzmann method is used to simulate the laminar flow in a concentric annulus. Then the particle equation of motion is solved in the lagrangian framework to investigate the dispersion and removal of particles. Drag, Saffman lift, gravity, buoyancy, Brownian motion and thermophoresis are forces that included in the particle tracking procedure.

2. Fluid flow simulation

2.1. Lattice Boltzmann method

A two-dimensional laminar natural convection flow is considered in a concentric annulus as the computational domain (Fig. 1).

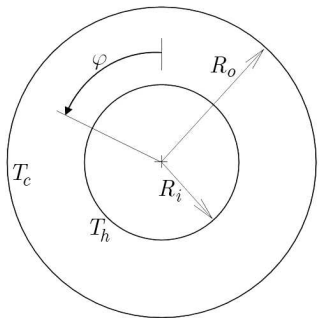

Fig. 1. Computational domain of the concentric annulus

The two-dimensional lattice Boltzmann method is used for flow simulations. A general form of the lattice Boltzmann equation with an external force can be written as (Hassanzade *et al.*, 2012)

$$f_k(\mathbf{x}+\mathbf{c}_k\Delta t, t+\Delta t) - f_k(\mathbf{x},t) = \Delta t \frac{f_k^{eq}(\mathbf{x},t) - f_k(\mathbf{x},t)}{\tau} + \Delta t \cdot \mathbf{F}_k \tag{2.1}$$

where f_k is the distribution function in the direction k, Δt is the lattice time step, $\mathbf{c}_k$ is the lattice velocity in the direction k, F_k is the external force in the direction of $\mathbf{c}_k$, τ denotes the lattice relaxation time which is defined as $\tau = (1/c_s^2)\upsilon + 1/2$, where υ is viscosity, f_k^{eq} is

the equilibrium distribution function dependent on the type of the problem. The equilibrium distribution functions for the fluid field are calculated (Hassanzade *et al.*, 2012) with eguation

$$f_k^{eq} = \omega_k \rho \Big[1 + \frac{\mathbf{c}_k \cdot \mathbf{u}}{c_s^2} + \frac{1}{2}\frac{(\mathbf{c}_k \cdot \mathbf{u})^2}{c_s^4} - \frac{1}{2}\frac{\mathbf{u} \cdot \mathbf{u}}{c_s^2} \Big] \tag{2.2}$$

where ω_k are weighting factors which k changes from 0 to 8. The values of $\omega_0 = 4/9$ for $|c_0| = 0$, $\omega_{1-4} = 1/9$ for $|c_{1-4}| = 1$ and $\omega_{5-8} = 1/36$ for $|c_{5-8}| = \sqrt{2}$ are assumed in this model (Abouei Mehrizi *et al.*, 2012). ρ and $\mathbf{u}$ are macroscopic fluid density and velocity which are calculated respectively as below

$$\rho = \sum_k f_k \qquad \rho \mathbf{u} = \sum_k f_k \mathbf{c}_k \tag{2.3}$$

The thermal lattice Boltzmann equation can be written as below

$$g_k(\mathbf{x}, t + \Delta t) - g_k(\mathbf{x}, t) = \Delta t \frac{g_k^{eq}(\mathbf{x}, t) - g_k(\mathbf{x}, t)}{\tau_c} \tag{2.4}$$

where the thermal equilibrium distribution functions are given as (Hassanzade *et al.*, 2012)

$$g_k^{eq} = \omega_k T \Big(1 + \frac{\mathbf{c}_k \cdot \mathbf{u}}{c_s^2} \Big) \tag{2.5}$$

where T is the fluid temperature evaluated from

$$T = \sum_k g_k^{eq} \tag{2.6}$$

The temperature relaxation time is calculated as a function of the diffusivity coefficient

$$\tau_c = \frac{1}{c_s^2}\alpha + \frac{1}{2} \tag{2.7}$$

In order to incorporate the buoyancy force in the model, the Boussinesq approximation has been applied, therefore the force term in Eq. (2.1) needs to be calculated as below in the vertical direction y

$$\mathbf{F}_y = 3\omega_k \mathbf{g}_y \beta \Delta T \tag{2.8}$$

where $\mathbf{g}_y$ is the acceleration of gravity acting in the y-direction of the lattice links, β is the thermal expansion coefficient and ΔT is the temperature difference.

2.2. Curved boundary treatment

In the present study, a second-order accurate method to define the curve boundary condition is used (Mei *et al.*, 1999). This boundary condition is used to implement the no slip condition for hydrodynamic and thermal treatment. The curve boundary for the no slip condition is used for both inner and outer cylinders. Figure 2 shows the lattice node treatment on the curved boundary condition, the gray nodes indicate the boundary nodes x_b, the white nods show the first fluid nodes x_f, and the solid block nodes on the boundary x_w indicate the intersections of the wall with various lattice links (Hassanzadeh Afrouzi *et al.*, 2012).

The fraction of an intersected link in the fluid region D, is determined by (Abouei Mehrizi *et al.*, 2012)

$$D = \frac{|x_f - x_w|}{|x_f - x_b|} \tag{2.9}$$

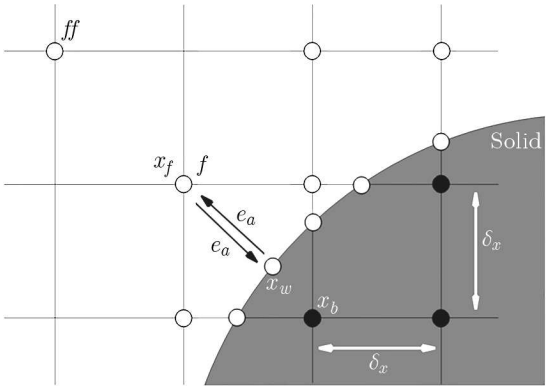

Fig. 2. Layout of the regularly spaced lattices and the curved wall boundary

At the collision step, the fluid side distribution function on the fluid side $\widetilde{f}_k$ is determined, but the solid side distribution function at the opposite direction $\widetilde{f}_{\overline{k}}$ is unknown. On the other hand, to finish the streaming step we need to know $\widetilde{f}_{\overline{k}}$ at the boundary node x_b. The detailed description of calculating velocity and temperature on boundary nodes was presented in our previous work (Hassanzadeh Afrouzi *et al.*, 2012) based on the ref. by Yu *et al.* (2003) and Guo *et al.* (2002)

3. Particle equation of motion

A particle suspended in a buoyancy driven flow is affected by some forces. The drag, Saffman lift, gravity, buoyancy, Brownian motion and thermophoresis are included in the particle equation of motion in this study. The corresponding particle equation of motion in the i-th direction is given as

$$\frac{du_p^i}{dx^i} = \frac{1}{\tau_p}(u_g^i - u_p^i) + L^i + N^i + \Big(1 - \frac{1}{S}\Big)g^i + Th^i \tag{3.1}$$

The first term in the right hand side of equations (3.1) is the drag force that is due to relative velocity between the particles and carrier gas. The relaxation time τ_p is the characteristic time scale (response time) of a particle. u_p^i and u_g^i are the corresponding particle and velocity in the direction of i, L is Saffman lift force, N – Brownian force, S is specific gravity, g_i is gravity acceleration and Th^i is the thermophoresis force. By increasing the relaxation time, the particle reaction decreases with variations of flow parameters. For submicron particles with the particle Knudsen number Kn_p larger than 0.1, when the particle diameter is in the range of the gas mean free path λ, the flow slips over the particle surface. Therefore, the Stokes drag must be modified by the Cunningham correction factor C_c as (Shams *et al.*, 2000)

$$C_c = 1 + \frac{2\lambda}{d_p}\left[1.257 + 0.4\mathrm{e}^{\left(\frac{-1.1d_p}{2\lambda_g}\right)}\right] \tag{3.2}$$

Small particles in a shear field experience a force perpendicular to the direction of flow. The shear lift originates from the inertia effects in the viscous flow around the particle and is different from the aerodynamic lift force. Saffman (1965) was the first to obtain an equation for this force

$$L = 1.615\rho^p\sqrt{\nu}(d^p)^2(u^g - u^p)\sqrt{\Big|\frac{du^f}{dy}\Big|}\,\mathrm{sgn}\Big(\frac{du^f}{dy}\Big) \tag{3.3}$$

Respectively, ρ^p and ν are density and kinematic viscosity of the gas phase. Brownian motion in the direction i is denoted by N^i. The instantaneous random momentum imparted to the

ultrafine particles is due to impacts of gas molecules which make the particle move on an erotic path known as the Brownian motion (Shams *et al.*, 2000; Li and Ahmadi, 1992)

$$N = G\sqrt{\frac{\pi S_0}{dt}} \qquad S_0 = \frac{216\nu K_1 T_g}{\pi^2 \rho_p (d_p)^5 S^2 C_c} \tag{3.4}$$

where T_g is gas temperature and K_1 is the Boltzmann constant. G is the unit variance zero mean Gaussian random numbers

$$G = \sqrt{-2\ln U_i}\cos(2\pi U_j) \tag{3.5}$$

where U_i and U_j are random numbers (between 0 and 1). Finally, Th^i denotes thermophoresis force which is defined as

$$Th^i = K_{Th}\frac{\partial T}{\partial x^i} \tag{3.6}$$

where K_{Th} is the thermophoresis coefficient suggested by Talbot *et al.* (1980)

$$K_{Th} = \frac{2C_s C_c\left(\frac{K_g}{K_p} + C_t \mathrm{Kn}_p\right)}{(1 + 3C_m \mathrm{Kn}_p)\left(1 + 2\frac{K_f}{K_p} + 2C_t \mathrm{Kn}_p\right)} \tag{3.7}$$

The values of C_t, C_m and C_s are 2.18, 1.14 and 1.17, respectively (Chein and Liao, 2005). K_f and K_p are thermal conductivity of the fluid and particle, respectively. By solving the particle equation of motion, the particles path is obtained from

$$\frac{dx^i}{dt} = u_p^i \tag{3.8}$$

4. Numerical procedure

The computational domain is considered to be two dimensional concentric cylindrical annulus with inner radius R_i and outer radius R_o. The aspect ratio is defined as the ratio of the outer radius to the inner radius. The cylinder surfaces are maintained at two different uniform temperatures. The simulation performed for the Rayleigh number (Ra), Eq. (4.1), from 10^3 to 10^5 and the aspect ratio from 2 to 4. The characteristics of the annulus are presented in Table 1

$$\mathrm{Ra} = \frac{g\beta \Delta T H^3}{\nu_g \alpha_g} \tag{4.1}$$

Table 1. Annulus characteristics at $\Delta t = 100$ and $R_o = 0.5\,\mathrm{cm}$

Aspect ratio (AR)	Inner cylinder diameter [cm]
2	0.25
3	0.167
4	0.125

Particle physical properties are listed in Table 2. The Runge-Kutta method is used to calculate particles trajectories. Particles are considered to be captured by surfaces when their distance from the cylinder surfaces becomes smaller than their radius.

Table 2. Physical properties of particles (silicon dioxide)

Density [kg/m^3]	2220
Specific heat [J/(kg K)]	745
Thermal conductivity [W/(m K)]	1.38

5. Results and discussion

5.1. Flow field and heat transfer

Two horizontal circular cylinders are considered. R_i, R_o, T_h, T_c stand for the inner and outer radius, temperature of the annulus, respectively. The flow field and heat transfer characteristics are validated by comparing the present results with those by Hauf and Grigull (1966) at the Grashof numbers of 120000 and 122000. The results show good compatibility between the present simulation and experimental results as shown in Fig. 3. For further validation of the numerical procedure, the local equivalent thermal conductivity is calculated at Ra of $5 \cdot 10^4$. The results have been compared with the study by Kuehn and Goldstein (1978). An equivalent thermal conductivity, K_{eq} is used to compare the accuracy of the present computations. The average equivalent heat conductivity is defined for the inner and outer cylinder by

$$\overline{K}_{eq\,i} = -\frac{\ln(rr)}{\pi(rr-1)} \int_0^\pi \frac{\partial T}{\partial r}\, d\varphi \qquad \overline{K}_{eq\,o} = -\frac{rr\ln(rr)}{\pi(rr-1)} \int_0^\pi \frac{\partial T}{\partial r}\, d\varphi \tag{5.1}$$

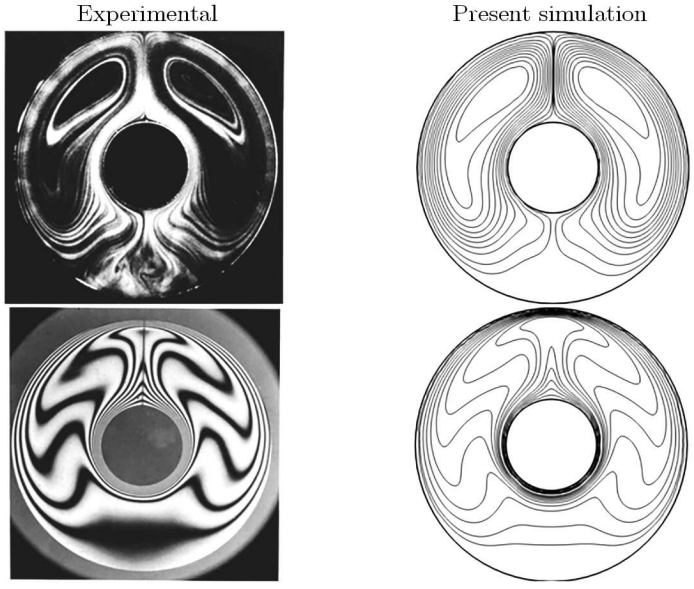

Fig. 3. The streamlines for Gr = 120000 (top) and isotherms for Gr = 122000 (bottom). Comparison with the experimental result by Hauf and Grigull (1966)

This parameter is defined as the actual heat flux divided by the heat flux that would occur due to pure conduction in the absence of fluid motion. The computed average equivalent heat conductivities are compared with the previous study by Kuehn and Goldstein (1978). The results for the local equivalent thermal conductivity are shown in Fig. 4 and represent good agreement. In particular, the present calculation of the local equivalent thermal conductivity is within ±3% of their benchmark data. The effect of the annulus aspect ratio on the flow and thermal fields is shown with streamlines (on the left) and the isotherms (on the right) in Figs. 5 to 7, respectively, for three Ra numbers (10^3, 10^4 and 10^5). The flow near the hot smaller cylinder becomes hotter

and reduces density (increase buoyancy). Then near the cold outer cylinder it becomes cold and starts to move down. This formss two large recirculation zones in the annulus at the left and right sides. The flow moves counterclockwise at the left side and clockwise at the right side of annulus. For the smallest Rayleigh number, the heat transfer is mainly due to conduction since the driven fluid motion is very slow (Fig. 5) due to the buoyancy force. As the Rayleigh number increases, the natural convection effect grows up. So the core of recirculation zones stretches in a larger region. The cores additionally move to the upper section of the annulus and this results in a plume shape of the isotherms. The effect of the increasing Ra number is more sensible at higher AR (AR = 4 in Figs. 5 to 7). In the bottom section, the relative position of hot and cold walls causes the power of convection to decrease. It is due to that the upper wall in this region is hotter and does not apply any movement to the flow. The increasing of AR causes isotherms to move to the upper section of the annulus gap at Ra = 10^3. Furthermore, the recirculation zones have less strength by increasing the aspect ratio. The buoyancy driven flow circulates in a narrow region because of the decreasing gap between the circles at a smaller aspect ratio. Therefore, the power of buoyancy becomes greater.

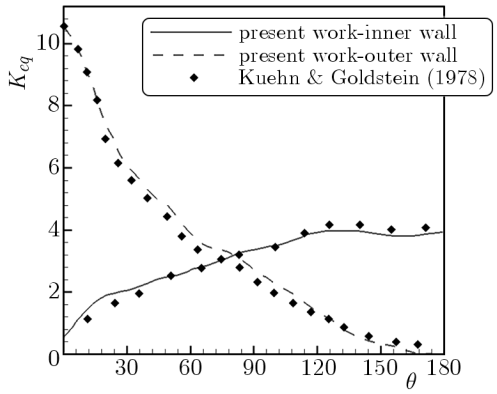

Fig. 4. Equivalent thermal conductivity on the inner and outer cylinder compared with the experiments by Kuehn and Goldstein (1976) for the annulus at Ra = $5 \cdot 10^4$

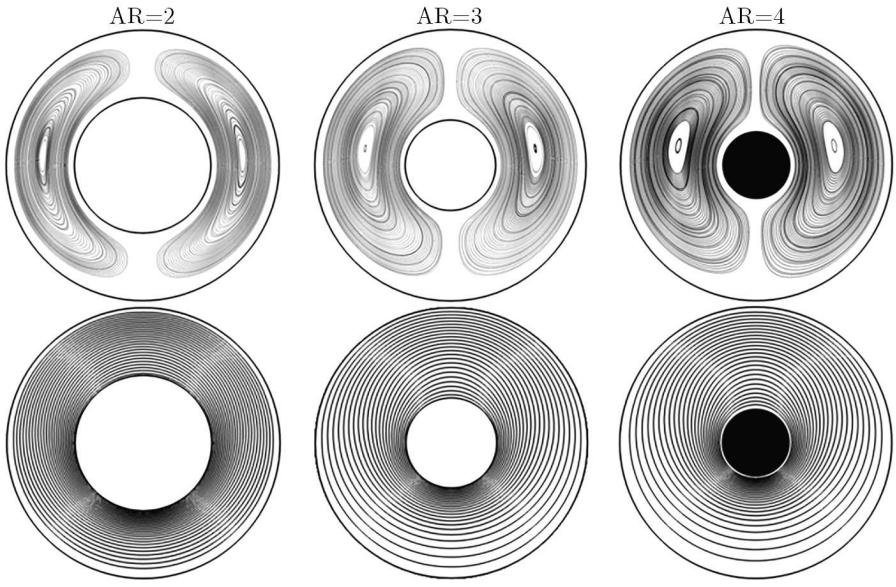

Fig. 5. Streamlines and isotherms for different aspect ratios at Ra = 10^3 (top: streamlines, bottom: isotherms)

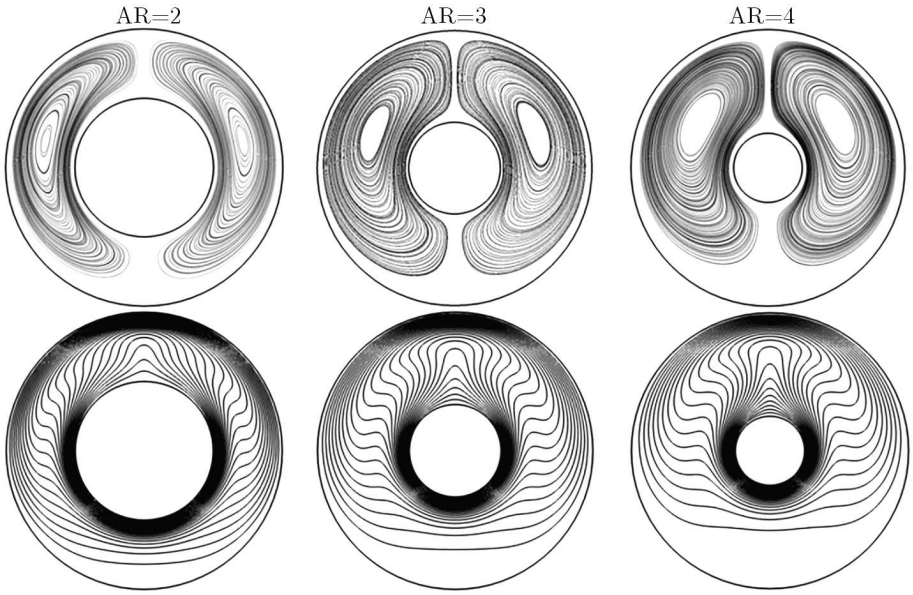

Fig. 6. Streamlines and isotherms for different aspect ratios at Ra = 10^4 (top: streamlines, bottom: isotherms)

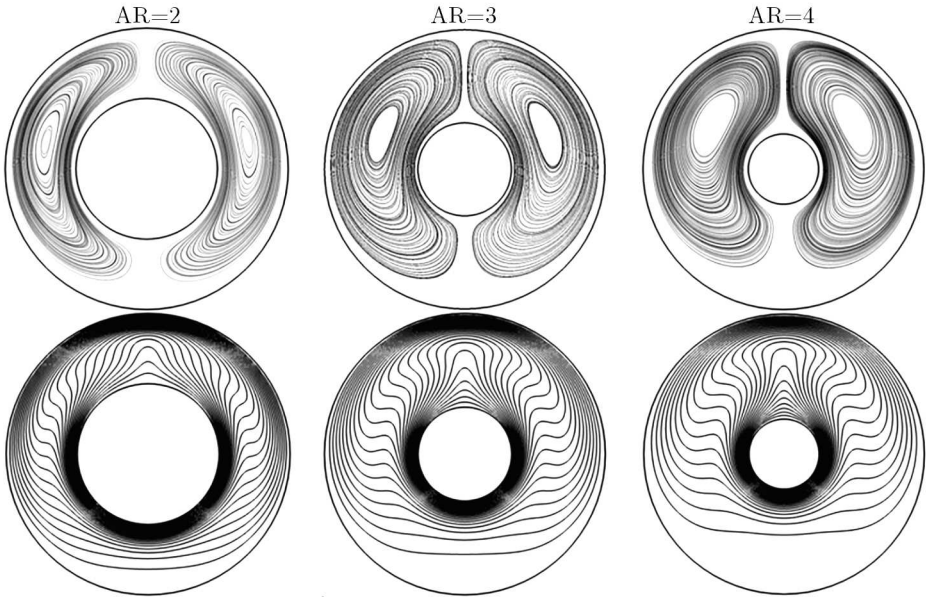

Fig. 7. Streamlines and isotherms for different aspect ratios at Ra = 10^5 (top: streamlines, bottom: isotherms)

5.2. Particles dispersion and removal

In the present study, the particles with sizes in the range of 10 to 150 nm at $S = 2220$ (Golovin and Putnam, 1962) are selected for simulation. The effects of the Rayleigh number, aspect ratio and particles diameter are investigated on the particles behavior such as removal and dispersion. In order to examine the relative significance of various particle transport mechanisms, some cases have been repeated in two new simulation approaches. In the first new approach, the thermophoresis force is neglected and, for the next approach, the effect of both thermophoresis and Brownian motion are not considered. The drag, gravity, buoyancy and lift forces have always been present in all the simulations. Hydrodynamics is usually the primary contributor to the particle dynamics. Since the magnitude and direction of the air velocity in the enclosure is

changing rapidly, the velocity slip between the air and particle develops. The air flow path is curved and the particles are unable to follow it precisely as a result of inertia. At one point the particles may even hit the wall and they are trapped there. This behavior is known as the inertial impaction. Brownian diffusion is dominant in the removal mechanism for finer particles. However, Brownian motion comes into account for particles with diameter within the range of present simulation.

Two recirculation regions tend to hold the particles within themselves due to hydrodynamic forces. The inertia force pushes the particles outwards and the gravity push them to the bottom. The thermophoretic force drives them toward the negative temperature gradient regions and the Brownian force makes them move along a stochastic path. The simultaneous effect of these forces creates a quasi-equilibrium zone at each side of the annulus gap. The trajectories of some particles are shown in Fig. 8 for $\mathrm{Ra} = 10^3$ and $\mathrm{AR} = 3$ when all forces are applied. The movement of particles with diameter of 10 nm clearly shows the effect of Brownian motion making the particles path stochastic (Fig. 8a). For these particles, a different removal mechanism is observed. The particles with the ID number of 1 and 2 start their migration from below of hot cylinder where the flow is weaker compared to other regions in the annulus. On the other hand, the power of the Brownian force becomes greater in the hot field. So, these particles are removed from the annulus by Brownian diffusion. The particles with ID numbers of 3 and 4 move through the streamline but the effects of Brownian motion and thermophoresis are observable. The particle with ID number 3 deposits on the inner cylinder by the contribution of Brownian motion and, maybe, gravity. The particles number 4 hit the outer cylinder because of thermophoresis. As the particles become larger, the effect of hydrodynamic forces increases and the particles tend to follow the streamlines exactly. This phenomenon is clearly observed in Figs. 8c and 8d). This figure additionally shows that by increasing the particles diameter from 100 nm up to 150 nm, no significant changes appear in the manner of particles dispersion in the annulus. It should be noted that the Brownian force causes the particles with diameter of 10 nm to require more time to follow the flow paths.

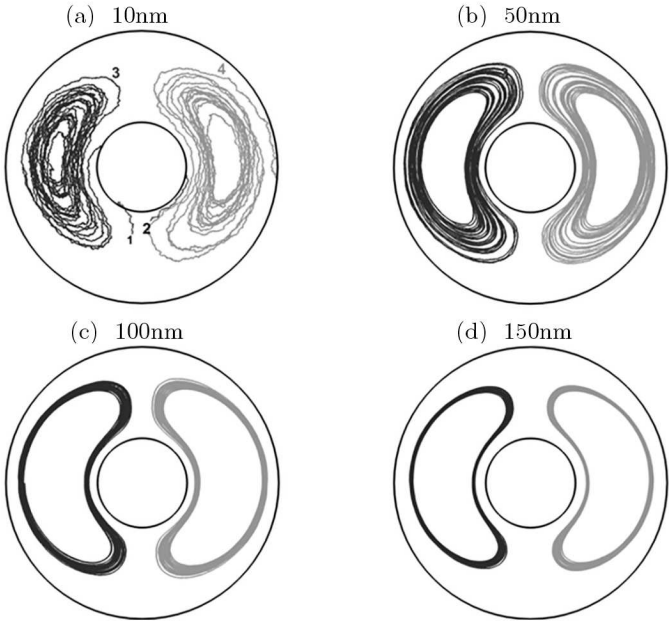

Fig. 8. Particle trajectories with all forces applied for $\mathrm{AR} = 3$ and $\mathrm{Ra} = 10^3$

By increasing the aspect ratio, the recirculation power decreases (Figs. 5 to 7), so the particles acceleration and their inertia decrease and the quasi-equilibrium zones cover a large part of the annulus gap (Fig. 8). The instant position of the suspended particles with diameter of 100 nm

is shown in Fig. 8 at the Ra number of 10000. It should be noted that the effect of different contributors to the particles transport are very complicated, and the forces have positive or negative effects on one particle in different locations.

The effects of the Ra number and AR of the annulus for particles with different diameters on the particles that remain suspended in the flow (concentration fraction) are presented in Fig. 9. The concentration fraction is smaller at AR = 4 for all particles. This shows that the hydrodynamic forces are dependent on the intensity of natural convection flow. By decreasing the aspect ratio, the number of particles that are removed from the flow by hitting the cylinders decreases. Additionally, by increasing the Ra number, the fraction of concentration at constant AR increases.

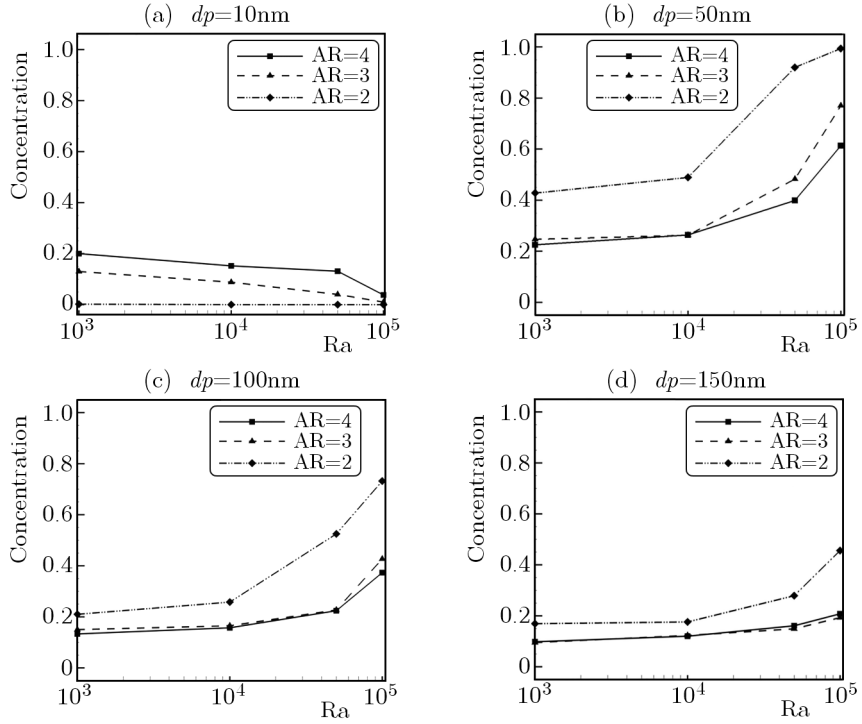

Fig. 9. Concentration fraction for particles with different radii versus the Ra number at various AR

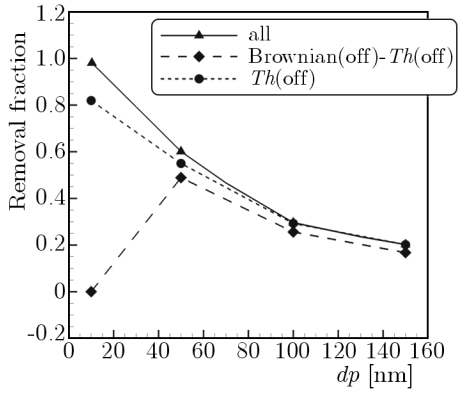

Fig. 10. Concentration versus *dp* with and without Brownian motion and thermophoresis

The mentioned trend is not observed for the particles with diameter of 10 nm. It is due to domination of Brownian diffusion and also the great effect of thermophoresis on these particles. The particles concentration increases by augmentation of AR. As discussed about the flow results, the quasi equilibrium zones form in a region closer to the cylinder walls at smaller

AR, and much more particles have chance to diffuse towards both cylinders. The cases with $AR = 0.5$ and $Ra = 10^4$ have been repeated two times, one by eliminating the Brownian motion and thermophoresis forces and another by eliminating just the thermophoresis force. The results indicate that the Brownian motion is the dominant removal mechanism, and thermophoresis is the second contributor. As the particles become larger, the effect of Brownian motion decreases while the effect of thermophoresis grows up (Fig. 10). The Brownian motion has no significant effect on the removal of the particles with diameter of 100 nm and greater. Removal fraction is shown in Fig. 10. It shows the fraction of deposited particles to the total distributed particles in the domain.

6. Conclusion

The flow and thermal fileds as well as the nano-particles transport have been investigated numerically by lattice Boltzmann method. The lagrangian particle equation of motion has been solved by employing the 4-th order Runge-Kutta algorithm. Simulations have been performed for the Rayleigh number changing from 10^3 to 10^5 and the particles specific density of 2220. Two experimental studies have been selected to validate the flow field and thermal characteristic of natural convection. The results show excellent agreement with them. The effects of the cylinder gap and particles size have been investigated on the removal and dispersion of particles at different Rayleigh numbers. Furthermore, the effect of absence and presence of the Brownian and thermophoresis force has been investigated for different cases. The results can be concluded as follows:

- The buoyancy effect increases by augmentation of the Rayleigh number at each aspect ratio and by decreasing the aspect ratio for each Rayleigh number. For a greater buoyancy effect, the strength of recirculation zones decreases.
- Brownian motion causes finer particles to follow stochastic pathlines in the natural convection flow.
- By decreasing the aspect ratio, more particles remove from the flow by hitting the cylinders.
- The final concentration of particles increases by augmentation of the aspect ratio.
- Brownian motion has a stronger more effect on the particles removal for greater nano-particles than the thermophoresis.

References

1. Abouei Mehrizi A., Farhadi M., Hassanzadeh Afrouzi H., Sedighi K., Rabienataj A.A., 2012, Mixed convection heat transfer in a ventilated cavity with hot obstacle: Effect of nano fluid and outlet port location, *International Communications in Heat and Mass Transfer*, **39**, 1000-1008

2. Abouei Mehrizi A., Farhadi M., Hassanzadeh Afrouzi H., Shayamehr S., 2013a, Lattice Boltzmann simulation of natural convection flow around a horizontal cylinder located beneath an insulation plate, *Journal of Theoretical and Applied Mechanics*, **51**, 360-367

3. Abouei Mehrizi A., Farhadi M., Sedighi K., Aghajani Delavar M., 2013b, Effect of fin position and porosity on heat transfer improvement in a plate porous media heat exchanger, *Journal of the Taiwan Institute of Chemical Engineers*, **44**, 3, 420-431

4. Abouei Mehrizi A., Farhadi M., Shayamehr S., 2013c, Natural convection flow of Cu-Water nanofluid in horizontal cylindrical annuli with inner triangular cylinder using lattice Boltzmann method, *International Communications in Heat and Mass Transfer*, **44**, 3, 147-156

5. Abouei Mehrizi A., Sedighi K., Farhadi M., Sheikholeslami M., 2013d, Lattice Boltzmann simulation of natural convection heat transfer in an elliptical-triangular annulus, *International Communications in Heat and Mass Transfer*, **48**, 164-177

6. Akbar M.K., Rahman M., Ghiaasiaan S.M., 2009, Particle transport in a small square enclosure in laminar natural convection, *Journal of Aerosol Science*, **40**, 747-761

7. Chein R., Liao W., 2005, Thermophoretic effects on nano-particle deposition in channel flow, *Heat and Mass Transfer*, **42**, 71-79

8. Chen F., Yu S.C.M., Lai A.C.K., 2006, Modeling particle distribution and deposition in indoor environments with a new drift–flux model, *Atmospheric Environment*, **40**, 357-367

9. Golkarfard V., Gandjalikhan Nasab S.A., Ansari A.B., Bagheri G.H., 2012, Numerical investigation on deposition of solid particles in a lid-driven square cavity with inner heated obstacles, *Advanced Powder Technology*, **23**, 6, 736-743

10. Golovin M., Putnam A., 1962, Inertial impaction on single elements, *Industrial and Engineering Chemistry Fundamentals*, **1**, 264-273

11. Guo Z., Shi B., Zheng C., 2002, A coupled lattice BGK model for the Boussinesq equations, *International Journal for Numerical Methods in Fluids*, **39**, 325-342

12. Hassanzadeh Afrouzi H., Farhadi M., 2013, Mix convection heat transfer in a lid driven enclosure filled by nanofluid, *Iranica Journal of Energy and Enviornment*, **4**, 4, 376-384

13. Hassanzadeh Afrouzi H., Farhadi M., Abouei Mehrizi A., 2012a, Numerical simulation of particles transport in a concentric annulus, *Advanced Powder Technology*, **24**, 3, 575-584

14. Hassanzadeh Afrouzi H., Sedighi K., Farhadi M., Fattahi E., 2012b, Dispersion and deposition of micro particles over two square obstacles in a channel via hybrid lattice Boltzmann method and discrete phase model, *International Journal of Engineering*, **25**, 3, 257-266

15. Hauf W., Grigull U., 1966, Measurements of the heat transfer at a horizontal cylindrical container – essential parameters, *Waerme- und Stoffuebertragung*, **9**, 1, 21-28

16. Jourabian M., Farhadi M., Rabienataj A.A., Abouei Mehrizi A., 2013, Lattice Boltzmann simulation of melting phenomenon with natural convection from an eccentric annulus, *Thermal Science*, **17**, 3, 877-890

17. Kuehn T., Goldstein R., 1976, An experimental and theoretical study of natural convection in the annulus between horizontal concentric cylinders, *Journal of Fluid Mechanics*, **74**, 695-719

18. Kuehn T., Goldstein R., 1978, An experimental study of natural convection heat transfer in concentric and eccentric horizontal cylindrical annuli, *Journal of Heat Transfer*, **100**, 635-644

19. Li A., Ahmadi G., 1992, Dispersion and deposition of spherical particles from point sources in a turbulent channel flow, *Aerosol Science and Technology*, **16**, 209-226

20. Mei R., Luo L.S., Shy W., 1999, An accurate curved boundary treatment in the lattice Boltzmann method, *Journal of Computational Physics*, **155**, 307-330

21. Puragliesi R., Dehbi A., Leriche E., Soldati A., Deville M.O., 2011, DNS of buoyancy-driven flows and Lagrangian particle tracking in a square cavity at high Rayleigh numbers, *International Journal of Heat and Fluid Flow*, **32**, 915-931

22. Rahman M.Md., Elias Md., Alim M.A., 2009, Mixed convection flow in a rectangular ventilated cavity with a heat conducting square cylinder at the center, *Journal of Engineering and Applied Sciences*, **4**, 5, 155-161

23. Saffman P.G., 1965, The lift on a small sphere in a slow shear flow, *Journal of Fluid Mechanics*, **22**, 385-400

24. Shams M., Ahmadi G., Rahimzadeh H., 2000, A sublayer model for deposition of nano-and micro-particles in turbulent flows, *Chemical Engineering Science*, **55**, 6097-6107

25. Talbot L., Cheng R., Schefer R., Willis D., 1980, Thermophoresis of particles in a heated boundary layer, *Journal of Fluid Mechanics*, **101**, 737-758

26. Vasak F., Bowen B., Chen C., Kastanek F., Epstein N., 1995, Fine particle deposition in laminar and turbulent flows, *Canadian Journal of Chemical Engineering*, **73**, 785-792

27. Vessakosol P., Charoensuk J., 2010, Numerical analysis of heat transfer and flow field around cross-flow heat exchanger tube with fouling, *Applied Thermal Engineering*, **30**, 1170-1178

28. Yu D., Mei R., Luo L.S., Shyy W., 2003, Viscous flow computations with the method of lattice Boltzmann equation, *Progress in Aerospace Sciences*, **39**, 329-367

Manuscript received November 9, 2014; accepted for print February 24, 2015

JOURNAL OF THEORETICAL AND APPLIED MECHANICS
53, 3, pp. 697-710, Warsaw 2015
DOI: 10.15632/jtam-pl.53.3.697

PRE-DESIGNING OF A MECHATRONIC SYSTEM USING AN ANALYTICAL APPROACH WITH DYMOLA

Ghazoi Hamza

Mechanics Modeling and Production Research Laboratory (LA2MP), National School of Engineers of Sfax (ENIS), Sfax, Tunisia and

Laboratory of Engineering of the Mechanical Structures and Materials (LISMMA), High Institute of Mechanic of Paris (SUPMECA), Saint-Ouen Cedex, France; e-mail: hamza.ghazoi@gmail.com

Jean-Yves Choley, Moncef Hammadi, Alain Riviere

Laboratory of Engineering of the Mechanical Structures and Materials (LISMMA), High Institute of Mechanic of Paris (SUPMECA), Saint-Ouen Cedex, France

Maher Barkallah, Jamel Louati, Mohamed Haddar

Mechanics Modeling and Production Research Laboratory (LA2MP), National School of Engineers of Sfax (ENIS), Sfax, Tunisia

This paper presents a pre-dimensioning method applied to a mechatronic system and regarding the vibrational aspect, through a simple modeling process in Dymola environment. We study the vibration transmission between dynamic exciters (motors) and receivers (electronic cards) which are located on a simply supported rectangular plate, using an analytical approach. This new method will allow us to perform representative and robust modeling and simulation. The solution for this issue would be a pre-sizing and pre-positioning procedure. It aims to determine a set of possible technical solutions and principal characteristics before the definitive choice of components and precise sizing of the system. The presented method predicts also behaviour of the mechatronic system. In order to validate the model with respect to the finite element method, selected simulation results are presented.

Keywords: pre-dimensioning, Dymola, analytical method, vibration, rectangular plate

1. Introduction

Mechatronics is the synergistic integration of a physical system, actuators, electronic components and sensors, etc., through the design process (Craig and Stolfi, 2002) and (Wang *et al.*, 2013) in order to develop new products more efficient and more reliable. It is very common in our daily life as well as in industry. In addition, it affects many applications in various fields such as transportation, automotive systems and production (Elmqvist *et al.*, 2001).

In order to minimize the cost as well as the time to market while improving their quality, it is important to take a great effort from the early phases of the design cycle of mechatronic systems. Thus, most important methodological efforts must be considered in the upstream phase of product development. The development process of a mechatronic system includes three phases which are the requirement analysis, pre-sizing and detailed sizing. The preliminary design is performed based on various feedback experiments and a set of specifications. Moreover, it should allow determining the system architecture and its setting (Liscouët *et al.*, 2012). For this reason, it may be necessary to describe the main phenomena involved in the system such as vibrational and thermal behaviour. Accordingly, a mechatronic designer uses different modeling tools to elaborate multi-physics models in the multidisciplinary design process of mechatronic systems.

In recent years, many researches, based on techniques such as multi-criteria decision making and poly-optimization, have been working on the integrated preliminary design and optimization of mechatronic systems. For instance, Hammadi *et al.* (2012b) proposed to aggregate several important criteria in one multi-criteria indicator to evaluate the mechatronic system performance in the preliminary design level. Moreover, Tarnowski *et al.* (2011) proposed the poly-optimization paradigm as an engineering design methodology for mechatronic system design. Every designer involved in the design process has to solve a design task as an inverse problem in an iterative way. The poly-optimization allows designers to make decision as a trade-off between conflicted criteria to find a sub-set of non-dominated solutions. Poly-optimization can be more interesting than aggregating many criteria in one multi-criteria indicator. However, a further development is required to automate the decision making based on poly-optimization.

To reduce the computing time during the system analysis and optimization of the mechatronic design, surrogate models can substitute the costly analysis models. A methodology based on the surrogate modeling technique combined with Modelica language was proposed by Hammadi *et al.* (2012a) for the optimization of electric vehicles. Although this method reduces the computing time during the optimization process, the elaboration of surrogate models is somewhat long and mechatronic designers have to verify the accuracy of the surrogate models before including them in the optimization process.

Long computing time in the analysis and optimization of mechatronic systems is due to the methods used to model and solve the governing equations of the mechatronic system and its components. In fact, the components modelled with partial differential equations (PDEs) are the major source of difficulties in the analysis and optimization of mechatronic systems. However, PDEs are strongly required to analyse the vibrating aspect of mechatronic systems. A vibrating component in mechatronic systems can be modelled with simple beams or plates. The governing equation of vibrating plate theories have been solved through three types of solutions: numerical methods, exact analytical methods and semi analytical methods.

In the case when the plate has all edges simply supported and a lateral force acts over the plate surface, Navier presented an exact method to obtain the solution of bending by using a double series Fourier approach, see Szilard (2004) and Ventsel and Krauthammer (2001). This method can be extended to an orthotropic plate subjected to dynamic excitation (Romanelli and Laura, 2001).

By using a single trigonometric series, Levy developed a method to solve the bending problem of a rectangular plate with two opposite sides simply supported and the remaining edges with arbitrary conditions (clamped, simply supported guided, etc.), see Ventsel and Krauthammer (2001).

In addition, Lagrange's multipliers approach was introduced by Vera *et al.* (2005) to study the problem of a plate supporting a 2-dof spring-mass system elastically mounted. However, it is not always possible to obtain analytical solutions, especially for complex structures. For this reason, many efforts have been dedicated to develop approximate methods, such as Galerkin's type approximate procedure. For instance, Laura and Duran (1975) used a simple polynomial approximation and Galerkin's method to determine the response of a thin rectangular plate clamped at four edges and subjected to uniformly distribute sinusoidal excitation. In this method, the approximate solution is expressed in terms of polynomials which satisfy all the prescribed boundary conditions. An untruncated infinite series superposition method (UISSM) was presented by Bhaskar and Sivaram (2008) for a rectangular plate with arbitrary boundary conditions and an arbitrary transverse load. The achieved solutions satisfy different requirements and they are obtained as a simple combination of analytically component solutions. The Rayleigh Ritz method is one of the most famous approximate methods; it is a useful approach for many eigenvalue problems (Leissa, 2005). This method belongs to the so-called variational methods; it assumes that the solution of the variational problem can be approximated by a suitable linear combina-

tion of the coordinate function. This method can be used for both thin and thick rectangular plates with different combinations of boundary conditions.

Various numerical methods have been developed to deal with the vibration problem of rectangular plates with mixed and non-uniform boundary conditions. Each of them can be classified as either a local method (finite difference method, finite element method) or a global method (differential quadratic method, Ritz method). In general, global methods are more accurate than the local ones. By contrast, local methods are more flexible to handle complex geometries and boundary conditions. A discrete singular convolution algorithm, as a potential approach, was introduced by Wei *et al.* (2001) to study this kind of problems. The mathematical fundamentals of this algorithm are based on the theory of distributions (Schwartz, 1951). This approach has the advantages of both methods (local and global).

The natural frequencies and the mode shapes of a rectangular plate, carrying any number of translational springs and point masses are determined by using the analytical and numerical combined method (ANCM) (Wu and Luo, 1997). By obtaining the analytical closed form solutions for the mode shapes and natural frequencies, based on the mode superposition theory, the eigenvalue equation of the plate with these elements can be derived. This approach prevents the algebraic difficulties of the analytical method. Moreover, it consumes less computation time if one compares it with the finite element method (FEM).

A plate vibrating in a mechatronic system can cause problems to various components which are interconnected such as electronic devices which are essential and vital components in any mechatronic systems. Moreover, they must be able to operate over the important life cycle and survive environmental issues such as temperature and vibration (Veprik and Babtisky, 2000) and (Mchira and Pecht, 2002) to which they are sensitive. Consequently, for the preliminary design phase, the objective is to predict how the electronic component will implement completely and correctly the functions specified in the requirements within the constraints of the device, the environments the component will function within and the defined interfaces. During this phase, the designer should maintain a system perspective and see the interaction with the rest of the system in order to identify inconsistencies and ambiguities.

The main purpose of this work is to present a pre-dimensioning method based on an analytical approach and taking into consideration the effect of vibration. More precisely, we focus on the effect of dynamic disturbances produced by motors and transmitted to the electronic cards through the plate. In order to predict the behaviour of the mechatronic system, robust modeling and simulations with DYMOLA are carried out. We investigate the sensitivity of the system for several parameters and different architectures in order to develop an accurate and reliable design.

The organization of this paper is as follows: the first section deals with the introduction, in Section 2 we introduce the analytical formulation of the problem, in Section 3 we present the modeling of the system. Results of simulations are presented and discussed in Section 4 with comparison to FEM. The conclusion of our paper is given in Section 5.

2. Theoretical background

2.1. Analytical formulation of plate vibration

Before developing the analytical model, we need to make some hypothesis and simplifications. Indeed, the simply supported rectangular plate will be considered as homogeneous, linearly elastic, isotropic and uniformly thin. Neither the shear deformations nor in plane forces are taken into account. The relatively low frequencies induced by electric motors and the small thickness of the plate compared to the other dimensions allow us to consider only transverse vibration. The excitations in many mechatronic systems can be considered as a random process.

However, for simplification reasons, we will deal only with deterministic structural parameters. Therefore, only a harmonic excitation is considered in this study.

The coordinate system of the plate is presented in Fig. 1. In these conditions, the classical plate governing differential equation of motion can be written as

$$D\nabla^4 w = -\rho h \frac{\partial^2 w}{\partial t^2} + f(x,y,t) \tag{2.1}$$

where

$$f(x,y,t) = \sum_{i=1}^{N} f_i \tag{2.2}$$

∇^2 is the Laplacian operator, $w(x,y,t)$ is the transverse deflection, N is the number of electric motors. D, ρ, h and $f(x,y,t)$ present respectively the flexural rigidity, density of the plate material, plate thickness and the transverse external loadings

$$D = \frac{Eh^3}{12(1-\upsilon^2)} \tag{2.3}$$

where E and υ are respectively Young's modulus and Poisson's ratio.

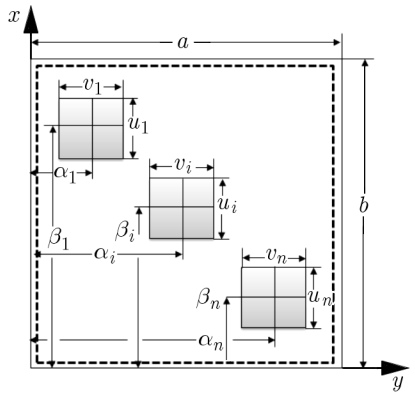

Fig. 1. Spatial distribution of dynamic pressures on the plate (top view)

We consider that every motor mounted on the plate induces a dynamic excitation over a finite area. In this case, we consider that a uniformly distributed $p\cos(\omega t)$ type force, equivalent to the excitation generated by the motor, acts over a rectangular portion of the plate of dimensions u_i and v_i, where the coordinates of the centroid are (α_i, β_i)

$$f_i = p_i \cos(\omega_i t) \tag{2.4}$$

where, p_i is the intensity of the distributed load, ω_i is the angular frequency of the dynamic excitation. Then

$$f(x,y,t) = \sum_{i=1}^{N} p_i \cos(\omega_i t) \tag{2.5}$$

The boundary conditions for a simply supported plate are the following

$$w = 0\Big|_{x=0,a} \qquad \frac{\partial^2 w}{\partial x^2} = 0\Big|_{x=0,a} \qquad w = 0\Big|_{y=0,b} \qquad \frac{\partial^2 w}{\partial y^2} = 0\Big|_{y=0,b} \tag{2.6}$$

In the following, we use Navier's principle to establish the dynamic equation of the structure.

The spatial distribution of the dynamical loading has been expanded into the double Fourier series (Szilard, 2004)

$$f_i(x,y,t) = \cos(\omega_i t) \sum_{n=1}^{\infty} \sum_{m=1}^{\infty} b_{nm}^i \sin\frac{n\pi x}{a} \sin\frac{m\pi y}{b} \tag{2.7}$$

The coefficients of the Fourier series can be calculated as

$$\begin{aligned} b_{nm}^i &= \frac{4p_i}{ab} \int_{\alpha_i - u_i/2}^{\alpha_i + u_i/2} \int_{\beta_i - v_i/2}^{\beta_i + v_i/2} \sin\frac{n\pi x}{a} \sin\frac{m\pi y}{b} = \frac{16p_i}{\pi^2} B_{nm}^i \\ B_{nm}^i &= \frac{1}{nm} \sin\frac{n\pi\alpha_i}{a} \sin\frac{n\pi u_i}{2a} \sin\frac{m\pi\beta_i}{b} \sin\frac{m\pi v_i}{2b} \end{aligned} \tag{2.8}$$

Following this approach, based on the superposition method, the expression of the deflected surface $W(x,y,t)$ can be written as in the following

$$w(x,y,t) = \sum_{i=1}^{N} w_i \cos(\omega_i t) = \sum_{i=1}^{N} \cos(\omega_i t) \sum_{n=1}^{\infty} \sum_{m=1}^{\infty} C_{nm}^i \sin\frac{n\pi x}{a} \sin\frac{m\pi y}{b} \tag{2.9}$$

then

$$\begin{aligned} w(x,y,t) = \cos(\omega_1 t) \sum_{n=1}^{\infty} \sum_{m=1}^{\infty} C_{nm}^1 \sin\frac{n\pi x}{a} \sin\frac{m\pi y}{b} + \cos(\omega_2 t) \sum_{n=1}^{\infty} \sum_{m=1}^{\infty} C_{nm}^2 \sin\frac{n\pi x}{a} \sin\frac{m\pi y}{b} \\ + \ldots + \cos(\omega_N t) \sum_{n=1}^{\infty} \sum_{m=1}^{\infty} C_{nm}^N \sin\frac{n\pi x}{a} \sin\frac{m\pi y}{b} \end{aligned} \tag{2.10}$$

with

$$\begin{aligned} C_{nm}^1 &= \frac{16p_1 B_{nm}^1}{\pi^2 \Big\{ D \Big[\Big(\frac{\pi n}{a}\Big)^2 + \Big(\frac{\pi m}{b}\Big)^2 \Big]^2 - \rho h \omega_1^2 \Big\}} \qquad C_{nm}^2 = \frac{16p_2 B_{nm}^2}{\pi^2 \Big\{ D \Big[\Big(\frac{\pi n}{a}\Big)^2 + \Big(\frac{\pi m}{b}\Big)^2 \Big]^2 - \rho h \omega_2^2 \Big\}} \\ &\vdots \\ C_{nm}^N &= \frac{16p_N B_{nm}^N}{\pi^2 \Big\{ D \Big[\Big(\frac{\pi n}{a}\Big)^2 + \Big(\frac{\pi m}{b}\Big)^2 \Big]^2 - \rho h \omega_N^2 \Big\}} \end{aligned} \tag{2.11}$$

Expression of deflection (2.12) automatically satisfies the prescribed boundary conditions.

For a simply supported plate, the natural frequencies are

$$\omega_{nm} = \pi^2 \Big[\Big(\frac{m}{a}\Big)^2 + \Big(\frac{n}{b}\Big)^2 \Big] \sqrt{\frac{D}{\rho h}} \tag{2.12}$$

For the case of one installed motor, the amplitudes of the plate bending moments are

$$M_x = D\Big(\frac{\partial^2 w}{\partial x^2} + \nu \frac{\partial^2 w}{\partial y^2}\Big) \qquad M_y = D\Big(\nu \frac{\partial^2 w}{\partial x^2} + \frac{\partial^2 w}{\partial y^2}\Big) \tag{2.13}$$

then

$$\begin{aligned} M_x &= \frac{16p_1 a^2}{\pi^2} \sum_{n=1}^{\infty} \sum_{m=1}^{\infty} \frac{B_{nm}}{F_{nm} - R^2 F_{11}} \Big[n^2 + \upsilon m^2 \Big(\frac{a}{b}\Big)^2 \Big] \sin\frac{n\pi x}{a} \sin\frac{m\pi y}{b} \\ M_y &= \frac{16p_1 a^2}{\pi^4} \sum_{n=1}^{\infty} \sum_{m=1}^{\infty} \frac{B_{nm}}{F_{mn} - R^2 F_{11}} \Big[\upsilon n^2 + \Big(\frac{ma}{b}\Big)^2 \Big] \sin\frac{n\pi x}{a} \sin\frac{m\pi y}{b} \end{aligned} \tag{2.14}$$

with

$$F_{nm} = \Big[n^2 + m^2\Big(\frac{a}{b}\Big)^2\Big]^2 \qquad R = \frac{\omega}{\omega_{11}} \tag{2.15}$$

The kinetic energy is

$$T = \frac{1}{2}\rho h \int\limits_S \Big(\frac{\partial w}{\partial t}\Big)^2 \, dxdy \tag{2.16}$$

In order to simplify the problem, we take $m = n = 1$ with $N = 1$. Then

$$\begin{aligned} w &= \cos(\omega_1 t) C_{11}^1 \sin\frac{\pi x}{a} \sin\frac{\pi y}{b} \\ T &= \frac{1}{2}\rho h \int\limits_0^a \int\limits_0^b \Big(-\omega_1 \sin(\omega_1 t) C_{11}^1 \sin\frac{\pi x}{a} \sin\frac{\pi y}{b}\Big)^2 \, dx\, dy \end{aligned} \tag{2.17}$$

so

$$T = \frac{1}{8}\rho h[-\omega_1 \sin(\omega_1 t) C_{11}^1]^2 ab \tag{2.18}$$

The expression of the strain energy of an isotropic plate is as follows

$$U = \frac{D}{2} \int\limits_s \Big(\frac{\partial^2 w}{\partial x^2} + \frac{\partial^2 w}{\partial y^2}\Big)^2 - 2(1-\upsilon)\Big[\frac{\partial^2 w}{\partial x^2}\frac{\partial^2 w}{\partial y^2} - \Big(\frac{\partial^2 w}{\partial x \partial y}\Big)^2\Big] \, ds \tag{2.19}$$

By calculating the derivatives of $w(x, y)$ we obtain

$$\begin{aligned} &\frac{\partial^2 w}{\partial x^2} = \cos(\omega_1) C_{11}^1 \frac{\pi^2}{a^2} \sin\frac{\pi x}{a} \sin\frac{\pi y}{b} \qquad \frac{\partial^2 w}{\partial y^2} = \cos(\omega_1) C_{11}^1 \frac{\pi^2}{b^2} \sin\frac{\pi x}{a} \sin\frac{\pi y}{b} \\ &\frac{\partial^2 w}{\partial y \partial x} = \cos(\omega_1) C_{11}^1 \frac{\pi^2}{ab} \sin\frac{\pi x}{a} \sin\frac{\pi y}{b} \end{aligned} \tag{2.20}$$

Substituting Eqs. (2.20) into (2.19) yields

$$U = \frac{Eh^3\pi^4 ab}{96(1-\upsilon^2)} \cos(\omega_1 t) C_{11}^1 \Big(\frac{1}{a} + \frac{1}{b}\Big)^2 \tag{2.21}$$

2.2. Modeling of the electronic card

The simplest model for a system under a vibration excitation is given by a rigid mass supported by a linear spring and damper (Piersol and Paez, 2010). Figure 2 shows schematically a model of the electronic card which is mounted resiliently over the vibrating plate. The mass of the internal box is generally very small in comparison with the entire box (Lahdenpera, 1992).

The equation of relative motion of the system is expressed in the form

$$Z_1 + 2\Omega_1 \zeta_1 \dot{Z}_1 + \Omega_1^2 Z_1 = -\ddot{Y} \tag{2.22}$$

where $\Omega_1 = \sqrt{k/m}$ is the angular frequency and m and k represent the moving mass and the corresponding spring stiffness, respectively. $\zeta_1 = c/C_c$ is the loss factor, where $C_c = 2\sqrt{km} = 2m\Omega_1$, and c is the damping coefficient.

The dynamic response of the plate is expressed as follows

$$Y(t) = w(x, y, t) = \sum_{i=1}^{N} w_i \cos(\omega_i t) \tag{2.23}$$

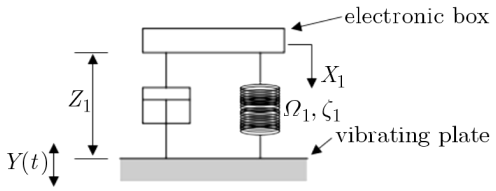

Fig. 2. Simple model of the electronic card; ζ_1 and Ω_1 denote, respectively, the loss factor and the natural frequency, $Y(t)$ is the plate motion, X_1 is the deflection of the system, $Z_1 = X_1 - Y$ denotes the relative deflection of the card to the plate

For two motors, the displacement function can be written as

$$\begin{aligned} Y(t) &= w(x,y,t) = w_1 \cos(\omega_1 t) + w_2 \cos(\omega_2 t) \\ \ddot{w}(x,y,t) &= -Y_1 \cos(\omega_1 t) - Y_2 \cos(\omega_2 t) \end{aligned} \tag{2.24}$$

where

$$Y_1 = \omega_1^2 w_1 \qquad Y_2 = \omega_2^2 w_2 \tag{2.25}$$

then

$$|Z| = |Z_1(\omega_1)| + |Z_2(\omega_2)| \tag{2.26}$$

where

$$|Z_1(\omega_1)| = \frac{Y_1}{\sqrt{(\Omega_1^2 - \omega_1^2)^2 + 4\omega_1^2 \Omega_1^2 \zeta^2}} \qquad |Z_2(\omega_2)| = \frac{Y_2}{\sqrt{(\Omega_1^2 - \omega_2^2)^2 + 4\omega_2^2 \Omega_1^2 \zeta^2}} \tag{2.27}$$

3. System modeling

Modeling language Modelica has been chosen to implement the models described above. As Modelica is an object oriented modeling language, it allows the realization of a complex system by simple gathering components (Schiavo *et al.*, 2006). The construction of this model (Fig. 3) includes elements developed expressly for this application such as the plate component and selection of the position component as well as parts that belong to Dymola/Modelica library.

The model of the system in Dymola is decomposed into a set of connected components; everyone is represented by a block containing the necessary information about the element, which can be changed by the user. The model can be divided into five main parts. The motor represents the dynamic excitation over the exterior surface of the plate. In this case, we model the motor by a uniformly distributed $p\cos(\omega t)$-type force acting over a rectangular subdomain of the plate. To choose the location of the card on the plate, the selection of the position element has been modelled. The simply supported plate object has been modelled with consideration of the necessary equations describing vibration propagation through the structure. Consideration has been given to the principal parameters that characterize the physical properties of this plate such as the dimensions, Poisson's ratio and Young's modulus.

In Fig. 3 components of the Modelica library are used: the linear 1D model composed of a spring and damper in parallel and the sliding mass, to model the electronic card. The sensors measure absolute position, absolute velocity and absolute acceleration in order to control the displacement, speed, and acceleration of the electronic card on the plate.

To describe the physical interfaces between these components, we use connectors which are associated with every component. In order to describe the physical interfaces between the motors

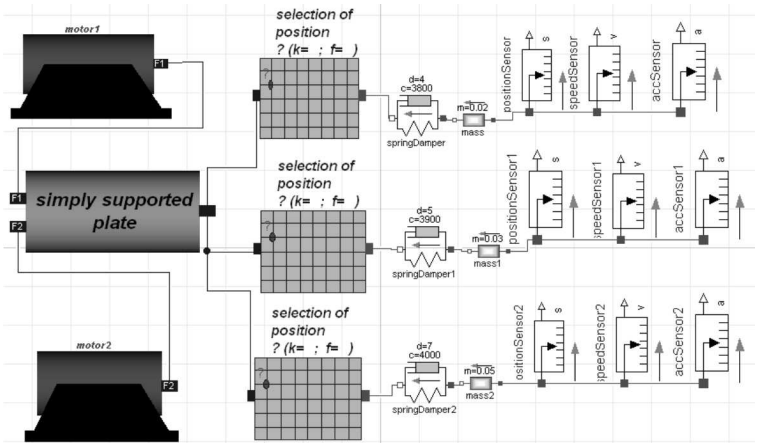

Fig. 3. Model of the system in Dymola/Modelica

Table 1. New connector properties

Type	Name	Description
Length	u_1	length [m]
Length	v	length [m]
Pressure	P_0	force magnitude [N/m^2]
Angular velocity	z	angular frequency [rad/s]

and the plate, we have introduced a new connector in Dymola. Table 1 shows the characteristics of the new connector used to connect new the models build in Dymola.

This new model will give us the possibility to have a simplified procedure which will enable us to perform behaviour simulations, technology completions and to estimate the vibrational behaviour of the mechatronic system.

4. Results and discussions

4.1. Case study presentation

According to the theoretical analysis in Section 2, two motors are considered in this study and two electronic cards which are located on the rectangular plate (Fig. 4a). The finite element analysis with ANSYS (Fig. 4b) has been used to validate the model implemented in Modelica.

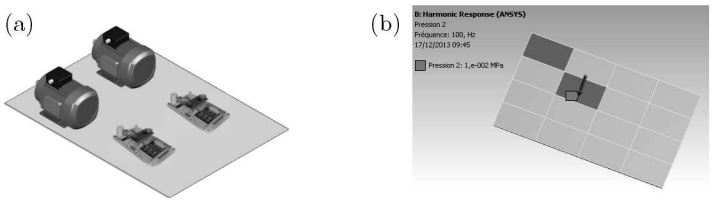

Fig. 4. (a) The studied model. (b) Modeling of the loaded plate with ANSYS

4.2. Validation with the finite element method

In order to validate the model implemented in Dymola/ Modelica, some results derived in this paper have been compared with those obtained with the finite element analysis using ANSYS.

Figure 4b illustrates the CAD model of the plate that has been used for this study in ANSYS WorkBench. The geometry is made of a set of rectangular faces with dimension (u, v) for each face, to make easy the application of the vibrating force represented with an arrow in the figure. The mesh is not represented in this figure.

The first five natural frequencies are listed in Table 2 along with analytical results and ANSYS output data. It can be seen that the natural frequencies obtained by this method are in good agreement with those obtained by the finite element analysis using ANSYS.

Table 2. Natural frequencies [Hz] of the simply supported plate. m and n are the mode numbers in the x and y direction, respectively

(m, n)	Analytical solution	ANSYS
(1,1)	169.88	170
(1,2)	423.36	426.8
(2,2)	676.32	682.9
(1,3)	848.29	853.67
(3,2)	1099	1109

Table 3 and 4 give the bending at the centre of the plate for several positions of the two motors and illustrate the error between the two methods.

Table 3. Bending at the centre of the plate, the two motors have the same amplitude of vibration, $p_1 = p_2 = 0.01\,\text{MPa}$ and the same frequency, $f_1 = f_2 = 100\,\text{Hz}$

Motors positions	Modelica	ANSYS	Error
$(\alpha_1, \beta_1) = (0.03\,\text{m}, 0.03\,\text{m})$ $(\alpha_2, \beta_2) = (0.03\,\text{m}, 0.09\,\text{m})$	0.094	0.095	0.15%
$(\alpha_1, \beta_1) = (0.03\,\text{m}, 0.03\,\text{m})$ $(\alpha_2, \beta_2) = (0.09\,\text{m}, 0.09\,\text{m})$	0.2	0.2	0%
$(\alpha_1, \beta_1) = (0.03\,\text{m}, 0.09\,\text{m})$ $(\alpha_2, \beta_2) = (0.09\,\text{m}, 0.09\,\text{m})$	0.241	0.234	2.99%
$(\alpha_1, \beta_1) = (0.09\,\text{m}, 0.09\,\text{m})$ $(\alpha_2, \beta_2) = (0.15\,\text{m}, 0.15\,\text{m})$	0.347	0.359	3.34%

The results are compared with those obtained with finite element analysis using ANSYS. It can be noticed that the error between two methods is less than 6%. Therefore, the results given by the analytical models and the FEM models are close to each other.

Table 4. Bending at the plate centre, the two motors have different amplitudes of vibration, $p_1 = 0.01\,\text{MPa}$, $p_2 = 0.02\,\text{MPa}$ and the same frequency, $f_1 = f_2 = 100\,\text{Hz}$

Motors positions	Modelica	ANSYS	Error
$(\alpha_1, \beta_1) = (0.03\,\text{m}, 0.03\,\text{m})$ $(\alpha_2, \beta_2) = (0.03\,\text{m}, 0.09\,\text{m})$	0.162	0.171	5.26%
$(\alpha_1, \beta_1) = (0.03\,\text{m}, 0.03\,\text{m})$ $(\alpha_2, \beta_2) = (0.09\,\text{m}, 0.09\,\text{m})$	0.374	0.383	2.34%
$(\alpha_1, \beta_1) = (0.03\,\text{m}, 0.09\,\text{m})$ $(\alpha_2, \beta_2) = (0.09\,\text{m}, 0.09\,\text{m})$	0.414	0.426	2.8%
$(\alpha_1, \beta_1) = (0.09\,\text{m}, 0.09\,\text{m})$ $(\alpha_2, \beta_2) = (0.15\,\text{m}, 0.15\,\text{m})$	0.520	0.541	3.88%

4.3. Parametric study

After the modeling of the entire system with Dymola/Modelica, an analysis has been carried out for different magnitudes. The plate is characterized by the parameters a and b which are lengths of the plate along, respectively, in the x and y direction, $a = b = 240\,\text{mm}$, plate thickness $h = 20\,\text{mm}$, density of the plate material $\rho = 7850\,\text{Kg/m}^3$, Poisson's ratio $\upsilon = 0.3$ and Young's modulus $E = 210000\,\text{MPa}$. Several simulations tests have been made. Figures 5a, 5b and 5c show, respectively, the displacement, speed and acceleration at the centre of the plate which is subjected to a bi-harmonic force that acts at positions $(\alpha_1, \beta_1) = (0.03\,\text{m}, 0.03\,\text{m})$ and $(\alpha_2, \beta_2) = (0.09\,\text{m}, 0.09\,\text{m})$. The excitation amplitudes are $p_1 = p_2 = 0.01\,\text{MPa}$ with excitation frequencies $f_1 = f_2 = 100\,\text{Hz}$.

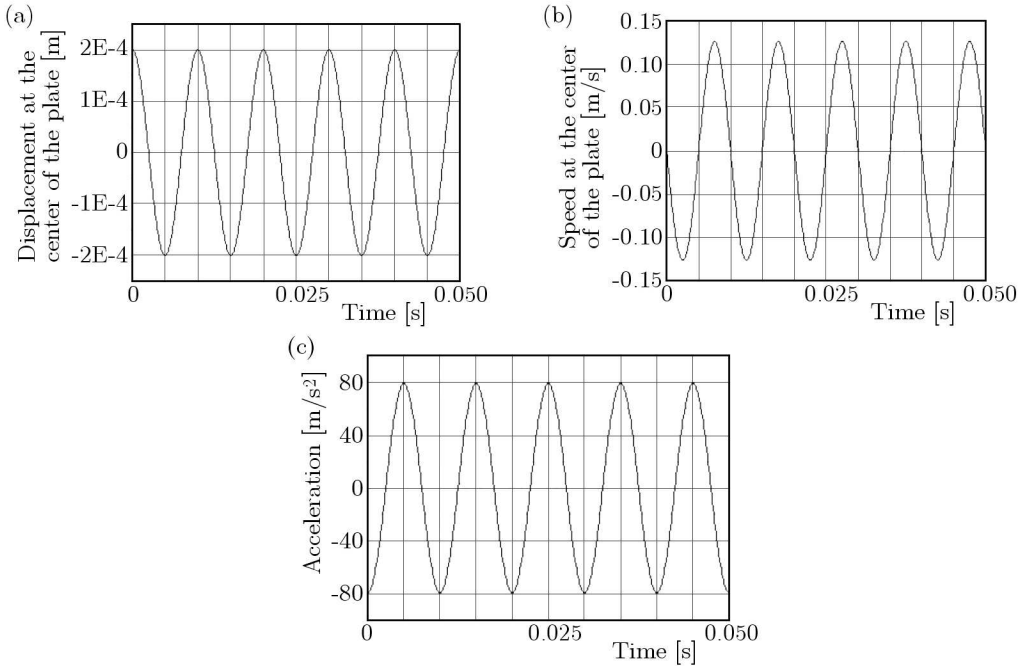

Fig. 5. Displacement (a), speed (b) and acceleration (c) at the plate centre

As it can be observed, the displacement, speed and acceleration at the centre of the plate have sinusoidal shapes with a frequency of 100 Hz (frequency of excitations) and they have, respectively, amplitudes of 0.2 mm, 0.125 m/s and 79.25 m/s^2. The speed and the acceleration are, respectively, $\pi/2$ and π phase-shifted with respect to the displacement.

Comparison between the amplitudes of vibration in the centre of the rectangular plate and that of the electronic card which is located in the same position is shown in Fig. 6. From the results presented in this figure, it can be observed that the two curves are in phases. But the amplitude of vibration of the mass is lower than that of the plate centre, which is due to the damping effect. Concerning the movement of the mass, a transient phenomenon occurs at the beginning of the movement. It represents the response of the system before stabilization, which strongly depends on the initial conditions. Then, there is a steady-state regime when the initial conditions have no longer influence.

Figure 7 shows the amplitudes of vibration of some points which are located in the middle line of the plate. As it can be observed, the deflections are different from one point to another. Moreover, the period of vibration is maintained and the curves are in phases. Then for the plate excited by two excitation forces acting at different locations, regardless the parameters, we can control the vibration amplitude in any point of the rectangular plate. The curve of transverse central deflection according to the plate width is given in Fig. 8. It is shown that the amplitude of vibration increases with increasing the plate width.

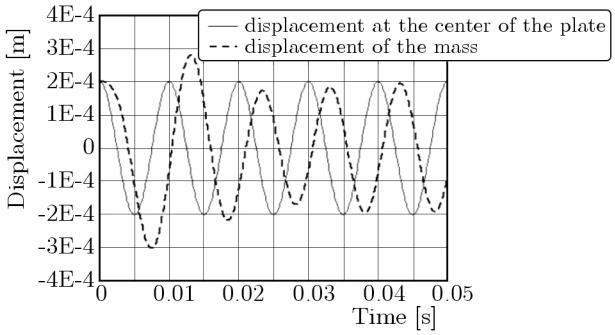

Fig. 6. Bending at the plate centre and displacement measured by the position sensor

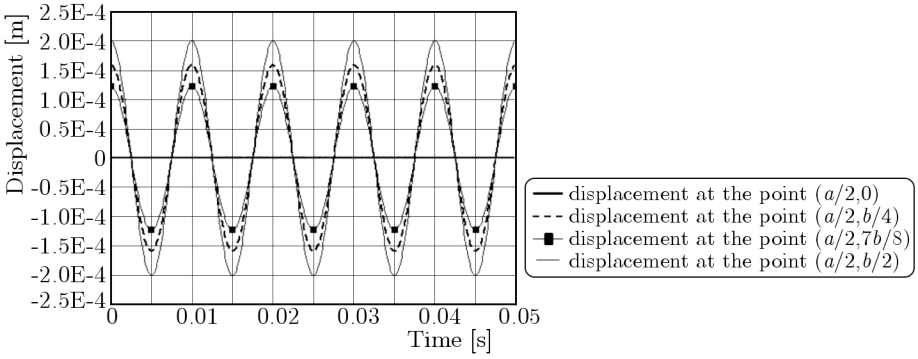

Fig. 7. Bending of the plate at different points in the middle line of the plate

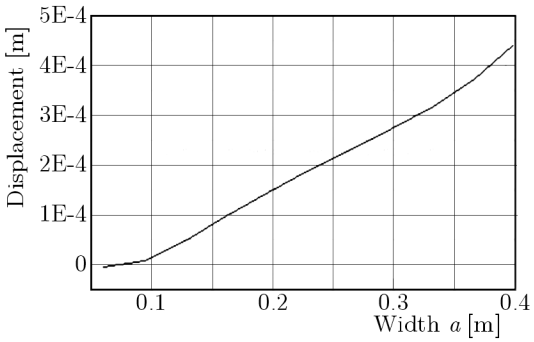

Fig. 8. Displacement at the plate centre according to its width a

The Navier approach is based on the thin plate theory. In this case, h is assumed to be negligible relatively to other dimensions (width and length). Yet, the height value has a great impact on the vibration propagation. Figure 9a represents the central deflection according to the plate height. As illustrated, the curve of the height has two parts. In the beginning, the vibration amplitude increases with the increasing height of the plate until reaching the value of 0.0029 m, then there is a decrease in the amplitude when the height increases, the amplitude of vibration tends to zero. Deflection of the plate depends mainly on its dimensions. Figure 9b clearly shows the variation of transverse displacement at the centre of the plate according to its dimensions (a, b). So, it can be seen that as the dimension values increase, the vibration amplitude increases.

Figures 10a and 10b depict, respectively, the central deflection of the plate according to the first motor dimensions and the motor positions on the rectangular plate while keeping other parameters fixed. The influence of the angular frequency on the vibrational response of the plate is given in Fig. 10c.

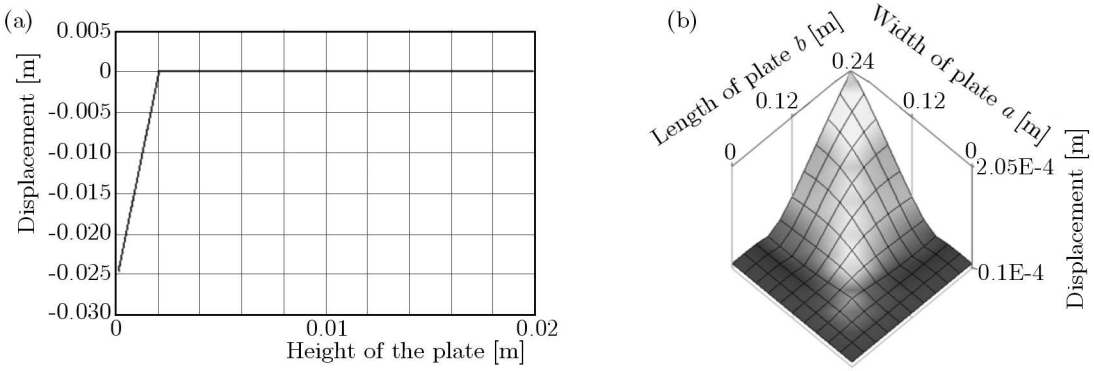

Fig. 9. Displacement at the plate centre according to: (a) its height h, (b) plate dimensions

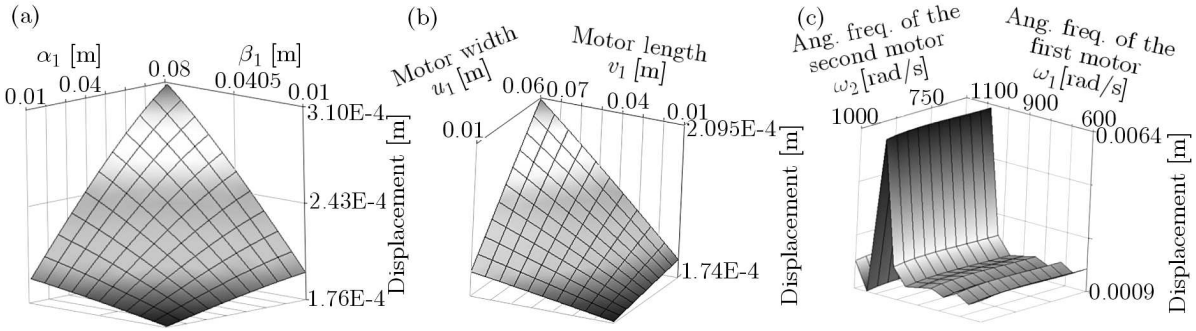

Fig. 10. Displacement at the plate centre according to: (a) dimensions of the first motor (α_1, β_1), (b) the motor positions (u_1, v_1), (c) the angular frequencies of the motors

Figures 11a and 11b show the effect of dimensions variation (width and length) on the strain and kinetic energy of the simply supported rectangular plate with uniform thickness. It can be observed that the kinetic energy increases with an increasing in the width a, in addition, the plate dimensions have a significant impact on the plate energies. At any position of the electronic card over the rectangular plate, we can control its motion.

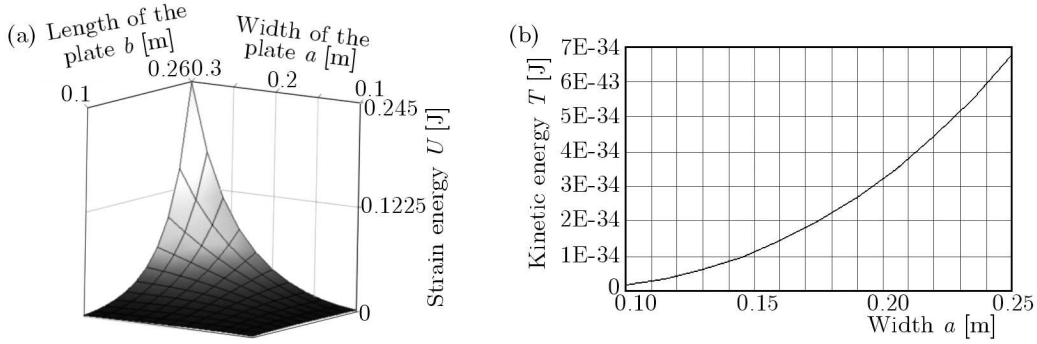

Fig. 11. (a) Strain energy of the plate according to its dimensions (a, b), $p_1 = 0.01\,\mathrm{MPa}$, $(\alpha_1, \beta_1) = (0.03\,\mathrm{m}, 0.03\,\mathrm{m})$. (b) Kinetic energy of the plate according to its width a

The simulation results of the speed and acceleration control of the electronic card are given in Figs. 12a and 12b. The card is located in the centre of the plate. As it is shown, the speed and acceleration are sinusoidal functions; both curves show a transient regime in the beginning, and then a steady-state regime is established. In addition, the two amplitudes depend strongly on the card characteristics as well as the card position on the plate.

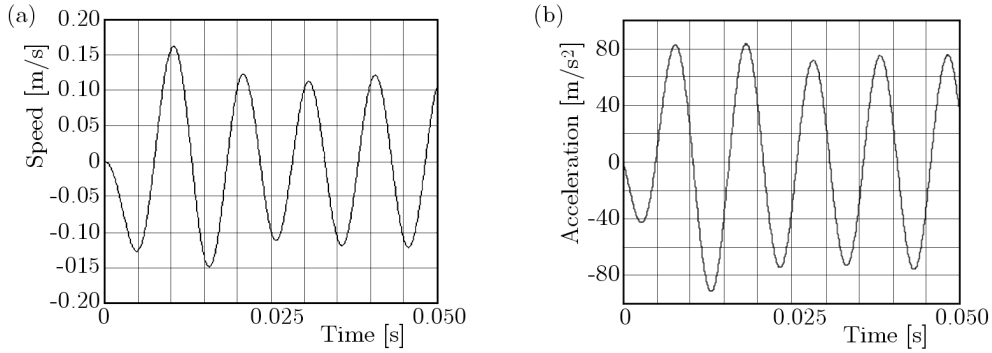

Fig. 12. (a) Speed measured by the speed sensor. (b) Acceleration response of the mass

5. Conclusions

In this paper, we have proposed a new approach for the preliminary design of a mechatronic system based on an analytical method. We defined a model that allows the predictability of the vibrational behaviour of the system. The model has been developed using the modeling language Modelica/Dymola. To show the capability of the model to help designers in pre-dimensioning, we have analysed several parameters having significant influence on the vibration propagation. The possibility of modifing the geometrical characteristic, the parameters and the evaluation of possible missions will serve as a strong positive point for this new method. This modeling process will serve to meet the system requirements with acceptable risks and to establish the basis for proceeding with a detailed design. The simulation results have been validated with the finite element analysis using ANSYS.

Only harmonic excitation has been considered in this study. This work will be extended to include the optimization of mechatronic systems under stochastic vibration.

References

1. Bhaskar K., Sivaram A., 2008, Untruncated infinite series superposition method for accurate flexural analysis of isotropic/orthotropic rectangular plates with arbitrary edge conditions, *Composite Structures*, **8**, 83-92

2. Craig K., Stolfi F., 2002, Teaching control system design through mechatronics: academic and industrial perspectives, *Mechatronics*, **12**, 371-381

3. Elmqvist H., Mattsson S.E., Otter M., 2001, Object-oriented and hybrid modeling in Modelica, *Journal Européen des Systèmes Automatisés*, **35**, 1-22

4. Hammadi M., Choley J.Y., Penas O., Rivère A., 2012a, Multidisciplinary approach for modelling and optimization of road electric vehicles in conceptual design level, *Electrical Systems for Aircraft, Railway and Ship Propulsion (ESARS), IEEE*, 1-6

5. Hammadi M., Choley J.Y., Penas O., Rivère A., Louati J., Haddar M., 2012b, A new multi-criteria indicator for mechatronic system performance evaluation in preliminary design level, *13th International Workshop on Mechatonics, 9th France-Japan and 7th Europe-Asia Congress on Research and Education in Mechatronics (REM)*, 409-416

6. Lahdenpera M., 1992, Severe environment electronics, *Mechatronics*, **2**, 301-309

7. Laura P.A.A., Duran R., 1975, A note on forced vibrations of a clamped rectangular plate, *Journal of Sound and Vibration*, **42**, 129-135

8. Leissa A.W., 2005, The historical bases of the Rayleigh and Ritz method, *Journal of Sound and Vibration*, **287**, 961-978

9. Liscouët J., Maré J.C., Budinger M., 2012, An integrated methodology for the preliminary design of highly reliable electromechanical actuators: search for architecture solutions, *Aerospace Science and Technology*, **22**, 9-18

10. Mishra S., Pecht M., 2002, Remaining life prediction of electronic products using life consumption monitoring approach, European Microelectronics Packaging and Interconnection Symposuim, Cracow, Poland, 16-18 June.

11. Piersol A.G., Paez T.L., 2010, *Harris' Shock and Vibration Handbook*, 6th edition, United States

12. Romanelli E., Laura P.A.A., 2001, Forced transverse vibrations of a simply supported rectangular orthotropic plate in the case where the force acts over a plate subdomain, *Ocean Engineering*, **28**, 1135-1144

13. Schiavo F., Vigano L., Ferretti G., 2006, Object-oriented modeling of flexible beams, *Multibody System Dynamics*, **15**, 3, 263-286

14. Schwartz L., 1951, *Theory of Distributions* (in French), tome 2, Paris, Hermann

15. Szilard R., 2004, *Theories and Applications of Plate Analysis: Classical, Numerical and Engineering Methods*, John Wiley & Sons, Inc., New Jersey

16. Tarnowski W., Krzyzynski T., Maciejewski I., Oleskiewicz R., 2011, Poly-optimization: a paradigm in engineering design in mechatronics, *Archive of Applied Mechanics*, **81**, 141-156

17. Ventsel E., Krauthammer T., 2001, *Thin Plates and Shells, Theory, Analysis, and Applications*, Basel, New York

18. Veprik A.M., Babtisky V.I., 2000, Vibration protection of sensitive electronic equipment from harsh harmonic vibration, *Journal of Sound and Vibration*, **238**, 19-30

19. Vera S.A., Febbo M., Mendez C.G., Paz R., 2005, Vibrations of a plate with an attached two degree of freedom system, *Journal of Sound and Vibration*, **285**, 457-466

20. Wang Y., Yu Y., Xie C., Zhang X., Jiang W., 2013, A proposed approach to mechatronics design education: integrating design methodology, simulation with projects, *Mechatronics*, **23**, 942-948

21. Wei G.W., Zhao Y.B., Xiang Y., 2001, The determination of natural frequencies of rectangular plates with mixed boundary conditions by discrete singular convolution, *International Journal of Mechanical Sciences*, **43**, 1731-1746

22. Wu J.S., Luo S.S., 1997, Use of the analytical and numerical combined method in the free vibration analysis of a rectangular plate with any number of point mass and translational springs, *Journal of Sound and Vibration*, **200**, 179-194

Manuscript received April 19, 2014; accepted for print February 24, 2015

JOURNAL OF THEORETICAL AND APPLIED MECHANICS
53, 3, pp. 711-722, Warsaw 2015
DOI: 10.15632/jtam-pl.53.3.711

REALIZATION OF COORDINATION TECHNOLOGY OF HIERARCHICAL SYSTEMS IN DESIGN OF ACTIVE MAGNETIC BEARINGS SYSTEM

Kanstantsin Miatliuk, Arkadiusz Mystkowski
Bialystok University of Technology, Department of Automatic Control and Robotics, Bialystok, Poland
e-mail: k.miatliuk@pb.edu.pl; a.mystkowski@pb.edu.pl

A cybernetic technology of mechatronic design of active magnetic bearings systems (AMB) originated from theory of systems is suggested in the paper. Traditional models of artificial intelligence and mathematics do not allow describing mechatronic systems being designed on all its levels in one common formal basis. They do not describe the systems structure (the set of dynamic subsystems with their interactions), their control units, and do not treat them as dynamic objects operating in some environment. They do not describe the environment structure either. Therefore, the coordination technology of hierarchical systems has been chosen as a theoretical means for realization of design and control. The theoretical basis of the given coordination technology is briefly considered. An example of technology realization in conceptual and detailed design of AMB system is also presented.

Keywords: hierarchical systems, design, coordination, mechatronic, magnetic bearings

1. Introduction

In the design process of active magnetic bearings (AMB) we deal with mechatronic objects which contain connected mechanical, electromechanical, electronic and computer subsystems. Various methods and models which are used for each system coordination (design and control) cannot describe all subsystems in common theoretical basis and, at the same time, describe the mechanism with all interactions in the structure of a higher level and the system as a unit in its environment. It is important to define the common theoretical means which will describe all subsystems of a mechatronic object being designed (AMB systems) and its coordination (design and control) system in a common formal basis. This task is topical for the systems of computer aided design (CAD). Besides, theoretical means of the coordination technology must allow performing the design and control tasks under condition of any information uncertainty, i.e. (1) to create and change mechatronic system construction and technology by selecting units of lower levels and settling their interactions to make the state and activity of the system in higher levels (environment) best coordinated with environmental aims (selection stratum); (2) to change the ways (strategies) of the design task performing when the designed unit is multiplied and the knowledge uncertainty is removed (learning stratum); (3) to change the above mentioned strata when new knowledge is created (self-coordination stratum).

The coordination technology must also cohere with traditional forms of information representation in mechatronics, i.e. numerical and geometrical systems. The theoretical basis of the design process in agreement with these requirements must be a hierarchical construction connecting any level unit with its lower and higher levels. Mathematical and cybernetic theories based on the set theory are incoherent with the above design requirements since the set theory describes one-level world outlook.

In this paper, the coordination technology of Hierarchical System by Mesarovich *et al.* (1970) with its standard block *aed* (ancient Greek word) by Novikava *et al.* (1990, 1995, 1997) Miatliuk

(2003), Novikava and Miatliuk (2007) has been chosen as the theoretical basis for performing a mechatronic design task. In comparison with traditional methods, *aed* technology allows presentation of the designed object structure, its dynamic representation as a unit in the environment, the environment itself and the control system in common formal basis together with easy formalization of the design process. In the paper, the *aed* formal basis and coordination technology of hierarchical systems are described. AMB system construction and the system conceptual and detailed design are presented as practical examples of the proposed technology. Finally, the developed technology for the design of exemplary AMB mechatronic systems is analysed.

2. Formal basis of design technology

The *aed* model S^ℓ considered below unites the codes of the two level system (Measarovic *et al.*, 1970) and general systems theory by Mesarovic and Takahara (1990), the number code L^S, geometry and cybernetics methods. The dynamic representation $(\overline{\rho}, \overline{\varphi})$ is the main means of the description of the named codes. *Aed* is a standard element of hierarchical systems (Novikava *et al.*, 1990, 1995, 1997; Miatliuk, 2003; Novikava and Miatliuk, 2007), which realizes the general laws of systems organization on each level and the inter-level connections. *Aed* S^ℓ contains ω^ℓ and σ^ℓ models which are connected by the coordinator S_0^ℓ

$$S^\ell \leftrightarrow \{\omega, S_0, \sigma\}^\ell \tag{2.1}$$

where ω^ℓ is a dynamic representation of any level $\ell \in L^S$ system in its environment, σ^ℓ is the system structure, S_0^ℓ is coordinator. The structure diagram of *aed* S^ℓ is presented in Fig. 1.

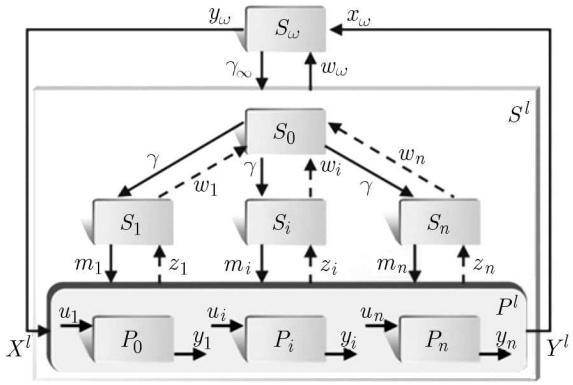

Fig. 1. Structure diagram of *aed* – standard block of Hierarchical Systems. S_0 is the coordinator, S_ω is the environment, S_i are subsystems, P_i are subprocesses, P^l is the process of level ℓ, X^l and Y^l are the input and output of the system S^l; m_i, zi, γ, w_i, u_i, y_i are interactions

Aggregated dynamic representations ω^ℓ of all *aed* connected elements, i.e. the object ${}_oS^\ell$, processes ${}_oP^\ell$, ${}_\omega P^\ell$ and environment ${}_\omega S^\ell$ are presented in form of the dynamic system $(\overline{\rho}, \overline{\varphi})^\ell$

$$\begin{aligned} \overline{\rho}^\ell &= \{\rho_t : \quad C_t \times X_t \to Y_t \quad \wedge \quad t \in T\}^\ell \\ \overline{\varphi}^\ell &= \{\phi_{tt'} : \quad C_t \times X_{tt'} \to C_{t'} \quad \wedge \quad t, t' \in T \quad \wedge \quad t' > t\}^\ell \end{aligned} \tag{2.2}$$

where C^ℓ is the state, X^ℓ – input, Y^ℓ – output, T^ℓ – time of level ℓ, $\overline{\rho}^\ell$ and $\overline{\varphi}^\ell$ are the reactions and state transition functions, respectively. Dynamic representations ω^ℓ of the object ${}_oS^\ell$, the processes ${}_oP^\ell$, ${}_\omega P^\ell$ and the environment ${}_\omega S^\ell$ are connected by their states, inputs and outputs.

The model of the system structure is defined as follows

$$\sigma^\ell = \{S_0^\ell, \{\overline{\omega}^{\ell-1}, {}_\sigma U^\ell\}\} = \{S_0^\ell, \widetilde{\sigma}^\ell\} \tag{2.3}$$

where S_0^ℓ is the coordinator, $\overline{\omega}^{\ell-1}$ are aggregated dynamic models of the subsystems $\overline{S}^{\ell-1} = \{S_i^{\ell-1} : \ i \in I^\ell\}$ of the lower level $\ell - 1$, ${}_\sigma U^\ell$ are structural connections ${}_\sigma U^\ell \supset {}_\omega \overline{U}^{\ell-1} = \{{}_\omega U_i^{\ell-1} : \ i \in I^\ell\}$ of the subsystems $\overline{S}^{\ell-1}$. $\widetilde{\sigma}^\ell$ is the connection of the dynamic systems $\overline{\omega}^{\ell-1}$ and their structural interactions ${}_\sigma U^\ell$ coordinated with the external ones ${}_\omega U^\ell = {}_\sigma U^{\ell+1} | S^\ell$.

The coordinator S_0^ℓ is the main element of hierarchical systems which realizes the processes of systems design and control (Novikava *et al.*, 1995; Miatliuk, 2003). It is defined according to *aed* presentation of Eq. (2.1) in the following form

$$S_0^\ell = \{\omega_0^\ell, S_{00}^\ell, \sigma_0^\ell\} \tag{2.4}$$

where ω_0^ℓ is the aggregated dynamic realization of S_0^ℓ, σ_0^ℓ is the structure of S_0^ℓ, S_{00}^ℓ is the coordinator control element. S_0^ℓ is defined recursively. The coordinator S_0^ℓ constructs its aggregated dynamic realization ω_0^ℓ and the structure σ_0^ℓ by itself. S_0^ℓ performs the design and control tasks on its selection, learning and self-organization strata (Miatliuk, 2003). All metric characteristics μ of systems being coordinated (designed and controlled) and the most significant geometry signs are determined in the frames of *aed* informational basis in the codes of numeric positional system L^S (Miatliuk, 2003; Novikava and Miatliuk, 2007).

The external connections ${}_\omega U^\ell$ of ω^ℓ with other objects are its coordinates in the environment ${}_\omega S^\ell$. The structures have two basic characteristics: ξ^ℓ (connection defect) and δ^ℓ (constructive dimension); μ^ℓ, ξ^ℓ and δ^ℓ are connected and described in the positional code of the L^S system (Miatliuk, 2003; Novikava and Miatliuk, 2007). For instance, the numeric characteristic (constructive dimension) $\delta^\ell \in \Delta^\ell$ of the system S^ℓ is presented in the L^S code as follows

$$\begin{aligned} &\widetilde{\delta}^\ell = (n_3, \ldots, n_0)_\delta && \widetilde{\delta}^\ell \in \{\delta_\sigma^\ell, \delta_\omega^\ell\} \\ &(n_i)_\delta = (n_{3-i})_\xi && (n_i)_\delta \in N \qquad i = 0, 1, 2, 3 \end{aligned} \tag{2.5}$$

where δ_ω^ℓ and δ_σ^ℓ are constructive dimensions of σ^ℓ and ω^ℓ, respectively. This representation of geometrical information allows execution of all operations with geometric images on the computer as operations with numeric codes.

The *aed* technology briefly described above presents a theoretical basis for AMB systems design and control. In comparison with the two-level system proposed by Mesarovic *et al.* (1970), the presented informational model of *aed* S^ℓ has new positive characteristic features (Novikava *et al.*, 1990, 1995, 1997; Miatliuk, 2003; Novikava and Miatliuk, 2007). Formalization, availability of the environment block ${}_\omega S^\ell$, description of the inter-level relations, coordination technology and information aggregation make the *aed* technology more efficient in the design tasks.

3. Coordination technology realization in the design of AMB system

3.1. Conceptual formal model of an AMB system

Formal description of the Active Magnetic Bearing (AMB) system in *aed* form is an example of the Hierarchical System (HS) (aed) coordination technology realization in the conceptual design of a mechatronic system. The AMBs systems are usually used in rotating machinery, flywheels, industrial turbomachinery, etc. (Schweitzer and Maslen, 2009). In this paper we focus on an AMB system which is a part of the experimental stand of a suspension system (Fig. 2) developed at Automation and Robotics Department, Bialystok University of Technology (Mystkowski and Gosiewski, 2007, Gosiewski and Mystkowski, 2006, 2008).

The AMB system is presented in *aed* form as follows

$${}_M S^\ell \leftrightarrow {}_M\{\omega, S_0, \sigma\}^\ell \tag{3.1}$$

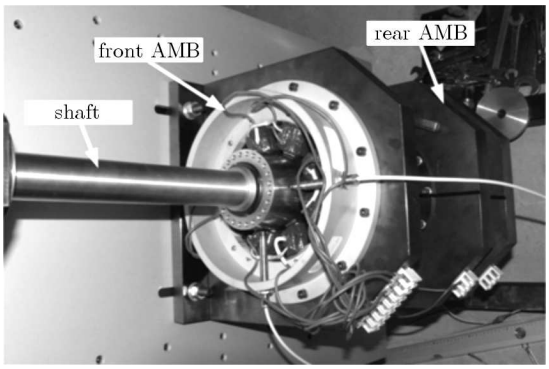

Fig. 2. AMB-beam test rig

where ${}_M\omega^\ell$ is an aggregated dynamic representation of the AMB system ${}_MS^\ell$, see Eq. (2.2), ${}_M\sigma^\ell$ is the system structure, ${}_MS_0^\ell$ is coordinator, i.e. design and control system, ℓ is the index of level.

The AMB system construction ${}_M\sigma^\ell$ contains the set of sub-systems $\overline{\omega}^{\ell-1}$ and their structural connections ${}_\sigma U^\ell$. Thus, according to Eq. (2.3), the structural subsystems presented in aggregated dynamic form $\overline{\omega}^{\ell-1}$ are:

- front AMB – ${}_M\omega_1^{\ell-1}$
- rear AMB – ${}_M\omega_2^{\ell-1}$
- thrust passive magnetic bearing (PMB) – ${}_M\omega_3^{\ell-1}$
- shaft – ${}_M\omega_4^{\ell-1}$.

In their turn, each subsystem has its own structural elements – the lower level $\ell-1$ subsystems. In the AMB subsystem ${}_M\omega_1^{\ell-1}$, these are eight $i=8$ electromagnetic coils ${}_M\omega_{1i}^{\ell-2}$ and the displacement sensors assembly ${}_M\omega_{1,9}^{\ell-2}$ which creates the external part of the AMB. The internal part is the magnetic core ${}_M\omega_{1,10}^{\ell-2}$ attached to the shaft. The subsystems ${}_M\overline{\omega}^{\ell-1}$ are connected by their common parts – the structural connections ${}_\sigma U^{\ell-1}$ that are elements of lower levels. For instance, the shaft ${}_M\omega_4^{\ell-1}$ and the front AMB ${}_M\omega_1^{\ell-1}$ are connected by their common element – the magnetic core ${}_\sigma U_{1,4}^{\ell-1} \leftrightarrow {}_M\omega_{1,10}^{\ell-2} \leftrightarrow {}_M\omega_{4,1}^{\ell-2}$, where ${}_M\omega_{1,10}^{\ell-2}$ is aggregated dynamic realization of the magnetic core being the subsystem of the front AMB ${}_M\omega_1^{\ell-1}$, and ${}_M\omega_{4,1}^{\ell-2}$ the realization of the magnetic core being the subsystem of the shaft ${}_M\omega_4^{\ell-1}$.

Aggregated dynamic realizations ${}_M\overline{\omega}^{\ell-1}$, i.e. dynamic models ${}_i(\overline{\rho},\overline{\varphi})^{\ell-1}$, Eq. (2.2), of the subsystems ${}_M\overline{S}^{\ell-1}$, are formed after definition of their inputs-outputs concerning each concrete sub-process they execute. Thus, for the shaft ${}_M\omega_4^{\ell-1}$ concerning its rotation process, the input ${}_MX_4^{\ell-1}$ is the torque M obtained from the loading system (motor), and the output ${}_MY_4^{\ell-1}$ is the angular velocity Ω of the shaft (Fig. 2). The shaft dynamic model ${}_M\omega_4^{\ell-1}$ in this case is presented at the detailed design stage in form of the differential equation described by Gosiewski and Mystkowski (2006, 2008).

The environment ${}_\omega S^\ell$ of the AMB system has its own structure and contains:

ω_1^ℓ – measuring and signal conditioning system (electronic),

ω_2^ℓ – loading system – motor/generator (electromechanical),

ω_3^ℓ – control systems in feedback loop of the general control AMB system (computer system).

Thus, the object being controlled ${}_MS^\ell$ (AMB system), environment subsystems, i.e. measuring ${}_\omega S_1^\ell$ (sensors, filters, estimators), loading ${}_\omega S_2^\ell$ (electromotor, generator, clutch) and control systems ${}_\omega S_3^\ell$ in the feedback loop (computer, processor, converters DAC and ADC) create the general control AMB system. The immediate input ${}_MX^\ell$ for the AMB system (which is at the

same time the output ${}_{\omega}Y_M^{\ell} = {}_M X^{\ell}$ of the environment of the AMB system) are signals from the loading system – the motor torque and control signal, i.e. the voltage/current or flux which come from internal or external controllers of the control system. The output of the AMB system is the axial displacement of the shaft in the plane orthogonal to the shaft symmetry axis, measured currents, flux, rotor angular speed, coil temperature, etc. The output ${}_M Y^{\ell}$ of the AMB system ${}_M S^{\ell}$, i.e. the displacement of the shaft, is at the same time the input ${}_{\omega}X_M^{\ell} = {}_M Y^{\ell}$ of the environment which is measured by eddy-current sensors or optical (laser) sensors. The states ${}_M C_i^{\ell}$ of the AMB system ${}_M S^{\ell}$ are:

${}_M c_1^{\ell}$ – displacements,

${}_M c_2^{\ell}$ – velocities,

${}_M c_3^{\ell}$ – accelerations,

${}_M c_4^{\ell}$ – magnetic forces.

The dynamic representation ${}_M\omega^{\ell}$ of the AMB system is constructed in form of Eq. (2.2) by the inputs ${}_M X^{\ell}$, states ${}_M C^{\ell}$ and outputs ${}_M Y^{\ell}$ mentioned above. The dynamic representation at the conceptual stage can be given in $(\overline{\rho}, \overline{\varphi})$, which is transformed into the state-space matrix form at the detailed design stage

$$\dot{\mathbf{x}} = \mathbf{A}\mathbf{x} + \mathbf{B}\mathbf{u} \qquad \mathbf{y} = \mathbf{C}\mathbf{x} \tag{3.2}$$

The first state equation in Eq. (3.2) corresponds to the state transition function $\overline{\varphi}$ in Eq. (2.2), and the second output equation corresponds to the reaction $\overline{\rho}$. Vectors $\mathbf{x}$, $\mathbf{y}$, $\mathbf{u}$ and matrices $\mathbf{A}$, $\mathbf{B}$, $\mathbf{C}$ of the equations are defined by Gosiewski and Mystkowski (2006). Therefore, Eq. (2.2) is the dynamic representation ${}_M\omega^{\ell}$ of the AMB system at the stage of conceptual design, and Eq. (3.2) is the AMB model which is used at the detailed design stage of the AMB system life circle (Ulman, 1992).

The AMB system process P^{ℓ} is a part of the higher-level process $P^{\ell+1}$ in the environment ${}_{\omega}S^{\ell}$, i.e. the general control AMB system. This process contains:

P_1^{ℓ} – control of the shaft displacement, vibration damping and machine diagnostics (by the AMB system ${}_M S^{\ell}$),

P_2^{ℓ} – measuring of output values of the AMB system by the measuring and signal conditioning system,

P_3^{ℓ} – reading of measured values and converting by the Digital Signal Processor (DSP) or any other real-time digital processor,

P_4^{ℓ} – processing and estimating,

P_5^{ℓ} – creation of the simulation model and sending it to DSP memory,

P_6^{ℓ} – sending control signals to the AMB system in real time,

P_7^{ℓ} – AMB system loading realized by the electromotor or generator that causes rotation of the shaft or convertion of the kinetic energy.

P_8^{ℓ} – shaft rotation.

P_1^{ℓ} and P_7^{ℓ} are realized by electromechanical subsystems of the general mechatronic system (general control AMB system), P_2^{ℓ}-P_6^{ℓ} are realized by the computer subsystem, and P_8^{ℓ} by the mechanical one. The general process is composed of sub-processes $\overline{P}^{\ell}$ executed by the general control AMB system, which includes the ABM system ${}_M S^{\ell}$ and its environment ${}_{\omega}S^{\ell}$.

So, all the subsystems of the general control AMB system, i.e. mechanical (shaft $S_4^{\ell-1}$), electromechanical (AMB system ${}_M S^{\ell}$ and motor ${}_{\omega}S_2^{\ell}$), computer-electronic (measuring ${}_{\omega}S_1^{\ell}$ and control system ${}_{\omega}S_3^{\ell}$) have their aggregated dynamic ω^{ℓ} and structural σ^{ℓ} descriptions. All the

connected descriptions of the subsystems $\overline{S}^{\ell}$ and processes $\overline{P}^{\ell}$ are presented in the informational resources (data bases) of the coordinator which realizes the design process connecting in this way the structure ${}_{M}\sigma^{\ell}$ and the functional dynamic realization ${}_{M}\omega^{\ell}$ of the AMB system being designed.

The coordinator ${}_{M}S_{0}^{\ell}$ in our case is realized in form of an automated design and control system of the AMB, which maintains its functional modes by the control system and realizes the design process by a higher level computer aided design (CAD) system (general supervisor) if necessary. The AMB control system is designed according to the hierarchical concept and contains low-level and high-level controllers (Fig. 4).

All metrical characteristics of the subsystems and processes described above are presented in form of numeric positional systems L^{S} (Novikava *et al.*, 1990, 1995, 1997; Miatliuk, 2003; Novikava and Miatliuk, 2007).

3.2. System architecture

The hierarchical system coordination technology allows one to describe active magnetic bearings (AMBs) coupled architecture and its coordination, i.e. design and control (Schweitzer and Maslen, 2009; Miatliuk *et al.*, 2010a). This technology enables one to allocate the inter-subsystems in the AMB structure. In this case, by using a novel approach, the conceptual design of the AMB system is considered as a multilevel model which enables introduction of further necessary changes into AMB construction and technology. This approach supports the design and assembling of AMB parts and can be considered as a self-optimization process. The main AMB model layers reflects AMB mechatronic subsystems, i.e. the mechanical subsystem, electrical subsystem and control software (supervisory intelligence), see Fig. 3. These subsystems can be

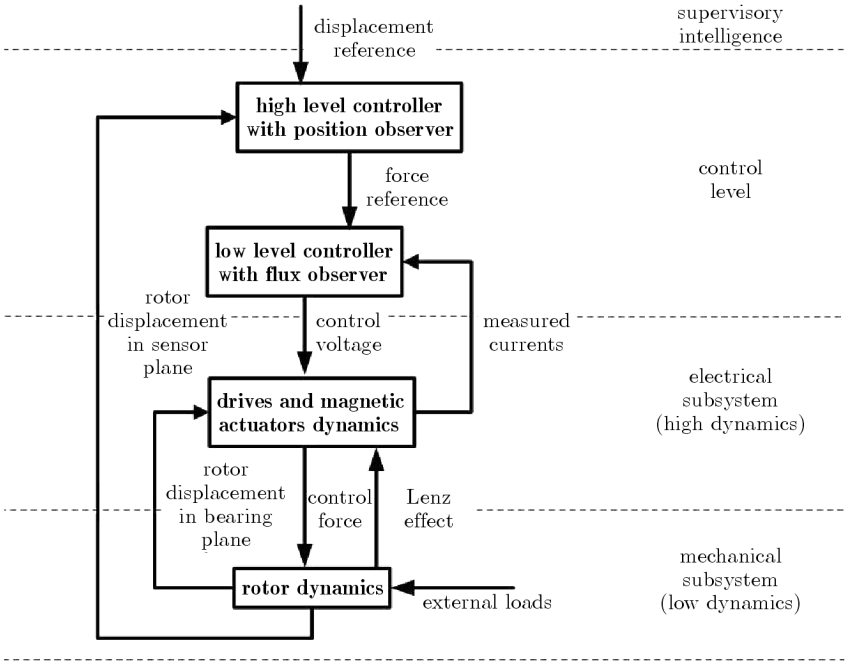

Fig. 3. Structure diagram of the AMB hierarchical system

constructed due to machine demands by selecting parts $\overline{\omega}^{\ell-1}$ and setting their interactions ${}_{\sigma}U^{\ell}$, see Eq. (2.3). Thus, the whole design process can be divided into engineering departments according to due knowledge. For example, high dynamics of the electrical AMB subsystem (at a low level) is faster than the mechanical one and requires different controller/actuators/sensors with a suitable bandwidth. Thus, these subsystems should be designed with taking into account their specified performances according to the whole system functional requirements. According to the

hierarchical control structure (see Fig. 1), the design technology realization steps are as follows. First, the low level (inner) closed-loop sub-system is designed in which the inner controller provides a fast response of the control loop with respect to the model of the electrical part of the AMB system (Schweitzer and Maslen, 2009). Here, since the electrical subsystem dynamics of the AMB model has uncertainties and consists of nonlinearities, the nonlinear control low is realized with robust controller (Gosiewski and Mystkowski, 2006, 2008). The robust controller overcomes control plant uncertainties and provides a fast response due to variations of the desired signals from the high level controller. Second, the high level control sub-system is designed based on the outer measured signals in the AMB mechanical sub-system. This high level control loop works slower than the inner controller since the dynamics of the AMB mechanical part refers to the significant inertia of AMB position control. The design process is formally presented in form of coordination strategies realized on the selection layer of the coordinator and described by the output functions λ of the coordinator canonical model (φ, λ) (Miatliuk, 2003). The change of coordination strategies in the coordinator learning and self-organization layers is described by the state transition functions φ.

3.3. Control structure

The hierarchical structure of the AMB control system consists of (at least) three layers. The first one (high level) consist of a complex AMB dynamic model (nonlinear) which refers to the concrete plant system. This plant model after simplification is used for controller synthesis and refers to the abstract system S^{ℓ}, Eq. (3.1). The second layer consists of the low level controller presented in form of the coordinator S_0^{ℓ}, Eq. (2.4), responding to the low level control task by direct impact on AMB dynamics and it is strongly nonlinear. The low level ℓ control subsystems represent a decentralized (local) control loop based on command signals from the high level $\ell+1$ control system. The last layer represents a high level controller (global) given in from of $S_0^{\ell+1}$ coordinator which performs high order tasks. The main advantage of such approaches is the decoupling of control laws for simpler evaluation by the designing engineers. For such a control structure, the high level controller is not dependent on the nonlinearities located in the low level layer. This enables designing a linear high level controller. However, the refinement of intercouplings due to the nonlinear nature of this dynamic system is the main challenge. Referring to the two-level control architecture as shown in Fig. 4, the plant S^{ℓ} behaviour is assumed to be described by the ${}_M\omega^{\ell}$ model built on the relation of AMB inputs X^{ℓ}, outputs Y^{ℓ} and states C^{ℓ}, see Eq. (2.2). C^{ℓ} is defined by the control inputs $G^{\ell-1}$ from the low level controller, i.e. the coordinator S_0^{ℓ}. The measured plant outputs $W^{\ell-1}$ are the feedback from the plant S^{ℓ} to the low level controller S_0^{ℓ}. The low level controller S_0^{ℓ} is directly connected by its input $X_0^{\ell} = \{G^{l}, W^{l-1}\}$ and output $Y_0^{\ell} = \{G^{l-1}, W^{1}\}$ with the plant model and with the high level controller $S_0^{\ell+1}$ where $\{G^{l-1}, W^{l-1}\}$ and $\{G^{l}, W^{l}\}$ are low level and high level signals, respectively. Similarly, the high level controller $S_0^{\ell+1}$ has its inputs $X_0^{\ell+1} = \{G^{l+1}, W^{l}\}$ and outputs $Y_0^{\ell+1} = \{G^{l}, W^{1+1}\}$ as well.

Ccontrol signals of the controllers are presented in form of coordinator strategies described by the output functions $\widehat{\lambda}_0^{\ell}$ of the coordinator canonical models $(\overline{\widehat{\varphi}}, \overline{\widehat{\lambda}})_0^{\ell}$ (Miatliuk, 2003) built on its inputs, outputs and states as follows

$$\widehat{\lambda}_{0t}^{\ell}: \quad C_0^{\ell} \times \widehat{\widetilde{X}}_0^{\ell} \to \widehat{\widetilde{Y}}_0^{\ell} \tag{3.3}$$

For instance, the control signal from the low-level $\ell/(\ell-1)$ controller S_0^{ℓ} to the plant is presented in form of the coordinator S_0^{ℓ} output function $\widehat{\lambda}_{0t}^{\ell/(\ell-1)}$

$$\overline{\widehat{\lambda}}_0^{\ell/(\ell-1)} = \left\{ \widehat{\lambda}_{0t}^{\ell/(\ell-1)}: \quad \widehat{\widetilde{C}}_0^{\ell} \times \widetilde{W}^{\ell-1} \to \widehat{\widetilde{G}}^{\ell-1} \right\} \tag{3.4}$$

where $\widehat{\widetilde{C}}_0^{\ell}$ is the controller (coordinator) states space.

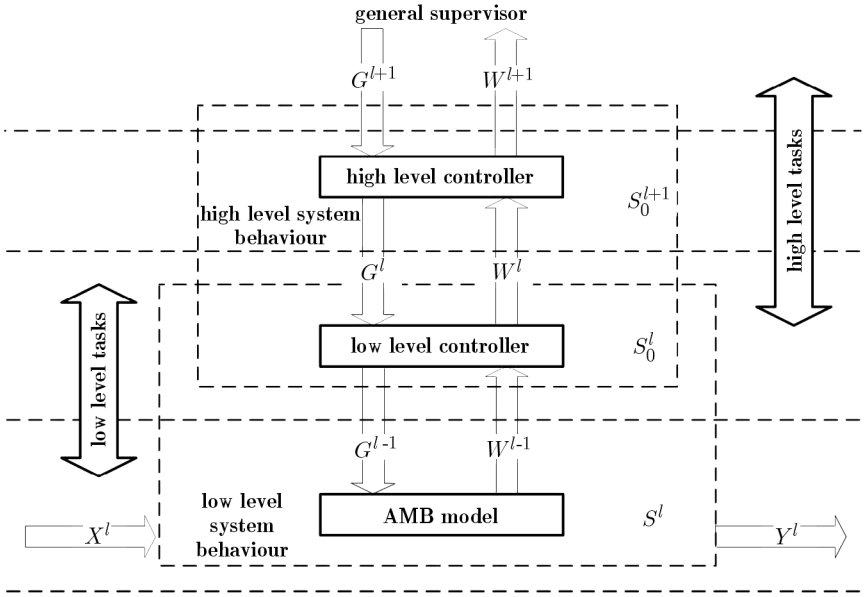

Fig. 4. Hierarchical AMB control architecture

The change of controller states is described by the state transition function $\overline{\widehat{\varphi}}_0^\ell$ of the coordinator canonic model (Miatliuk, 2003)

$$\overline{\widehat{\varphi}}_0^\ell = \{\widehat{\varphi}_{0tt'}^\ell : \quad C_0^\ell \times X_{0tt'}^\ell \to C_0^\ell\} \tag{3.5}$$

For the current (or flux) controlled AMB, the high level controller provides the vector of 4 control currents which after biasing the vector of 8 reference currents (reference forces) are presented by the signals G^ℓ (Fig. 4). The reference forces are provided to the low level control loops. The referenced voltages $G^{\ell-1}$ are input to the drives and actuators of the AMB system. The rotor displacements in the bearing planes ($W^{\ell-1}$) are estimated based on the measured rotor displacements in the sensor planes ($W^{\ell-1}$). They are provided to the low level controller. The desired rotor position is the reference signal of the high level (rotor position) controller and the desired electromagnetic force is the reference signal of the low level (current/flux) controller, respectively.

In order to simplify the design of the control system, the one-degree-of-freedom (1 DOF) AMB dynamic control model (Fig. 4) is considered as the hierarchical system. Its control model is considered as a cascade of two simple systems consisting of high level (electrical) and low level (mechanical) mechatronic subsystems with their coordinators. In this case, the AMB controller structure is coupled to the position and flux feedback, which refers to global and local control loops, respectively. The given conceptual model of the AMB system is concretized at its detailed design stage.

4. Exemplary detailed design of an AMB system

4.1. Simplified AMB model

At the detailed design stage which follows the conceptual one in the AMB system life circle (Ullman, 1992) the simplified 1 DOF (one degree of freedom) AMB model is used. The AMB consists of two opposite and identical magnetic actuators (electromagnets), which are generating the attractive forces F_1 and F_2, on the rotor (Schweitzer and Maslen, 2009). To control the position x of the rotor of mass m to the equilibrium state $x = 0$, the voltage inputs of the electromagnets V_1 and V_2 are used to design the control law, see Fig. 5.

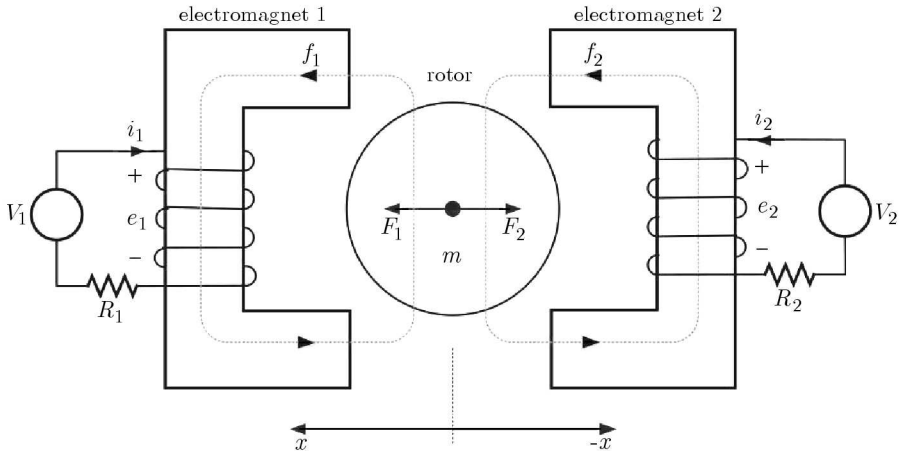

Fig. 5. A simplified one-dimensional AMB (Schweitzer and Maslen, 2009)

The simplified mechatronic model of the AMB is nonlinear and coupled with mechanical and electrical dynamics. Referring to Fig. 5, neglecting gravity, the dynamic equation is given by Schweitzer and Maslen (2009)

$$m\frac{d^2x}{dt^2} = \frac{\Phi|\Phi|}{\mu_0 A} = F(\Phi) \tag{4.1}$$

where Φ is the total magnetic flux through each active coil, A is the cross area of each electromagnet pole and μ_0 is the permeability of vacuum ($4\pi \cdot 10^{-7}$ Vs/Am). Equation (4.1) corresponds to the dynamic representation $(\overline{\rho}, \overline{\varphi})$ given at the AMB conceptual design stage.

The system nonlinearity in Eq. (4.1) is given by the function $\eta(\Phi) = \Phi|\Phi|$, and it is non-decreasing. The total flux generated by the i-th electromagnet is $\Phi_i = \Phi_0 + \phi_i$. In the case of zero-bias operation, the bias flux Φ_0 equals zero and the total flux is equal to the control flux ϕ_i. Then, we define the generalized flux which is given by

$$\phi := \phi_1 - \phi_2 = \frac{1}{N}\left(\int (V_1 - Ri_1)\, dt - \int (V_2 - Ri_2)\, dt\right) \qquad i = 1, 2 \tag{4.2}$$

where N is the number of turns of the coil of each electromagnet, V is applied control voltage, and i is current in the electromagnet with resistance R.

4.2. Low level controller

The fast inner controller (low level coordinator S_0^ℓ) generates the required fluxes in the AMB structure due to nonlinear characteristics of the controlled flux ϕ versus the generated force F. Since the magnetic flux sensors may complicate significantly the electrical and mechanical structure of the AMB system, a low level flux observer can be applied. The low level observer estimates the flux ϕ based on current measurements in the electrical part of the AMB system. The low level control loop consists of the electrical dynamics of the AMB system. The governing equations for this dynamics are given by Schweitzer and Maslen (2009)

$$\frac{d}{dt}\phi_1 = \frac{1}{N}(V_1 - Ri_1) \qquad \frac{d}{dt}\phi_2 = \frac{1}{N}(V_2 - Ri_2) \tag{4.3}$$

After neglecting the resistance in Eq. (4.3), the electrical dynamics is simplified

$$\dot{\phi}_i = \frac{V_i}{N} \qquad i = 1, 2 \tag{4.4}$$

The low level controller works in the inner flux loop. The reference force signal f_r for the low level flux controller is provided by the high level position controller. Thus, the transform function for the low level control feedback rule in the s-domain

$$G_l(s) = \frac{f_c(s)}{f_r(s)} := \frac{\phi_c(s)}{\phi_r(s)} \tag{4.5}$$

The control force f_c depends on the control flux ϕ_c which fulfils the condition of switching scheme:
— when $\phi_c \geqslant 0$

$$\phi_c = \phi_1 \qquad \phi_2 = 0$$

— when $\phi_c < 0$

$$\phi_c = -\phi_2 \qquad \phi_1 = 0$$

The low level control law $u_\phi = -f_\phi(\phi_r - \phi_c)$, where f_ϕ is a nonlinear control function which also ensures the bounds of ϕ_i, i.e. $\lim_{t\to\infty} \phi_i(t) = \min\{\phi_1(0), \phi_2(0)\}$.

Equations (4.3)-(4.5) correspond to the dynamic representation $(\widehat{\varphi}, \widehat{\lambda})_0^\ell$ of the low level coordinator S_0^ℓ given at the AMB conceptual design stage.

4.3. High level controller

Now, with respect to the outer controller (high level coordinator $S_0^{\ell+1}$), since the AMB model from the force f to the position x is linear, no linearization is needed and, therefore, the position control law can be linear. Moreover, the high level controller is not coupled with the low level control loop. The high level control loop provides the reference force f_r and consists the mechanical dynamics of the AMB system. The high level position feedback control rule in s-domain is based on the measured rotor displacement x_{mat} at the magnetic bearing plane and the referenced displacement x_r

$$G_h(s) = \frac{x_m(s)}{x_r(s)} \tag{4.6}$$

where the displacement x_m is estimated (by the linear high level position observer) based on the measured mass displacement x.

In order to provide the equilibrium state of dynamics Eq. (4.1) the time derivatives in Eq. (4.1) go to zero

$$\frac{d^2x}{dt^2} = \frac{\Phi|\Phi|}{\mu_0 m A} \to 0 \tag{4.7}$$

If the static gain of the control loop of G_h is defined as the state feedback controller (static gain matrix $\mathbf{K}$), then

$$\lim_{s\to 0} G_h = K \qquad \text{when} \qquad \frac{d^2x}{dt^2} \to 0 \tag{4.8}$$

Therefore, Eqs. (4.1)-(4.8) present detailed design models of the AMB system and its controllers. Equation (4.1) corresponds to the dynamic model $(\overline{\rho}, \overline{\varphi})$ of the AMB given at the AMB conceptual design stage, and Eqs. (4.3)-(4.5) and Eqs. (4.6)-(4.8) correspond to the dynamic models of the low-level and high-level controllers, respectively.

5. Conclusions

The realization of the coordination technology for AMB mechatronic systems (design and control) in the formal basis of hierarchical systems is briefly given in the paper. In comparison with traditional methods of mathematics and artificial intelligence, the proposed formal model contains connected descriptions of the designed object structure, its aggregated dynamic representation as a unit in its environment, the environment model and the control system. All the descriptions are connected by the coordinator which performs the design and control tasks on its strata. Besides, the proposed *aed* technology coheres with traditional systems of information presentation in mechatronics: numeric, graphic and natural language forms (Novikava and Miatliuk, 2007). The technology is also coordinated with general requirements of the design and control systems (Novikava *et al.*, 1990, 1995) as it considers mechatronic subsystems of different nature (mechanical, electromechanical, electronic, computer) in common theoretical basis.

The presentation of the AMB system in the formal basis of HS allows creation of the AMB conceptual model necessary for its transition to concrete mathematical models used at the detailed design stage of the AMB. At the detailed design stage, the low level and high level control loops of the AMB control structure are introduced. Each sub-system consists of the controller and observer structures which provide reference signals to each other. In this approach, the high level control loop is not dependent on the low level one. Thus, the magnetic force field nonlinearities in the low level sub-subsystem are not dependent on the high level position control loop. In the proposed approach, the electromagnetic nonlinearities are shifted from the high level control loop into the low level control loop. At the detailed design stage, the AMB (control) subsystems are described by traditional DE. At the conceptual design stage, the subsystems are presented in form of (ρ, φ) which are generalizations of DE and algebra systems. So, the transition from the conceptual to the detailed design stage in frames of the proposed technology is convenient and requires concretisation of the abstract dynamic system only.

The given technology brings new informational means for the conceptual and detailed design of mechatronic systems and AMB systems in particular. The described *aed* technology has been also applied to the design and control of other engineering objects (Miatliuk and Siemieniako, 2005; Miatliuk *et al.*, 2006; Miatliuk and Diaz-Cabrera, 2013), in biomechanics (Miatliuk *et al.*, 2009a,b) and mechatronics (Miatliuk *et al.*, 2010a; Miatliuk and Kim, 2013).

Acknowledgment

The work has been supported with Statutory Work of the Department of Automatic Control and Robotics, Faculty of Mechanical Engineering, Bialystok University of Technology, No. S/WM/1/2012.

References

1. Delaleau E., Stanković A.M., 2004, Flatness-based hierarchical control of the PM synchronous motor, *Proceedings of the American Control Conference*, Boston, USA, 65-70
2. Gosiewski Z., Mystkowski A., 2006, One DoF robust control of shaft supported magnetically, *Archives of Control Sciences*, **16**, 3, 247-259
3. Gosiewski Z., Mystkowski A., 2008, Robust control of active magnetic suspension: analytical and experimental results, *Mechanical Systems and Signal Processing*, **22**, 6, 1297-1303
4. Mesarovic M., Macko D., Takahara Y., 1970, *Theory of Hierarchical Multilevel Systems*, Academic Press, New York and London
5. Mesarovic M., Takahara Y., 1990, *Abstract Systems Theory*, Springer Verlag
6. Miatliuk K., 2003, Coordination processes of geometric design of hierarchical multilevel systems (in Polish), *Budowa i Eksploatacja Maszyn*, **11**, 163-178

7. Miatliuk K., Diaz-Cabrera M., 2013, Application of hierarchical systems technology in design and testing of circuit boards, *Lecture Notes in Computer Science*, **8112**, 521-526

8. Miatliuk K., Gosiewski Z., Siemieniako F., 2006, Coordination technology in the assembly operations design, *Proceedings of IEEE SICE-ICCAS Conference*, Busan, Korea, 2243-2246

9. Miatliuk K., Gosiewski Z., Siemieniako F., 2010a, Theoretical means of hierarchical systems for design of magnetic bearings, *Proceedings of 8th IFToMM International Conference on Rotor Dynamics, KIST*, Seoul, Korea, 1035-1039

10. Miatliuk K., Kim Y.H., 2013, Application of hierarchical systems technology in conceptual design of biomechatronic system, *Advances in Intelligent Systems and Computing*, Springer, **240**, 77-86

11. Miatliuk K., Kim Y.H., Kim K., 2009a, Human motion design in hierarchical space, *Kybernetes*, **38**, 9, 1532-1540

12. Miatliuk K., Kim Y.H., Kim K., 2009b, Motion control based on the coordination method of hierarchical systems, *Journal of Vibroengineering*, **11**, 3, 523-529

13. Miatliuk K., Kim Y.H., Kim K., Siemieniako F., 2010b, Use of hierarchical system technology in mechatronic design, *Mechatronics*, **20**, 2, 335-339

14. Miatliuk K., Siemieniako F., 2005, Theoretical basis of coordination technology for systems design in robotics, *Proceedings of 11th IEEE MMAR Conference*, Miedzyzdroje, 1165-1170

15. Mystkowski A., Gosiewski Z., 2007, Dynamic optimal control of active magnetic bearings system (in Polish), *Proceedings of I Congress of Polish Mechanics*, Warsaw

16. Novikava S., Ananich G., Miatliuk K., 1990, The structure and the dynamics of information in design systems, *Proceedings of 7th International Conference on Engineering Design, ICED'90*, **2**, 946-953

17. Novikava S., Miatliuk K., 2007, Hierarchical system of natural grammars and process of innovations exchange in polylingual fields, *Kybernetes*, **36**, 7, 36-48

18. Novikava S., Miatliuk K., Gancharova S., Kaliada W., 1995, *Aed* construction and technology in design, *Proceedings of 7th IFAC LSS Symposium*, Pergamon, London, 379-381

19. Novikava S., Miatliuk K., et al., 1997, *Aed* theory in hierarchical knowledge networks, *International Journal Studies in Informatics and Control*, **6**, 1,75-85

20. Schweitzer G., Maslen E.H., Eds., 2009, *Magnetic Bearings: Theory, Design, and Application to Rotating Machinery*, Springer

21. Ullman D.G., 1992, *The Mechanical Design Process*, USA: McGraw-Hill, Inc.

22. Xinyu W., Lei G., 2010, Composite hierarchical control for magnetic bearing based on disturbance observer, *Proceedings of the 29th Chinese Control Conference*, Beijing, China, 6173-6178

23. Zhou K., Doyle J.C., 1998, *Essentials of Robust Control*, Prentice Hall

Manuscript received May 7, 2014; accepted for print March 3, 2015

JOURNAL OF THEORETICAL AND APPLIED MECHANICS
53, 3, pp. 723-730, Warsaw 2015
DOI: 10.15632/jtam-pl.53.3.723

GAS TURBINE RELIABILITY MODEL BASED ON TANGENT HYPERBOLIC RELIABILITY FUNCTION

Ahmed Zohair Djeddi, Ahmed Hafaifa
University of Djelfa, Faculty of Science and Technology, Djelfa, Algeria
e-mail: a_z_djeddi@univ-djelfa.dz; hafaifa.ahmed.dz@ieee.org

Abudura Salam
University of Médéa, Faculty of Science and Technology, Médéa, Algeria
e-mail: abudura.salam@univ-medea.dz

The present work deals with the exploration of a new model proposed for the reliability analysis of industrial production systems. This proposed model is mainly based on the tangent hyperbolic function, where the survival function is determined and used in the lifetime distribution modeling taking into account of estimation the parameters of the proposed function. On the other side, tests validation is performed using the real data of a gas turbine installation. The obtained results allow the modeling of damage effects, hence the prediction of the performance of the examined gas turbine using the proposed model gives good results in terms of validity.

Keywords: reliability estimation, reliability algorithms, lifetime distribution, Weibull distribution, availability

1. Introduction

Actually, the complexity of industrial plants and their equipment behavior led practically to very complex maintenance strategies that are containing a number of different tasks. Moreover, the random nature of degradation and failure that may occur makes the determination of the required strategy to fulfill the best decisions regarding their maintenance a very difficult practical task (Costa *et al.*, 2014; Lai, 1994; Guemana *et al.*, 2011; Rao *et al.*, 2005; Hasumi *et al.*, 2009). The main aim of the proposed model is to analyze and measure industrial system reliability parameters to achieve the best time determination for making decision on the maintenance actions. Whereas, in the present work, this study is based on a model of a gas turbine which is considered as the main important equipment of the compressor stations, gas pumps, oil pumps and petrol production. The reliability model proposed in this paper is based essentially on the elementary function of tangent hyperbolic which is proved in this paper to be theoretically and practically similar to the well know Weibull distribution which was introduced by the Swedish mathematician in 1951 (Weibull, 1951). The Weibull distribution is considered the first distribution used in reliability analysis due to its very big capacity to adapt a very large number of data sets. However, many lifetime distributions that have a bathtub-shaped hazard rate function have been introduced after Weibull distribution, in which the main aim was to improve the systems reliability. A survey presenting the state-of-the-art on the class of such distributions was presented by Moeini *et al.* (2013), Scott (1979), Lai *et al.* (1998, 2001, 2003).

This work proposes an exploration of a new model which will contribute to the enhancement of the industrial systems reliability. It is obvious that the hyperbolic tangent function has a curve similar to the cumulative function of the probability distribution. Hence, a new model based on a tangent hyperbolic function defined on $\Re^+$ can be proposed. It is very clear that

its form is similar to the form of Weibull's model. In this model, the survival function will be studied based on it.

For validation of the proposed model, a practical application has been made with real data. These data have been collected from a gas turbine operating in a natural gas transportation system which is used in the south of Algeria. The reliability approach developed in this paper allows the modeling of the effects of damage to predict the performance of the examined gas turbine operation and give good results in terms of validity compared with the Weibull approach.

2. Reliability model based on the tangent hyperbolic function

The availability of the industrial equipment control allows the industries to act positively on the conformity of production, the exploitation costs and the production successful competitiveness. Indeed, the life managing of the equipment that is being used in oil and gas facilities is based on taking into account the aspects of aging, the economic and regulatory factors in order to optimize the operation, maintenance and lifespan of the system structures and components. The main goal is to maintain the level of safety and reliability as well as to maximize the investment return on the overall lifespan. The reliability of industrial systems is always essential and attracts much attention among scientific researches. It is especially important for components whose failure can cause major problems in terms of maintainability, availability and security (Halimi *et al.*, 2014; Hafaifa *et al.*, 2013a,b; Sturges, 1926; Ruji, 1990; Trofimov *et al.*, 1978). As it is aforementioned, a new model based on the tangent hyperbolic function is proposed to be used for the analysis and the study of the survival function in the reliability modeling. The tangent hyperbolic function considered in this paper is defined as a function on $\Re^+$ (Fig. 1). It is expressed as follows

$$F(x) = \begin{cases} 0 & \text{for} \quad x \in \Re^+ \\ \tanh(x) & \text{for} \quad x \geqslant 0 \end{cases} \tag{2.1}$$

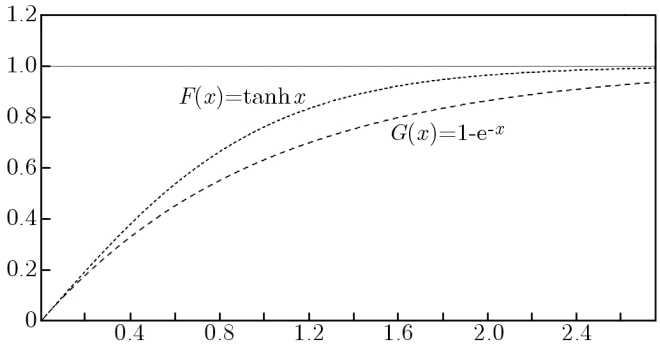

Fig. 1. Tangent hyperbolic function

To assess the impact of the aging effects on the equipment by annual frequency and to identify the sensitive equipment and the requested strategies for service priority to manage the risks that are associated with the age of the facilities, a cumulative distribution function is used. In this case it is the limit of $F(x)$ equal to 1 when x tends to +infinity and is equal to 0 when x tends to 0. The proposed function is a non-decreasing and a right-continuous function, so the proposed tangent hyperbolic function is fulfils these requirements and it presents a good choice as a candidate cumulative distribution function (Costa *et al.*, 2014; Guaily and Epstein, 2013)

$$\lim_{x \to 0} F(x) = 0 \qquad \lim_{x \to +\infty} F(x) = 1 \tag{2.2}$$

The distribution lifespan in the proposed tangent hyperbolic distribution form is deduced from the Weibull distribution. The survival function is represented as follows

$$R(t) = 1 - \tanh(\lambda t)^{\beta} \tag{2.3}$$

where β is the shape parameter and λ is the scale parameter. The cumulative distribution function is expressed as follows

$$F(t) = 1 - R(t) = \tanh(\lambda t)^{\beta} \tag{2.4}$$

Based on the derivative of the last function, the probability density function is obtained as follows:.

$$f(t) = \frac{dF(t)}{dt} = \frac{(\lambda t)^{\beta-1}\lambda\beta}{\cosh^2(\lambda t)^{\beta}} \tag{2.5}$$

The hazard function is determined in the flowing equations

$$P_r(t < T \leqslant t + \Delta t \Big| T > t) = \frac{f(t)}{R(t)}\Delta t = h(t)\Delta t \tag{2.6}$$

where

$$h(t) = \frac{f(t)}{R(t)} = \frac{(\lambda t)^{\beta-1}\frac{\lambda\beta}{\cosh^2(\lambda t)^{\beta}}}{1 - \tanh(\lambda t)^{\beta}}$$

Using a variable converting the reliability $R(t)$ replaced by the hyperbolic function, $h(t)$ can be rewritten using exponential form as follows

$$h(t) = \frac{2\lambda\beta(\lambda t)^{\beta-1}}{1 + \mathrm{e}^{-2(\lambda t)^{\beta}}} \tag{2.7}$$

2.1. Hazard and density functions

The hazard function in the proposed tangent hyperbolic model is expressed by equation (2.7) and is shown in Fig. 2. It is obvious that the curve of this function depends only on the parameter β. Therefore, the curve of this function can be discussed based on the value of β:

- In the case when $\beta = 1$, the hazard function tends quickly to 2λ

$$\lim_{t\to\infty} h(t) = 2\lambda \tag{2.8}$$

- In the case when $\beta = 2$, the hazard function becomes

$$h(t) = \frac{4t\lambda^2}{1 + \mathrm{e}^{-2(\lambda t)^2}} \to 4t\lambda^2 \tag{2.9}$$

  The hazard function $h(t)$ is a straight line with slope equal to $4\lambda^2$.

- In the case when $0 < \beta < 1$, the hazard function becomes

$$h(t) \to 2\lambda\beta(\lambda t)^{\beta-1} \tag{2.10}$$

  The hazard function curve follows t^p form with $-1 < p < 0$.

- In the case when $\beta > 2$, the hazard function curve follows t^p with $p > 1$ (convex form).
- In the case when $1 < \beta < 2$, the hazard function curve follows t^p with $0 > p > 1$ (concave form).

It can be concluded that the curves of the hazard function have their Weibull equivalents curves. On the other side, the density function of the proposed tangent hyperbolic model presented in equation (2.5) is presented in Fig. 3 for different values of β.

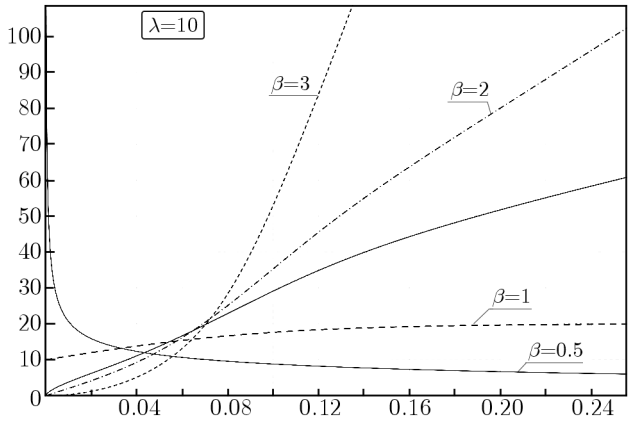

Fig. 2. Hazard function determined using the tangent hyperbolic algorithm

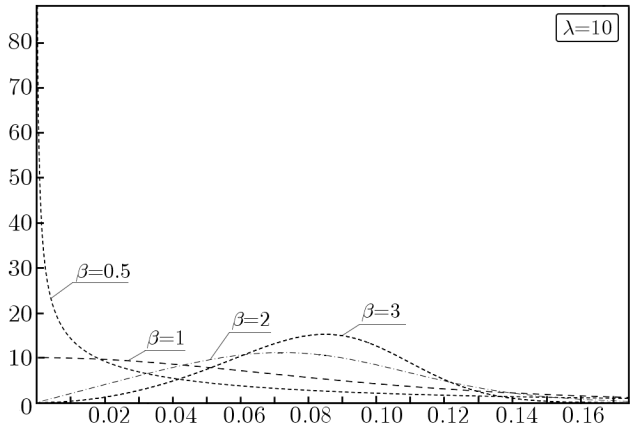

Fig. 3. Density function found using the hyperbolic model

3. Application results

The data used in this paper are taken from the data history of a gas turbine (PGT10) used for natural gas transportation and installed in a gas plant located in the south of Algeria. Those data are presented in Table 1.

Table 1. Examined gas turbine data

N	1	2	3	4	5	6	7	8	9	10
TBF*	240	264	384	552	624	648	696	720	720	768
N	11	12	13	14	15	16	17	18	19	20
TBF	768	792	960	1272	1344	1464	1632	1680	1776	1944
N	21	22	23	24	25	26	27	28	29	30
TBF	1968	1992	2064	2136	2208	2376	2448	2448	2472	2664
N	31	32	33	34	35	36	37	38	39	40
TBF	2832	2880	3000	3600	3672	3720	4272	4656	5592	5856

$*$ TBF is the Time Between Failures given in hours

3.1. Esytimation of the model parameters

Using equation (2.4), the inverse of the tangent hyperbolic function can be obtained as follows

$$\tanh^{-1} y = (\lambda t)^{\beta} \tag{3.1}$$

The tangent hyperbolic can be eliminated from this equation based on the following well known expression

$$\tanh^{-1} y = \frac{1}{2} \log \frac{1+y}{1-y} \tag{3.2}$$

Furthermore, if the log is used to the two members of equation (3.1), the obtained expression is as follows

$$\log\Big(\frac{1}{2} \log \frac{1+y}{1-y}\Big) = \beta \log \lambda + \beta \log t \tag{3.3}$$

which can be transformed into a linear expression

$$Y = A + BX \tag{3.4}$$

where

$$Y = \log\Big(\frac{1}{2} \log \frac{1+y}{1-y}\Big) \qquad X = \log t \qquad A = \beta \log \lambda \qquad B = \beta$$

To estimate A and B, any graphical or analytical methods can be used, a possible approach is the simple regression analysis using (3.2). The estimation of the parameters based on the least--squares fit is shown in Fig. 4. The parameters of the examined gas turbine using the proposed approach are presented in Table 2. The obtained estimated parameters are $\lambda = 0.00034$ and $\beta = 1.24568$.

Table 2. The obtained parameters for the examined gas turbine

	Estimate	Std. Error	t value	$\Pr(>\|t\|)$
β	1.24569	0.03435	36.27	< 2E-16
$\beta \log \lambda$	−7.98420	0.02801	−285.07	< 2E-16

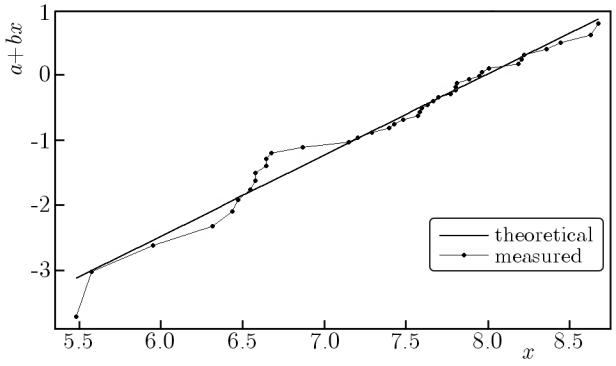

Fig. 4. The distribution function of the examined gas turbine determined using the hyperbolic algorithm

The plots of Y versus X which are related to the cumulative distribution function and time for the examined gas turbine determined using the proposed tangent hyperbolic algorithm are shown in Fig. 4, where the plotted data are scattered close to the fitted straight line. It can be said that this model is acceptable (Murthy *et al.*, 2004; Yang and Scott, 2013).

3.1.1. Cumulative distribution function

The cumulative distribution function of the examined gas turbine found using the tangent hyperbolic model is shown in Fig. 5. The plotted data are scattered close to the fitted curve. Following the cumulative distribution function expressed in equation (2.4), the parameters $\lambda = 0.00034$ and $\beta = 1.24568$.

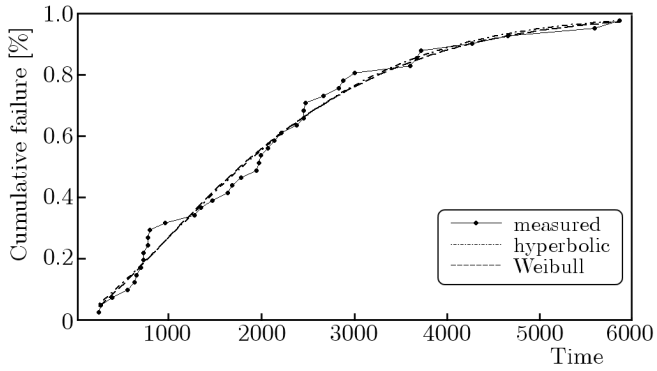

Fig. 5. The cumulative failure rate of the examined gas turbine using the hyperbolic model

3.1.2. Density and hazard functions

The density function and the hazard function of the examined gas turbine determined by using the tangent hyperbolic function model are shown respectively in Figs. 6 and 7. These functions are obtained by using equation (2.5) and taking into account the estimated parameter values $\lambda = 0.00034$ and $\beta = 1.24568$.

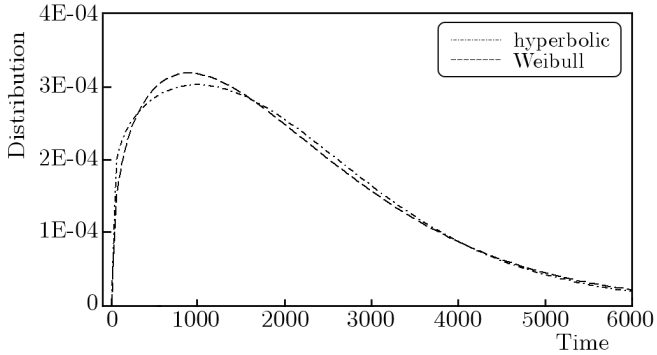

Fig. 6. The distribution function of the model of the examined gas turbine using the hyperbolic model

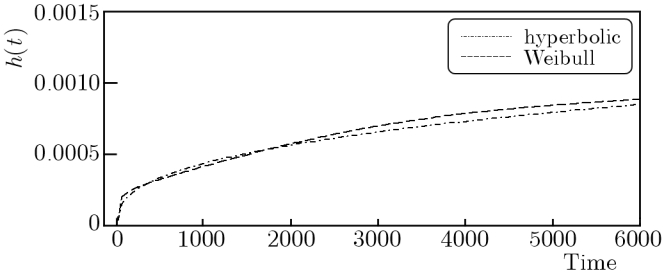

Fig. 7. The hazard function of the examined gas turbine using the hyperbolic model

3.1.3. Mean time between failures

The Mean Time Between Failures (MTBF) is the predicted elapsed time between inherent failures of the system during exploitation (Yang and Scott, 2013) which is expressed as follows

$$\text{MTBF} = \int_0^{+\infty} t f(t)\, dt = \int_0^{+\infty} t \frac{(\lambda t)^{\beta-1}\lambda\beta}{\cosh^2(\lambda t)^{\beta}}\, dt \tag{3.5}$$

It is worth noting that there is an alternative way for computing the expected value (Murthy *et al.*, 2004)

$$\text{MTBF} = \int_0^{+\infty} S(t)\,dt = \int_0^{+\infty} 1 - \tanh(\lambda t)^{\beta}\,dt \tag{3.6}$$

Table 3

Model	Weibull	Hyperbolic function
MTBF	2088.623 h	2075.40 h

4. Conclusion

The goal achieved in this paper is concerned with industrial reliability, which requires the specialists to be more competitive and more responsive to variable market conditions. It is obvious that to achieve better management of the facilities performance, it is necessary to improve the reliability. It has been shown that with the application of the proposed method based on the tangent hyperbolic function good results can be obtained. The main objective is to analyze and to measure the reliability parameters of the examined system in order to determine the best time to take maintenance action based on reliability analysis. The developed in this paper reliability approach allows the modeling of the damage effects to predict the performance of the examined gas turbine operation and to lead to good results in terms of validity compared with the Weibull approach. This model can be improved to have a bathtub-shaped hazard form.

Refernces

1. Costa F.M.P., Rocha A.M.A.C., Fernandes E.M.G.P., 2014, An artificial fish swarm algorithm based hyperbolic augmented Lagrangian method, *Journal of Computational and Applied Mathematics*, **259**, Part B, 868-876

2. Guaily A.G., Epstein M., 2013, Boundary conditions for hyperbolic systems of partial differentials equations, *Journal of Advanced Research*, **4**, 4, 321-329

3. Guemana M., Aissani S., Hafaifa A., 2011, Use a new calibration method for gas pipelines: an advanced method improves calibrating orifice flowmeters while reducing maintenance costs, *Hydrocarbon Processing Journal*, **90**, 8, 63-68

4. Hafaifa A., Belhadef R., Guemana M., 2013a, Reliability model exploitation in industrial system maintainability using expert system evaluation, *Proceedings of the 4th International Conference on Integrity, Reliability and Failure, IRF2013*, Funchal, Madeira, Portugal, 387-388

5. Hafaifa A., Guemana M., Daoudi A., 2013b, Vibrations supervision in gas turbine based on parity space approach to increasing efficiency, *Journal of Vibration and Control*, doi: 10.1177/1077546313499927

6. Halimi D., Hafaifa A., Bouali E., 2014, Maintenance actions planning in industrial centrifugal compressor based on failure analysis, *Journal of Maintenance and Reliability*, **16**, 1, 17-21

7. Hasumi T., Akimoto T., Aizawa Y., 2009, The Weibull-log Weibull distribution for interoccurrence times of earthquakes, *Physica A: Statistical Mechanics and its Applications*, **388**, 4, 491-498

8. Lai C.D., 1994, Tests of univariate and bivariate stochastic ageing, *IEEE Transactions on Reliability*, **43**, 2, 233-241

9. Lai C.D., Moore T., Xie M., 1998, The beta integrated model, *Prococeding of the International Workshop on Reliability Modeling and Analysis: from Theory to Practice*, 153-159

10. Lai C.D., Xie M., Murthy D.N.P., 2001, Bathtub shaped failure rate distributions, *Handbook in Reliability*, **20**, 69-104

11. Lai C.D., Xie M., Murthy D.N.P., 2003, A modified Weibull distribution, *IEEE Transactions on Reliability*, **52**, 1, 33-37

12. Moeini A., Jenab K., Mohammadi M., Foumani M., 2013, Fitting the three-parameter Weibull distribution with Cross Entropy, *Applied Mathematical Modelling*, **37**, 9, 6354-6363

13. Murthy P.D.N., Xie M., Jiang R., 2004, *Weibull Models*, John Wiley & Sons

14. Rao C.R., Wegman E.J., Solka J.L., 2005, *Handbook of Statistics: Data Mining and Data Visualization*, Volume 24 *de Handbook of Statistics*, Elsevier Science

15. Ruji H., 1990, State space tree method and exact decomposition algorithm for finding network overall reliability, *Journal of Electronics (China)*, **7**, 4, 296-305

16. Scott D.W., 1979, On optimal and data-based histograms, *Biometrika*, **66**, 3, 605-610

17. Sturges H.A., 1926, The choice of a class interval, *Journal of the American Statistical Association*, **21**, 153, 65-66

18. Trofimov N.G., Kravchenko B.A., Kramarovskii B.I., Baturov V.B., Kostina G.N., 1978, Increasing the strength and reliability of turbine blades by thermoplastic hardening methods, *Strength of Materials*, **10**, 8, 990-996

19. Weibull W., 1951, A statistical distribution function of wide applicability, *Journal of Applied Mechanics*, **1**, 18, 293-297

20. Yang J., Scott D.W., 2013, Robust fitting of a Weibull model with optional censoring, *Computational Statistics and Data Analysis*, **67**, 1, 149-161

Manuscript received October 3, 2014; accepted for print March 11, 2015

JOURNAL OF THEORETICAL AND APPLIED MECHANICS
53, 3, pp. 731-743, Warsaw 2015
DOI: 10.15632/jtam-pl.53.3.731

NON-LINEAR VIBRATION OF TIMOSHENKO BEAMS BY FINITE ELEMENT METHOD

Jerzy Rakowski, Michał Guminiak
Poznań University of Technology, Institute of Structural Engineering, Poznań, Poland
e-mail: jerzy.rakowski@put.poznan.pl; michal.guminiak@put.poznan.pl

The paper is concerned with free vibrations of geometrically non-linear elastic Timoshenko beams with immovable supports. The equations of motion are derived by applying the Hamilton principle. The approximate solutions are based on the negligence of longitudinal inertia forces but inclusion of longitudinal deformations. The Ritz method is used to determine non-linear modes and the associated non-linear natural frequencies depending on the vibration amplitude. The beam is discretized into linear elements with independent displacement fields. Consideration of the beams divided into the regular mesh enables one to express the equilibrium conditions for an arbitrary large number of elements in form of one difference equation. Owing to this, it is possible to obtain an analytical solution of the dynamic problem although it has been formulated by the finite element method. Some numerical results are given to show the effects of vibration amplitude, shear deformation, thickness ratio, rotary inertia, mass distribution and boundary conditions on the non-linear natural frequencies of discrete Timoshenko beams.

Keywords: Timoshenko beams, non-linear vibrations, eigenvalue problem, finite elements

1. Introduction

The linear free vibration of Timoshenko beams was studied by Levinson and Cooke (1982). Bhashyam and Prathap (1981) applied the Finite Element Method and elements with linear shape functions to determine natural frequencies of Timoshenko beams. The authors eliminated the shear locking by a selective reduced integrations procedure. The studies of beams with immovable supports weere carried out by Woinowsky-Krieger (1950), Hsu (1960), Evensen (1968) and Lewandowski (1987). The authors used a continuum approach as well as the finite element approach proposed by Levinson and Cooke (1982), Sarma and Varadan (1983) and Kitipornchai *et al.* (2009). The exact solutions given in form of elliptic functions were presented by Woinowsky-Krieger (1950) and Hsu (1960). Evensen (1968) analysed beams with various boundary conditions using the perturbation method. Lewandowski (1987) applied the Ritz method to obtain the frequency-amplitude relationship for elastically supported beams. The solutions presented by Bhashyam and Prathap (1980) as well as Sarma and Varadan (1983) are based on the assumption that the equation of motion is satisfied only at the instant of the maximum deformation. Dumir and Bhaskar (1988) compared the results of analysis of non-linear vibrations of beams and plates obtained by various methods. They also brought out the source of errors which appear in some finite elements formulations, e.g. presented by Mei and Decha-Umphai (1985). Marur and Prathap (2005) solved the non-linear vibration problem of Timoshenko beams by applying variational formulations, and similar isssues for thick asymetric beams were inastigated in a wide range by Singh and Rao (1998). The problem of non-linear vibration of Timoshenko beams taking into account cracking was invastigated by Kitipornchai *et al.* (2009). The non-linear formulation of the Timoshenko beam based on the modified couple stress theory was applied by Asghari *et al.* (2010) to static and free vibration analysis of beams.

Effectiveness of the Finite Element Method depends e.g. on the type of finite elements taken in the analysis. Many of them induce undesirable parasitic effects as shear locking. A critical analysis of a class of finite elements was carried out by Rakowski (1990, 1991a, 1991b). In the present work the linear finite element developed by Rakowski (1990) is used in the analysis of non-linear vibration of the Timoshenko beam. Such an improved linear element does not lock and gives a better convergence to the exact results than the reduced-integrated one, and the division of considered beams into the regular mesh of identical elements enables one to formulate the equilibrium conditions in form of one difference equation. The advantage of this FEM formulation idea is that the solution of the considered dynamic problem can be obtained in an analytical closed form and that it facilitates analyses regardless of the number of finite elements. The solving procedure is analogous to that used for continuous systems, but in this case the nodal displacements are spatial functions of the discrete variable (the index number of a node). This methodology was adopted to solve the problem of vibrations of infinite Bernoulli-Euler beams by Rakowski and Wielentejczyk (1996, 2002). In the present approach, the equations of motion for a continuous beam are derived from the variational formulation by applying Hamilton's principle. The approximate time function is assumed to be harmonic and the solution of the problem is based on the idea presented by Rosenberg (1966) and Szemplińska-Stupnicka (1983) where non-linear normal modes and natural frequencies of vibrations are unknown and amplitude dependent. The effects of shear deformation, thickness ratio and rotary inertia on the non-linear natural frequencies are analysed. The element stiffness matrix and the consistent mass matrix are derived using the simple linear elements with independent displacement fields. The shear locking in exactly integrated elements is eliminated by introducing a scalling factor into the stiffness matrix (Rakowski, 1990). Beams with different boundary conditions are considered. The comparison of results obtained for the evaluated elements and the reduced-integrated ones is given.

2. Theoretical considerations

The equation for the strain energy for a beam of length l, including shear deformation, axial force, longitudal and the large transverse displacement effect, is

$$U = \int_0^l \frac{EA}{2}\Big(u_{,x} - \frac{1}{2}w_{,x}^2\Big)^2\,dx + \int_0^l \frac{EJ}{2}\theta_{,x}^2\,dx + \int_0^l \frac{\kappa GA}{2}(w_{,x} - \theta)^2\,dx + \int_0^l H\Big(u_{,x} - \frac{1}{2}w_{,x}^2\Big)^2\,dx \tag{2.1}$$

where u, w are the longitudinal and transverse displacements of the centroidal axis, θ is the rotation of the beam section, E, G are the elastic and shear moduli, J, A are the moment of inertia and the cross-section area, respectively, H is the initial axis force and κ is the shear coefficient. The kinetic energy including horizontal and rotary inertias can be expressed as

$$T = \int_0^l \frac{m}{2}u_{,t}^2\,dx + \int_0^l \frac{m}{2}w_{,t}^2\,dx + \int_0^l \frac{m\rho^2}{2}\theta_{,t}^2\,dx \tag{2.2}$$

where m is mass per unit length and ρ is the radius of gyration of the cross section.

Equations (2.1) and (2.2) give, on applying Hamilton's principle, the following equations of motion

$$
\begin{aligned}
&EA\Big[u_{,x}+\frac{1}{2}(w_{,x})^2\Big]_{,x}-mu_{,tt}=0\\
&\Big\{Hw_{,x}+EA\Big[u_{,x}+\frac{1}{2}(w_{,x})^2\Big]w_{,x}\Big\}_{,x}+\kappa GA[w_{,x}-\theta]_{,x}-m_{,tt}=0\\
&EJ\theta_{,xx}+\kappa GA(w_{,x}-\theta)-m\rho^2\theta_{,tt}=0
\end{aligned}
\tag{2.3}
$$

Neglecting the horizontal inertia forces in the second equation of (2.3), yields

$$
C=EA\Big[u_{,x}+\frac{1}{2}(w_{,x})^2\Big]_{,x}=\text{ const} \tag{2.4}
$$

Integrating expression (2.4) in the range from 0 to l for an immovable beam, we have

$$
C=\int_0^l \frac{EA}{2a}w_{,x}^2\,dx \tag{2.5}
$$

Substituting (2.4) into equation (2.3) and eliminating the unknown function θ, yields

$$
\begin{aligned}
&\Big(\frac{H+C}{\kappa GA}+1\Big)\frac{\partial^4 w}{\partial x^4}-\frac{H+C}{EJ}\frac{\partial^2 w}{\partial x^2}-\Big[\frac{m}{\kappa GA}+\frac{m\rho^2}{EJ}\Big(\frac{H+C}{\kappa GA}+1\Big)\Big]\frac{\partial^4 w}{\partial x^2\partial t^2}\\
&\quad+\frac{m}{EJ}\frac{\partial^2 w}{\partial t^2}+\frac{m^2\rho^2}{\kappa EJGA}\frac{\partial^4 w}{\partial t^4}=0
\end{aligned}
\tag{2.6}
$$

Let us assume the approximate solution to equation (2.6) to be harmonic function of time (Woinowsky-Krieger, 1950)

$$
w(x,t)=\alpha W(x)\cos\omega t \tag{2.7}
$$

where $W(x)$ is a function of the spatial variable (not given *a priori*), α is the vibration amplitude of an arbitrary point x_0 of the beam axis for which $W(x_0)=1$. The non-linear normal mode $W(x)$ and the free frequency vibrations ω depend on the boundary conditions and on the vibration amplitude α. The above solution does not satisfy non-linear equation (2.6) at every time. We minimize the error by equating the weighed residual of equation (2.6) to zero for one time period with the weighting function $\cos\omega t$ (Dumir and Bhaskar, 1988; Szemplińska-Stupnicka, 1983). As a result, the equilibrium equation in the dimensionless form is obtained

$$
\frac{d^4W}{d\xi^4}+\frac{1}{F}\Big[\Omega^2\frac{F+f}{\lambda^2}-(s+c)\lambda^2\Big]\frac{d^2W}{d\xi^2}+\frac{\Omega^2}{F}\Big(f\frac{\Omega^2}{\lambda^4}-1\Big)W=0 \tag{2.8}
$$

where

$$
\begin{aligned}
&W=W(\xi) && \xi=\frac{x}{L} && f=\frac{2(1+\nu)}{\kappa}\\
&s=\frac{H}{EA} && \lambda=\frac{L}{\rho} && \Omega=\frac{m\omega^2L^4}{EJ}\\
&c=\frac{3}{8}\frac{\delta^2}{\lambda^2}\int_0^1\frac{dW}{d\xi}\,d\xi && \delta=\frac{\alpha}{\rho} && F=\frac{s+c}{f}+1
\end{aligned}
$$

and ν is Poisson's ratio. The solution tf equation (2.8) is

$$
W(x)=C_1\sinh\mu_1\xi+C_2\cosh\mu_1\xi+C_3\sin\mu_2\xi+C_4\cos\mu_2\xi \tag{2.9}
$$

where C_i are arbitrary constants and

$$
\begin{aligned}
&\mu_1^2=\sqrt{\frac{b^2}{4}-\frac{\Omega}{F}\Big(\frac{f\Omega^2}{\lambda^4}-1\Big)}+\frac{b}{2} && \mu_2^2=\sqrt{\frac{b^2}{4}-\frac{\Omega}{F}\Big(\frac{f\Omega^2}{\lambda^4}-1\Big)}-\frac{b}{2}\\
&b=\frac{1}{F}\Big[\frac{\Omega^2}{\lambda^2}(F+f)-(s+c)\lambda^2\Big]
\end{aligned}
$$

From the third equation of (2.3) one finds that the dimensionless rotation function depending on the spatial variable is of the form

$$\phi(\xi) = (C_1 \sinh \mu_1 \xi + C_2 \cosh \mu_1 \xi)\frac{\beta_1}{\mu_1} - (C_3 \cos \mu_2 \xi + C_4 \sin \mu_2 \xi)\frac{\beta_2}{\mu_2} \tag{2.10}$$

where $\beta_1 = f\Omega^2/\lambda^2 + F\mu_1^2$ and $\beta_2 = f\Omega^2/\lambda^2 - F\mu_2^2$.

The boundary conditions for beams with immovable supports are:
— for the hinged end

$$W = 0 \qquad M = EJ\frac{d\phi}{d\xi} = 0$$

— for the clamped end

$$W = 0 \qquad \phi = 0$$

The frequency equations derived for several combinations of the boundary conditions are:
— for the hinged-hinged beam

$$\sinh \mu_1 \sin \mu_2 = 0 \tag{2.11}$$

— for the clamped-clamped beam

$$2 + \frac{\beta_2^2\mu_1^2 - \beta_1^2\mu_2^2}{\beta_1\beta_2\mu_1\mu_2}\sinh \mu_1 \sin \mu_2 - 2\cosh \mu_1 \cos \mu_2 = 0 \tag{2.12}$$

— for the clamped-hinged beam

$$\beta_2\mu_1 \tanh \mu_1 + \beta_1\mu_2 \tanh \mu_2 = 0 \tag{2.13}$$

Since the non-linear frequency parameter Ω^2 and the non-linear vibration mode W depend on the vibration amplitude α, the eigenvalue problem of non-linear equation (2.8) is solved iteratively (Lewandowski, 1987). For hinged-hinged beams, the non-linear mode is identical to the linear one and independent of the amplitude. Hence the frequency parameter Ω^2 can be expressed in an analytical form as the root of the quadratic equation

$$f\frac{\Omega^4}{\lambda^4} - \Omega^2\Big[(F+k)\frac{k^2\pi^2}{\lambda^2} + 1\Big] + k^2\pi^2[Fk^2\pi^2 + \lambda(s+c)] = 0 \tag{2.14}$$

where $c = (3/16)(k^2\pi^2\delta^2/\lambda^2)$, k is the number of the vibration mode. Ommiting the rotary inertia effect, yields

$$\Omega^2 = k^2\pi^2\frac{Fk^2\pi^2 + \lambda^2(s+c)}{1 + f\frac{k^2\pi^2}{\lambda^2}} \tag{2.15}$$

By assuming in (2.14) or (2.15) $f = 0$, one obtains non-linear frequencies for the Bernoulli--Euler beam in which the axial force effect is taken into account. Table 1 presents the rotary inertia effect I_ρ on the non-linear frequency ratio ω/ω_1 for the fundamental vibration mode of simply-supported beams (α is the amplitude in the middle of the beam, Ω_1 is the frequency parameter determined for linear vibration). The calculations have been carried out for $\nu = 0.3$, $\kappa = 5/6$ and $H = 0$, respectively.

The backbone curves for various slenderness ratios for two modes of vibration of a simply-supported Timoshenko beam are shown in Fig. 1.

For the first mode ($k = 1$), α is the amplitude in the middle of the beam ($\xi = 1/2$), for $k = 2$, $\xi = 1/4$ (L is the beam length). One can see that the frequency ratio for the simply-supported Timoshenko beam depends on the kind of mode.

Table 1. Non-linear frequency ratio ω/ω_1 for simply-supported continuous beams

α/ρ	Bernoulli-Euler beam				Timoshenko beam			
	$\lambda = 30$		$\lambda = 10$		$\lambda = 20$		$\lambda = 30$	
	$I_\rho \neq 0$	$I_\rho = 0$	$I_\rho \neq 0$	$I_\rho = 0$	$I_\rho \neq 0$	$I_\rho = 0$	$I_\rho \neq 0$	$I_\rho = 0$
1.0	1.0897	1.0897	1.1158	1.1159	1.0963	1.0963	1.0927	1.0927
2.0	1.3229	1.3229	1.4068	1.4075	1.3445	1.3445	1.3325	1.3325
3.0	1.6394	1.6394	1.7889	1.7908	1.6785	1.6785	1.6559	1.6559
4.0	2.0000	2.0000	2.2146	2.2190	2.0568	2.0569	2.0255	2.0255
Ω_1	9.8159	9.8696	8.3874	8.6299	9.4106	9.5103	9.6556	9.7050

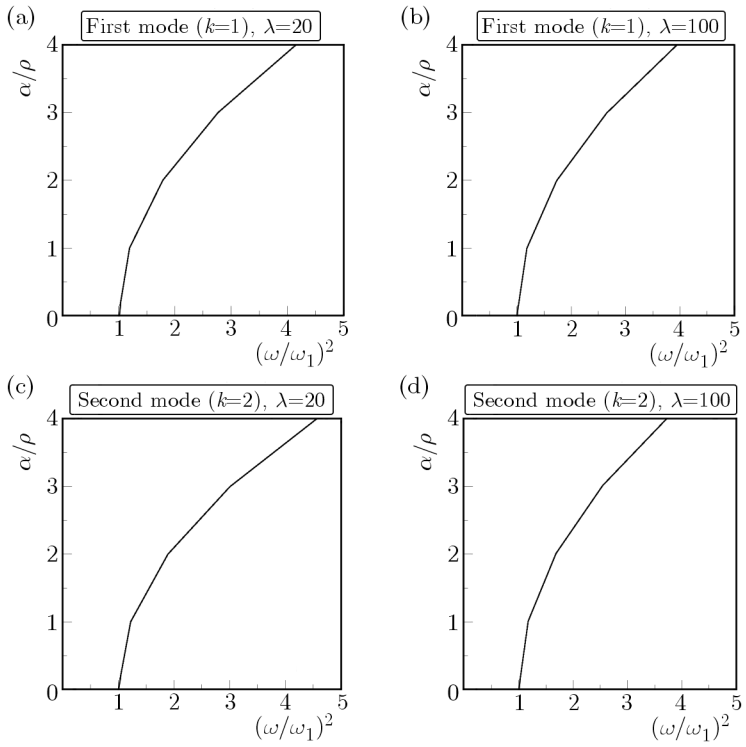

Fig. 1. The backbone curves for various slenderness ratios for two modes of vibration of a simply-supported Timoshenko beam

3. Finite Element Method formulation

Let us assume the element shape functions to be linear and independent

$$\begin{aligned} u(x,t) &= u_1(t) + [u_2(t) - u_1(t)]\frac{x}{a} \\ w(x,t) &= w_1(t) + [w_2(t) - w_1(t)]\frac{x}{a} \\ \theta(x,t) &= \theta_1(t) + [\theta_2(t) - \theta_1(t)]\frac{x}{a} \end{aligned} \tag{3.1}$$

The beam element convention is presented in Fig. 2.

Substituting (3.1) into (2.1), we obtain the element stiffness matrix in which the non-linear part corresponding to the nodal quantities $\{u_1 \quad u_2 \quad w_1 \quad \theta_1 \quad w_2 \quad \theta_2\}^{\mathrm{T}}$ can be written in the following form

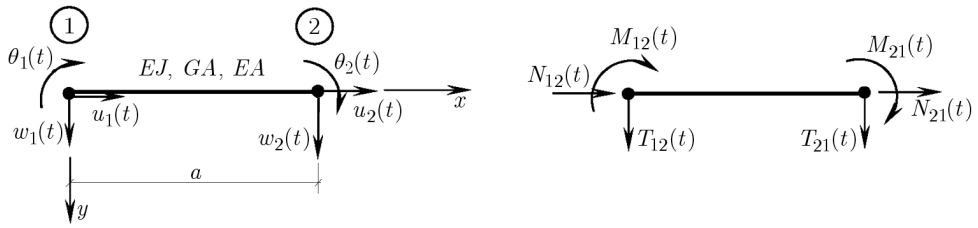

Fig. 2. Timoshenko beam convention

$$\mathbf{K}_N^* = \frac{EA}{a}\begin{bmatrix} 1 & -1 & (w_2-w_1)/(2a) & 0 & -(w_2-w_1)/(2a) & 0 \\ -1 & 1 & -(w_2-w_1)/(2a) & 0 & (w_2-w_1)/a & 0 \\ (w_2-w_1)/a & -(w_2-w_1)/a & (w_2-w_1)^2/(2a^2) & 0 & -(w_2-w_1)^2/(2a^2) & 0 \\ 0 & 0 & 0 & 0 & 0 & 0 \\ -(w_2-w_1)/a & (w_2-w_1)/a & -(w_2-w_1)^2/(2a^2) & 0 & (w_2-w_1)^2/(2a^2) & 0 \\ 0 & 0 & 0 & 0 & 0 & 0 \end{bmatrix}$$

Neglecting the horizontal forces in the calculations yields for each element the following relationship

$$C = \frac{EA}{a}\Big[u_1 - u_2 + \frac{w_1(w_2-w_1)}{2a} - \frac{w_2(w_2-w_1)}{2a}\Big] = \text{const} \tag{3.2}$$

Assuming that the considered Timoshenko beam with immovable supports is divided into elements with equally spaced nodes and summing up both sides of equation (3.2) in the range from 0 to R (R is the number of beam elements), we have

$$C = \frac{EA}{2Ra}\sum_{r=0}^{R-1}(w_{r+1}-w_r)^2 \tag{3.3}$$

In order to avoid the shear locking which occurs in linear elements and leads to erroneous results, we improve the elements by introducing a scaling factor $d/(d+1)$ into the flexural and shear matrices (Rakowski, 1990). Replacing E and G by $Ed/(d+1)$ and $Gd/(d+1)$, respectively, and eliminating the unknowns u_i, the element stiffness matrix can be expressed as follows

$$\mathbf{K} = \frac{EJ}{a^3}\frac{1}{d+1}[d\mathbf{K}_F + \mathbf{K}_S + (d+1)(\mathbf{K}_G + \mathbf{K}_N)] \tag{3.4}$$

where $d = [24(1+\nu)\rho^2]/(\kappa a^4)$, $\mathbf{K}_F$, $\mathbf{K}_S$, $\mathbf{K}_G$ and $\mathbf{K}_N$ are the flexural, shear, geometrical and non-linear matrices, respectively. They refer to the nodal quantities $\{w_1 \quad a\theta_1 \quad w_2 \quad a\theta_2\}^{\mathrm{T}}$ and have the form

$$\begin{aligned} \mathbf{K}_F &= \begin{bmatrix} 0 & 0 & 0 & 0 \\ 0 & 1 & 0 & -1 \\ 0 & 0 & 0 & 0 \\ 0 & -1 & 0 & 1 \end{bmatrix} \qquad \mathbf{K}_S = \begin{bmatrix} 12 & 6 & -12 & 6 \\ 6 & 4 & -6 & 2 \\ -12 & -6 & 12 & -6 \\ 6 & 2 & -6 & 4 \end{bmatrix} \\ \mathbf{K}_G &= \frac{a^2}{EJ}\begin{bmatrix} H & 0 & -H & 0 \\ 0 & 0 & 0 & 0 \\ -H & 0 & H & 0 \\ 0 & 0 & 0 & 0 \end{bmatrix} \qquad \mathbf{K}_N = \frac{a^2}{EJ}\begin{bmatrix} C & 0 & -C & 0 \\ 0 & 0 & 0 & 0 \\ -C & 0 & C & 0 \\ 0 & 0 & 0 & 0 \end{bmatrix} \end{aligned} \tag{3.5}$$

We assume the nodal displacements to be harmonic

$$w_r = \alpha W_r \cos\omega t \qquad \theta_r = \frac{\alpha}{a}\phi_r \cos\omega t \tag{3.6}$$

where α is the amplitude of an arbitrarly chosen node i, W_r and ϕ_r are dimensionless functions of the discrete variable r (r is the index number of the node), $r \in \langle 0, R\rangle$. By using the shape functions given in (3.1), the consistent matrix is obtained as

$$\mathbf{M}_C = \frac{am}{6}\begin{bmatrix} 2 & 0 & 1 & 0 \\ 0 & 2\rho^2/a^2 & 0 & \rho^2/a^2 \\ 1 & 0 & 2 & 0 \\ 0 & \rho^2/a^2 & 0 & 2\rho^2/a^2 \end{bmatrix} \tag{3.7}$$

If the beam, divided into a regular mesh, consists of identical elements, the dynamic equilibrium conditions can be derived according to the following way. We substitute (3.5) into (3.4) and take into account element mass matrix (3.7). Having assembled the two adjacent beam elements $(r-1, r)$ and $(r, r+1)$, we can write the equilibrium of moments and forces for an arbitrary node r as

$$\begin{aligned} &6(W_{r-1} - W_r) + 2(\phi_{r-1} + 2\phi_r) + 6(W_r - W_{r+1}) + 2(2\phi_r + \phi_{r+1}) - d(\phi_{r-1} + \phi_r) \\ &\quad + d(\phi_r - \phi_{r+1}) - 4\Lambda^2(d+1)e^2(\phi_{r-1} + 4\phi_r + \phi_{r+1}) = 0 \\ &-[12 + 6(d+1)](W_{r-1} - W_r) + [12 + 6(d+1)D](W_r - W_{r+1}) - 6(\phi_{r-1} - \phi_r) \\ &\quad + 6(\phi_r - \phi_{r+1}) - 4\Lambda^2(d+1)(W_{r-1} + 4W_r + W_{r+1}) = 0 \end{aligned} \tag{3.8}$$

Introducing the shifting operator E_r^n and central difference operator Δ_r^n into equations (3.8), we obtain two difference equations with unknown nodal variables ϕ_r and W_r

$$\begin{aligned} &\Big[(\Delta^2 + 6) - \frac{d}{2}\Delta^2\Big]\phi_r - 3(\mathrm{E} - \mathrm{E}^{-1})W_r - 2\Lambda^2(d+1)e^2(\Delta^2 + 6)\phi_r = 0 \\ &(\mathrm{E} - \mathrm{E}^{-1})\phi_\mathrm{r} - 2[2 + \mathrm{D(d+1)}]\Delta^2\mathrm{W_r} - \frac{2}{3}\Lambda^2\mathrm{(d+1)}(\Delta^2 + 6)\mathrm{W_r} = 0 \end{aligned} \tag{3.9}$$

where

$$\Delta^2 = \Delta_r^2 = \mathrm{E} + \mathrm{E}^{-1} - 2 \qquad \mathrm{E}^n = \mathrm{E}_r^n \qquad \Lambda = \frac{\Omega^2}{24R^4}$$

$$\Omega^2 = \frac{m\omega^2 L^4}{EJ} \qquad D = \frac{a^2(H+C)}{6EJ} \qquad e = \frac{R}{\lambda}$$

L is length of the beam ($L = aR$), λ is the slenderness ratio ($\lambda = L/\rho$.

Equating to zero the weighed residual of equation (3.9) for one time period $(0 - 2\pi)$ with the weighting function $\cos\omega t$ (Marur and Prathap, 2005)

$$\int_0^{2\pi} \varepsilon_i(r,t)\cos\omega t \; d(\omega t) = 0 \qquad i = 1, 2 \tag{3.10}$$

(ε_1, ε_2 are the left-hand sides of the first and second equation of (3.9) multiplied by $\cos\omega t$) one obtains the equilibrium conditions given in the form of equations (3.9) where now

$$D = \frac{a^2}{6EJ}\Big(H + \frac{3}{4}C\Big) \qquad C = \frac{EAR\delta^2}{2\lambda^2}\sum_{r=0}^{R-1}(W_{r+1} - W_r)^2 \tag{3.11}$$

After elimination of ϕ_r from coupled equation (3.9), we can rewrite them in form of a single fourth-order homogenous difference equation

$$B_1\Delta^4 W_r + B_2\Delta^2 W_r + B_3 W_r = 0 \tag{3.12}$$

where

$$B_1 = 1 - D\Big(1 - \frac{d}{2}\Big) + \frac{\Lambda^2}{3}(d - 2 + 12e^2) + 2\Lambda^2 De^2(d+1) + \frac{4}{3}\Lambda^4 e^2(d+1)$$
$$B_2 = -6D + 2\Lambda^2(d - 4 + 12e^2) + 12\Lambda^2 De^2(d+1) + 16\Lambda^4 e(d+1)$$
$$B_3 = -24\Lambda^2 + 48\Lambda^4 e^2(d+1)$$

The analytical solution to equation (3.12) is

$$W_r = C_1 \sinh\mu_1 r + C_2 \cosh\mu_1 r + C_3 \sinh\mu_2 r + C_4 \cosh\mu_2 r \tag{3.13}$$

where μ_1, μ_2 can be real, imaginary or complex, and they must fulfill the characteristic quadratic equation

$$B_1 \cosh^2\mu + \Big(-2B_1 + \frac{B_2}{2}\Big)\cosh\mu + B_1 - B_2 + \frac{B_4}{4} = 0 \tag{3.14}$$

The function ϕ_r can be derived from the second equation of (3.9) in the form

$$\phi_r = D_2 \sinh\mu_1 r + D_1 \cosh\mu_1 r + D_4 \sinh\mu_2 r + D_3 \cosh\mu_2 r \tag{3.15}$$

where

$$D_1 = \beta_1 C_1 \qquad D_2 = \beta_1 C_2 \qquad D_3 = \beta_2 C_3 \qquad D_4 = \beta_2 C_4$$
$$\beta_1 = \frac{2}{\sinh\mu_1}\Big\{(\cosh\mu_1 - 1)\Big[1 + \frac{D}{2}(d+1)\Big] + \frac{\Lambda^2}{3}(\cosh\mu_1 + 2)(d+1)\Big\}$$
$$\beta_2 = \frac{2}{\sinh\mu_2}\Big\{(\cosh\mu_2 - 1)\Big[1 + \frac{D}{2}(d+1)\Big] + \frac{\Lambda^2}{3}(\cosh\mu_2 + 2)(d+1)\Big\}$$

If a lumped mass model of the Timoshenko beam is considered, the element mass matrix has the following form

$$\mathbf{M}_1 = \frac{am}{2}\begin{bmatrix} 1 & 0 & 1 & 0 \\ 0 & \rho^2/ + a^2 & 0 & \rho^2/a^2 \\ 1 & 0 & 1 & 0 \\ 0 & \rho^2/a^2 & 0 & \rho^2/a^2a^2 \end{bmatrix} \tag{3.16}$$

The difference equilibrium equations corresponding to element mass matrix $\mathbf{M}_1$ (3.16) are

$$\begin{aligned} &\Big[(\Delta^2 + 6) - \frac{d}{2}\Delta^2\Big]\phi_r - 3(\mathrm{E} - \mathrm{E}^{-1})\mathrm{W_r} - 12\Lambda^2\mathrm{e}^2(\mathrm{d}+1)\phi_\mathrm{r} = 0 \\ &(\mathrm{E} - \mathrm{E}^{-1})\phi_r - 2[2 + D(d+1)]\Delta^2 W_r - 4\Delta^2(d+1)W_r = 0 \end{aligned} \tag{3.17}$$

or expressed in form of an equation with one unknown W_r

$$B_1\Delta^4 W_r + B_2\Delta^2 W_r + B_3 W_r = 0$$

where

$$B_1 = 1 - D\Big(1 - \frac{d}{2}\Big) \qquad B_2 = -6D + 2\Lambda^2[d - 2 + 12e^2 + 6De^2(d+1)]$$
$$B_3 = -24\Lambda^2 + 48\Lambda^4 e^2(d+1)$$

The solution to this equation and the expression of the characteristic equation are identical to those given in (3.13) and (3.14), respectively. But in this case, the quantities β_i present in the relationship between D_i and C_i (see (3.15)), derived from (3.17), are defined as

$$\beta_1 = \frac{2}{\sinh\mu_i}\Big\{\cosh\mu_i - 1)\Big[1 + \frac{D}{2}(d+1)\Big] + \Lambda^2(d+1)\Big\} \qquad i = 1,2$$

Since the non-linear frequency parameter Λ and the non-linear vibration modes W_r and ϕ_r depend on the amplitude α, the eigenvalue problem of non-linear equation (3.12) is solved iteratively. The iteration starts by assuming the magnitude of the constant D (it is convenient in the first step of iteration to use the value calculated for the linear case). From the frequency equations adequate to the considered boundary conditions, one finds μ_1 and μ_2. Then the vibration mode W_r is determined and the resulting parameter $\overline{D}$ is compared with the given D. The iterative computation is continued until the difference $|\overline{D} - D|$ is less than the adopted tolerance. The boundary conditions are considered below.

3.1. Simply-supported beam

For a simply supported beam with the boundary nodes 0 and R, the boundary conditions $W_0 = W_R = 0$, $M_0 = M_R = 0$ lead to the following mode of vibrations which is independent of the vibration amplitude

$$W_r = C_1 \sin(k\pi r) \tag{3.18}$$

and k being the number of mode. The frequency parameter Λ can be determined as the root of the quadratic equation

$$a_k\Lambda^2 + b_k\Lambda + c_k = 0 \tag{3.19}$$

where

$$\begin{aligned}
a_k &= 4e^2(d+1)\Big\{\frac{1}{3}\Big[\cos\Big(\frac{k\pi}{R}\Big) - 1\Big]^2 + 2\Big[\cos\Big(\frac{k\pi}{R}\Big) - 1\Big] + 3\Big\}\\
b_k &= \Big[\cos\Big(\frac{k\pi}{R}\Big) - 1\Big]^2\Big[-\frac{2}{3} + \frac{d}{3} + 4e^2 + 2e^2(d+1)D\Big]\\
&\quad + \Big[\cos\Big(\frac{k\pi}{R}\Big) - 1\Big][-4 + d + 12e^2 + 6e^2(d+1)D] - 6\\
c_k &= \Big[\cos\Big(\frac{k\pi}{R}\Big) - 1\Big]\Big\{\Big[\cos\Big(\frac{k\pi}{R}\Big) - 1\Big]\Big[1 - D\Big(1 - \frac{d}{2}\Big)\Big] - 3D\Big\}
\end{aligned}$$

When the lumped mass model is considered, the above coefficients must be replaced by

$$\begin{aligned}
a_k &= 4e^2(d+1)\\
b_k &= \Big[\cos\Big(\frac{k\pi}{R}\Big) - 1\Big]^2[-2 + d + 12e^2 + 6e^2(d+1)D] - 6\\
c_k &= \Big[\cos\Big(\frac{k\pi}{R}\Big) - 1\Big]\Big\{\Big[\cos\Big(\frac{k\pi}{R}\Big) - 1\Big]\Big[1 - D\Big(1 - \frac{d}{2}\Big)\Big] - 3D\Big\}
\end{aligned}$$

3.2. Clamped-clamped beam

The boundary conditions $W_0 = W_R = 0$, $\phi_0 = \phi_R = 0$ request the following equations to be fulfilled

$$\begin{aligned}
&C_1[\beta_2\sinh(\mu_1 R) - \beta_1\sinh(\mu_2 R)] + C_2\beta_2[\cosh(\mu_1 R) - \cosh(\mu_2 R)] = 0\\
&C_1\beta_1[\cosh(\mu_1 R) - \cosh(\mu_2 R)] + C_2[\beta_1\sinh(\mu_1 R) - \beta_2\sinh(\mu_2 R)] = 0
\end{aligned} \tag{3.20}$$

Equating to zero the determinant of the set of equations (3.20) yields the characteristic equation

$$2\beta_1\beta_2[\cosh(\mu_1 R)\cosh(\mu_2 R)-1]-(\beta_1^2+\beta_2^2)\sinh(\mu_1 R)\sinh(\mu_1 R)=0 \tag{3.21}$$

The modes of vibrations are

$$W_r = C_1\Big\{\sinh(\mu_1 r)-\frac{\beta_1}{\beta_2}\sinh(\mu_2 r)-\beta[\cosh(\mu_1 r)-\cosh(\mu_2 r)]\Big\} \tag{3.22}$$

where

$$\beta=\frac{\beta_1[\cosh(\mu_1 R)-\cosh(\mu_2 R)]}{\beta_1\sinh(\mu_1 R)-\beta_2\sinh(\mu_2 R)}$$

3.3. Hinged-clamped beam

In this case, the boundary conditions are given by $W_0 = W_R = 0$, $M_0 = 0$, $\phi_R = 0$, which refer to the homogenous equations

$$\begin{aligned} &C_1\sinh(\mu_1 R)+C_3\sinh(\mu_2 R)=0\\ &C_1\beta_1\cosh(\mu_1 R)+C_3\beta_2\cosh(\mu_2 R)=0 \end{aligned} \tag{3.23}$$

and give the characteristic equation

$$\beta_2\tanh(\mu_1 R)-\beta_1\tanh(\mu_2 R)=0 \tag{3.24}$$

The modes of vibrations can be expressed as

$$W_r = C_1\Big[\sinh(\mu_1 r)-\frac{\sinh(\mu_1 R)}{\sinh(\mu_2 R)}\sinh(\mu_2 r)\Big] \tag{3.25}$$

Let us now analyse the reduced-integrated linear elements. When the one-point quadrature is applied to the shear term of strain energy (2.1), the element stiffness matrix becomes

$$\mathbf{K}=\frac{EJ}{a^3}\frac{1}{d}[(d-1)\mathbf{K}_F+\mathbf{K}_S+d(\mathbf{K}_G+\mathbf{K}_N)] \tag{3.26}$$

where $\mathbf{K}_F$, $\mathbf{K}_S$, $\mathbf{K}_G$ and $\mathbf{K}_N$ are defined as in (3.4). The difference between the above matrix and that given in (3.4) is that in (3.26) the expression $(d-1)$ is used instead of d.

4. Numerical examples

The non-linear frequency ratios are determined for beams with various boundary conditions and for a wide spectrum of the thickness ratio. The consistent and lumped mass model of beams are considered. The results of computation are compared with the results obtained for linear elements to which the reduced-selective integration technique has been applied. The calculations have been carried out with the values $\nu = 0.3$, $\kappa = 5/6$ and $H = 0$. The following indications are accepted:

- CONT – the beam with continuous mass distribution,
- MOD – the beam divided into modified finite elements proposed by Rakowski (1990),
- RI – the beam divided into linear elements with reduced integration correction.

Numerical results are obtained for the lumped mass model. Values in the parentheses refer to the consistent mass model.

Table 2. Comparison of the frequency ratio (ω/ω_1) for continuous and discrete ($R = 8$) simply-supported Timoshenko beams

α/ρ	$\lambda = 20$			$\lambda = 100$		
	CONT	MOD	RI	CONT	MOD	RI
First mode ($k = 1$)						
Ω_1	9.411	9.528 (9.406)	9.584 (9.461)	9.850	9.977 (9.849)	10.042 (9.914)
1.0	1.0963	1.0941	1.0930	1.0900	1.0878	1.0867
2.0	1.3445	1.3371	1.3336	1.3237	1.3165	1.3129
3.0	1.6785	1.6652	1.6587	1.6409	1.6278	1.6212
4.0	2.0568	2.0375	2.0281	2.0023	1.9832	1.9736
Second mode ($k = 2$)						
Ω_1	33.550	35.115 (33.357)	35.772 (33.981)	39.162	41.201 (39.138)	42.338 (40.218)
1.0	1.1158	1.1062	1.1021	1.0908	1.0823	1.0781
2.0	1.4048	1.3763	1.3629	1.3264	1.2983	1.2841
3.0	1.7889	1.7346	1.7108	1.6457	1.5945	1.5685
4.0	2.2146	2.1363	2.1021	2.0092	1.9345	1.8962

Table 3. Frequency ratio (ω/ω_1) of the first mode for the clamped-clamped beam ($R = 8$)

α/ρ	$\lambda = 20$		$\lambda = 40$		$\lambda = 100$	
	MOD	RI	MOD	RI	MOD	RI
1.0	1.0251 (1.0251)	1.0242 (1.0242)	1.0211 (1.0212)	1.0204 (1.0294)	1.0202 (1.0202)	1.0195 (1.0195)
2.0	1.0963 (1.0965)	1.0929 (1.0931)	1.0817 (1.0819)	1.0789 (1.0790)	1.0781 (1.0783)	1.0756 (1.0757)
3.0	1.2045 (1.2049)	1.1975 (1.1979)	1.1746 (1.1750)	1.1689 (1.1693)	1.1675 (1.1678)	1.1625 (1.1628)
4.0	1.3400 (1.3407)	1.3286 (1.3294)	1.2918 (1.2925)	1.2830 (1.2836)	1.2807 (1.2814)	1.2734 (1.2739)
5.0	1.4952 (1.4962)	1.4789 (1.4800)	1.4265 (1.4276)	1.4144 (1.4154)	1.4114 (1.4123)	1.4021 (1.4028)
Ω_1	19.082 (18.801)	19.539 (19.247)	21.609 (21.282)	22.281 (21.937)	22.529 (22.185)	23.295 (22.932)
	CONT					
Ω_1	18.837		21.296		22.189	

5. Concluding remarks

The analytical solution to the non-linear free vibration problem formulated by the finite element method for the Timoshenko beam is presented. The simple modified linear element is used in the solution. This improved element gives a better convergence to the solution for the continuous system than the reduced-integrated one. The good accuracy is achieved for a wide range of the thickness ratio for the consistent and lumped mass models of the beam. The concept of the finite difference method is introduced. The main advantage of the presented idea is that even for a large number of elements it suffices to consider the non-linear eigenvalue problem of only one difference equation which is equivalent to a set of FEM equilibrium conditions.

Table 4. Frequency ratio (ω/ω_1) of the second mode for the clamped-clamped beam ($R = 8$)

α/ρ	$\lambda = 20$		$\lambda = 40$		$\lambda = 100$	
	MOD	RI	MOD	RI	MOD	RI
1.0	1.0649	1.0604	1.0452	1.0413	1.0402	1.0367
	(1.0652)	(1.0608)	(1.0457)	(1.0418)	(1.407)	(1.10371)
2.0	1.2372	1.2216	1.1680	1.1540	1.1502	1.1379
	(1.2383)	(1.2228)	(1.1697)	(1.1557)	(1.1519)	(1.1393)
3.0	1.4780	1.4480	1.3431	1.3154	1.3079	1.2845
	(1.4796)	(1.4499)	(1.3462)	(1.3188)	(1.3114)	(1.2875)
4.0	1.7591	1.7134	1.5506	1.5068	1.4950	1.4590
	(1.7611)	(1.7158)	(1.5552)	(1.5120)	(1.5004)	(1.4641)
5.0	2.0640	2.0024	1.7790	1.7169	1.7003	1.6499
	(2.0662)	(2.0050)	(1.7846)	(1.7236)	(1.7074)	(1.6572)
Ω_1	46.229	48.146	58.332	62.197	63.945	69.172
	(43.863)	(45.585)	(55.152)	(58.717)	(60.409)	(65.225)
	CONT					
Ω_1	44.330		55.423		60.519	

Table 5. Frequency ratio (ω/ω_1) of the third mode for the clamped-clamped beam ($R = 8$)

α/ρ	$\lambda = 20$		$\lambda = 40$		$\lambda = 100$	
	MOD	RI	MOD	RI	MOD	RI
1.0	1.1095	1.0989	1.0586	1.0473	1.0442	1.0335
	(1.1117)	(1.1009)	(1.0603)	(1.0489)	(1.0457)	(1.0347)
2.0	1.3768	1.3433	1.2124	1.1737	1.1630	1.1254
	(1.3799)	(1.3461)	(1.2126)	(1.1777)	(1.1671)	(1.1290)
3.0	1.7252	1.6652	1.4268	1.3532	1.3329	1.2599
	(1.7262)	(1.6657)	(1.4310)	(1.3581)	(1.3384)	(1.2652)
4.0	2.1172	2.0290	1.6793	1.5673	1.5367	1.4234
	(2.1133)	(2.0241)	(1.6825)	(1.5717)	(1.5425)	(1.4300)
5.0	2.5518	2.4235	1.9562	1.8047	1.7774	1.6234
	(2.5283)	(2.4042)	(1.9579)	(1.8082)	(1.7694)	(1.6152)
Ω_1	81.697	85.847	112.487	124.642	130.900	151.802
	(72.825)	(76.475)	(99.927)	(110.404)	(116.090)	(133.961)
	CONT					
Ω_1	75.077		101.659		117.002	

References

1. Asghari M., Kahrobaiyan M.H., Ahmadian M.T., 2010, A nonlinear Timoshenko beam formulation based on the modified couple stress theory, *International Journal of Engineering Science*, **48**, 1749-1776

2. Bhashyam G.R., Prathap G., 1980, Galerkin finite element method for non-linear beam vibrations, *Journal of Sound and Vibration*, **72**, 191-203

3. Bhashyam G.R., Prathap G., 1981, The second frequency spectrum of Timoshenko beams, *Journal of Sound and Vibration*, **76**, 407-420

4. Dumir P.C., Bhaskar A., 1988, Some erroneous finite element formulations of non-linear vibrations of beams and plates, *Journal of Sound and Vibration*, **123**, 517-527

5. Evensen D.A., 1968, Non-linear vibrations of beams with various boundary conditions, *American Institute of Aeronatics and Astronomics Journal*, **6**, 370-372

6. Hsu C.S., 1960, On the application of elliptic functions in non-linear forced oscillations, *Quarterly of Applied Mathematics*, **17**, 393-407

7. Kitipornchai S., Ke L.L., Yang J., Xiang Y., 2009, Nonlinear vibration of edge cracked functionally graded Timoshenko beams, *Journal of Sound and Vibration*, **324**, 962-982

8. Lewandowski R., 1987, Application of the Ritz method to the analysis of non-linear free vibration of beams, *Journal of Sound and Vibration*, **114**, 91-101

9. Levinson M., Cooke D.W., 1982, On the two frequency spectra of Timoshenko beams, *Journal of Sound and Vibration*, **84**, 319-326

10. Marur S.R., Prathap G., 2005, Non-linear beam vibration problems and simplifications in finite element models, *Computational Mechanics*, **35**, 352-360

11. Mei C., Decha-Umphai K., 1985, A finite element method for non-linear forced vibrations of beams, *Journal of Sound and Vibration*, **102**, 369-380

12. Rakowski J., 1990, The interpretation of shear locking in beam elements, *Computers and Structures*, **37**, 5, 769-776

13. Rakowski J., 1991a, A critical analysis of quadratic beam finite elements, *International Journal for Numerical Methods in Engineering*, **31**, 949-966

14. Rakowski J., 1991b, A new methodology of evaluation of C0 bending finite elements, *Computer Methods in Applied Mechanics and Engineering*, **91**, 1327-1338

15. Rakowski J., Wielentejczyk P., 1996, Vibrations of infinite periodic beams by finite element method, *Zeitschrift für Angewandte Mathemetic und Mechanik*, **76**, 411-412

16. Rakowski J., Wielentejczyk P., 2002, Dynamic analysis of infinite discrete structures, *Foundations of Civil and Environmental Engineering*, **3**, 91-106

17. Rosenberg R.M., 1966, On non-linear vibrations of systems with many degree of freedom, *Advanced in Applied Mechanics*, **9**, 154-242

18. Sarma B., Varadan T.K., 1983, Lagrange-type formulation for finite element analysis of non-linear beam vibrations, *Journal of Sound and Vibration*, **86**, 61-70

19. Singh G., Rao G.V., 1998, Nonlinear oscillations of thick asymmetric cross-ply beams, *Acta Mechanics*, **127**, 135-146

20. Szemplińska-Stupnicka W., 1983, Non-linear normal modes and generalized Ritz method in the problems of vibrations of non-linear elastic continuous systems, *International Journal of Non-linear Mechanics*, **18**, 154-242

21. Woinowsky-Krieger S., 1950, The effect of an axial force on the vibration of hinged bars, *Journal of Applied Mechanics*, **17**, 35-36

Manuscript received January 30, 2014; accepted for print March 12, 2015

JOURNAL OF THEORETICAL AND APPLIED MECHANICS
53, 3, pp. 745-755, Warsaw 2015
DOI: 10.15632/jtam-pl.53.3.745

ANALYSIS OF LATERAL VIBRATIONS OF THE AXIALLY LOADED HELICAL SPRING

Krzysztof Michalczyk
AGH University of Science and Technology, Faculty of Mechanical Engineering and Robotics, Kraków, Poland
e-mail: kmichal@agh.edu.pl

It is shown in this paper that the proposed concept by Krużelecki and Życzkowski (1990) of the equivalent rod can be applied in calculations of natural lateral vibrations of springs and that the obtained results will be nearer FEM results than the standard model based on the Timoshenko equivalent beam. The model, created on this base, allows one to calculate natural frequencies of the clamped-clamped spring. It is also shown that models based on the equivalent beam concept, which are easier to apply than the models treating the spring as the spatially curved rod, have only a slightly smaller accuracy. It is also indicated that in the most common practice making of manufacturing end coils of springs, the natural frequencies differ significantly from the frequencies calculated by means of all tested methods. The performed simulations show that differences between the first and the second as well as the third and the fourth natural frequency of the spring are small and, therefore, the axially symmetrical equivalent beam model can be used without a large error. The diagram allowing one to determine whether the desired frequencies are lower or higher than the cut-off frequency is developed for the presented model.

Keywords: helical spring vibrations, axially loaded spring,coil spring, Timoshenko equivalent beam

1. Introduction

Lateral vibrations of helical springs constitute essential hazards for their operation safety, since they can cause high stress amplitudes and contribute to the loss of stability. On account of that, looking for ways of limiting natural vibrations of helical springs and the development of calculation methods allowing one to determine these limitations efficiency is essential. Equally essential is the accurate determination of natural frequencies.

Problems related to determination the above value can be considered when the spring is treated as a spatially curved rod or using the concept of the equivalent beam. Analyses of spring vibrations treated as the spatially curved rod were presented, among others, by Love (1899), Wittrick (1966), Mottershead (1980), Pearson and Wittrick (1986) Jiang *et al.* (1991), Yıldırım (1999) Becker *et al.* (2002), Lee and Thompson (2001), Lee (2007), Stander and Du Preez (1992), Nagaya *et al.* (1986), Taktak *et al.* (2008), Yu and Yang (2010). The analyses enabled a relatively accurate description of the effect, but due to problem complexity it was very difficult to apply and – depending on assumptions – to obtain analytical results in a closed form. For practical reasons much more suitable is the equivalent rod or beam model (Haringx, 1949; Della Pietra and Della Valle, 1982; Kobelev, 2014; Michalczyk, 2014). However, the beam model does not take into account several factors related to dynamic effects in springs. It assumes, among others, that the equivalent beam modelling the spring in the case of lateral vibrations is prismatic and has axially symmetrical parameters characterising stiffness and mass distribution. It can be expected that this assumption in the case of clamped-clamped springs (with fixed ends) – the most often met case in practice – can be the reason of significant errors, since the spring lateral

stiffness is not the same in all directions and its distribution round the axis depends on the partial coil number. The problem of lateral vibrations of helical springs treated as the equivalent beam was considered in the paper by Kobelev (2014). However, only the simplest case, such as the simply-supported beam, was solved in that study.

A new concept of an equivalent rod, which could be applied to analysis of the helical spring static stability was proposed by Krużelecki and Życzkowski (1990). That idea, in contrast to the model of Timoshenko and Gere (1961), took into account the influence of the lead angle of the helix line on its flexural, shearing and compression rigidities. In addition, that concept allowed the analysis of spring buckling in two planes.

The aim of the hereby paper is the analysis of the possibility of application of the Krużelecki and Życzkowski (1990) concept to the determination of lateral vibrations of axially loaded helical springs. The results obtained on the basis of such formulated model will be compared with the classical model of the Timoshenko equivalent beam, with the numerical simulation results and with the results achieved by other authors. The presented model additionally takes into account the non-rotational way of mounting of the end coils.

2. Analysis

For an element of the equivalent beam modelling the axially helical spring loaded by a force P, as shown in Fig. 1, the following equations of motion can be written (Haringx, 1949)

$$\frac{\partial N}{\partial \psi} + Q = 0 \qquad m_e \frac{\partial^2 y}{\partial t^2} = N\frac{\partial \psi}{\partial x} - \frac{\partial Q}{\partial x} \qquad m_e r_g^2 \frac{\partial^2 \psi}{\partial t^2} = N\varphi + Q + \frac{\partial M}{\partial x} \tag{2.1}$$

The angle ψ originates only from bending, while the angle φ originates only from the equivalent beam shearing

$$\psi + \varphi = -\frac{\partial y}{\partial x} \qquad \frac{\partial \psi}{\partial x} = \frac{M}{\alpha} \qquad \varphi = \frac{Q}{\beta} \tag{2.2}$$

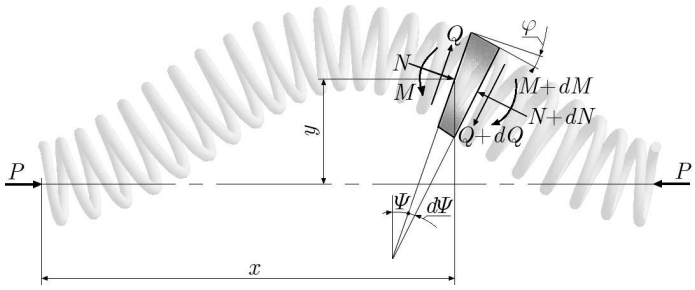

Fig. 1. Model of the equivalent rod for analysis of lateral vibrations of the helical spring

The coefficients α and β are up-to-date flexural and shearing rigidities of the equivalent beam, respectively. The spring mass for its length unit is marked by m_e, while the radius of gyration of the equivalent beam cross-section is marked by r_g. Limiting the vibration analysis to small deflections only, it can be assumed that $N \approx P$. Making use of (2.2) in (2.1) on this assumption, after transformations, we obtain

$$\beta\Big(1 + \frac{P}{\beta}\Big)\varphi = m_e r_g^2 \frac{\partial^2 \psi}{\partial t^2} - \alpha \frac{\partial^2 \psi}{\partial x^2} \qquad -m_e \frac{\partial^2 \varphi}{\partial t^2} + \beta \frac{\partial^2 \varphi}{\partial x^2} = m_e \frac{\partial^2 \psi}{\partial t^2} + P\frac{\partial^2 \psi}{\partial x^2} \tag{2.3}$$

Eliminating φ from equations (2.3) and transforming, we obtain the wave equation of lateral vibrations of the spring under the axial static load (Haringx, 1949)

$$\frac{\partial^4\psi}{\partial x^4} - \Big(\frac{m_e}{\beta} + \frac{m_e r_g^2}{\alpha}\Big)\frac{\partial^4\psi}{\partial x^2\partial t^2} + \frac{m_e^2 r_g^2}{\alpha\beta}\frac{\partial^4\psi}{\partial t^4} + \frac{P}{\alpha}\Big(1+\frac{P}{\beta}\Big)\frac{\partial^2\psi}{\partial x^2} + \frac{m_e}{\alpha}\Big(1+\frac{P}{\beta}\Big)\frac{\partial^2\psi}{\partial t^2} = 0 \tag{2.4}$$

Since we are considering the model with undamped vibrations, separating variables in equation (2.4), the function $\psi(x,t)$ can be written as the product of the amplitude $\Psi(x)$ and the time function $T(t) = \sin\omega t$. Analogous expressions can be also written for the functions φ and y

$$\psi(x,t) = \Psi(x)\sin\omega t \qquad \varphi(x,t) = \Phi(x)\sin\omega t \qquad y(x,t) = Y(x)\sin\omega t \tag{2.5}$$

Substituting proper derivatives $(2.5)_1$ into equation (2.4) and performing transformations, we obtain the equation for amplitudes in the form

$$\Psi^{IV} + \Big[\Big(\frac{m_e}{\beta} + \frac{m_e r_g^2}{\alpha}\Big)\omega^2 + \frac{P}{\alpha}\Big(1+\frac{P}{\beta}\Big)\Big]\Psi^{II} - \Big[\frac{m_e}{\alpha}\Big(1+\frac{P}{\beta}\Big)\omega^2 - \frac{m_e^2 r_g^2}{\alpha\beta}\omega^4\Big]\Psi = 0 \tag{2.6}$$

Denoting for simplification

$$b = \Big(\frac{m_e}{\beta} + \frac{m_e r_g^2}{\alpha}\Big)\omega^2 + \frac{P}{\alpha}\Big(1+\frac{P}{\beta}\Big) \qquad c = \frac{m_e}{\alpha}\Big(1+\frac{P}{\beta}\Big)\omega^2 - \frac{m_e^2 r_g^2}{\alpha\beta}\omega^4 \tag{2.7}$$

The characteristic equation for (2.6), after substituting $\Psi(x) = C\mathrm{e}^{rx}$, takes the form

$$r^4 + br^2 - c = 0 \tag{2.8}$$

Substituting $q = r^2$, we obtain a quadratic equation $q^2 + bq - c = 0$, whose roots are

$$q_1 = \frac{1}{2}\Big(-b + \sqrt{b^2+4c}\Big) \qquad q_2 = \frac{1}{2}\Big(-b - \sqrt{b^2+4c}\Big) \tag{2.9}$$

The expression, which occurs in square roots in (2.9) can be transformed, using (2.7), into

$$b^2 + 4c = \frac{m_e^2}{\alpha^2\beta^2}(\alpha - r_g^2\beta)^2\omega^4 + 2\frac{m_e}{\alpha}\Big(1+\frac{P}{\beta}\Big)\Big(\frac{P}{\beta} + \frac{Pr_g^2}{\alpha} + 2\Big)\omega^2 + \frac{P^2}{\alpha^2}\Big(1+\frac{P}{\beta}\Big)^2 \tag{2.10}$$

This expression, similarly as b, is higher than null for an arbitrary frequency ω, which means

$$\bigwedge_{\omega\geqslant 0} q_2 < 0$$

Thus, the solution form of equation (2.6) depends on sign of the root q_1. The cut-off frequency value ω_b at which the solution form of equation (2.8) changes, is calculated by equating the right-hand side of equation $(2.9)_1$ to null

$$\omega_b = \sqrt{\frac{\beta}{m_e r_g^2}\Big(1+\frac{P}{\beta}\Big)} \tag{2.11}$$

Thus

$$\bigwedge_{\omega<\omega_b} \Psi(x) = C_1\cosh(k_1 x) + C_2\sinh(k_1 x) + C_3\cos(k_2 x) + C_4\sin(k_2 x) \tag{2.12}$$

where

$$k_1 = \sqrt{\frac{1}{2}\Big(-b + \sqrt{b^2+4c}\Big)} \qquad k_2 = \sqrt{\frac{1}{2}\Big(b + \sqrt{b^2+4c}\Big)} \tag{2.13}$$

and

$$\bigwedge_{\omega>\omega_b} \Psi(x) = C_5\cos(k_3x) + C_6\sin(k_3x) + C_7\cos(k_4x) + C_8\sin(k_4x) \tag{2.14}$$

where

$$k_3 = \sqrt{\frac{1}{2}\Big(b - \sqrt{b^2+4c}\Big)} \qquad k_4 = k_2 \tag{2.15}$$

The way of determining the cut-off frequency ω_b for short, not loaded beams, was studied by Stephen and Puchegger (2006) and Majkut (2009). From the investigations of the author (which are presented in the further part of this paper) it results that even for relatively short springs, the first natural frequencies of lateral vibrations are lower than the cut-off frequency ω_b. Therefore, in further considerations, expression (2.12) is used.

The spring deflection angle resulting only from shearing, on the basis of $(2.3)_1$, equals

$$\varphi = \frac{1}{\beta\Big(1+\frac{P}{\beta}\Big)}\Big(m_e r_g^2\frac{\partial^2\psi}{\partial t^2} - \alpha\frac{\partial^2\psi}{\partial x^2}\Big) \tag{2.16}$$

Making use of $(2.2)_3$, $(2.5)_{2,3}$ and (2.16) in equation $(2.1)_2$, after transformations, we obtain the equation of amplitudes in the form

$$Y = -\left[\frac{P\Big(1+\frac{P}{\beta}\Big) + m_e\omega^2 r_g^2}{m_e\omega^2\Big(1+\frac{P}{\beta}\Big)}\Psi^I + \frac{\alpha}{m_e\omega^2\Big(1+\frac{P}{\beta}\Big)}\Psi^{III}\right] \tag{2.17}$$

Using derivatives (2.12) in equation (2.17) and transforming, we finally obtain the equation of displacements in the form

$$\begin{aligned} Y(x) = {} & (-Ak_1 - Bk_1^3)C_1\sinh(k_1x) + (-Ak_1 - Bk_1^3)C_2\cosh(k_1x) \\ & + (Ak_2 - Bk_2^3)C_3\sin(k_2x) + (-Ak_2 + Bk_2^3)C_4\cos(k_2x) \end{aligned} \tag{2.18}$$

where, for notation simplification, the following marks are introduced

$$A = \frac{P\Big(1+\frac{P}{\beta}\Big) + m_e\omega^2 r_g^2}{m_e\omega^2\Big(1+\frac{P}{\beta}\Big)} \qquad B = \frac{\alpha}{m_e\omega^2\Big(1+\frac{P}{\beta}\Big)} \tag{2.19}$$

The boundary conditions, being the clamped-clamped spring, correspond properly with the real operation conditions of a majority of springs applied in industry and, therefore, such a model will be considered. These conditions are

$$\textbf{1)}\ \ y(0,t) = 0 \qquad \textbf{2)}\ \ y(L,t) = 0 \qquad \textbf{3)}\ \ \psi(0,t) = 0 \qquad \textbf{4)}\ \ \psi(L,t) = 0 \tag{2.20}$$

where L is the real height of the spring.

From conditions **1**, **3** and **4**, we obtain the following relationships

$$\begin{aligned} & C_2 = \frac{-\cosh(k_1L) + \cos(k_2L)}{\sinh(k_1L) + \frac{Ak_1+Bk_1^3}{-Ak_2+Bk_2^3}\sin(k_2L)}C_1 \qquad C_3 = -C_1 \\ & C_4 = \frac{Ak_1 + Bk_1^3}{-Ak_2 + Bk_2^3}C_2 \end{aligned} \tag{2.21}$$

On the basis of the second boundary condition (2.20), we obtain the frequency equation

$$\begin{aligned} 0 = {} & (-Ak_1 - Bk_1^3)C_1 \sinh(k_1 L) + (-Ak_1 - Bk_1^3)C_2 \cosh(k_1 L) \\ & + (Ak_2 - Bk_2^3)C_3 \sin(k_2 L) + (-Ak_2 + Bk_2^3)C_4 \cos(k_2 L) \end{aligned} \tag{2.22}$$

The models proposed by Krużelecki and Życzkowski (1990) have been used for the determination of the equivalent stiffness of the beam modelling the spring. The equivalent flexural rigidity and shear stiffness are expressed by

$$\alpha = \frac{2EJ \sin\delta}{2 + \nu \cos^2\delta} \qquad \beta = \frac{EJ \sin\delta}{R^2(1 + \nu \sin^2\delta)} \frac{2\pi n}{\int\limits_{\phi_0}^{\phi_0 + 2\pi n_0} \sin^2\phi \, d\phi} \tag{2.23}$$

where EJ is the product of Young's modulus and area moment of inertia of the wire section, ν is Poisson's ratio. The values δ and R are the lead angle of the helix and half of the diameter of the nominal spring for an arbitrary force P, respectively. The angle ϕ, occurring in $(2.23)_2$, is the angle marked by the lead radius between the transverse force vector and an arbitrary cross-section of the spring wire. Since the transverse force direction may not coincide with the direction determined by the spring axis and the beginning of the helix line, the angle coordinate of the spring beginning ϕ_0 can generally differ from zero.

As compared to the widely applied in the references equivalent stiffness, see e.g. Timoshenko and Gere (1961), Guido *et al.* (1978), in which the lead angle of the helix δ is assumed as constant and equal to zero, expressions (2.23) allow one to take into account a non-zero value of the angle δ dependent on the axial force P. The relationships given by Krużelecki and Życzkowski (1990) take also into account the nominal spring radius R change as well as the change of the active coils number n, under the influence of the force P. The authors assumed that the way of supporting the spring ends enables their free rotation. In such a case, during compression of the spring the number of its coils usually decreases (Michalczyk, 2009). Since the wire length is constant, it results in an additional increase in its nominal radius R. Its value as well as the value of the up-to-date helix line pitch angle δ can be determined by rearrangement of the relationships between the torsion and curvature of the helix wire and the force P given by Haringx (1948)

$$\frac{PR^2(1+\nu)\cos\delta}{EJ} = \sin\delta\cos\delta - \frac{R}{R_0}\sin\delta_0\cos\delta_0 \qquad \frac{PR^2\sin\delta}{EJ} = \cos^2\delta - \frac{R}{R_0}\cos^2\delta_0 \tag{2.24}$$

In order to realise the condition of free rotation of the spring ends, one of them has to be supported on a thrust bearing. Only in such a case equations (2.24) can be used for calculating R and δ.

However, most often, springs are supported in a way making free rotations of the end coils impossible and, therefore, this case will be considered further. The number of active coils n of the spring loaded by the force P is equal – due to the clamped-clamped condition – to the number of active coils n_0 of the not loaded spring. On this assumption and making use of the geometrical relations, it is possible to determine the helix line pitch angle δ and the spring nominal radius R under load

$$\delta = \arcsin\left(\left(1 - \frac{P}{\gamma_0}\right)\sin\delta_0\right) \qquad R = R_0 \frac{\cos\delta}{\cos\delta_0} \tag{2.25}$$

The equivalent shear stiffness γ_0 occurring in equation $(2.25)_1$ can be expressed by the equation (Krużelecki and Życzkowski, 1990)

$$\gamma_0 = \frac{EJ \sin\delta_0}{R_0^2(1 + \nu\cos^2\delta_0)} \tag{2.26}$$

Knowing the nominal radius R of the axially loaded clamped-clamped spring, it is possible to calculate its equivalent radius of gyration r_g. In the case of modelling the radius of gyration of cylindrical helical springs, the equivalent rod constitutes the thin-walled cylinder of the average radius equal to the nominal spring radius R and of the mass equal to the spring mass. On this assumption, making use of $(2.25)_2$, the equivalent radius of gyration r_g can be written in the form

$$r_g = \frac{\sqrt{2}}{2} R_0 \frac{\cos\delta}{\cos\delta_0} \tag{2.27}$$

Introducing $(2.25)_1$, (2.26), (2.27) into (2.11), (2.22), (2.23), we can calculate cut-off frequencies and natural frequencies of lateral vibrations.

3. Simulations, results and discussion

3.1. Analysis of natural frequencies of lateral vibrations of not axially loaded springs

Comparisons of the results obtained on the basis of numerical FEM simulations of models (given in references) in which the spring is considered as a spatially curved rod of the classic model of the Timoshenko equivalent beam (applied up-to-date in all investigations concerning lateral vibrations of the spring modelled as the equivalent rod) with the proposed in this paper model using the concept of the equivalent beam given by Krużelecki and Życzkowski (1990) is presented below. As the first example, the spring of the same parameters as those used in work by Lee and Thompson (2001) is analysed. These parameters are as follows: total spring length $L = 332\,\text{mm}$, spring nominal radius $R_0 = 65\,\text{mm}$, wire radius $r = 6\,\text{mm}$, density $\rho = 7800\,\text{kg/m}^3$, number of active coils $n = 6$, Young's modulus $E = 209000\,\text{MPa}$, Poisson's ratio $\nu = 0.28$. The first four forms of lateral vibrations of the clamped-clamped spring not loaded by a longitudinal force obtained by the FEM in the ANSYS software are presented in Fig. 2.

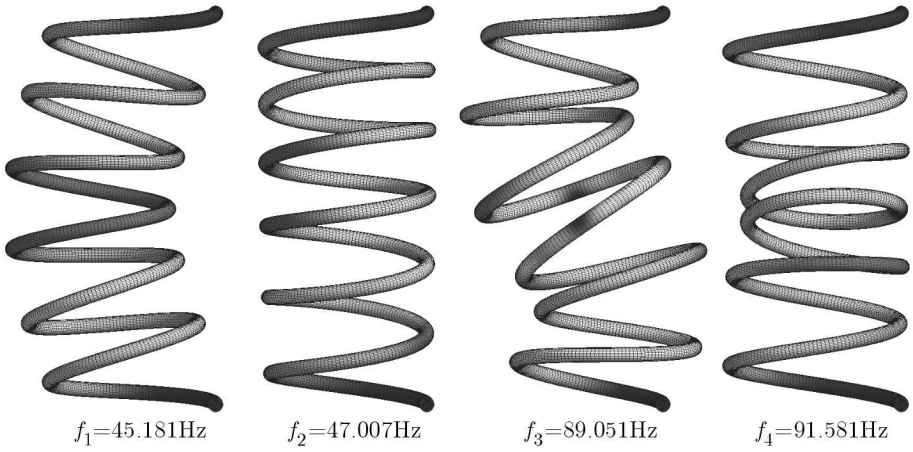

Fig. 2. Forms and frequencies of lateral natural vibrations of the clamped-clamped spring

As can be seen in Fig. 2, the frequency f_2 is only insignificantly higher than f_1. In the case of frequencies f_4 and f_3, the difference is even smaller.

The comparison of natural frequencies of the spring not loaded by a longitudinal force obtained by means of FEM, the dynamic stiffness method (Lee and Thompson, 2001), transfer matrix method (Pearson, 1982), standard model of the Timoshenko equivalent beam (STB) and the model presented in this paper (MTB) is presented in Table 1. In the methods presented by Lee and Thompson (2001) and Pearson (1982), the spring is treated as a spatially curved rod. The solution, in both methods, is obtained by means of a numerical method.

It should be noticed, that in methods using the concept of the equivalent rod modelled as acylinder, all frequencies of lateral vibrations are doubled due to the axial symmetry.

Table 1

	f_1	f_2	f_3	f_4
FEM model (Fig. 2)	45.181	47.007	89.051	91.581
Dynamic stiffness method	45.135	46.951	88.976	91.586
Transfer matrix method	45.13	46.95	88.97	91.59
Equivalent Timoshenko beam (STB)	45.975	45.975	94.088	94.088
Model presented in the work (MTB)	45.764	45.764	93.62	93.62

Comparing the results given in Table 1 it is seen that the application of the modified Timoshenko beam model (MTB) with taking into account non-rotational ends support and using stiffness given in the paper by Krużelecki and Życzkowski (1990) provides, in the case of the analysed not axially loaded spring, results very similar to those ones obtained on the basis of the standard Timoshenko beam model (STB). The largest difference between the frequencies obtained from the FEM simulation and the frequencies obtained from the two last models did not exceed 6%.

The most often occurring case in the engineering practice is the spring of end coils bent and ground off, since only this way of support (except cases of using special spring holders or spring guided on a pin or in a cylindrical sleeve) ensures its stable operation. It can be expected that the way of making the end coils has an influence on the natural frequencies. In order to illustrate this problem, FEM analyses have been performed for a spring of the same parameters as before but with different shapes of neutral coils. The model of such spring and its first four lateral vibration modes are presented in Fig. 3.

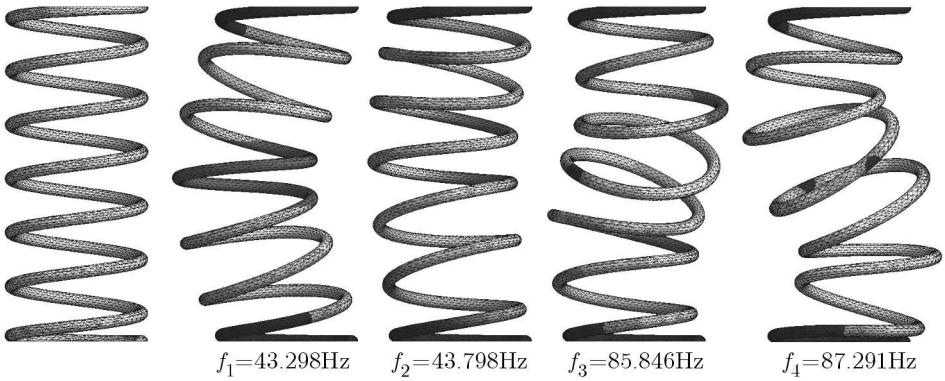

Fig. 3. Forms and frequencies of lateral natural vibrations of the clamped-clamped spring with typical industrial end coils

Comparing data contained in Table 1 and 2, it can be noticed that in the case of the spring with end coils bent and ground off, a better similarity of the FEM results for the models proposed by Lee and Thompson (2001) and Pearson (1982) is not obtained (at least for the first two frequencies) than the results obtained on the basis of the models based on the equivalent beam concept.

Table 2

	f_1	f_2	f_3	f_4
FEM model with bent coils (Fig. 3)	43.298	43.798	85.846	87.291

3.2. Analysis of natural frequencies of lateral vibrations of axially loaded springs

Helical springs applied in the industry most often operate under a certain preliminary axial load, usually caused by the supported machine, weight or preliminary tension, e.g. in overload clutches, valves or in variable-speed transmission systems. Thus, the influence of the axial force (approximately statical) on natural frequency vibrations of helical springs is essential. Diagrams of the first four natural frequencies of lateral vibrations obtained (as before) from FEM analyses and from the solution presented in this study are presented in Fig. 4. The FEM simulations were carried out in two stages: in the first one, the statistical analysis was performed at the determined spring load, while in the second, the modal analysis was performed for such a loaded model. Analyses and calculations were performed for the following spring relative deflections: 0; 0.125; 0.25; 0.375; 0.5. Simulations were carried out in the ANSYS packet, Mechanical APDL module.

As can be seen in Fig. 4, along with an increase in the axial force P and thus an increase in the spring relative deflection, the model presented in this study improves convergence with the FEM in relation to the standard model of the equivalent beam.

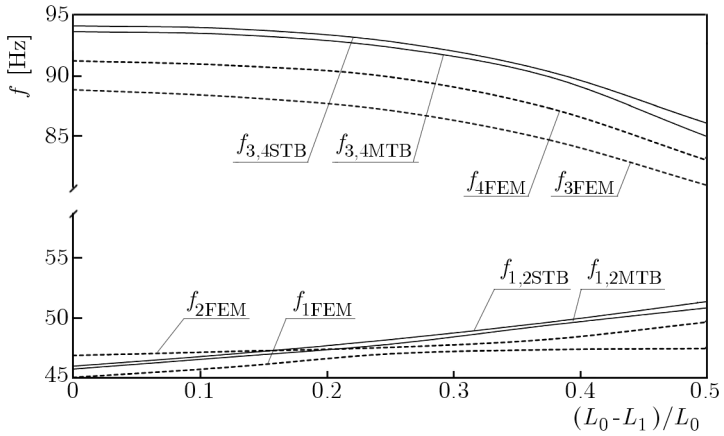

Fig. 4. Comparison of the first four natural frequencies of lateral vibrations obtained from FEM simulations with the first two double frequencies calculated on the basis of the standard model of the equivalent beam (STB) and the model presented in this study (MTB)

3.3. Cut-off frequencies of lateral vibrations of helical springs according to the presented model

As has been mentioned above, equations (2.12), (2.18) and (2.22) are applicable only in the case when the cut-off frequency ω_b determined by equation (2.11) is larger than the looked for natural frequencies. Thus, from the point of view of analysis of spring lateral vibrations, it is important to find out whether the looked for vibrations form is above or below the cut-off frequency ω_b. This problem was analysed by Guido *et al.* (1978), where the authors indicated that for slenderness $L_0/D_0 = 1$ (or less) natural frequencies always correspond to solution (2.13). However, they did not provide neither slenderness values nor relative deflections at which the successive natural frequencies can be calculated from (2.12). On the basis of the studies performed at various material and geometrical parameters, it can be stated that the spring slenderness and its deflection decide whether the given natural frequency is higher or lower than the cut-off frequency.

The diagram allowing one to determine whether equation (2.12) or (2.14) should be used in calculations of natural frequencies of lateral vibrations is presented in Fig. 5. The up-to-date spring length L_1 related to the length of a not loaded spring L_0 is marked in the vertical axis,

while the not loaded spring slenderness $L_0/2R_0$ in the horizontal axis. If, e.g. we are interested in natural frequencies of lateral vibrations of the clamped-clamped spring of a slenderness being 2.5 and compressed to 0.6 of its initial height (point A in Fig. 5), then the first two double frequencies $\omega_{1,2}$ and $\omega_{3,4}$ can be calculated using the solution in form (2.12) and (2.22), while in order to find the parameters of higher frequencies, the solution in form (2.14) should be used.

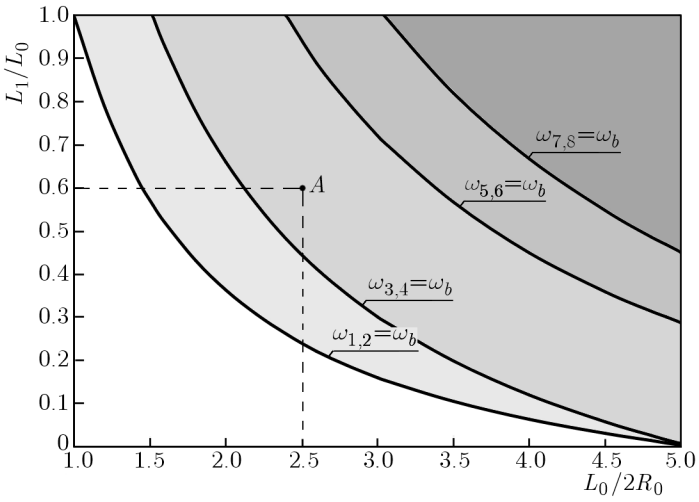

Fig. 5. Curves separating the zones in which the cut-off frequency ω_b is higher than the successive frequencies of lateral natural vibrations

4. Conclusions

The modified model of the equivalent beam, presented in this study, allows one to determine form (2.18) and frequencies (2.22) of lateral natural vibrations of the axially loaded spring. The results obtained on the basis of the presented model, using the concept given by Krużelecki and Życzkowski (1990) are slightly closer to the results of the FEM analysis than the standard model based on the Timoshenko equivalent beam. The developed model allows calculation of natural frequencies of the axially loaded spring and supported in a way making free rotations of its end coils impossible. It is also shown that the models based on the equivalent beam concept, easier in applications than models treating the spring as a spatially curved rod, have only insignificantly smaller accuracy. The largest difference between the frequencies obtained from the FEM simulation for the spring without bent end coils (Fig. 2) and the frequencies obtained from the presented model is a little bit above 5%. Comparing the frequencies obtained from the FEM simulation for the spring without bent end coils (Fig. 2) with the frequencies obtained from the FEM simulation for the spring of typical industrial end coils (Fig. 3) can be noticed that the differences are even larger – the maximum difference for the second frequency exceeded 6%. Thus, the way of making the end coils significantly influences the natural frequencies. In the most often met in practice case of spring end coils being bent and ground off, the natural frequencies differ significantly from the frequencies calculated by all tested methods. The performed simulations indicated also that the differences between the first and the second as well as the third and the fourth natural frequency are small for springs and, therefore, the axially symmetric equivalent beam model can be applied for calculating (without large error) these frequencies. The diagram (Fig. 5) allowing one to determine which form of the solution to equation (2.6) should be applied in calculating frequencies and forms of natural vibrations of the spring of the given slenderness and static deflection has also been developed for the presented model.

References

1. Becker L. E., Chassie G. G., Cleghorn W. L., 2002, On the natural frequencies of helical compression springs, *International Journal of Mechanical Sciences*, **44**, 825-841
2. Della Pietra L., Della Valle S., 1982, On the dynamic behavior of axially excited helical springs, *Meccanica*, **17**, 31-43
3. Guido A.R., Della Pietra L., Della Valle S., 1978, Transverse vibrations of helical springs, *Meccanica*, **13**, 2, 90-108
4. Haringx J.A., 1948, On highly compressible helical springs and rubber rods, and their application for vibration-free mountings, I, *Philips Research Reports*, **3**, 401-449
5. Haringx J. A., 1949, On highly compressible helical springs and rubber rods, and their application for vibration-free mountings, II, *Philips Research Reports*, **4**, 49-80
6. Jiang W., Jones W.K., Wang T.L., Wu K.H., 1991, Free vibrations of helical springsm, *Transactions of ASME*, **58**, 222-228
7. Kobelev V., 2014, Effect of static axial compression on the natural frequencies of helical springs, *MMMS*, issue 3
8. Krużelecki J., Życzkowski M., 1990, On the concept of an equivalent column in the problem of stability of compressed helical springs, *Ingenieur-Archiv*, **60**, 367-377
9. Lee J., 2007, Free vibration analysis of cylindrical helical springs by the pseudospectral method, *Journal of Sound and Vibration*, **302**, 185-196
10. Lee J., Thompson D. J., 2001, Dynamic stiffness formulation, free vibration and wave motion of helical springs, *Journal of Sound and Vibration*, **239**, 297-320
11. Love A.E.M., 1899, The propagation of waves of elastic displacement along a helical wire, *Transactions of the Cambridge Philosophical Society*, **18**, 364-374
12. Majkut L., 2009, Free and forced vibrations of Timoshenko beams described by single difference equation, *Journal of Theoretical and Applied Mechanics*, **47**, 1,193-210
13. Michalczyk K., 2009, Analysis of helical compression spring support influence on its deformation, *The Archive of Mechanical Engineering*, **56**, 4, 349-362
14. Michalczyk K., 2014, Influence of the elastomeric coating on parameters of steady state vibrations of coil springs in the resonance and outside it, *Journal of Theoretical and Applied Mechanics*, **52**, 2, 507-518
15. Mottershead J.E., 1980, Finite elements for dynamical analysis of helical rods, *International Journal of Mechanical Sciences*, **22**, 267-283
16. Nagaya K., Takeda S., Nakata Y., 1986, Free vibration of coil springs of arbitrary shape, *International Journal for Numerical Methods in Engineering*, **23**, 1081-1099
17. Pearson D., 1982, The transfer matrix method for the vibration of compressed helical springs, *Journal of Mechanical Engineering Sciences*, **24**, 163-171
18. Pearson D., Wittrick W.H., 1986, An exact solution for the vibration of helical springs using a Bernoulli-Euler model, *International Journal of Mechanical Sciences*, **28**, 83-96
19. Stander N., Du Preez R.J., 1992, Vibration analysis of coil springs by means of isoparametric curved beam finie elements, *Communications in Applied Numerical Methods*, **8**, 373-383
20. Stephen N.G., Puchegger S., 2006, On the valid frequency range of Timoshenko beam theory, *Journal of Sound and Vibration*, **297**, 1082-1087
21. Taktak M., Dammak F., Abid S., Haddar M., 2008, A finite element for dynamic analysis of a cylindrical isotropic helical spring, *Journal of Materials and Structures*, **3**, 641-658

22. Timoshenko S., Gere J.M., 1961, *Theory of Elastic Stability*, New York and London: McGraw Hill, p. 140

23. Wittrick W.H., 1966, On elastic wave propagation in helical springs. International, *Journal of Mechanical Sciences*, **8**, 25-47

24. Yildrim V., 1999, An efficient numerical method for predicting the natural frequencies of cylindrical helical springs, *International Journal of Mechanical Sciences*, **41**, 919-939

25. Yu A.M., Yang C.J., 2010, Formulation and evaluation of an analytical study for cylindrical helical springs, *Acta Mechanica Solida Sinica*, **23**, 1, 85-94

Manuscript received August 13, 2014; accepted for print March 13, 2015

JOURNAL OF THEORETICAL
AND APPLIED MECHANICS
53, 3, pp. 757-762, Warsaw 2015
DOI: 10.15632/jtam-pl.53.3.757

SHORT RESEARCH COMMUNICATION

EXPERIMENTAL INVESTIGATION OF THIN BRASS SHEETS UNDER TENSION-COMPRESSION CYCLIC LOADING

Zbigniew L. Kowalewski, Lech Dietrich
Institute of Fundamental Technological Research, Polish Academy of Sciences, Warsaw, Poland
e-mail: zkowalew@ippt.pan.pl

Grzegorz Socha
Institute of Aviation, Warsaw, Poland

Strength and durability of thin-walled structures are usually calculated with the use of computer simulations. To perform such simulations using Finite Element Method, characteristics of a material subjected to monotonic tension or compression and tension-compression cyclic loading are necessary. Experimental determination of such kind of characteristics is usually performed on specimens cut out from a metal or composite thin sheet. Problems associated with testing on flat specimens under large deformation are discussed in this paper. A new design of fixture proposed by the authors for this kind of testing is shortly described. The results of investigations carried out on brass using the new fixture for flat specimens testing are also presented.

Keywords: fixture, large deformations, tension-compression tests, thin metal sheet

1. Introduction

Problems associated with material testing on flat specimens under compression within a large deformation range procure many difficulties. It seems that buckling is regarded as the most significant. Many propositions of experimental setups enabling compression testing of flat specimens were given by researchers (see References). In 1978, Dietrich and Turski (1978) elaborated solution of the side-supporting fixture. The main advantage of this design was the ability to support the entire specimen gage length during a test. This was due to the fact that the side-supporting block was able to change its length together with gradual shortening of the specimen during compression. A detailed description of the fixture was given in the monograph published by Szczepiński (1990).

The fixture is shown in Fig. 1a. The main principle of operation is explained in Fig. 1b where two expanded views of parts of the fixture are shown. The maximum and minimum height of the compression fixture is given in Fig. 1a. The side-support of the specimen has been realized by two sets of thin plates perpendicular to the specimen surface supporting its both sides. Each set, consisting the same type of the plate is positioned by two pins: the first is inserted into the pin-hole at one end of the plate and the second is inserted into U-shape cut on the opposite side of the plate. The neighboring plates are rotated with respect to each other by an angle equal to 180 deg, see Fig. 1b. The upper and lower yoke support both pins. The screws connecting two parts of the yoke allow the adjustment of the fixture to fit the specimen thickness.

In this paper, a modified version of the fixture developed in the 70's (Dietrich and Turski, 1978) is applied to execute experimental investigations of thin metal sheets under tension-compression cyclic loading. It enables application of cyclic tension-compression to the flat specimen in a wide strain range due to coupling of the side-supporting blocks with the standard grips of the testing machine. The main principle of the fixture assembly is explained in Fig. 2,

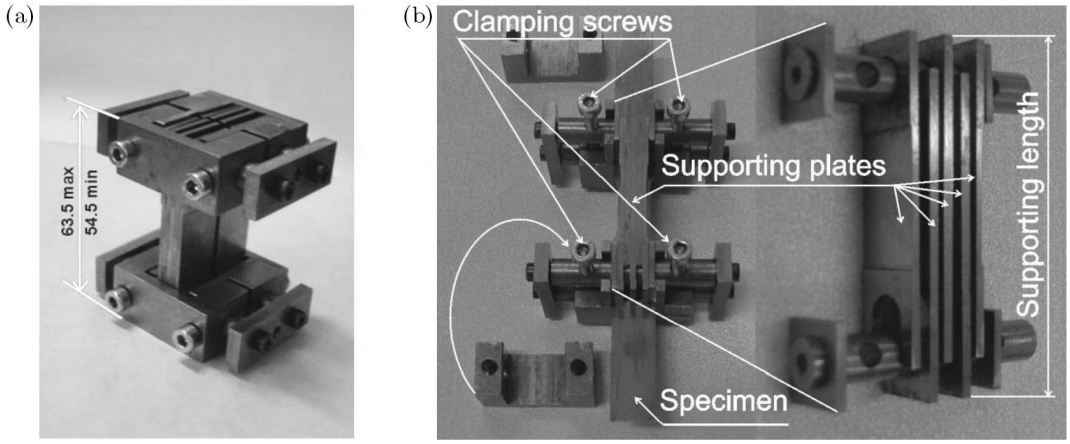

Fig. 1. (a) A special fixture for compressive tests. (b) Expanded views of supporting plates and the fixture with mounted specimen and four clamping bolts

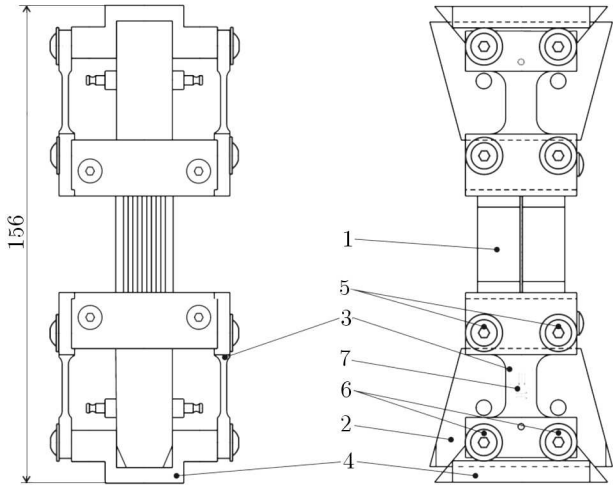

Fig. 2. Technical drawing of the fixture and numbered component parts: front and side view

where engineering drawing of the fixture is presented. The main part of the fixture placed in the middle (1) is exactly the same design of the side-supporting block as that developed in 1978. The gripped part of the specimen is held by wedges (2) comprising the standard grip assembly of the testing machine and operated thanks to hydraulic pressure supplying that machine. The complete assembly of the sliding block is fixed to the testing machine using screws (5, 6), connectors (3) and base (4). More details of this device can be found in (Dietrich *et al.*, 2014).

The design from the 70's could have been used only for monotonic compression since supporting blocks once shortened remained in this position. Another important advantage of the modified design is the ability of monitoring the friction force between the specimen and supporting blocks, which allows avoiding the error during stress determination. The measurement of the friction force is realized by strain gages (7) cemented to connector (3).

2. Experimental details

2.1. Specimen and material

All tension-compression tests have been carried out on thin sheet specimens with nominal thickness equal to 1 mm using the fixture that is briefly presented in the previous Section. Dimensions of the specimen are shown in Fig. 3.

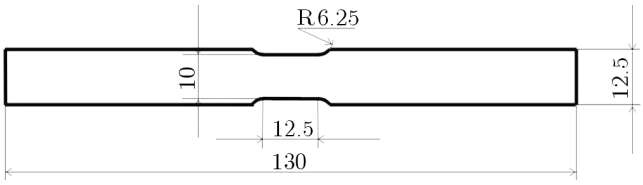

Fig. 3. The specimen manufactured from a 1 mm thickness sheet of brass

The material tested has been M63 brass used in deep-drawing processes. The chemical composition of the alloy is presented in Table 1 according to Polish Standards.

Table 1. Chemical composition of M63 brass (CW508L notation according to EN)

Cu	Ni	Fe	Pb	Zn
62-64	max 0.30	max 0.10	max 0.10	rest

2.2. Preliminary tensile tests

Before tension-compression cycles, the standard tensile test has been carried out in order to determine mechanical properties of the brass tested. It has been performed without application of the anti-buckling fixture. Instead of it, typical grips and mechanical extensometer have been used. The determined mechanical parameters are shown in Table 2. The results of tensile test are also used to validate the experimental data from tension-compression cycles.

Table 2. Mechanical parameters of M63 brass

Young's modulus	Yield point	Tensile strength	Total elongation
110 GPa	550 MPa	680 MPa	14%

2.3. Experimental program

The cyclic loading has been carried out under displacement control with the rate 0.05 mm/s. The conditions on the engineering strain have been set to limit the strain range during cycling.

In the first type of tests (tension-compression), 10 cycles within a strain range ± 0.040 (strain varied between 0.02 and -0.02) have been executed starting in the tensile direction. The last cycle ended with force equal to zero.

In the second type of tests, a similar program has been realized in the compressive range of strain changing from -0.002 to -0.020. As in the former case, 10 cycles have been executed ending with the zero force.

All tests have been carried out using an extensometer with the range of ± 0.2. The load cell has been calibrated in the range of ± 25 kN. The special set-up for friction force measurement has been applied. It consisted of two coupling bars with strain gauges calibrated in the range of ± 2 kN.

3. The results of cyclic tests

The results of the first type of tests carried out on M63 brass under cyclic loading are presented in Fig. 4. The first cycle is illustrated by the solid black line denoted as 1. The tensile stress-strain curve obtained under simple tension without using the anti-buckling fixture is also shown in Fig. 4 (gray dotted line denoted as 2).

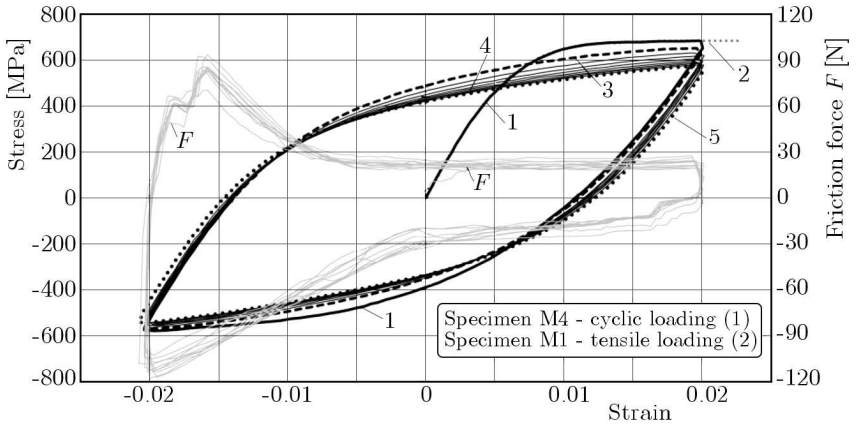

Fig. 4. Hysteresis loops of the brass and variation of the friction force during the test

The second cycle is represented by black dashed line (3). The last two cycles are denoted by black dotted lines (4 and 5). Figure 4 also presents the evolution of the friction force (gray lines, denoted as F). The friction force is also shown as a function of time in Fig. 5a as well as the total force for all recorded cycles. Changes of strain corresponding to the force variations are shown in Fig. 5b for all cycles carried out.

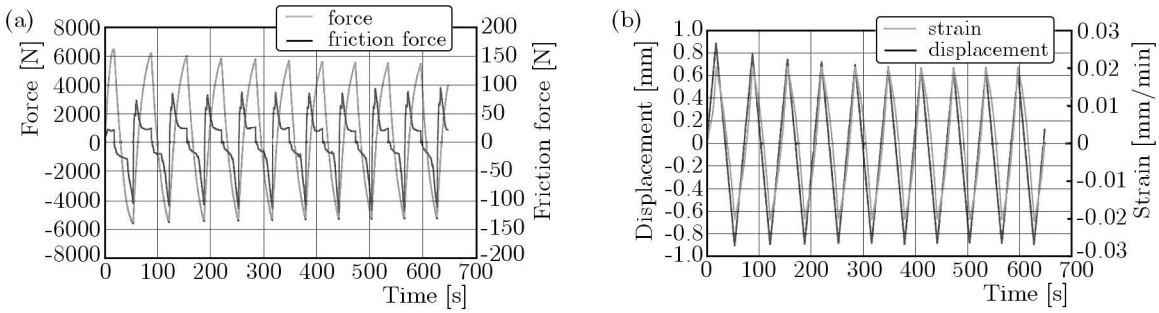

Fig. 5. Variation of the specimen load and friction force (a) and variation of displacement and strain (b) versus time during cyclic loading (type 1)

The brass exhibited the softening effect reflected by a significant decrease in the stress amplitude, especially in the first two cycles, see Fig. 5a.

The level of the friction force was also monitored during the test. Its variation is presented in Figs. 4 and 5a. The friction force has a similar course in all cycles and does not change clearly under tension and grows up at compression. It has to be emphasized, however, that values of the friction force are relatively small and they do not change the cyclic stress-strain characteristic.

In the second scheme of tests, the cyclic loading has been applied for the strain level varying between -0.002 and -0.020. Also ten cycles have been carried out, however in that case, the loading process started in the compression direction. The results of the second type of tests are presented in Fig. 6.

The softening effect tokes place for the material in question. It is most remarkable for the first two cycles. During subsequent cycles, the saturation state is almost achieved, i.e. hysteresis loops coincide themselves. As it is clearly seen in Figs. 7a and 7b, the friction force has rather low magnitudes. As in the previous cases, the friction force variation data are subsequently used to correct the stress-strain characteristic of the brass tested.

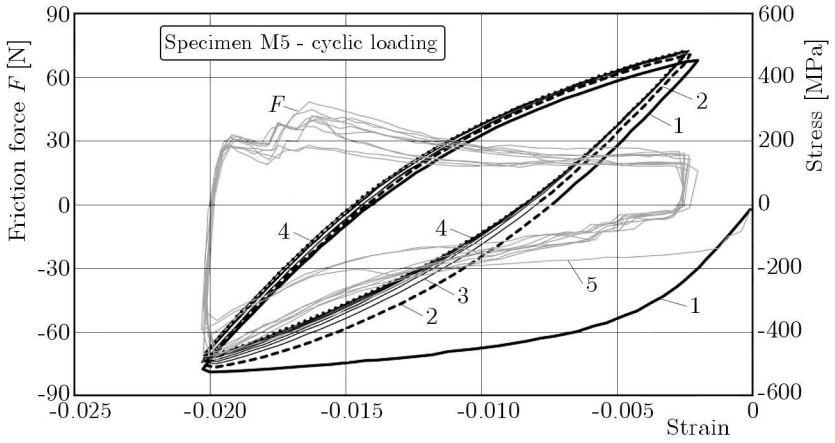

Fig. 6. Hysteresis loops of the brass and variation of the friction force during the test

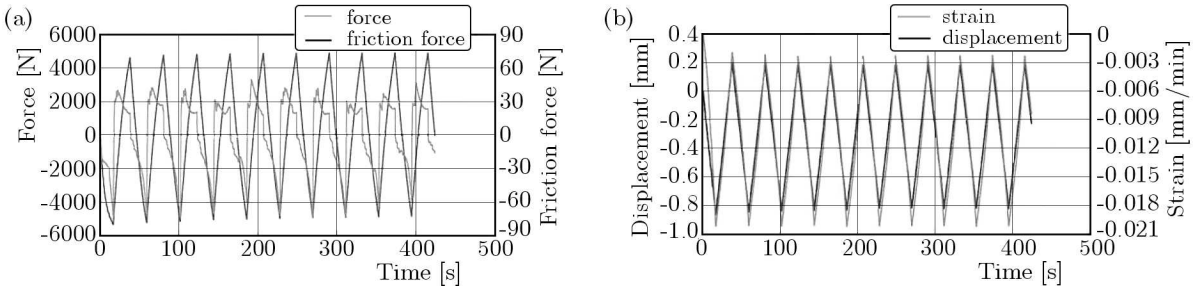

Fig. 7. Variation of the specimen load and friction force (a) and variation of displacement and strain (b) versus time during cyclic loading (type 2)

4. Concluding remarks

Taking into account all data captured by means of the new fixture, one can conclude that the technique is promising with respect to providing data for the modeling of cyclic deformation behavior for shell structures. It enables one to avoid buckling during compression of specimens made of thin metal sheets. The fixture changes its length with specimen elongation or shrinkage during a test which allows application of the cyclic load.

Although in the case of the presented tests the strain range has been set to ± 0.02, the fixture nominal strain capacity is much greater. Depending on mutual location of the supporting plates, the testing technique allows tension-compression tests to be performed at the displacement amplitude within the range ± 5 mm what corresponds to the maximum strain amplitude of ± 0.4 for the specimen gage length to be equal 12.5 mm.

The friction force, which is generated due to movement of both parts of the fixture, is measured by the special strain gauge system during each test. It allows essential reduction of the friction force influence on the stress-strain characteristics.

References

1. Aitchison C.S., Tuckerman L.B., 1939, The "pack" method for compressive tests of thin specimens of materials used in thin-wall structures, *NACA*, **649**

2. Cao J., Lee W., Cheng H. S., Seniw M., Wang H. P., Czung K., 2009, Experimental and numerical investigation of combined isotropic-kinematic hardening behavior of sheet metals, *International Journal of Plasticity*, **25**, 942-972

3. Dietrich L., Socha G., Kowalewski Z.L., 2014, Anti-buckling fixture for large deformation tension-compression cyclic loading of thin metal sheets, *Strain International Journal of Experimental Mechanics*, **50**, 174-183

4. Dietrich L., Turski K., 1978, A new method of thin sheets testing under compression (in Polish), *Engineering Transactions*, **26**, 1, 91-99

5. Jackman K. R., 1944, Improved methods for determining the compression properties of sheet metal, *Automotive and Aviation Industries*, **90**, 11, 36

6. Kuwabara T., 2007, Advances in experiments on metal sheets and tubes in support of constitutive modeling and forming simulations, *International Journal of Plasticity*, **23**, 385-419

7. Kuwabara T., Kumanto Y., Ziegelheim J., Kurasaki I., 2009, Tension-compression asymmetry of phosphor bronze for electric parts and its effect on bending behavior, *International Journal of Plasticity*, **25**, 1759-1776

8. LaTour H., Wolford S., 1945, Single-strip compression test for sheet materials, Proc. ASTM, 45, 675

9. Miller J. A., 1946, A fixture for compressive tests of thin sheet metal between lubricated steel guides, NACA, 1022

10. Sandorff P.E., Dillon R.K., 1946, Compressive stress-strain properties of some aircraft materials, Proc. ASTM, 46, 1039

11. Standard methods of compression testing of metallic materials, ASTM E9-61

12. Szczepiński W., edit., 1990, Experimental Methods in Mechanics of Solids, PWN, Warszawa, Elsevier, Amsterdam-Oxford-New York-Tokyo

Manuscript received March 2, 2015; accepted for print April 27, 2015

INFORMATION FOR AUTHORS

Journal of Theoretical and Applied Mechanics (***JTAM***) is devoted to all aspects of solid mechanics, fluid mechanics, thermodynamics and applied problems of structural mechanics, mechatronics, biomechanics and robotics. Both theoretical and experimental papers as well as survey papers can be proposed.

We accept articles in English only. The text of a *JTAM* paper should not exceed **12 pages of standard format A4** (11-point type size, including abstract, figures, tables and references).

- The material for publication should be sent to the Editorial Office via electronic journal system: http://www.ptmts.org.pl/jtam/index.php/jtam

Papers are accepted for publication after the review process. Blind review model is applied, which means that the reviewers' names are kept confidential to the authors. The final decision on paper acceptance belongs to the Editorial Board.

- After qualifying your paper for publication we will require the following:
  - LaTeX or TeX or Word document file
  - graphical files in grey scale, 300 dpi, in print quality (e.g.: ∗.png, ∗.bmp, ∗.jpg, ∗.eps).

Requirements for paper preparation

Contents of the manuscripts should appear in the following order:

- Title of the paper
- Authors' full name, affiliation and e-mail
- Short abstract (maximum 100 words) and 3-5 key words (1 line)
- Article text (equations should be numbered separately in each section; each reference should be cited in the text by the last name(s) of the author(s) and the publication year)
- References in alphabetical order. See the following:

  1. Achen S.C., 1989, A new boundary integral equation formulation, *Journal of Applied Mechanics*, **56**, 2, 297-303
  2. Boley B.A., Weiner J.H., 1960, *Theory of Thermal Stresses*, Wiley, New York
  3. Canon W., 1955, Vibrations of heated beams, Ph.D. Thesis, Columbia University, New York
  4. Deresiewicz H., 1958, Solution of the equations of thermoelasticity, *Proceedings of Third U.S. National Congress of Applied Mechanics*, 287-305

- Titles of references originally published not in English, should be translated into English and formulated as follows:

  5. Huber M.T., 1904, Specific work of strain as a measure of material effort (in Polish), *Czasopismo Techniczne*, **XXII**, 3, 80-81

All the data should be reported in SI units.

New *JTAM* offer for short communication!

Since July 2013, short research communications have been accepted for publication in *JTAM* with all the requirements concerning standard publications, except for their volume that is limited to 4 pages.
